Journal of Cosmology and
Astroparticle Physics

Dark matter implications of the WMAP-Planck Haze

To cite this article: Andrey E. Egorov *et al* JCAP03(2016)060

View the article online for updates and enhancements.

Related content

- Testing the dark matter origin of the WMAP-Planck haze with radio observations of spiral galaxies
  Eric Carlson, Dan Hooper, Tim Linden et al.
- On The gamma-ray emission from Reticulum II and other dwarf galaxies
  Dan Hooper and Tim Linden
- Constraints on dark matter annihilation by Planck
  Chalit Muanglay, Maneenate Wechakama and Brandon K. Cantlay

Recent citations

- Light weakly interacting massive particles
  Graciela B Gelmini
- A review of indirect searches for particle dark matter
  Jennifer M. Gaskins
- Investigating the uniformity of the excess gamma rays towards the galactic center region
  Shunsaku Horiuchi *et al*

This content was downloaded from IP address 193.232.69.1 on 02/10/2017 at 17:26

Journal of Cosmology and Astroparticle Physics
An IOP and SISSA journal

Dark matter implications of the WMAP-Planck Haze

Andrey E. Egorov,[a] **Jennifer M. Gaskins,**[b,c] **Elena Pierpaoli**[a] **and Davide Pietrobon**[d,e,f]

[a]University of Southern California,
3620 McClintock Ave., SGM 408, Los Angeles, CA 90089, U.S.A.
[b]California Institute of Technology,
1200 E. California Blvd., Pasadena, CA 91125, U.S.A.
[c]GRAPPA, University of Amsterdam,
Science Park 904, 1098 XH Amsterdam, Netherlands
[d]University of California, Berkeley, Space Sciences Laboratory,
7 Gauss Rd, Berkeley CA 94720, U.S.A.
[e]Lawrence Berkeley National Laboratory,
1 Cyclotron Road, Berkeley, CA 94720, U.S.A.
[f]HERE,
2075 Allston Way, Berkeley CA 94704, U.S.A.

E-mail: egorov@usc.edu, jgaskins@uva.nl, pierpaol@usc.edu, daddeptr@gmail.com

Received October 14, 2015
Revised January 20, 2016
Accepted February 24, 2016
Published March 31, 2016

Abstract. Gamma rays and microwave observations of the Galactic Center and surrounding areas indicate the presence of anomalous emission, whose origin remains ambiguous. The possibility of dark matter annihilation explaining both signals through prompt emission at gamma rays and secondary emission at microwave frequencies from interactions of high-energy electrons produced in annihilation with the Galactic magnetic fields has attracted much interest in recent years. We investigate the dark matter interpretation of the Galactic Center gamma-ray excess by searching for the associated synchrotron emission in the WMAP and Planck microwave data. Considering various magnetic field and cosmic-ray propagation models, we predict the synchrotron emission due to dark matter annihilation in our Galaxy, and compare it with the WMAP and Planck data at 23–70 GHz. In addition to standard microwave foregrounds, we separately model the microwave counterpart to the Fermi Bubbles and the signal due to dark matter annihilation, and use component separation techniques to extract the signal associated with each template from the total emission. We confirm the presence of the Haze at the level of ≈7% of the total sky intensity at 23 GHz in our chosen region of interest, with a harder spectrum ($I \sim \nu^{-0.8}$) than the synchrotron from regular

© 2016 IOP Publishing Ltd and Sissa Medialab srl
doi:10.1088/1475-7516/2016/03/060

JCAP03(2016)060

cosmic-ray electrons. The data do not show a strong preference towards fitting the Haze by either the Bubbles or dark matter emission only. Inclusion of both components provides a better fit with a dark matter contribution to the Haze emission of ≈20% at 23 GHz, however, due to significant uncertainties in foreground modeling, we do not consider this a clear detection of a dark matter signal. We set robust upper limits on the annihilation cross section by ignoring foregrounds, and also report best-fit dark matter annihilation parameters obtained from a complete template analysis. We conclude that the WMAP and Planck data are consistent with a dark matter interpretation of the gamma-ray excess.

Keywords: dark matter theory, cosmic ray theory, absorption and radiation processes

ArXiv ePrint: 1509.05135

JCAP03(2016)060

Contents

1 Introduction **1**

2 Microwave emission from DM annihilation **3**
- 2.1 DM distribution 4
- 2.2 Electron injection from DM annihilation 4
- 2.3 Magnetic field distribution 5
- 2.4 CR propagation using GALPROP 5
- 2.5 Diffusion model 7
- 2.6 DM emission maps 8

3 Regions of interest on the sky **8**

4 DM microwave spectra in the Haze region **10**

5 Conservative constraints on DM annihilation **12**

6 DM constraints from a component separation approach **16**
- 6.1 The WMAP-Planck Haze: history 16
- 6.2 Methodology 17
- 6.3 Fitting results 20
- 6.4 DM implications 24

7 Discussion and conclusions **26**

1 Introduction

The existence of dark matter (DM) has been firmly established by a variety of observations [1], however its nature remains a compelling mystery. DM is often assumed to be in the form of Weakly Interacting Massive Particles (WIMPs), which may pair annihilate and/or decay to produce Standard Model particles. Indirect searches for the detectable products of DM annihilation and decay, including photons, charged cosmic rays (CRs), and neutrinos, offer the possibility of detecting this elusive particle and constraining its properties, as well as determining its spatial distribution. For typical WIMP DM models, the Standard Model particles immediately resulting from annihilation or decay are in the MeV to TeV energy range, making gamma rays a particularly promising channel for DM detection.

With the great leap in capabilities for detection of GeV gamma rays provided by the Fermi Large Area Telescope (LAT) aboard the Fermi Gamma-ray Space Telescope [2], much progress has been made in indirect searches for gamma rays from DM annihilation and decay. Analyses of Fermi LAT observations of possible sources of annihilation signals have provided strong constraints on the WIMP mass and annihilation cross section [3–5]. These studies probed annihilation cross sections below the canonical value for a thermal relic WIMP DM particle $\langle \sigma v \rangle = 3 \cdot 10^{-26}$ cm^3/s, for WIMP masses below a few tens of GeV for some Standard Model final states.

The Galactic Center (GC) is expected to be the brightest source in the sky of gamma rays from DM annihilation due to its large overdensity of DM and its close proximity. In

JCAP03(2016)060

recent years, numerous studies have firmly revealed the presence of an excess at GeV energies over the expected astrophysical gamma-ray emission from the GC and Inner Galaxy that is consistent with expectations for a DM annihilation signal (e.g., [6–12]). In this work we will use GC to refer to the dynamical center of the Galaxy, and Inner Galaxy to refer to the region extending as much as tens of degrees away from the GC. In addition to the DM interpretation, other explanations considered for this excess include a population of unresolved gamma-ray millisecond pulsars (MSPs) [9, 11, 13–17] and gamma rays from CRs injected in bursts near the GC [18–20]. Recent results suggest that the majority of the excess emission arises from a population of unresolved sources such as MSPs [21, 22], however those sources have not been identified in multi-wavelength studies (see, e.g., [23]), and there remains some debate in the community, leaving open the exciting possibility that the excess represents a detection of DM annihilation.

Multi-wavelength observations can provide critical tests of DM interpretations of high-energy signals, particularly in a complex environment like the GC. Along with prompt gamma-ray emission, WIMP annihilation can also inject other energetic particles into the interstellar medium, including electrons and protons and their antiparticles, which give rise to lower-energy photons. Protons propagate and participate in hadronic interactions with gas, yielding neutral pions which produce gamma-ray photons when they decay. Electrons and positrons (referred as electrons in our paper, since they behave equivalently for our purposes in producing secondary emission), on the other hand, generate substantial secondary emission via inverse Compton scattering (ICS) on the interstellar radiation fields, bremsstrahlung on ionized gas, and synchrotron emission in magnetic fields (MF). DM annihilation in the Inner Galaxy thus generates associated radiation from radio to gamma rays (with a rather broad spectrum from each mechanism mentioned above). Thus, to test the DM interpretation for the GC gamma-ray excess, one may look for the associated lower-frequency emission. In particular, one can look for the synchrotron emission at microwave frequencies from the propagation of injected high-energy electrons in Galactic MF.

A similarly intriguing excess over conventional astrophysical models at microwave frequencies was identified several years ago: the WMAP Haze [24, 25]. The WMAP Haze refers to excess emission in the Inner Galaxy identified in the WMAP data, observed to be approximately symmetric around the GC, extending tens of degrees away from the GC, and exhibiting a harder spectral index than expected for synchrotron associated with the Galactic CR population from astrophysical sources. The spectrum of the WMAP Haze suggests that it originates from a distinct population of high-energy electrons. Initially, secondary emission from WIMP annihilation was proposed as a possible explanation for the Haze, and an associated gamma-ray signal was predicted [25].

More recently, a new feature in the gamma-ray sky has been identified: the Fermi Bubbles [26, 27]. The Bubbles are a bipolar structure centered on the GC and extending above and below it out to $|b| \approx 50^\circ$, and they are clearly visible in the LAT gamma-ray data. Similar structures had previously been identified in X-ray and 408 MHz radio data [28] as well as in IR maps [29], and they had been suggested to result from starburst-driven winds in the GC. Refined observations in microwave with Planck confirmed the presence of the excess emission previously identified as the Haze in WMAP data, and revealed a correlated morphology between the Haze and Fermi Bubbles [30]. This indicates a potentially common origin of these two phenomena. In addition, recent observations of polarized radio emission with the S-PASS survey at 2.3 GHz revealed that the radio features are also closely aligned with those observed in gamma rays [31], again pointing to a consistent interpretation (e.g., [32]).

JCAP03(2016)060

The Bubble-like structures observed over a broad range of energies are now presumed to be multi-wavelength views of the same phenomenon, and compelling non-exotic explanations have been put forth (e.g. reverse shocks in the GC's giant outflows [32]). Moreover, due to the unique morphology of these structures, it is quite unlikely that they are associated with DM annihilation. Thus, a search for a DM signal in the WMAP-Planck data requires an understanding of not only "standard" astrophysical foregrounds but also the microwave emission associated with the Fermi Bubbles. Despite the presence of the Bubbles in multi-frequency observations, and its likely presence in the microwave band, it is still possible that some part of the observed Haze is due to DM annihilation. Throughout this paper, the term "Haze" will refer to the microwave emission not accounted for by common foregrounds (i.e. Bubbles and/or DM annihilation), and "Bubbles" will refer to the microwave counterpart of the Fermi Bubbles.

In this work, we revisit the problem of multi-wavelength DM searches in the Galaxy using the WMAP-9 and Planck 2013 data sets, focusing on DM models that could explain the observed GC gamma-ray excess. We calculate the microwave emission associated with WIMP annihilation in the Galaxy, and test the consistency of that signal with the observations by performing a complete model-fitting analysis of the WMAP-Planck data. The predicted microwave emission due to WIMP annihilation is subject to uncertainties in the modeling of the Galactic environment. In particular, uncertainties in the MF distribution in the Galaxy and in the propagation parameters for electrons in the interstellar medium can lead to significant variations in the expected emission. We address these sources of uncertainty by varying the MF and propagation models in order to understand their impact on our results. We then compare our models with the data in order to assess the potential contribution of DM to the total signal.

We adopt two different approaches for model-data comparison: first we assume that the data only contain noise, CMB fluctuations and DM signal (but no other foregrounds or Bubbles). This leads to an overestimate of the potential DM contribution which translates to a conservative but robust upper limit on the DM annihilation cross section. Next, we perform a component separation procedure based on template fitting, this time also considering all relevant foregrounds and the Bubbles. In this case, we present the best-fit DM parameters obtained. With these analyses we aim to address the following issues: *i)* the nature of the Haze — whether the data favor (and at what significance) a DM component in the Haze emission; and *ii)* the compatibility of WIMP models needed to fit the GC gamma-ray excess with the microwave data.

We present the DM models and the computation of the microwave emission from DM annihilation in section 2. In section 3 we define the two regions of interest (ROIs) we consider, and in section 4 we show the predicted DM spectra in the Haze region. Section 5 is dedicated to conservative WIMP model constraints obtained from the data when considering CMB and DM emission as the only contributions, neglecting all other foregrounds. A comprehensive component separation procedure, which includes models of expected foregrounds, is described along with its results in section 6. We discuss the implications of these findings for DM models and a DM interpretation of the GC gamma-ray excess in section 7.

2 Microwave emission from DM annihilation

The propagation of high-energy electrons in the Galactic MF gives rise to synchrotron emission at microwave frequencies. The emission associated with DM annihilation depends on

JCAP03(2016)060

the spatial distribution of the injection sites, the injected spectrum of these particles, as well as the Galactic environment.

2.1 DM distribution

The exact DM density distribution in our Galaxy is a matter of active debate. A wide range of DM density profiles from cored to very cuspy are in agreement with numerical simulations and observational data (e.g., [33–37]). In this work we restrict our analysis to profile shapes that have been shown to provide a good fit to the GeV excess in the Inner Galaxy [6–11, 38]. In particular, we adopt for the DM distribution a generalized form of the Navarro-Frenk-White (NFW) density profile [39]

$$\rho_{\rm DM}(r) = \frac{\rho_{\rm s}}{\left(\frac{r}{r_{\rm s}}\right)^{\gamma}\left(1+\left(\frac{r}{r_{\rm s}}\right)^{\alpha}\right)^{(\beta-\gamma)/\alpha}}, \tag{2.1}$$

where $\rho_{\rm DM}(r)$ is the DM density at radius r from the center of the halo, $\rho_{\rm s}$ is a scale density, $r_{\rm s}$ is a scale radius, and α, β, and γ are shape parameters. We adopt the common convention to fix $\alpha = 1$ and $\beta = 3$, and allow only the inner profile slope, parametrized by γ, to vary. Following the results of [6–11, 38], we consider values of γ ranging between 1.1 and 1.3 (considering three discrete values 1.1, 1.2 and 1.3). We adopt $r_{\rm s} = 23$ kpc and fix the local density at the solar position to $\rho_{\rm DM}(r_\odot = 8.3\ {\rm kpc}) = 0.34\,{\rm GeV/cm^3}$ (which are similar to the values adopted in [6–11, 38]).

The density distribution is indeed highly uncertain in a very close vicinity of the center. For this reason, authors typically do not extrapolate profiles like eq. (2.1) down to zero radius and instead truncate it at some distance $r_{\rm core}$ leaving the density constant inside $r_{\rm core}$. A natural lower limit on $r_{\rm core}$ is about the Schwarzschild radius of the central black hole $4.2 \cdot 10^{-7}$ pc. An upper limit allowed by the fit of the gamma excess was found to be ~ 10 pc [10]. We computed that the DM emission intensities in our relevant ROIs only vary by about $\sim 1\%$ when we vary $r_{\rm core}$ over the mentioned allowed range $4.2 \cdot 10^{-7}$ pc $\lesssim r_{\rm core} \lesssim 10$ pc. Hence, although this parameter is highly uncertain, its specific choice does not matter in our case.

Substructures are also known to play an important role in boosting the luminosity of a DM halo (see e.g. [40]). We modeled the substructure contribution with a local boost factor to the annihilation rate everywhere in the Galaxy $\xi_{\rm DM}(r)$, taking its radial distance dependence from figure 4 of [40]. We found that substructure increases the signal in our chosen ROI (discussed in section 3) only by $\approx (30-35)\%$. This is because the majority of our signal comes from areas close to the GC where, due to tidal disruption, we do not expect a large amount of substructure.

2.2 Electron injection from DM annihilation

The spectrum of electrons produced by DM annihilation depends on the DM mass and the branching ratios to different Standard Model final states. We consider DM masses from 7.0 to 52 GeV, broadly motivated by the range of WIMP masses found in prior work to be able to provide, for some choice of final state(s), a good fit to the spectrum of the observed gamma-ray excess around the GC.

Also in line with much prior work on the gamma-ray excess, in this work we consider two benchmark annihilation channels: $b\bar{b}$ and $\tau^+\tau^-$. The former represents a typical hadronic channel which yields a soft spectrum of injected electrons, while the latter is a leptonic

JCAP03(2016)060

channel that produces more electrons with a harder spectrum. We take the yields of electrons from WIMP annihilation from the PPPC4DMID package [41, 42] (including electroweak corrections; see, e.g. [43]).

2.3 Magnetic field distribution

Synchrotron emission depends crucially on the MF distribution in the Galaxy. Although sophisticated MF configurations are possible (see, e.g., [44]), for the sake of simplicity we model the MF with an axisymmetric distribution, as also adopted in earlier works, e.g. [45, 46]:

$$B(R, z) = B_0 \exp(-(R - R_\odot)/R_B - |z|/z_B), \tag{2.2}$$

where R and z represent radial-in-plane and plane-orthogonal distances in the Galaxy, respectively.

The parameter B_0 in eq. (2.2) represents the total MF value at the Solar location and is taken to be 6 μG following [47]. The radial scale R_B in eq. (2.2) naturally sets the central field value and is more uncertain. On this point, we rely on the lower limit $B(0, 0) = 50$ μG derived in [48] as our preferred choice. This sets the respective $R_B = 4.0$ kpc, which we consider to be the most realistic value. However, we also compute our results for $B(0, 0) = 100$ μG as a limiting case which would produce higher DM emission. Such high central MF values are encountered in the literature [49]. However, the field would reach these values only very close to the GC (within ~ 0.2 kpc), and in that case the field radial dependence in eq. (2.2) might not be steep enough to produce the proper field attenuation at larger radii. For this reason, we consider the $B(0, 0) = 100$ μG (with respective $R_B = 3.0$ kpc) configuration to be generally less realistic.

The z_B parameter in eq. (2.2) sets the vertical characteristic scale of the MF, which is also somewhat uncertain. Various studies of the MF distribution in the Milky Way and other similar galaxies (e.g. [50–52]) estimate z_B to be robustly constrained in the range $\approx (1 - 10)$ kpc with a characteristic "average" value of 4-6 kpc. At the same time, z_B is naturally linked to the CR propagation parameters (discussed in section 2.5), as the MF is the driving reason for CR diffusion, and where the MF is small or null CR can freely propagate. We therefore expect the MF spatial extent z_B to be comparable to the spatial extent of the diffusion region, parametrized by h (the vertical half-height of the diffusion zone). Proportionality between these two parameters was employed in multiple earlier works to estimate z_B (e.g. [46, 47]). We follow this approach and, similarly to [47], we compute all our results for two values of z_B: $z_B = \delta \cdot h$ and $z_B = 0.5 \cdot h$. The parameter δ denotes the spectral slope of the spatial diffusion coefficient (described below).

2.4 CR propagation using GALPROP

We computed all-sky intensity maps of the synchrotron emission from DM annihilation using the GALPROP package [53]. GALPROP is a sophisticated code designed to compute CR propagation in the Milky Way. It solves the transport equation in its most general version for a given distribution of CR sources in 2 or 3 spatial + time + particle momenta dimensions. It also incorporates detailed knowledge about the Galaxy such as the neutral and ionized gas distributions, interstellar radiation field, and astrophysical CR sources. Moreover, GALPROP is able to compute all sky maps of secondary emission from CRs resulting from a variety of processes, including synchrotron emission.

JCAP03(2016)060

We employed GALPROP v54r2423 to model the propagation of electrons from DM annihilation in the Galaxy. Specifically, GALPROP was used to numerically solve the following transport equation:

$$\frac{\partial n}{\partial t} = q(r,p) + D_{xx}(p)\nabla^2 n + \frac{\partial}{\partial p}p^2 D_{pp}(p)\frac{\partial}{\partial p}\frac{1}{p^2}n - \frac{\partial}{\partial p}(\dot{p}n), \tag{2.3}$$

where p is the electron momentum and $n \equiv n(\vec{r},p,t)$ is the electron concentration per unit momentum range everywhere in the Galaxy. GALPROP solves eq. (2.3) in time until a stationary solution $n(\vec{r},p,t) \to n(\vec{r},p)$ is achieved.

The various terms in eq. (2.3) are defined as follows:

- $q(r,p)$ represents the spherically symmetric source term, which defines the electron production rate per unit volume per unit momentum range. The current public version of GALPROP does not offer the option to include a DM annihilation source. For this reason, we modified the source code to introduce a DM source of CRs, by injecting CRs according to the following equation:

$$q(r,p) = \frac{1}{2}\langle\sigma v\rangle\left(\frac{\rho_{\rm DM}(r)}{m_\chi}\right)^2 \xi_{\rm DM}(r)\frac{dN_e}{dp}(p), \tag{2.4}$$

  where $\langle\sigma v\rangle$ denotes the WIMP annihilation cross section, $\rho_{\rm DM}(r)$ is the DM density distribution defined by eq. (2.1), m_χ is the WIMP mass, $\xi_{\rm DM}(r)$ is the DM annihilation rate boost factor due to substructures taken from [40], and $\frac{dN_e}{dp}(p)$ represents the energy spectrum of electrons per annihilation (from the PPPC4DMID package [42]). As the standard astrophysical foregrounds are accounted for in our analysis using existing templates for microwave data analysis described in section 6, we do not include any astrophysical (non-DM) sources of CRs in the GALPROP model.

- $D_{xx}(p)$ is the spatial diffusion coefficient (assumed to be isotropic and spatially-independent):

$$D_{xx}(p) = D_0\left(\frac{p}{p_0}\right)^\delta, \tag{2.5}$$

  where p_0 is set to the constant value 1 GeV/c (e.g., [47]). The choice of D_0 and δ constants is explained below.

- $D_{pp}(p)$ is the electron reacceleration coefficient. Particle reacceleration in the interstellar medium happens due to interactions with MHD waves. $D_{pp}(p)$ is defined here through the spatial diffusion coefficient (eq. (2.5)), see [54] for further details:

$$D_{pp}(p)D_{xx}(p) = \frac{4p^2 v_a^2}{3\delta(4-\delta^2)(4-\delta)w}, \tag{2.6}$$

  where v_a is the Alfven speed in the media and w is the ratio of MHD waves energy density to MF energy density, assumed to be 1 in GALPROP.

- $\dot{p} \equiv dp/dt$ is the electron momentum loss rate due to various cooling processes: synchrotron radiation (computed using the MF distribution eq. (2.2)), emission from ICS on the interstellar radiation field (composed by starlight, CMB, and dust emission photons), bremsstrahlung radiation on ionized gas, and others. We refer to reader to [53] for further details.

JCAP03(2016)060

Parameter	MED	MAX	Reacc
Half-height of the diffusion box h, kpc	4.0	15	5.4
Diffusion coefficient normalization D_0, cm^2/s	$3.4 \cdot 10^{27}$	$2.3 \cdot 10^{28}$	$5.4 \cdot 10^{28}$
Diffusion coefficient energy dependence power δ	0.70	0.46	0.31
Alfven speed in the intragalactic media v_a, km/s	0	0	38
MF vertical scale height, version 1 $z_{B1} = \delta \cdot h$, kpc	2.8	6.9	1.7
MF vertical scale height, version 2 $z_{B2} = 0.5 \cdot h$, kpc	2.0	-	2.7

Table 1. Diffusion parameter values for the electron propagation (which enter eqs. (2.3)–(2.6)) and MF vertical scale heights (which enter eq. (2.2)) used in our work.

We run the version of GALPROP that is implemented in 3 spatial dimensions. For the spatial dimensions we choose a resolution of 200 pc, which is sufficient for our purposes as our region of interest is somewhat far from the GC and therefore large variations in emissivity are not expected within this box size. Reducing the box size to 100 pc varies the emission by $\approx (1-10)\%$, at the cost of highly increasing computing time. Our implementation of the DM source in GALPROP was validated by comparison with similar calculations in the literature that were obtained by a variety of methods [45, 47, 55]. Our GALPROP version with DM can be downloaded for a public use at [77].

2.5 Diffusion model

For the choice of the propagation parameters in eqs. (2.3)–(2.6), to begin we followed the canonical MIN/MED/MAX paradigm which has been used extensively in earlier works (see, e.g., [41, 46, 47]). These three diffusion parameter configurations were derived from various CR data sets. MED is an average "best-fit" configuration, while MIN and MAX are intended to represent possible extremes. Because recent CR data seem to reliably exclude the MIN model [56], we discarded this case and considered instead a newly proposed model derived in [57], which includes CR reacceleration effects in the fit. Specifically, we used the posterior mean parameter values from table 2 of [57].

Recalling that we consider two values for the MF vertical scale height z_B (referred to as z_{B1} and z_{B2}), which is related to h, we now define combined MF and propagation models. In principle we would consider both values of z_B with the three propagation models described above, however we discovered empirically that the intensity for the two z_B values is very similar for the MAX propagation configuration, and so we use only the z_{B1} case with the MAX model. This results in five z_B/propagation models. Table 1 summarizes the parameter values for these five configurations.

For each of these five models, we consider the two central MF values mentioned previously, for a total of ten MF/propagation models. These are meant to represent current systematic uncertainties on this aspect of the analysis. For each of these models, we calculate the emission from each of the DM models described in section 2.1 and section 2.2. In section 2.6 we show the dependence of the DM emission intensity on the MF and propagation configuration.

Section 2.3 described the vertical sizes of the rectangular 3D diffusion box; for the horizontal size, we set the box edges to be $+/-15$ kpc along both x- and y-axes to approximately enclose the Galactic disc (see e.g. [47]). Boundary conditions were set to the free escape mode. For the energy boundaries, we take 0.01 to 200 GeV. The lower boundary is mainly defined by the fact that the electrons with smaller energies have no contribution to the syn-

JCAP03(2016)060

chrotron radiation at the frequencies of interest. The upper boundary has to contain the most energetic electrons produced by our DM source. One might naively assume that they would approximately correspond to the largest DM particle rest mass involved ($\sim 50\,\mathrm{GeV}$), however particle reacceleration (as in our Reacc model) can in principle raise the electron energies much beyond $m_\chi c^2$. We empirically found that 200 GeV is an effective upper limit on the energies the electrons attain in our cases.

Further details on all parameters we adopted in the GALPROP runs can be requested from the authors.

2.6 DM emission maps

We implemented the modeling described in the previous sections in GALPROP and produced multi-frequency maps for all DM models needed to cover the parameter space. In total, we computed 300 parameter configurations, which are constituted by 5 different WIMP masses over the range of interest (we interpolated our results between the computed points), 2 annihilation channels ($b\bar{b}$, $\tau^+\tau^-$), 3 profile slopes (see section 2.1), and 10 MF/propagation models (see section 2.3 and section 2.5). The maps have a resolution of $\approx 0.5^\circ$ (HEALPix [58] resolution $N_{side} = 128$) and are produced at the WMAP and Planck frequencies of 23, 28, 33, 41, 44, 61, and 70 GHz.

Figure 1, top left panel, shows the DM intensity map for the reference model of the data ("REF"); this is also the best-fit configuration found in section 6. The figure shows an intensity distribution around the GC that is highly concentrated, spanning six orders of magnitude between the center and anti-center. The other panels of figure 1 show examples of the dependence of the emission on various parameters in terms of the ratio to the REF case.

We comment now on some general features. The difference between the maps typically grows with distance from the GC. This is seen when changing the DM particle mass (top right), and also interestingly, for the frequency dependence (middle row, left). However the steeper DM density profile map ($\gamma = 1.3$ vs. $\gamma = 1.1$ for the REF model) differs noticeably only very close to the GC (middle row, right); this indicates that the profile slope does not have an important impact on the emission at higher Galactic latitudes. The $b\bar{b}$ annihilation channel produces significantly smaller intensities than $\tau^+\tau^-$ one, everywhere on the sky, as expected (bottom left). A more conservative MF/propagation model (bottom right) differs non-trivially from the REF model: the intensity is much smaller around the center and much larger around the anti-center. This can be primarily attributed to an overall smaller MF, which generates weaker synchrotron around the GC and cools electrons less efficiently, allowing them to diffuse further while still emitting.

3 Regions of interest on the sky

For each of the two approaches to testing a DM contribution to the data, we selected a ROI in the sky on which to perform the analysis. For the first approach, in which we derive conservative limits by assuming the total data is composed of only the CMB and a DM component, we chose a ROI inside which we compute the average intensity at every frequency, to be compared to the analogous quantity as derived from DM maps.

The ROI choice was based on the Planck collaboration's study of the Haze [30], and consists of a rectangular area in Galactic coordinates $-35^\circ \leq b \leq -10^\circ$, $|l| \leq 35^\circ$. This choice is well-motivated for a DM search, since that ROI is sufficiently far from the bright

JCAP03(2016)060

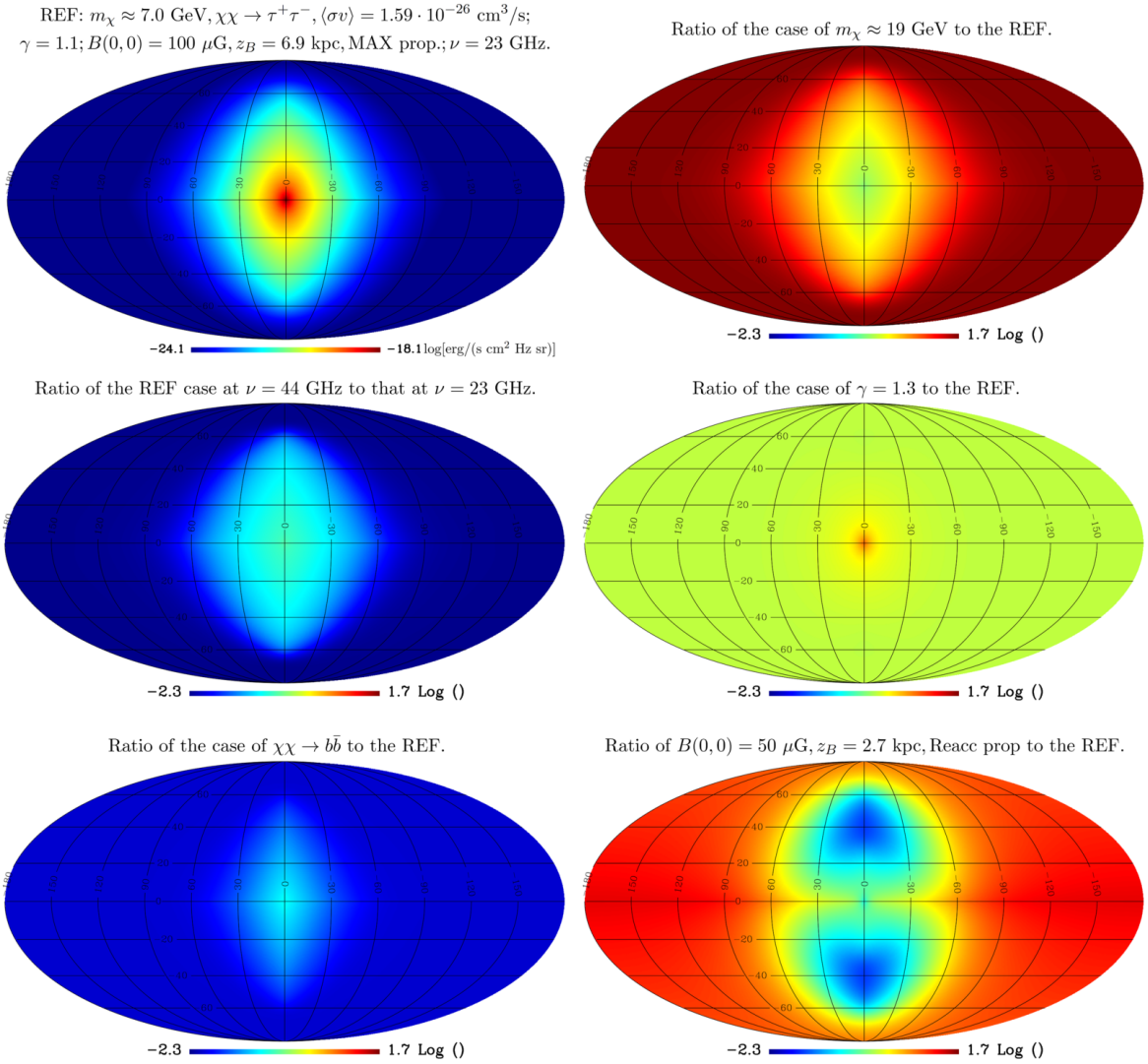


Figure 1. (COLOR ONLINE FOR ALL FIGURES) Examples of DM emission intensity maps in Galactic coordinates, at the frequencies indicated. The top left map represents a reference DM parameter configuration ("REF"). Specific parameters of the configuration are given above the map. Other maps show the difference with respect to the REF map when the model parameters are changed as noted. The difference is shown as the ratio $I_x(b,l)/I_{\rm REF}(b,l)$, where I_x is the intensity of the map with one of parameters being changed and $I_{\rm REF}$ is the intensity of the REF map. To illustrate dependence on MF/propagation we changed the relevant parameters. For more details see section 2.6.

foreground emission in the Galactic plane but still in a region where the DM emission is relatively strong. We also masked bright compact sources inside the ROI using the product of the WMAP and Planck source masks for each channel, smoothed to 1° [59, 60]. Our final ROI for the conservative analysis is shown in figure 2 (left panel).

For the component separation analysis in which we determine the contribution to the data from DM by modeling Galactic foregrounds and the Bubbles, we adopt a slightly different ROI. The ROI for this analysis is shown in right panel of figure 2. It is a 60° semi-disc centered on the GC, with bright compact sources masked as in the first ROI, and also strong

JCAP03(2016)060

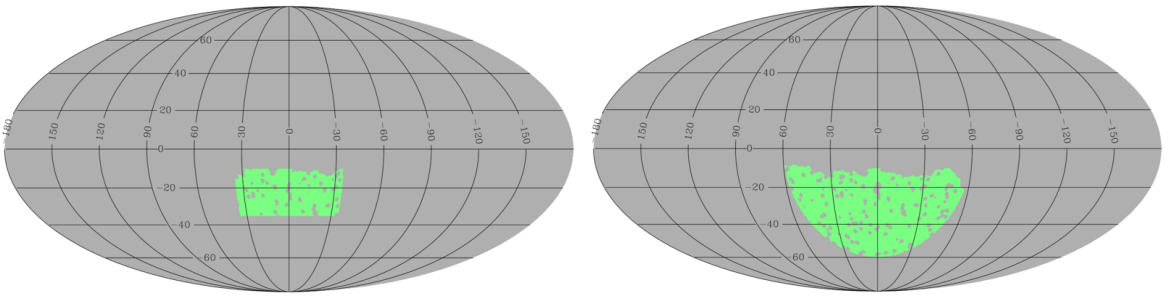


Figure 2. *Left:* our ROI with masked compact sources chosen to produce the conservative DM constraints with CMB subtraction only. It was constructed as the rectangle $-35^\circ \leq b \leq -10^\circ$, $|l| \leq 35^\circ$. *Right:* our ROI with masked compact sources chosen for the regional fitting in the component separation procedure (see more in section 6). Before point source masking it was constructed as a half-disc of 60° radius around GC, with very bright areas around the Galactic plane also masked. This ROI is also used in the presentation of example DM emission spectra in section 4.

Galactic plane emission masked [59]. The choice of 60° addresses additional challenges for this approach, namely avoiding strong foreground degeneracies due to using too small an area while still selecting an area in which each foreground has a spatially-uniform frequency dependence and including the relevant Haze emission.

4 DM microwave spectra in the Haze region

Considering the ROIs we have defined, it is useful to examine the frequency dependence of the DM component from our simulated maps. For this purpose, we consider the larger ROI used later in the component fitting analysis in section 6, shown in the right panel of figure 2. Inside this ROI we average the DM intensity and plot it versus frequency of emission in figure 3. In general a simple power law is not sufficient to describe the spectra, as a mild spectral index evolution is observed within the frequency range considered. Intensities for the $\tau^+\tau^-$ channel are typically five to ten times larger than those for $b\bar{b}$, for the same WIMP mass, density profile and MF/propagation model.

In addition to the amplitude of the emission, the slope of the spectrum strongly depends on the DM particle mass. Approximating the spectra by a simple power law $I \sim \nu^\beta$, we found that for the $b\bar{b}$ case β grows with mass over the range $-3.3 \lesssim \beta \lesssim -1.6$. For $\tau^+\tau^-$ the variation is even slightly larger: $-3.2 \lesssim \beta \lesssim -1.2$. Essentially no dependence of the intensity or slope on the inner profile slope γ is observed, as expected from inspecting the relevant maps in figure 1.

As for the MF and propagation model, higher MFs produce larger intensities. The spectral slope seems to be largely independent of the MF and propagation models, however the overall amplitude strongly depends on the propagation model, varying by up to one order of magnitude. As expected, configurations with higher vertical MF extent z_B produce larger emission. For the same $B(0,0)$ and z_B, models with reacceleration generate slightly larger intensities than those without reacceleration. Such inferences about DM spectra have interesting implications for a comparison with real sky data. In particular, the Planck team claimed in [30] that the average spectral index of synchrotron emission from electrons from Galactic astrophysical sources is ≈ -1.1. The anomalous microwave excess around GC, on the other hand, has a very different index ≈ -0.6. This is one of the main motivations for

JCAP03(2016)060

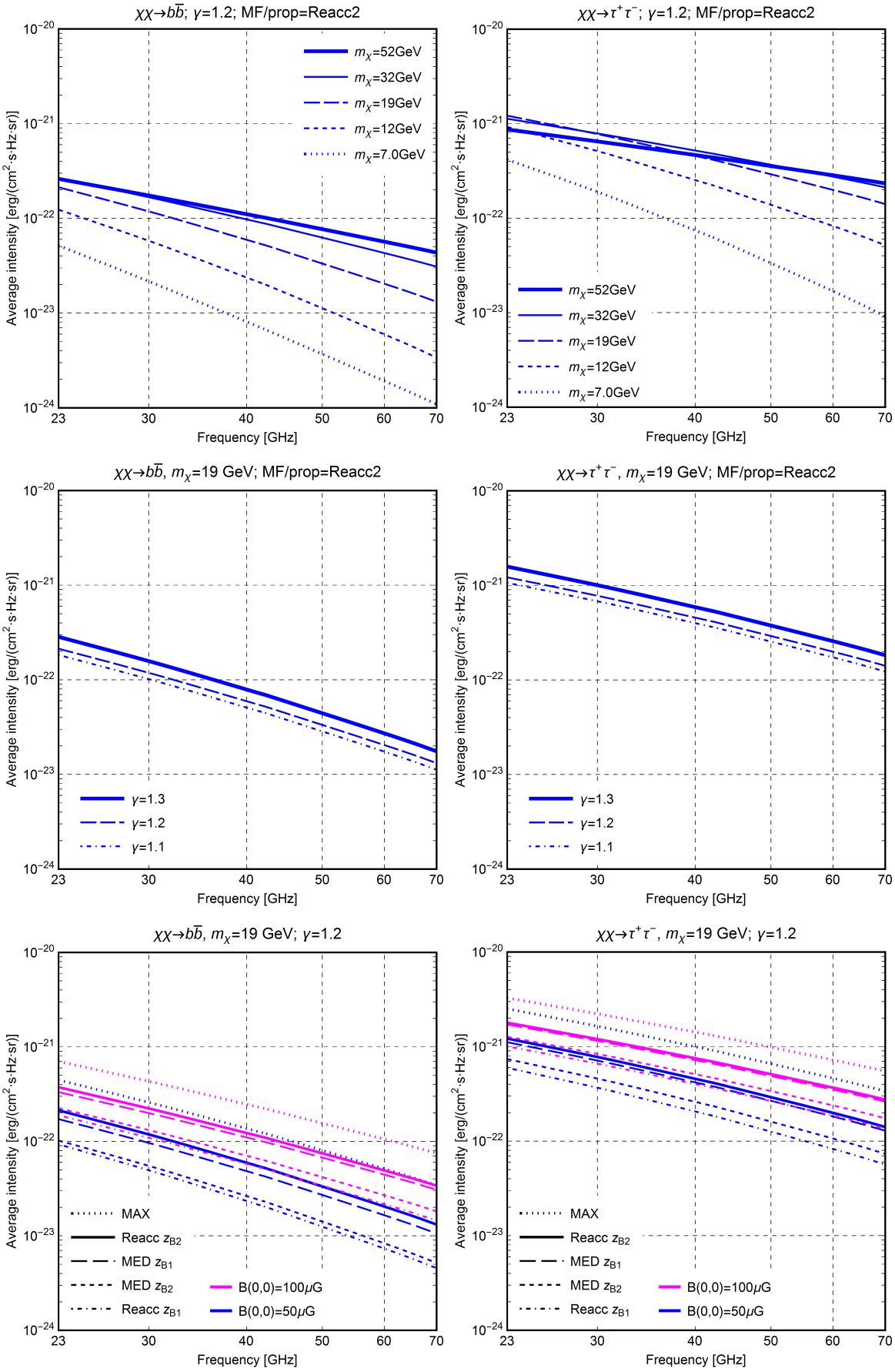


Figure 3. *Continue.*

JCAP03(2016)060

Figure 3. *(preceding page)* Dependence of the DM emission spectrum on various model parameters. The ROI over which the DM intensity was averaged is shown in the right panel of figure 2. Left column in this figure represents the $b\bar{b}$ annihilation channel, while the right column shows results for the $\tau^+\tau^-$ channel. The annihilation cross section $\langle\sigma v\rangle = 3 \cdot 10^{-26}$ cm^3/s in all panels. Points were calculated from the DM maps at each frequency and then interpolated. The first row shows the spectral dependence on the DM mass, the second row shows the dependence on the inner profile slope γ, and the third row shows the dependence on the MF and propagation model.

the suggestion that the Haze comes from a distinct population of electrons, such as from DM annihilation. Comparing the DM indexes estimated above with the ones derived for the Haze and the synchrotron component of the WMAP and Planck data, we notice that while DM is able to generate an arbitrary amplitude for the intensity, the spectrum of the emission has a limited range of slopes (at least for DM masses of interest). Therefore, the DM component is only marginally able to mimic / contribute to regular synchrotron (for the largest WIMP masses considered), and at the same time its spectrum is too steep to fit the excess, which has $\beta \approx -0.6$. These simple considerations suggest that, even in the case that a DM signal is present, it is likely that another mechanism contributes the majority of the Haze signal. This was one of the motivations for us to include a possible counterpart of the Fermi Bubbles in the component separation procedure presented in section 6 too. Indeed, higher WIMP masses ~ 100 GeV may potentially provide the spectral slopes needed for the Haze. However, in this work we intentionally restricted our analysis to only those DM models which fit the gamma-ray excess.

5 Conservative constraints on DM annihilation

In this section we present conservative DM constraints derived from the Planck sky maps when the emission is assumed to be composed only of CMB emission and DM emission, with no other foregrounds considered. Since the intensity of the DM emission is linearly proportional to the annihilation cross section $\langle\sigma v\rangle$, an upper limit on the total observed non-CMB emission at a given frequency can be directly converted into an upper limit on $\langle\sigma v\rangle$ for all WIMP masses of interest. In performing this estimate, we consider only the CMB emission as it is very bright and well characterized and thus very simple to model extremely accurately.

For this analysis, we chose to use Planck Low Frequency Instrument (LFI) channels only (28, 44 and 70 GHz) as the Planck noise level is far superior to that of WMAP while the frequency range covered is comparable.

The Planck 2013 maps that have been released have the monopole and dipole largely subtracted, but, after careful component separation, an estimate of the residual monopole and dipole in the maps was made and published by the Planck team. These residual values with their errors are shown in table 2 of [61]. We performed subtraction of the quoted residual monopole and dipole values from all three Planck LFI channels. We then computed the average intensities in each frequency map. The impact of subtracting residual monopole and dipole on the average intensity is shown in table 2. The first line of this table shows the average intensity inside our ROI from figure 2 (left panel) without any map processing. The second and third lines of table 2 show the ROI intensities after subtraction of the residual monopole and monopole+dipole respectively. These have a significant impact on the 70 GHz channel in particular, where the intensity decreases by about a factor of two.

JCAP03(2016)060

Map	28 GHz	44 GHz	70 GHz
Nominal Planck LFI maps	$3.69 \cdot 10^{-20}$	$2.38 \cdot 10^{-20}$	$3.79 \cdot 10^{-20}$
Maps after residual monopole subtraction	$3.50 \cdot 10^{-20}$	$2.27 \cdot 10^{-20}$	$1.79 \cdot 10^{-20}$
Maps after residual mono/dipole subtraction	$3.64 \cdot 10^{-20}$	$2.27 \cdot 10^{-20}$	$1.79 \cdot 10^{-20}$
Standard deviation of residual monopole	$4.72 \cdot 10^{-22}$	$5.66 \cdot 10^{-22}$	$1.33 \cdot 10^{-21}$
Standard deviation of residual dipole	$6.17 \cdot 10^{-22}$	0	0
Standard deviation of CMB fluctuations	$6.00 \cdot 10^{-21}$	$1.44 \cdot 10^{-20}$	$3.37 \cdot 10^{-20}$
Total standard deviation	$6.05 \cdot 10^{-21}$	$1.44 \cdot 10^{-20}$	$3.38 \cdot 10^{-20}$

Table 2. Average intensities in our ROI from the Planck LFI temperature maps and their associated uncertainties (all in units of erg/(cm^2 s sr Hz), converted from CMB temperature units using: $\Delta I(\nu) = \frac{\partial B_{bb}(\nu,T)}{\partial T}\Big|_{T=2.726K} \Delta T(\nu)$). These were used to derive the intensity upper limits from the data for the subsequent derivation of DM constraints. See section 5 for more details.

Once the monopole and dipole were subtracted and the average intensities in the ROI were computed, we proceeded to estimate uncertainties due to Planck noise, errors in the residual monopole and dipole, and CMB fluctuations. The instrumental noise level was estimated using the maps provided as a part of the Planck data products, and it was found to be largely subdominant compared to the other uncertainties. The monopole and dipole uncertainties were taken from table 2 of [61] and assumed to be the standard deviations of respective Gaussian distributions. Numerical values for the monopole and dipole "noise" (denoted $\sigma_\nu^{\rm mon}$, $\sigma_\nu^{\rm dip}$) are shown in the fourth and fifth line respectively of table 2. The dipole-induced uncertainty slightly exceeds the monopole uncertainty for 28 GHz and does not exist for other channels by construction as it was not modeled in the Planck team fitting.

The most important contribution to the intensity uncertainty comes from the CMB temperature fluctuations, which we take to be an unknown realization of the underlying cosmological model, in our specific ROI. Here we aim at deriving the standard deviation $\sigma_\nu^{\rm CMB}$ of the mean ROI intensity $I = 1/n \sum_{i=1}^n T_i$, where $n = 6427$ denotes the number of map pixels in our ROI at our resolution and T_i is the intensity (or, equivalently, thermodynamic temperature) value in each pixel i.

The variance of I was calculated as follows:

$$\langle (I - \langle I \rangle)^2 \rangle = \langle I^2 \rangle = \langle \frac{1}{n^2} \sum_{i=1}^n T_i \sum_{j=1}^n T_j \rangle = \frac{1}{n^2} \sum_{i,j=1}^n \langle T_i T_j \rangle$$
$$= \frac{1}{n^2} \sum_{i,j=1}^n \sum_l \frac{2l+1}{4\pi} C_l B_l^2 W_l^2 P_l(\cos\theta_{ij}). \quad (5.1)$$

Here the brackets $\langle\rangle$ mean averaging effectively over all possible realizations of the underlying cosmological model in an area that matches our ROI. When considering CMB fluctuations, $\langle I \rangle = 0$. The well-known expression for $\langle T_i T_j \rangle$ in terms of the CMB power spectrum C_l can be found in, e.g., eq. (18.29) in [62].

The beam B_l and pixel window function W_l in eq. (5.1) account for the smoothing procedure we applied to the data (we smoothed the Planck maps down to 1° convolving them with a 2D Gaussian function) and map pixel size ($\sim 0.5°$ in our case). $P_l(x)$ denotes the Legendre polynomials of order l and θ_{ij} the angular distance between the i'th and j'th

JCAP03(2016)060

pixels. The standard deviation given by eq. (5.1) was computed using the HEALPix tools [58] and summing from $l = 2$ to $l_{\rm max} = 60$; it was found to be 25.4 $\mu K_{\rm CMB}$ (identical for all frequencies). As input C_l's we used the power spectrum theoretically derived from the conventional best-fit ΛCDM model [63]. Specifically, we took numerical values of C_l's from the "Ancillary Data" section of [64] and the Planck+WP+highL+lensing parameter set there. The σ_ν^{CMB} values are shown in the sixth line of table 2.

The three sources of noise described above are uncorrelated, so the total noise is the sum in quadrature of $\sigma_\nu^{\rm mon}$, $\sigma_\nu^{\rm dip}$, and $\sigma_\nu^{\rm CMB}$. Numerical values are shown in the last line of table 2, where we see that the CMB fluctuations contribution completely dominates over the others. Regarding the signal to noise ratio, the CMB noise is at the level $\approx 20\%$ with respect to the mean intensity at 28 GHz, but it increases fast with frequency, and at 70 GHz it already exceeds the mean signal. We compute the 95% confidence level (CL) limit by setting $I_\nu + 1.64\sigma_\nu$ as the upper limit at each frequency. This chosen cut corresponds to the 95% upper limit for a one-dimensional Gaussian distribution. Our choice is justified by the fact that the main source of noise is CMB fluctuations, which are correlated between frequency channels.

After setting $I_\nu + 1.64\sigma_\nu$ as the intensity upper limit, we required that the DM emission intensity in our ROI should not exceed these limits in *any* of the frequency channels. Since the DM intensity is proportional to $\langle\sigma v\rangle$, this requirement translates to an upper limit for the cross section, which we display in figure 4. In general, our exclusion curves are quite far from the canonical thermal relic cross section $\langle\sigma v\rangle = 3 \cdot 10^{-26}$ cm^3/s (red dashed line) for all considered configurations. The best constraint among all is $\langle\sigma v\rangle \lesssim 2 \cdot 10^{-25}$ cm^3/s. No clear dependence of the exclusions on the profile slope γ is apparent. However, the dependence on the annihilation channel is quite strong: constraints for $\tau^+\tau^-$ are $\gtrsim 3$ times stronger than for $b\bar{b}$ for the same MF/propagation models. Also the $\tau^+\tau^-$ channel forms a slightly narrower band of exclusion lines. Increases in both z_B and $B(0,0)$ values strengthen the constraints. All these parameter dependencies are indeed in agreement with those for DM intensities, which were described in section 4. The most pessimistic constraints are typically realized by the Reacc z_{B1} $B(0,0) = 50$ μG configuration, while the most optimistic ones by MAX $B(0,0) = 100$ μG. The more moderate configuration is Reacc z_{B2} $B(0,0) = 50$ μG, which we set as our representative constraint (shown by the blue solid line in figures 3, 4 and 9). For this we chose the $B(0,0) = 50$ μG case rather than $B(0,0) = 100$ μG due to the MF considerations explained in section 2.3. Note also that the fiducial configuration corresponds to the Reacc diffusion model, which is expected to be newest and most accurate among all three considered.

Along with our exclusion lines, figure 4 shows the parameter regions at 95% CL (unless stated otherwise), which are required to fit the GC gamma-ray excess by WIMP annihilation; see figure caption for details. In general, there is a good agreement between the parameter regions derived in independent studies for the same channel and profile slope pairs. While all these works only include DM prompt gamma rays in the fit, [65] showed that including secondary gammas from ICS and bremsstrahlung from DM leptons marginally changes the result (their signal region, derived for the configuration $\chi\chi \to b\bar{b}$; $\gamma = 1.2$, is almost completely inside the brown region shown). Therefore, overall our constraints on the cross section show no tension with the signal regions derived from gamma-ray data analyses of the excess. An alternative way to account for CMB fluctuations in the emission map is to subtract at every frequency the reconstructed CMB fluctuation map as provided by the Planck team (see "all-sky-maps" folder at [64]). This map is the result of the emission component

JCAP03(2016)060

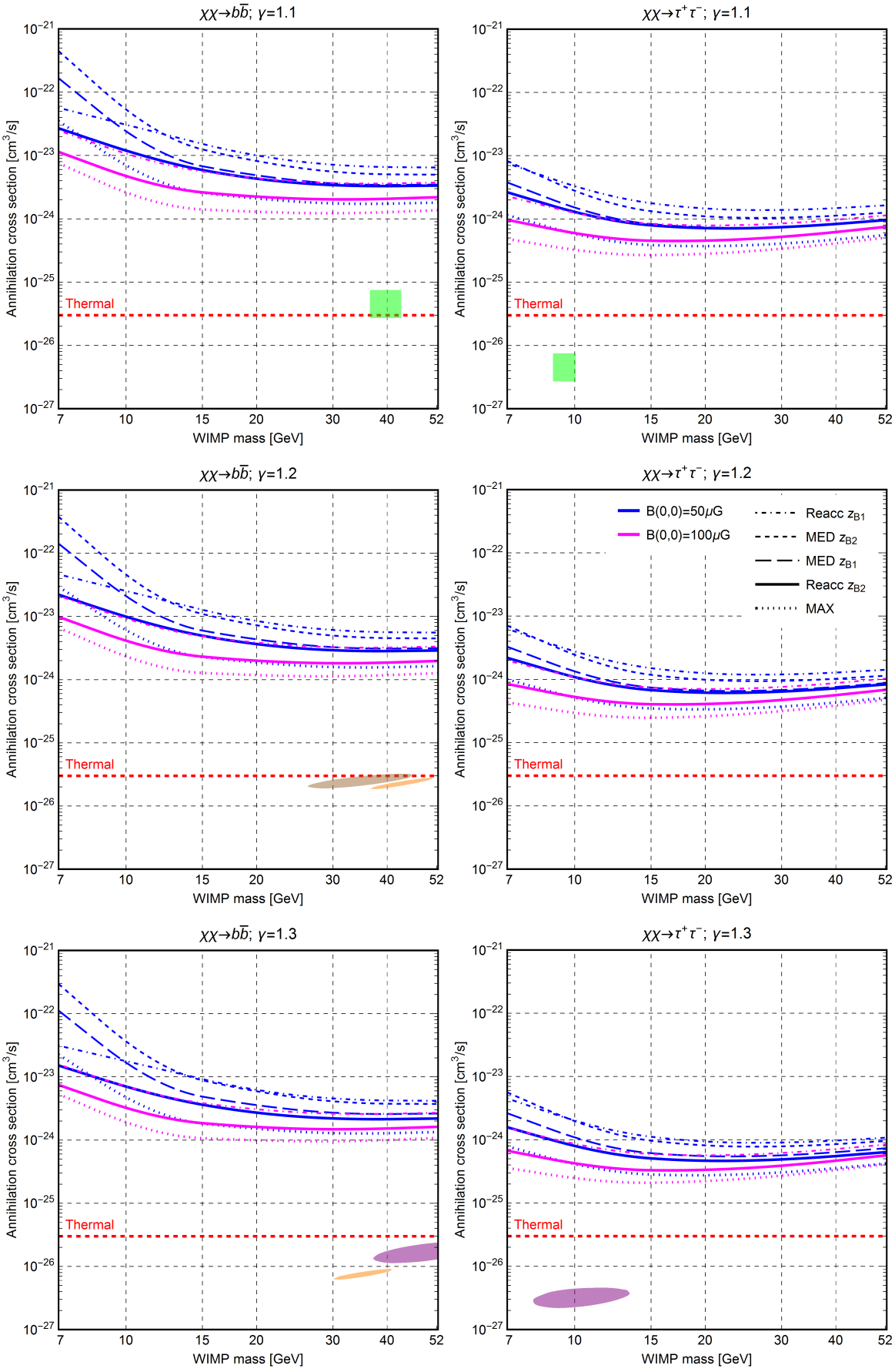


Figure 4. *Continue.*

JCAP03(2016)060

Figure 4. *(preceding page)* DM constraints derived at 95% CL resulting from the Planck temperature maps with subtraction of the CMB emission only for various DM/MF/propagation models ($\langle\sigma v\rangle$ above the lines are excluded). The red dashed horizontal line indicates the thermal relic cross section $\langle\sigma v\rangle = 3\cdot 10^{-26}$ cm^3/s. Besides exclusion curves we also show here WIMP parameter regions (at 95% CL unless stated otherwise) needed to fit the GC gamma-ray excess. The brown region for the case $\chi\chi \to b\bar{b}$; $\gamma = 1.2$ was derived in the work [9], the orange ones for $\chi\chi \to b\bar{b}$ in [10], the green ones for $\gamma = 1.1$ in [11] (68% CL regions), and the purple ones for $\gamma = 1.3$ in [38]. For the optimistic high MF models with $B(0,0) = 100$ μG, only three exclusion curves out of five computed in total are shown. The two curves not shown lie inside the other curves. More details are in section 5.

separation procedure performed by the team and reflects the most up-to-date knowledge of the actual realization of CMB fluctuation field. We attempted this strategy and found a relatively minor improvement in our derived constraints of $\approx 16\%$. Although more stringent, these constraints depend on the specific component separation procedure adopted to derive the map, and therefore we opted instead to show the results from the procedure described earlier in this section.

The DM limits described in this section are relatively weak, however we expect that foregrounds other than the CMB play a potentially important role in this region of the sky: dust, free-free from ionized hydrogen, synchrotron from regular CRs and the Bubbles. In the following section we perform a full component separation analysis to more accurately characterize a possible DM contribution.

6 DM constraints from a component separation approach

6.1 The WMAP-Planck Haze: history

A mysterious microwave excess above the canonical astrophysical foregrounds was first reported with the first WMAP data release [24], and was later interpreted as a possible signal of DM annihilation [25]. Further WMAP-based studies confirmed the existence of the Haze and characterized it in detail [66–68]. The most recent and comprehensive Haze study was performed after the Planck data releases in [30]. This work combined WMAP-9 and Planck data to separate out the Haze emission at 6 frequencies via frequency-by-frequency template fitting. The results showed the Haze properties to be highly consistent between the two data sets. This can be seen in figure 8 in [30], where the derived Haze spectrum is presented. As we already mentioned, those authors claimed that the Haze spectrum $I \sim \nu^{-0.56}$ is indeed significantly harder than the usual synchrotron $I \sim \nu^{-1.1}$, which suggests the origin to be from a distinct population of electrons. The overall amplitude of the Haze emission was found to constitute $\approx 33\%$ of the total synchrotron and $\approx 23\%$ of the total Galactic emission at 23 GHz in the relevant region (figure 2, left). Figures 9–10 in [30] show the Haze morphology, which appears to be consistent with that of the Fermi Bubbles. This fact and other considerations (see, e.g., [32]), led the community to favor a scenario where the Haze is simply the microwave counterpart of the Fermi Bubbles.

The DM and the Bubbles interpretation of the Haze are in fact not mutually exclusive, and thus it is necessary to consider both in the analysis. In what follows, we will investigate whether the data are best fit with one of these components at a time, or both together. In this part of the analysis, we will adopt the ROI shown in the right panel of figure 2 for the component separation analysis.

JCAP03(2016)060

6.2 Methodology

Our procedure relies on template fitting, which is described by the following equation:

$$d(\nu, b, l) = \sum_i a_i(\nu) t_i(\nu, b, l) + r(\nu, b, l), \tag{6.1}$$

where $d(\nu, b, l)$ is the data map at frequency ν in a pixel with coordinates (b, l); $t_i(\nu, b, l)$ is an assumed template intensity of the i-th component; $r(\nu, b, l)$ are residuals; $a_i(\nu)$ is a dimensionless amplitude of the i-th component, which is determined by the fitting. As for the sky maps $d(\nu, b, l)$, we used four WMAP channels: 23, 33, 41, 61 GHz (K, Ka, Q, and V bands from [69]) and three Planck LFI channels: 28, 44, 70 GHz from [64]. In contrast to [30], we also include in the fit the 70 GHz frequency channel, which provides further leverage for DM fitting and allows a better investigation of the frequency dependence of foregrounds.

In addition to DM, we included in the fit as foregrounds: dust, free-free, synchrotron and the Bubbles. A monopole and dipole component, as well as the CMB, are initially fit to the whole sky map, and removed from the data, so there is no monopole, dipole, or CMB fitting performed in the chosen ROI. As described in section 2, the DM emission modeling predicts a specific emission at each frequency, therefore the DM has only one free parameter, namely an overall amplitude a_{DM}, which sets the annihilation cross section value required by the fit. We ran the fitting procedure separately for each DM/MF/propagation model. We assume spatially-constant power laws for all Galactic foregrounds. This means that the templates are rescaled by a single number, $a_i(\nu)$, in the ROI at every frequency independently. Therefore, unlike for the DM component, we do not impose a frequency dependence to foregrounds in the fit. We compute it, however, a posteriori.

The data at 23 GHz and the foreground templates are shown in figure 5. Note that our units can be converted into thermodynamic units: 10^{-20} erg/(s cm^2 Hz sr) $\approx 62\ \mu K_{\rm CMB}$ at 23 GHz at temperatures of interest. For the CMB template we employed the Internal Linear Combination from Planck HFI channels (weights were derived from one single region, outside of the type-III Planck 2013 CO-based mask [70]). The reason for this choice rather than the Planck official map (SMICA) is that we wanted to avoid any of the LFI channels contributing to the CMB solution in order to avoid any circularity in the fit. The Galactic dust emission map is described in [71, 72]. Free-free emission naturally correlates with H_α, which provides an estimate of its morphology [73]. The synchrotron from conventional astrophysical CRs is assumed to have a similar morphology at radio and microwave frequencies (which is essentially equivalent to an assumption of constant spectral index across the sky). This allows us to use the canonical Haslam 408 MHz map as the synchrotron template [74]. Finally for the Bubbles we adopted the elliptical Gaussian template (with $\sigma_l = 15^\circ$ and $\sigma_b = 25^\circ$) proposed by [30] for the Haze emission, which was suggested to be suitable for the Fermi Bubbles counterpart. Indeed an exact Bubbles morphology is not known and may be quite complicated with both vertical and horizontal asymmetries (see, e.g., [31] for the morphology in radio). Our choice has the advantage of allowing comparison of our results with existing results in the literature (see [30] and references therein).

Additional foreground components could also be considered. For example, the authors of [30] also introduced a "disc" component (an elliptical Gaussian with $\sigma_l = 20^\circ$ and $\sigma_b = 5^\circ$) to account for a potential difference in the synchrotron morphology between 408 MHz and the typical CMB frequency range. This was intended to account for the energy dependence of the electron propagation length. Our attempt to add such component to the fitting provided unphysical results. Also, considering the relatively minor importance of the disc reported

JCAP03(2016)060

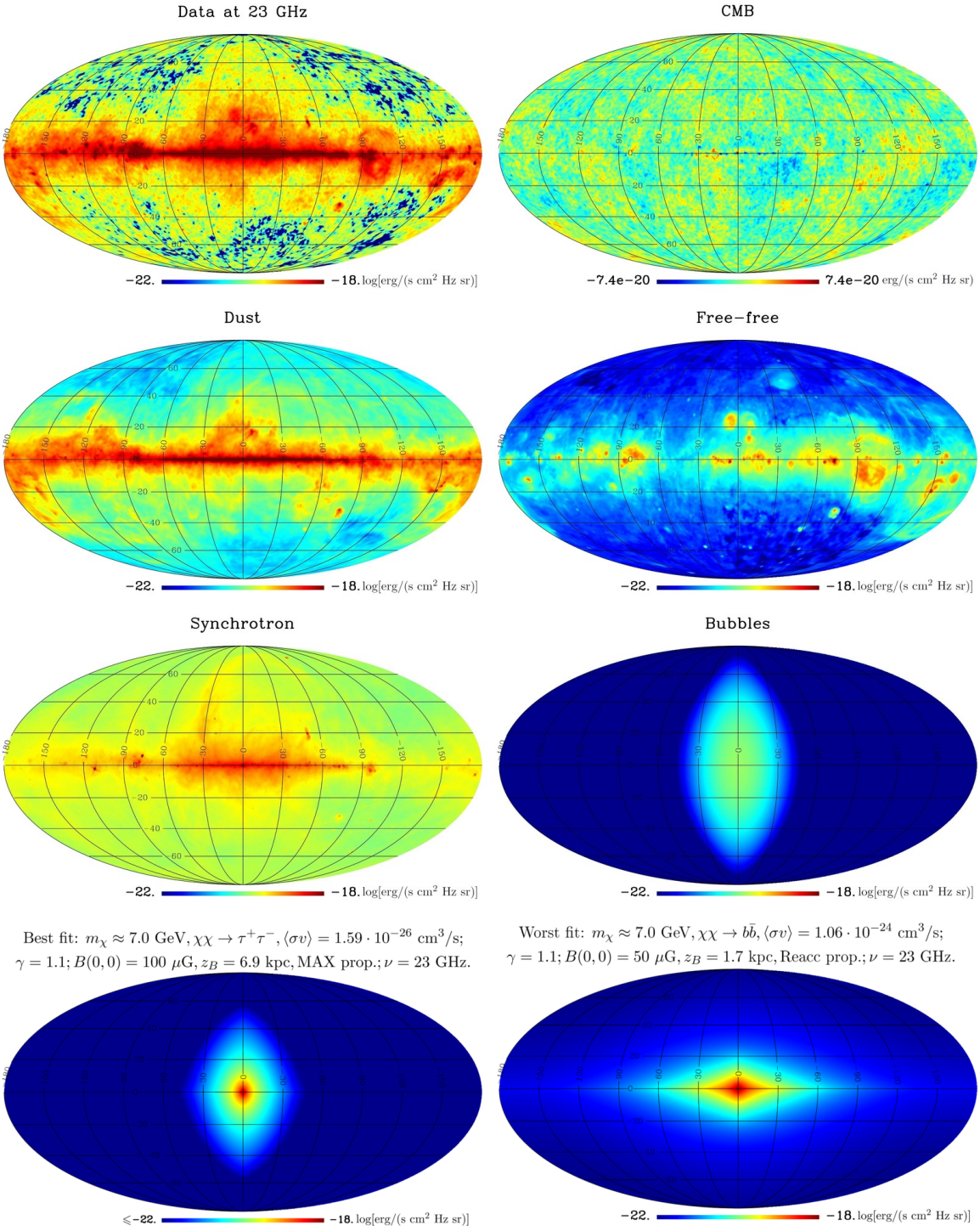


Figure 5. Data (total observed intensity at 23 GHz, top left panel) and templates (all other panels) used in the analysis. Morphology of all components except DM was assumed to be frequency-independent. Normalization of each template corresponds to that of the best-fit model at 23 GHz. The bottom panels show the best-fit and worst-fit DM sky maps among all the models considered. See more details in section 6.2.

JCAP03(2016)060

in [30], we decided not to include any further correction to the synchrotron emission in our final procedure.

The fitting procedure determines the amplitudes $a_i(\nu)$ by minimizing the residuals $r(\nu, b, l)$ in eq. (6.1). They are the solution of the following set of equations:

$$\frac{\partial \chi^2}{\partial a_i(\nu)} = 0. \tag{6.2}$$

If the sky model only included free amplitudes for each component at each frequency, the solution of the linear system eq. (6.2) would be:

$$\mathbf{a}(\nu) = \mathbf{T}^{-1} B_\nu \tag{6.3}$$

$$\Delta a(\nu)^2 = \mathrm{diag} \frac{1}{2} \mathbf{T}^{-1} \tag{6.4}$$

where $B_\nu = (d(\nu, b, l)/\sigma(\nu, b, l)) \cdot (t(b, l)/\sigma(\nu, b, l))$ and $T_{ij} = t_i(b, l)/\sigma(\nu, b, l) \cdot t_j(b, l)/\sigma(\nu, b, l)$. However, our DM modeling couples all frequencies so that we have to resort to a Markov-Chain procedure to find the values and errors for $a_i(\nu)$.

Modeling foregrounds by means of templates and assuming spatially-constant spectral indexes across the whole sky is a very crude approximation. Moreover, we expect the DM signal to be prominent near the GC but not everywhere. On the other hand, a residual monopole and dipole might be present in the WMAP and Planck maps, as well as in the templates, as result of the map-making and calibration procedures, and on small areas of the sky these components are not properly fit.

For these reasons, we decided to perform the fit in two steps. First, we fit the data masking the Galactic plane and bright sources with a mask very similar to the one used by [30], and obtained the template amplitudes at all frequencies; we did not include the DM in this nearly full-sky fit. We then subtracted the CMB and monopole and dipole from the data and solved for the dust, free-free, synchrotron, Bubbles, and DM amplitudes in the larger ROI (right panel of figure 2).

In order to determine the best-fitting DM/foreground amplitudes in our chosen ROI, we ran our own Markov Chain Monte Carlo (MCMC) sampler to study the multi-parameter likelihood, which is assumed to be:

$$L \sim \exp(-0.5\chi^2), \;\; \chi^2 = \sum_{j=1}^{7} \sum_{i=1}^{n_2} \frac{r_{ij}^2}{\sigma_{ij}^2}, \tag{6.5}$$

where r_{ij} is the residual in pixel i at frequency channel j according to eq. (6.1), σ_{ij} are map noise, and the summation runs over all seven frequencies and all $n_2 = 15481$ pixels in our ROI. The reduced χ^2 ($\chi^2_{\rm r}$), is computed dividing the full χ^2 in eq. (6.5) by the number of degrees of freedom $N_{\rm dof} = 7 \cdot n_2 - 7 \cdot 4 - 1 = 108338$.

Eq. (6.5) implicitly assumes that the noise in each pixel is uncorrelated. In fact, noise correlations are expected because of the spacecraft scanning strategy and the adopted smoothing procedure. Despite being sub-optimal, this procedure is commonly used (e.g., [30]) because of the difficulty to treat the full complexity of the noise at intermediate and high resolution. The noise maps were computed as the standard deviation of full resolution Gaussian noise realizations, smoothed to one degree and downgraded to $N_{side} = 128$ (to match the DM template). The RMS maps derived were further rescaled to match the noise power spectrum level of the full-resolution smoothed maps. We did not put any prior on the amplitudes, aside from imposing that they should be positive.

JCAP03(2016)060

Model/ χ^2_r	Cross section $\langle\sigma v\rangle$ [cm^3/s]	Mass m_χ [GeV]	Channel	Profile slope γ	Central MF $B(0,0)$ [μG]	Vertical MF scale z_B [kpc]	Diffusion model
BF/ 6.87	$1.6 \cdot 10^{-26}$	7.0	$\tau^+\tau^-$	1.1	100	6.9	MAX
WF/ 7.03	$1.1 \cdot 10^{-24}$	7.0	$b\bar{b}$	1.1	50	1.7	Reacc
6.92	$1.9 \cdot 10^{-26}$	19					
6.99	$4.7 \cdot 10^{-26}$	52					
6.91	$1.3 \cdot 10^{-25}$		$b\bar{b}$				
6.89	$9.2 \cdot 10^{-27}$			1.3			
6.89	$2.9 \cdot 10^{-26}$				50		
6.91	$1.8 \cdot 10^{-26}$					2.7	Reacc
6.89	$6.3 \cdot 10^{-26}$	19	$b\bar{b}$				
6.92	$8.8 \cdot 10^{-26}$	52	$b\bar{b}$				

Table 3. All parameter values for the best-fitting (BF, the first row) and worst-fitting (WF, the second row) DM/MF/propagation models. Lower rows illustrate the fit quality for other models, which differ from the BF model by one or two parameters indicated in the respective columns.

6.3 Fitting results

We ran the MCMC fit for our grid of DM/MF/propagation models and obtained χ^2_r for each of them. Overall the quality of the fit is quite poor, with a χ^2_r ranging between 6.87 and 7.03. This is simply a confirmation of the challenge that the component separation poses, the limitations we face with the current, non-Planck-based foreground templates, and the simplicity of template fitting. As a result, the χ^2_r difference cannot be considered as a powerful discriminant between models. Nonetheless, we can rank the models based on their likelihood and draw conclusions. The parameter values of the best-fitting (BF) and worst-fitting (WF) configurations are presented in table 3. This table also shows for an illustration the fit quality of the other representative DM/MF/propagation models, which differ from the BF model by one or two parameters.

While overall the poor χ^2_r values indicate a poor fit, it is sensible to ask whether the Bubbles and/or DM substantially improve the fit, with respect to the case in which only standard foregrounds are included. The respective fit qualities for various setups are shown in table 4, with fits to each individual frequency and all frequencies together reported. If only standard foregrounds are considered, the fit is very poor. The lowest frequencies show the largest residuals, hence they likely contain the largest contribution from the Haze. Above 40 GHz, residuals are less pronounced and quite acceptable, with a possible overfitting in the 60 GHz channel where the foregrounds are typically at their minimum. When adding the Bubbles template, we see a very significant improvement at low frequencies. Similarly, when adding only DM, there is an improvement in the fit. The value of $|\Delta\chi^2_r|$ is slightly less than in the Bubbles-only case, but quite comparable. When allowing for both Bubbles and DM in the fit, χ^2_r reduces by almost a factor of two; however remaining quite large (since naively we expect it to take the value of one in the case of a good fit).

JCAP03(2016)060

ν	χ^2_r with CMB, mono/dipole, f-f, synchr., dust	$\Delta\chi^2_r$ after addition of the Bubbles	$\Delta\chi^2_r$ after addition of the BF DM model	$\Delta\chi^2_r$ after addition of the Bubbles and BF DM model
23	37.4	-15.9	-15.4	-17.8
28	21.4	-6.35	-5.42	-6.86
33	10.0	-3.13	-2.67	-3.47
41	2.23	-0.475	-0.363	-0.533
44	3.31	-0.343	-0.219	-0.379
61	0.563	-0.023	-0.013	-0.023
70	2.29	-0.078	-0.007	-0.077
Gl.	11.0	-3.75	-3.44	-4.16

Table 4. Effects of addition of the Bubbles and DM on the quality of the fit. The BF DM model shown is described in table 3. The second column shows results with "standard" foregrounds only. The third column shows the χ^2_r improvement after adding the Bubbles. The fourth column shows improvements after adding the BF DM model only (no Bubbles). The last column shows improvements in the most general case of the Bubbles and DM considered together.

In figure 6 we show maps of the relative residuals $r(\nu, b, l)/[d(\nu, b, l) - md(\nu, b, l)]$ with $r(\nu, b, l)$ and $d(\nu, b, l)$ defined as in eq. (6.1) and $md(\nu, b, l)$ the fitted mono/dipole. The top row of figure 6 shows the frequency dependence of the residuals with neither DM nor the Bubbles in the fit. At 23 GHz the Haze is very clearly visible, reaching up to about 50% of the total sky intensity at peak points. Note the vertically-elongated Haze morphology (which would be absorbed by the Bubbles template) slightly bent to the right relative to zero longitude (which visually matches the shape derived in [31]). The Haze becomes less prominent with frequency, and is almost absent at 70 GHz. This spectral trend agrees well with that in table 4, which shows that χ^2_r reaches considerably lower values at higher frequencies, even if only standard foregrounds are considered. Moreover, looking at the top left panel, it is clear that the Haze tends to have rather irregular morphology with sharp edges, which seems more consistent with the Bubbles origin rather than smooth DM emission (e.g., figure 1). The bottom row shows the residuals at the lowest and most relevant frequency for the cases of DM only, DM+Bubbles WF and DM+Bubbles BF. We can see that the addition of DM alone reduces residuals somewhat. Adding both the Bubbles and DM further improves the results, almost entirely absorbing the Haze. There is, however, essentially no difference in the DM BF and WF cases, which is consistent with our previous finding that the χ^2_r differs very little for these two models.

The computation of the fitting coefficients $a_i(\nu)$ also allows us to evaluate the average intensity of each component within the ROI and its frequency dependence, as well as the components' relative amplitudes. This is reported in figure 7 for the BF DM model. Other models did not show significant qualitative differences. Hence, for simplicity, in what follows we focus on the BF case. At essentially all frequencies, there is a hierarchy in intensity (from higher to lower): synchrotron, dust, Bubbles, free-free and DM. The CMB fluctuations average is negative in our ROI, and its absolute value grows from a subdominant 2.9% at 23 GHz up to a significant 61% at 70 GHz, which reflects the black-body spectrum and the overall foreground frequency dependence. DM has the smallest contribution at all frequencies,

JCAP03(2016)060

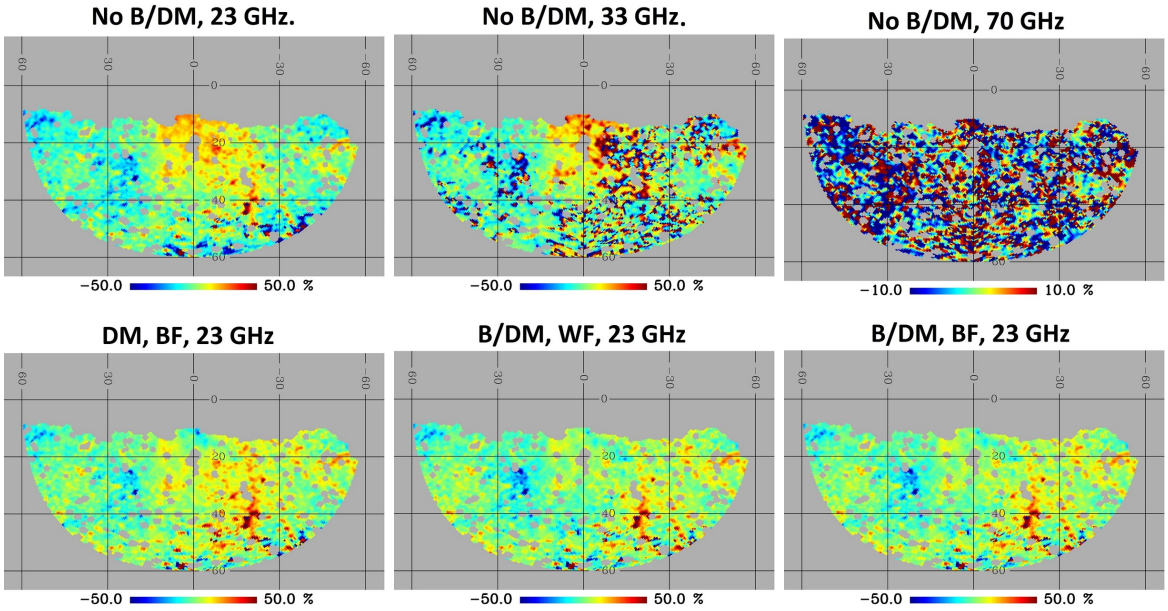


Figure 6. Residuals resulting from our component separation procedure in units of the total measured sky intensity. The top row shows the residuals at different frequencies without introducing either the Bubbles or DM template. We can see a clear excess in this case at low frequencies. The bottom row shows residuals at 23 GHz with DM only and Bubbles+DM. Adding DM improves residuals slightly, while adding both the Bubbles and DM improves the residuals much more. At the same time the difference between the BF and WF configurations is almost absent. More details are in section 6.3.

ranging from 2.2% to 0.27%. The synchrotron dominates at almost all frequencies, decreasing from 61% to 51%. Also we see that we reproduced well the canonically-expected (e.g., [30]) synchrotron spectral index $I \sim \nu^{-1.1}$. The dust spectrum is not monotonic; it contributes 29% at 23 GHz. The free-free contributes 2.7% and matches quite well the expected slope $I \sim \nu^{-0.15}$ (e.g., [75]). The Bubbles contribution is relatively flat in frequency and equal to 5-9%. Our Bubbles spectrum agrees very well with $I \sim \nu^{-0.56}$ derived in [30].

We also compare our foreground component intensities with those derived in [30], for the frequency where the Haze is most pronounced. For this exercise, we considered the ROI used in [30] and shown in figure 2 (left panel). This comparison is shown in table 5. While all standard astrophysical components have similar derived properties in both that work and ours, the Haze component in this work is about a factor of two smaller. This might be due to the mono/dipole removal strategy described above and/or to the modeling of the Haze which receives contributions from both Bubbles and DM in our work. Lastly, note that the sum of all components is well within the 3σ error bars on the data in all channels.

We also investigate the model dependence of the Bubbles and DM contributions. In table 6 we report the mean and variation ranges of the contributions of all DM/MF/propagation models at 23 and 70 GHz. The Haze contribution does not significantly fluctuate from model to model. At 23 GHz its amplitude is well above systematics due to model variations, whereas at higher frequencies it is of the same order of magnitude as the residuals. The mean flux of the Haze represents 7.8% of the total sky emission compared to the best-fit amplitude of 7.2%. DM contributes a significant part of the Haze at 23 GHz: 21% on average (30% in the BF case). Because DM spectra usually fall off with frequency faster than the Bubbles spectrum, the DM contribution to the Haze decreases with frequency.

JCAP03(2016)060

Component	Planck team	Our work
Synchrotron	43	56
Dust	30	26
Free-free	4	3.1
Haze (DM+Bubbles)	23	12

Table 5. The breakdowns of the Galactic components (in % of the total non-CMB emission) at 23 GHz in the ROI (figure 2, left) obtained in our work (BF case) and by the Planck team in [30]. More details are in section 6.3.

JCAP03(2016)060

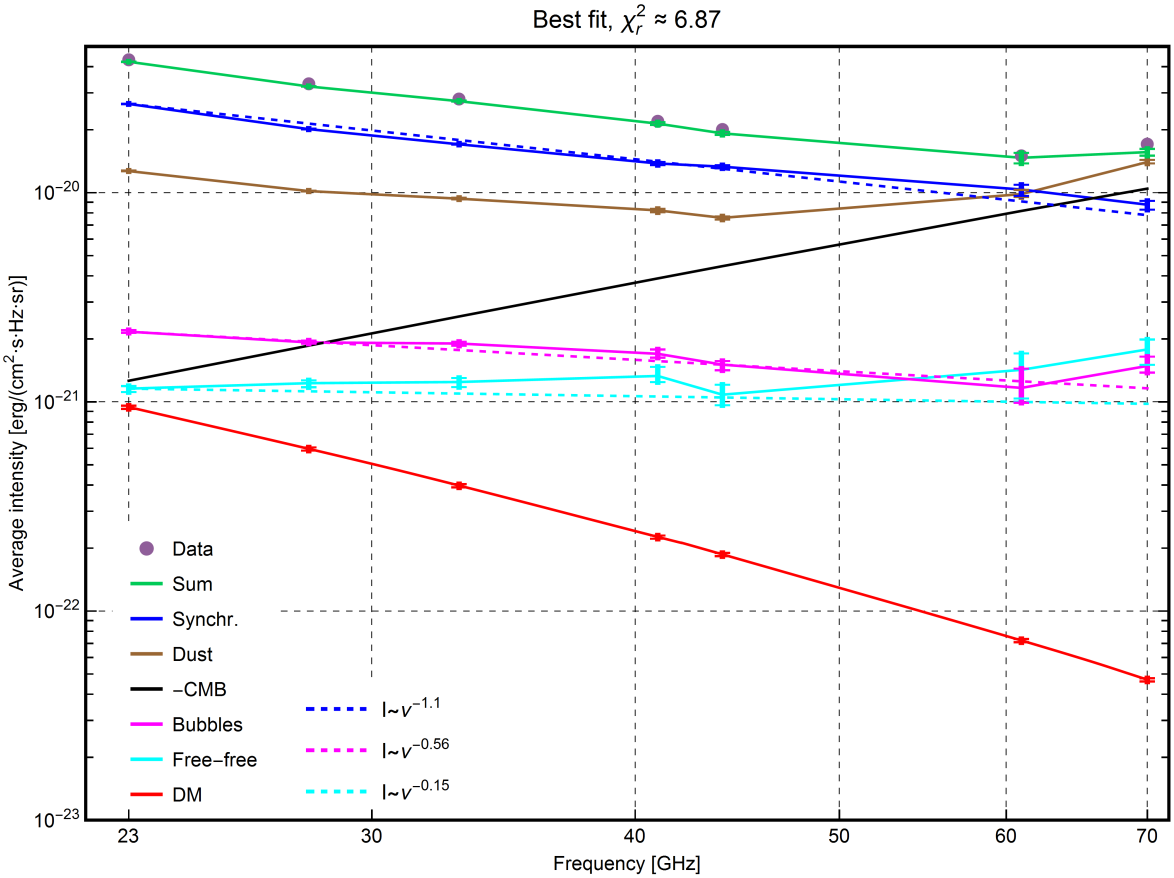


Figure 7. Spectra of all physical components (and their sum) for the BF DM configuration. Error bars correspond to statistical 68% CL. The data reported here have monopole and dipole subtracted, and the noise does not exceed the marker size used. Solid lines are results of this work, dashed lines are power-law spectra typically expected for the components considered. More details are in section 6.3.

Parameter	23 GHz	70 GHz
Range/mean of Haze contribution to the data, %	[7.2-10]/7.8	[8.7-10]/9.2
Range/mean of DM contribution to the data, %	[0.43-6.3]/1.7	[0.0043-4.7]/0.59
Range/mean of DM contribution to the Haze, %	[5.5-62]/21	[0.047-45]/6.5
Range/mean of the residuals, %	[1.7-2.1]/2.0	[7.7-9.1]/8.6

Table 6. Variation ranges and mean of the contributions for all our DM/MF/propagation models. The last row shows the residuals normalized to data. More details are in section 6.3 and section 6.4.

Note that in table 6 we also quote the range and mean of the residuals normalized to the data, which can give an indication of the systematic uncertainties (error bars in figure 7 reflect statistical errors only). Systematic uncertainties may be due to inaccuracy in the templates, the foreground modeling error introduced by our component separation setup, as well as residual systematics in the WMAP and Planck data (e.g., calibration and map-making). Studying these in detail is beyond the scope of our work, however note that they are below 10% of the sky signal at all frequencies.

Statistical uncertainties in figure 7 rarely exceed a few percent. The largest uncertainties are at high frequencies for the Bubbles and free-free component. Given the low map noise, our component separation strategy yields quite narrow N-dimensional likelihoods (N=29) for all parameters. Figure 8 shows some examples of the marginalized likelihoods, for some components' amplitudes. The distributions are typically symmetric but not necessarily Gaussian, and the dispersion is below a few percent. Two of the bottom panels also show the 2D marginalized confidence regions for the most correlated pairs of components in the BF case. Thus, we see that the largest correlation is observed between the DM and Bubbles amplitudes at 23 GHz with the correlation coefficient $R = 0.70$ (defined in the standard way as the covariance divided by the square root of the product of the variances). This degeneracy between DM and the Bubbles is likely caused by similarity in the templates. The second largest correlation, with $R = 0.65$, is seen between the dust and synchrotron at 70 GHz.

6.4 DM implications

Table 6 shows that the derived DM contribution to the data, considering all DM/MF/propagation models, is small: at 23 GHz the mean contribution is 1.7% and the BF model 2.2%. This is at the level of the residuals at 23 GHz, implying no robust detection of DM. The signal-to-noise ratio does not improve at higher frequencies because the DM emission is less pronounced and the noise increases. Some models show a 6% contribution of DM to the data at 23GHz, which is well above the residuals. However, this is also not a highly significant detection, and the global fit is, in general, poor with $\chi^2_{\rm r} \simeq 7$ for all models.

We now examine correlations between the fit quality and DM parameters. For example, one may naively expect a preference for a specific DM spectral slope by the data. The DM spectral slope β (defined as $I \sim \nu^\beta$) varies over a wide range $-5.0 < \beta < -1.1$ for all models. The best fitting models have $\beta \approx -2.7$, which is much smaller than that of both the Bubbles and synchrotron (for which we find fitted values of -0.44 ± 0.05 and -1.17 ± 0.01 respectively). However, β is not linked unambiguously to any single DM/MF/propagation parameter. Looking at more physical parameters, one can see the following correlations. The fit quality mainly depends on the MF/propagation model, it depends significantly on WIMP mass, and is almost insensitive to the annihilation channel and profile slope γ. The smallest $\chi^2_{\rm r}$ typically corresponds to the strongest MF ($B(0,0) = 100$ μG) with medium to high

JCAP03(2016)060

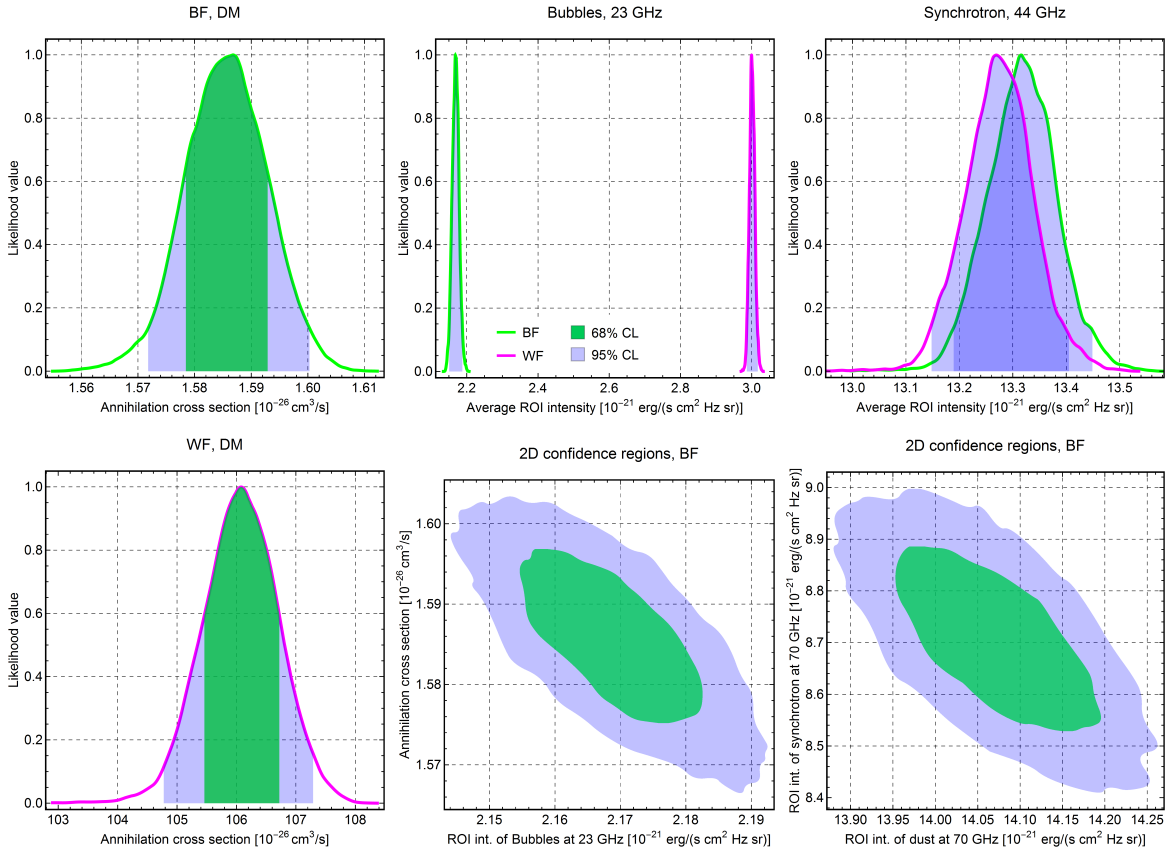


Figure 8. Examples of the marginalized 1D and 2D likelihoods for the components mentioned on each plot. The green regions show 68% confidence intervals while the blue regions 95%. 1D likelihoods are shown for both the BF and WF cases. 2D confidence regions are shown for the pairs of most correlated component intensities in the BF case. More details are in section 6.3.

vertical extent (z_B = 2.7, 6.9 kpc), strong diffusion models MAX and Reacc (see table 1), and intermediate WIMP masses around 19 GeV. Instead, the worst fits are observed for low z_B = 1.7-2.0 kpc, MED and Reacc diffusion, and low WIMP masses around 7 GeV. These general trends should not be considered in a strict sense. Particularly, one may notice that the same WIMP mass 7 GeV serves for both BF and WF models (table 3), which suggests only a weak correlation with mass. The correlation with MF/propagation configuration is stronger, and this has a quite straightforward interpretation. Comparing the BF and WF DM maps in figure 5 two main differences are apparent: the BF map has a steeper brightness profile and a vertically elongated morphology instead of the horizontal morphology observed in the WF. The vertical elongation can be naturally explained by a strong and highly extended MF with the parameters mentioned above. The reason for such a preference by the fit could be related to the degeneracy between DM and the Bubbles: the BF DM template looks much more similar to the Bubbles template than the WF template.

Figure 9 presents our main result: the best-fitting WIMP annihilation cross sections and masses for various DM/MF/propagation models. As for the more conservative constraints (figure 4), $\langle\sigma v\rangle$ values vary over an order of magnitude for different MF/propagation models, with the $\tau^+\tau^-$ channel showing less of a spread than $b\bar{b}$ does. Indeed, the MF/propagation model uncertainties significantly exceed the statistical ones. The BF $\langle\sigma v\rangle$ values reside close

JCAP03(2016)060

to the canonical cross section $3 \cdot 10^{-26}$ cm^3/s, especially for $\tau^+\tau^-$ channel. It is interesting to compare the constraints in the $\langle\sigma v\rangle - m_\chi$ plane with those required to fit the GC gamma-ray excess, also reported in figure 9. In most cases we see no intersections between the allowed regions determined by gamma-ray data analysis and our BF values. A small intersection is visible only in the case $\chi\chi \to b\bar{b}$, $\gamma = 1.1$. On one hand, very optimistic MF/propagation models with $B(0,0) = 100$ μG would be required in this case. On the other hand, the green rectangles reflect just 68% CL regions, which strengthen the potential overlap. Thus, we can conclude that for realistic parameter configurations our fit of the microwave data with DM does not prefer similar DM parameters as the gamma-ray data fits [9–11, 38], but rather favors higher cross section values (by a factor $\sim (2-7)$) for similar masses and annihilation channels. However, in case of a push of both the gamma-ray fit and MF/propagation parameters towards an optimistic side, one can reconcile the DM parameters in the case $\chi\chi \to b\bar{b}$, $\gamma = 1.1$.

Finally, comparing DM best-fit values resulting from the component separation and the more conservative constraints derived in section 5 (figure 9 vs. figure 4), it is apparent that foreground cleaning may improve the sensitivity of a DM search by a factor of 10-100. However, as was already mentioned in section 5, any component separation procedure yields results whose validity depends on the foreground and signal modeling.

7 Discussion and conclusions

In this paper, we addressed the DM implications of the WMAP-Planck Haze in the context of models that could explain the GC gamma-ray excess. We investigated whether the microwave observations are compatible with a DM contribution to the Haze emission, derived constraints on DM particle parameters, and compared them to those needed to fit the GC gamma-ray excess.

We modeled the synchrotron emission in the microwave portion of the electromagnetic spectrum due to DM annihilation, making various assumptions about the DM density distribution, the DM particle model, as well as the MF and CR propagation models. DM emission intensity sky maps for various DM/MF/propagation models were created and compared with the data at seven WMAP-Planck frequencies. To test the consistency of the DM models with the data, we adopted two approaches. First we adopted a conservative approach which only considered CMB fluctuations and DM as contributing to the total sky intensity, while second we attempted to separate all the emission components including a potential DM signal using template fitting. The first approach yields relatively weak, but very robust DM constraints (see figure 4). The second one probes much lower cross sections, with the best-fit cross-sections reaching the thermal relic expectation $\langle\sigma v\rangle = 3 \cdot 10^{-26}$ cm^3/s (see figure 9), however this approach is more dependent on the details of the modeling and the results are less straightforward to interpret due to degeneracies between DM and other model components.

We summarize our results as follows:

- The (weak) upper limits obtained with the conservative approach are compatible with both the thermal cross section and the signal regions of DM models that fit the gamma-ray excess that have been determined in other works.

- In the component separation analysis, the overall quality of our fits is poor, indicating that we lack sufficient understanding of foregrounds, or that template fitting is a too

JCAP03(2016)060

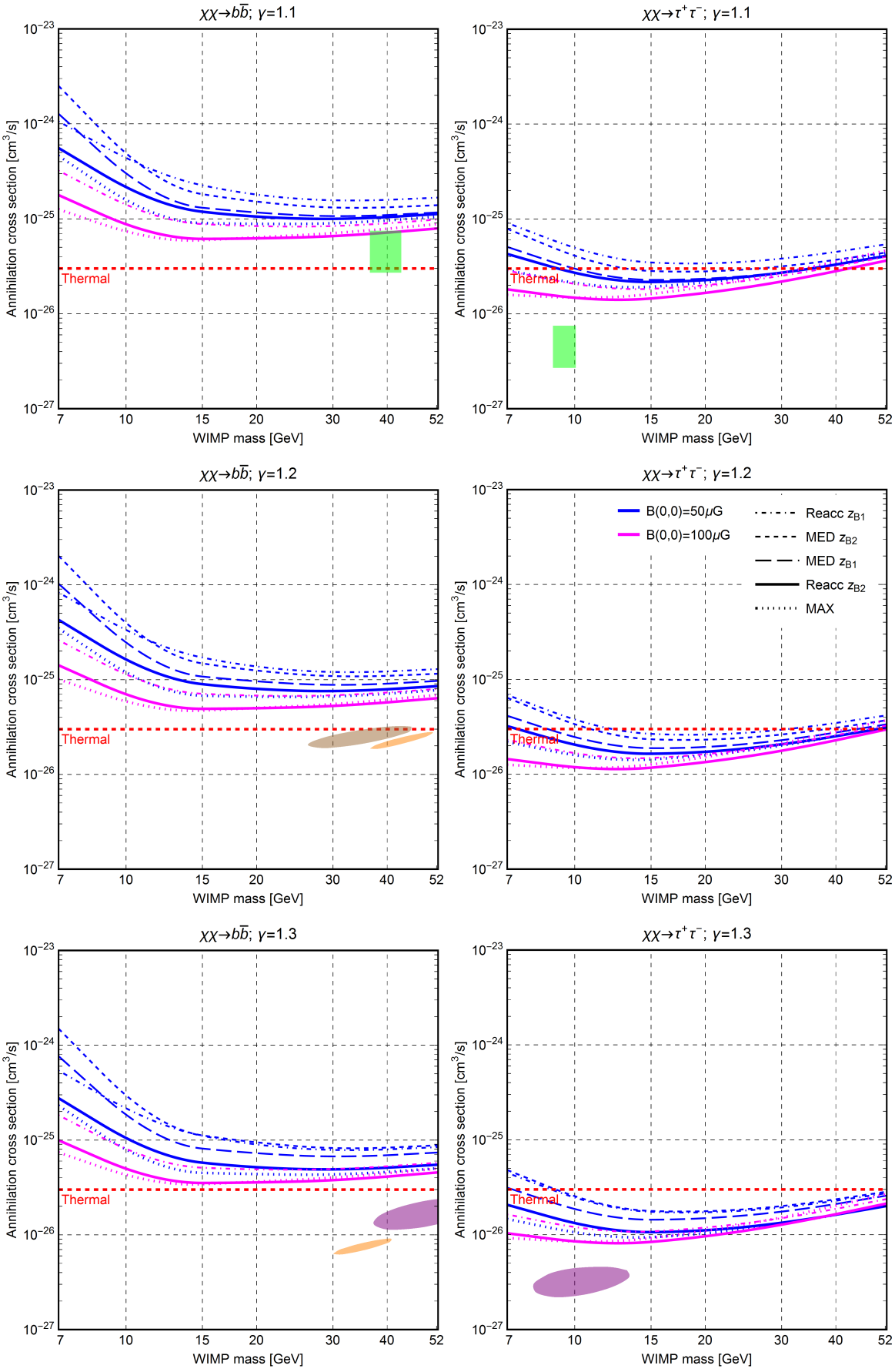


Figure 9. *Continue.*

JCAP03(2016)060

Figure 9. *(preceding page)* DM constraints derived at 95% CL resulting from our component separation procedure for various DM/MF/propagation models. Limiting cross section values are indistinguishable from the BF ones at this line resolution. The red dashed horizontal line indicates the thermal relic cross section $\langle\sigma v\rangle = 3 \cdot 10^{-26}$ cm^3/s. In addition to the best-fit curves we also present here DM parameter regions (same as in figure 4) needed to fit the GC gamma-ray excess. We see again that our constraints mainly do not contradict them. See more details in section 6.4.

simplistic procedure for explaining the observed signal in the sky area under consideration.

- Adding additional components that produce emission at tens of degrees around the GC to the standard astrophysical foregrounds and CMB considerably improves the fit. Thus we confirm the clear presence of the Haze: a microwave excess not explained by the CMB, (spinning) dust, free-free, and synchrotron emission, which contributes (7.2-10)% of the intensity at 23 GHz and (8.7-10)% at 70 GHz in our selected sky region near the GC. We also derive the Haze spectrum (here represented by the sum of the DM and Bubbles components), obtaining $I \sim \nu^{-0.84\pm0.04}$. This is somewhat different from the slope of -0.56 reported in [30]. However, this is not a completely equivalent comparison due to the presence of the DM template in our Haze fit. Our derived Haze spectrum significantly differs from that of the usual synchrotron ($I \sim \nu^{-1.17\pm0.01}$), which suggests the Haze originates from a population of electrons distinct from typical Galactic CR electrons.

- We considered two possible origins of the Haze in constructing our templates: i) DM annihilation and ii) a counterpart of the Fermi Bubbles. We showed that the data do not have a strong preference for either of these two components when considered separately; they provide comparable fit qualities with a mild preference towards the Bubbles. However, inclusion of both templates together provides a better fit than adding either template individually. Thus, both emission mechanisms can be contributing to the Haze. In this scenario, DM constitutes (5.5-62)% (on average 21%) of the Haze emission and (0.43-6.3)% (on average 1.7%) of the total emission at 23 GHz. The DM spectrum, as derived from our modeling of the DM emission, is generally steeper than the Bubbles fit-inferred spectrum. The amplitude of the latter exceeds that of the DM, especially at high frequencies.

- Given the overall poor quality of the fits, it is not possible to confidently attribute any of the emission to a DM model, nor to single out a particular DM model as the one preferred by the data. In general the data show a mild preference for a strong MF that is extended above the plane. This kind of MF generates DM emission with a vertically elongated morphology that is aligned with the Bubbles observed in gamma rays.

- For realistic MF/propagation parameter values, the best-fit cross sections as determined by the component separation procedure are a factor ≈(2-7) higher than those favored to explain the GC gamma-ray excess, and are in tension with other constraints from indirect DM searches (e.g., [4]). Note, however, that in the case of $\chi\chi \to b\bar{b}$, $\gamma = 1.1$ an agreement between microwave and gamma-ray fits exists for optimistic MF/propagation configurations.

JCAP03(2016)060

Looking forward, although multi-frequency studies clearly offer complementary information to that from indirect searches in gamma rays, to make these searches competitive it will be necessary to better understand the various non-DM contributions to the total microwave emission. This could be pursued by considering other component separation strategies and an optimization of the ROI.

Acknowledgments

It is a pleasure to thank Loris Colombo for extensive help with the CMB emission modeling and Planck data interpretation, Andrew Strong for valuable consultations on GALPROP, and Antony Lewis for assistance with GetDist. AE and EP acknowledge the support of NASA grant NNX13AP25G and the usage of the computers at the USC High Performance Computing Center. JG acknowledges support from NASA through Einstein Postdoctoral Fellowship grant PF1-120089 awarded by the Chandra X-ray Center, which is operated by the Smithsonian Astrophysical Observatory for NASA under contract NAS8-03060, and from a Marie Curie International Incoming Fellowship in the project "IGMultiWave (PIIF-GA-2013-628997) – ADD". We also acknowledge the use of the LevelScheme package for Mathematica developed by Mark Caprio [76], it greatly helped in preparation of high-quality plots. In addition, this research used resources of the National Energy Research Scientific Computing Center, which is supported by the Office of Science of the U.S. Department of Energy under Contract No. DE-AC02-05CH11231. Some of the results in this paper have been derived using the HEALPix [58] package.

References

[1] G. Bertone, *Particle dark matter - observations, models and searches*, Cambridge University Press (2010).

[2] Fermi-LAT collaboration, W.B. Atwood et al., *The Large Area Telescope on the Fermi Gamma-ray Space Telescope Mission*, *Astrophys. J.* **697** (2009) 1071 [arXiv:0902.1089] [INSPIRE].

[3] D. Hooper, C. Kelso and F.S. Queiroz, *Stringent and Robust Constraints on the Dark Matter Annihilation Cross Section From the Region of the Galactic Center*, *Astropart. Phys.* **46** (2013) 55 [arXiv:1209.3015] [INSPIRE].

[4] Fermi-LAT collaboration, M. Ackermann et al., *Searching for Dark Matter Annihilation from Milky-Way Dwarf Spheroidal Galaxies with Six Years of Fermi Large Area Telescope Data*, *Phys. Rev. Lett.* **115** (2015) 231301 [arXiv:1503.02641] [INSPIRE].

[5] M.R. Buckley, E. Charles, J.M. Gaskins, A.M. Brooks, A. Drlica-Wagner et al., *Search for Gamma-ray Emission from Dark Matter Annihilation in the Large Magellanic Cloud with the Fermi Large Area Telescope*, *Phys. Rev.* **D 91** (2015) 102001 [arXiv:1502.01020] [INSPIRE].

[6] L. Goodenough and D. Hooper, *Possible Evidence For Dark Matter Annihilation In The Inner Milky Way From The Fermi Gamma Ray Space Telescope*, arXiv:0910.2998 [INSPIRE].

[7] D. Hooper and L. Goodenough, *Dark Matter Annihilation in The Galactic Center As Seen by the Fermi Gamma Ray Space Telescope*, *Phys. Lett.* **B 697** (2011) 412 [arXiv:1010.2752] [INSPIRE].

[8] K.N. Abazajian and M. Kaplinghat, *Detection of a Gamma-Ray Source in the Galactic Center Consistent with Extended Emission from Dark Matter Annihilation and Concentrated Astrophysical Emission*, *Phys. Rev.* **D 86** (2012) 083511 [*Erratum ibid.* **D 87** (2013) 129902] [arXiv:1207.6047] [INSPIRE].

JCAP03(2016)060

[9] C. Gordon and O. Macias, *Dark Matter and Pulsar Model Constraints from Galactic Center Fermi-LAT Gamma Ray Observations*, *Phys. Rev.* **D 88** (2013) 083521 [arXiv:1306.5725] [INSPIRE].

[10] T. Daylan, D.P. Finkbeiner, D. Hooper, T. Linden, S.K.N. Portillo et al., *The characterization of the gamma-ray signal from the central Milky Way: A case for annihilating dark matter*, *Phys. Dark Univ.* **12** (2016) 1 [arXiv:1402.6703] [INSPIRE].

[11] K.N. Abazajian, N. Canac, S. Horiuchi and M. Kaplinghat, *Astrophysical and Dark Matter Interpretations of Extended Gamma-Ray Emission from the Galactic Center*, *Phys. Rev.* **D 90** (2014) 023526 [arXiv:1402.4090] [INSPIRE].

[12] F. Calore, I. Cholis and C. Weniger, *Background model systematics for the Fermi GeV excess*, *JCAP* **03** (2015) 038 [arXiv:1409.0042] [INSPIRE].

[13] D. Hooper, I. Cholis, T. Linden, J. Siegal-Gaskins and T. Slatyer, *Pulsars Cannot Account for the Inner Galaxy's GeV Excess*, *Phys. Rev.* **D 88** (2013) 083009 [arXiv:1305.0830] [INSPIRE].

[14] I. Cholis, D. Hooper and T. Linden, *Challenges in Explaining the Galactic Center Gamma-Ray Excess with Millisecond Pulsars*, *JCAP* **06** (2015) 043 [arXiv:1407.5625] [INSPIRE].

[15] Q. Yuan and B. Zhang, *Millisecond pulsar interpretation of the Galactic center gamma-ray excess*, *JHEAp* **3-4** (2014) 1 [arXiv:1404.2318] [INSPIRE].

[16] J. Petrović, P.D. Serpico and G. Zaharijaš, *Millisecond pulsars and the Galactic Center gamma-ray excess: the importance of luminosity function and secondary emission*, *JCAP* **02** (2015) 023 [arXiv:1411.2980] [INSPIRE].

[17] T.D. Brandt and B. Kocsis, *Disrupted Globular Clusters Can Explain the Galactic Center Gamma Ray Excess*, *Astrophys. J.* **812** (2015) 15 [arXiv:1507.05616] [INSPIRE].

[18] J. Petrović, P.D. Serpico and G. Zaharijaš, *Galactic Center gamma-ray "excess" from an active past of the Galactic Centre?*, *JCAP* **10** (2014) 052 [arXiv:1405.7928] [INSPIRE].

[19] E. Carlson and S. Profumo, *Cosmic Ray Protons in the Inner Galaxy and the Galactic Center Gamma-Ray Excess*, *Phys. Rev.* **D 90** (2014) 023015 [arXiv:1405.7685] [INSPIRE].

[20] I. Cholis, C. Evoli, F. Calore, T. Linden, C. Weniger and D. Hooper, *The Galactic Center GeV Excess from a Series of Leptonic Cosmic-Ray Outbursts*, *JCAP* **12** (2015) 005 [arXiv:1506.05119] [INSPIRE].

[21] R. Bartels, S. Krishnamurthy and C. Weniger, *Strong support for the millisecond pulsar origin of the Galactic center GeV excess*, *Phys. Rev. Lett.* **116** (2016) 051102 [arXiv:1506.05104] [INSPIRE].

[22] S.K. Lee, M. Lisanti, B.R. Safdi, T.R. Slatyer and W. Xue, *Evidence for Unresolved γ-Ray Point Sources in the Inner Galaxy*, *Phys. Rev. Lett.* **116** (2016) 051103 [arXiv:1506.05124] [INSPIRE].

[23] T. Linden, *Known Radio Pulsars Do Not Contribute to the Galactic Center Gamma-Ray Excess*, *Phys. Rev.* **D 93** (2016) 063003 [arXiv:1509.02928] [INSPIRE].

[24] D.P. Finkbeiner, *Microwave ism emission observed by wmap*, *Astrophys. J.* **614** (2004) 186 [astro-ph/0311547] [INSPIRE].

[25] D. Hooper, D.P. Finkbeiner and G. Dobler, *Possible evidence for dark matter annihilations from the excess microwave emission around the center of the Galaxy seen by the Wilkinson Microwave Anisotropy Probe*, *Phys. Rev.* **D 76** (2007) 083012 [arXiv:0705.3655] [INSPIRE].

[26] M. Su, T.R. Slatyer and D.P. Finkbeiner, *Giant Gamma-ray Bubbles from Fermi-LAT: AGN Activity or Bipolar Galactic Wind?*, *Astrophys. J.* **724** (2010) 1044 [arXiv:1005.5480] [INSPIRE].

JCAP03(2016)060

[27] Fermi-LAT collaboration, M. Ackermann et al., *The Spectrum and Morphology of the Fermi Bubbles*, *Astrophys. J.* **793** (2014) 64 [arXiv:1407.7905] [INSPIRE].

[28] Y. Sofue, *Bipolar-hyper-shell galactic center statrburst model: further evidence from rosat data and new radio and x-ray simulations*, *Astrophys. J.* **540** (2000) 224 [astro-ph/9912528] [INSPIRE].

[29] J. Bland-Hawthorn and M. Cohen, *The Large scale bipolar wind in the Galactic Center*, *Astrophys. J.* **582** (2003) 246 [astro-ph/0208553] [INSPIRE].

[30] Planck collaboration, P.A.R. Ade et al., *Planck Intermediate Results. IX. Detection of the Galactic haze with Planck*, *Astron. Astrophys.* **554** (2013) A139 [arXiv:1208.5483] [INSPIRE].

[31] E. Carretti, R.M. Crocker, L. Staveley-Smith, M. Haverkorn, C. Purcell, B.M. Gaensler et al., *Giant Magnetized Outflows from the Centre of the Milky Way*, *Nature* **493** (2013) 66 [arXiv:1301.0512] [INSPIRE].

[32] R.M. Crocker, G.V. Bicknell, A.M. Taylor and E. Carretti, *A Unified Model of the Fermi Bubbles, Microwave Haze and Polarized Radio Lobes: Reverse Shocks in the Galactic Center's Giant Outflows*, *Astrophys. J.* **808** (2015) 107 [arXiv:1412.7510] [INSPIRE].

[33] F. Iocco, M. Pato, G. Bertone and P. Jetzer, *Dark Matter distribution in the Milky Way: microlensing and dynamical constraints*, *JCAP* **11** (2011) 029 [arXiv:1107.5810] [INSPIRE].

[34] F. Nesti and P. Salucci, *The Dark Matter halo of the Milky Way, AD 2013*, *JCAP* **07** (2013) 016 [arXiv:1304.5127] [INSPIRE].

[35] F. Calore, N. Bozorgnia, M. Lovell, G. Bertone, M. Schaller, C.S. Frenk et al., *Simulated Milky Way analogues: implications for dark matter indirect searches*, *JCAP* **12** (2015) 053 [arXiv:1509.02164] [INSPIRE].

[36] M. Pato, F. Iocco and G. Bertone, *Dynamical constraints on the dark matter distribution in the Milky Way*, *JCAP* **12** (2015) 001 [arXiv:1504.06324] [INSPIRE].

[37] F. Iocco, M. Pato and G. Bertone, *Evidence for dark matter in the inner Milky Way*, *Nature Phys.* **11** (2015) 245–248 [arXiv:1502.03821] [INSPIRE].

[38] F. Calore, I. Cholis, C. McCabe and C. Weniger, *A Tale of Tails: Dark Matter Interpretations of the Fermi GeV Excess in Light of Background Model Systematics*, *Phys. Rev.* **D 91** (2015) 063003 [arXiv:1411.4647] [INSPIRE].

[39] J.F. Navarro, C.S. Frenk and S.D.M. White, *A Universal density profile from hierarchical clustering*, *Astrophys. J.* **490** (1997) 493 [astro-ph/9611107] [INSPIRE].

[40] M. Kamionkowski, S.M. Koushiappas and M. Kuhlen, *Galactic Substructure and Dark Matter Annihilation in the Milky Way Halo*, *Phys. Rev.* **D 81** (2010) 043532 [arXiv:1001.3144] [INSPIRE].

[41] M. Cirelli, G. Corcella, A. Hektor, G. Hutsi, M. Kadastik, P. Panci et al., *PPPC 4 DM ID: A Poor Particle Physicist Cookbook for Dark Matter Indirect Detection*, *JCAP* **03** (2011) 051 [*Erratum ibid.* **1210** (2012) E01] [arXiv:1012.4515] [INSPIRE].

[42] *PPPC 4 DM ID - A Poor Particle Physicist Cookbook for Dark Matter Indirect Detection*, http://www.marcocirelli.net/PPPC4DMID.html.

[43] P. Ciafaloni, D. Comelli, A. Riotto, F. Sala, A. Strumia and A. Urbano, *Weak Corrections are Relevant for Dark Matter Indirect Detection*, *JCAP* **03** (2011) 019 [arXiv:1009.0224] [INSPIRE].

[44] G. Dobler, I. Cholis and N. Weiner, *The Fermi Gamma-Ray Haze from Dark Matter Annihilations and Anisotropic Diffusion*, *Astrophys. J.* **741** (2011) 25 [arXiv:1102.5095] [INSPIRE].

JCAP03(2016)060

[45] D. Malyshev, I. Cholis and J.D. Gelfand, *Fermi Gamma-ray Haze via Dark Matter and Millisecond Pulsars*, *Astrophys. J.* **722** (2010) 1939 [arXiv:1002.0587] [INSPIRE].

[46] Y. Mambrini, M.H.G. Tytgat, G. Zaharijaš and B. Zaldivar, *Complementarity of Galactic radio and collider data in constraining WIMP dark matter models*, *JCAP* **11** (2012) 038 [arXiv:1206.2352] [INSPIRE].

[47] N. Fornengo, R.A. Lineros, M. Regis and M. Taoso, *Galactic synchrotron emission from WIMPs at radio frequencies*, *JCAP* **01** (2012) 005 [arXiv:1110.4337] [INSPIRE].

[48] R.M. Crocker, D. Jones, F. Melia, J. Ott and R.J. Protheroe, *A lower limit of 50 microGauss for the magnetic field near the Galactic Centre*, *Nature* **468** (2010) 65 [arXiv:1001.1275] [INSPIRE].

[49] R.M. Crocker, D.I. Jones, F. Aharonian, C.J. Law, F. Melia and J. Ott, *Gamma-Rays and the Far-Infrared-Radio Continuum Correlation Reveal a Powerful Galactic Center Wind*, *Mon. Not. Roy. Astron. Soc.* **411** (2011) L11 [arXiv:1009.4340] [INSPIRE].

[50] R. Stepanov, T.G. Arshakian, R. Beck, P. Frick and M. Krause, *Magnetic field structures of galaxies derived from analysis of Faraday rotation measures and perspectives for the SKA*, *Astron. Astrophys.* **480** (2008) 45 [arXiv:0711.1267] [INSPIRE].

[51] M. Haverkorn and V. Heesen, *Magnetic fields in galactic haloes*, *Space Sci. Rev.* **166** (2012) 133 [arXiv:1102.3701] [INSPIRE].

[52] M. Haverkorn, *Magnetic Fields in the Milky Way*, arXiv:1406.0283 [INSPIRE].

[53] *The GALPROP code for cosmic-ray transport and diffuse emission production*, https://sourceforge.net/projects/galprop [http://galprop.stanford.edu/].

[54] A.W. Strong and I.V. Moskalenko, *Propagation of cosmic-ray nucleons in the galaxy*, *Astrophys. J.* **509** (1998) 212 [astro-ph/9807150] [INSPIRE].

[55] D. Hooper and T. Linden, *Gamma Rays From The Galactic Center and the WMAP Haze*, *Phys. Rev.* **D 83** (2011) 083517 [arXiv:1011.4520] [INSPIRE].

[56] J. Lavalle, D. Maurin and A. Putze, *Direct constraints on diffusion models from cosmic-ray positron data: Excluding the minimal model for dark matter searches*, *Phys. Rev.* **D 90** (2014) 081301 [arXiv:1407.2540] [INSPIRE].

[57] R. Trotta, G. Johannesson, I.V. Moskalenko, T.A. Porter, R.R. de Austri and A.W. Strong, *Constraints on cosmic-ray propagation models from a global Bayesian analysis*, *Astrophys. J.* **729** (2011) 106 [arXiv:1011.0037] [INSPIRE].

[58] K.M. Gorski, E. Hivon, A.J. Banday, B.D. Wandelt, F.K. Hansen, M. Reinecke et al., *HEALPix - A Framework for high resolution discretization and fast analysis of data distributed on the sphere*, *Astrophys. J.* **622** (2005) 759 [astro-ph/0409513] [INSPIRE].

[59] *Wilkinson Microwave Anisotropy Probe*, http://lambda.gsfc.nasa.gov/product/map/dr5/masks_info.cfm.

[60] *Planck Public Data Release 2 Mission Ancillary Data*, http://irsa.ipac.caltech.edu/data/Planck/release_2/ancillary-data/.

[61] PLANCK collaboration, P.A.R. Ade et al., *Planck 2013 results. XII. Diffuse component separation*, *Astron. Astrophys.* **571** (2014) A12 [arXiv:1303.5072] [INSPIRE].

[62] J. Peacock, *Cosmological physics*, Cambridge University Press (1999).

[63] PLANCK collaboration, P.A.R. Ade et al., *Planck 2013 results. XVI. Cosmological parameters*, *Astron. Astrophys.* **571** (2014) A16 [arXiv:1303.5076] [INSPIRE].

[64] http://irsa.ipac.caltech.edu/data/Planck/release_1/.

JCAP03(2016)060

[65] T. Lacroix, C. Boehm and J. Silk, *Fitting the Fermi-LAT GeV excess: On the importance of including the propagation of electrons from dark matter*, *Phys. Rev.* **D 90** (2014) 043508 [arXiv:1403.1987] [INSPIRE].

[66] G. Dobler and D.P. Finkbeiner, *Extended Anomalous Foreground Emission in the WMAP 3-Year Data*, *Astrophys. J.* **680** (2008) 1222 [arXiv:0712.1038] [INSPIRE].

[67] D. Pietrobon et al., *Analysis of WMAP 7-year Temperature Data: Astrophysics of the Galactic Haze*, *Astrophys. J.* **755** (2012) 69 [arXiv:1110.5418] [INSPIRE].

[68] G. Dobler, *Identifying the Radio Bubble Nature of the Microwave Haze*, *Astrophys. J.* **760** (2012) L8 [arXiv:1208.2690] [INSPIRE].

[69] *Data Hosted on LAMBDA*, http://lambda.gsfc.nasa.gov/product/.

[70] PLANCK collaboration, P.A.R. Ade et al., *Planck 2013 results. XIII. Galactic CO emission*, *Astron. Astrophys.* **571** (2014) A13 [arXiv:1303.5073] [INSPIRE].

[71] D.J. Schlegel, D.P. Finkbeiner and M. Davis, *Maps of dust IR emission for use in estimation of reddening and CMBR foregrounds*, *Astrophys. J.* **500** (1998) 525 [astro-ph/9710327] [INSPIRE].

[72] D.P. Finkbeiner, M. Davis and D.J. Schlegel, *Extrapolation of galactic dust emission at 100 microns to CMBR frequencies using FIRAS*, *Astrophys. J.* **524** (1999) 867 [astro-ph/9905128] [INSPIRE].

[73] D.P. Finkbeiner, *A Full-Sky Hα template for microwave foreground prediction*, *Astrophys. J. Suppl.* **146** (2003) 407 [astro-ph/0301558] [INSPIRE].

[74] C.G.T. Haslam, C.J. Salter, H. Stoffel and W.E. Wilson, *A 408 MHz all-sky continuum survey. II. The ATLAS of contour maps*, *Astron. Astrophys. Suppl. Ser.* **47** (1982) 1 [INSPIRE].

[75] PLANCK collaboration, R. Adam et al., *Planck 2015 results. X. Diffuse component separation: Foreground maps*, arXiv:1502.01588 [INSPIRE].

[76] *LevelScheme*, http://scidraw.nd.edu/levelscheme/.

[77] *GALPROP code with DM component*, https://github.com/a-e-egorov/GALPROP_DM.git.

JCAP03(2016)060

Journal of Cosmology and Astroparticle Physics
An IOP and SISSA journal

Dark matter searches by the planned gamma-ray telescope GAMMA-400

Andrey E. Egorov,[a,1] **Nikolay P. Topchiev,**[a] **Arkadiy M. Galper,**[a,b] **Oleg D. Dalkarov,**[a] **Alexey A. Leonov,**[a,b] **Sergey I. Suchkov**[a] **and Yuriy T. Yurkin**[b]

[a]Nuclear Physics and Astrophysics Division, Lebedev Physical Institute, Leninskii prospect, 53, Moscow, Russia
[b]National Research Nuclear University MEPhI, Kashirskoe highway, 31, Moscow, Russia
E-mail: eae14@yandex.ru, tnp51@yandex.ru, amgalper@mephi.ru, dalkarovod@lebedev.ru, alexeyanatolievich@rambler.ru, soutch@mail.ru, YTYurkin@mephi.ru

Received May 23, 2020
Accepted September 29, 2020
Published November 24, 2020

Abstract. Our paper reviews the planned space-based gamma-ray telescope GAMMA-400 and evaluates in details its opportunities in the field of dark matter (DM) indirect searches. We estimated the GAMMA-400 mean sensitivity to the diphoton DM annihilation cross section in the Galactic center for DM particle masses in the range of 1–500 GeV. We obtained the sensitivity gain at least by 1.2–1.5 times (depending on DM particle mass) with respect to the expected constraints from 12 years of observations by Fermi-LAT for the case of Einasto DM density profile. The joint analysis of the data from both telescopes may yield the gain up to 1.8–2.3 times. Thus the sensitivity reaches the level of annihilation cross section $\langle\sigma v\rangle_{\gamma\gamma}(m_\chi = 100\,\text{GeV}) \approx 10^{-28}\,\text{cm}^3/\text{s}$. This will allow us to test the hypothesized narrow lines predicted by specific DM models, particularly the recently proposed pseudo-Goldstone boson DM model. We also considered the decaying DM — in this case the joint analysis may yield the sensitivity gain up to 1.1–2.0 times reaching the level of DM lifetime $\tau_{\gamma\nu}(m_\chi = 100\,\text{GeV}) \approx 2 \cdot 10^{29}\,\text{s}$. We estimated the GAMMA-400 sensitivity to axion-like particle (ALP) parameters by a potential observation of the supernova explosion in the Local Group. This is very sensitive probe of ALPs reaching the level of ALP-photon coupling constant $g_{a\gamma} \sim 10^{-13}\,\text{GeV}^{-1}$ for ALP masses $m_a \lesssim 1\,\text{neV}$. We also calculated the sensitivity to ALPs by constraining the modulations in the spectra of the Galactic gamma-ray pulsars due to possible ALP-photon conversion. GAMMA-400 is expected to be more sensitive than the CAST helioscope for ALP masses $m_a \approx (1\text{–}10)\,\text{neV}$ reaching $g_{a\gamma}^{\text{min}} \approx 2 \cdot 10^{-11}\,\text{GeV}^{-1}$. Other potentially interesting targets and candidates are briefly considered too.

Keywords: axions, dark matter experiments, dark matter theory, gamma ray experiments
ArXiv ePrint: 2005.09032

[1]Corresponding author.

© 2020 IOP Publishing Ltd and Sissa Medialab
https://doi.org/10.1088/1475-7516/2020/11/049

JCAP11(2020)049

Contents

1 A brief overview of the GAMMA-400 project 1

2 GAMMA-400 sensitivity to the spectral lines due to DM annihilation or decay in the Galactic center 4

3 ALP discovery potential by an observation of the supernova explosion in the Local Group 10

4 ALP constraining potential by observations of bright gamma-ray pulsars 16

5 Miscellaneous targets 19

6 Conclusions 21

JCAP11(2020)049

1 A brief overview of the GAMMA-400 project

GAMMA-400 (Gamma-ray Astronomical Multifunctional Modular Apparatus up to (initially) $\approx 400\,\mathrm{GeV}$) is the Russian space-based pair-converting calorimetric gamma-ray telescope planned for a launch after 2026 (e.g. [1]). It is expected to continue gamma-ray astronomy development after Fermi-LAT and other instruments using better characteristics. One of the key mission objectives is indeed DM indirect searches, where the gamma-ray range is historically the most promising channel (e.g. [2]). Our paper describes quantitatively the main directions in the field for GAMMA-400, where it can bring a significant progress. Mainly this refers to the two most popular DM candidates — WIMPs and ALPs. But other candidates are being considered too, especially in section 2. Thus section 2 is dedicated to estimation of GAMMA-400 sensitivity to the narrow spectral lines due to DM annihilation or decay in the Galactic center (GC) for a quite generic DM candidate. Section 3 analyzes the potential to discover/constrain ALPs by an observation of a nearby supernova explosion. Section 4 is dedicated to estimation of GAMMA-400 sensitivity to ALPs by observations of bright gamma-ray pulsars. Section 5 briefly discusses other targets: globular clusters, AGNs and others. And section 6 summarizes the obtained results.

In this section we briefly describe the expected GAMMA-400 performance based on our detailed simulations. In general, our telescope is capable for both photon and electron/positron detection (without a possibility to distinguish between electrons and positrons). The lower boundary of sensitivity range is $\approx 20\,\mathrm{MeV}$ and determined by a sophisticated combination of various factors like backgrounds, detector noises, Coulomb scattering of a pair produced in the converter-tracker etc. The upper boundary is determined mainly by statistical flux limitations and reaches $\sim 10\,\mathrm{TeV}$ for $e^{\pm}$ and $\sim 1\,\mathrm{TeV}$ for gammas. The telescope field of view determined analogously to that of Fermi-LAT is $\approx 1\,\mathrm{sr}$. In general, our instrument is designed for the dedicated pointed deep observations of several interesting regions of the gamma-ray sky oppositely to the uniform survey strategy of Fermi-LAT.

Figure 1 shows the GAMMA-400 physical scheme, figure 2 demonstrates the dependence of all key characteristics on the energy inside the sensitivity range in comparison with other gamma-ray telescopes. The effective area, angular and energy resolutions are shown in comparison with Fermi-LAT for two cases — using the whole converter-tracker and only its "thin" part. The latter for Fermi-LAT is also often referred as Fermi-Front [3]. GAMMA-400 has essentially the same feature in the form of 4 thin tungsten layers of $0.025X_0$ (radiation length units) and 2 layers without tungsten at the back of the converter-tracker (see figure 1). These

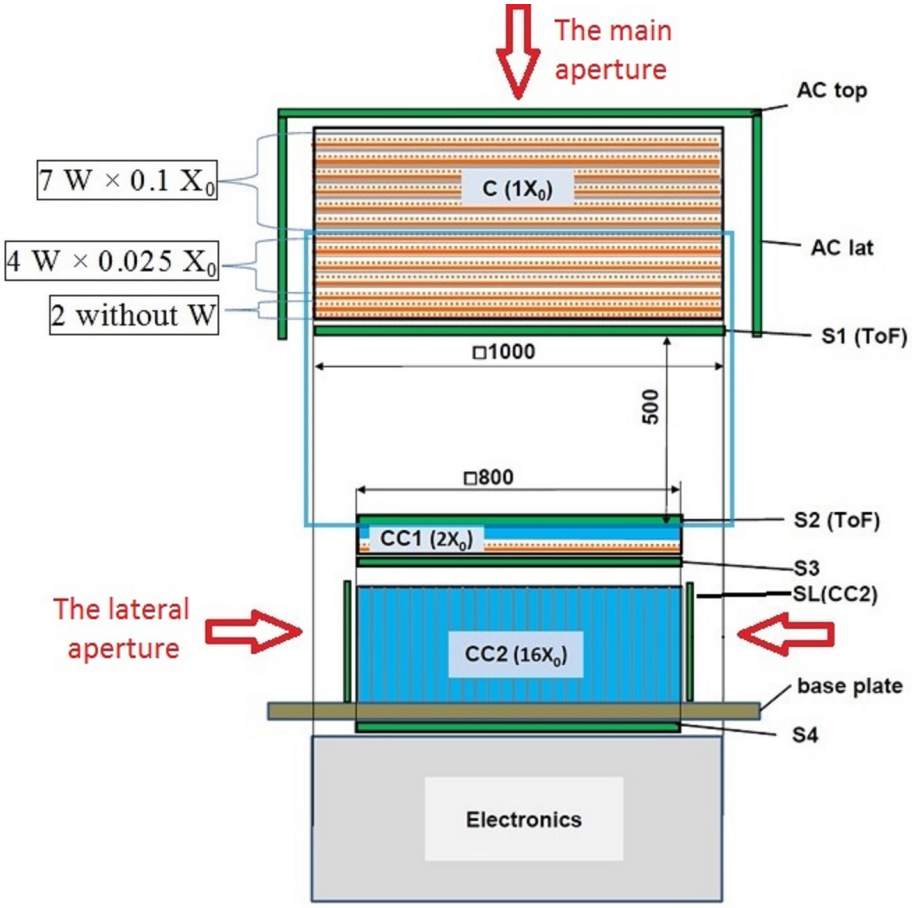


Figure 1. The GAMMA-400 physical scheme. All sizes are in mm. "AC" denotes the anticoincidence system, "C" is the converter-tracker, "ToF" is the time-of-flight system and "CC" is the coordinate calorimeter. The big cyan rectangle encloses the part of the telescope used in the detection mode of low-energy photons by the thin layers of the converter-tracker referred below as the thin converter. More details see in section 1.

thin layers provide significantly better angular and energy resolutions (see the dashed lines in figure 2) due to reduced Coulomb scattering of the produced pair being tracked. Indeed the effective area of the thin converter is significantly lower than the total area. However at low energies it is compensated by large photon fluxes. In summary, we can see that the angular resolution of the thin converter of GAMMA-400 significantly exceeds that of Fermi-LAT at any energy. The whole converter of GAMMA-400 outperforms Fermi-LAT at energies above $\approx 10\,\mathrm{GeV}$ and reaches $\sim 0.01^\circ$ at 100 GeV. The energy resolution superiority is even greater: it begins from $\approx 200\,\mathrm{MeV}$ (for the whole converter) and reaches $\approx 2\%$ at 100 GeV (the thin converter of Fermi-LAT does not differ much from the whole one by energy resolution [3]). The comparison with DAMPE and ground-based telescopes is also shown.

All characteristics described above refer to the classical mode of photon detection, when the photon enters the converter without interaction in the anticoincidence system and produces a pair, which releases its energy in the calorimeter. Such a mode can be called the main aperture detection. However, in principle one can detect photons entering the calorimeter directly from its lateral surfaces (see figure 1). For this purpose our telescope will have the lateral detectors of calorimeter (SL(CC2)). We call this mode the lateral aperture detection. Indeed it has a photon direction reconstruction worse than that for the main aperture. How-

JCAP11(2020)049

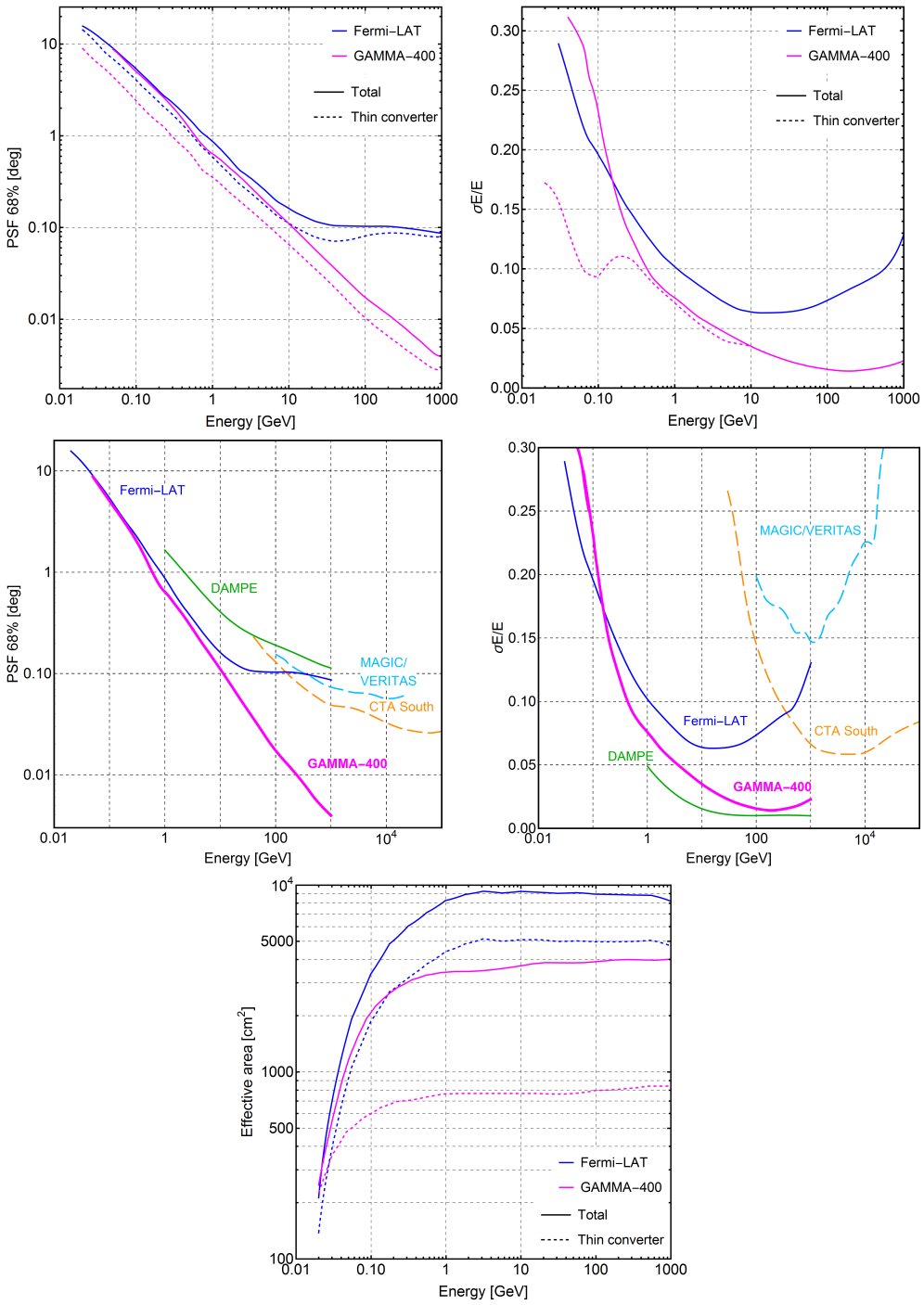


Figure 2. The energy dependence of the key characteristics of GAMMA-400 in comparison with other telescopes (performance data for Fermi-LAT was taken from [3]). *Top left*: the angular resolution as the radius of point spread function (PSF) at the level of 68% containment. *Top right*: the energy resolution as the relative standard deviation of the measured photon energy distribution. *Middle left*: GAMMA-400 and Fermi-LAT (whole converter-tracker) angular resolution in comparison with DAMPE [4] and the ground-based Cherenkov telescopes MAGIC [5], VERITAS [6] and CTA South [7]. *Middle right*: same for the energy resolution. *Bottom left*: the effective area for the cases of using the whole converter-tracker and only its "thin" part, which provides better performance at low energies. See more details in section 1.

JCAP11(2020)049

ever, it may be still useful for some tasks like a narrow line search in a large-scale diffuse background, detection of GRBs and other transients etc. For this reason we conduct a dedicated modeling of the lateral aperture [8]. The preliminary modeling results showed a good performance of the lateral aperture: the lower detection threshold is $\sim 10\,\mathrm{MeV}$, the effective area is up to $\approx 2000\,\mathrm{cm}^2$ for each side and a large total field of view is about 2–3 sr.

Also we would like to clarify in this section one important aspect: our telescope is under designing stage yet and, hence, several differences in its description exist in the papers published in different years. The telescope version described in this paper is already quite stable. At the same time, as can be seen in other papers (e.g. [9]), a larger version of GAMMA-400 is also under consideration. This version has a bigger calorimeter in all three dimensions ($1 \times 1\,\mathrm{m}^2$ and $\approx 25X_0$), which provides the effective area up to $5500\,\mathrm{cm}^2$ and the energy resolution $\approx 1\%$ at high energies. But such an extended version has the mass of $\approx 4\,\mathrm{t}$ instead of $\approx 2\,\mathrm{t}$ for the base version described in the previous paragraphs. Currently we do not have a certainty yet which launch vehicle will be provided for GAMMA-400. Hence we consider essentially both versions: the base one as rather guaranteed and the extended one as an optimistic case, when a heavy enough launch vehicle and additional funds will be provided. In this paper we mainly describe and build predictions for the base version.

2 GAMMA-400 sensitivity to the spectral lines due to DM annihilation or decay in the Galactic center

Historically GAMMA-400 was designed to have the thick calorimeter ($\gtrsim 20X_0$) in order to provide an excellent energy resolution and, hence, the sensitivity to narrow spectral lines. The latter can be generated by a big variety of DM candidates through annihilation or decay. Besides traditional WIMPs annihilating directly to photons, this variety includes: Kaluza-Klein particles [10], the hidden sector DM [11], gravitino [12], pseudo-Goldstone DM [13], secluded DM [14] and others. Thus the line search represents a very generic and powerful DM search method — it is not tuned to a specific candidate, but rather tests many different candidates simultaneously.

According to the preliminary observational program GAMMA-400 will conduct the deep continuous observations of the GC during 2–4 years. The GC is known to be the best target in the sky for the search of lines from annihilating DM — notwithstanding bright backgrounds — since it has the biggest J-factor among all the targets. There were published already several papers on the line constraints by Fermi-LAT observations [12, 15]. We followed the standard methodology used in these papers in order to estimate the line sensitivity of GAMMA-400 alone and together with Fermi-LAT. We calculated the sensitivity to both annihilating and decaying DM, i.e. the limiting velocity-averaged diphoton annihilation cross section $\langle\sigma v\rangle_{\chi\chi\to\gamma\gamma}$ for the range of DM particle masses m_χ from 1 to 450 GeV and the limiting DM lifetime $\tau_{\chi\to\gamma\nu}$ for the mass range (1–900) GeV (analogically to [15]). We calculated the limiting cross sections and lifetimes for ~ 10 discrete mass values in those ranges and then interpolated between the values. To estimate the line sensitivity we largely followed the methodology described in [12]. Thus we constructed the following likelihood function, which is essentially the probability density for $\mu_{\mathrm{sig}}\left(\begin{smallmatrix}\langle\sigma v\rangle_{\gamma\gamma}\\ \tau_{\gamma\nu}\end{smallmatrix}, m_\chi\right)$ — the average number of photons in the bin from DM line in the case of observation of n photons in total and expectation of μ_b background photons (in the bin-bin index is omitted, bins are independent):

$$L\left(\mu_{\mathrm{sig}}\left(\begin{smallmatrix}\langle\sigma v\rangle_{\gamma\gamma}\\ \tau_{\gamma\nu}\end{smallmatrix}, m_\chi\right), n_s|n, \mu_b\right) \propto P_s(n_s, \mu_b) \times P(\mu|n) = \frac{1}{\sqrt{2\pi}\sigma_s}\exp\left(-\frac{n_s^2}{2\sigma_s^2}\right) \times \frac{\mu^n}{n!}e^{-\mu}, \tag{2.1}$$

JCAP11(2020)049

where $P_s(n_s, \mu_b)$ reflects the systematic flux uncertainty and modeled by the normal distribution, $P(\mu|n)$ is the standard Poisson distribution of the photon count, in a general case $n = n_b + n_{\rm sig} + n_s$, $\mu = \mu_b + \mu_{\rm sig} + n_s$, n_s is the photon number systematic offset due to CR contamination etc. (nuisance parameter), n_b (μ_b) is the measured (average) number of background photons, σ_s is the standard deviation of the systematic offset and taken to be $\sigma_s = \delta f_s \times \mu_b$ analogically to [12]. The fractional systematic uncertainty δf_s is assumed to be the same for both telescopes and equal to 0.015 according to [15] except the case of the search of decaying DM by Fermi-LAT, when it collects the signal from the whole sky with larger $\delta f_s = 0.018$. To estimate the median sensitivity we put $n = \mu_b$. Let us expand in details μ_b and $\mu_{\rm sig}$:

$$\mu_b(m_\chi) = \int\limits_{m_\chi - k(m_\chi)\sigma_E(m_\chi)}^{m_\chi + k(m_\chi)\sigma_E(m_\chi)} dE' \int dE f_b(E) \frac{1}{\sqrt{2\pi}\sigma_E(E)} \exp\left(-\frac{(E-E')^2}{2\sigma_E^2(E)}\right) \varepsilon(E), \qquad (2.2)$$

where $f_b(E)$ is the background spectrum and $\varepsilon(E) = \int A_{\rm eff}(E,t)dt$ is the exposure with $A_{\rm eff}(E,t)$ being the telescope effective area, which is observing the target at an arbitrary moment. This number of photons is calculated (for the annihilation case) inside the energy bin $m_\chi \pm k(m_\chi)\sigma_E(m_\chi)$, where $k(m_\chi)$ is the energy bin half-width in the units of $\sigma_E(E = m_\chi)$, i.e. the RMS of energy dispersion of the telescope or essentially its energy resolution (shown in figure 2). We tuned $k(m_\chi)$ to maximize the sensitivity being estimated for each DM particle mass (see also below). However the sensitivity does not depend strongly on $k(m_\chi)$. The second integral over E in (2.2) technically goes over all energies. However practically we integrated over the range $E' \pm 5\sigma_E(E')$, which is absolutely enough. The background spectrum $f_b(E)$ inside the chosen region of interest (ROI, will be described below) is assumed to be a priori known: we extracted it from the Fermi-LAT background model map [16] using the Aladin sky atlas [17]. Here we included only the Galactic diffuse component, since the contribution of point sources and the isotropic background in the GC region is small ($\lesssim 10\%$, see e.g. figure 1 in [18]) and was checked to be negligible. The exponent function in (2.2) models the energy dispersion of telescopes.

As the first step we reproduced the Fermi-LAT line limits published in [15] based on 6 years of observations in order to verify a correctness of our procedure. For this calculation we needed in the Fermi-LAT exposure $\varepsilon(E)$ and took it from [19]. Although [19] provides the exposure value only at 1 GeV for 8 years of operation, we extrapolated it to an arbitrary energy and operation time by simple rescaling through the effective area: $\varepsilon_F(E,T) \approx \varepsilon_F(1\,\text{GeV}, 8\text{ years}) \frac{A_{\rm eff}(E)}{A_{\rm eff}(1\,\text{GeV})} \frac{T}{8\,\text{years}}$.

Now let us discuss calculation of the expected DM line signal $\mu_{\rm sig}\left(\begin{smallmatrix}\langle\sigma v\rangle_{\gamma\gamma}\\ \tau_{\gamma\nu}\end{smallmatrix}, m_\chi\right)$ and the ROI for the line search. The DM signal (as the photon flux density) is calculated through the well-known equations (e.g. [15]):

$$\frac{d\Phi_\gamma^{\rm ann}}{dE} = \frac{1}{8\pi}\frac{\langle\sigma v\rangle_{\gamma\gamma}}{m_\chi^2}\left(\frac{dN_\gamma}{dE}\right)_{\gamma\gamma} J(\Omega_{\rm ROI}), \quad \frac{d\Phi_\gamma^{\rm dec}}{dE} = \frac{1}{4\pi\tau_{\gamma\nu}m_\chi}\left(\frac{dN_\gamma}{dE}\right)_{\gamma\nu} D(\Omega_{\rm ROI}), \qquad (2.3)$$

$$J(\Omega_{\rm ROI})||D(\Omega_{\rm ROI}) = \int\limits_{\rm l.o.s.} dl \int\limits_{\rm ROI} d\Omega\ \rho^{2||1}\left(r = \sqrt{r_\odot^2 + l^2 - 2r_\odot l\cos\theta}\right), \qquad (2.4)$$

JCAP11(2020)049

where $\rho(r)$ is the DM density dependence on the distance from the GC and $\left(\frac{dN_\gamma}{dE}\right)_{\gamma\gamma/\gamma\nu}$ is the photon spectrum from one annihilation/decay. One annihilation yields two photons with the energies equal to the rest energy of DM particle. One decay may yield various pairs: two photons, photon and neutrino, photon and Z-boson etc. We followed the choice of [15], where DM decays to the photon and neutrino with energies equal to the half of DM rest energy. The majority of papers dedicated to the line searches (e.g. [12, 15, 20, 21]) assumes the spectrum to be essentially the delta-function: $\left(\frac{dN_\gamma}{dE}\right)_{\gamma\gamma} = 2\delta(E - m_\chi)$ and $\left(\frac{dN_\gamma}{dE}\right)_{\gamma\nu} = \delta\left(E - \frac{m_\chi}{2}\right)$. This is indeed true for virtually still DM particles. However any DM halo has a velocity dispersion, which inevitably leads to the Doppler broadening of the line. This is especially relevant for large halos like galaxy clusters considered in e.g. [20]. For the case of our Galaxy we expect the relative Doppler broadening to be $\sim 10^{-3}$. However with GAMMA-400 we deal with energy resolutions down to $\sim 10^{-2}$ level, which is not drastically larger than the line width mentioned. For this reason we decided to check precisely whether we can safely ignore the finite line width. For that we modeled the line shape as follows (the annihilation case, decay line width is the same):

$$\left(\frac{dN_\gamma}{dE}\right)_{\gamma\gamma} \approx \frac{1700}{m_\chi} \exp\left(-\frac{(E - m_\chi)^2}{2\sigma_l^2(m_\chi)}\right), \qquad \sigma_l(m_\chi) = \frac{\langle v_{\text{l.o.s.}}\rangle m_\chi}{\sqrt{2\ln 2}c}, \tag{2.5}$$

where $\langle v_{\text{l.o.s.}}\rangle \approx 200\,\text{km/s}$ [22] and the normalization coefficient was obtained from the simple condition $\int \left(\frac{dN_\gamma}{dE}\right)_{\gamma\gamma} dE = 2$. Then we tested the difference in the number of photons from line calculated with the simple delta-like line shape and the Gaussian one (2.5) inside the (narrowest) energy bin. We obtained a negligible difference and then confidently proceeded to work with effectively monochromatic photons from the line.

As the DM density profile we chose a very typical one — Einasto profile with parameters from [15]:

$$\rho(r) = \rho_s \exp\left(-\frac{2}{\alpha}\left(\left(\frac{r}{r_s}\right)^\alpha - 1\right)\right), \tag{2.6}$$

where $\rho_s = 0.081\,\text{GeV/cm}^3$, $r_s = 20\,\text{kpc}$ and $\alpha = 0.17$. This yields $\rho(r = 8.5\,\text{kpc}) = 0.4\,\text{GeV/cm}^3$. We did not include substructure boost due to its smallness in the central region of the halo [23]. Meanwhile, one basic sanity check for DM density profile is to test whether it yields the correct whole halo mass, which is quite well known for our Galaxy to be $M_{200} \approx 1.2 \cdot 10^{12} M_\odot$ [24]. To calculate the whole halo mass for our chosen profile (2.6) we used the following equation for the Einasto enclosed mass from [25, 26]:

$$M(r < R, r_s, \rho_s, \alpha) = \int_0^R 4\pi r^2 \rho(r) dr = \frac{4\pi\rho_s r_s^3}{\alpha}\left(\frac{2}{\alpha}\right)^{-\frac{3}{\alpha}} e^{2/\alpha}\left(\Gamma\left(\frac{3}{\alpha}\right) - \Gamma\left(\frac{3}{\alpha}, \frac{2}{\alpha}\left(\frac{R}{r_s}\right)^\alpha\right)\right), \tag{2.7}$$

where $\Gamma(z) = \int_0^\infty x^{z-1}e^{-x}dx$ is the usual and $\Gamma(z,a) = \int_a^\infty x^{z-1}e^{-x}dx$ is the upper incomplete gamma functions. The equation above yielded $M(R \approx 10 r_s) \approx 1.4 \cdot 10^{12} M_\odot$, which is in a reasonable agreement with the value cited above from [24] (neglecting by substructures and baryons) taking into account their uncertainties.

For the ROI for the annihilation case we naturally chose the one from [15] in their case of Einasto profile, i.e. the disk with radius $\theta_{\text{max}} = 16^\circ$ around the GC. We essentially copied the density profile and ROI from [15] due to two reasons: at first, as was already mentioned,

JCAP11(2020)049

we wanted to check whether our algorithm correctly reproduces the Fermi-LAT constraints. And secondly we would like to make a pure comparison of GAMMA-400 line sensitivity with that of Fermi-LAT under the similar circumstances. For the decay case the situation is more tricky. The decay signal is less concentrated towards GC in the sky, and it is more efficient to collect such signal from a large part of the sky. Thus in [15] the whole sky (i.e. $\theta_{\max} = 180^\circ$) was used for this purpose. However as was mentioned above, GAMMA-400 is intended to deeply observe only several selected areas of interest in the sky with the biggest exposure dedicated to the GC. Hence in order to estimate our sensitivity to decaying DM we naturally chose the same ROI as for the annihilation case. For this ROI the chosen profile (2.6) yields for (2.4) $J(\theta_{\max} = 16^\circ) \approx 1.1 \cdot 10^{23}\,\mathrm{GeV}^2/\mathrm{cm}^5$ and $D(\theta_{\max} = 16^\circ) \approx 2.6 \cdot 10^{22}\,\mathrm{GeV}/\mathrm{cm}^2$.

At this point we could determine $\mu_{\mathrm{sig}}\left(\substack{\langle\sigma v\rangle_{\gamma\gamma} \\ \tau_{\gamma\nu}}, m_\chi\right)$ for (2.1):

$$\begin{aligned}
\mu_{\mathrm{sig}}(\langle\sigma v\rangle_{\gamma\gamma}, m_\chi) &= \int\limits_{m_\chi - k(m_\chi)\sigma_E(m_\chi)}^{m_\chi + k(m_\chi)\sigma_E(m_\chi)} dE' \int dE \frac{d\Phi_\gamma^{\mathrm{ann}}}{dE}(E) \frac{1}{\sqrt{2\pi}\sigma_E(E)} \exp\left(-\frac{(E-E')^2}{2\sigma_E^2(E)}\right) \varepsilon(E) \\
&= \frac{\langle\sigma v\rangle_{\gamma\gamma}}{4\pi m_\chi^2} J(\Omega_{\mathrm{ROI}}) \mathrm{erf}\left(\frac{k(m_\chi)}{\sqrt{2}}\right) \varepsilon(m_\chi), \\
\mu_{\mathrm{sig}}(\tau_{\gamma\nu}, m_\chi) &= \int\limits_{\frac{m_\chi}{2} - k\left(\frac{m_\chi}{2}\right)\sigma_E\left(\frac{m_\chi}{2}\right)}^{\frac{m_\chi}{2} + k\left(\frac{m_\chi}{2}\right)\sigma_E\left(\frac{m_\chi}{2}\right)} dE' \int dE \frac{d\Phi_\gamma^{\mathrm{dec}}}{dE}(E) \frac{1}{\sqrt{2\pi}\sigma_E(E)} \exp\left(-\frac{(E-E')^2}{2\sigma_E^2(E)}\right) \varepsilon(E) \\
&= \frac{1}{4\pi\tau_{\gamma\nu} m_\chi} D(\Omega_{\mathrm{ROI}}) \mathrm{erf}\left(\frac{k(m_\chi/2)}{\sqrt{2}}\right) \varepsilon(m_\chi/2),
\end{aligned} \tag{2.8}$$

where $\mathrm{erf}(x) = \frac{2}{\sqrt{\pi}} \int_0^x e^{-t^2} dt$ is the error function, and we took into account the approximation of the line shape by delta-function discussed above. Finally we determined the following condition for the median sensitivity at 95% confidence level:

$$\begin{aligned}
\int\limits_0^{\langle\sigma v\rangle_{\gamma\gamma}^{\mathrm{lim}}} d\langle\sigma v\rangle_{\gamma\gamma} \int dn_s L(\mu_{\mathrm{sig}}(\langle\sigma v\rangle_{\gamma\gamma}, m_\chi), n_s | n = \mu_b, \mu_b) = 0.95, \\
\int\limits_{\tau_{\gamma\nu}^{\mathrm{lim}}}^{\infty} d\tau_{\gamma\nu} \int dn_s L(\mu_{\mathrm{sig}}(\tau_{\gamma\nu}, m_\chi), n_s | n = \mu_b, \mu_b) = 0.95,
\end{aligned} \tag{2.9}$$

i.e. we marginalized the likelihood over the nuisance parameter n_s. This is also often called the Bayesian approach (with the flat prior, see e.g. [27]). Then we substituted (2.1), (2.2), (2.8) into (2.9) and found numerically the limiting values of $\langle\sigma v\rangle_{\gamma\gamma}^{\mathrm{lim}}$ and $\tau_{\gamma\nu}^{\mathrm{lim}}$ for each m_χ. For masses $m_\chi \lesssim 100\,\mathrm{GeV}$ the photon counts are large, and we used the well-known approximation of the Poisson distribution $P(\mu|n) = \frac{\mu^n}{n!} e^{-\mu} \approx \frac{1}{\sqrt{2\pi\mu}} \exp\left(-\frac{(n-\mu)^2}{2\mu}\right)$ for large μ.

As we already mentioned, firstly we obtained the sensitivity (i.e. $\langle\sigma v\rangle_{\gamma\gamma}^{\mathrm{lim}}(m_\chi)$ and $\tau_{\gamma\nu}^{\mathrm{lim}}(m_\chi)$) for Fermi-LAT by 5.8 years of observations in order to compare our result with [15] to be sure in the correctness of our algorithm. Our obtained sensitivity is shown by the blue lines in figures 3–4. It matches the sensitivity obtained in [15] with the accuracy not worse than $\approx 20\%$ for all the masses. In our view this is a very good concordance for our relatively

JCAP11(2020)049

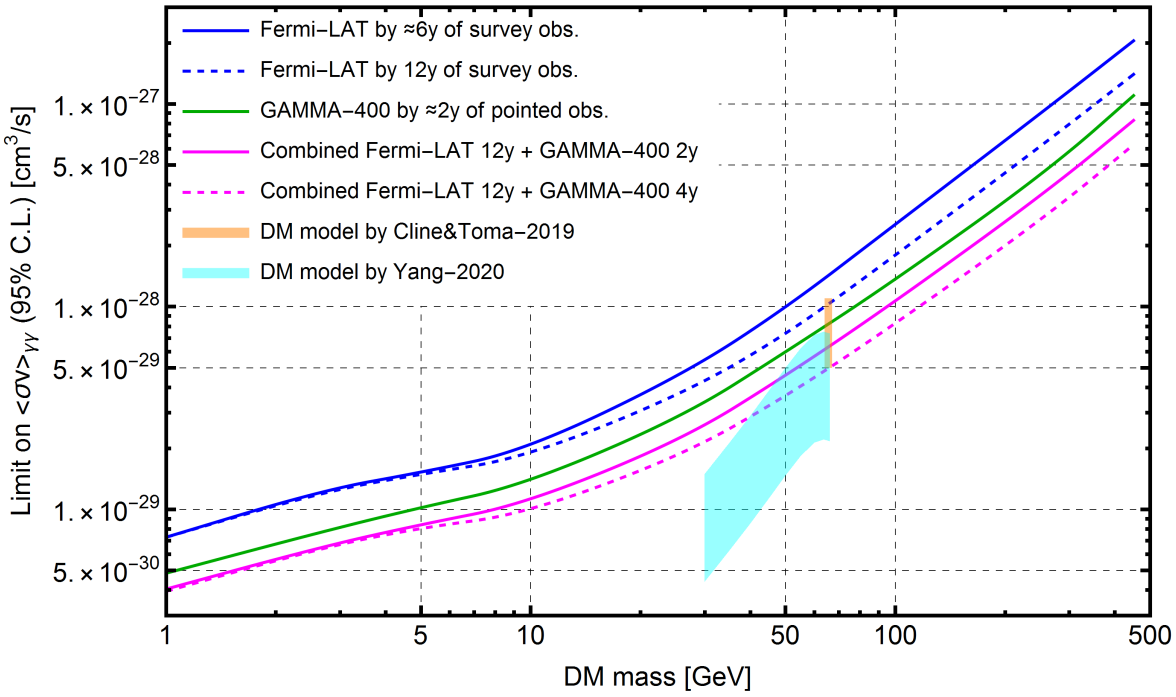


Figure 3. GAMMA-400 median sensitivity to the diphoton annihilation cross section in comparison with that of Fermi-LAT (alone and combined) for the case of Einasto DM density profile and the ROI radius of 16° around the GC. The predictions of two specific DM models [13, 14] are also shown, which could be directly tested. More details see in section 2.

simplistic procedure.[1] This assured us and we proceeded to the next step: prediction of Fermi-LAT sensitivity for its current data set, i.e. ≈ 12 years of observations. This prediction is shown by the blue dashed lines in figures 3–4. We may conclude the following: at low DM masses $m_\chi \lesssim 10\,\text{GeV}$ Fermi-LAT has clearly reached a saturation, i.e. an increase of exposure does not increase the sensitivity at all (background-dominated regime). In other words, the telescope's energy resolution sets a fundamental limit to the line sensitivity, which can not be overcome by an exposure increase. At higher DM masses the signal to background ratio is larger, and the sensitivity still increases with exposure, however not so much.

Then we calculated GAMMA-400 sensitivity for the annihilation case for the pointed (targeted) observations of the GC during ≈ 2 years, which is the minimal anticipated exposure time according to the preliminary GAMMA-400 observational program. As we already mentioned, we optimized the energy bin half-width $k(m_\chi)$ to maximize the sensitivity. We obtained that the optimal half-width monotonically increases with DM mass from $k(m_\chi = 1\,\text{GeV}) = 0.35$ to $k(m_\chi = 450\,\text{GeV}) = 1.65$. The calculated GAMMA-400 sensitivity is shown by the green line in figure 3. We see that it exceeds the sensitivity of Fermi-LAT even in the case of 12 years of its observations for all DM masses. The sensitivity gain is 1.2–1.5 times depending on DM mass. Such sensitivity is achievable by GAMMA-400 thanks to both a good energy resolution and the pointed observation mode. Thus the latter provides the exposure $\varepsilon_G(E = 100\,\text{GeV}, T = 2\,\text{years}) \approx 2 \cdot 10^{11}\,\text{cm}^2\,\text{s}$. For comparison, Fermi-LAT during 12 years has accumulated $\varepsilon_F(E = 100\,\text{GeV}, T = 12\,\text{years}) \approx 6 \cdot 10^{11}\,\text{cm}^2\,\text{s}$.

[1] A little detail worthy to mention is that [15] used NFW density profile for the case of decaying DM. However D-factors (2.4) are almost exactly the same for NFW and Einasto profiles (for $\Omega_{\text{ROI}} = 4\pi\,\text{sr}$). Hence our sensitivity with Einasto profile corresponds directly to that with NFW in [15] (figure 9 there).

JCAP11(2020)049

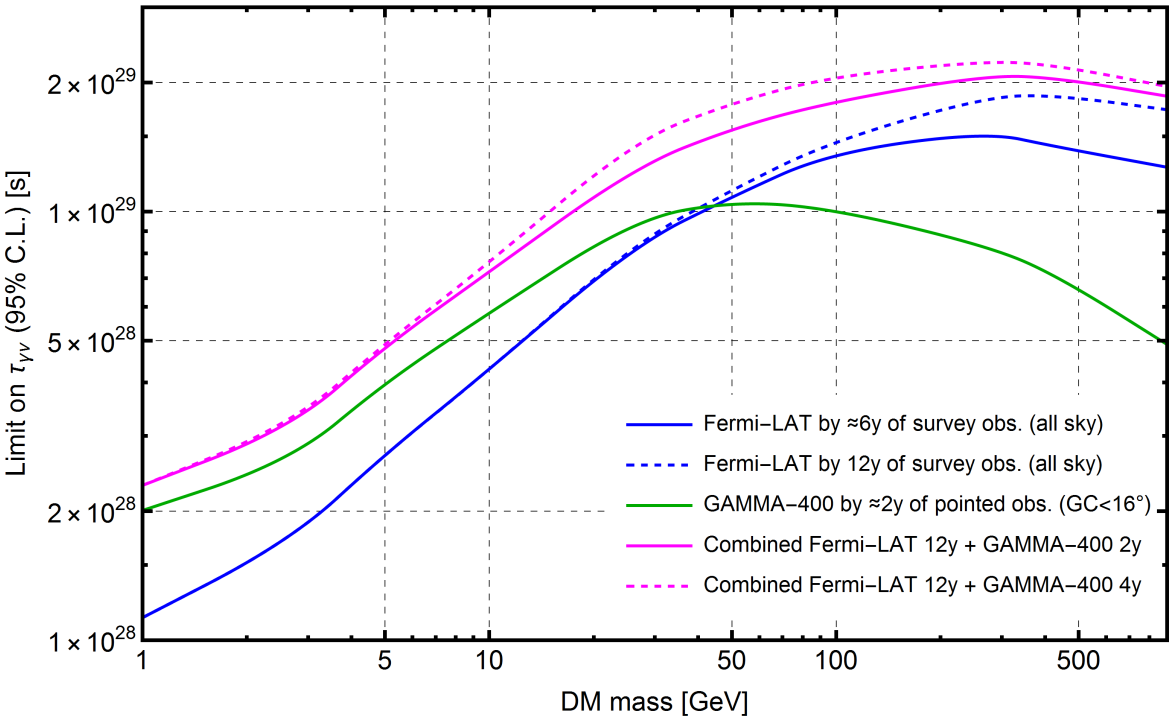


Figure 4. GAMMA-400 median sensitivity to the DM lifetime in comparison with that of Fermi-LAT (alone and combined) for the case of Einasto DM density profile. GAMMA-400 collects the signal from the disk with 16° radius around the GC, Fermi-LAT — from all sky. More details see in section 2.

Then we naturally assumed that the future GAMMA-400 data can be jointly analyzed with the already existing Fermi-LAT data and estimated the combined sensitivity of both telescopes. For this we constructed the joint likelihood function as the product of likelihood functions for each telescope. Then our median sensitivity condition (2.9) transforms to (up to a normalization factor):

$$\int_0^{\langle\sigma v\rangle_{\gamma\gamma}^{\lim}} d\langle\sigma v\rangle_{\gamma\gamma} \int dn_{sF} \int dn_{sG} L_F(\mu_{\mathrm{sig},F}(\langle\sigma v\rangle_{\gamma\gamma}, m_\chi), n_{sF}|n=\mu_{bF},\mu_{bF})\times \\ \times L_G(\mu_{\mathrm{sig},G}(\langle\sigma v\rangle_{\gamma\gamma}, m_\chi), n_{sG}|n=\mu_{bG},\mu_{bG}) = 0.95, \tag{2.10}$$

where index "F" denotes everything for Fermi-LAT, "G" — for GAMMA-400. The combined sensitivity of Fermi-LAT by 12 years of survey observations and GAMMA-400 by 2 years of the pointed observations of the GC is shown by the magenta line in figure 3. As can be seen, such a joint analysis increases the sensitivity even further: by 1.6–1.8 times depending on DM mass with respect to Fermi-LAT by 12 years limits. Also we naturally expect that the combined limits will have much smaller uncertainty than the limits from a single telescope, although we did not evaluate the limit uncertainties here quantitatively. In the best case scenario our telescope can be operating during up to 10 years. In such case, in principle it can observe the GC during ≈ 4 years. We estimated the combined sensitivity for this case — it is shown by the dashed magenta line in figure 3 and considered to be an optimistic scenario providing the sensitivity gain by 1.8–2.3 times. And in the meanwhile, we also estimated the sensitivity of the possible extended (4 t) version of GAMMA-400 mentioned in section 1.

JCAP11(2020)049

The joint sensitivity of Fermi-LAT and such version of GAMMA-400 (4 years of exposure) will exceed Fermi-LAT alone by even much more — 1.8–3.5 times!

Figure 3 also contains the predictions of two specific DM models [13, 14]. In [13] the recent pseudo-Goldstone boson DM model was presented with $m_\chi = (64\text{–}67)\,\text{GeV}$, which can explain the GC gamma-ray excess and the antiproton excess in CRs by the annihilation mainly into $b\bar{b}$. Also it can solve certain anomalies observed in LEP and CMS experiments. And at the same time this model predicts some non-zero annihilation branching ratio to photons, which implies the narrow line with the parameters marked by the orange region in figure 3. We see that Fermi-LAT alone can not reach this region to test. But together with GAMMA-400 the whole orange region can be tested! Similarly the cyan region shows the predictions of another model [14], where DM has the form of secluded (vector) particles, which firstly annihilate into mediators with subsequent decay of the latter into SM particles including photons. This model also explains the GC gamma-ray excess and predicts the narrow line. However for this model the prediction is not so well-localized in the plane $\langle\sigma v\rangle_{\gamma\gamma} - m_\chi$ — we see that Fermi-LAT together with GAMMA-400 will be able to probe just a top part of the cyan region. Just to clarify we notice that indeed this vector DM does not annihilate to gammas directly. The cyan region in the figure reflects the effectively expected parameter values, if one would pretend diphoton annihilation to treat this candidate on the same parameter plane. Speaking more generally about other possible DM candidates including traditional WIMPs, theoretically we can expect to find them everywhere on the parameter plane below the level $\sim 0.1\langle\sigma v\rangle_{\text{thermal}} \sim 10^{-27}\,\text{cm}^3/\text{s}$ [15]. As shown in figure 3 we achieve this level of sensitivity for all DM masses up to $m_\chi \approx 500\,\text{GeV}$. Thus we can conclude that the addition of the future GAMMA-400 high-quality data to the existing Fermi-LAT data significantly increases the sensitivity to the diphoton annihilation cross section (up to factor of 2, at least for the steep density profiles) and may reveal DM at any mass in the considered range $\approx (1\text{–}500)\,\text{GeV}$.

The sensitivity being estimated appeared to depend strongly on the fractional flux systematic uncertainty δf_s mentioned above. As a natural basic scenario we assumed $\delta f_{sG} = \delta f_{sF} = 0.015$. To study the sensitivity dependence on this parameter we also calculated the sensitivity gains for the optimistic case of reduction of our systematics down to $\delta f_{sG} = 0.01$. The latter would yield the following gains with respect to Fermi-LAT by 12 years: 1.3–2.1 times for GAMMA-400 by 2 years alone and 2.1–2.7 times for GAMMA-400 by 4 years + Fermi-LAT by 12 years. Thus such potential optimization of systematics would provide an additional significant growth of sensitivity.

And finally we calculated GAMMA-400 sensitivity to the decaying DM for the similar exposures — the result is shown in figure 4. Here expectedly the sensitivity gain is not so large due to our limited sky coverage: GAMMA-400 by 2 years alone overtakes Fermi-LAT up to $m_\chi \approx 40\,\text{GeV}$. However the combined analysis with 4 years of GAMMA-400 data will still provide the sensitivity gain by 1.1–2.0 times for the whole mass range! In this case the gain monotonically increases with the mass decrease.

3 ALP discovery potential by an observation of the supernova explosion in the Local Group

As was described in [28], gamma-ray telescopes has a high potential to discover ALPs by an observation of a nearby supernova (SN) explosion. In this section we aimed to estimate the GAMMA-400 sensitivity to photon-ALP coupling constant $g_{a\gamma}$ depending on the ALP mass

JCAP11(2020)049

m_a by such an observation. Here we largely followed the methodology developed in [28]. ALPs can be copiously produced in SN interiors during the explosion. Then they freely leave an SN, propagate and partially convert to photons in ambient magnetic fields. This may cause a gamma-ray burst from the SN during its explosion simultaneously with the neutrino burst. Such a gamma-ray burst typically peaks at 50–100 MeV [29], which fits well into the GAMMA-400 operating energy range. The first key step in this section was to model the expected spectrum of the burst. The time-integrated spectral flux has the form:

$$\frac{dN_\gamma}{dE} = \frac{dN_a}{dE} \frac{P_{a\to\gamma}(E, m_a, g_{a\gamma}, \vec{r}_{\rm SN})}{4\pi d^2}, \tag{3.1}$$

where $\frac{dN_a}{dE}$ is the energy distribution of the produced ALPs, $P_{a\to\gamma}(E, m_a, g_{a\gamma}, \vec{r}_{\rm SN})$ is their conversion probability on the way to observer and d is the distance to SN. Let us write out the former two based on [28] and [30]:

$$\frac{dN_a}{dE} = C_a \left(\frac{g_{a\gamma}}{\rm GeV^{-1}}\right)^2 \left(\frac{E}{E_a}\right)^{\beta_a} \exp\left(-\frac{(\beta_a+1)E}{E_a}\right). \tag{3.2}$$

The constants C_a, E_a, β_a moderately depend on the progenitor mass (see table 1 in [28]). However, as was shown in [28], the final limits on $g_{a\gamma}$ depend on the progenitor mass very weakly. For this reason and the fact that the progenitor mass distribution is very steep we decided to fix C_a, E_a, β_a to the following constant values, which reflect the most probable case of (10–20)$M_\odot$ progenitor: $C_a = 8 \cdot 10^{75}\,\mathrm{GeV}^{-1}, E_a = 99\,\mathrm{MeV}, \beta_a = 2.2$. The conversion probability in (3.1) has the form (in the natural units $c = \hbar = k_B = 1$, see eqs. (4)–(8) in [30]):

$$\begin{aligned} P_{a\leftrightarrow\gamma}(E, m_a, g_{a\gamma}, \vec{r}_{\rm SN}) &= \frac{1}{1+(E_c/E)^2} \sin^2\left(\frac{g_{a\gamma} B_\perp d}{2} \sqrt{1+\left(\frac{E_c}{E}\right)^2}\right), \\ E_c &\simeq 2.5 \frac{|m_a^2 - \omega_{pl}^2|}{\mathrm{neV}^2} \left(\frac{\mu\mathrm{G}}{B_\perp}\right) \left(\frac{10^{-11}\,\mathrm{GeV}^{-1}}{g_{a\gamma}}\right) \mathrm{GeV} \end{aligned} \tag{3.3}$$

for the case of a uniform transverse magnetic field between the SN and observer. In reality the field is indeed not uniform. However, as will be shown below, the uniform field approximation can yield reasonably precise sensitivity estimates.

We calculated our sensitivity for three specific representative targets: SN at GC, in M 31 and Betelgeuse. These targets were also explored in [28] for Fermi-LAT. As was outlined there, the magnetic field distribution uncertainties influence the limits on $g_{a\gamma}$ significantly: by factor of ≈ 2 for the case of GC and by 4–5 for M 31/Betelgeuse. These uncertainty ranges are shown in figure 5 by the shaded areas bounded by the dashed lines. We found that such large ranges can easily enclose the sensitivity curves calculated with the simplified models of the uniform transverse magnetic field. This reduces a necessity to conduct a complicated procedure of numerical solving of the photon-ALP beam transport equation with the coordinate-dependent field. With the constant field model one can calculate the gamma-ray spectrum (3.1) analytically with the exactly known dependence on all the parameters. We decided to employ such an advantage and chose the simplified uniform field model for all our calculations. For this model we had to determine the effective transverse field value between the target and observer and the effective ALP path length. For the cases of GC and Betelgeuse

JCAP11(2020)049

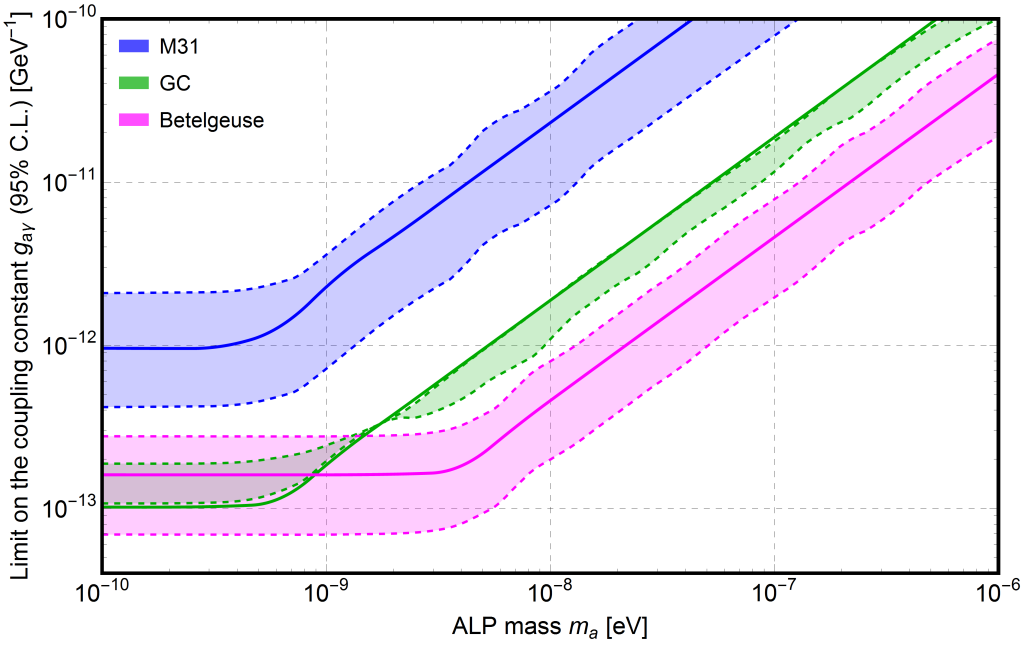


Figure 5. Fermi-LAT sensitivity to the ALP-photon coupling constant. The shaded areas reflect uncertainties in the limits due to uncertainties in the magnetic field distribution along the line of sight according to [28]. The solid lines reflect the sensitivity in our simplified constant-field model with the chosen field values cited in table 1. See more details in section 3.

the path lengths were naturally set to distances to these targets (see all the parameter values in table 1). For M 31 the path length is less obvious, since the major intergalactic portion of the propagation path practically does not contribute into the conversion probability. Hence we estimated the path length as the sum of portions inside Milky Way and M 31. For this we approximated the galaxies by cylinders with half-heights equal to the scale heights of their magnetic field distributions. These scale heights were taken from [31, 32]. Finally this yielded the effective path length $l_{\rm eff} \approx 14\,{\rm kpc}$. Having set path lengths we found the effective transverse field values $B_{\perp{\rm eff}}$, which yield approximately the average sensitivity of Fermi-LAT with respect to the boundary cases of field models reflected by the dashed lines in figure 5. To do this we used (3.1)–(3.3), Fermi-LAT characteristics and the data from table 2 in [28]. The fitted field values are shown in table 1 and respective $g_{a\gamma}$ Fermi-LAT limits are shown in figure 5 by the solid lines. We see that these lines indeed fit rather well into the uncertainty ranges. Thus we consider our uniform field model as a model yielding middling conservative constraints with uncertainties about factor of 2. In other words, our model would reflect approximately an average sensitivity between the extreme cases. In general, the obtained field values are reasonable for the galactic medium (see e.g. [31, 32]). The field value for Betelgeuse is naturally much lower than that for the GC, since the former is located near the Galactic anticenter.

At this point we determined all the ingredients for calculation of the gamma-ray spectrum. The next big step was to deduce the GAMMA-400 sensitivity to such a spectrum depending on $g_{a\gamma}$ and m_a. We integrated the spectrum over the energy range (50–400) MeV, which was found to be optimal for all the targets and is slightly narrower than in [28]. Similarly to [28] we set the signal integration time to be $\tau = 20\,{\rm s}$. To obtain the achievable observational upper limit on the mean number of signal photons ($\mu_{\rm sig}$) during this time inter-

JCAP11(2020)049

	Betelgeuse	GC	M 31
Galactic longitude, deg	200	0	121
Galactic latitude, deg	−8.96	0	−21.6
Effective beam path $l_{\rm eff}$, kpc	$\equiv d_{\rm Bet} \approx 0.20$	$\equiv d_{\rm GC} \approx 8.4$	14
Effective transverse magnetic field $B_{\perp{\rm eff}}$, μG	3.0	8.0	4.0
Expected number of background counts μ_b	0.2	1.0	0.1
95% limit on the number of signal counts $\mu_{\rm sig,UL}$	3.0	4.2	3.0
Probability to catch SN for GAMMA-400, %	?	3–6	1–2

Table 1. The parameters of three considered trial cases of SN explosion observations.

val in the presence of background we constructed the following simple Poissonian likelihood function:

$$L_{\rm SN}(\mu_{\rm sig}(g_{a\gamma}, m_a)|n, \mu_b) \propto \frac{(\mu_{\rm sig} + \mu_b)^n}{n!} \exp(-\mu_{\rm sig} - \mu_b), \tag{3.4}$$

where μ_b is the mean number of background photons and n is the measured counts. Similarly to the previous section 2 we assumed here $n = \mu_b$ rounding μ_b to the nearest integer (i.e. no apparent signal). Systematic flux uncertainties ($\sim 1\%$) are irrelevant here. The mean photon numbers were calculated by the following way:

$$\mu_{\rm sig} \equiv \mu_{\rm sig}(g_{a\gamma}, m_a) \ = 0.68 \int\limits_{50\,{\rm MeV}}^{400\,{\rm MeV}} \frac{dN_\gamma}{dE}(E, g_{a\gamma}, m_a) A_{\rm eff}(E) dE, \tag{3.5}$$

$$\mu_b \ \approx \int\limits_{50\,{\rm MeV}}^{400\,{\rm MeV}} f_b(E, b, l, \Omega_{\rm PSF}(E = 70\,{\rm MeV})) A_{\rm eff}(E) \tau dE. \tag{3.6}$$

The coefficient 0.68 in (3.5) reflects the choice of ROI size as the size of PSF at 68% containment. f_b in (3.6) is the background spectral flux inside the ROI, which depends on a sky position and ROI/PSF size. For the latter we chose PSF at 70 MeV, since the spectrum (3.1) typically peaks around this energy. In general, f_b includes all the components of gamma-ray sky. For our estimates we included only the diffuse backgrounds (Galactic and isotropic, from [16] using [17]), since the contribution of point sources is expected to be subdominant (see e.g. figure 1 in [18]). The obtained backgrounds are provided in table 1. We see that only the GC has rather significant background. Betelgeuse and M 31 can be considered as essentially background-free cases. And we neglected by the photon energy dispersion effect calculating (3.5)–(3.6), since it was checked to be irrelevant for the case of integration over so wide energy range.

To obtain the 95% C.L. upper limit on the mean number of signal photons $\mu_{\rm sig,UL}$ we implied the following condition analogically to (2.9):

$$\int\limits_0^{\mu_{\rm sig,UL}(g_{a\gamma}^{\rm lim}, m_a)} L_{\rm SN}(\mu_{\rm sig}|n = [\mu_b], \mu_b) d\mu_{\rm sig} = 0.95. \tag{3.7}$$

The obtained upper limits are presented in table 1. Then we substituted the obtained $\mu_{\rm sig,UL}$'s in (3.5) and found numerically the limiting coupling constant as a function of ALP mass

JCAP11(2020)049

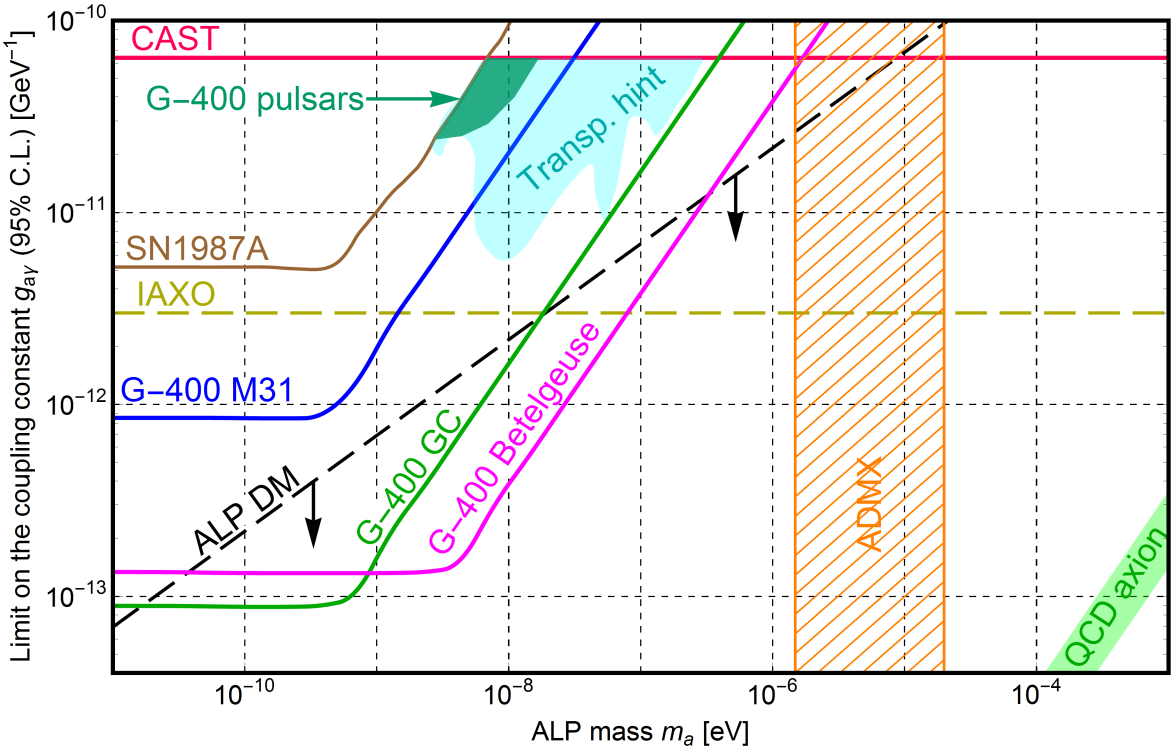


Figure 6. GAMMA-400 (G-400) sensitivity to the ALP-photon coupling constant by the observation of supernova in the GC, M 31; or Betelgeuse explosion. Other limits are also shown for comparison: CAST [33]; future IAXO in its best configuration [33]; absence of the gamma-ray burst from SN1987A [28]; ADMX [36], which reaches the QCD axion band (outside of the plot range). See more details in section 3. Also the sensitivity region by observations of pulsars is shown, which overlaps with the anomalous TeV transparency hint region — see details in section 4.

$g^{\rm lim}_{a\gamma}(m_a)$. The resulting curves are presented in figure 6 together with other constraints for comparison. Overall we see that the obtained GAMMA-400 sensitivity is very similar to that of Fermi-LAT, which is shown by the solid lines in figure 5 (for the same ALP propagation model). This is quite expected due to a comparable performance of both telescopes at the relevant energies. From figure 6 we deduce that the sensitivity curves for GC and Betelgeuse do not differ drastically. For other locations of the SN in the Galactic disk we can expect intuitively the sensitivity curve lying somewhere between the curves for GC and Betelgeuse. Thus for $m_a \lesssim (10\text{–}100)$ neV an observation of the Galactic SN represents the most sensitive ALP search experiment among all existing. This would allow to explore completely the region of parameter space needed to explain the tentative anomalous transparency of the Universe at very high energies by ALPs [33]. Also this observation would probe the certain portion of parameter space below the black dashed line in figure 6, where ALPs can accommodate all DM. It realizes for the mass range $m_a \sim (0.1\text{–}100)$ neV. However, it is still very hard to reach the well-motivated QCD axion parameter band, which is shown by green and represents the band enclosed between DFSZ and KSVZ axion models [33]. So far this band has been reached only by ADMX experiment at $m_a \sim (1\text{–}10)\,\mu$eV.

A non-trivial question here is indeed the probability to catch such an SN for GAMMA-400. The probability is the biggest for the case of GC, since as was mentioned in section 2, according to the preliminary observational program we are going to observe the GC dur-

JCAP11(2020)049

ing 2–4 years. Let us estimate the probability of the catch based on the average Galactic rate of core-collapse SNe. The latter was thoroughly estimated in [34] to be ≈ 3 SNe per century. We can naturally expect that mainly this rate is "localized" inside the Galactic disk. GAMMA-400 field of view centered on the GC captures $\approx 40\%$ of the whole Galactic disk. Counting that the star formation in the Galaxy is slightly concentrated towards the center, it would be reasonable to assume that at least $\approx 3/2$ SNe/century can be expected in average for GAMMA-400 looking at the GC. Considering the SNe explosions to be a Poissonian process, one can easily get that the probability of one or more SNe during 2–4 years of quasi-continuous observations is 3–6%. According to preliminary plans GAMMA-400 will also observe a significant part of the Galactic plane beyond the GC region during ≈ 1.5 years. In such a case this would add another $\approx 1\%$ of probability to the total chance. M 31 is expected to be inside the field of view during 0.4–0.7 years, which adds 1–2%. We do not really consider the Magellanic clouds and M 33 due to very low chances from them. Thus the total chance is estimated to be 5–9%. Besides that we may keep in mind two famous supergiants, which are very close to the explosion — η Car Foramen and α Ori Betelgeuse. The latter is especially interesting due to its proximity, which would allow to predict the explosion several days in advance thanks to the pre-supernova steady neutrino signal [35]. This would provide a great opportunity to point GAMMA-400 at Betelgeuse in advance and observe the explosion with a guarantee in case it will happen during the telescope lifetime. In general, as was also noted in [28], the neutrino signal accompanying the explosion is very useful timing trigger for searches of the gamma-ray burst being considered. Neutrino telescopes will easily detect the neutrino burst from any Galactic SN. However, M 31 in this aspect is less favorable being too far for the neutrino burst to be detectable.

And finally we would like to discuss briefly potential uncertainties of the sensitivity estimated here. For this purpose we investigated the dependence of the limiting coupling constant value on the key parameters and obtained approximately the following for the relevant values of other parameters: $g_{a\gamma}^{\rm lim} \propto B_{\perp}^{-1/2} \mu_{\rm sig,UL}^{1/4}$. Thus the dependence on the number of signal photons is very weak and on the magnetic field is mild. Above we mentioned that we neglected by the contribution of point sources in μ_b. This approximation may lower μ_b and, hence, $\mu_{\rm sig,UL}$. However $g_{a\gamma}^{\rm lim}$ practically would not change even if we would double or triple μ_b — due to so weak dependence on $\mu_{\rm sig,UL}$. Thus our sensitivity estimate is quite realistic with respect to the background model. As we already mentioned, the main source of uncertainty is the magnetic field model. We would estimate the respective systematic uncertainty of $g_{a\gamma}^{\rm lim}$ to be at the level of factor of ≈ 2. Meanwhile, we also studied two possibilities to detect the gamma-ray burst — by the whole converter and only by its thin part. The latter has much smaller PSF (see details in section 1), which would reduce the background. However, we found that the sensitivity of both variants is approximately the same due to the reduced effective area in the "thin" mode. Another advantage could be obtained from using the lateral aperture mentioned in section 1. Together with the main aperture the total field of view may reach $\approx 1/3$ of the whole sky. This significantly increases the probability of the catch estimated above for the main aperture by $\approx 3\%$ bringing the total chances to 8–12%. The lateral aperture will presumably have a large background level. However the sensitivity to $g_{a\gamma}$ may still be at the relevant level due to very weak dependence of the former on $\mu_{\rm sig,UL}$. Overall, although we are not ready to really quantify exact predictions for the lateral aperture, we consider it to be a useful mode for the detection of SNe and other transients.

JCAP11(2020)049

4 ALP constraining potential by observations of bright gamma-ray pulsars

Bright gamma-ray pulsars located near the Galactic plane represent a good target for ALP searches by GAMMA-400. For certain values of ALP mass and photon coupling constant a significant part of photons can convert to ALPs during propagation in the Galactic magnetic field forming the oscillations in the pulsar spectra according to (3.3). Galactic pulsars are generally better than AGNs for ALP searches due to much better knowledge of the magnetic field distribution between the source and observer. In [37] an attempt was made to find such oscillations based on Fermi-LAT data and resulted in a tentatively positive detection of ALP with $m_a \approx 3.6\,\mathrm{neV}$, $g_{a\gamma} \approx 2.3 \cdot 10^{-10}\,\mathrm{GeV}^{-1}$. In this section we conducted the estimation of GAMMA-400 sensitivity to such oscillations and respective ALP parameters. In general, one can intuitively expect a comparable sensitivity of GAMMA-400 and Fermi-LAT to ALPs. However better angular and energy resolutions of GAMMA-400 (figure 2) may enable better sensitivity by decreased background subtraction systematics and spectral smearing. In our estimates we decided to study the sensitivity on the "m_a–$g_{a\gamma}$" parameter plane outside of the regions excluded by CAST and non-observation of gammas from SN1987A (see figure 6). We used the same 6 pulsars employed by [37] (PSRs J1420-6048, J1648-4611, J1702-4128, J1718-3825, J2021+3651, J2240+5832) as well-suitable for our purposes: they are bright to provide good photon statistics, distant to gain a significant ALP-photon conversion probability and located very close to the Galactic plane, where the magnetic field is the strongest. Only one modification to the pulsar sample we made is the assumed distance to PSR J2021+3651. [37] assumed the distance of 10 kpc. However the dedicated study of this pulsar [38] emphasizes a generally big uncertainty in the distance, which can be in the range 1–12 kpc. Their additional study allowed to constrain the distance to the range $1.8^{+1.7}_{-1.4}\,\mathrm{kpc}$. In such a situation we decided that 10 kpc would be too optimistic (for our purposes) assumption. Also for such a distance the pulsar appear suspiciously bright in gamma rays. Thus we decided to stay conservative and placed it at the upper distance obtained in [38], i.e. 3.5 kpc. Distances to other pulsars were taken from [37].

Our algorithm of sensitivity estimation is based on the likelihood function, which joins together all the pulsars and all the relevant energy bins of each pulsar. Briefly the steps of our procedure are the following: we

1. Took the intrinsic spectra of pulsars, which were obtained in [37] (red dashed lines in their figures with spectra) and are supposed to be cleaned out of instrumental systematics and modulations due to ALPs.

2. Chose an optimal binning for our telescope (can be seen in figure 7) and simulated the data points assuming no ALPs and taking into account both the statistical and systematical fluctuations (the latter was described in section 2).

3. Chose a particular $(m_a, g_{a\gamma})$ values being tested and generated the spectra of pulsars with ALPs by multiplication of the intrinsic spectra by the probability of photon-ALP conversion (3.3) as function of energy.

4. Constructed the following joint likelihood function:

$$L(m_a, g_{a\gamma}) \propto \prod_{j=1}^{6\mathrm{PSRs}} \prod_{i=1}^{\#\mathrm{bins}_j} L_{ij}(\mu_{ij}(m_a, g_{a\gamma}), n_{s,ij}|n_{ij}), \tag{4.1}$$

JCAP11(2020)049

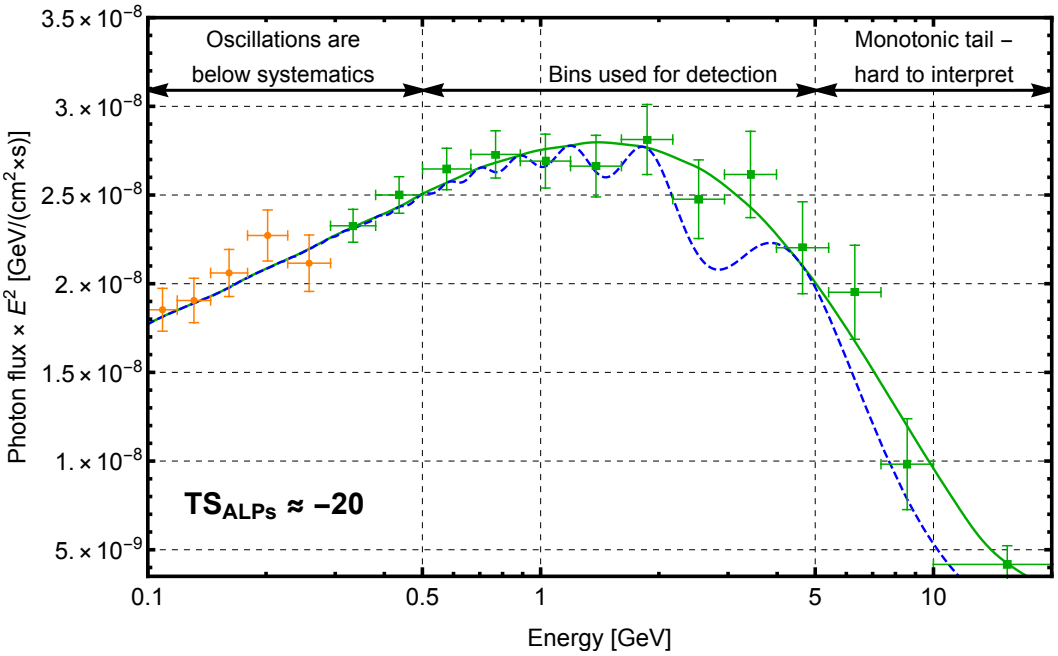


Figure 7. The spectra of PSR J1420-6048 with (blue dashed) and without (green) oscillations caused by ALPs ($m_a = 7.0\,\text{neV}$, $g_{a\gamma} = 4.6 \cdot 10^{-11}\,\text{GeV}^{-1}$) together with the simulated GAMMA-400 data points. The exposure time is 0.5 years. The orange data points at low energies reflect the usage of the thin converter. More details are in section 4.

where L_{ij} is the individual likelihoods for each bin. It has the form similar to (2.1) with $n_{s,ij}$ being systematic offsets, n_{ij} — measured (i.e. simulated at step 2) numbers of photons and μ_{ij} — the expected (average) numbers of photons:

$$\mu_{ij}(m_a, g_{a\gamma}) = \int_{E_{il}}^{E_{iu}} dE \int dE' f_j(E') \times \left\{ \begin{array}{l} 1 \text{ for null likelihood} \\ 1 - P_{\gamma\to a}(E', m_a, g_{a\gamma}, B_{\perp\text{eff}}, d_j) \end{array} \right\} \times \\ \times \frac{1}{\sqrt{2\pi}\sigma_E(E')} \exp\left(-\frac{(E-E')^2}{2\sigma_E^2(E')}\right) \varepsilon_j(E'), \tag{4.2}$$

where E_{il}, E_{iu} are the energy bin margins, $f_j(E')$ are the intrinsic photon spectra of pulsars and d_j are the pulsar distances.

5. Constructed the criterion of rejection of the hypothesis of ALPs presence in the spectra through the standard test statistic approach:

$$\text{TS}_{\text{ALPs}}(m_a, g_{a\gamma}) = 2 \ln \frac{L(m_a, g_{a\gamma}, \vec{n}_s^{\max})}{L(m_a = 0, g_{a\gamma} = 0, \vec{n}_{s0}^{\max})} \equiv 2(\ln L - \ln L_0), \tag{4.3}$$

where $\vec{n}_s^{\max}, \vec{n}_{s0}^{\max}$ vectors of nuisance systematic offsets are fitted in each bin to maximize L and L_0 respectively. This approach is actually different from the one used in section 2, where we marginalized the likelihood over the nuisance parameters. Here the latter approach is practically inconvenient, so we decided to employ the likelihood ratio test approach, which is also widely used and often called the frequentist approach

JCAP11(2020)049

(see e.g. [27] for a general methodological review). Then we set the following typical model rejection criterion (see also [12]): $\mathrm{TS}_{\mathrm{ALPs}}(m_a, g_{a\gamma}^{\mathrm{lim}}) = -2.71$. Physically by construction it means that for each ALP mass m_a the coupling constant values $g_{a\gamma} \geqslant g_{a\gamma}^{\mathrm{lim}}$ are excluded with the confidence level $\geqslant 95\%$. In other words, the spectral oscillations produced by $g_{a\gamma} \geqslant g_{a\gamma}^{\mathrm{lim}}$ would be large enough to be inevitably distinguishable from the smooth spectra without ALPs.

6. Repeated steps 3–5 for all relevant discrete pairs of values $(m_a, g_{a\gamma})$ and obtained the interpolated mean sensitivity exclusion contour $g_{a\gamma}^{\mathrm{lim}}(m_a)$ at 95% confidence level. The obtained sensitivity region is drawn by the aquamarine color in figure 6.

Let us discuss several essential details about the procedure outlined above. The conversion probability $P_{\gamma\to a}$ determined by (3.3) and participating in (4.2) indeed requires the specification of magnetic field between the pulsars and observer. Here similarly to section 3 we set the uniform field, which was shown there to provide approximately the medium sensitivity among various possible field models. We set $B_{\perp\mathrm{eff}} = 5\,\mu G$ for all the pulsars as an average value between those obtained in section 3 as representative values for the directions towards the Galactic center and anticenter (the cases of GC and Betelgeuse in table 1 respectively). Such choice is motivated by the fact that all the participating pulsars lie far from both the center and anticenter — their average angular distance from the GC is $\approx 50^\circ$. As for the assumed effective exposure times, they vary between 0.25 and 1.8 years depending on the pulsar location. The pulsars located closer to the GC get longer exposure times — they will be captured in the field of view during the preliminary planned deep 2+ year observations of the GC. In order to calculate the mean sensitivity realistically we simulated 1000 random data samples n_{ij} and took those $g_{a\gamma}^{\mathrm{lim}}(m_a)$, which yields $\langle \mathrm{TS}_{\mathrm{ALPs}}(m_a, g_{a\gamma}^{\mathrm{lim}}) \rangle = -2.71$ with the latter being averaged over the ensemble of samples.

Figure 7 shows the example of particular pulsar spectra with respective data points for the case of $(m_a, g_{a\gamma})$ values, which are approximately central for the sensitivity region in figure 6. The non-trivial question for the procedure above was — which bins should we include in the likelihood (4.1)? Figure 7 illustrates the choice of bins: we did not include the bins at low energies where $P_{\gamma\to a} \lesssim 0.01$, since the oscillations there would be indistinguishable from systematics; and the bins at high energies where the coupling is strong, and $P_{\gamma\to a}$ does not oscillate anymore increasing monotonically. Such a high energy "tail" was not included in the analysis simply because it is unclear how to distinguish between the intrinsic spectral slope, which can be not known exactly a priori, and the possible absorption by ALPs at these energies. Thus the obtained sensitivity is rather conservative in this respect. The first 5 bins in the energy range of 100–300 MeV were generated by the thin converter for all the pulsars, since the whole converter has large PSF at these energies and, hence, will inevitably intrude large background systematics in the data. In general, by looking at figure 7 one can not see that the data points (i.e. 8 bins used for detection) prefer the smooth spectrum really obviously. However the obtained sensitivity is achieved by stacking together the multiple bins and pulsars. From figure 6 the sensitivity reaches $g_{a\gamma}^{\mathrm{lim,min}} \approx 2.4 \times 10^{-11}\,\mathrm{GeV}^{-1}$ at $m_a \approx 3\,\mathrm{neV}$ and then worsens as m_a both decreases and increases up to the CAST limit at $m_a \sim 1, 10\,\mathrm{neV}$. This reproduces a typical sensitivity mass range for the space-based gamma-ray telescopes, see e.g. [39]. With increase of m_a the spectral oscillations generally shift to higher energies.

Meanwhile our estimated sensitivity is by an order of magnitude better than the mentioned coupling constant value obtained in [37] as a tentative signal. We can not compare

JCAP11(2020)049

it with our sensitivity directly due to different magnetic field model, which indeed influences $P_{\gamma\to a}$ and, hence, the sensitivity. However we suppose that $g_{a\gamma} \approx 10 g_{a\gamma}^{\rm lim}$ would produce big oscillations detectable by GAMMA-400 for any reasonable case of magnetic fields, especially taking into account an opportunity of the joint data analysis of GAMMA-400 and Fermi-LAT. Thus we anticipate to confirm or deny robustly the tentative detection [37] by GAMMA-400, even if such ALP evaded by somehow CAST and SN1987A constraints. If the detection will not be confirmed, then the joint data analysis from both telescopes may expand the GAMMA-400 sensitivity region further and test a major part of the blue region in figure 6, which reflects the parameter values needed to fit the anomalous transparency of the Universe at very high energies by ALPs. Estimation of the joint sensitivity of both telescopes requires a bit of extrapolation and is left for a future work. Also the GAMMA-400 sensitivity region can be further expanded by an increase of the pulsar exposures, which were assumed here to be minimally anticipated and can be significantly larger in the optimistic case of telescope operation during 10 years. Indeed our estimates here are based on the simplistic uniform magnetic field model. But in this respect we would like to note that in order to study properly the systematical uncertainties related to the field model, it is not enough to model realistically the Galactic magnetic field only like it was done in [28, 37]. One also has to evaluate the potential influence of the intrinsic/PWN and heliomagnetic fields, which inevitably exist along the line of sight. Finally, the sensitivity can indeed be further increased by adding other objects into the sample including supernova remnants [40].

5 Miscellaneous targets

Globular clusters. Recently the detection of gamma rays from the globular clusters 47 Tuc and ω Cen was reported, and DM annihilation as one of the possible emission sources was proposed [41, 42]. However soon after publication [42] 5 millisecond radio pulsars were discovered in ω Cen [43]. The latter makes pulsars to be much more probable gamma-ray source than DM annihilation. However still considering both options we estimated that GAMMA-400 will be potentially able to distinguish robustly these two sources employing a good angular resolution at low energies. Figure 3 in [42] shows the fits of the ω Cen spectrum (measured by Fermi-LAT) by pulsars and annihilating WIMPs. From this figure one can see that both possible sources have very similar spectra above $\approx 300\,$MeV, which makes them hard to disentangle. Below this energy the spectra differ significantly. But over there Fermi-LAT does not really see the object presumably due to large systematics, which are caused by large PSF (even for Fermi-Front) and, hence, high background contamination from the nearby Galactic plane etc. Thus better measurements at low energies may provide a crucial information to finally determine the emission mechanism. This information could be gathered employing the thin converter of GAMMA-400, which has the PSF ≈ 2 times smaller than that of Fermi-Front and, hence, smaller background systematics. Assuming the spectrum of DM, we simulated the idealized (i.e. no background systematics) GAMMA-400 data points for ω Cen at low energies — see figure 8. We see quite perfect distinction between two possible sources with $\mathrm{TS_{DM}} = 57$. Although it is generally unlikely to find DM in this object, this is a good example, which demonstrates the advantage of GAMMA-400 at low energies.

Subhalos and dwarfs. They continue to be interesting targets for DM searches in gamma rays. We provided some estimates of subhalo detectability by GAMMA-400 in [44]. As for the dwarf Milky Way satellites, although GAMMA-400 primarily is not designated for such

JCAP11(2020)049

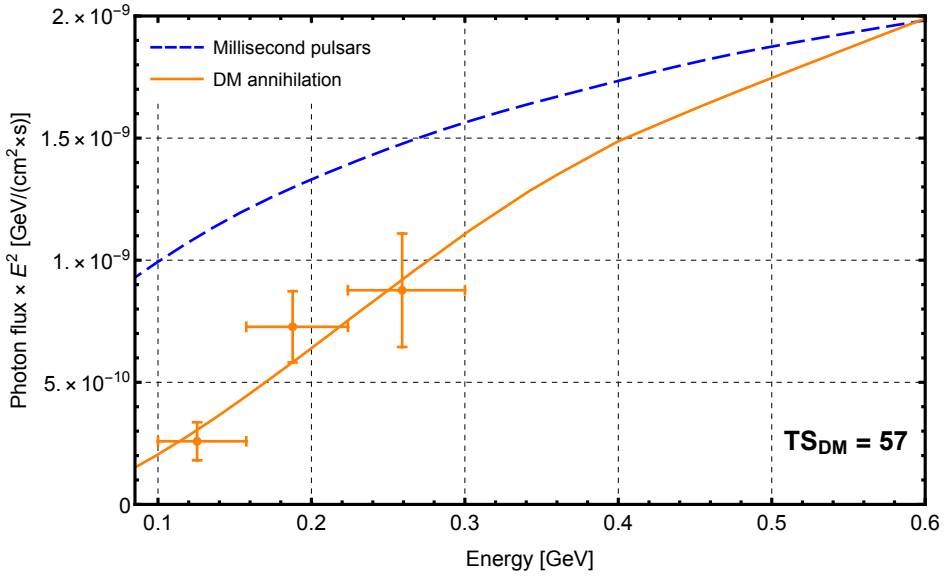


Figure 8. The fitted spectra of the globular cluster ω Cen assuming millisecond pulsars and annihilating DM as the sources of emission (from [42]) together with the simulated GAMMA-400 data points at low energies. Two spectra can be reliably distinguished. The assumed exposure time is 0.7 years.

faint high-latitude objects, potentially it may provide an improvement in the sensitivity to WIMPs annihilating there with the masses around $m_\chi \sim 100$ GeV. Such WIMP masses (assuming the thermal cross section) are poorly reached by both Fermi-LAT and ground-based Cherenkov telescopes including CTA, see e.g. figure 3 in [45]. Thus additional observations by GAMMA-400 with an excellent quality of photons above 10 GeV may play a significant role in "bridging" this mass gap.

Galactic center. It historically has the well-known gamma-ray excess (e.g. [18, 46]). The debate on its origin is still actively going on with strong arguments favoring both opportunities: the annihilating DM origin [47] and the origin from millisecond pulsars [48]. GAMMA-400 again can help to resolve finally this puzzle adding a new high quality data by the planned deep observations of the GC. Especially big progress may come from low energies: the line of reasoning similar to the one developed above for ω Cen applies to the GC as well. Also besides traditional WIMPs another recently proposed peculiar DM candidate in the form of the Bose-Einstein condensate of the hexaquark d*(2380) particles [49] has the best search prospects at sub-GeV energies in the GC as was studied in [50]!

NGC 1275 and other galaxies. NGC 1275 is a gamma-ray bright galaxy at the center of the Perseus galaxy cluster, which is supposed to host high central magnetic fields. Hence this is a good target for ALP searches, which are actively going on [39]. Although we plan to observe this object, we do not rely on it as much as on pulsars described in section 4. The reason is simply that the magnetic field distribution around NGC 1275 is less known, which produces big uncertainties in the ALP constraints derived from this object as was shown in the recent paper [51]. Thus according to [51] some alternative magnetic field models are able to elevate the limiting coupling constant values above the CAST limit (!), making the constraints from this target too model-dependent and, hence, ambiguous. Nevertheless, other

JCAP11(2020)049

similar sources — particularly, M 87 — can be studied too. Finally, the recent paper [52] identified hints of annihilating WIMPs in the outer halo of M 31 in gamma rays. This makes M 31 a potentially interesting target for GAMMA-400 too.

Other axion-related probes. Recently the paper [53] proposed another way to probe $\sim$ meV-scale axions: they can be produced inside neutron stars, escape them and then subsequently decay into gamma photons, which could be detectable as an extended halo around the neutron star. This halo is expected to have the angular radius $\approx 2^\circ$ at 10–200 MeV energies for the neutron star at distance ~ 100 pc. Such halo could be resolved as an extended source by the thin converter of GAMMA-400 (see figure 2). Other work [54] points to the opportunities at low energies too: more exotic DM in the form of axino and/or gravitino can be detected through the spectral lines from their decay in the GC.

6 Conclusions

We analyzed the capabilities of the planned space-based gamma-ray telescope GAMMA-400 for DM indirect detection. We mainly (but not only) focused on the two most popular DM candidates — WIMPs and ALPs. GAMMA-400 is expected to have improved angular and energy resolutions in comparison with Fermi-LAT, which would provide new opportunities in several directions of DM searches. The preliminary observational program of GAMMA-400 includes the deep pointed observations of the GC region during 2–4 years, deep survey of the selected parts of the Galactic plane during 1.5–2 years and other targets. Such program is expected to enable the following opportunities.

We estimated the mean sensitivity of GAMMA-400 to the narrow lines due to DM annihilation or decay in the GC and compared it with the estimated sensitivity of Fermi-LAT after 12 years of work assuming Einasto density profile for the range of DM particle masses (1–450) GeV ((1–900) GeV for decay). We obtained that with the mentioned 2–4 years exposure GAMMA-400 is more sensitive to the annihilating DM in the whole mass range and will be able to test the diphoton annihilation cross sections at least by 1.2–1.5 times smaller than that for Fermi-LAT by 12 years (figure 3). The joint analysis of Fermi-LAT and GAMMA-400 data will yield in the optimistic case the sensitivity gain up to a factor 1.8–2.3 depending on DM mass reaching $\langle\sigma v\rangle_{\gamma\gamma}(m_\chi = 100\,\text{GeV}) \approx 10^{-28}\,\text{cm}^3/\text{s}$. This in turn will allow to test comprehensively the hypothesized line at $E_\gamma = m_\chi = (64\text{–}67)$ GeV predicted by the specific DM model [13], as well as model [14] partially. This gives a good hope to reveal DM in case it is composed of those candidates. For the decaying DM the joint analysis may provide the gain of sensitivity to the DM lifetime up to a factor 1.1–2.0 reaching $\tau_{\gamma\nu}(m_\chi = 100\,\text{GeV}) \approx 2 \cdot 10^{29}$ s (figure 4).

Another promising direction is the ALP search by a potential observation of SN explosion in the Local Group. ALPs are very popular DM candidate, can be produced and emitted in SN and then detected as gamma-ray burst due to conversion to photons during propagation. Such a burst typically peaks at 50–100 MeV and represents a very sensitive probe of ALP parameters. Thus we showed that the observation of Galactic SN by GAMMA-400 can constrain the photon-ALP coupling constant down to the level $g_{a\gamma} \sim 10^{-13}\,\text{GeV}^{-1}$ for ALP masses $m_a \lesssim 1$ neV (figure 6). This represents the most sensitive indirect probe of ALPs, which allows to test some part of the ALP parameter space, where ALPs can explain all DM. For the case of SN in M 31 the sensitivity is lower by about an order of magnitude. We estimated our sensitivity in the frame of the simplified uniform magnetic field model. However,

JCAP11(2020)049

as we noted, the sensitivity dependence on the assumed magnetic field model is medium. The total chance to catch SN in the Local Group during the mission lifetime is ≈ 8–12%.

ALPs can be also constrained by observations of bright and distant Galactic gamma-ray pulsars. ALPs with certain parameter values would produce noticeable modulations in the pulsar spectra due to photon-ALP conversion in the Galactic magnetic fields. We estimated the GAMMA-400 sensitivity to ALP parameters causing such modulations by the simulation of observations of 6 convenient pulsars. GAMMA-400 appeared to be more sensitive than CAST in the mass range $m_a \approx (1-10)\,\mathrm{neV}$ reaching $g_{a\gamma}^{\min} \approx 2 \cdot 10^{-11}\,\mathrm{GeV}^{-1}$ (figure 6). This will allow to robustly test the tentative ALP detection in the spectra of these pulsars by Fermi-LAT reported in [37].

Other potentially interesting targets for WIMP searches include: the Galactic center, globular clusters, subhalos and dwarf satellites. For ALPs these are AGNs, particularly NGC 1275 and M 87. These targets are briefly described in section 5.

Indeed further development of our activities is anticipated as the mission will be approaching to the launch. The directions of development are mainly elaboration of other possible targets for DM searches, especially those outlined in section 5; refinement of the physical models involved and keeping the mission objectives up-to-date according to the developments in the field. This paper aimed to provide the sensitivity estimates at the first approximation using the current level of knowledge in the gamma-ray astronomy. The obtained sensitivity of GAMMA-400 to various DM candidates allow us to expect a significant contribution of this planned telescope to the field of DM indirect searches.

Acknowledgments

For a major part of all our calculations we use Wolfram Mathematica package and would like to acknowledge its excellent performance for the scientific computing and visualization. Our research has made use of "Aladin sky atlas" developed at CDS, Strasbourg Observatory, France [17] and the WebPlotDigitizer [55]. This study was supported by the Russian State Space Corporation ROSCOSMOS (contract no. 024-5004/16/224).

References

[1] A.M. Galper et al., *Precision Measurements of High-Energy Cosmic Gamma-Ray Emission with the GAMMA-400 Gamma-Ray Telescope*, *Phys. Atom. Nucl.* **80** (2017) 1141 [*Yad. Fiz.* **80** (2017) 660] [INSPIRE].

[2] L. Roszkowski, E.M. Sessolo and S. Trojanowski, *WIMP dark matter candidates and searches—current status and future prospects*, *Rept. Prog. Phys.* **81** (2018) 066201 [arXiv:1707.06277] [INSPIRE].

[3] https://www.slac.stanford.edu/exp/glast/groups/canda/lat_Performance.htm.

[4] K. Duan, Y.F. Liang, Z.Q. Shen, Z.L. Xu and C. Yue, *The performance of DAMPE for gamma-ray detection*, *PoS* **ICRC2017** (2018) 775 [INSPIRE].

[5] J. Aleksić et al., *The major upgrade of the MAGIC telescopes, Part II: A performance study using observations of the Crab Nebula*, *Astropart. Phys.* **72** (2016) 76 [arXiv:1409.5594] [INSPIRE].

[6] N. Park, *Performance of the VERITAS experiment*, *PoS* **ICRC2015** (2016) 771 [arXiv:1508.07070] [INSPIRE].

[7] https://www.cta-observatory.org/science/cta-performance/.

JCAP11(2020)049

[8] I.V. Arkhangelskaja et al., *Gammas and Charged Particles Identification in Lateral and Additional Apertures of GAMMA-400*, *Phys. Atom. Nucl.* **82** (2020) 845 [INSPIRE].

[9] N.P. Topchiev et al., *Space-based GAMMA-400 mission for direct gamma- and cosmic-ray observations*, *J. Phys. Conf. Ser.* **1181** (2019) 012041 [INSPIRE].

[10] G. Bertone, C.B. Jackson, G. Shaughnessy, T.M.P. Tait and A. Vallinotto, *Gamma Ray Lines from a Universal Extra Dimension*, *JCAP* **03** (2012) 020 [arXiv:1009.5107] [INSPIRE].

[11] P. Fileviez Pérez and C. Murgui, *Gamma Lines from the Hidden Sector*, *Phys. Rev. D* **100** (2019) 123007 [arXiv:1901.10483] [INSPIRE].

[12] A. Albert et al., *Search for* 100 *MeV to* 10 *GeV* γ*-ray lines in the Fermi-LAT data and implications for gravitino dark matter in* $\mu\nu$*SSM*, *JCAP* **10** (2014) 023 [arXiv:1406.3430] [INSPIRE].

[13] J.M. Cline and T. Toma, *Pseudo-Goldstone dark matter confronts cosmic ray and collider anomalies*, *Phys. Rev. D* **100** (2019) 035023 [arXiv:1906.02175] [INSPIRE].

[14] K.-C. Yang, *A potentially detectable gamma-ray line in the Fermi Galactic center excess — in light of one-step cascade annihilations of secluded (vector) dark matter via the Higgs portal*, *JHEP* **07** (2020) 148 [arXiv:2001.04946] [INSPIRE].

[15] M. Ackermann et al., *Updated search for spectral lines from Galactic dark matter interactions with pass 8 data from the Fermi Large Area Telescope*, *Phys. Rev. D* **91** (2015) 122002 [arXiv:1506.00013] [INSPIRE].

[16] https://fermi.gsfc.nasa.gov/ssc/data/access/lat/BackgroundModels.html.

[17] F. Bonnarel et al., *The ALADIN interactive sky ATLAS. A reference tool for identification of astronomical sources*, *Astron. Astrophys. Suppl. Ser.* **143** (2000) 33.

[18] M. Ackermann et al., *The Fermi Galactic Center GeV Excess and Implications for Dark Matter*, *Astrophys. J.* **840** (2017) 43 [arXiv:1704.03910] [INSPIRE].

[19] Fermi-LAT collaboration, *Fermi Large Area Telescope Fourth Source Catalog*, *Astrophys. J. Suppl.* **247** (2020) 33 [arXiv:1902.10045] [INSPIRE].

[20] B. Anderson, S. Zimmer, J. Conrad, M. Gustafsson, M. Sánchez-Conde and R. Caputo, *Search for Gamma-Ray Lines towards Galaxy Clusters with the Fermi-LAT*, *JCAP* **02** (2016) 026 [arXiv:1511.00014] [INSPIRE].

[21] Y.-F. Liang, Z.-Q. Xia, K.-K. Duan, Z.-Q. Shen, X. Li and Y.-Z. Fan, *Limits on dark matter annihilation cross sections to gamma-ray lines with subhalo distributions in N -body simulations and Fermi LAT data*, *Phys. Rev. D* **95** (2017) 063531 [arXiv:1703.07078] [INSPIRE].

[22] G. Bertone, *Particle Dark Matter: Observations, Models and Searches*, Cambridge University Press, Cambridge U.K. (2010) [https://doi.org/10.1017/CBO9780511770739] [INSPIRE].

[23] M. Kamionkowski, S.M. Koushiappas and M. Kuhlen, *Galactic Substructure and Dark Matter Annihilation in the Milky Way Halo*, *Phys. Rev. D* **81** (2010) 043532 [arXiv:1001.3144] [INSPIRE].

[24] T.M. Callingham et al., *The mass of the Milky Way from satellite dynamics*, *Mon. Not. Roy. Astron. Soc.* **484** (2019) 5453 [arXiv:1808.10456] [INSPIRE].

[25] V.F. Cardone, E. Piedipalumbo and C. Tortora, *Spherical galaxy models with power law logarithmic slope*, *Mon. Not. Roy. Astron. Soc.* **358** (2005) 1325 [astro-ph/0501151] [INSPIRE].

[26] G.A. Mamon and E.L. Łokas, *Dark matter in elliptical galaxies. 1. Is the total mass density profile of the NFW form or even steeper?*, *Mon. Not. Roy. Astron. Soc.* **362** (2005) 95 [*Erratum ibid.* **370** (2006) 1581] [astro-ph/0405466] [INSPIRE].

JCAP11(2020)049

[27] S. Hoof, A. Geringer-Sameth and R. Trotta, *A Global Analysis of Dark Matter Signals from 27 Dwarf Spheroidal Galaxies using 11 Years of Fermi-LAT Observations*, *JCAP* **02** (2020) 012 [arXiv:1812.06986] [INSPIRE].

[28] M. Meyer, M. Giannotti, A. Mirizzi, J. Conrad and M.A. Sánchez-Conde, *Fermi Large Area Telescope as a Galactic Supernovae Axionscope*, *Phys. Rev. Lett.* **118** (2017) 011103 [arXiv:1609.02350] [INSPIRE].

[29] A. Payez, C. Evoli, T. Fischer, M. Giannotti, A. Mirizzi and A. Ringwald, *Revisiting the SN1987A gamma-ray limit on ultralight axion-like particles*, *JCAP* **02** (2015) 006 [arXiv:1410.3747] [INSPIRE].

[30] D. Horns, L. Maccione, M. Meyer, A. Mirizzi, D. Montanino and M. Roncadelli, *Hardening of TeV gamma spectrum of AGNs in galaxy clusters by conversions of photons into axion-like particles*, *Phys. Rev. D* **86** (2012) 075024 [arXiv:1207.0776] [INSPIRE].

[31] A.E. Egorov and E. Pierpaoli, *Constraints on dark matter annihilation by radio observations of M31*, *Phys. Rev. D* **88** (2013) 023504 [arXiv:1304.0517] [INSPIRE].

[32] A.E. Egorov, J.M. Gaskins, E. Pierpaoli and D. Pietrobon, *Dark matter implications of the WMAP-Planck Haze*, *JCAP* **03** (2016) 060 [arXiv:1509.05135] [INSPIRE].

[33] P. Di Vecchia, M. Giannotti, M. Lattanzi and A. Lindner, *Round Table on Axions and Axion-like Particles*, *PoS* **Confinement2018** (2019) 034 [arXiv:1902.06567] [INSPIRE].

[34] S.M. Adams, C.S. Kochanek, J.F. Beacom, M.R. Vagins and K.Z. Stanek, *Observing the Next Galactic Supernova*, *Astrophys. J.* **778** (2013) 164 [arXiv:1306.0559] [INSPIRE].

[35] A. Odrzywolek, M. Misiaszek and M. Kutschera, *Detection possibility of the pair - annihilation neutrinos from the neutrino - cooled pre-supernova star*, *Astropart. Phys.* **21** (2004) 303 [astro-ph/0311012] [INSPIRE].

[36] L.J. Rosenberg, *Dark-matter QCD-axion searches*, *Proc. Nat. Acad. Sci.* **112** (2015) 12278 [INSPIRE].

[37] J. Majumdar, F. Calore and D. Horns, *Search for gamma-ray spectral modulations in Galactic pulsars*, *JCAP* **04** (2018) 048 [arXiv:1801.08813] [INSPIRE].

[38] A. Kirichenko et al., *Optical observations of PSR J2021+3651 in the Dragonfly Nebula with the GTC*, *Astrophys. J.* **802** (2015) 17 [arXiv:1501.04594] [INSPIRE].

[39] Fermi-LAT collaboration, *Search for Spectral Irregularities due to Photon-Axionlike-Particle Oscillations with the Fermi Large Area Telescope*, *Phys. Rev. Lett.* **116** (2016) 161101 [arXiv:1603.06978] [INSPIRE].

[40] Z.-Q. Xia, Y.-F. Liang, L. Feng, Q. Yuan, Y.-Z. Fan and J. Wu, *Searching for the possible signal of the photon-axionlike particle oscillation in the combined GeV and TeV spectra of supernova remnants*, *Phys. Rev. D* **100** (2019) 123004 [arXiv:1911.08096] [INSPIRE].

[41] A.M. Brown, T. Lacroix, S. Lloyd, C. Bœhm and P. Chadwick, *Understanding the γ-ray emission from the globular cluster 47 Tuc: evidence for dark matter?*, *Phys. Rev. D* **98** (2018) 041301(R) [arXiv:1806.01866] [INSPIRE].

[42] A.M. Brown, R. Massey, T. Lacroix, L.E. Strigari, A. Fattahi and C. Bœhm, *The glow of annihilating dark matter in Omega Centauri*, arXiv:1907.08564 [INSPIRE].

[43] S. Dai et al., *Discovery of Millisecond Pulsars in the Globular Cluster Omega Centauri*, *Astrophys. J. Lett.* **888** (2020) L18 [arXiv:1912.08079] [INSPIRE].

[44] A.E. Egorov et al., *Detactability of Dark Matter Subhalos by Means of the GAMMA-400 Telescope*, *Phys. Atom. Nucl.* **81** (2018) 373 [*Yad. Fiz.* **81** (2018) 360] [arXiv:1710.02492] [INSPIRE].

JCAP11(2020)049

[45] N. Hiroshima, M. Hayashida and K. Kohri, *Dependence of accessible dark matter annihilation cross-sections on the density profiles of dwarf spheroidal galaxies with the Cherenkov Telescope Array*, *Phys. Rev. D* **99** (2019) 123017 [arXiv:1905.12940] [INSPIRE].

[46] K.N. Abazajian, N. Canac, S. Horiuchi and M. Kaplinghat, *Astrophysical and Dark Matter Interpretations of Extended Gamma-Ray Emission from the Galactic Center*, *Phys. Rev. D* **90** (2014) 023526 [arXiv:1402.4090] [INSPIRE].

[47] R.K. Leane and T.R. Slatyer, *Revival of the Dark Matter Hypothesis for the Galactic Center Gamma-Ray Excess*, *Phys. Rev. Lett.* **123** (2019) 241101 [arXiv:1904.08430] [INSPIRE].

[48] K.N. Abazajian, S. Horiuchi, M. Kaplinghat, R.E. Keeley and O. Macias, *Strong constraints on thermal relic dark matter from Fermi-LAT observations of the Galactic Center*, *Phys. Rev. D* **102** (2020) 043012 [arXiv:2003.10416] [INSPIRE].

[49] M. Bashkanov and D.P. Watts, *A new possibility for light-quark Dark Matter*, *J. Phys. G* **47** (2020) 03LT01 [arXiv:2001.08654] [INSPIRE].

[50] G. Beck, *Indirect detection prospects for $d^*(2380)$ dark matter*, arXiv:2003.09283 [INSPIRE].

[51] M. Libanov and S. Troitsky, *On the impact of magnetic-field models in galaxy clusters on constraints on axion-like particles from the lack of irregularities in high-energy spectra of astrophysical sources*, *Phys. Lett. B* **802** (2020) 135252 [arXiv:1908.03084] [INSPIRE].

[52] C. Karwin, S. Murgia, S. Campbell and I. Moskalenko, *Fermi-LAT Observations of Gamma-Ray Emission Towards the Outer Halo of M31*, in proceedings of the *8th International Fermi Symposium: Celebrating 10 Year of Fermi*, Baltimore, MD, U.S.A., 14–19 October 2018, [arXiv:1812.02958] [INSPIRE].

[53] B. Berenji, *Constraints on Axions from Spatially-Extended Gamma-Ray Emission from Neutron Stars*, arXiv:2004.08785 [INSPIRE].

[54] G.A. Gómez-Vargas, D.E. López-Fogliani, C. Muñoz and A.D. Perez, *MeV-GeV γ-ray telescopes probing axino LSP/gravitino NLSP as dark matter in the $\mu\nu$SSM*, *JCAP* **01** (2020) 058 [arXiv:1911.03191] [INSPIRE].

[55] https://apps.automeris.io/wpd/.

JCAP11(2020)049

Updated constraints on WIMP dark matter annihilation by radio observations of M31

Andrei E. Egorov*

Nuclear Physics and Astrophysics Division, Lebedev Physical Institute, Leninskii prospect—53, 119333 Moscow, Russia

(Received 4 May 2022; accepted 7 July 2022; published 21 July 2022)

The present work derived the robust constraints on annihilating weakly interacting massive particle (WIMP) parameters utilizing new radio observations of M31 as well as new studies of its dark matter distribution and other properties. The characteristics of emission due to dark matter (DM) annihilation were computed in the frame of a 2D galactic model employing GALPROP code adapted specifically for M31. This enabled us to refine various inaccuracies of previous studies on the subject. DM constraints were obtained for two representative annihilation channels: $\chi\chi \to b\bar{b}$ and $\chi\chi \to \tau^+\tau^-$. A wide variety of radio data was utilized in the frequency range $\approx$(0.1–10) GHz. As the result, the thermal WIMP lighter than fiducially $\approx$70 GeV for $b\bar{b}$ channel and $\approx$40 GeV for $\tau^+\tau^-$ was excluded. The corresponding mass threshold uncertainty ranges were estimated to be 20–210 GeV and 18–89 GeV. The obtained exclusions are competitive to those from Fermi-LAT observations of dwarfs and AMS-02 measurements of antiprotons. Our constraints do not exclude the explanation of the γ-ray outer halo of M31 and the Galactic Center excess by annihilating DM. The thermal WIMP with $m_x \approx 70$ GeV, which explains the outer halo, would make a significant contribution to the nonthermal radio flux in M31 nucleus, fitting well both the spectrum and morphology. And, finally, we questioned the possibility claimed in other studies to robustly constrain heavy thermal WIMP with $m_x > 100$ GeV by radio data on M31.

DOI: 10.1103/PhysRevD.106.023023

I. INTRODUCTION AND MOTIVATION

The physical nature of dark matter (DM) remains to be one of the biggest puzzles in modern physics and astronomy. Currently, we may outline three most popular candidates for the role of DM: weakly interacting massive particles (WIMPs), axionlike particles (ALPs), and sterile neutrinos (see, e.g., Ref. [1] for a review). This work is dedicated to indirect searches of the first candidate—WIMPs, which historically have been the most anticipated. The idea of indirect searches is based on the opportunity of pair annihilation of WIMPs, which are assumed to be Majorana fermions, particularly, e.g., neutralinos. This annihilation produces various highly energetic Standard Model particles, whose signatures can be potentially detected or constrained astrophysically. Historically, this idea was introduced and explored for the first time probably in [2]. For a review of the contemporary status of this field, one may see, e.g., Ref. [3]. In our case, we consider DM halo of the big neighbor galaxy M31 (or Andromeda galaxy, or NGC 224). Annihilating WIMPs in its halo would produce relativistic electrons and positrons ($e^{\pm}$), which in turn would generate synchrotron emission in the galactic magnetic field (MF) at radio frequencies. Hence, the radio observations of the galaxy may infer some constraints on annihilating DM or even hints of DM signal.

This work mainly aims to derive the conservative and robust constraints on WIMP parameters—mass and annihilation cross section. The considered WIMP mass range is 10–1000 GeV. Indeed, theoretically, WIMPs may exist beyond this range. However, WIMPs lighter than $\sim$10 GeV with the cross section around the thermal value are already excluded robustly by various strategies [3], at least for canonical annihilation channels. And WIMPs heavier than $\sim$1 TeV produce too faint radio signals to be separable from other astrophysical emissions. Then inside the chosen mass range, thermal WIMPs lighter than $\approx$(20–100) GeV were excluded by Fermi-LAT observations of dwarf Milky Way (MW) satellites [4,5]. The quoted mass threshold is so uncertain due to uncertainties in the assumed DM densities in dwarfs and a variety of possible annihilation channels. Then the masses above $\approx$100 GeV are expected to be probed by future Cherenkov Telescope Array (CTA) observations of the Galactic halo [6]. Thus, γ-ray observations, although producing rather model-independent constraints, tend to have some sensitivity gap around $m_x = 100$ GeV. Hence, other independent probes should be utilized in order to complement searches in the γ-ray band, also verifying them independently. And radio observations are one such probe. Unlike the prompt gamma

*aegorov@runbox.com

 © 2022 American Physical Society

radiation, the radio emission is produced by secondary $e^{\pm}$, which makes the respective constraints more model dependent. However, the advantage of the radio band is much higher angular and spectral resolutions in comparison with the γ-ray band, which provides very detailed imaging of targets. The polarization information can be utilized too, which enhances the sensitivity even further [7]. Thus, the ultimate goal of our work is to probe WIMP masses up to $\approx$100 GeV at the level of thermal cross section as the most physically motivated one.

M31 is one of the best targets in the sky for DM searches in radio due to its proximity, which allows detailed imaging and studies of the galactic environment—particularly mass and MF distributions. Dwarf MW satellites are not so attractive in radio as in the γ-ray band due to the absence of any direct measurements of their MF. Objects beyond the Local Group are more distant and, hence, would have fainter annihilation signals. Our own Galaxy MW might be worse target than M31 due to brighter central region, which is illustrated by Table I at a couple of relevant frequencies. The total radio emission is indeed composed by a wide variety of mechanisms, and it is quite difficult to separate the various emission components. Hence, in general, a lower total emission intensity would imply a lower limit on the intensity of emission due to DM annihilation and, therefore, stronger DM constraints. A majority of the emission from DM is concentrated in a small region around the galactic center with radius $R \sim 1$ kpc; since typically DM density falls off with distance fast, and the volumic annihilation rate is proportional to the square of DM density. We see from Table I that M31 nucleus is fainter than that of MW by more than an order of magnitude. This suggests potentially high sensitivity to weak DM contribution and motivates us to study M31 very thoroughly as a promising target.

At the frequencies relevant for WIMP searches, the galactic radio emission has two main components—thermal and nonthermal (illustrated in Fig. 3 below). The thermal emission is generated by ionized galactic gas and can be relatively easily subtracted due to a distinct spectral shape. The nonthermal emission represents the synchrotron from relativistic $e^{\pm}$ of cosmic rays (CR) and may contain the component from $e^{\pm}$ of DM. To distinguish these two populations, they are refereed as CR and DM $e^{\pm}$, respectively. It is difficult in general to separate these two components of synchrotron emission, since they have quite similar spectral shapes as shown below. For this reason, in order to derive conservative and robust DM constraints, I separated out only the thermal emission when possible and did not attempt to estimate the level of CR synchrotron. Such an attempt would indeed strengthen the constraints but make them very model dependent at the same time.

In order to derive DM constraints, at first, we have to model theoretically the characteristics of anticipated emission due to DM, i.e., its intensity dependence on frequency and direction. This is done by utilization of GALPROP code and is described in Sec. III. The obtained DM emission maps and spectra are discussed in Sec. IV. Then the relevant observational data were collected and compared with the theoretically calculated DM emission intensity. The latter is linearly proportional to the annihilation cross section. This fact allows us to calculate the limits on cross section relatively easily for a fixed WIMP mass. The derivation of constraints is described in Sec. V. Then Sec. VI relates the derived constraints with those from γ-ray band and antiprotons. And Sec. VII discusses semi-qualitatively possible DM contribution into the central radio emission in M31.

In fact, this paper continues our previous work on the subject [11]. Currently, an attempt of comprehensive study has been made, which includes the following key novelties and improvements:

(1) Multiple inaccuracies made in the previous works (they are discussed in Sec. II) were refined.
(2) New information on DM density distribution and galactic environment emerged over last 10 years were incorporated.
(3) For the first time, the transport equation for DM $e^{\pm}$ was solved in 2D including the diffusion of $e^{\pm}$, before only 1D (i.e., spherically symmetric) approximation was implemented—more in Sec. II.
(4) New radio observational data were included, particularly very valuable low-frequency images from LOFAR.
(5) Emission component separation was included: at some frequencies, the utilized maps are cleaned of the discrete projected nuisance sources and diffuse thermal emission.

Table II shows the utilized parameters of M31, which define its position with respect to the observer. Over the text of the paper, the variable R denotes the 3D radial distance,

TABLE I. The estimated intensities of the nuclear regions ($R \leqslant 1$ kpc) of MW and M31 at relevant frequencies with respective references.

Galaxy	Intensity at 0.408 GHz, kJy/sr	Intensity at 1.42 GHz, kJy/sr
MW	1400 [8]	440 [9]
M31	78 [10]	32 [10]

TABLE II. The values of basic parameters of M31 used in this work.

Parameter	Value	Reference
Galactic longitude of center	121.17°	[12]
Galactic latitude of center	−21.57°	[12]
Distance d	760 kpc	[13]
Inclination	74°	[13]

while (r, z) are cylindrical coordinates attached to the galactic plane. They correspond to (ρ', z') coordinates in our paper [11].

II. CRITICAL REVIEW OF THE PREVIOUS WORKS ON THE SUBJECT

Here is the list of papers dedicated to DM searches in M31 in radio best to the author's knowledge—[11,14–17]. Each of these works has certain weaknesses, which are briefly reviewed below.

Reference [11] (our work) was the first approximation to the task. In that study, we neglected by the spatial diffusion of DM $e^{\pm}$ in the central region. Then Eqs. (8) and (10) there, which define the energy loss rates for $e^{\pm}$, are unfortunately incorrect at some level, which was revealed in verification procedure conducted now. Thus, inverse Compton scattering (ICS) losses (8) must have the prefactor 1.0 instead of 0.76. Then the bremsstrahlung losses (10) there must have the form as (12) here below. Moreover, historically, these errors propagated through many papers due to copying without checking. Thus, the following nonexhaustive list of papers has wrong expressions for some of the energy loss components—[14,16,18–23]. These loss rates play an important role in the calculations. For this reason, the verified expressions for them are provided below—Eqs. (10)–(13). Another possible problem in the above papers is the expression for electron's synchrotron power. This can be seen, for example, in [[18], Eq. (38)]: the physical meaning of the factor $(1 + (\gamma\nu_p/\nu)^2)^{3/2}$ is unclear; its explanation can not be found. Returning back to the discussion of [11]: we assumed there for the interstellar radiation field (ISRF) energy density to be constant and equal to that in MW center. This energy density defines the ICS loss rate [Eq. (11)]. Indeed, the density is not uniform in the galactic environment and, as shown in Sec. III D below, larger in M31 nucleus by ≈2 times with respect to that in MW nucleus.

Reference [14] calculated multifrequency emissions from annihilating WIMPs, which would fit the γ-ray excess around M31 center seen by Fermi-LAT [24]. For this purpose, the authors solved analytically the transport equation for DM $e^{\pm}$ with spatial diffusion in the spherically symmetric approximation employing their RX-DMFIT tool [23]. Although such universal tools are generally useful, 1D approximation presumably applies well to dwarf spheroidals and virialized galaxy clusters, but not to spiral galaxies, which inherently have (at least) 2D geometry. Also, each target has its own peculiar properties. The authors extrapolated (similarly to [11]) MW central ISRF energy density to M31, which would overestimate the emission intensity from $e^{\pm}$ due to underestimated cooling rate.

Reference [15] claimed abnormally strong DM constraints from their observations of M31 at 5 GHz (just one frequency) by 26 m single-dish radio telescope. Thus, these authors stated the exclusion of WIMP masses up to ≈300 GeV for all annihilation channels. They claimed that by somehow their observational technique called "cross scans" managed to avoid the majority of usual astrophysical emissions and left mainly the diffuse large-scale emission potentially attributable to DM. The described technique is not understandable, especially taking into account their angular resolution FWHM ≈ 10′. They utilized the region, which captures essentially the whole galaxy, for the derivation of constraints. The measured diffuse signal looks to be around the noise level from their Fig. 1. Likely, the authors severely underestimated the large-scale diffuse flux, getting its value much below other independent measurements. Then in the calculations, they neglected completely by the spatial diffusion of DM $e^{\pm}$ in the whole galaxy, and by spatial variations of MF and ISRF density. These are clearly crude approximations, as can be seen, e.g., from [[14], Fig. 6], where the impact of diffusion coefficient value on the radio flux is shown for the central kiloparsec. This impact is significant even in the central region, where $e^{\pm}$ cool fast. In outer regions, $e^{\pm}$ cool much slower, hence migrate much further sinking into the halo—and the diffusion is much more important. Thus, overall the claimed constraints can not be considered as justified.

Reference [16] basically solved the transport equation again in 1D and possibly (not really clear from the text) neglected by the diffusion too, producing even stronger constraints than [15] with large region of interests (ROIs) up to 50′. Thus, the reasoning from the previous two paragraphs applies here directly, too. One advantage here in comparison with [15] is the spatially dependent MF (1D). However, MF model in [16] [their Eq. (4.2), taken from [25]] likely has the wrong meaning of "r" variable: originally in [25], it means 2D (radial-in-plane) distance, but the author of [16] interpreted "r" as 3D distance, hence distorting the model significantly. Meanwhile, the same misinterpretation likely happened in [15] too. Then the author claimed that the derived constraints rule out DM interpretation of Galactic Center (GC) γ-ray and antiproton CR excesses. However, the derived constraints are again doubtful, as it is shown below.

Reference [17] utilized the radio data [26] at 5–8 GHz and claimed a possible presence of DM contribution in the central emission, with the former being well-fitted by the thermal WIMP with $m_x \approx 30$ GeV. However, the least understandable fact in the story is that the authors seem to ignore, that they robustly ruled out such a WIMP in their work [15] a couple of years ago! Thus, their two papers seem to require different WIMPs for the inner and outer parts of M31. Besides this, their model of observational uncertainties is not transparent; e.g., a map noise and systematics are not mentioned. Also, the authors assumed the stellar density profile to be the tracer of non-DM radio emission. However, CR synchrotron must not necessarily

follow the stellar density, since the former is defined by the distribution of CR accelerators and $e^{\pm}$ diffusion. Also, such a frequency range is not optimal for WIMP detection as shown below.

Thus, this section pedagogically demonstrated that the current situation is not really satisfactory—all the works discussed above have certain inaccuracies. Therefore, M31 still lacks the comprehensive and precise analysis. This created the motivation to build the full 2D model and derive more precise DM constraints. The comparison of newly derived constraints with those from papers above is discussed in Secs. VI, VIII.

III. MODELING THE EMISSION DUE TO DM ANNIHILATION BY GALPROP

In this section, I describe the first key step—the computation of theoretically expected emission maps and spectra due to WIMPs annihilation. In general, there are two possible ways of this computation: one is to create a new code specifically for this purpose like we did in our previous work [11] or to adapt widely used codes, which compute CR propagation and emission. The latter way has a big advantage: we do not need to do an extensive calibration and checking of the whole code, instead we only have to check the part modified for our purpose. Moreover, in the past, we had already developed the extension for GALPROP package, which accurately computes DM annihilation. This was done in the frame of our work [27] on DM searches in MW for version 54 of GALPROP. Later, the new version 56 was released, which has many new functionalities including an arbitrary observer placement in the Galaxy [28,29]. The latter opportunity allows us in principle to apply GALPROP to *any* galaxy—not just to the MW. These circumstances evidently defined my choice to employ GALPROP v56 for the task. Only two essential procedures were needed: adaptation of our DM extension for v56, and then—v56 for M31. Our DM extension for both versions of GALPROP is made public at [30] for convenient usage by astrophysical community. The detailed explanations are also provided there. The extension for v56 includes some features specifically related to M31.

The source term in the transport equation incorporated by our extension defines injection of $e^{\pm}$ produced by WIMP annihilation and has the following form:

$$q(R,E) = \frac{1}{2}\langle\sigma v\rangle\left(\frac{\rho(R)}{m_x}\right)^2 \xi(R)\frac{dN_e}{dE}(E), \qquad (1)$$

where $\langle\sigma v\rangle$ denotes WIMP annihilation cross section, $\rho(R)$ is DM density distribution, m_x is WIMP mass, $\xi(R)$ is the DM annihilation rate boost factor due to substructures, and $\frac{dN_e}{dE}(E)$ represents the energy spectrum of $e^{\pm}$ per annihilation. For the latter, the same spectra were used as in our previous works cited above. These spectra were taken from PPPC 4 DM ID resource [31,32].

Modeling the emission due to DM annihilation indeed suffers from various significant uncertainties, which include and are not limited to those in DM density and MF distributions, propagation parameters of galactic environment. And it is very important to include and quantify all significant uncertainties in the procedure of DM constraints derivation. To quantify uncertainties, the popular MIN-MED-MAX paradigm (like, e.g., in [33]) was utilized, when MIN and MAX model setups provide, respectively, the lowest and highest DM emission intensities and hence, the weakest and strongest constraints. And MED setup represents some middle or "average expectation" scenario. It is not constructed to yield exactly the average intensity between MIN and MAX. In this respect, MED is probably less informative, since MIN and MAX represent rather hard limits, and the real intensity lives somewhere between them. MIN-MED-MAX models were built separately for the DM density profile and MF distribution together with the propagation parameters (MF/prop. with "/" meaning "and")—i.e., three independent density profiles and three independent MF/prop. configurations were tested. MF and propagation parameters were treated jointly in order to reduce the computational heaviness of the task. Also, it is not so necessary to vary propagation parameters independently, since the impact of their uncertainties is much smaller than that of DM and MF distributions. Thus, for each WIMP mass and annihilation channel 3 DM density profiles $\times 3$ MF/prop. configurations $= 9$ independent models were computed, providing a good coverage of the parameter space. DM intensities were computed for 13 log-evenly spaced WIMP masses over our range of interest 10–1000 GeV, which provides sufficiently dense coverage for further interpolation. And so far, I computed only two representative and popular annihilation channels—$\chi\chi \to b\bar{b}$ and $\chi\chi \to \tau^+\tau^-$. Just with two channels, the total number of computed models, i.e., separate GALPROP runs, is thus $13 \times 2 \times 9 = 234$. Such a model grid required a significant amount of computational time. For this reason, other annihilation channels were left for future work. Also, as can be seen, e.g., at [[34], Fig. 9], the exclusion limits for other channels can be expected to lie approximately between those for $b\bar{b}$ and $\tau^+\tau^-$. The next subsections describe in detail all the essential ingredients needed for modeling of the emission due to DM annihilation. The dependence of thermal annihilation cross section on WIMP mass was gathered from the updated work on the subject [35,36].

A. Adaptation of GALPROP for M31

The main difference between MW and M31 cases in the frame of modeling by GALPROP is the location of observer. Fortunately, GALPROP from v56 allows us to set an arbitrary location. However, if one would set the true distance

to M31, then the map pixels would be too large to achieve an acceptable angular resolution. For this reason, M31 was placed at the fake distance $d_f = 50$ kpc, and all the angular quantities were rescaled by the following relation from a simple geometry: $d \tan\alpha \approx d_f \tan\alpha_f$. The fake distance value was chosen from two obvious requirements: on one hand, it must be much larger than the relevant ROIs; on the other hand, it must be small enough to provide sufficient angular resolution about the angular size of GALPROP spatial grid step. It was checked empirically that the rescaling by relation above with the chosen value of d_f does not introduce any significant intensity distortions. Thus, the introduced d_f allowed us to have a comfortable (not too large) number of pixels on the produced HEALPix maps.

Another aspect is the choice between 2D and 3D solution of the transport equation. Since practically all the model ingredients are 2D, this was an obvious choice to speed up computation. Also, the difference between 2D and 3D solutions was checked to be negligible for the small enough spatial grid step in 2D. The numerical values of general GALPROP parameters, which are the same for all MIN-MED-MAX setups, are written out in the Appendix.

Then it was very important to establish/check the consistency between our previous setups [11,27] and the current one. After long and deep investigations, it was concluded that all three setups agree at the level not worse than ≈10%, which is a very good agreement. [11] used the code, which is completely independent with respect to GALPROP. Hence, the obtained agreement provides the mutual check between all three setups and their results.

B. Modeling DM density distribution

The first important question here one may have is whether traditional spherically symmetric density profiles would describe M31 dark halo adequately. Besides many spherically symmetric models, two papers were found, which claimed both significantly oblate and prolate halo shapes—[37] and [38], respectively. Thus, no systematic and robust deviation from the spherical symmetry seems to be detected. Hence, the spherically symmetric DM density distributions were employed.

Many studies concerning DM distribution in M31 were considered, and [39–45] were utilized among them. Overall, they have quite a good agreement with each other. As was outlined above, I aimed to choose three representative density profiles among many ones derived in the above papers: one "average expectation" case (MED) and two boundary cases around it, which would majorly enclose the uncertainty range (MIN/MAX). Usually, stellar and gas kinematics do not allow us to deduce reliably DM distribution in the inner regions of big galaxies; since baryons dominate the potential there, noncircular motions arise etc. Thus, almost all the above studies derived DM density distribution at distances above 7–8 kpc, leaving it very poorly constrained in the inner kiloparsecs. At the same time, the density in this inner region majorly defines the DM constraints that we are looking for, since the signal from DM is very concentrated towards the center (see, e.g., [[11], Fig. 5]). Hence, our constraints would be very uncertain, if we would just formally extrapolate the profiles derived for an outer region into the inner region. Thus, the estimates showed that the most cored (Burkert) profile from [43] allows thermal WIMPs with almost *any* mass in our range of interest (for MED MF/prop.), while the most cuspy/contracted (Moore) profile would exclude WIMP masses up to almost 1 TeV. Fortunately, the new works [44,45] allow us to shrink reasonably such a huge uncertainty range. The team [44] introduced newer data and sophisticated two-bulge 2D-model for M31, which yielded satisfactory estimates of DM density in the inner region—Fig. 12 there. Their estimates reliably exclude both extreme cases—very shallow profile like Burkert and very contracted one like Moore. The authors of [45] pointed out that "the giant stellar stream and the shell-like features of M31 are probably results of accretion of the satellites from highly eccentric orbits." They modeled the influence of such accretion of DM-rich satellite on the central DM cusp and found, that even if the initial DM distribution in M31 was very cuspy, the central cusp would be unavoidably washed out after the accretion. Thus, the final profile is expected to be rather cored, although with quite high central densities—see [[45], Figs. 5 and 8]. Based on these results, both extremely cuspy and cored profiles were excluded from consideration. Other profiles derived in [39–44] (with sane fit qualities) form the corresponding uncertainty range. I ranked all these profiles by central densities and chose MIN-MED-MAX, which have approximately minimal-medium-maximum central densities and hence, would generate respective intensities of DM emission.

The minimal profile, which would yield the most conservative DM constraints, appeared to be Einasto from [44]. I took for MIN their lowest allowed density profile rather than the best fit to stay conservative. The chosen profile can be seen at [[44], Fig. 12] as the bottom edge of violet-shaded family of acceptable Einasto profiles. The exact definition of Einasto profile is the following:

$$\rho_{\mathrm{Ein}}(R) = \rho_{-2} \exp\left(-\frac{2}{\alpha}\left(\left(\frac{R}{R_{-2}}\right)^{\alpha} - 1\right)\right), \qquad (2)$$

where R_{-2} and ρ_{-2} are the radius and density, where the profile slope (logarithmic hereafter) goes over -2 (more details can be seen in [[43], Appendix B]). The numerical values of these parameters are provided in Table III. I note that in fact the density profiles in [44] are 2D and have a mild flattening $q = 0.85$ as a fiducial value (the definition of flattening parameter q can be seen in [[44], Eqs. (22)–(23)]). Such flattened DM halos are physically motivated by the gravitational pull from baryons towards the galactic

TABLE III. Parameter values of the employed models of DM density and MF distributions, and propagation.

Model	MIN	MED	MAX
DM density profile			
Type	Einasto	NFW	Einasto
Scale radius $R_{-2(s)}$, kpc	8.9	10.4	17.4
Scale density $\rho_{-2(s)}$, $\frac{\text{GeV}}{\text{cm}^3}$	0.383	0.585	0.0892
α slope	0.73	–	0.17
Central cusp	–	+	+
Substructure boost	–	–	+
MF distribution			
Central cusp	–	+	+
Central field value, μG	14	50	100
Vertical scale z_B, kpc	0.88	1.2	1.6
Propagation parameters			
Half-height of diffusion cylinder $z_{\max}$, kpc	2.2	2.7	3.2
Diffusion coefficient at 1 GeV D_0, cm^2/s	10×10^{27}	6×10^{27}	2×10^{27}
Diffusion coefficient slope δ	0.4	0.45	0.5
Alfven speed V_A for reacceleration coefficient, km/s	0	0	5
Optical ISRF density factor with respect to MW	2.5	2.0	1.6

plane, since the baryonic matter dominates the potential in the central region and is concentrated around the plane. However, according to estimates $q = 0.85$ and $q = 1$ (i.e., spherically symmetric) profiles yield very close J factors for the relevant ROIs—the former differ just by few percents. Such small difference is negligible in our context, hence, $q = 1$ was adopted. A J factor by definition means the following quantity:

$$J = \int_{\text{FoV}} \int_{\text{LoS}} \rho^2(\vec{r'}) d\Omega dl'; \tag{3}$$

i.e., this is the squared DM density integrated over the solid angle of ROI and the line of sight (primed coordinates originate at the observer's position). The J factor exactly defines the flux of prompt γ rays due to DM annihilation (see, e.g., Refs. [3,5] for details). The radio flux can be assumed to be roughly proportional to a J factor, too.

I would like to note that the profile above does not reproduce correctly the total halo mass, which is profile independent and well-constrained to lie in the range $(0.7–1.3) \times 10^{12}\ M_\odot$ (e.g., [[43], Table V]). The reason is that the authors [44] aimed to reconstruct the density profile only up to radius of 15 kpc, and their profiles are not precise beyond this distance. However, it does not hamper to use it for our purposes, since, as shown below, DM emissivity is too weak at radial distances above ~10 kpc and hence, does not render much relevance there.

As the opposite MAX case, the Einasto profile derived in [43] was employed. This profile has approximately the biggest central density allowed by [44,45]. Also, it is well-known that besides the smooth DM component, numerous subhalos with a very wide mass spectrum may reside in the host halo and boost the signal from annihilating DM significantly. For this reason, I included the signal boost due to substructure on top of the regular smooth component according to the boost factor model [46] in order to get a bit optimistic DM constraints in MAX case. However, we do not expect a significant signal increase due to substructure, since the latter do not survive much in the central regions of galaxies due to tidal disruption. And DM signal is mainly localized around the center.

Then finally, we have to choose the MED density profile, which would represent approximately medium constraints between the margins provided by MIN and MAX. Such MED model can be naturally considered as more probable/expected case, or fiducial model. It was found that Navarro-Frenck-White (NFW) best-fitting profile in [44] is the closest to such MED case. The exact functional form for NFW, which is employed in GALPROP, is the following:

$$\rho_{\text{NFW}}(R) = \frac{\rho_s}{\text{Max}[R, R_{tr}]/R_s (1 + \text{Max}[R, R_{tr}]/R_s)^2}. \tag{4}$$

It is the traditional NFW (firstly introduced by [47]) truncated at $R = R_{tr}$, below which the density stays constant. $R_{tr} = 0.01$ kpc was chosen, since no N-body simulations are able to resolve anything below such scale (e.g., [45]). Hence, this truncation radius was introduced in order to stay conservative and avoid unphysical divergence at the central point. However, such small scale does not have any significant influence on the final constraints. The parameter values of all selected profiles are provided in Table III, and Fig. 1 shows the density radial dependencies. As a sanity check, we can see from the figure, that all the accepted profiles reproduce well DM density at the solar

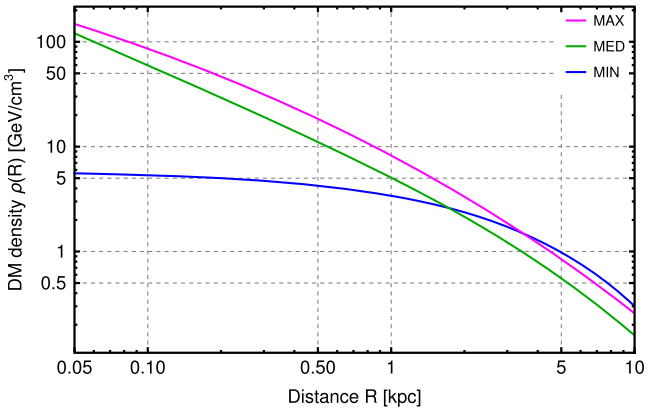


FIG. 1. DM density distributions selected as MIN-MED-MAX models. Their parameters are listed in Table III.

radius (one may expect rather similar DM halos in M31 and MW).

C. Modeling the magnetic field distribution

As was already mentioned in Sec. II, it is very important to model MF properly for the computation of synchrotron emission. Indeed, knowledge about MF distribution in M31 is much more limited than that in MW, which implies corresponding uncertainties for the expected emission. As with modeling of DM density, various available literature concerning MF in M31 was analyzed. Also, a similarity between M31 and MW was naturally utilized: some aspects, which were unclear for M31, were extrapolated from MW.

A basic structure of the utilized 2D MF model comprises piecewise-linear dependence on the radius r multiplied by the exponential dependence along the vertical coordinate z. Then MED and MAX models have additional central cusps. Such a choice of the functional form was motivated by the fact that quite all MF measurements in M31 were done inside its disk; hence, the typical simple exponential z dependence was assumed for the halo. To model the radial profile of MF in the plane, the results of mainly two papers [48,49] were utilized. Thus, [48] reported the following equipartition total field estimates in the central region: $B(0.2<r<0.4\,\mathrm{kpc})=15\pm3\,\mu\mathrm{G}$, $B(0.8<r<1.0\ \mathrm{kpc})=19\pm3\ \mu\mathrm{G}$. I took uncertainties of these and other field values in the disk as one of the factors, which defined the MIN-MED-MAX range of models. Thus, for example, for MIN, $B(0.2<r<0.4\,\mathrm{kpc})=15-3=12\,\mu\mathrm{G}$ was used, for MED—$B(0.2<r<0.4\ \mathrm{kpc})=15\ \mu\mathrm{G}$ and for MAX—$B(0.2<r<0.4\ \mathrm{kpc})=15+3=18\ \mu\mathrm{G}$. The field value in the very center $0<r<0.2$ kpc was assumed to be equal to that in the range $0.2<r<0.4$ kpc. Then [[49], Table I] provides the field values in the radial range 6–14 kpc (so-called star-forming ring, with 4 sub-ranges) at the level $B\approx6\div7\mu G\pm20\%$. And no reliable estimates in the range $1<r<6$ kpc seem to be available. Regarding this gap between the nucleus and ring [26] states, that MF exists there too, but it is just not illuminated by CR $e^{\pm}$, which are confined in the nucleus and ring. But it is hard to measure the field value in the gap, since it does not show a radio emission, and really few background sources shine through the gap (for Faraday rotation measurements) [50].

The field does not differ much among the measured ranges and, hence, changes with r relatively slowly. Considering this fact, a simple connection of the measured ranges by linear interpolation was applied in order to build the full radial dependence. Such procedure yielded the continuous radial profile. Another important circumstance, which is usually not taken into account, is that the cited field values must not be considered as values at a point or plane. Instead, these are always values effectively averaged over some volume, which is inevitably nonzero due to, e.g., a finite size of telescope beam, which is used for MF measurement (through the nonthermal emission intensity or rotation measure). The size of this volume along r coordinate is explicitly provided by the results cited above. Considering that the cited radial ranges are quite narrow, and the field changes slowly with r, this averaging effect along r was neglected. However, the field changes much faster along z in any spiral galaxy; i.e., the field falls down exponentially (in first approximation) with the scale ~1 kpc. Hence, it is important to take into account this averaging effect along z in order to model properly the values in the galactic plane. This requires one to choose the effective averaging volume size $\pm z_{av}$ along z. A natural choice, also suggested by [49], would be the characteristic thickness of the nonthermal emission layer, which can be considered as the vertical beam path length in the layer. [[49], Table I] provides the value of this thickness $z_{av}\approx0.3$ kpc. Then by the definition of volumic average, which in our case comes down to the average over z due to $B(r)\approx\mathrm{const}$ locally, we have

$$\langle B\rangle=\int_{-z_{av}}^{z_{av}}B_{pl}\exp\left(-\frac{|z|}{z_B}\right)dz\Big/\int_{-z_{av}}^{z_{av}}dz=B_{pl}\frac{z_B}{z_{av}}\left(1-\exp\left(-\frac{z_{av}}{z_B}\right)\right).\tag{5}$$

Here, z_B means the vertical scale height, $\langle B\rangle$—the effectively measured field in a certain radial range, and B_{pl}—the physical value in galactic plane, which we look for to construct MF distribution. Such averaging correction in practice is relatively small. Thus, for example, the measured MED MF value cited above for the central region $\langle B\rangle=15\ \mu\mathrm{G}$ yields $B_{pl}=17\ \mu\mathrm{G}$ with the corresponding z_B value. Having conducted the whole procedure described above, we can write out our basic MIN MF model, which is described by Eq. (6) below.

Our MIN model is based on the assumption of equipartition between the field energy density and that of CR $e^{\pm}$. Such a model represents the minimal anticipated MF. However, according to [51], the equipartition assumption may significantly underestimate the real field in irregular dense environments like galactic nuclei with fast $e^{\pm}$ cooling. This was evidently demonstrated in the work [52] for the nucleus of our Galaxy. These authors considered an approximately ellipsoidal region around the GC with semimajor and minor axes $(r_1,z_1)=(0.42,0.14)$ kpc. The simple equipartition assumption gives the field strength of just $\sim10\ \mu\mathrm{G}$ inside for fiducial model parameter values. However, the independent comprehensive multiwavelength analysis revealed the necessary minimal field strength of $50\ \mu\mathrm{G}$ (effective volumic average), with a possibility for the real field to be even at the level $\approx100\ \mu\mathrm{G}$ (see also Ref. [53]). In principle, as [52] says, equipartition may also yield $100\ \mu\mathrm{G}$, but with extremal parameter values. Such a situation may naturally exist in M31 nucleus too. For this reason, it was decided to

introduce the same MF "cusps" as in MW into MED and MAX distributions. Such MF profiles are somewhat analogous to DM density profiles in the aspect of cusp or core presence in the central region. MF cusps were embedded into MED and MAX profiles through the following way. MF was assumed to be constant with the strength 50 and 100 μG for MED and MAX profiles correspondingly inside the ellipsoidal region with semiaxes $(r_1, z_1) = (0.42, 0.14)$ kpc similar to MW. Indeed, in reality, MF likely has some internal nonuniform structure inside this region. However, it would be too speculative to assume any specific nonuniformity. For this reason, the effective volumic-average values according to the results of [52] were set. This cusp is embedded into MF outside the central region, where the environment is less dense, and the equipartition field is expected to be a better estimate. Hence, this MF outside can be described by the same piecewise-linear on r and exponential on z model discussed above for MIN profile. However, it is necessary to connect smoothly the central cusp with its surroundings avoiding unphysical field discontinuity. To do this, the transition zone was introduced, where the field is naturally assumed to transform gradually from the central non-equipartition regime down to the equipartition "state" outside. This transition zone was assumed to be restricted from outside by the ellipsoidal surface too with semiaxes $(r_2, z_2) = 2 \times (r_1, z_1) = (0.84, 0.28)$ kpc. From the inside, it is indeed restricted by the central cusp of the constant field. Thus, the transition zone can be imagined as the ellipsoidal layer around the concentrical ellipsoid with constant field. As for the field distribution in the transition zone, it was defined through the linear interpolation between field values on the boundary surfaces of the zone. Such interpolation reflects the smooth transition mentioned above. The internal surface possesses indeed the central field value 50 or 100 μG. And the external surface in turn—the corresponding piecewise-linear on r and exponential on z values. Equations (7)–(8) below summarize the structure of MED and MAX models with the formal mathematical description of the ellipsoidal surfaces,

$$B^{\mathrm{MIN}}_{\mu\mathrm{G}}(r_{\mathrm{kpc}}, z) = \exp\left(-\frac{|z|}{z_B}\right) \times \begin{cases} 14, \text{if } r < 0.4; \\ 12r + 9, \text{if } 0.4 \leqslant r < 0.8; \\ 19, \text{if } 0.8 \leqslant r < 1; \\ -2.1r + 21, \text{if } 1 \leqslant r < 6; \\ -0.36r + 11, \text{if } r \geqslant 6. \end{cases} \tag{6}$$

$$B^{\mathrm{MED}}_{\mu\mathrm{G}}(r_{\mathrm{kpc}}, z) = \begin{cases} 50, \text{if } r < r_1, |z| < z_1\sqrt{1-(r/r_1)^2}; \\ \text{transition zone} \downarrow, \text{if } r < r_2, \mathrm{Max}[0, z_1^2(1-(r/r_1)^2)] \leqslant z^2 < z_2^2(1-(r/r_2)^2); \\ \exp\left(-\frac{|z|}{z_B}\right) \times \begin{cases} 17, \text{if } r < r_1, |z| \geqslant z_2\sqrt{1-(r/r_2)^2}; \\ 9.1r + 13, \text{if } r_1 \leqslant r < r_2, |z| \geqslant z_2\sqrt{1-(r/r_2)^2}; \\ 21, \text{if } r_2 \leqslant r < 1; \\ -2.4r + 23, \text{if } 1 \leqslant r < 6; \\ -0.27r + 11, \text{if } r \geqslant 6. \end{cases} \end{cases} \tag{7}$$

$$B^{\mathrm{MAX}}_{\mu\mathrm{G}}(r_{\mathrm{kpc}}, z) = \begin{cases} 100, \text{if } r < r_1, |z| < z_1\sqrt{1-(r/r_1)^2}; \\ \text{transition zone} \downarrow, \text{if } r < r_2, \mathrm{Max}[0, z_1^2(1-(r/r_1)^2)] \leqslant z^2 < z_2^2(1-(r/r_2)^2); \\ \exp\left(-\frac{|z|}{z_B}\right) \times \begin{cases} 20, \text{if } r < r_1, |z| \geqslant z_2\sqrt{1-(r/r_2)^2}; \\ 9.5r + 16, \text{if } r_1 \leqslant r < r_2, |z| \geqslant z_2\sqrt{1-(r/r_2)^2}; \\ 24, \text{if } r_2 \leqslant r < 1; \\ -2.8r + 27, \text{if } 1 \leqslant r < 6; \\ -0.35r + 12, \text{if } r \geqslant 6. \end{cases} \end{cases} \tag{8}$$

"↓" sign above means the transition between the zones described by the rows above and below the sign.

Now let us discuss the choice of vertical scale height z_B. As a typical rule, [54,55] suggest that $z_B \approx 4h_s$ with h_s being the synchrotron emission scale height. The latter is provided by [[49], Table 1]. Then naturally I set the following z_B values for MIN-MED-MAX MF models: $z_B = 4 \times (\mathrm{Min}[h_s], \langle h_s \rangle, \mathrm{Max}[h_s]) = (0.88, 1.2, 1.6)$ kpc,

where min/max attributes to the radial and frequency variations of h_s. Thus, M31 has the relatively thin synchrotron and magnetic disks in comparison with other galaxies, as it is also stated in, e.g., [56] as a consequence of the peculiar absence of so-called thick synchrotron disk.

GALPROP internally averages $e^{\pm}$ synchrotron emission intensity over directions regardless of the field direction. This makes the synchrotron emission isotropic from any volume of interest. Thus, such model effectively assumes MF to be purely random; i.e., the total field has the strength (6)–(8) and a random direction at every point. Indeed, the real field has both regular and random components. However, this is a very challenging task to model both these components realistically, and the outcome will be likely model dependent. A direct application of the comprehensive MW MF models to M31 like Jansson and Farrar one [57], which include both regular and random components, is not particularly helpful here, since such models reconstruct the field on large spatial scales and have a relatively poor information about the central kiloparsec, which plays a key role for our purposes.

At this point, we have defined the MF distribution in M31. Indeed, the real distribution is likely more sophisticated. Thus, an obvious sophistication could be, for example, the dependence of scale height z_B on r. However, the chosen model should at least cover reasonably the possible uncertainty range for the finally expected DM constraints. The key MF model parameters are written out in Table III.

D. Propagation parameters

Another important set of parameters attributes to the diffusion of DM $e^{\pm}$ in both coordinate and energy space. Let us begin the modeling of this set from defining the size of diffusion cylinder, inside which we solve the transport equation by GALPROP. The cylinder radius is usually assumed to be about the radius of a stellar disk. However, in our case, the $e^{\pm}$ source is very concentrated towards the center, and $r_{\max} = 15$ kpc was checked and set as an absolutely sufficient radius. As for the vertical size $z_{\max}$—i.e. the half-height of the diffusion cylinder, it is naturally linked to the vertical extent of MF, since the latter holds $e^{\pm}$ inside the diffusion region. For this reason, usually a linear proportionality is assumed between $z_{\max}$ and z_B, and I set $z_B = \delta \times z_{\max}$ according to, e.g., [[58], Eq. (4.5)]. δ here denotes the energy-dependence slope of the diffusion coefficient defined as follows:

$$D(E) = D_0 \left(\frac{E}{\mathrm{GeV}}\right)^{\delta}. \tag{9}$$

Thus, now we have to determine the diffusion coefficient parameters D_0 and δ. Here, the results of detailed study [59] were utilized. This study examined the CR $e^{\pm}$ propagation in M31 and M33. These authors estimated the diffusion coefficient at several GeV and reported the results in their Table V. They found a slight anisotropy of the diffusion coefficient: it is larger by $\approx$2 times along the galactic plane than in the orthogonal direction. However, GALPROP v56 allows only isotropic diffusion; hence, the coefficients were averaged over directions. The estimates in [59] are too approximate to recover δ reliably. For this reason, the data on diffusion parameters in MW were also employed—particularly from [33]. And δ values were extrapolated from there. This work derived the updated diffusion parameters for DM searches in MW in the frame of MIN-MED-MAX paradigm. These authors outlined the parameter values for various propagation setups. These setups differ by the functional form of the diffusion coefficient, presence of reacceleration, and convection. The closest setup to our GALPROP is called "QUAINT" in their notation. The respective parameter values are provided in [[33], Table VII], which yields $\delta = 0.4$–0.5. These values reasonably agree with the results of [59] and therefore, were adopted for M31. Having set δ, D_0 values were derived by Eq. (9) using $D(E)$ values from [[59], Table V]. MIN-MED-MAX D_0 values were calculated, respectively, as $(\mathrm{Min}[D_0], \langle D_0 \rangle, \mathrm{Max}[D_0])$; i.e., the range is formed by all possible values obtained in [59] by various methods and observational frequencies. All the accepted parameter values for M31 are written out in Table III. The accepted D_0 values are rather close to those for MW cited in [[33], Table VII]—the values for M31 are lower by 2–3 times.

Another important aspect of the propagation model is a possible reacceleration of $e^{\pm}$ by magnetohydrodynamic (MHD) waves. The reacceleration together with energy losses defines the diffusion in energy space. GALPROP defines the reacceleration coefficient through essentially the single parameter $V_A/\sqrt{w}$ with V_A being Alfven speed and w—the ratio of energy densities of the MHD waves and MF. However, it is very difficult to model such fine effects as reacceleration in M31—no papers were found on this topic. Another difficulty is a lack of knowledge about w and the thickness of layer around the galactic plane, where reacceleration works. Also, there are some doubts whether the reacceleration is modeled fully correctly by GALPROP, since substitution of the typically recommended value $V_A = 30$ km/s (e.g., [60]) yields a very abnormal increase of our synchrotron emission intensity. Taking all these into account, it would be too rough to assume any specific reacceleration in our model. At the same time, "QUAINT" setup for MW mentioned above requires significant V_A for all MIN-MED-MAX cases. In such an uncertain situation, the following conservative choice was made: the reacceleration was switched off in our MIN and MED models, and was included only into MAX model with the minimal possible $V_A = 5$ km/s according to the recipe in [[33], Appendix B] (assuming $w = 1$). Such a conservative choice ensures that our emission intensities of interest would not be overestimated. And the convection of $e^{\pm}$ was

not included too, as an uncertain and insignificant effect: "QUAINT" setup suggests tiny convective speeds $V_c \sim 0.1$ km/s. η parameter from [[33], Eq. (B1)] was fixed to $\eta = -2$ and checked to be irrelevant at the energies of interest.

Finally, we have to discuss probably the most important propagation aspect—energy losses of $e^{\pm}$ in the galactic environment. These losses are composed by synchrotron, ICS, bremsstrahlung, Coulomb, and ionization losses. As was discussed above in Sec. II, many studies used incorrect expressions for these losses. Therefore, below I provide the verified expressions for the key loss components $b \equiv -dE/dt$ in $\mathbf{GeV/s}$ as they are implemented in GALPROP based mainly on [61],

$$b_{\rm synch} = 6.60 \times 10^{-25} B^2_{\mu\rm G}(\gamma^2 - 1), \tag{10}$$

$$b_{\rm ICS} = 2.66 \times 10^{-23} U_{\rm eV/cm^3}(\gamma^2 - 1), \tag{11}$$

$$b_{\rm brems} \simeq 7.1 \times 10^{-20} \gamma n_e (\ln\gamma + 0.36), \tag{12}$$

$$b_{\rm Coul} \simeq 7.6 \times 10^{-18} n_e (\ln(\gamma/n_e) + 73); \tag{13}$$

where γ is $e^{\pm}$ Lorentz factor, U is the energy density of ambient radiation field, and n_e is the concentration of ambient (fully) ionized gas in $\mathbf{cm^{-3}}$. MF strength for the synchrotron losses is defined by Eqs. (6)–(8). As for the ISRF energy density U in (11), its determination is highly nontrivial. In general, ISRF comprises three major components: CMB emission, which is the same everywhere with $U_{\rm CMB} = 0.26$ eV/cm^3, the infrared emission from a galactic dust and the starlight. As for the spatial profiles of energy densities of the last two components, they were adopted from MW (taken from GALPROP). Then ISRF densities were globally rescaled (i.e., the profiles were renormalized) according to the individual properties of M31. GALPROP easily allows us to do such rescaling of each component by an arbitrary factor with respect to the typical density in MW. Let us begin this discussion from modeling the infrared rescaling factor. Generally, as, e.g., [62] says, M31 is a relatively dust-poor galaxy with low infrared luminosity. Hence, we expect a lower infrared radiation density in comparison with that in MW. In order to estimate the rescaling factor quantitatively, the infrared intensities of the central regions [$(r, |z|) \leqslant 0.5$ kpc] of MW and M31 were obtained. The central region was chosen as the most important again, since DM is highly confined there. The infrared intensity of the GC region was extracted from DIRBE-COBE and IRIS missions data in the frequency range 1–5 THz. The intensity of M31 nucleus was taken from the dedicated paper [63] by Planck Collaboration. Then the ratio of intensities was obtained—M31 appeared to be fainter by 10–30 times depending on frequency. Assuming approximate proportionality between the emission intensity and energy density, I set the infrared ISRF energy density factor for M31 to be 0.1 for all MIN-MED-MAX cases. Overall, this factor has a relatively little influence (as well as CMB) on the total ICS losses. But this is opposite for the optical ISRF density, which dominates in ICS losses around the galactic center—i.e., in the bulge region. To compare the optical bulge intensities of MW and M31, the information from [64–67] on the bulge luminosities were utilized. The ratio of luminosities would be equal approximately to the ratio of intensities, since according to [[65], Table V] and [[66], Table I] the bulges of MW and M31 have very similar size. These tables clearly demonstrate that M31 bulge is more luminous than MW bulge. Combining the values of M31 and MW bulge masses, their mass-to-light ratios, optical luminosities of both galaxies, and their bulge light fractions collected from [64–67], the ratio of M31 to MW bulge luminosity (and hence, intensity) was obtained to be $\approx 2.0 \pm 0.5$ depending on a filter band. In the absolute units, it corresponds to $U_{\rm opt} \approx$ (12–25) eV/cm^3 in M31 center. Thus, we see that the optical radiation energy density in M31 central region is significantly higher than that in MW, which would imply in turn faster cooling of DM $e^{\pm}$, therefore lower synchrotron intensity and, unfortunately, weaker DM constraints. The optical ISRF density factor was set to 2.5 for MIN scenario, 2.0 for MED, and 1.6 for MAX to cover the potential uncertainty range. This choice provides the same increment 1.25 between MIN and MED, MED and MAX: $2.5 = 2.0 \times 1.25 = 1.6 \times 1.25^2$.

At this point, we have defined the synchrotron and ICS energy losses, which play the main role in the overall loss budget. Then in order to determine bremsstrahlung, Coulomb, and ionization losses (which are subdominant), I had to model and substitute into GALPROP the spatial distributions of the ionized, atomic, and molecular gas in M31. As for the first one, combining the relevant information from [49,54], the following approximate profile was set:

$$n_e(r_{\rm kpc}, z_{\rm kpc}) = 0.03 \exp\left(-\left(\frac{r}{10}\right)^2 - \frac{|z|}{1}\right) \ {\rm cm}^{-3}. \tag{14}$$

The description of neutral gas distributions and other secondary parameters are placed into the Appendix in order to not overload the main body of paper.

E. Emission absorption

It is important to take into account possible emission absorption along the line of sight. We estimated in [[11], Appendix A] that the synchrotron self-absorption is not relevant in the circumnuclear environment of M31 at the frequencies of interest. Then we have to estimate the thermal free-free absorption both in M31 and MW. For both GALPROP was used—it has the functionality to model both free-free emission and absorption by an ionized gas. In order to estimate the absorption in MW by

GALPROP, the observer was placed at the Sun's position, and the test source was generated outside MW in the direction of M31. *A priori*, we do not expect a significant free-free absorption in this direction, since M31 is located quite far from the GC in the sky—M31 Galactic coordinates can be seen in Table II. The level of absorption was checked with a couple of representative ionized gas distributions for MW contained in GALPROP. The emission intensity decreases by no more than ≈1.5% at our lowest frequency of interest 74 MHz. The free-free absorption coefficient indeed decreases with frequency increase. Therefore, the absorption inside MW was justifiably neglected.

The free-free absorption inside M31 was basically modeled by three entities: the thermal electrons' spatial distribution, their temperature, and clumping factor. The first entity is our ionized gas distribution (14)—this is fixed. The electrons' temperature was fixed to the value 7000 K according to [[68], Fig. 1]. Then the electrons' clumping factor was adjusted as a free parameter to reproduce the global M31 free-free emission flux density, which is indeed produced by the same ionized gas. Thus, the thermal emission measurements help to model the thermal absorption. The former was taken from [[63], Fig. 15] and [[69], Fig. 3] at the frequency about 0.5 GHz. These independent studies found approximately the following flux densities of free-free emission from the whole galaxy at the mentioned frequency: 0.9 Jy and 0.5 Jy, respectively. Then the electrons' clumping factor in GALPROP was fitted to the value 21, which provides approximately the average free-free flux between the cited values. This value of clumping factor lies inside the expected range 10–100 suggested by GALPROP manual [70]. The corresponding free-free emission flux density generated by GALPROP can be seen in Fig. 3. The described procedure yielded the synchrotron emission absorption at the level 0.5%–1.0% for the relevant ROIs with $R = 1$–2 kpc at 74 MHz. Thus, the free-free absorption inside M31 can be neglected too, though it was still included in calculations at no cost. However, in general, it is important to model it carefully at $\nu \lesssim 50$ MHz. Another very important aspect here is that a significant absorption may break the linear proportionality between DM $e^{\pm}$ synchrotron intensity and annihilation cross section. This linearity in turn is fundamental for the whole procedure of DM constraints derivation. Here, the absorption was included into the calculations by the simple single model, since the absorption is tiny and hence, does not require much attention in the frequency range of interest. Our range lies essentially in the domain, where the optically transparent medium approximation works. However, one should be very careful in the case of going outside the optical transparency regime.

At this point, we have discussed all essential galactic model parameters and their uncertainties. The constructed MIN-MED-MAX configurations are expected to form the comprehensive uncertainty range for the final DM constraints. Uncertainties of the model parameters, which are not varied by MIN-MED-MAX, have a negligible contribution into the final uncertainties.

IV. OBTAINED EMISSION MAPS AND SPECTRA

Combining together all the ingredients described above GALPROP solved the transport equation for each of 234 DM models and generated the respective synchrotron intensity maps in HEALPix format at eight frequencies of interest listed in Table IV. Figure 2 depicts the example of representative DM intensity map in comparison with the observed nonthermal diffuse emission map of M31 at 1.5 GHz. A benchmark thermal WIMP with $m_x = 100$ GeV annihilating evenly to $b\bar{b}$ and $\tau^+\tau^-$ is assumed there (MED configuration). At the nonthermal (top) image, we see very bright central region and the well-known star-forming ring around $r \approx 10$ kpc. The central emission has a remarkably circular shape. This can not be said about DM emission morphology: it clearly shows a mild ellipticity, which reflects primarily the asymmetry of MF distribution in r and z directions. The observed intensity in the center is larger by ≈5 times than that on DM map, which preliminary indicates that it is rather tricky to constrain even 100 GeV WIMP mass scale. DM emission intensity decreases fast with the angular distance from center waning down

TABLE IV. Characteristics of the radio images of M31 used for derivation of constraints. The last column indicates the availability of emission intensity cleaned of the thermal emission.

Frequency, GHz	Reference	Bandwidth, GHz	Targeted observation or sky survey name	Beam FWHM, arcmin	rms noise, mJy/beam	Systematic uncertainty, %	Nonthermal intensity available
0.074	[73,74]	0.0016	VLSSr	1.25	100	10	−
0.15	[75]	0.048	LoTSS	0.33	≈0.25	10	−
0.34	[76]	≈0.07	Targeted	5	3	8	−
1.5	[71]	≈0.02	Targeted	1.5	0.3	≈10	+
2.6	[77]	0.07	Targeted	4.4	1.2	≈5	−
4.9	[26,77]	0.3	Targeted	0.25, 3	0.0075, 0.35	≈5, 10	−, +
6.6	[78]	1.2	Targeted	2.9	0.43	28	+
8.4	[26,77]	1.1	Targeted	0.25, 1.4	0.0055, 0.25	≈5	−

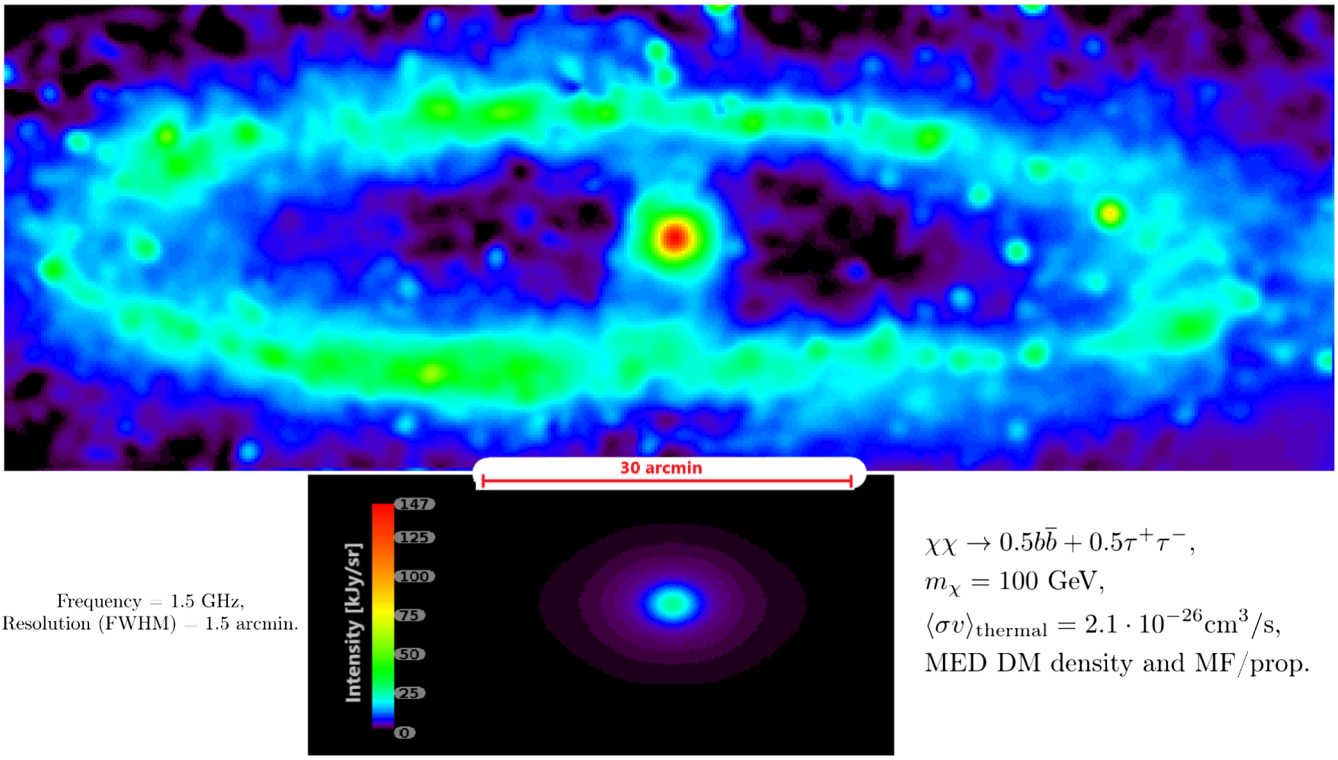


FIG. 2. Top: the observed nonthermal emission (source-subtracted) map of M31 at 1.5 GHz from [71,72]. Bottom: the intensity map due to DM annihilation computed by GALPROP for the specified configuration of parameters. 1 arcmin corresponds to $R \approx 0.22$ kpc.

completely beyond $\approx 15'$. This fast decrease reflects the steepness of annihilation rate profile, which is proportional to ρ^2.

Figure 3 displays the emission spectra integrated over the whole galaxy (ROI radius is $\approx 2°$). The separation of all regular emission components was done in the dedicated study of M31 by Planck Collaboration [63]. Their results generally agree with the similar independent study [69]. Then the spectra of specified benchmark DM models were superimposed on the plot to compare them with various emission components. First of all, we can see that DM component expectedly decreases fast with the mass increase. The ratio of fluxes between $b\bar{b}$ and $\tau^+\tau^-$ channels depends both on the mass and frequency. Also, we see that the slope of DM spectra is rather similar to that of the total synchrotron. DM component (if it exists) would contribute to the synchrotron spectrum drawn by the magenta line. Hence, it is optimal to search DM at frequencies, where the synchrotron dominates the total emission, in order to avoid a contamination by other components. The synchrotron absolutely dominates up to ≈ 1 GHz, then free-free adds slightly between 1 and 10 GHz. Thus, we can infer approximately the optimal frequency range for DM detection/constraining: below ≈ 1 GHz is the best situation, where we can work with the total emission; then between 1 and 10 GHz, it is preferential to remove the free-free component; and it does not make sense to go beyond 10 GHz, since many other components arise there, but DM

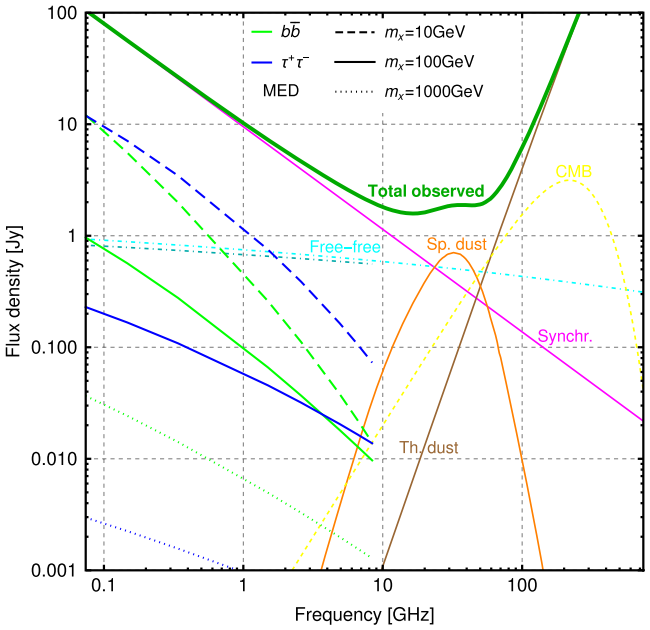


FIG. 3. The flux density spectrum of the whole M31 galaxy. The total observed emission spectrum and all its specified components (except DM) are taken from [[63], Fig. 15]. The green and blue lines show our representative DM models commented on the plot. DM annihilation cross section is thermal, the density profile and MF/prop. model are MED. The truncated dot-dashed line shows the free-free spectrum obtained by GALPROP in our calculations.

rapidly faints. This justifies my choice of the frequency range $\approx(0.1–10)$ GHz for derivation of constraints: below this range, the free-free absorption hinders, above—DM signal drowns among other emissions. Also, we see that working with the emission integrated over the whole galaxy would not be able to yield any useful constraints: even the lightest WIMP with $m_x = 10$ GeV produces the flux by an order of magnitude lower than the observed synchrotron. Hence, the ROI optimization is necessary.

Figure 4 shows the azimuthally averaged radial emission intensity profiles at the frequency of LOFAR Two-meter Sky Survey (LoTSS). As pointed out above, only the synchrotron exists at such low frequencies. At angular radii above $5'$–$10'$ the observed emission intensity is an approximate estimate, since LOFAR does not see completely diffuse structures with such big sizes according to [75]. We see that DM emission is expectedly highly concentrated around the center, and its potential contribution into the total emission decreases strongly beyond $10'$–$15'$, especially counting that LOFAR does not see all the intensity there. Then at large radii $\gtrsim 20'$, the bright star-forming ring enters the ROI, and the DM signal—to—nonthermal noise ratio drops even further. Thus, the plot suggests that the optimal ROI radii for DM searches are likely not larger than $10'$–$15'$. Also, we may notice that the radial profiles of different channels are very parallel.

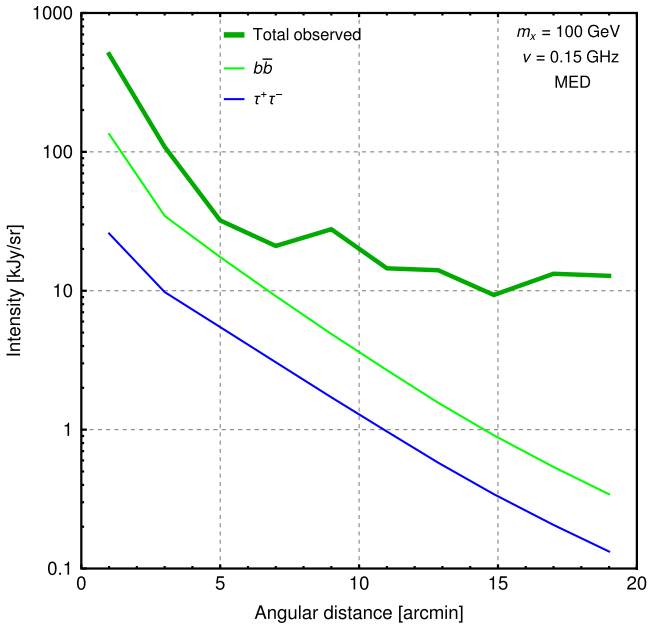


FIG. 4. The radial dependence of the emission intensity at the frequency 0.15 GHz. The intensity is averaged over concentric annuli with $2'$ width. An estimate of the total observed emission was extracted from LoTSS maps [75]. DM annihilation cross section is thermal, the density profile, and MF/prop. model are MED. Beyond $5'$–$10'$ the estimated observed emission intensity is very approximate due to the limitations of LOFAR ability to see large scales.

Then Figs. 5 and 6 illustrate the dependence of radial profiles on DM density distribution and MF/prop. setup respectively for both channels. Regarding the dependence on density profile, MED and MAX curves are quite parallel and differ mainly by their amplitudes. But MIN intensity decreases slower: in the center, it is the lowest, and at $20'$, it is almost the highest among three. This likely reflects the

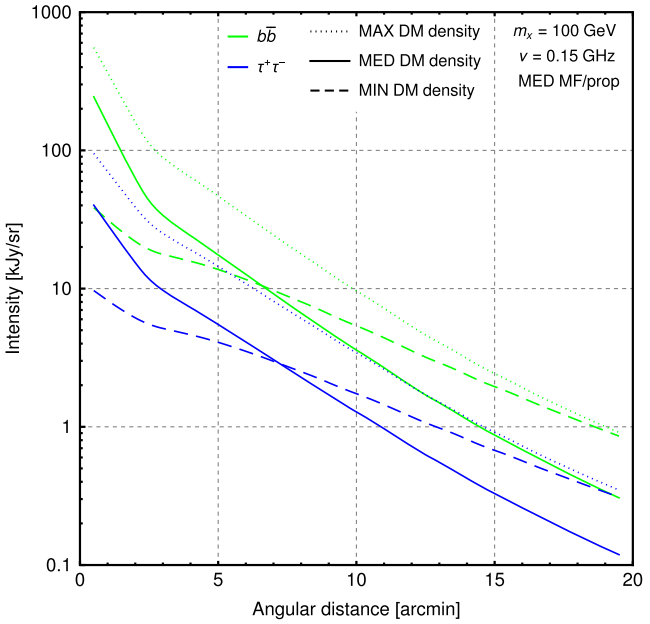


FIG. 5. The radial DM intensity distribution dependence on DM density profile for the specified benchmark configurations.

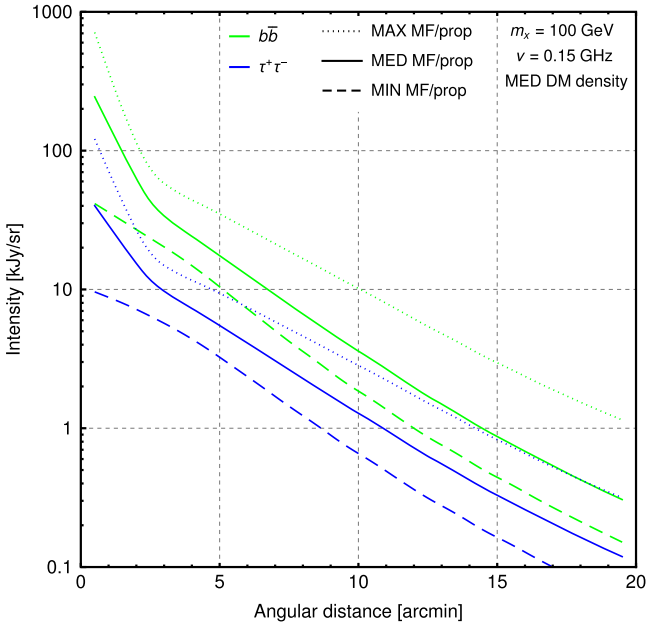


FIG. 6. The radial DM intensity distribution dependence on MF/prop. model for the specified benchmark configurations.

fact that MIN density overtakes both MED and MAX at $R \gtrsim 3$ kpc, which is visible at Fig. 1. Regarding the dependence on MF/prop. model, all three curves here are rather parallel. The main difference is due to the presence or absence of the central MF cusp: MED and MAX cases elevate up the intensity steeply in the cusp zone. And MIN evolves with the distance more smoothly. The ratio of MAX to MED intensity is comparable to the ratio of MED to MIN.

The main inference from this section is the optimal frequency and spatial domains for the derivation of DM constraints, which is described in the next section.

V. DERIVATION OF DM CONSTRAINTS FROM VARIOUS RADIO DATA

For comparison of the theoretically calculated DM maps with the observed maps, all the relevant radio data on M31 was thoroughly collected in the frequency range of interest $\approx$(0.1–10) GHz. The selected radio surveys and targeted observations are listed in Table IV with their characteristics. We can see that a large variety of high-quality data is currently available, which evenly covers our frequency range. Ideally, one would prefer to have an image, which is cleared off both projected discrete sources and thermal diffuse emission (especially, above 1 GHz) by the image authors. Availability of such images among the selected sample is marked by "+" in the last column of the table. Just for three (out of eight) frequency channels such images were found. However, in principle, the presence of nuisance emissions would spoil the produced constraints towards a weaker side (i.e., more conservative); hence, it is not dangerous. Also, as was explained above, the free-free component is negligible below $\approx$1 GHz. Let us now briefly discuss the data at each frequency. 0.074 GHz survey (VLSSr) represents the redux of VLSS (VLA Low-frequency Sky Survey). Being interferometric sky survey, it inevitably has a limitation of the largest visible angular scale, which is $36'$ according to the survey description [73]. Such a scale is sufficient for our purposes. Then 0.15 GHz is very new and high-quality LOFAR Two-meter Sky Survey (LoTSS). Its largest scale is estimated to be $\approx 10'$ from the description [75]. Another peculiarity of this survey is a very wideband. In order to count the finite bandwidth effect, DM maps around this frequency were averaged over the band assuming the power-law spectra. The rest of data is targeted imaging by (mainly) single-dish antennas. These maps have a typical systematic intensity uncertainty around 5%. When the thermal emission subtraction is performed, it inevitably introduces additional systematics. Thus, at 1.5 and 4.9 GHz, the systematic uncertainty is assumed to be 10% according to [[77], Table III] (for small ROIs). And at 6.6 GHz, I utilized only the synchrotron flux from the central disk with $6'$ radius provided in [[78], Table VII], and the large systematics of 28% here reflects the total uncertainty of their component separation procedure. At 4.9 and 8.4 GHz, there are two independent datasets—with low and high resolution. The latter is produced by combining the observations made on Effelsberg telescope and VLA.

Then let us discuss the construction of ROIs for the derivation of constraints. ROIs must satisfy several basic requirements: 1) they must not overlap in order to enter the likelihood function independently, 2) their size along any direction must not be smaller than the image resolution (beam FWHM), 3) and they must not be larger than the largest survey visible scale discussed above. According to these requirements, the circular disk around the center and several concentric annuli around it were utilized at each frequency. Such structure looks like ◎ as an example of disk and one annulus. The circular ROIs are very convenient in practice, since they are invariant on the position (azimuthal) angle in the sky plane. The angular radius of disk and the width of annuli were set to be about the respective image resolution at each frequency in order to cover the radial emission profile densely, since *a priori* it is not known which radial range yields the strongest constraints. The radius of the biggest (most outer) annulus is defined by either the survey scale limitation or the distance, where the ratio of DM intensity to the observed intensity becomes too low. Thus, for example, 0.15 GHz (LOFAR) channel has the following ROIs: the central disk with $1'$ radius and 4 concentric annuli with $1'$ widths covering up to $5'$. In total, 33 ROIs were utilized (from one to five at each frequency) covering the distances up to $15'$ from the center. Beyond $15'$, the bright star-forming ring begins to enter, worsening significantly the signal-to-noise ratio. Meanwhile, the inner $6'$ is almost free from the projected nuisance sources. One may also use in principle the off-center ROIs. The dark gaps between the nucleus and ring well visible at Fig. 2 (top) are particularly attractive in this respect. It was calculated that these gaps (especially, the right one) actually provide very high signal-to-noise ratio; i.e., DM constraints, which are even stronger than those derived from the nuclear region. However, as was explained in details in Sec. III C, these regions lack any direct MF measurements. MF there was defined in our model just by linear interpolation between the nuclear and ring regions. Hence, it would be too speculative and unreliable to claim strong constraints based on the gap region only. And I made the decision to utilize only the central ROIs, where MF was more or less certainly measured.

Meanwhile, the following alternative selection of the central ROIs was also tested. This selection uses the disks only. Firstly, at each frequency, the optimal disk is being searched, i.e., the disk with the radius, which provides the best sensitivity. Then one such optimal ROI for each frequency is being substituted in the joint likelihood. In this case, the latter would have just eight ROIs in total instead of 33 as in the method described above. However, this strategy with disks only demonstrated a

worse sensitivity for all DM models. Hence, the strategy with 33 ROIs was employed.

Another important step in the preparation of ROI intensities for substitution into the final likelihood was the map smoothing in order to take into account the angular resolution at each frequency. The effective pixel size of DM maps generated by GALPROP before smoothing is $\approx 0.3'$. Then smoothing by a Gaussian beam was applied to each map (except very high-resolution maps) with the corresponding beam FWHM (listed in the fifth column of Table IV).

Now we can move to the construction of the likelihood function $L(\vec{c}|\vec{\Theta})$, which represents the probability density for the parameter vector $\vec{\Theta}$ in case of the observational data $\vec{c}$. $\vec{c}$ in our case is the observed mean intensities inside ROIs, and $\vec{\Theta}$ contains the annihilation cross section and various nuisance parameters. The likelihood (assumed to be Gaussian) takes into account both the statistical and systematical uncertainties of the observed intensities—$L = L_{\rm stat} \times L_{\rm syst}$,

$$L \propto \prod_{i=1}^{8\text{freq.}} \prod_{j=1}^{\#\text{ROI}_i} \exp\left(-\frac{n_{ij}^2}{2\sigma_{ij}^2}\right) \times \exp\left(-\frac{(s_{ij}-c_{ij})^2}{2\sigma_{s,ij}^2}\right), \quad (15)$$

where n_{ij} is the map noise inside jth ROI at ith frequency with rms σ_{ij}, $s_{ij} - c_{ij}$ is the systematical offset between the measured mean intensity c_{ij} and the true one s_{ij}. The systematic map uncertainties listed in the 7th column of Table IV (let us denote them by u_i) represent essentially the sky-averaged values. However, the systematic offset in any specific ROI is not known apriori. Hence, it is essentially the random variable, which is being modeled by the Gaussian distribution with $\sigma_{s,ij} = u_i c_{ij}$. Then the total offset-corrected intensity is composed by the following terms: $s_{ij} = n_{ij} + a_{ij} + w_{ij}$, where a is all the standard astrophysical emissions (mainly CR synchrotron and free-free) and w is the potential DM contribution. The noise rms for an arbitrary ROI is calculated as $\sigma_{ij} = \sigma_{m,i}/\sqrt{N_{ij}}$ with $\sigma_{m,i}$ being the map noise in Jy/beam listed in the sixth column of Table IV and N_{ij}—the number of beams inside jth ROI. A reminder here just in case: all the calculations are done in terms of the ROI-averaged intensity (i.e., in Jy/sr), not the flux density [Jy]. Then in the absolute units $\sigma_{ij} = \sigma_{m,i}/\sqrt{\Omega_{b,i}\Omega_{ij}}$, where Ω is the ROI size in sr. Thus, in order to convert all the map intensities and noises into telescope-independent units, one has to calculate the effective beam sizes $\Omega_{b,i}$. For this purpose, the Gaussian telescope beam was assumed,

$$\Omega_{b,i} = \int_{4\pi} \exp\left(-\frac{\theta^2}{2\sigma_{b,i}^2}\right) d\Omega = 2\pi \int_0^{\pi} \exp\left(-\frac{4\ln 2\theta^2}{\text{FWHM}_i^2}\right) \sin\theta d\theta, \quad (16)$$

with the beam FWHM being listed in the fifth column of Table IV.

After likelihood construction, it was an important step to decide which statistical framework to apply for the derivation of constraints—Bayesian or frequentist. The latter employs Wilks' theorem, and the constraints are derived from the test statistic $\text{TS} = 2\ln(L/L_0)$. However, as was meaningfully pointed out in [5], Wilks' theorem strictly applies only if the hypothesis being tested does not lie at the boundary of parameter space, meaning that the null likelihood L_0 with $\langle\sigma v\rangle = 0$ is not suitable. A violation of this applicability condition causes a deviation of TS from χ^2 distribution and finally may spoil the constraints by several times towards weaker side, as was shown in [5]. Hence, I employed the Bayesian inference, when the likelihood function is being marginalized over nuisance parameters inferring the probability density for the variables of interest. Similar methodology was utilized in our previous work [[11], Sec. III]. The nuisance parameters in our case are the intensities of usual astrophysical emission a_{ij} and the systematic-free observed intensities s_{ij}. An important decision is what to assume for a_{ij}. As was intended initially, the constraints being derived here must be conservative and minimally model dependent. Hence, the flat prior uncorrelated between frequencies was assumed for a_{ij}, meaning that *any* astrophysical intensities are equally allowed. The prior for s_{ij} is flat too. With flat priors, we can straightly marginalize the likelihood (15) to get the probability density for the annihilation cross section (other DM parameters are fixed),

$$L(\langle\sigma v\rangle|\vec{c}) \propto \int_{-\infty}^{\infty}\int_{0}^{\infty} \prod_{i,j} \exp\left(-\frac{(s_{ij}-a_{ij}-w_{ij}(\langle\sigma v\rangle))^2}{2\sigma_{ij}^2}\right) \times \exp\left(-\frac{(s_{ij}-c_{ij})^2}{2\sigma_{s,ij}^2}\right) ds_{ij} da_{ij}. \quad (17)$$

The integral above was calculated analytically yielding

$$L(\langle\sigma v\rangle|\vec{c}) \propto \prod_{i=1}^{8\text{freq.}} \prod_{j=1}^{\#\text{ROI}_i} \left(1 + \text{erf}\left(\frac{c_{ij} - w_{ij}(\langle\sigma v\rangle)}{\sqrt{2(\sigma_{ij}^2 + \sigma_{s,ij}^2)}}\right)\right), \quad (18)$$

where $\text{erf}(x) = 2/\sqrt{\pi}\int_0^x e^{-t^2} dt$. The double product above has 33 multipliers in total. Then the following equation derives the constraint on $\langle\sigma v\rangle$ at the typical 95% confidence level:

$$\int_0^{\langle\sigma v\rangle_{\rm lim}} L(\langle\sigma v\rangle|\vec{c}) d\langle\sigma v\rangle \Big/ \int_0^{\infty} L(\langle\sigma v\rangle|\vec{c}) d\langle\sigma v\rangle = 0.95. \quad (19)$$

The limiting cross section $\langle\sigma v\rangle_{\rm lim}$ was found numerically from the equation above individually for each of 234 DM

models computed by GALPROP. These models enter (18) through the mean intensities w_{ij}, which are linearly proportional to $\langle\sigma v\rangle$.

Before drawing the final constraints, which join all the frequencies together, the frequency-individual constraints were derived for MED parameter configuration in order to see the influence of each frequency. In this case, the product over i in (18) is absent. The result is shown in Fig. 7 for both annihilation channels. We see that in $\chi\chi \to b\bar{b}$ case the LoTSS data dominate the constraints for almost all WIMP masses considered. At low masses, VLSSr also helps. LoTSS domination was naturally anticipated: this is the highest sensitivity data at low frequencies, where DM synchrotron is expected to be bright. Other frequencies influence the likelihood weakly, since for a strong influence the exclusion lines should be packed densely to each other, creating the multiplication effect, as the plot demonstrates. For the $\chi\chi \to \tau^+\tau^-$ channel, the "cloud" of lines is narrower. Here LoTSS defines the exclusion until $m_x \approx 30$ GeV, then the nonthermal map at 4.9 GHz dominates absolutely. However, the picture could be different for MIN and MAX setups.

Then Fig. 8 demonstrates the exclusions for each of our nine DM density and MF/prop. setups. We can see that they generate quite wide uncertainty range—its vertical width slightly exceeds an order of magnitude, especially for $b\bar{b}$. In general, the obtained constrains are meaningful in a sense that some thermal WIMP masses inside our range are excluded, even in the most conservative MIN case for both channels. We can also note that the separation between the MIN and MED curves is smaller than that between MED and MAX with our log axes. This can be explained mainly by the presence of substructure boost and reacceleration in MAX models, which cause a significant pull towards larger DM signal intensities and hence, stronger constraints.

More meaningful exclusions are probably those which enclose the whole uncertainty band, since they represent quite hard limits for possible reality. These hard limits are set by MIN and MAX density/MF/prop. setups. However, one would prefer also to have some representative (or effective) average exclusion. Selection of MED scenario for the role of such exclusion would not be correct, since MED reflects just a particular parameter configuration. Instead, all nine possible parameter configurations must be averaged. This was done by geometric averaging, since MIN-MED-MAX tend to form the geometric progression rather than the arithmetic one. The resulting exclusion is shown by the green thick line at Fig. 9 and can be considered as the effective average exclusion. The green-shaded area around it reflects the uncertainties of DM density distribution (with MED MF/prop.). The blue- and magenta-shaded areas add MF/prop. uncertainties. We can notice (also from Fig. 8) that the width of uncertainty band due to uncertainties in DM density is comparable to that due to uncertainties in MF/prop. in many cases. Thus, both factors have important contributions into the total uncertainty budget. Then WIMP mass limits for the thermal cross section were numerically calculated for the cases displayed in Fig. 9. The results are written out in Table V. The mass for the case of $\tau^+\tau^-$ channel is confined significantly better than for $b\bar{b}$. In the latter case, the total uncertainty reaches an order of magnitude. Assuming that the exclusions for other

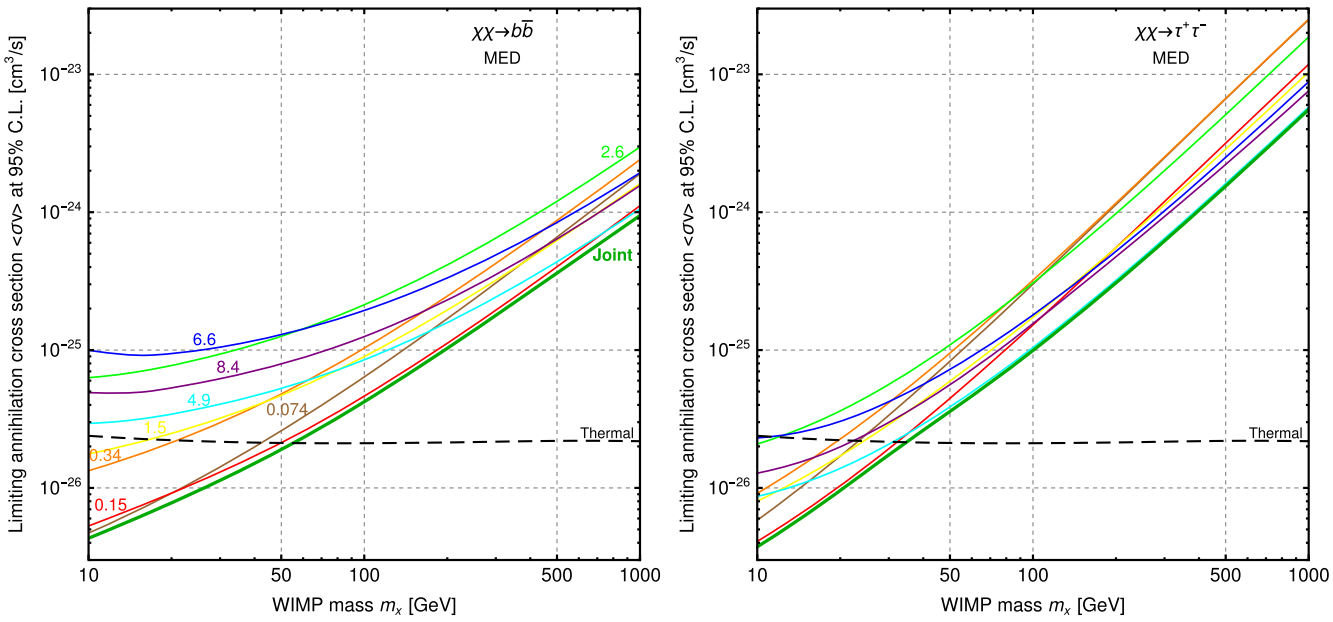


FIG. 7. The limits on annihilation cross section vs WIMP mass for both annihilation channels (MED DM density and MF/prop.) split by frequency, which is marked in GHz near each curve. The thick green line represents the joint exclusion from all frequencies together. The excluded cross section values are above the lines. The (almost) horizontal dashed line shows the thermal relic cross section.

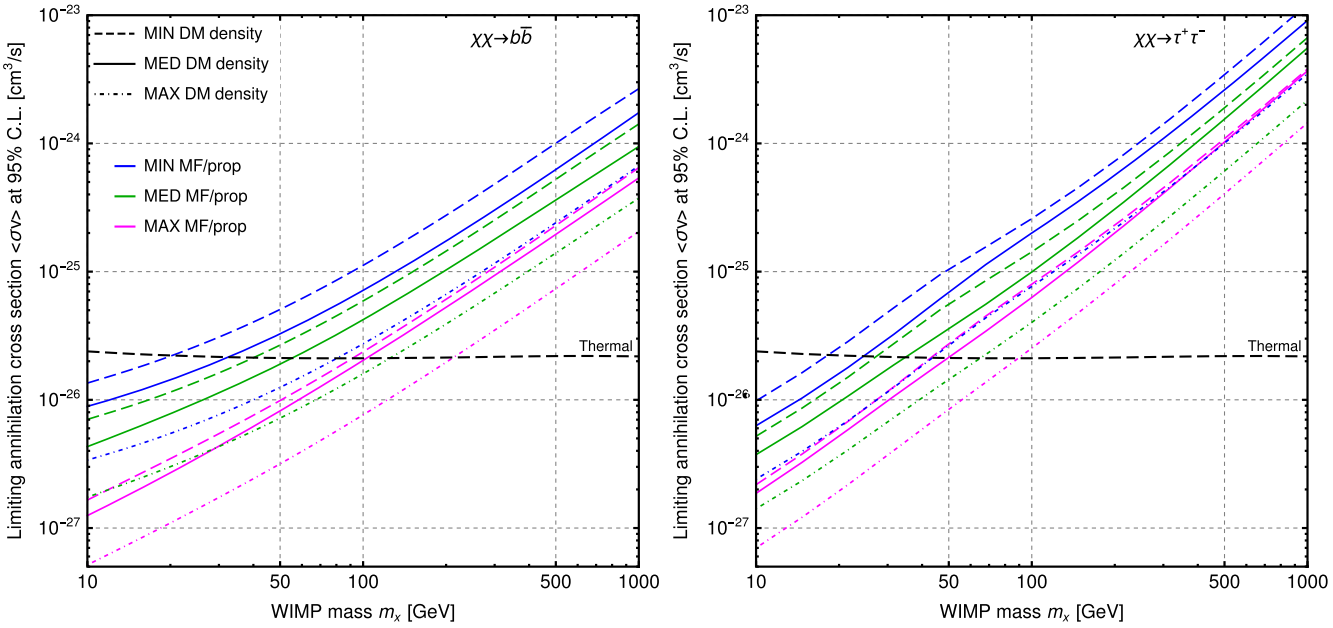


FIG. 8. The joint constraints for all nine DM density and MF/prop. models for both annihilation channels.

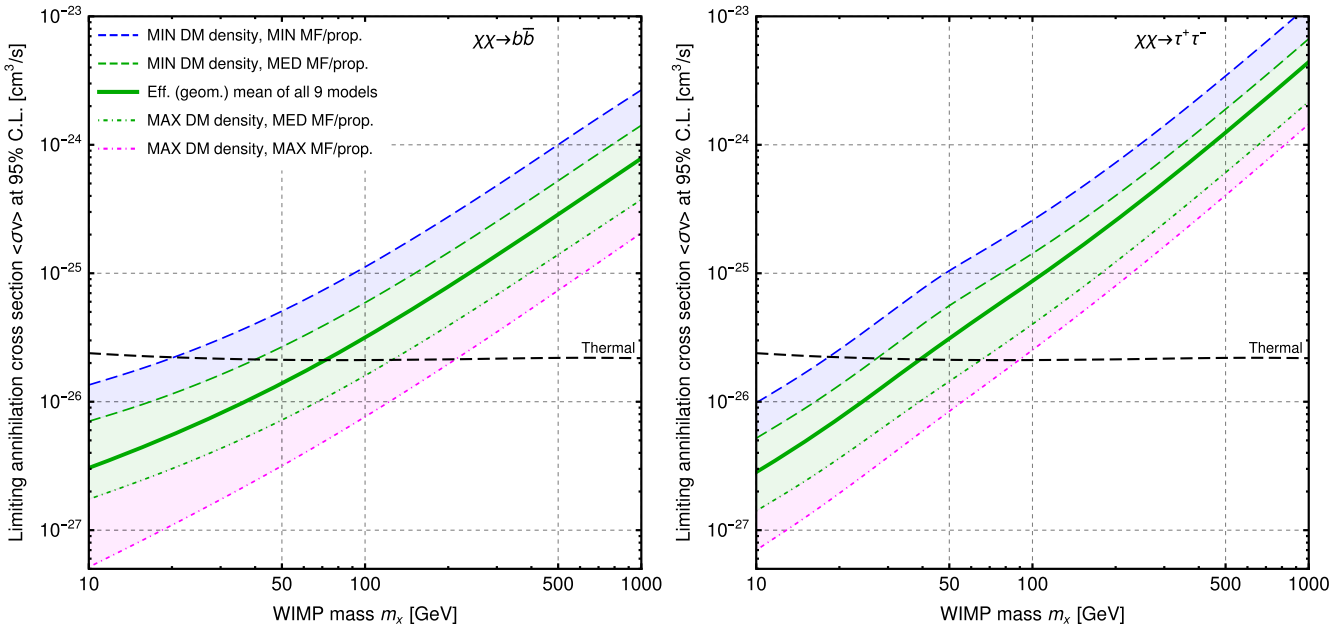


FIG. 9. The constraints' uncertainty ranges formed by the uncertainties of DM density profile only (the green-shaded zone), and both DM density and MF/prop. (the blue- and magenta-shaded zones). The green thick line represents the geometric average of all nine density/MF/prop. models and can be considered as the effective average limit.

annihilation channels lie somewhere between the tested cases, it can be claimed that the thermal WIMP with $m_x \lesssim 20$ GeV is robustly excluded under *any* reasonable choice of DM density and MF/prop. models. In the opposite case of the optimistic models, the mass threshold is in the range $\approx$(90–200) GeV. And finally, the *average* expectation for the *thermal WIMP is* $m_x \lesssim$ (40–70) GeV, which reflects essentially the moderately conservative models. Indeed, the conducted procedure does not yield any probabilistic inference for the thermal WIMP mass thresholds inside the obtained uncertainty ranges quoted in Table V. The threshold value probability density can be assumed quasiuniform over these ranges with a slight preference toward the effective averages just from a general intuition.

TABLE V. The obtained lower limits on the thermal WIMP mass and their uncertainty ranges. See the details in Sec. V.

	$\chi\chi \to b\bar{b}$	$\chi\chi \to \tau^+\tau^-$
Effective (geometric) average	**72**	**39**
Range due to DM density uncertainties	40–120	27–65
Range due to DM density and MF/prop. uncertainties	20–210	18–89

VI. RELATION WITH THE γ-RAY BAND AND ANTIPROTONS

Bedsides $e^{\pm}$, WIMP annihilation produces other particles including antiprotons, neutrons, antideutrons, and photons (more details are in, e.g., [32]). The latter is often called the final state or prompt radiation and falls to the γ-ray band. In this context, [14] analyzed whether M31 radio brightness allows to fit the central γ-ray emission (seen by Fermi-LAT [24]) by annihilating DM only. As was mentioned in Sec. II, [14] concluded that such fit is not allowed, but their model contains some imprecise assumptions. Having more precise model developed here, we can check whether the conclusion of [14] still holds. According to their Fig. 3, WIMP must have the following parameters to fit the γ emission: $m_x \approx 10$ GeV, $\langle\sigma v\rangle \approx 10^{-25}$ cm^3/s. This is for NFW density profile with the inner slope $\gamma_{\rm NFW} = 1$, which is quite similar to our MED profile. According to our Fig. 9, such a WIMP is excluded absolutely robustly. Then for larger values of $\gamma_{\rm NFW}$, they indeed obtained smaller required cross sections. Our constraints would strengthen for steeper profiles too, down to at least $\langle\sigma v\rangle \approx 10^{-27}$ cm^3/s. Therefore, we conclude that the main claim of [14] is verified to be valid in spite of their model approximations. This is generally anticipated, since it is unlikely that the γ-ray emission around M31 center is generated by DM only—some contributions from usual astrophysical sources like CR interactions, millisecond pulsars, etc. are expected too.

More interesting situation was revealed for the outer halo of M31, which was claimed to manifest the γ-ray emission too in [79]. And DM annihilation was found to be the plausible mechanism for this emission in [80]. A domination of DM source is more probable in the outer halo, since CR interactions with the environment generate gammas mainly inside the disk. Figure 10 shows by the red crosses WIMP parameter ranges required to fit the outer halo emission according to [80]. The top cross reflects the model, in which only M31 dark halo contributes into the signal. The bottom cross takes into account both MW and M31 halo contributions along the line of sight. We see that in both cases the vertical uncertainty range is quite large. However, our constraints robustly exclude the first case, when only the M31 J factor (3) is included. This is generally anticipated, since DM must inevitably annihilate in both halos. The second case is allowed very partially;

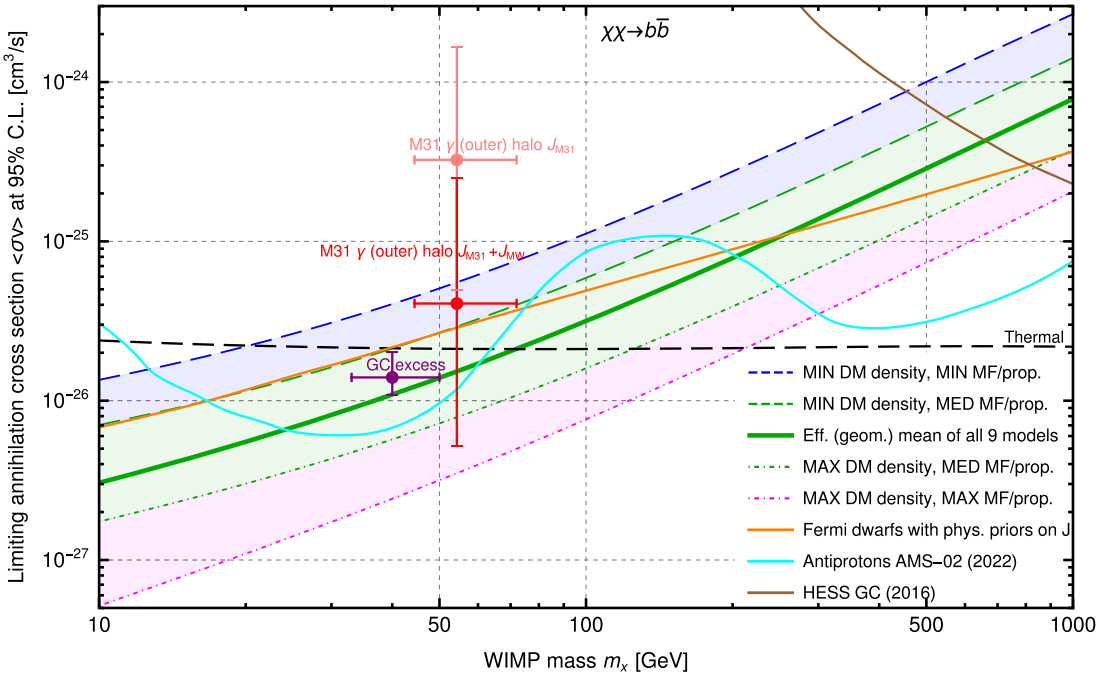


FIG. 10. Our constraints for $b\bar{b}$ annihilation channel in comparison with the WIMP parameter ranges required to fit the γ-ray emission from the outer halo of M31 (red crosses, taken from [[80], Fig. 7]) and GC excess (purple cross, taken from [81]). Also, the constraints from Fermi-LAT observations of dwarfs [[4], Fig. 4], AMS-02 data on antiprotons [[82], Fig. 6] and HESS observations of GC [[83], Fig. 4S] are shown.

i.e., nonconservative assumptions are needed for the fit, particularly regarding the J-factor values.

Then the purple cross in Fig. 10 shows the parameter values required to fit the well-known γ-ray excess around the GC according to the newest study [81]. Our derived constraints in principle allow these values, although for slightly "pessimistic" models of DM density and MF/prop. in M31. Thus, in summary, both the γ-ray phenomena—M31 outer halo and GC excess—can be explained by DM annihilation without an apparent contradiction with the radio constraints, although some restrictions and cautions exist. Hence, these phenomena persist to be promising directions for DM indirect searches. The community needs new higher-quality γ-ray data on both GC and M31 in order to progress understanding of the nature of both phenomena. Such new data in future may come from (besides other projects) our space-based γ-ray telescope GAMMA-400 being developed currently. Its anticipated sensitivity to various types of DM signals are reviewed in details in [84].

Figure 10 also demonstrates Fermi-LAT constraints from the dwarf MW satellites. These constraints are generally comparable to our effective average exclusion. Fermi-LAT constraints significantly depend on the assumed J-factor values for dwarfs, which lack the direct measurements of J factors. As pointed out in [4], the optimistic J-factor values yield the constraints slightly stronger than those derived here and exclude thermal WIMP up to ≈100 GeV. More realistic scenario shown by the orange line in Fig. 10 yields the exclusion, which is weaker than our one until ≈200 GeV.

The constraints for heavy WIMPs come from ground-based γ-ray telescopes. Thus, the brown line in Fig. 10 shows the limit from HESS observations of the GC region [83]. This limit was obtained from 254 hours of pure observational time gathered over 10 years of telescope operations. As can be seen from, e.g., [[83], Fig. 2], [85], Imaging Atmospheric Cherenkov Telescopes (IACTs) develop much better sensitivity, when they target GC rather than dwarf satellites. However, the constraints from observations of GC are more model dependent due to large uncertainties of DM density in the central kiloparsec. IACTs are generally unable to mitigate this uncertainty by observing a bigger part of the Galactic halo due to a relatively small field of view (see, e.g., [[6], Sec. 5.3]). Overall, we may conclude that currently IACTs overtake the limits derived here at WIMP masses above ≈500 GeV.

And finally, Fig. 10 also contains the limit from AMS-02 antiproton data derived in the newest study [82], which meanwhile disproved a significance of the antiproton excess attributed to DM. We see that the antiproton exclusion line jumps below and above our exclusion until ≈200 GeV, where overtakes finally. Thus, overall, our approach is very competitive to both Fermi-LAT observations of dwarfs and CR antiproton measurements.

VII. POSSIBLE DM CONTRIBUTION INTO THE NONTHERMAL EMISSION IN THE CENTRAL REGION

This section is dedicated to the semiqualitative discussion on the following interesting question: what kind of a radio signal in M31 nucleus would be produced by WIMP, which fits the γ-ray outer halo? For this purpose, I decided to test WIMP with the thermal annihilation cross section (as the most motivated value) and $m_x = (60–70)$ GeV. This WIMP lies inside the range bounded by the red bottom cross in Fig. 10, and it is "partially" (i.e., for certain reasonable parameter configurations) allowed by all the main constraints: our radio, Fermi-LAT gamma by dwarfs and antiprotons. The lighter thermal WIMP is severely constrained, and the heavier one would not fit the outer halo. $m_x = 68$ GeV was set due to practical convenience. Then, the spectrum of radio emission due to such a WIMP and the radial intensity profile were generated (for MED configuration) for the disk with 5′ radius around the center. The results are displayed by the light-green lines at Figs. 11 and 12. The spectrum was compared with the observed nonthermal spectrum, which was obtained from the data at 0.074, 0.15, 0.34, 1.5, and 4.9 GHz. The observed spectrum was fitted by a simple power law yielding $I_\nu \propto \nu^{-0.76}$ (machine fit)—it is shown by the thick green line. We see that the slopes of the observed and DM spectra are quite similar. The blue line shows the case of $\tau^+\tau^-$ channel just for comparison ($\tau^+\tau^-$ was not used to fit the outer halo).

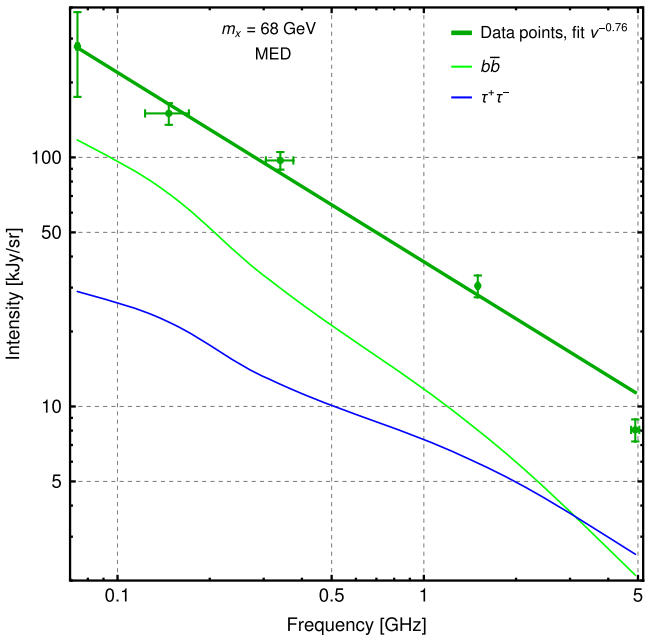


FIG. 11. The observed nonthermal spectrum in the disk with 5′ radius around the center and the spectra of annihilating thermal WIMP with $m_x = 68$ GeV. The case of $b\bar{b}$ channel fits the γ-ray emission from the outer halo of M31.

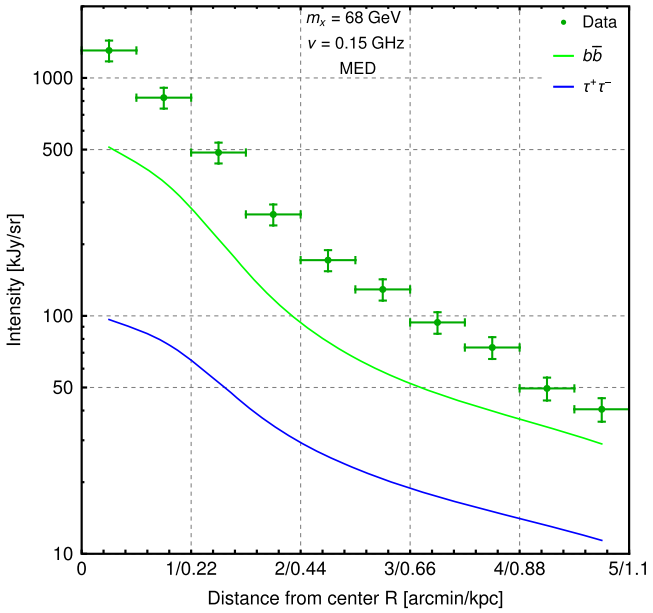


FIG. 12. The observed radial intensity profile from LoTSS data and that from the annihilating thermal WIMP with $m_x = 68$ GeV. The case of $b\bar{b}$ channel fits the γ-ray emission from the outer halo of M31.

The radial intensity profile from DM also follows the observed one very well, just from a visual inspection. Thus, such a WIMP can easily mimic both the spectrum and morphology of the central emission contributing up to about half of the total emission intensity. Another contribution can naturally come from CR $e^{\pm}$. And a good consistency of the spectrum and morphology was seen with just first near-at hand parameter configuration without any tuning, i.e., with MED DM density profile and MF/prop. configuration. An intentional tuning would further improve consistency. DM model variation causes a significant variation of the spectral index. As an illustration of this fact, all our computed 234 DM models show the spectral indices in the wide range 0.39–1.77, if to approximate the spectra by the power law inside inner 5′. The branching ratio of the annihilation to different channels is another free parameter. Thus, overall there are wide opportunities to achieve the necessary fit for the spectrum, morphology and amplitude.

The obtained good consistency between the considered DM emission spectrum/morphology and the observed ones may in principle indicate indirectly in favor of the presence of DM contribution in the central emission. Meanwhile, [26] noticed, that the source of CRs, which produce the radio emission in the nucleus, is unclear; since the star formation and hence, CR acceleration sites are located in the outer zone $r \gtrsim 3$ kpc. The possibility of diffusion of CRs from there to the central region is also doubted. Hence, it is not easy to find a conventional explanation for the relatively bright central radio emission.

VIII. CONCLUSIONS AND DISCUSSION

The present work aimed to obtain the robust and model-independent WIMP annihilation constraints from radio observations of M31. Various new observational data on M31 were implemented, including very recent high-quality images obtained in LOFAR Two-meter Sky Survey. For the first time, the transport equation for DM $e^{\pm}$ was properly solved in 2D taking into account the spatial diffusion. Solution of the transport equation and generation of DM synchrotron emission maps were performed by the specific adaptation of GALPROP code (v56). This is the first (known to the author) application of GALPROP to another galaxy. A wide variety of radio data in the frequency range $\approx$(0.1–10) GHz were utilized to derive the constraints. The systematic uncertainties of the derived constraints were quantified by three benchmark MIN-MED-MAX scenarios (individual) for both DM density distribution and MF/prop. parameters. The constraints were obtained for two representative annihilation channels—into $b\bar{b}$ and $\tau^+\tau^-$. The final results can be viewed in Figs. 8, 9, and Table V. Thus, WIMP mass lower threshold is constrained to lie in the range 20–210 GeV for $b\bar{b}$ channel and 18–89 GeV for $\tau^+\tau^-$ channel for the case of thermal annihilation cross section. If one would like to have some representative effective average limits, then the exclusion drawn by the thick green line at Fig. 9 is suggested to be used for that. This exclusion presents the geometric mean of all nine computed parameter configurations and yields $m_x \gtrsim 70$ GeV for $b\bar{b}$, $m_x \gtrsim 40$ GeV for $\tau^+\tau^-$. However, one has to keep in mind that indeed these average limits are somewhat fiducial rather than statistically hard. Our limits are rather model independent in the sense that no specific assumptions were made regarding the intensity of usual CR synchrotron emission; i.e., the flat priors were assumed for it at all frequencies.

Let us compare the derived constraints with the results of previous studies on the subject. First of all, it is very interesting to make the comparison with our previous work [11]. There, we claimed the (average effective) exclusion of thermal WIMP lighter than 55–100 GeV (the same annihilation channels). The little difference with respect to the new results appeared to be fully caused by the change of the thermal cross section value: the older value used 10 years ago is larger by $\approx$1.5 times than the modern refined value utilized here. Rescaling the thermal cross section would bring the old and new results into nearly ideal agreement. The supposed reason of such a remarkable reconciliation is the following. On one hand, the new study introduced various refining aspects to the model, which lowered DM intensities (hence, weakened the constraints). These aspects include the spatial diffusion, more realistic MF distribution, and energy losses, etc. On the other hand, newer and more sensitive radio images were utilized. Some of these images are cleaned of nuisance emissions. A better sensitivity allowed us to constrain the observed nonthermal emission

intensity better, which strengthened DM constraints. And it looks like these two opposite effects exactly canceled each other. The uncertainty ranges of the final constraints were slightly shrunk by the new model.

Regarding the studies made by other authors, we basically disprove the strong constraints claimed in [15,16], which excluded heavy thermal WIMPs with $m_x \gg 100$ GeV. These studies obtained the constraints utilizing very large ROIs comparable by size to the whole galaxy. Figure 3 above indicates semi-intuitively impossibility of such strong constraints, even if MED configuration there would be replaced by MAX, which produces the largest possible DM flux (from the whole galaxy). The latter reaches the level of observed flux just for the lightest WIMP with $m_x \approx 10$ GeV, meaning that only such low masses can be constrained. The natural question is what does cause such a big discrepancy between the results here and in [15,16]? Although the precise answer would require us to do specific calculations; on a qualitative level, the main supposed reason is the deficient 1D MF model in [15,16] together with abandoning the spatial diffusion, as was discussed in Sec. II. Their MF models extrapolate spherically symmetrically significant field values of several μG up to huge distances of decades kpc. However, no direct field measurements are available at such distances, especially outside the disk. From a general reasoning, one would not expect for MF to extend significantly beyond the disk, since the typical field generation by a dynamo would not work there. For this reason, the exponential field decline is usually assumed in the halo. Thus, [15,16] presumably boosted DM flux from the halo abnormally due to filling an unrealistically large volume by the significant MF. More realistic 2D MF models like those employed here [Eqs. (6)–(8)] are needed instead, especially taking into account the mentioned thinness of M31 magnetic disk.

The obtained exclusions are competitive and comparable to those from Fermi-LAT observations of MW satellites and AMS-02 measurements of CR antiprotons. Rather conservative scenarios of our constraints allow the explanations of the γ-ray M31 outer halo and GC excess by annihilating DM.

It was found that the thermal WIMP with $m_x \approx 70$ GeV, which fits the γ-ray outer halo and is not strongly excluded by all the main constraints, would make a significant contribution into the nonthermal emission in the central region of M31 fitting well both the emission spectrum and radial intensity profile. This is demonstrated at Figs. 11 and 12 particularly for MED DM density and MF/prop. configuration. In that case, DM emission intensity reaches up to about half of the total observed intensity.

As a further development of this work, it is planned to extend this methodology to all other possible annihilation channels in order to study them in details and obtain the channel-independent exclusions. Then the future data from LOFAR LBA Sky Survey (LoLSS) [86] are anticipated for further sensitivity improvement. The study similar to the present work can be conducted for MW too, since the most recent such study [34] utilized rather approximate solution of the transport equation. And the information on the emission polarization can be employed for an ultimate improvement of the sensitivity (for both galaxies). This was already probed in [7].

ACKNOWLEDGMENTS

I greatly appreciate the following software, which is very useful in my work: Wolfram *Mathematica*; "Aladin sky atlas" developed at CDS, Strasbourg Observatory, France [87]; NumPy [88]; Healpy [89]; WebPlotDigitizer [90]. I am very grateful to Mikhail Zavertyaev for providing the server for long computations, Rainer Beck for providing the radio maps of M31, also to George Heald, Nikolay Topchiev, and Mikhail Razumeiko.

APPENDIX: ADDITIONAL ASPECTS OF MODELING OF DM $e^{\pm}$ PROPAGATION AND EMISSION FROM THEM IN GALPROP

Here, I describe the aspects, which were not covered in the main text. Table VI below lists the values of various relevant parameters, which were used in GALPROP. These parameters are the same for all MIN-MED-MAX configurations. The spatial and energy grid step sizes, as well as the propagation energy range cited in the table, were empirically adjusted to achieve a good precision of the intensity calculation at the level of few percents. In fact, the step sizes are very small. Such small steps were needed in the numerical procedure, because both DM density and $e^{\pm}$ injection spectra changes very steeply.

Then let us discuss the neutral gas concentration profiles, which were needed to calculate $e^{\pm}$ bremsstrahlung and ionization energy losses mentioned in Sec. III D. The measured surface density profiles of the atomic and molecular gas were taken from [[66], Fig. 1]. Then I assumed the vertical profiles of gases to be similar to those in MW. Usually, these vertical profiles are assumed to be Gaussian—e.g., [91]. The vertical scale heights (i.e., Gaussian rms) were adopted from [91,92]: $\sigma_{\rm HI} = 0.06$ kpc and $\sigma_{\rm H_2} = 0.03$ kpc,

TABLE VI. Values of various parameters used in GALPROP.

Parameter	Value
Radius of the diffusion cylinder $r_{\rm max}$	15 kpc
Spatial grid step size $\Delta r = \Delta z$	0.05 kpc
Propagation energy range	10 MeV–$1.2m_xc^2$
Energy grid step increment	1.04
Infrared ISRF density factor with respect to MW	0.1
HEALPix resolution of maps $N_{\rm side}$	$2^{10} = 1024$
Temperature of free e^- in galactic gas T_e	7000 K
Free electrons' clumping factor	21
He/H ratio in galactic gas	0.1

which are attributed to the bulge region. Then the normalization coefficients for the concentration profiles were calculated, requiring that each profile must reasonably reproduce the total gas mass in M31: $\int n_{\rm gas}(r,z) m_p dV \approx M_{\rm gas}$. The total gas masses in M31 were taken from [[66], Table I] and [93]. This procedure produced the following fitting functions for the gas distributions, which were substituted into GALPROP,

$$n_{\rm HI}(r_{\rm kpc},z) = 0.269(10\hat{}(\sin((r/8.23)^{1.35}) - 0.377) + (r/23)^2 + 0.23/(r+1.8)^{0.7}) \times \exp(-0.5z^2/\sigma_{\rm HI}^2)\ {\rm cm}^{-3}, \quad \text{(A1)}$$

$$n_{\rm H_2}(r_{\rm kpc},z) = 0.538(0.073 + 0.42\exp(-(r-4.35)^2) + \exp(-(r-10.8)^2/3.5)) \times \exp(-0.5z^2/\sigma_{\rm H_2}^2)\ {\rm cm}^{-3}. \quad \text{(A2)}$$

Indeed, these are quite simple distributions, which track only the large-scale structure of the gas over the whole disk and do not contain small-scale irregularities like dense clouds. As an overall sanity check of the gas profiles constructed above [including (14)], I compared the synchrotron flux from the relevant ROI ($R \leqslant 1$ kpc) produced with the profiles above and that with the standard MW profiles. The replacement of $n_e(r,z)$ and $n_{\rm HI}(r,z)$ has a minor effect on the flux—less than 10%. This agrees with the data presented in [[66], Table 1, Fig. 1] for HI—its disk surface density and total mass are very similar in MW and M31. However, the replacement of $n_{\rm H_2}(r,z)$ profile lowers the flux more—by 10%–30% depending on frequency. This also agrees with the mentioned source of data—H_2 surface density and mass in M31 are lower than those in MW by several times. Thus, the constructed profiles look realistic in the first approximation. Also, the fact that the emission fluxes depend mildly on the gas concentrations releases a necessity to vary the latter with the purpose of studying the corresponding uncertainty range. That is, the potential uncertainties in the synchrotron intensity due to the uncertainties in gas distributions are negligible in comparison with those driven by, e.g., the uncertainties in DM density distribution. Thus, I set the same gas distributions for all MIN-MED-MAX scenarios.

Full galdef files for GALPROP runs can be requested from the author by e-mail.

[1] V. A. Rubakov, Cosmology and dark matter, arXiv:1912.04727.

[2] Y. B. Zeldovich, A. Klypin, M. Y. Khlopov, and V. M. Chechetkin, Astrophysical bounds on the mass of heavy stable neutral leptons, Sov. J. Nucl. Phys. **31**, 664 (1980).

[3] T. R. Slatyer, Les Houches lectures on indirect detection of dark matter, SciPost Phys. Lect. Notes 53 (2022).10.21468/SciPostPhysLectNotes.53

[4] S. Ando, A. Geringer-Sameth, N. Hiroshima, S. Hoof, R. Trotta, and M. G. Walker, Structure formation models weaken limits on WIMP dark matter from dwarf spheroidal galaxies, Phys. Rev. D **102**, 061302 (2020).

[5] S. Hoof, A. Geringer-Sameth, and R. Trotta, A global analysis of dark matter signals from 27 dwarf spheroidal galaxies using 11 years of Fermi-LAT observations, J. Cosmol. Astropart. Phys. 02 (**2020**) 012.

[6] A. Acharyya, R. Adam, C. Adams, I. Agudo, A. Aguirre-Santaella, R. Alfaro, J. Alfaro, C. Alispach, R. Aloisio, R. Alves Batista *et al.*, Sensitivity of the Cherenkov Telescope Array to a dark matter signal from the Galactic centre, J. Cosmol. Astropart. Phys. 01 (2021) 057.

[7] S. Manconi, A. Cuoco, and J. Lesgourgues, Dark matter constraints from Planck observations of the galactic polarized synchrotron emission, arXiv:2204.04232.

[8] Haslam 408 MHz all-sky map from https://lambda.gsfc.nasa.gov/product/foreground/fg_2014_haslam_408_info.cfm.

[9] P. Reich, J. C. Testori, and W. Reich, A radio continuum survey of the southern sky at 1420 MHz. The atlas of contour maps, Astron. Astrophys. **376**, 861 (2001).

[10] R. A. M. Walterbos and R. Graeve, Radio continuum emission from the nuclear region of M 31: Evidence for a nuclear radio spiral, Astron. Astrophys. **150**, L1 (1985).

[11] A. E. Egorov and E. Pierpaoli, Constraints on dark matter annihilation by radio observations of M31, Phys. Rev. D **88**, 023504 (2013).

[12] NASA/IPAC Extragalactic Database https://ned.ipac.caltech.edu/.

[13] S. Li, A. G. Riess, M. P. Busch, S. Casertano, L. M. Macri, and W. Yuan, A Sub-2 distance to M31 from photometrically homogeneous near-infrared cepheid period-luminosity relations measured with the Hubble space telescope, Astrophys. J. **920**, 84 (2021).

[14] A. McDaniel, T. Jeltema, and S. Profumo, Multiwavelength analysis of annihilating dark matter as the origin of the gamma-ray emission from M31, Phys. Rev. D **97**, 103021 (2018).

[15] M. H. Chan, L. Cui, J. Liu, and C. S. Leung, Ruling out ~100–300 GeV thermal relic annihilating dark matter by radio observation of the Andromeda galaxy, Astrophys. J. **872**, 177 (2019).

[16] G. Beck, An excess of excesses examined via dark matter radio emissions from galaxies, J. Cosmol. Astropart. Phys. 08 (2019) 019.

[17] M. H. Chan, C. F. Yeung, L. Cui, and C. S. Leung, Analysing the radio flux density profile of the M31 galaxy: A possible dark matter interpretation, Mon. Not. R. Astron. Soc. **501**, 5692 (2021).
[18] S. Colafrancesco, S. Profumo, and P. Ullio, Multi-frequency analysis of neutralino dark matter annihilations in the Coma cluster, Astron. Astrophys. **455**, 21 (2006).
[19] M. H. Chan, C. M. Lee, C. Y. Ng, and C. S. Leung, Constraining Annihilating Dark Matter Mass by the Radio Continuum Spectral Data of a High-redshift Galaxy Cluster, Astrophys. J. **900**, 126 (2020).
[20] M. H. Chan and C. M. Lee, Fitting dark matter mass with the radio continuum spectral data of the Ophiuchus cluster, Phys. Dark Universe **26**, 100355 (2019).
[21] E. Storm, T. E. Jeltema, S. Profumo, and L. Rudnick, Constraints on dark matter annihilation in clusters of galaxies from diffuse radio emission, Astrophys. J. **768**, 106 (2013).
[22] M. H. Chan, Radio constraints of dark matter: A review and some future perspectives, Galaxy **9**, 11 (2021).
[23] A. McDaniel, T. Jeltema, S. Profumo, and E. Storm, Multiwavelength analysis of dark matter annihilation and RX-DMFIT, J. Cosmol. Astropart. Phys. 09 (2017) 027.
[24] M. Ackermann *et al.*, Observations of M31 and M33 with the Fermi large area telescope: A galactic center excess in Andromeda?, Astrophys. J. **836**, 208 (2017).
[25] B. Ruiz-Granados, J. A. Rubiño-Martín, E. Florido, and E. Battaner, Magnetic fields and the outer rotation curve of M31, Astrophys. J. Lett. **723**, L44 (2010).
[26] R. Gießübel and R. Beck, The magnetic field structure of the central region in M 31, Astron. Astrophys. **571**, A61 (2014).
[27] A. E. Egorov, J. M. Gaskins, E. Pierpaoli, and D. Pietrobon, Dark matter implications of the WMAP-Planck Haze, J. Cosmol. Astropart. Phys. 03 (**2016**) 060.
[28] http://galprop.stanford.edu/.
[29] I. Moskalenko, G. Johannesson, and T. Porter, GALPROP Code for Galactic Cosmic Ray Propagation and Associated Photon Emissions, in *36th International Cosmic Ray Conference (ICRC2019)* (Proceedings of Science, Madison, 2019), Vol. 36, p. 111.
[30] https://github.com/a-e-egorov/GALPROP_DM.
[31] http://www.marcocirelli.net/PPPC4DMID.html.
[32] M. Cirelli, G. Corcella, A. Hektor, G. Hütsi, M. Kadastik, P. Panci, M. Raidal, F. Sala, and A. Strumia, PPPC 4 DM ID: a poor particle physicist cookbook for dark matter indirect detection, J. Cosmol. Astropart. Phys. 03 (2011) 051.
[33] Y. Génolini, M. Boudaud, M. Cirelli, L. Derome, J. Lavalle, D. Maurin, P. Salati, and N. Weinrich, New minimal, median, and maximal propagation models for dark matter searches with Galactic cosmic rays, Phys. Rev. D **104**, 083005 (2021).
[34] M. Cirelli and M. Taoso, Updated galactic radio constraints on Dark Matter, J. Cosmol. Astropart. Phys. 07 (2016) 041.
[35] K. Saikawa and S. Shirai, Precise WIMP dark matter abundance and Standard Model thermodynamics, J. Cosmol. Astropart. Phys. 08 (2020) 011.
[36] https://member.ipmu.jp/satoshi.shirai/DM2020/.
[37] A. Banerjee and C. J. Jog, The flattened dark matter halo of M31 as deduced from the observed H I scale heights, Astrophys. J. **685**, 254 (2008).
[38] K. Hayashi and M. Chiba, The prolate dark matter halo of the Andromeda galaxy, Astrophys. J. **789**, 62 (2014).
[39] J. J. Geehan, M. A. Fardal, A. Babul, and P. Guhathakurta, Investigating the Andromeda stream—I. Simple analytic bulge-disc-halo model for M31, Mon. Not. R. Astron. Soc. **366**, 996 (2006).
[40] M. S. Seigar, A. J. Barth, and J. S. Bullock, A revised ΛCDM mass model for the Andromeda galaxy, Mon. Not. R. Astron. Soc. **389**, 1911 (2008).
[41] L. Chemin, C. Carignan, and T. Foster, H I kinematics and dynamics of Messier 31, Astrophys. J. **705**, 1395 (2009).
[42] E. Corbelli, S. Lorenzoni, R. Walterbos, R. Braun, and D. Thilker, A wide-field H I mosaic of Messier 31. II. The disk warp, rotation, and the dark matter halo, Astron. Astrophys. **511**, A89 (2010).
[43] A. Tamm, E. Tempel, P. Tenjes, O. Tihhonova, and T. Tuvikene, Stellar mass map and dark matter distribution in M 31, Astron. Astrophys. **546**, A4 (2012).
[44] M. Blaña Díaz, O. Gerhard, C. Wegg, M. Portail, M. Opitsch, R. Saglia, M. Fabricius, P. Erwin, and R. Bender, Sculpting Andromeda—made-to-measure models for M31's bar and composite bulge: Dynamics, stellar and dark matter mass, Mon. Not. R. Astron. Soc. **481**, 3210 (2018).
[45] P. Boldrini, R. Mohayaee, and J. Silk, Flattening of dark matter cusps during mergers: Model of M31, Astrophys. J. **919**, 86 (2021).
[46] M. Kamionkowski, S. M. Koushiappas, and M. Kuhlen, Galactic substructure and dark-matter annihilation in the Milky Way halo, Phys. Rev. D **81**, 043532 (2010).
[47] J. F. Navarro, C. S. Frenk, and S. D. M. White, A universal density profile from hierarchical clustering, Astrophys. J. **490**, 493 (1997).
[48] P. Hoernes, R. Beck, and E. M. Berkhuijsen, *Properties of synchrotron emission and magnetic fields in the central region of M31, in The Central Regions of the Galaxy and Galaxies*, edited by Y. Sofue (Kluwer, Dordrecht, 1998), Vol. 184, p. 351.
[49] A. Fletcher, E. M. Berkhuijsen, R. Beck, and A. Shukurov, The magnetic field of M31 from multi-wavelength radio polarization observations, Astron. Astrophys. **414**, 53 (2004).
[50] J. L. Han, R. Beck, and E. M. Berkhuijsen, New clues to the magnetic field structure of M 31, Astron. Astrophys. **335**, 1117 (1998).
[51] R. Beck, Magnetic fields in galaxies, Space Sci. Rev. **166**, 215 (2012).
[52] R. M. Crocker, D. I. Jones, F. Melia, J. Ott, and R. J. Protheroe, A lower limit of 50 microgauss for the magnetic field near the galactic centre, Nature (London) **463**, 65 (2010).
[53] R. M. Crocker, D. I. Jones, F. Aharonian, C. J. Law, F. Melia, and J. Ott, γ-rays and the far-infrared-radio continuum correlation reveal a powerful Galactic Centre wind, Mon. Not. R. Astron. Soc. **411**, L11 (2011).
[54] R. Stepanov, T. G. Arshakian, R. Beck, P. Frick, and M. Krause, Magnetic field structures of galaxies derived

from analysis of Faraday rotation measures, and perspectives for the SKA, Astron. Astrophys. **480**, 45 (2008).
[55] M. Haverkorn and V. Heesen, Magnetic fields in galactic haloes, Space Sci. Rev. **166**, 133 (2012).
[56] R. Beck, L. Chamandy, E. Elson, and E. G. Blackman, Synthesizing observations and theory to understand galactic magnetic fields: Progress and challenges, Galaxy **8**, 4 (2019).
[57] R. Jansson and G. R. Farrar, A new model of the galactic magnetic field, Astrophys. J. **757**, 14 (2012).
[58] N. Fornengo, R. A. Lineros, M. Regis, and M. Taoso, Galactic synchrotron emission from WIMPs at radio frequencies, J. Cosmol. Astropart. Phys. 01 (2012) 005.
[59] E. M. Berkhuijsen, R. Beck, and F. S. Tabatabaei, How cosmic ray electron propagation affects radio-far-infrared correlations in M 31 and M 33, Mon. Not. R. Astron. Soc. **435**, 1598 (2013).
[60] L. O. C. Drury and A. W. Strong, Power requirements for cosmic ray propagation models involving diffusive reacceleration; estimates and implications for the damping of interstellar turbulence, Astron. Astrophys. **597**, A117 (2017).
[61] V. Ginzburg, *Theoretical Physics and Astrophysics* (Pergamon Press, New York, 1979).
[62] B. Groves and O. Krause, Hot & cold dust in M31: The resolved SED of Andromeda, in *The Spectral Energy Distribution of Galaxies—SED 2011*, edited by R. J. Tuffs and C. C. Popescu (2012), Vol. 284, pp. 112–116.
[63] Planck Collaboration, P. A. R. Ade, N. Aghanim, M. Arnaud, M. Ashdown, J. Aumont, C. Baccigalupi, A. J. Banday, R. B. Barreiro, N. Bartolo *et al.*, Planck intermediate results. XXV. The Andromeda galaxy as seen by Planck, Astron. Astrophys. **582**, A28 (2015).
[64] S. M. Kent, An improved bulge model for M31, Astron. J. **97**, 1614 (1989).
[65] S. van den Bergh, The local group of galaxies, Astron. Astrophys. Rev. **9**, 273 (1999).
[66] J. Yin, J. L. Hou, N. Prantzos, S. Boissier, R. X. Chang, S. Y. Shen, and B. Zhang, Milky Way versus Andromeda: A tale of two disks, Astron. Astrophys. **505**, 497 (2009).
[67] T. C. Licquia, J. A. Newman, and J. Brinchmann, Unveiling the milky way: A new technique for determining the optical color and luminosity of our galaxy, Astrophys. J. **809**, 96 (2015).
[68] F. S. Tabatabaei, E. M. Berkhuijsen, P. Frick, R. Beck, and E. Schinnerer, Multi-scale radio-infrared correlations in M 31 and M 33: The role of magnetic fields and star formation, Astron. Astrophys. **557**, A129 (2013).
[69] E. S. Battistelli *et al.*, Strong evidence of anomalous microwave emission from the flux density spectrum of M 31, Astrophys. J. Lett. **877**, L31 (2019).
[70] GALPROP explanatory supplement at http://galprop.stanford.edu/code.php?option=manual.
[71] R. Beck, E. M. Berkhuijsen, and P. Hoernes, A deep lambda 20 CM radio continuum survey of M 31, Astron. Astrophys. Suppl. Ser. **129**, 329 (1998).
[72] R. Beck (private communication).
[73] W. M. Lane, W. D. Cotton, S. van Velzen, T. E. Clarke, N. E. Kassim, J. F. Helmboldt, T. J. W. Lazio, and A. S. Cohen, The very large array low-frequency sky survey redux (VLSSr). Mon. Not. R. Astron. Soc. **440**, 327 (2014).
[74] A. S. Cohen, W. M. Lane, W. D. Cotton, N. E. Kassim, T. J. W. Lazio, R. A. Perley, J. J. Condon, and W. C. Erickson, The VLA low-frequency sky survey, Astron. J. **134**, 1245 (2007).
[75] T. W. Shimwell *et al.*, The LOFAR two-metre sky survey. V. Second data release, Astron. Astrophys. **659**, A1 (2022).
[76] R. Gießübel, G. Heald, R. Beck, and T. G. Arshakian, Polarized synchrotron radiation from the Andromeda galaxy M 31 and background sources at 350 MHz, Astron. Astrophys. **559**, A27 (2013).
[77] R. Beck, E. M. Berkhuijsen, R. Gießübel, and D. D. Mulcahy, Magnetic fields and cosmic rays in M 31. I. Spectral indices, scale lengths, Faraday rotation, and magnetic field pattern, Astron. Astrophys. **633**, A5 (2020).
[78] S. Fatigoni *et al.*, Study of the thermal and nonthermal emission components in M 31: The Sardinia Radio Telescope view at 6.6 GHz, Astron. Astrophys. **651**, A98 (2021).
[79] C. M. Karwin, S. Murgia, S. Campbell, and I. V. Moskalenko, Fermi-LAT Observations of γ-ray emission toward the outer halo of M31, Astrophys. J. **880**, 95 (2019).
[80] C. M. Karwin, S. Murgia, I. V. Moskalenko, S. P. Fillingham, A.-K. Burns, and M. Fieg, Dark matter interpretation of the Fermi-LAT observations toward the outer halo of M31, Phys. Rev. D **103**, 023027 (2021).
[81] I. Cholis, Y.-M. Zhong, S. D. McDermott, and J. P. Surdutovich, The return of the templates: Revisiting the galactic center excess with multi-messenger observations, Phys. Rev. D **105**, 103023 (2022).
[82] F. Calore, M. Cirelli, L. Derome, Y. Genolini, D. Maurin, P. Salati, and P. D. Serpico, AMS-02 antiprotons and dark matter: Trimmed hints and robust bounds, SciPost Phys. **12**, 163 (2022).
[83] H. Abdallah, A. Abramowski, F. Aharonian, F. Ait Benkhali, A. G. Akhperjanian, E. Angüner, M. Arrieta, P. Aubert, M. Backes, A. Balzer *et al.*, Search for Dark Matter Annihilations Towards the Inner Galactic Halo from 10 Years of Observations with H.E.S.S., Phys. Rev. Lett. **117**, 111301 (2016).
[84] A. E. Egorov, N. P. Topchiev, A. M. Galper, O. D. Dalkarov, A. A. Leonov, S. I. Suchkov, and Y. T. Yurkin, Dark matter searches by the planned gamma-ray telescope GAMMA-400, J. Cosmol. Astropart. Phys. 11 (2020) 049.
[85] V. A. Acciari *et al.* (MAGIC Collaboration), Combined searches for dark matter in dwarf spheroidal galaxies observed with the MAGIC telescopes, including new data from Coma Berenices and Draco, Phys. Dark Universe **35**, 100912 (2022).
[86] F. de Gasperin *et al.*, The LOFAR LBA Sky Survey. I. Survey description and preliminary data release, Astron. Astrophys. **648**, A104 (2021).
[87] F. Bonnarel, P. Fernique, O. Bienaymé, D. Egret, F. Genova, M. Louys, F. Ochsenbein, M. Wenger, and J. G. Bartlett, The ALADIN interactive sky atlas. A reference tool for identification of astronomical sources, Astron. Astrophys. Suppl. Ser. **143**, 33 (2000).

[88] https://numpy.org/.
[89] https://github.com/healpy.
[90] https://apps.automeris.io/wpd/.
[91] K. Ferrière, W. Gillard, and P. Jean, Spatial distribution of interstellar gas in the innermost 3 kpc of our galaxy, Astron. Astrophys. **467**, 611 (2007).
[92] J. M. Dickey and F. J. Lockman, H I in the galaxy., Annu. Rev. Astron. Astrophys. **28**, 215 (1990).
[93] C. Nieten, N. Neininger, M. Guélin, H. Ungerechts, R. Lucas, E. M. Berkhuijsen, R. Beck, and R. Wielebinski, Molecular gas in the Andromeda galaxy, Astron. Astrophys. **453**, 459 (2006).

Nature of M31 gamma-ray halo in relation to dark matter annihilation

Andrei E. Egorov*

Nuclear Physics and Astrophysics Division, Lebedev Physical Institute, Leninskii prospect—53, 119333, Moscow, Russia

(Received 12 May 2023; accepted 26 July 2023; published 25 August 2023)

The present work analyzes various aspects of M31 gamma-ray halo emission in its relation to annihilating dark matter (DM). The main aspect is the predicted effect of asymmetry of the intensity of emission due to inverse Compton scattering (ICS) of a possible population of relativistic electrons and positrons ($e^{\pm}$) in the galactic halo on starlight photons. This asymmetry is expected to exist around the major galactic axis, and arises due to anisotropy of the interstellar radiation field and the inclination of M31. ICS emission and its asymmetry were modeled by GALPROP code for the trial case of $e^{\pm}$ generated by annihilating weakly interacting massive particles (WIMPs) with various properties. The asymmetry was obtained to appear at photon energies above ∼0.1 MeV. Morphological and spectral properties of the asymmetry were studied in detail. Potential observational detection of the asymmetry may allow to infer the leptonic fraction in the emission generation mechanism, thus providing valuable inferences for understanding the nature of M31 gamma-ray halo emission. Specific asymmetry predictions were made for the recently claimed DM interpretation of the outer halo emission. The paper also studied the role of secondary—ICS and bremsstrahlung—emissions due to DM annihilation for that interpretation. And, finally, the latter was shown to be somewhat restricted by the recently derived WIMP constraints from radio data on M31.

DOI: 10.1103/PhysRevD.108.043028

I. INTRODUCTION AND MOTIVATION

M31 (Andromeda galaxy) is the closest large spiral galaxy. Its proximity allows to study in detail a wide variety of astrophysical phenomena under a view and environment, which are alternatives to our own Galaxy, Milky Way (MW). This paper concerns the results of gamma-ray band observations of M31 in their possible relation to annihilating dark matter (DM). M31 was detected in gamma rays for the first time by Fermi-LAT during the first years of its operation [1]. Later, more observational data was accumulating, which enabled certain detailing of both the emission spectrum and morphology. Thus, [2] reported that the gamma-ray emission source at M31 center is extended, has the angular radius ≈0.4° and presumably has a uniform brightness distribution. The emission spectrum was measured up to ≈10 GeV. Then [3] (among other works on the subject) confirmed the cited results of [2] and also reported a possible presence of another emission component, which extends up to ≈1°. At about the same time, [4] also found out a tentative presence of very large outer gamma-ray halo, which extends up to at least ≈9°. And very recently, [5] elaborated that the central source, which was previously thought to be extended with the radius 0.4°, in fact represents two point sources: one is in the center and one is ≈0.4° away from the center. And it is not very clear whether the noncentral source belongs to M31.

Simultaneously with the observational progress briefly described above, extensive theoretical modeling of the possible gamma-ray emission mechanisms in M31 was developing. A wide variety of emission sources has been proposed: a population of millisecond pulsars (MSPs) [6], cosmic rays (CRs) [7,8], and DM annihilation (e.g., [9]). It is very possible that more than one emission mechanisms work together, and different processes are responsible for the emission generation in different regions of the galaxy.

Many works studied the possibility of presence of DM contribution in the gamma-ray emission [6,9–12] and derived the respective constraints. One brief conclusion from these studies is impossibility to explain all the emission by annihilating DM only. Thus, the fit of the inner halo (IH) region spectrum requires the mass of DM particle (traditional weakly interacting massive particles (WIMPs) are being considered) to be very small—$m_x \approx (6\text{–}11)$ GeV according to [11], while the outer halo (OH) region spectrum can be fitted by heavier WIMP with $m_x \approx (45\text{–}72)$ GeV [9]. But this is an absolutely natural situation: we would primarily expect for DM contribution to be minor, while the majority of emission is generated by usual astrophysical processes, like it is in our own Galaxy. And it is very interesting and promising to understand the emission nature in detail, which

*aegorov@runbox.com

 © 2023 American Physical Society

may eventually lead to a robust detection of DM signal among other emission components. Thus, M31 studies in the gamma-ray band represent a valuable direction in the field of DM indirect searches.

One potential emission generation mechanism is leptonic, i.e., through the inverse Compton scattering (ICS) process between the photon field in the galaxy and relativistic electrons/positrons. This mechanism has a big relevance: [7,8] showed that both the IH and OH emissions could be explained by CR interactions, when a significant contribution comes from ICS of CR $e^{\pm}$. The emission due to WIMP annihilation (or decay) would also necessarily have the leptonic (secondary) component; since besides the prompt gammas, the annihilation produces relativistic $e^{\pm}$ too (DM $e^{\pm}$ hereafter). However, among all the works cited above, only [10] paid attention to the ICS emission component due to WIMPs.

The main goal of this work is to conduct comprehensive theoretical modeling of the interesting effect of ICS emission intensity asymmetry between M31 hemispheres. This effect was pointed out for the first time in [13] (see Fig. 2 there): we view M31 under the certain inclination angle; hence, there must be some difference in the upscattered photon spectra from the regions above and below M31 major axis, since the starlight radiation field in any disk galaxy has a significant anisotropy. The physical nature of such asymmetry will be explained in more details below. The authors of [13] provided just simple analytical estimates of this effect, concluding that an average upscattered photon energy would differ by ∼10% between the hemispheres. Here I aim to study this asymmetry effect much more precisely and in detail, since the former may potentially provide a valuable observational test for the physical nature of the gamma-ray emission from the halo. GALPROP code [14] was employed for the modeling of ICS emission in M31. As the source of $e^{\pm}$ population in the halo, WIMP annihilation was assumed in connection with the results of [9], where WIMP annihilation in both MW and M31 was shown to be the plausible explanation of the gamma-ray emission toward the OH. The study here is majorly theoretical and does not aim so far to derive any observational constraints or implications, although some minor qualitative discussion of the observational prospects is given. Section II below is dedicated to the asymmetry effect and represents the main content of this paper. Then Secs. III and IV discuss somewhat different but important aspects of DM interpretation of the OH emission. The authors of [9] performed the fit of the OH by only the prompt gamma-ray emission from annihilating WIMPs and did not take into account the secondary (ICS and bremsstrahlung) emissions. Section III analyzes the role of secondary emission contributions due to WIMPs. Section IV debates the relation between the OH fit and WIMP radio constraints. And Sec. V summarizes the findings.

In general, this work continues our series of papers [15–17] dedicated to WIMP searches/constraints in M31 and utilizes the methodology developed previously there. M31 model parameters assumed here are the same as in [16], if it is not explicitly stated otherwise.

II. ICS EMISSION ASYMMETRY

An interstellar radiation field (ISRF), i.e., the photon field produced by stars, gas and dust, is anisotropic at some level in any disk galaxy due to its nonspherical shape. Let us imagine that a disk galaxy, particularly M31 in our case, possesses a population of relativistic $e^{\pm}$ of any origin, they produce gamma rays through ICS at ISRF, and we observe the galaxy in the gamma-ray band from aside under the certain inclination angle—see Fig. 1. In our case $E_e > E_\gamma \gg E_{\gamma 0}$, where E_e is the electron or positron energy before scattering, $E_{\gamma 0}$ and E_γ are the photon energies before and after scattering. Such energy ratio implies, that the momentum of upscattered photon would have almost exactly the same direction as the initial $e^{\pm}$ momentum. This fact is quite obvious from just a general intuition, but can also be obtained from the equation for the differential cross section of the ICS process derived in quantum electrodynamics (e.g., [[18], Eq. (86.6)]). Hence, we would see the gamma-ray photons produced by $e^{\pm}$, which move toward the observer. Then we can deduce from Fig. 1, that the effective average angle between the initial momenta of photons and emitting $e^{\pm}$ slightly differs for the lines of sight lying above and below the major axis of the galaxy. The energy of upscattered photons strongly depends on that angle through the following relation (taken from [[19], Eq. (16.54)]):

$$E_\gamma = \frac{E_{\gamma 0}(1-\beta_e \cos\theta_i)}{1-\beta_e \cos\theta_f + (1-\cos(\theta_i-\theta_f))E_{\gamma 0}/E_e}, \quad (1)$$

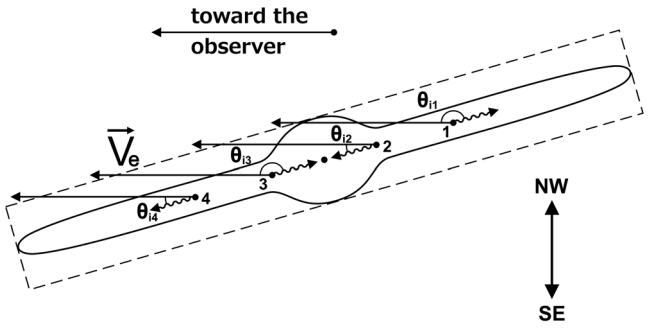


FIG. 1. The schematic central vertical section of M31 with four trial points of interest in regard to ICS process. The dashed line denotes the approximate boundary of the assumed diffusion zone; $\vec{V}_e$—the velocities of $e^{\pm}$, which produce the upscattered photons visible for the observer; and the wavy lines—the purportive slightly predominant directions of ISRF photons at the corresponding points.

where $\beta_e \equiv V_e/c$, θ_i is the angle between the initial momenta of $e^{\pm}$ and photon, $\theta_f \approx 0$ is the angle after the collision (which nearly vanishes according to the considerations above). Therefore, we can expect slightly different ICS emission spectra from regions of interest (ROIs), which are located above and below the major axis, and are symmetric with respect to it. This is the ICS emission asymmetry effect in its essence. Roughly speaking, one hemisphere is expected to be brighter than the other at the same photon energy. Such effect does not exist for our own Galaxy, since we are located at its plane and view the ISRF from both hemispheres symmetrically. However, for M31 the asymmetry may be substantial. And potential observational studies of this asymmetry may allow to derive or constrain the leptonic fraction in the total gamma-ray emission, facilitating the unraveling of the emission mechanism.

The asymmetry effect is modeled here specifically for the case of $e^{\pm}$ population produced by annihilating DM, whose properties fit the outer gamma-ray halo of M31 according to [9]. The primary motivation for such choice is to build precise and testable predictions for this specific model of the OH emission. At the same time, we may expect rather similar asymmetry properties for other cases of $e^{\pm}$ population, since the properties of the latter primarily influence the ICS emission intensity amplitude and spectral shape rather than the asymmetry. The latter is primarily defined by the galaxy inclination and ISRF directionality, which are the same for any $e^{\pm}$ population. Hence, in the first approximation, we may extrapolate the obtained asymmetry picture from our particular case of interest to other cases. Nevertheless, I computed the asymmetry properties for some alternative $e^{\pm}$ populations too in order to study the parameter dependence to a certain extent. It is not easy to compute a large grid of various $e^{\pm}$ model populations due to the computational heaviness of the task.

A. Modeling the ICS emission due to WIMP annihilation

This subsection describes the details of the ICS emission modeling procedure. WIMP mass was set to $m_x = 60$ GeV as the main value of interest. This is the approximate average value among those derived in [9] for the fit of OH. The primary annihilation products are assumed to be $b\bar{b}$ quark pairs. The annihilation cross section is set to the thermal value $\langle\sigma v\rangle(m_x = 60\ \mathrm{GeV}) = 2.1 \times 10^{-26}\ \mathrm{cm}^3/\mathrm{s}$ according to [20]. Actually, [9] found very large uncertainty range for the cross section value, which fits the OH (Table II there): $\langle\sigma v\rangle \sim (10^{-26}\text{–}10^{-23})\ \mathrm{cm}^3/\mathrm{s}$ depending on a variety of their model parameters and assumptions. Only the thermal cross section is mainly considered here, because it represents the most natural and motivated value in cosmology and particle physics. But also the intensity of emission of any kind due to WIMP annihilation is linearly proportional to the cross section; hence, the intensity can be easily rescaled for an arbitrary cross section value. And the asymmetry, defined as the intensity ratio between the hemispheres, would not depend on the cross section at all.

Regarding DM density profile, [9] utilized two profiles for the fit: Einasto profile from [21] and Navarro-Frenck-White (NFW) profile from [4,9]. These profiles yield rather similar densities (see [[9], Fig. 3]). I utilized Einasto profile for main calculations, though some alternative profile with lower density was substituted too (see Table III below) in order to study the parameter dependence. Meanwhile, Einasto profile exactly corresponds to MAX DM density profile in [16] (its parameters can be seen in Table III there). MIN-MED-MAX here have the traditional meaning of parameter configurations, which provide respectively the minimal, medium and maximal emission intensities due to DM.

Another important aspect is DM annihilation rate boost due to substructures in DM halo. This aspect is highly uncertain. The boost factor has the biggest influence on the annihilation rate at the largest radii ~100 kpc. The authors of [9] quantify the uncertainty in the boost factor by employing of four various models: the smooth density profile (i.e., no boost at all) and "low–mid–high" boost configurations (Table II there). A higher boost implies a lower annihilation cross section required for the outer gamma-ray halo fit. The boost factor radial profile adapted here is based on [22] and closely resembles the "high" case in [9]. In general, we do not expect a high influence of details of the boost factor model on the characteristics of the secondary emissions due to WIMPs, which we are interested in. This is because DM $e^{\pm}$ live only in the diffusion zone, which is typically assumed to extend up to at most $R \approx 20$ kpc (e.g., [23]). And the annihilation rate boost factor is not yet significant at such distances (see, e.g., [[22], Fig. 4]). Thus, although the boost factor is included in the calculations here, it does not play a big role for the final results. But speaking technically, the model setup here was made to be consistent with [9] in the following sense: the thermal annihilation cross section requires the "high" boost at least in MW for the OH fit according to Table II there; MW and M31 have quite similar DM halos; hence, the high substructure boost in MW likely implies the same for M31.

The computation of all the emission maps was performed by GALPROP code v57 [24] paired with the addition [25] developed by the author. This addition enables a precise computation of all DM-related particles and emissions, and incorporates the energy spectra of stable annihilation products (at injection) from PPPC 4 DM ID resource [26–28]. GALPROP solves the transport equation for DM $e^{\pm}$, computes their emissivity and integrates it along a line of sight, yielding emission intensity sky maps. GALPROP provides the powerful capability to compute the ICS emission precisely in the frame of full anisotropic

TABLE I. The total luminosities and gas masses of MW and M31 with respective references.

Parameter	MW	M31
Optical (V-band) luminosity [$L_\odot$]	2.1×10^{10} [31]	2.7×10^{10} [31]
IR (dust) luminosity [$L_\odot$]	7.4×10^{9} [32]	4.3×10^{9} [33]
Gas mass [$M_\odot$]	7×10^{9} [31]	8×10^{9} [34,35]

formalism, which is described in [29]. Indeed, GALPROP had to be specifically adapted for modeling of M31. In this aspect, the experience, which was developed in the frame of work [16], was widely used. Our model is 2D, i.e., the axial symmetry of the galaxy is assumed. An important model element for the ICS emission computation is ISRF, i.e., the model of distribution of the intensity of field target photons over energy, spatial coordinates and direction. In general, GALPROP naturally includes three distinct components of ISRF: CMB, a far-infrared (IR) emission from dust and an optical emission from stars. The standard MW 2D ISRF model created by GALPROP authors [30] was utilized for M31 here with one modification: the energy densities of IR and optical components were globally rescaled according to the ratio of M31 and MW IR/optical total luminosities. GALPROP lacks the dedicated model of M31 ISRF. But MW and M31 are rather similar galaxies in their structure and size. Hence, it is a reasonable approximation to extrapolate MW ISRF to M31 for estimation purposes. And the ratio of M31 and MW luminosities serves as an estimator of the ratio of the photon field energy densities (again assuming the same size for both galaxies), since a radiation energy density is linearly proportional to an intensity. Table I provides the relevant luminosities of both galaxies. The corresponding ISRF energy density global rescaling factors are listed in Table II together with other important GALPROP model parameters. It is implicitly assumed here that there are no causes for the ICS emission asymmetry other than the galaxy inclination. It means that $e^{\pm}$ population and ISRF are constructed in such a way, that they are both axisymmetric and symmetric with respect to the galactic plane. These are generally natural assumptions for a disk galaxy modeled in 2D. And all the used ISRF models were empirically checked to satisfy those symmetries by making test GALPROP runs with the observer placed at the galactic plane. These test runs yielded no ICS asymmetry, as anticipated.

Another essential model ingredient for the computation of ICS emission due to DM $e^{\pm}$ is their cooling and propagation. The cooling mechanisms include ICS, synchrotron, bremsstrahlung radiative energy losses; Coulomb scattering and ionization losses. The respective energy loss rates (as they are implemented in GALPROP) are written out in [[16], Eqs. (10)–(13)]. The ICS energy loss rate is defined by the energy density of ISRF, which is described above. The synchrotron loss rate is defined by the magnetic field (MF) strength. M31 MF model developed in [16] (Sec. IIIC there) was naturally adopted here. Specifically, MED (i.e., medium) MF configuration with the central field strength of 50 μG was used as the base scenario here. The energy losses of other kinds require to set the gas distributions in M31. The former is described in [[16], Eq. (14), Appendix]. Regarding $e^{\pm}$ propagation (prop.) parameters, the experience gained in [16] was again utilized: MED propagation parameter configuration, described in Sec. IIID there, was adopted as the base scenario. Thus, $e^{\pm}$ population is assumed to be residing and emitting inside the diffusion cylinder with the radius $r_{\max} = 20$ kpc and the half-height $z_{\max} = 2.7$ kpc. Indeed, such cylinder is a conventional modeling abstraction—there is no sharp physical boundary at the cylinder edges. In reality, MF vanishes smoothly, and, hence, the diffusion coefficient diverges gradually too near the boundaries of the diffusion zone. For this reason, our model calculations of the ICS emission intensity might be unreliable for the lines of sight passing near the edges of the diffusion zone.

TABLE II. Values of various parameters used in GALPROP.

Parameter	Value
Radius of the diffusion cylinder $r_{\max}$	20 kpc
Spatial grid step size $\Delta r = \Delta z$	0.05 kpc
$e^{\pm}$ propagation energy range	$(5 \times 10^{-4} - 1)m_x c^2$
Energy grid step increment	1.1
Optical ISRF energy density factor with respect to MW	1.3
IR ISRF energy density factor with respect to MW	0.57
HEALPix resolution of maps N_{side}	$2^{12} = 4096$
Conversion factor from CO intensity to H_2 column density X_{CO}	1.9×10^{20} $\text{mol cm}^{-2}(\text{K km/s})^{-1}$
He/H ratio in the galactic gas	0.1

M31 was placed at the real distance in the model setup here, which differs from the model in [16], where a smaller than real distance was used in order to reduce computational efforts without a loss of precision. But it would be unreliable to alter the distance in the current task of the ICS emission asymmetry calculation, since such alteration may introduce unphysical asymmetry; geometrical proportions are more important here. The real distance required, in turn, very high angular resolution of sky maps, which were computed in the traditional HEALPix format [36]. It was found empirically, that ≈1 arcmin resolution is sufficient for mitigating the finite pixelization effects on relevant angular scales. HEALPix resolution parameter N_{side} was set to $2^{12} = 4096$ in order to achieve the mentioned pixel size. The anisotropic ICS computation in GALPROP is heavy, and so high angular resolution required to employ the computing cluster with 64 CPU cores in order to compute the whole task in a few weeks.

B. Obtained emission characteristics

Putting together all the model ingredients described in the previous subsection, the ICS emission maps were computed at discrete photon energies over the wide range 1 keV–10 GeV with the photon energy increment factor of 10. Let us start the analysis of obtained maps from the selection of relevant ROIs. Historically, as was described in Sec. I, two radial zones around M31 center were considered separately: inside and outside $R \approx 5$ kpc $\leftrightarrow 0.4°$. They seem to have different mechanisms of the gamma-ray emission generation. Based on these considerations, as a natural and intuitive choice, the following ROIs were constructed for the analysis here—they are depicted in Fig. 2. The first ROI resembles the IH and is the disk with 5 kpc radius around the center. The second ROI is the annulus fragment restricted by $R = 5$ kpc and $R = 10$ kpc circles; and the lines, which are parallel to the major axis and are 5 kpc away from it. The major axis divides each of these ROIs into symmetric halves. One half is closer to the northwest, the other—to the southeast. Let us briefly call them the northern and southern parts. These parts are designed for their intensity comparison in the study of ICS emission asymmetry. The second ROI is intended to represent the OH. Both ROIs are constructed in a way, that they do not approach too close to the boundary of the sky projection of the diffusion cylinder, where the intensity values might be imprecise according to the explanation above. Thus, it would not make sense to study the OH by, for example, the full 5–10 kpc annulus, since it goes far beyond the diffusion cylinder projection at the upper and bottom areas. Another potentially useful feature of the chosen ROIs, if to consider separately their halves, is that they both have the characteristic size of about 5 kpc, which approximately matches the resolution of Fermi-LAT in the angular measure at the energies 1–10 GeV [37]. One detail about the OH ROI is that, generally speaking, there are two such ROIs—one on each side from the minor axis. However, it does not matter which of these two ROIs is considered, since the emission intensity map is symmetric about the minor axis. As was explained above, the asymmetry is anticipated only about the major (horizontal in Fig. 2) axis. And let us declare the exact definition of the asymmetry, which is used through this paper: this is the relative difference between the ICS emission intensities in the northern and southern halves of the designated ROIs, i.e., $I_N/I_S - 1$. An intensity inside any region means the value averaged over all map pixels in that region.

As the next step, let us discuss an important test of accuracy of the obtained maps. As was mentioned above, our constructed model of M31 implies, that the ICS emission asymmetry is caused by the ISRF anisotropy and inclination *only*. Hence, the ICS emission maps must be perfectly symmetric about the major axis in the case of isotropic ISRF. And CMB ISRF component is very helpful

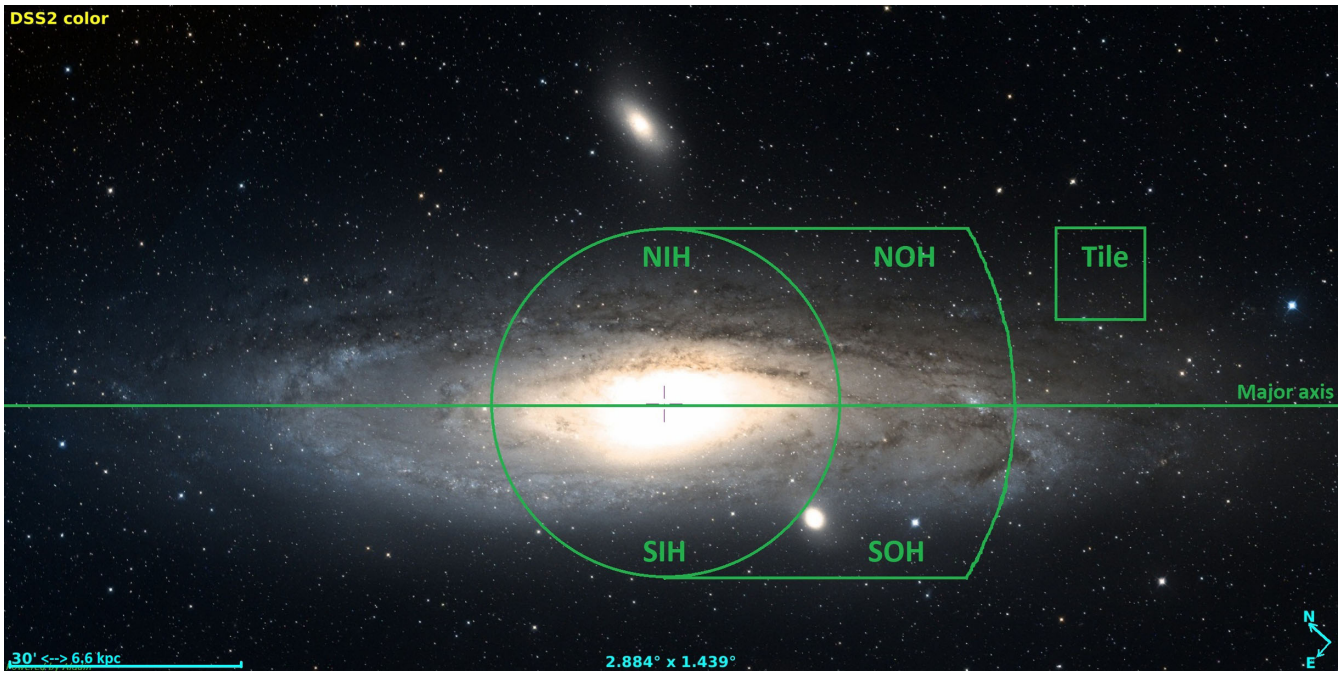


FIG. 2. The visual image of M31 (obtained from Aladin sky atlas) with the border lines of ROIs chosen for our analysis. The abbreviations have the following meanings: NIH—northern inner halo ROI (i.e., the northern half of the inner halo ROI), SIH—southern inner halo ROI, NOH—northern outer halo ROI and SOH—southern outer halo ROI. The square marked as "Tile" represents the uppermost and rightmost tile in Fig. 4. The approximate angular size of the diffusion cylinder sky projection is $3.0° \times 1.2°$ (major × minor axes, base (MED) case). More details are in Sec. II.

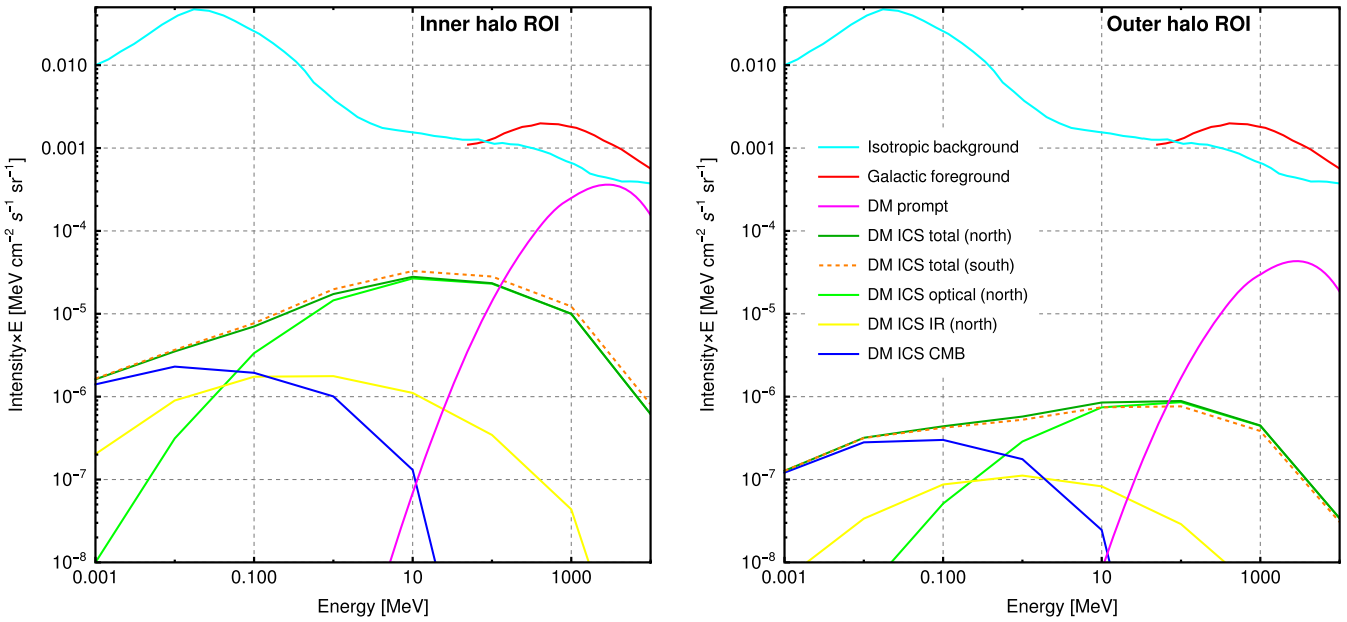


FIG. 3. The obtained ICS emission spectra in the IH ROI (left) and in the OH ROI (right) for our model $e^{\pm}$ population produced by the thermal WIMPs with $m_x = 60$ GeV ($\chi\chi \to b\bar{b}$), which fit the OH gamma-ray emission according to [9]. ICS emission from various ISRF components are shown individually. "North" and "south" mean respective ROI halves. The estimated spectrum of the isotropic background was taken from [[38], Fig. 3]. The measured spectrum of the Galactic foreground at M31 location was taken from Fermi-LAT diffuse Galactic emission map [39]. More details are in Sec. II.

in testing this implication, since the CMB emission is almost absolutely isotropic everywhere by its nature. CMB ICS emission component may have only a minor asymmetry of the second order due to the following peculiar mechanism. The primary asymmetry of the IR and optical ICS components implies the difference in ICS cooling rates for $e^{\pm}$, which reside in different hemispheres. In other words, $e^{\pm}$ from the brighter hemisphere radiate out their energy faster. And a faster cooling rate implies, in turn, a lower equilibrium concentration of emitting $e^{\pm}$. Therefore, we may expect a minor second order anisotropy with the opposite sign due to such a difference in cooling rates. And it may be notable mainly for the CMB ICS component, which lacks the first order anisotropy.

The asymmetry of CMB ICS emission component in all the computed parameter configurations at all photon energies in both ROIs does not exceed ≈1% by absolute value. I attribute this small residual asymmetry to a combination of two effects: the described second order asymmetry and the finite map pixelization. A nearly perfect symmetry of the obtained CMB ICS emission maps confirms the overall correctness of the whole calculation algorithm. And the cited ≈1% residual asymmetry represents and is accepted as a fair estimate of the uncertainty of all the asymmetry values calculated in the frame of our model in the selected ROIs. Indeed, this uncertainty does not include all systematical model uncertainties, like those related to a difference between the real M31 ISRF and the benchmark MW ISRF utilized here.

Now we can look at the obtained ICS emission spectra in the prepared ROIs. The spectra are shown in Fig. 3 separately for IH and OH ROIs. For definiteness, the northern ROI halves were mainly used for Fig. 3 (shown by the solid lines). Besides the total ICS emission spectra, the spectra from all three main ISRF components are also shown individually. According to the basic Eq. (1) above, the energies of photon before and after the scattering act are linearly proportional to each other. This fact is clearly reflected in Fig. 3: the ICS spectrum from CMB photons peaks at 0.01–0.1 MeV in the chosen units, from IR photons—at 0.1–1 MeV and from optical photons (as well as the total)—at 10–100 MeV. Overall, the contribution from optical photons dominates at energies above 0.1–1 MeV. The IH ROI is brighter than the OH ROI by more than an order of magnitude. This reflects a very steep radial dependence of DM annihilation rate. The spectral shape does not differ much between the IH and OH ROIs. The magenta lines represent the prompt (primary) gammas due to annihilation of the same WIMPs. The prompt gamma-ray emission maps were computed by the absolutely same GALPROP framework with only one difference: the medium emissivity integration along the line of sight was done up to $R \approx 200$ kpc, which approximately corresponds to the virial radius of M31 DM halo. The prompt emission component is expectedly brighter than the ICS component, although the latter peaks at significantly lower energies. The dashed lines mark the total ICS spectrum in the southern ROI halves. And in spite of the very large range

over the vertical axis, we can clearly see the difference between the northern and southern ROI spectra, meaning that the predicted ICS emission asymmetry effect truly exists! And the asymmetry has different signs in the IH and OH ROIs. In order to have some connection with the real sky, Fig. 3 also contains the approximate measured spectra of the isotropic background and Galactic foreground at M31 location. The former does not continue below 50 MeV due to a scarcity of data. Another relevant aspect is the actual observed intensity of M31. Concerning the IH ROI, according to [5] the point source (if to spread it over the whole IH) in M31 center produces the intensity, which is approximately the same as the Galactic foreground shown by the red line in Fig. 3. For the OH, a good estimate of M31 intensity would be the prompt DM emission spectrum shown by the magenta line, since DM model used here fits all the OH emission according to [9].

Then let us analyze the morphology of the ICS emission. In order to visualize the intensity and asymmetry map, I tiled the sky projection of the diffusion cylinder at the representative photon energy of 1 GeV by the squares with 2.5 kpc sides symmetrically about M31 center—see Fig. 4. The thick line there denotes the major axis, the thick dot—M31 center. Also, Fig. 2 illustrates the position of the uppermost rightmost tile on the sky. The specific size of 2.5 kpc was chosen due to the following reasons. It provides a convenient tiling of the diffusion cylinder projection without too close approach to the boundary and with the sufficient number of map pixels (≈170) inside every tile for mitigating pixel "noise." Also, 2.5 kpc corresponds to the angular resolution, which may be achievable in the near future with new gamma-ray telescopes (see, e.g., [[38], Fig. 19]). The tiles contain their ICS emission intensity value, and the asymmetry values of the total intensity and its component from CMB ISRF (in brackets). The asymmetry in Fig. 4 means the relative intensity difference between the tiles in the rows above the major axis and their symmetric counterparts below.

Looking at Fig. 4 we may notice, first of all, that the intensity distribution is almost perfectly symmetric about the minor galactic axis. This matches expectations from our model of M31. The intensity steeply decreases with the central distance. Considering the asymmetry distribution, we see a peculiar picture. Naively, we might expect the asymmetry to have the same sign over the whole hemisphere, i.e., when one hemisphere is uniformly brighter than the other one. However, the asymmetry is very nonuniform: it is negative close to the center in the bulge region and positive elsewhere. The asymmetry goes down to −18% near the center and rises up to 170% in the corners. The asymmetry of CMB component serves as an indicator of the correctness of the calculation algorithm. As was explained above, the CMB component must be nearly symmetric. It is indeed so in the second row from the top. However, the first row demonstrates some minor systematically negative CMB asymmetry at the level of few %, which slightly exceeds our uncertainty estimate of 1%. This asymmetry can be attributed to two possible natural reasons. One is the second order asymmetry due to the difference in cooling rates described above. Indeed, the primary asymmetry in the first row tiles is very large, therefore $e^{\pm}$ cool down much faster there. And the second reason may be geometrical: the upper (northwest) part of M31 disk is further from us than the lower (southeast) part according to [40]. Then the difference in distances to the emitting regions corresponding to the tiles in the first and

3.6e-8 171; (-4) ***2.5 kpc***	7.7e-8 143; (-2)	1.7e-7 110; (-2)	3.7e-7 76; (-3)	8.1e-7 52; (0)	1.2e-6 33; (-3)	8.1e-7 52; (0)	3.7e-7 76; (-3)	1.7e-7 110; (-2)	7.7e-8 143; (-2)	3.6e-8 171; (-4)
0.19° 9.2e-8 21; (0)	2.4e-7 12; (0)	6.9e-7 2; (1)	2.2e-6 -8; (1)	9.5e-6 -16; (1)	5.0e-5 -18; (0)	9.4e-6 -16; (1)	2.2e-6 -8; (1)	6.8e-7 2; (1)	2.4e-7 12; (0)	9.2e-8 21; (0)
7.6e-8	2.1e-7	6.8e-7	2.4e-6	1.1e-5	6.1e-5	1.1e-5	2.4e-6	6.7e-7	2.1e-7	7.6e-8
1.3e-8	3.2e-8	8.1e-8	2.1e-7	5.3e-7	9.0e-7	5.3e-7	2.1e-7	8.0e-8	3.2e-8	1.3e-8

FIG. 4. The ICS emission intensity and asymmetry map at $E_\gamma = 1$ GeV for the base parameter configuration by means of the square tiling. The thick line marks M31 major axis, the thick dot—the galactic center. Each tile contains the following values: the average intensity (multiplied by the photon energy) in the units [MeV cm^{-2} s^{-1} sr^{-1}] (with "e" meaning $\times 10\hat{}$), the total asymmetry defined here as the relative intensity difference in % between the upper row tiles and their symmetric lower counterparts, and the asymmetry of CMB ICS component (in brackets). The upward direction corresponds to northwest.

fourth rows is larger than that to the tiles in the second and third rows (see also Fig. 1). Therefore, the tiles in the first row may look fainter than their counterparts in the fourth row, but for the second row, this effect is still not pronounced. Thus, we may conclude again, that our model reasonably reproduces the symmetry of CMB component.

Now let us try to deduce an intuitive physical interpretation of the obtained nonuniform asymmetry distribution. Fig. 1 serves for this purpose. In general, we may expect, that the biggest ICS emissivity is reached in the places with the highest ISRF density, i.e. inside M31 bulge and disk. Let us choose four trial points (1–4 at Fig. 1) there in order to study the geometry of ICS process. Let us assume that the near vicinity of these points produces a defining contribution to the emission intensity integrated along the whole line of sight inside the diffusion cylinder. The points 1 and 4 represent pairs of locations outside the bulge, the points 2 and 3—inside. $\vec{V}_e$ is the velocity of emitting $e^{\pm}$ before scattering. And the photon symbols represent the supposed prevailing momentum direction of ISRF target photons before scattering. Thus, θ_i are the angles between the initial momenta of photons and $e^{\pm}$. According to Eq. (1) above, the energy of upscattered photon grows monotonically with θ_i. It means that the energy transfer between $e^{\pm}$ and a photon happens most efficiently in head-on collisions and least efficiently, when $e^{\pm}$ chases a photon moving in nearly the same direction. Therefore, the ICS emission intensity increases with θ_i, if to consider the latter as the effective average angle, which is defined by the prevailing direction of photon motion. I attempted to guess such directions at Fig. 1. Considering points 1 and 4, the ISRF intensity in the direction along the galactic plane should be much higher than across. And the intensity in the direction outward from the nucleus is probably slightly higher than toward, at least because ISRF density is generally expected to decrease with the radius. These intuitive considerations led to the marked prevailing photon momenta directions at points 1 and 4. $\theta_{i1} > \theta_{i4}$, hence the upper (northern) hemisphere outside the bulge region must be brighter than the lower (southern) one, which reconciles with Fig. 4. But when our line of sight dives into the bulge, the situation is less obvious—see points 2 and 3. The bulge has a spheroidal shape, and ISRF is expected to be rather isotropic inside. Hence, the bulge by itself does not seem to provide any significantly prevailing direction of photon momenta. The former may be produced by the photons from the disk parts, which are closest to points 2 and 3, as shown in Fig. 1. Then $\theta_{i2} < \theta_{i3}$, which explains the negative asymmetry in the bulge region according to Fig. 4. This is a qualitative interpretation of the peculiarities of obtained asymmetry distribution best to the author's imagination. However, other mechanisms may indeed work too. Thus, we have also keep in mind, that the medium ICS emissivity also depends on $e^{\pm}$ concentration, which has a steep radial profile defined majorly by DM density profile. And the interpretation above considered, for simplicity, just the plane section of the system, although the volumic picture does not seem to introduce anything essentially else.

Finally, let us analyze the asymmetry dependence on the photon energy and other model parameters. Table III serves for this purpose. It lists the asymmetry values starting from $E_\gamma = 0.1$ MeV for both IH and OH ROIs (the same ROIs as were used for Fig. 3). Below $E_\gamma \sim 0.1$ MeV the asymmetry vanishes, because the CMB ISRF component dominates in the production of ICS emission and makes it symmetric at those energies, as can be seen in Fig. 3. We can see from the table, that the absolute value of asymmetry generally grows with energy for all the computed parameter configurations. At low energies this trend is caused again by a decrease of CMB ICS contribution with the energy increase. Considering the IH ROI, the growth of asymmetry is monotonous there over the whole energy range. In the OH ROI the asymmetry reaches its maximum typically around $E_\gamma \sim 1$ GeV and then decreases. The first row of the table represents the base parameter configuration, which was described in Sec. II A and fits the OH emission according to [9]. We may note for this case, that the asymmetry is quite substantial: it reaches −21% in the IH ROI and 16% in the OH ROI. The second row reflects

TABLE III. The ICS emission asymmetry [%] dependence on the photon energy and model parameters configuration. The asymmetry values are provided for both IH ROI and OH ROI (separated by ";", "[,]" means a range of values).

Parameter configuration	0.1 MeV	1 MeV	10 MeV	100 MeV	1 GeV	10 (100) GeV
Base: $m_x = 60$ GeV, $\chi\chi \to b\bar{b}$, MAX DM density, MED MF/prop.	−7; 4	−11; 8	−13; 13	−14; 15	−16; 16	−21; 10
Base with DM prompt gammas added.	−7; 4	−11; 8	−13; 13	−10; 5	−1; 0	−1; 0
Base with misc parameter variations: $i = [70°, 77°]$, [MIN, MAX] MF/prop.	[−7, −2]; [3, 8]	[−11, −3]; [6, 17]	[−13, −5]; [10, 24]	[−14, −8]; [11, 26]	[−16, −10]; [12, 27]	[−21, −17]; [6, 22]
Base with misc parameter variations and DM prompt gammas added.	[−7, −2]; [3, 8]	[−11, −3]; [6, 17]	[−13, −5]; [10, 24]	[−10, −5]; [4, 8]	−1; 0	−1; 0
Base except $m_x = 600$ GeV.	−4; 1	−7; 3	−10; 8	−12; 14	−14; 18	−15; 16 (−17; 13)
Base except $\chi\chi \to \tau^+\tau^-$.	−3; 0	−5; 2	−9; 10	−12; 18	−14; 18	−18; 15
Base except MIN DM density.	−3; 3	−5; 6	−7; 8	−9; 7	−12; 6	−19; 0

the same parameter configuration, but when the prompt gamma-ray emission due to WIMP annihilation is added on top of the ICS emission. The prompt emission spectrum is relatively narrow: as can be seen in Fig. 3, it is narrower than the ICS emission spectrum. The prompt emission reaches a significant contribution and begins to influence the asymmetry around $E_\gamma \sim 100$ MeV, and then vanishes the asymmetry completely at $E_\gamma \gtrsim 1$ GeV due to a full dominance over the ICS emission at those energies.

The third and fourth rows of Table III illustrate the ranges of asymmetry values (around the base scenario) due to the uncertainties in M31 inclination and MF/prop. model parameters. The inclination angle (i) value has key importance for the ICS emission asymmetry effect. For the base scenario $i = 74°$ was assumed as the average value among various determinations cited in [41]. Those determinations obtained values ranging from 70° to 77°. And I computed the asymmetry values for these boundary inclination values too in order to study the respective uncertainties. MF/prop. parameters were also varied together with the inclination, although the former are expected to play a secondary role. The ranges of possible values of MF/prop. parameters were taken from [[16], Table III]. As can be seen in Table III, the resulting uncertainty ranges of the asymmetry are quite substantial, especially in the OH ROI. The IH ROI did not show a clear correlation between the asymmetry and the varied model parameter values. A low sensitivity to the inclination value in the IH ROI could be due to the fact, that the bulge and ISRF there have quasispherical geometry.

The next rows of the table show the asymmetry for alternative DM models: heavier (by an order of magnitude) WIMPs with $m_x = 600$ GeV, another important annihilation channel $\chi\chi \to \tau^+\tau^-$ and MIN DM density profile (from [[16], Sec. IIIB]). In each of these three cases, only the mentioned model element was changed, other parameters correspond to the base configuration. The listed DM models do not have direct relevance for the fit of outer gamma-ray halo. They were computed for a somewhat different purpose—to study the asymmetry dependence on the properties of $e^\pm$ population. In a broader view, WIMP mass (i.e., the rest energy) can be considered as the upper limit for the energy of $e^\pm$. WIMP annihilation channel defines the shape of $e^\pm$ energy spectrum (at the injection). DM density profile defines the degree of concentration of $e^\pm$ source. Hence, by varying these DM model parameters, we may explore to some extent an overall possible variation of the asymmetry due to a variation of the properties of $e^\pm$ population. The thermal WIMPs much lighter than 60 GeV were not considered, because they are quite robustly excluded by various indirect searches and, hence, are not interesting. The fifth row of Table III reflects the case of heavier WIMPs. In this case we may note slightly smaller asymmetry at low photon energies and a confident propagation of the asymmetry to very high energies $E_\gamma \sim 100$ GeV. This can be explained by an overall shift of $e^\pm$ population toward higher energies. The noted persistence of the asymmetry at $E_\gamma \sim 100$ GeV can be considered as an indication of possibility of the asymmetry existence at an arbitrarily high energy, as far as $e^\pm$ exist with that energy. The sixth row shows the case of $\chi\chi \to \tau^+\tau^-$: at low photon energies it shows appreciably lower asymmetry with respect to the base configuration. And the last row of the table reflects the case of very different DM density profile: MIN, i.e. the cored profile, which is opposite to the MAX cusped profile. As was discussed in [[16], Sec. IIIB], MIN and MAX profiles approximately enclose the range of possible DM densities in the central region (inner several kpc) of M31 DM halo. MIN profile demonstrates significantly lower asymmetry values at all the energies in both ROIs in comparison with the base case. Thus, the degree of concentration, i.e., the radial steepness of $e^\pm$ source distribution, substantially influences the asymmetry. The zero value of the asymmetry in the OH ROI at $E_\gamma = 10$ GeV does not necessarily mean full symmetry: likely, it is just the result of superposition of negative and positive asymmetries in different parts of the OH ROI.

Looking at Table III overall, we can find out, that the negative asymmetry in the IH ROI reaches at most −21%, while the positive asymmetry in the OH ROI— +27%. Indeed, the computed trial cases do not provide full and smooth coverage of the whole parameter space. But they outline well the characteristic asymmetry values, which we may anticipate from some arbitrary $e^\pm$ population. Thus, concluding broadly, the ICS emission from any reasonable $e^\pm$ population is expected to possess an asymmetry at the level of 10%–20% (at least at some energies) in the selected ROIs.

C. Observational prospects

Although this paper aims mainly at the theoretical modeling of the ICS emission asymmetry effect, this subsection discusses some general considerations of the effect's observability. Let us go back to Fig. 3, which reflects the base thermal WIMP scenario for the outer gamma-ray halo fit. Considering the ICS emission intensity averaged over IH and OH ROIs, we see that, unfortunately, it is smaller than the background and foreground emission intensities by more than one order of magnitude at all photon energies in both ROIs. Hence, it would be very challenging to separate even just the ICS component itself from other emission components in the direction of M31. The asymmetry, i.e., the intensity difference between the ROI halves, is even smaller: it can be seen as the difference between the dark-green and dashed lines. In comparison with the backgrounds/foregrounds, this difference is tiny at all. However, one may consider other regions, where the asymmetry values are larger: according to Fig. 4, the asymmetry exceeds 100% in the locations far from M31

center, i.e., the intensity ratio exceeds factor of 2 there. But the problem for such locations is a very small intensity amplitude, since the latter steeply decreases with the distance from center. Hence, changing the ROIs does not seem to provide an obvious sensitivity gain. Thus, at first glance, the overall picture appears to be quite pessimistic in the sense; that the predicted asymmetry effect indeed exists, but mainly theoretically, since its observational detection requires a virtually unlimited instrumental sensitivity.

At the same time, there are some reasons for optimism. One reason is that, according to Fig. 3, the prompt and ICS emission spectra peak at significantly different energies. This circumstance and a relative narrowness of the prompt spectrum loosen an observational degeneracy between these two components: the bright prompt signal does not "interfere" much with the weaker ICS signal and its asymmetry at $E_\gamma \lesssim 100$ MeV. The latter energy range can be optimal for a search of the asymmetry also due to another reason: photon fluxes are relatively high there, since they steeply decrease with energy. At higher gamma-ray energies $E_\gamma \gtrsim 1$ GeV precise intensity measurements are very limited due to small photon counts and, hence, large statistical errors. But at lower energies photon counts are large (for the same detector area); which may allow, in principle, precise intensity measurements and, hence, separation of faint emission components. Another challenge is the angular resolution: that achievable now by Fermi-LAT at low energies is insufficient. However, in general, we may anticipate significant progress in both the sensitivity and angular resolution of gamma-ray telescopes in the future. The relevant future missions, which are expected to have a good sensitivity at low energies, include e-ASTROGAM [38], AMEGO [42], HERD [43] and GAMMA-400 [44,45].

So far, the discussion has been tied solely to the specific thermal WIMP, which is needed for the fit of OH. However, according to [[9], Table II], the fit may require higher than thermal cross sections even for the same (high) J-factor values (the exact definition of J-factor notion is given by Eq. (7) there). The required cross section value is highly uncertain due to the complicated systematic uncertainties described there. The ICS emission intensity is linearly proportional to the cross section. Hence, in the case of higher cross sections, the ICS signal would be proportionally brighter and, therefore, easier to detect over backgrounds.

As was emphasized in Sec. I, the observed gamma-ray emission in M31, speaking generally, must not necessarily originate from DM. The emission may come from a population of CRs through both the leptonic and hadronic mechanisms. If the leptonic component, i.e., the ICS emission from CR $e^\pm$, is nonzero, then the asymmetry of the total emission would indeed be nonzero too. The asymmetry of ICS emission from CR $e^\pm$ is even easier to detect in comparison with DM $e^\pm$ case; because in the latter case the ICS emission has a secondary role, and the asymmetry is present only inside a relatively narrow energy range. In the CR case there is no prompt gamma-ray component, i.e., the ICS component is primary, and only a potential hadronic component may "interfere" with the ICS emission of interest. Also in this case the ICS emission spectrum and its asymmetry do not have a steep cutoff near WIMP rest energy—at $E_\gamma \sim 10$ GeV in our case. The spectrum from CR $e^\pm$ would be much wider over the energy. The asymmetry is naturally expected to be the most prominent in the case, when all the observed emission comes from CR $e^\pm$. Summarizing, detection of the asymmetry effect is a very challenging task, but potentially not hopeless for future highly sensitive gamma-ray telescopes.

III. ESTIMATION OF DM $e^\pm$ ICS AND BREMSSTRAHLUNG EMISSION CONTRIBUTIONS

This section is dedicated to a somewhat different aspect of DM interpretation of the outer gamma-ray halo. Best to the author's understanding, the work [9] took into account only the prompt emission component due to DM annihilation for the fit of OH emission and neglected by the secondary components—ICS and bremsstrahlung from DM $e^\pm$. This section aims to check the validity of such approximation by estimating the emission fluxes from these secondary contributions and comparing them with the prompt emission flux. This estimation was done for the same thermal WIMP with $m_x = 60$ GeV annihilating to $b\bar{b}$, which fits the OH. The secondary emission fluxes were calculated for the annular region on the sky, which was used in [9] for the fitting procedure and called "spherical halo (SH)" there. This annulus is centered at M31 center, and has angular radii 0.4° and 8.5°. For definiteness, I consider here the case "I" according to the classification in [9]; i.e., when annihilating WIMPs in both MW and M31 form the signal along M31 line of sight, and there is no effect of absorption of MW DM signal by isotropic emission template. The secondary emission fluxes were computed here individually for MW and M31. Regarding DM density profile, it is the same here as in the previous section (Einasto MAX). The profile parameters for MW were obtained according to the recipe in [9]. And MED MF/prop. configuration was employed.

Let us start the discussion from the ICS component of secondary emissions. M31 ICS emission intensity maps were already calculated by GALPROP in the frame of modeling conducted in the previous section. Here we need in the emission flux from the annular region cited above for a convenient comparison with the prompt fluxes in [9]. This region encloses the whole M31 diffusion zone sky projection except the central disk with 0.4° radius. MW ICS

TABLE IV. The emission fluxes in the units [MeV cm^{-2} s^{-1}] of various components due to DM annihilation in MW and M31 from the annular ROI centered at M31 center with angular radii 0.4° and 8.5°. The prompt emission fluxes above the vertical space are taken from [9]. DM parameters correspond to the OH fit.

Emission component	Flux at 0.1 GeV	Flux at 1 GeV	Flux at 10 GeV
Total observed =	3×10^{-7}	6×10^{-6}	4×10^{-6}
MW prompt +	3×10^{-7}	5×10^{-6}	3×10^{-6}
M31 prompt	4×10^{-8}	7×10^{-7}	4×10^{-7}
MW ICS +	2×10^{-8}	1×10^{-8}	7×10^{-10}
MW bremsstrahlung =	6×10^{-9}	4×10^{-9}	2×10^{-10}
MW secondary	3×10^{-8}	1×10^{-8}	8×10^{-10}
M31 ICS +	2×10^{-10}	8×10^{-11}	6×10^{-12}
M31 bremsstrahlung =	7×10^{-12}	6×10^{-12}	3×10^{-13}
M31 secondary	2×10^{-10}	9×10^{-11}	7×10^{-12}

emission intensity maps were calculated by the same way with DM density and MF/prop. parameters adapted for MW. MW ICS emission spreads over the whole sky, indeed, since we look at the sky from the inside of MW diffusion cylinder (meanwhile, [46] has a relevance in this context). The extracted ICS emission fluxes from the annular ROI at three representative energies are written out in Table IV.

Another potentially relevant emission mechanism is bremsstrahlung from DM $e^{\pm}$. Bremsstrahlung emission maps were computed by GALPROP too. This calculation requires knowledge of the interstellar gas distribution in both galaxies. GALPROP conveniently provides the relevant gas distributions for MW. This allows to compute quite detailed all-sky bremsstrahlung intensity maps. For M31 such detailed gas maps do not exist, and MW gas maps were substituted. Such a rough approximation is acceptable due to the following reasons. First, contrary to MW, we do not need in the detailed intensity map of M31. Instead, we need in just the total flux from almost the whole galaxy (without its central part). The total bremsstrahlung flux from the whole galaxy is presumably proportional to the total galactic gas mass. MW and M31 have very similar total gas mass values—they are provided in Table I. Hence, MW gas distributions are expected to provide a reasonable estimate of the total bremsstrahlung flux from M31. Also, Table II displays the values of certain parameters used in the bremsstrahlung calculation procedure. The resulting bremsstrahlung fluxes are displayed in Table IV.

Now we can compare the obtained secondary emission fluxes with the prompt ones. The latter were extracted from [[9], Fig. 2 (right), the whole SH] and are written out above the vertical space in Table IV. In general, we can note that the prompt emission flux is much larger than the ICS one, and the latter in turn is much larger than the bremsstrahlung flux. Thus, the latter plays the least role among three components and, by the way, would not create much of a nuisance background for detection of the ICS emission asymmetry. All MW emissions are much brighter than M31 ones. [9] used the photon energy range starting from 1 GeV for the fit. We see from Table IV, that all the secondary components are negligible in comparison with both MW and M31 prompt components at $E_\gamma \gtrsim 1$ GeV. Thus, it is valid to neglect by secondary emissions in the fit at those energies. However, at $E_\gamma = 0.1$ GeV we can see, that MW secondary flux becomes comparable to M31 prompt flux. Hence, if one would employ lower energies $E_\gamma \lesssim 1$ GeV for the fit, then it is necessary to take into account at least MW ICS component (if the scheme "I" is realized, when both galaxies are included).

And there is another important caveat, which concerns the annihilation cross section value. So far we have discussed the case of thermal cross section, which is the most natural and approximately corresponds to the parameter configuration described by the first row of Table II in [9]. However, other rows of this table represent alternative viable parameter configurations: they have less extreme substructure boosts, but require more exotic DM with high annihilation cross sections. Lowering the boost factor would not decrease the secondary emission fluxes significantly, since the boost factor works mainly on the largest radii $R \sim 100$ kpc and does not affect the annihilation rate all that much inside the diffusion cylinder, i.e., at $R \lesssim 20$ kpc. But increasing the cross section would linearly increase the secondary fluxes. Hence, for lower boost factor cases, the secondary emission fluxes would be higher and contribute more to the total flux. Thus, one may need to take into account certain secondary components, if the cross sections higher than thermal are employed for the fit.

Speaking very generally, there is another—the fourth—gamma-ray emission type due to annihilating WIMPs: the emission from decaying pions, which are produced by DM proton and antiproton collisions with an interstellar gas. However, hadronic emissions are beyond the scope of this work.

IV. INTERRELATION BETWEEN DM RADIO CONSTRAINTS AND FIT OF THE OUTER HALO

This section aims to discuss another aspect, which is very relevant for DM explanation of the outer gamma-ray halo emission: how WIMP parameter values, which are needed for the fit, relate to the constraints obtained from radio observational data on M31. DM $e^{\pm}$ inevitably produce synchrotron emission too in the galactic MF in the radio band. And radio observations provide a powerful tool for constraining the properties of any $e^{\pm}$ population. This aspect was already discussed briefly in [[16], Sec. VI]. Here more details are revealed.

The main difficulty here is the fact, that the radio and gamma-ray data are being compared in essentially non-overlapping spatial regions of M31. Thus, [9] conducted the fit avoiding the IH region, i.e., the fit was done over the radial distances $R \gtrsim 5$ kpc $\leftrightarrow 0.4°$. However, the radio constraints [16] were derived oppositely inside the IH region using $R \lesssim 3$ kpc (outside, these constraints are weak). DM density profile is determined quite precisely in the OH region—this can be seen in, e.g., [[9], Fig. 3]. However, this cannot be said about the IH region—DM density is constrained rather poorly there (e.g., [21]). [[16], Fig. 1] demonstrates the range of possible DM densities in the IH region. This wide range translates into a large uncertainty of WIMP parameter constraints derived from the IH. Figure 5 shows WIMP parameter plane (the annihilation cross section vs. mass plane) with the constraints derived in [16] from the radio nonthermal emission maps of M31 bulge region and the parameter region required for the outer gamma-ray halo fit. The fitting parameter region (displayed by the green rectangle) was taken from [9], the cross section values are from the last two columns of Table II there. Both scenarios I and II were included here. These cross section values were taken without the uncertainties related to those in J-factor values (columns 7–9 there). The exclusion limits in Fig. 5 came from [[16], Fig. 8(left)]. Their line style encodes the type of DM density profile, line color—MF/prop. configuration according to [16]. Strictly speaking, we must be comparing WIMP parameters in the radio and gamma-ray bands for *exactly* similar DM density profiles in order to draw meaningful inferences, because every profile requires its own fitting cross section values. The exact similarity holds only for the MAX profile among three profile cases depicted. MED and MIN profiles may require slightly different cross sections for the outer gamma-ray halo fit, i.e., the top and bottom green rectangle borders at Fig. 5 for them may be shifted with respect to the MAX profile case depicted. It is important to keep this caveat in mind interpreting this figure.

Another relevant circumstance is the difference in substructure boost factor model between DM density profiles used in [9,16]. However, this difference does not have a significant impact in our case. The reason is that the radio

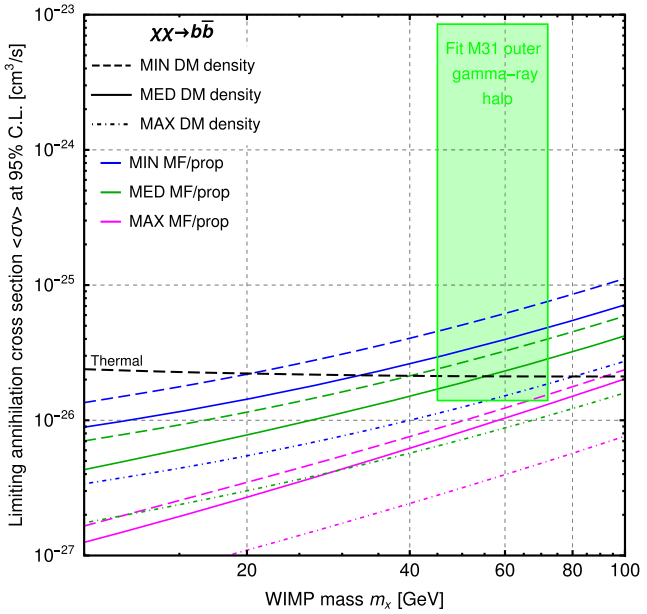


FIG. 5. WIMP parameter plane. The green rectangle shows the parameter region, which fits the outer gamma-ray halo according to [[9], Table II] (both I and II scenarios, Einasto profile). The lines represent the parameter constraints from radio observations at 95% confidence level from [16] for various commented DM density and MF/prop. parameter configurations. The black dashed line reflects the thermal cross section (taken from [20,47]). More details are in Sec. IV.

constraints were derived employing mainly only the central region of M31 with $R \lesssim 3$ kpc, where the role of substructures is very small due to their tidal disruption. Thus, it was calculated that the cross section radio limits differ just by 4%–6% between the cases with and without the substructure boost of MAX DM density profile (the boost factor radial profile was from [22] for this case). Hence, the radio limits are quite universal with respect to the assumed boost factor model, and they can be compared directly (in *this* aspect) to any cases outlined in [[9], Table II] within ≈10% precision.

We see from Fig. 5, that in the case of MAX DM density profile, which provides the "pure" comparison, the radio limits exclude the gamma-ray fit nearly completely for all MF/prop. configurations. However, this cannot be said about other profile cases. Low DM density and MF strength values in the central region of M31 allow some part of the green parameter region. But even the weakest MIN limit (the dashed blue line) allows, in fact, only a very small (<1% by relative area in the linear measure) part of the gamma-ray fitting region. We can also notice, that the case II, when all the gamma-ray emission in OH comes from M31 only, is completely excluded by the radio limits.

One possible caveat to the conclusions above is the uncertainties in the fitting cross section values due to the uncertainties in J-factor values for both MW and M31. These uncertainties are written out in [[9], Table II, columns

7–9] and are related mainly to a possible asphericity of DM halos of both galaxies. We can see from those columns, that the cross section may deviate by up to 2–3 times from the average fitting value in the last two columns. This deviation may stretch the green rectangle in Fig. 5 over the vertical direction. The shift of the upper rectangle border does not matter, since the upper cross section values are absolutely excluded. Only the bottom border has relevance. The bottom border is defined by the first row of [[9], Table II]. This row shows, that J-factor uncertainties may provide the maximal cross section decrease with respect to the average value by $1.52 \times 1.32 \times 1.38 \approx 2.8$ times. However, at the same time, there is another systematical uncertainty of observational origin. [9] analyzed individually the whole OH (SH in their terminology) and its northern/southern halves (SHN/SHS), and obtained the fitting cross sections for all three cases. The cross section values for the whole halo and the southern half match quite well. But the northern half requires the cross section value by ≈2 times larger. This discrepancy can be attributed to significant observational systematics due to an overall weakness of the purported OH emission. Here I would like to note, that there is a mistake in the text of [9], where the cross section ratios for the different halo parts are described. This mistake was confirmed by the author of [9] in private communication. Thus, the text must state "SH/SHS ≈ 1" and "SH/SHN ≈ 0.5" instead of "SH/SHS = 1.8" and "SH/SHN = 1.0". Table II there provides the cross section values for the whole halo (SH), i.e., the minimal values with respect to this observational systematics, since SHN requires ≈2 times higher cross section. Therefore, this observational systematics is able to counteract the cross section decrease by 2.8 times, which may be provided by J-factor uncertainties described above. Summarizing, we would need in extremely fine-tuned circumstances in order to push the bottom border of the green rectangle significantly lower in Fig. 5. These circumstances include: an extreme boost factor configuration, high and tuned asphericity of DM halos of both galaxies, favorably tuned observational systematics and other. A random coincidence of all these factors is unrealistic. Thus, the caveat described in this paragraph does not seem to be able to change noticeably our conclusions about certain tension with the radio constraints.

Summarizing a somewhat qualitative discussion in this section, we can state the following. The cuspy M31 DM density profiles like Einasto MAX cannot fit the outer gamma-ray halo without violation of the radio constraints. But rather cored profiles may accommodate the requirements from both radio and gamma-ray bands, if the latter would require the fitting cross section values comparable to those for the cuspy profiles. Such cored profiles are possible due to, e.g., sophisticated effects of long-term washing out of the initial cusp [48] and are not excluded observationally. However, the cored profiles would likely require a significant or even dominant gamma-ray signal contribution from MW along the OH line of sight and quite high boost factor (at least in MW) for the OH fit. This follows from [[9], Table II] and the fact, that high cross sections $\langle \sigma v \rangle \gtrsim 10^{-25}$ cm^3/s are robustly excluded for any scenarios in Fig. 5. And, finally, just to clarify, the discussion here does not make any inferences on the cuspy/cored property of MW DM density profile in the context of OH fit.

V. CONCLUSIONS AND DISCUSSION

The main goal of this work was to model theoretically the interesting effect of the asymmetry of ICS emission from a population of relativistic $e^{\pm}$ in M31 halo. This effect was pointed out for the first time in [13]. The asymmetry arises, because the ISRF of a disk galaxy is anisotropic, and we view M31 under certain inclination angle. The asymmetry appears as the difference in ICS emission intensity between the points, which are located symmetrically with respect to the major galactic axis.

ICS emission intensity maps were computed by GALPROP code (v57). As the source of $e^{\pm}$ population, the thermal WIMPs with $m_x = 60$ GeV annihilating to $b\bar{b}$ were set. This WIMP may be responsible for the gamma-ray emission from M31 OH according to [9]. This $e^{\pm}$ population was chosen as a trial example to study the effect in general and, at the same time, in order to build specific observational predictions for DM interpretation of the OH emission. Some alternative $e^{\pm}$ populations from DM were studied too.

The conducted computation confirmed the asymmetry effect presence at a significant level. Table III displays the main results of calculations: the asymmetry dependence on the energy and model parameters in the IH and OH ROIs. We can emphasize the following key properties of the asymmetry: (1) it appears at the energies $E_\gamma \gtrsim 0.1$ MeV; (2) has the opposite sign in the IH and OH ROIs; (3) by absolute value it is comparable in the IH and OH ROIs; (4) has a moderate sensitivity to the galactic and $e^{\pm}$ population model parameters; (5) ranges at most from 0 to ≈30% by absolute value in the IH and OH ROIs; (6) addition of the prompt emission from DM annihilation vanishes the asymmetry at $E_\gamma \gtrsim 1$ GeV.

A potential observational detection of the asymmetry would provide valuable inferences for the emission mechanism understanding. We can outline the following semi-qualitative classification in this regard:

(1) If a diffuse gamma-ray emission is absolutely symmetric at all energies with respect to the major axis of M31, this implies likely a purely hadronic emission mechanism.
(2) A mild emission asymmetry at the level of few % implies likely a mixed leptonic/hadronic emission scenario.

(3) A significant asymmetry at the level $\gtrsim 10\%$ implies a dominance of the leptonic sources; which may include $e^{\pm}$ from CRs, DM and even probably MSPs.
(4) The asymmetry in the case of DM $e^{\pm}$ appears over a significantly narrower energy range than in the case of CR $e^{\pm}$.

This scheme is outlined in the context of considered ROIs, indeed, and does not necessarily need to be applied to both of them simultaneously. Different parts of the galactic halo may have different emission mechanisms, and the latter can be tested through the asymmetry measurements regionally. Overall, the logic here indeed applies to only a large-scale diffuse emission and does not apply to an emission from discrete sources. And, of course, the above scheme is majorly idealistic in the sense, that it ignores possible nuisance asymmetries due to, e.g., inhomogeneities of the galactic medium. Considering specifically DM interpretation of the outer gamma-ray halo, this emission component is expected to manifest the following distinct feature: $\approx 10\%$ asymmetry in the energy range $\sim(1\text{–}100)$ MeV in both the IH and OH ROIs (see the third row of Table III). Thus, potential asymmetry measurements may provide a valuable observational tool for diagnosing the emission generation mechanism. Particularly, such tool may confirm DM origin of the emission and, thus, unravel DM nature eventually. However, from an observational point of view, such measurements are very challenging and require very high sensitivity; since M31 is rather faint object on the gamma-ray sky. It is generally hard to separate various emission components inside M31. And it would be especially difficult to detect the asymmetry of the potential DM signal, since its ICS component has the intensity much lower than both the Galactic foreground and isotropic background, as illustrated in Fig. 3. And hadronic emissions inside M31 may create additional nuisance background too. Summarizing, the revealed ICS emission asymmetry effect is rather theoretical so far, since its observational detection may require virtually unlimited sensitivity. However, if, for example, the brightest (central) region of M31 is shining through ICS, the asymmetry detection there may be achievable in the near future. In general, it is a very sophisticated task to model the quantitative observational predictions for any specific gamma-ray telescope, this is beyond the scope of this work.

Meanwhile, as was already mentioned in Sec. IV, [9] reported the observed intensity difference between the northern and southern halves of OH by ≈ 2 times. One may naturally ask whether this observed asymmetry can be explained by the ICS emission asymmetry being discussed. Considering DM as the source of $e^{\pm}$, the answer is absolutely no, since, as was noted above, the bright prompt DM emission component vanishes the asymmetry in the energy range $E_\gamma \geq 1$ GeV employed in [9].

The ICS emission asymmetry effect would, in principle, exist in any disk galaxy, which is viewed under the inclination angle different from 0° or 90°. Examples of such nearby galaxies include Large Magellanic Cloud (LMC), M81, M33 and others. However, all of them except LMC are farther than M31. Hence, it would be even more difficult to study their gamma-ray emission details.

A potential direction for further development of this topic is to conduct the same asymmetry modeling for the case of CR $e^{\pm}$ population and compare the results with DM case. The results may differ due to the differences in both the $e^{\pm}$ source spatial distribution and energy spectrum at injection.

Other sections of the paper discussed other aspects, which are directly relevant for DM interpretation of the outer gamma-ray halo. One aspect is the role of the secondary, i.e., ICS and bremsstrahlung, emissions due to DM annihilation in both MW and M31. It was proved that these secondary components can be neglected in the fit of OH in the relevant energy range $E_\gamma \gtrsim 1$ GeV for the case of nearly thermal annihilation cross section. However, at lower energies or/and in the case of higher cross sections, one may need to take into account some of the secondary components. The second aspect is the relation between WIMP radio constraints derived recently in [16] and the outer gamma-ray halo fit. These constraints imply certain restrictions on the possibility of the fit (from Fig. 5): a significant contribution from MW to the gamma-ray signal along M31 OH line of sight is inevitably necessary, as well as quite high boost factor due to substructures (at least in MW DM halo). Regarding M31, only rather cored DM density profiles are suitable. Overall, we may conclude, that DM explanation of M31 OH is still possible in a view of radio constraints. However, this explanation does not look all that natural, since it requires certain fine tuning of the model ingredients. Particularly, a bit optimistic boost factor values are needed. Also, WIMP constraints from observations of other objects, particularly dwarf MW satellites, may provide another independent restrictions. Thus, it is probably premature now to consider M31 outer gamma-ray halo phenomenon as definite DM manifestation. More observational data on M31 is needed in order to unravel large systematical uncertainties and understand the emission mechanisms better.

It is indeed difficult to provide full coverage of such a complicated topic in the frame of one single paper. The modeling here was tied mainly to the quite standard thermal WIMPs and the diffusion of their annihilation products. However, more exotic scenarios may be relevant. E.g., the so-called leptophilic DM [49], which produces a lot of $e^{\pm}$, which in turn would produce a bright ICS emission. Regarding the diffusion model, one may consider a larger size of the diffusion zone (e.g., [8]).

ACKNOWLEDGMENTS

I greatly appreciate the following software, which is very useful: Wolfram Mathematica; "Aladin sky atlas" developed at CDS, Strasbourg Observatory, France [50]; NumPy [51]; HEALPY [52]; WebPlotDigitizer [53]. I am very grateful to Alexei Alexeev for providing access to high-performance computing cluster, Mikhail Zavertyaev for providing another server and also to Mikhail Razumeyko.

[1] A. A. Abdo, M. Ackermann, M. Ajello, A. Allafort, W. B. Atwood, L. Baldini, J. Ballet, G. Barbiellini, D. Bastieri, K. Bechtol, R. Bellazzini, B. Berenji, R. D. Blandford, E. D. Bloom, E. Bonamente *et al.*, Astron. Astrophys. **523**, L2 (2010).
[2] M. Ackermann, M. Ajello, A. Albert, L. Baldini, J. Ballet, G. Barbiellini, D. Bastieri, R. Bellazzini, E. Bissaldi, E. D. Bloom, R. Bonino, E. Bottacini, T. J. Brandt, J. Bregeon, P. Bruel *et al.*, Astrophys. J. **836**, 208 (2017).
[3] C. Armand and F. Calore, Phys. Rev. D **103**, 083023 (2021).
[4] C. M. Karwin, S. Murgia, S. Campbell, and I. V. Moskalenko, Astrophys. J. **880**, 95 (2019).
[5] Y. Xing, Z. Wang, D. Zheng, and J. Li, Astrophys. J. Lett. **945**, L22 (2023).
[6] F. Zimmer, O. Macias, S. Ando, R. M. Crocker, and S. Horiuchi, Mon. Not. R. Astron. Soc. **516**, 4469 (2022).
[7] A. McDaniel, T. Jeltema, and S. Profumo, Phys. Rev. D **100**, 023014 (2019).
[8] A. Do, M. Duong, A. McDaniel, C. O'Connor, S. Profumo, J. Rafael, C. Sweeney, and W. Vera, Phys. Rev. D **104**, 123016 (2021).
[9] C. M. Karwin, S. Murgia, I. V. Moskalenko, S. P. Fillingham, A.-K. Burns, and M. Fieg, Phys. Rev. D **103**, 023027 (2021).
[10] Z. Li, X. Huang, Q. Yuan, and Y. Xu, J. Cosmol. Astropart. Phys. 12 (2016) 028.
[11] A. McDaniel, T. Jeltema, and S. Profumo, Phys. Rev. D **97**, 103021 (2018).
[12] M. Di Mauro, X. Hou, C. Eckner, G. Zaharijas, and E. Charles, Phys. Rev. D **99**, 123027 (2019).
[13] K. M. Belotsky, E. S. Shlepkina, and M. L. Soloviev, arXiv:2011.04689.
[14] http://galprop.stanford.edu/.
[15] A. E. Egorov and E. Pierpaoli, Phys. Rev. D **88**, 023504 (2013).
[16] A. E. Egorov, Phys. Rev. D **106**, 023023 (2022).
[17] A. E. Egorov, Proc. Sci. 423 (**2023**) 120.
[18] V. Berestetskii, E. Lifshitz, and L. Pitaevskii, *Quantum Electrodynamics (Vol. IV)* (Nauka, Moscow (in Russian), 1989).
[19] V. Ginzburg, *Theoretical Physics and Astrophysics* (Pergamon Press, New York, 1979).
[20] https://member.ipmu.jp/satoshi.shirai/DM2020/.
[21] A. Tamm, E. Tempel, P. Tenjes, O. Tihhonova, and T. Tuvikene, Astron. Astrophys. **546**, A4 (2012).
[22] M. Kamionkowski, S. M. Koushiappas, and M. Kuhlen, Phys. Rev. D **81**, 043532 (2010).
[23] N. Fornengo, R. A. Lineros, M. Regis, and M. Taoso, J. Cosmol. Astropart. Phys. 01 (2012) 005.
[24] T. A. Porter, G. Jóhannesson, and I. V. Moskalenko, Astrophys. J. Suppl. Ser. **262**, 30 (2022).
[25] https://github.com/a-e-egorov/GALPROP_DM.
[26] http://www.marcocirelli.net/PPPC4DMID.html.
[27] M. Cirelli, G. Corcella, A. Hektor, G. Hütsi, M. Kadastik, P. Panci, M. Raidal, F. Sala, and A. Strumia, J. Cosmol. Astropart. Phys. 03 (2011) 051.
[28] P. Ciafaloni, D. Comelli, A. Riotto, F. Sala, A. Strumia, and A. Urbano, J. Cosmol. Astropart. Phys. 03 (2011) 019.
[29] I. V. Moskalenko and A. W. Strong, Astrophys. J. **528**, 357 (2000).
[30] T. A. Porter and A. W. Strong, in *Proceedings of the 29th International Cosmic Ray Conference (ICRC29)*, International Cosmic Ray Conference Vol. 4 (Tata Institute of Fundamental Research, Mumbai, 2005), p. 77.
[31] J. Yin, J. L. Hou, N. Prantzos, S. Boissier, R. X. Chang, S. Y. Shen, and B. Zhang, Astron. Astrophys. **505**, 497 (2009).
[32] T. J. Sodroski, N. Odegard, R. G. Arendt, E. Dwek, J. L. Weiland, M. G. Hauser, and T. Kelsall, Astrophys. J. **480**, 173 (1997).
[33] B. T. Draine, G. Aniano, O. Krause, B. Groves, K. Sandstrom, R. Braun, A. Leroy, U. Klaas, H. Linz, H.-W. Rix, E. Schinnerer, A. Schmiedeke, and F. Walter, Astrophys. J. **780**, 172 (2014).
[34] R. Braun, D. A. Thilker, R. A. M. Walterbos, and E. Corbelli, Astrophys. J. **695**, 937 (2009).
[35] C. Nieten, N. Neininger, M. Guélin, H. Ungerechts, R. Lucas, E. M. Berkhuijsen, R. Beck, and R. Wielebinski, Astron. Astrophys. **453**, 459 (2006).
[36] K. M. Górski, E. Hivon, A. J. Banday, B. D. Wandelt, F. K. Hansen, M. Reinecke, and M. Bartelmann, Astrophys. J. **622**, 759 (2005).
[37] https://www.slac.stanford.edu/exp/glast/groups/canda/lat_Performance.htm.
[38] A. De Angelis, V. Tatischeff, M. Tavani, U. Oberlack, I. Grenier, L. Hanlon, R. Walter, A. Argan, P. von Ballmoos, A. Bulgarelli, I. Donnarumma, M. Hernanz, I. Kuvvetli, M. Pearce, A. Zdziarski *et al.*, Exp. Astron. **44**, 25 (2017).
[39] https://fermi.gsfc.nasa.gov/ssc/data/access/lat/BackgroundModels.html.
[40] E. Tempel, A. Tamm, and P. Tenjes, Astron. Astrophys. **509**, A91 (2010).
[41] S. Li, A. G. Riess, M. P. Busch, S. Casertano, L. M. Macri, and W. Yuan, Astrophys. J. **920**, 84 (2021).
[42] J. McEnery, A. van der Horst, A. Dominguez, A. Moiseev, A. Marcowith, A. Harding, A. Lien, A. Giuliani, A. Inglis,

S. Ansoldi, A. Stamerra, A. Manousakis, A. Strong, C. Bambi, B. Patricelli *et al.*, Bull. Am. Astron. Soc. **51**, 245 (2019).
[43] L. Fariña, L. Jouvin, J. Rico, N. Mori, F. Gargano, V. Formato, F. de Palma, C. Pizzolotto, J. Casaus, M. N. Mazziota, X. Wu, P. Bordas, D. Gascon, D. Simons, A. Tykhonov, C. Altomare, L. Silveri, D. Gasparrini (HERD Collaboration), in *Proceedings of the 37th International Cosmic Ray Conference, 2021, Berlin* (2022), p. 651, 10.22323/1.395.0651.
[44] A. E. Egorov, A. M. Galper, N. P. Topchiev, A. A. Leonov, S. I. Suchkov, M. D. Kheymits, and Y. T. Yurkin, Phys. At. Nucl. **81**, 373 (2018).
[45] A. E. Egorov, N. P. Topchiev, A. M. Galper, O. D. Dalkarov, A. A. Leonov, S. I. Suchkov, and Y. T. Yurkin, J. Cosmol. Astropart. Phys. 11 (2020) 049.
[46] J. I. Djuvsland, J. Hinton, and B. Reville, Phys. Dark Universe **39**, 101157 (2023).
[47] K. Saikawa and S. Shirai, J. Cosmol. Astropart. Phys. 08 (2020) 011.
[48] P. Boldrini, R. Mohayaee, and J. Silk, Astrophys. J. **919**, 86 (2021).
[49] S. Ghosh, A. Dutta Banik, E. J. Chun, and D. Majumdar, Phys. Rev. D **104**, 075016 (2021).
[50] F. Bonnarel, P. Fernique, O. Bienaymé, D. Egret, F. Genova, M. Louys, F. Ochsenbein, M. Wenger, and J. G. Bartlett, Astron. Astrophys. Suppl. Ser. **143**, 33 (2000).
[51] https://numpy.org/.
[52] https://github.com/healpy.
[53] https://apps.automeris.io/wpd/.

PHYSICAL REVIEW D **88,** 023504 (2013)

Constraints on dark matter annihilation by radio observations of M31

A. E. Egorov* and E. Pierpaoli†

Department of Physics and Astronomy, University of Southern California, 3620 McClintock Avenue, SGM 408, Los Angeles, California 90089, USA

(Received 29 March 2013; published 2 July 2013)

We used radio observations of the neighbor galaxy M31 in order to put constraints on the dark matter particle mass and annihilation cross section. Dark matter annihilation in M31 halo produces highly energetic leptons, which emit synchrotron radiation on radio frequencies in the galactic magnetic field. We predicted expected radio fluxes for the two annihilation channels: $\chi\chi \to b\bar{b}$ and $\chi\chi \to \tau^+\tau^-$. We then compared them with available data on the central radio emission of M31 as observed by four radio surveys: VLSS (74 MHz), WENSS (325 MHz), NVSS (1400 MHz), and GB6 (4850 MHz). Assuming a standard Navarro-Frenk-White dark matter density profile and a conservative magnetic field distribution inside the Andromeda galaxy, we find that the thermal relic annihilation cross section or higher $\langle\sigma v\rangle \geq 3 \times 10^{-26}$ cm^3/s are only allowed for weakly interacting massive particle masses greater than $\approx$100 and $\approx$55 GeV for annihilation into $b\bar{b}$ and $\tau^+\tau^-$, respectively. Taking into account potential uncertainties in the distributions of dark matter density and the magnetic field, the mentioned weakly interacting massive particle limiting masses can be as low as 23 GeV for both channels, and as high as 280 and 130 GeV for annihilation into $b\bar{b}$ and $\tau^+\tau^-$, respectively. These mass values exceed the best up-to-date known constraints from Fermi gamma observations: 40 and 19 GeV, respectively [A. Geringer-Sameth and S. M. Koushiappas, Phys. Rev. Lett. **107**, 241303 (2011)]. Precise measurements of the magnetic field in the relevant region and better reconstruction of the dark matter density profile of M31 will be able to reduce the uncertainties of our exclusion limits.

DOI: 10.1103/PhysRevD.88.023504 PACS numbers: 95.35.+d, 95.85.Bh, 98.56.Ne

I. INTRODUCTION

The physical nature of the dark matter (DM) is continuing to be not understood. The most probable candidate for the role of DM is a weakly interacting massive particle (WIMP): a supersymmetric partner of a Standard Model (SM) particle. There are three main approaches in attempts to detect WIMPs: accelerator searches, direct searches, and indirect searches. Although great efforts have been dedicated already to all of these directions, the DM puzzle still seems to be very far from its final and clear solution.

This article is related to the last mentioned search strategy: indirect detection. The idea of indirect detection is based on the opportunity of pair annihilation of WIMPs causing production of different highly energetic SM particles, which eventually decay into stable particles like leptons, protons, and others. These yields may emit electromagnetic radiation through various mechanisms like synchrotron emission, inverse Compton scattering (ICS), etc. in different astrophysical objects. By detecting such radiation we can infer WIMP properties. Since there are evidences of DM existence in any object from dwarf galaxies to largest galaxy clusters, any of these objects are potentially a good target for indirect DM searches. Indirect searches of dark matter have been already extensively exploited considering all wavelength ranges from radio to gamma rays (see [1] for a review). The conventional Lambda cold dark matter model of cosmology suggests a WIMP velocity averaged annihilation cross section $\langle\sigma v\rangle \approx 3 \times 10^{-26}$ cm^3/s, which yields the correct current DM abundance in the Universe in case the DM is thermally produced (see, e.g., [1]). Indirect searches may either lead to the discovery of DM with a given particle annihilation cross section and mass,[1] or constrain the cross section to be below the level of a thermal relic over all plausible ranges of WIMP masses (from several GeV to several TeV). The latter case may imply that, in fact, we do not understand the DM phenomenon in cosmology all that well, and a more sophisticated DM production mechanism is needed.

Currently the most promising direction in indirect detection seems to be related to Fermi searches of the primary gamma emission produced directly by WIMP annihilation (see [3]). At the moment, these constraints are the strongest: they exclude WIMP masses smaller than about 40 and 19 GeV for $b\bar{b}$ and $\tau^+\tau^-$ annihilation channels, respectively, for the standard thermal relic annihilation cross section. While the allowed region of WIMP

*astrotula@gmail.com

†Also at California Institute of Technology, MC 249-17, 1200 East California Blvd, Pasadena, CA 91125, USA. pierpaol@usc.edu

[1]Note that the annihilation cross section at the current epoch can be larger in more general models than the standard thermal value even in the case of thermal production due to effects like Sommerfeld enhancement; see, e.g., [2].

 © 2013 American Physical Society

parameters space is gradually shrinking, WIMP masses of hundreds and thousands GeV are still allowed. Indirect searches may allow further insights in the DM phenomenon. Wavelength bands ranging from the radio to the gamma rays and various astrophysical objects may be exploited further to this aim. In this work we studied, in particular, radio observations of the closest big galaxy M31. Relativistic leptons produced by DM annihilation in its halo emit synchrotron radiation on radio frequencies due to Andromeda's magnetic field. Given the size of the galaxy and its DM halo, the strength of its magnetic field and its close distance, large radio fluxes from DM annihilation may be expected from M31. Therefore M31's radio properties may be exploited in order to put strong upper limits on the annihilation cross section. Surprisingly, almost no attempts in this direction have been made in the past: in the literature only few articles can be found dedicated to indirect searches in M31. The most remarkable among them is [4]. These authors obtained some constraints on WIMP parameter space by Cherenkov ground based gamma observations. However, those observations did not have enough sensitivity to probe the relevant region of DM parameters (at least for the conventional WIMPs). Another work, which can be mentioned in the context of WIMP searches in M31 is [5], where the authors studied a detectability of DM minihalos formed around the hypothetical intermediate mass black holes. The conclusion was that such minihalos can be detectable by modern gamma instruments. However, in a contrast with this work, the authors [5] did not aim to put any constraints on the WIMP parameter space. And since the time of these publications [4,5] no significant progress has been made on this object in indirect searches, if we would consider only searches of the ''minimal'' cold dark matter WIMPs.

We computed the expected radio flux due to DM annihilation (Sec. II), and then compared it with available data of radio observations of M31, which allowed us to put upper limits on the annihilation cross section (Sec. III). For comparison with real observations we chose all appropriate radio surveys, which cover a wide range of frequencies: VLSS (74 MHz), WENSS (325 MHz), NVSS (1400 MHz), and GB6 (4850 MHz). The limits obtained can be considered as conservative because we did not make any specific assumptions about the radio emission other than the one from DM in the center of M31, and allowed for an unconstrained contribution from all other unknown backgrounds.

We calculated the constraints for two annihilation channels, specifically the ones annihilating into $b\bar{b}$ and $\tau^+\tau^-$ pairs. We chose these channels among all possibilities because, as explained, e.g., in [6], $b\bar{b}$ and $\tau^+\tau^-$ nearly present the channels with the softest and hardest lepton yields, respectively. Any other case would therefore produce radio fluxes at intermediate levels with respect to these two. In this sense, these can be considered as the two limiting cases.

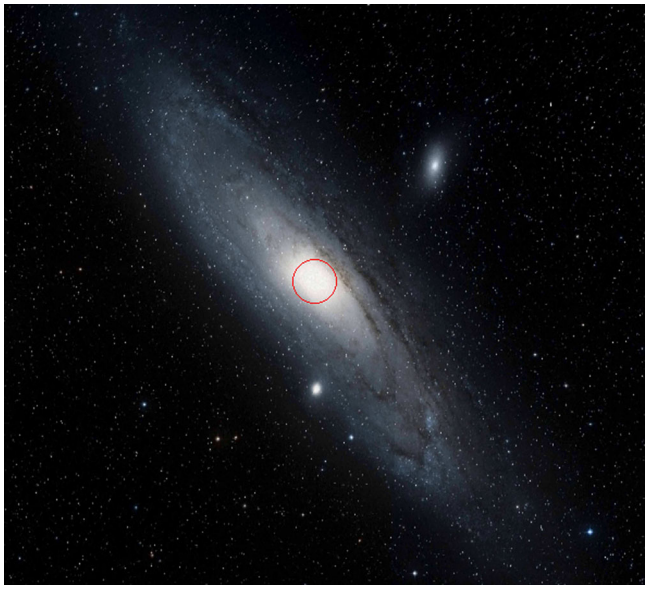


FIG. 1 (color online). Optical image of M31 with the marked ROI, selected for our purposes. Circle radius is $5'$.

In our analysis, we considered only the central part of M31, and specifically the bulge area of a circular shape with the angular radius $\alpha \approx 5'$ around the Galactic center (see Fig. 1). We chose this specific region of interest (ROI) as a target of indirect searches because of the following considerations: (i) the radio quietness of the M31 nucleus, which indicates low contamination in the radio band by other standard astrophysical processes, (ii) the absence of any projected point source inside it, and (iii) sufficient halo size to produce a relevant signal. More details about the ROI choice will be explained below.

Through our paper we adopted the Hubble constant value $H_0 = 71\ \mathrm{km}/(\mathrm{s}\cdot\mathrm{Mpc})$, which was taken from the WMAP7 data at [7].

This paper is organized as follows: Sec. II describes computation of the expected radio emission properties due to WIMP annihilation in M31, in Sec. III we derived the actual constraints by comparison of the predicted fluxes with observational data, and Sec. IV summarizes the results of our work.

II. COMPUTING THE RADIO FLUX

A. General theory

In this section we present the procedure for the computation of the radio flux density from the center of M31. We neglected here the potential absorption of radio emission between the source and the observer, since our estimates showed that it occurs at a negligible level (see Appendix A). In the case of an optically transparent emitting medium, the total flux density from our ROI in

M31 can be obtained just by integrating the local medium emissivity $j(\nu, \vec{r})$ over the volume of halo contained in our ROI:

$$S = \frac{\int j(\nu, \vec{r}) dV}{4\pi d^2}, \tag{1}$$

where $d = 785 \pm 25$ kpc is the distance between us and the Andromeda center [8]; $\vec{r}$ is the position vector inside the M31 halo originating in the M31 center. We disregarded here all (small) redshift effects. Then as a next step we needed to compute the local emission coefficient at an arbitrary position in M31 halo $j(\nu, \vec{r})$. The synchrotron emissivity of leptons produced by WIMP annihilation has the form

$$\begin{aligned} j(\nu, \vec{r}) &= \int_{m_e c^2}^{m_\chi c^2} \left(P_{e^+}(E_{e^+}, \nu, \vec{r}) \frac{dn_{e^+}}{dE_{e^+}} dE_{e^+} \right. \\ &\quad \left. + P_{e^-}(E_{e^-}, \nu, \vec{r}) \frac{dn_{e^-}}{dE_{e^-}} dE_{e^-} \right) \\ &= 2 \int_{m_e c^2}^{m_\chi c^2} P_e(E, \nu, \vec{r}) \frac{dn_e}{dE} dE, \end{aligned} \tag{2}$$

where e^+ and e^- represent positrons and electrons, respectively, $P_e(E, \nu, \vec{r})$ is the synchrotron emission power of one lepton with energy E on a frequency ν [measured in erg/(s · Hz) in CGS], and $\frac{dn_e}{dE}$ is the energy distribution of leptons—the number of leptons per unit volume per unit energy range. We assumed electron and positron terms in Eq. (2) to be equal to each other, which is reasonable because these both species behave similarly in all relevant aspects. According to [9]

$$P_e(E, \nu, \vec{r}) = \int_0^\pi d\theta' \pi \sqrt{3} \sin^2\theta' r_e m_e c \nu_0 F\left(\frac{x}{\sin\theta'}\right), \tag{3}$$

where

$$\begin{cases} r_e = \frac{e^2}{m_e c^2}, \\ x = \frac{2\nu}{3\nu_0 \gamma^2}\left(1 + \left(\frac{\gamma \nu_{\rm pl}}{\nu}\right)^2\right)^{3/2}, \\ \nu_0(\vec{r}) = \frac{eB(\vec{r})}{2\pi m_e c}, \\ \nu_{\rm pl} = \sqrt{\frac{e^2 n}{\pi m_e}} - \text{plasma frequency of ambient plasma}, \\ F(t) \approx 1.25(648)^{1/12} t^{1/3} e^{-t} - \text{synchrotron spectrum}, \\ \gamma = \frac{E}{m_e c^2} - \text{lepton Lorentz-factor}. \end{cases} \tag{4}$$

This set of formulas describes the synchrotron power of a lepton in a magnetic field $B(\vec{r})$ in the presence of an ambient plasma with concentration n. Integration over θ' in Eq. (3) represents the averaging over all possible random angles between a lepton's velocity and magnetic field.

In order to proceed with our computation of the radio flux expected, we needed to derive the energy distribution $\frac{dn_e}{dE}$. For this purpose we applied the standard diffusion equation:

$$\frac{\partial}{\partial t}\frac{dn_e}{dE} = \nabla\left(D\nabla\frac{dn_e}{dE}\right) + \frac{\partial}{\partial E}\left(b(E, \vec{r})\frac{dn_e}{dE}\right) + q_e(E, r), \tag{5}$$

where D is the spatial diffusion coefficient, $b(E, \vec{r})$ is the energy loss rate for a lepton through various energy dissipation mechanisms (measured in the units of energy per time), $q_e(E, r)$ is the source function—how many electrons (or positrons—but only one of these two species) are produced by WIMP annihilation per unit time per unit volume per unit energy range. We can simplify this equation, assuming the stationary limit $\frac{\partial}{\partial t} = 0$, as commonly done for the diffusion of DM annihilation products in galaxies and clusters (see, e.g., [10]). Another useful simplification is the absence of the spatial diffusion of annihilation products, which will make the first term in the rhs vanish. We investigated the validity of such an assumption by comparing the characteristic diffusion length of newly injected leptons with the size of our ROI and concluded that it could be done without significant effect on our results (see Appendix B for details). With these two simplifications we can easily solve the diffusion equation:

$$\frac{dn_e}{dE}(E, \vec{r}) = \frac{1}{b(E, \vec{r})} \int_E^{m_\chi c^2} q_e(E', r) dE'. \tag{6}$$

At this point we should specify the functions $b(E, \vec{r})$ and $q_e(E, r)$. The energy loss rate $b(E, \vec{r})$ is constituted mainly by four different cooling processes: ICS emission, synchrotron emission, bremsstrahlung, and Coulomb scattering:

$$b(E, \vec{r}) = b_{\rm ICS} + b_{\rm sync} + b_{\rm brem} + b_{\rm Col}. \tag{7}$$

Using previous results presented in the literature [1,9,11] we constructed each of these four terms, respectively, as follows:

$$b_{\rm ICS} = 0.76 \frac{U_{\rm ph}}{1\ \text{eV} \cdot \text{cm}^{-3}} \left(\frac{E}{1\ \text{GeV}}\right)^2; \tag{8}$$

here, and in other loss terms, numerical prefactors like 0.76 follow from the exact analytical computation of the corresponding loss rate for a lepton. $U_{\rm ph}$ denotes the total energy density of radiation at relevant locations. For the Galactic center region it is constituted mainly by star light photons. We substituted for this quantity the fixed value $U_{\rm ph} = 8\ \text{eV} \cdot \text{cm}^{-3}$, which is quoted in [1] as a characteristic value for the Milky Way (MW) center.

$$b_{\rm sync} = 0.025 \left(\frac{B(\vec{r})}{1\ \mu\text{G}}\right)^2 \left(\frac{E}{1\ \text{GeV}}\right)^2, \tag{9}$$

$$b_{\rm brem} = 4.70 \frac{n}{1\ {\rm cm}^{-3}} \frac{E}{1\ {\rm GeV}}, \quad (10)$$

where n denotes the concentration of ambient plasma in ${\rm cm}^{-3}$.[2] For this quantity we also used the constant value $n = 0.1\ {\rm cm}^{-3}$ relying on the results of the study in Ref. [12], where such a plasma concentration was derived as a typical average value for the Galactic center region.

$$b_{\rm Col} = 6.13 \frac{n}{1\ {\rm cm}^{-3}} \left(1 + \frac{1}{75} \log\left(\frac{E}{m_e c^2 n}\right)\right). \quad (11)$$

All loss rates here are measured in the units 10^{-16} GeV/s. For illustrative purposes, we showed in Fig. 2 the energy dependences of each term in Eqs. (8)–(11) over the relevant range of lepton energies. We can clearly see that the synchrotron losses term depends on the location through $B(\vec{r})$. For this reason, we presented $b_{\rm sync}$ in Fig. 2 for three relevant trial locations, which are away from the M31 center by 0, 1, and 2 kpc. More details about $B(\vec{r})$ distribution will be discussed in Sec. II C. In the most general case, the quantities $U_{\rm ph}$ and n depend on $\vec{r}$ as well, indeed. However, at the current level of accuracy of our model we made two simplifying assumptions. First, we assumed constant values for these quantities with conservative choices, and second, we adopted the values for the MW relying on high similarity between these two galaxies.

As for the source function $q_e(E, r)$, it is computed essentially as a product of the number of leptons produced by one WIMP annihilation per unit energy range $\frac{dN_e}{dE}$ and the number of annihilations per unit time per unit volume:

$$q_e(E, r) = \frac{1}{2}\left(\frac{\rho_{\rm DM}(r)}{m_\chi}\right)^2 \langle\sigma v\rangle \frac{dN_e}{dE}, \quad (12)$$

where $\rho_{\rm DM}(r)$ is the local DM density, $\langle\sigma v\rangle$ is thermally averaged annihilation cross section, and m_χ is the WIMP mass. Annihilation yields of leptons $\frac{dN_e}{dE}$ for two necessary channels $\chi\chi \to b\bar{b}$, $\tau^+\tau^-$ were taken from Ref. [13]. A detailed description of this resource is presented in [14]. We took the precomputed annihilation yields from this resource in their last version, which includes electroweak corrections. The importance of these corrections for a yields computation was justified in [15]. Inclusion of electroweak corrections leads to slightly different secondary lepton yields from annihilation into primary products with different polarizations: left- or right-polarized tau leptons, transversely or longitudinally polarized W bosons, etc. But as practice showed, the difference in the final radiation flux is very minor due to this splitting. For example, the final flux for the case of the M31 DM halo concentration $c_{100} = 12$, observational frequency $\nu = 74$ MHz, WIMP mass $m_\chi = 100$ GeV, and annihilation into $\tau^+\tau^-$ differs just by $<1\%$ for different polarizations, which is much smaller than other total flux uncertainties presented. That is why we did not further distinguish different polarizations of primary annihilation products.

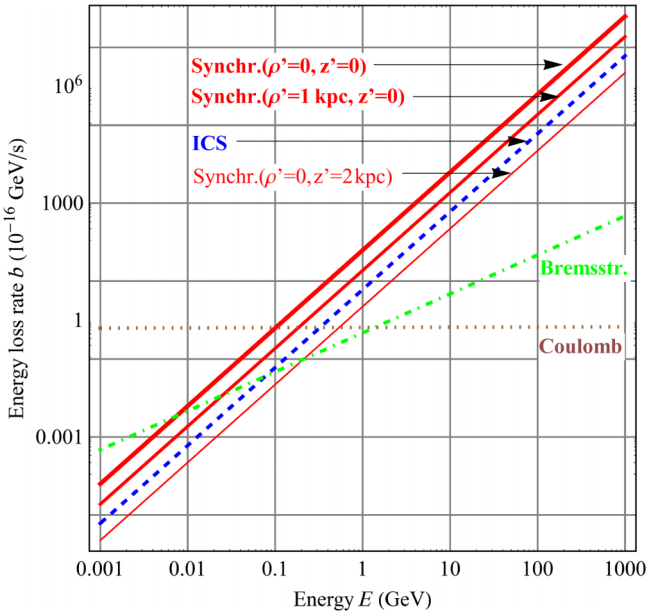


FIG. 2 (color online). The energy dependence of various types of lepton energy losses. Synchrotron losses are shown for three representative locations around the M31 center. For more details see Secs. II A and II C.

For the next step we needed to specify the DM density distribution $\rho_{\rm DM}(r)$, which appears in formula (12). The next subsection is dedicated to the DM density profile derivation.

B. DM density distribution

As a model of DM density distribution $\rho_{\rm DM}(r)$, in M31 halo we used the standard Navarro-Frenk-White (NFW) profile, firstly introduced in [16] and widely used since that due to its universality. Some other profiles potentially describe a DM distribution in galactic halos even better than NFW—this was demonstrated, e.g., in [17] for the Einasto density profile. However, we did not use any other profiles further, except NFW, due to the following reasons. First, all currently available models of the DM density distribution in M31 were made in the frame of the NFW profile. The second reason is that among all profiles, the NFW yields moderate emission fluxes due to DM annihilation (lower than, e.g., the Moore profile—see [10]), and this makes our constraints conservative with respect to the assumptions on the adopted density profile. Also, the NFW profile is specified by only two free parameters, while a larger number of parameters is required by some other

[2]This loss term $b_{\rm brem}$ was presented in another form in Ref. [9]. However, we suspect a mistake at this point in [9], because our verification of this loss rate did not confirm the expression there. For this reason, we use here the expression precisely derived in [11] [formula (6.74) there], which appears to have better justification.

profiles. This choice therefore minimizes the overall number of "degrees of freedom" in our model.

Quantitatively, the DM density distribution of our choice is the following:

$$\rho_{\mathrm{DM}}(r) = \begin{cases} \rho_{\mathrm{DM}}(r = 50\ \mathrm{pc}), & \text{if } 0 \le r < 50\ \mathrm{pc}; \\ \frac{\rho_s}{\frac{r}{r_s}(1+\frac{r}{r_s})^2}, & \text{if } r \ge 50\ \mathrm{pc}. \end{cases} \quad (13)$$

It presents the exact NFW profile with a minor modification, which can be called as a flat core: we do not extrapolate the density below the radial distance of $r_t = 50$ pc, inside this central region we leave DM density at the constant level of $\rho_{\mathrm{DM}}(r = 50\ \mathrm{pc})$. This choice is motivated by the divergence of the NFW distribution toward the central point of the halo, which prevents us from estimating the DM density reliably in the very central region. The NFW profile provides a reliable density estimate down to the radius ~50 pc for a M31-size halo (see, e.g., Fig. 4 in [18]). That's why in order to be conservative in our computation of the medium emissivity, which depends quadratically on the local DM density, we truncated the NFW profile at $r = r_t = 50$ pc and left the density at smaller radii on the level of $\rho_{\mathrm{DM}}(r = 50\ \mathrm{pc})$. We tested the dependence of our results on the specific arbitrary choice of the truncation radius r_t. This study showed that a decrease (increase) of r_t by a factor of 2 (a factor of 4) produce an increase (decrease) of ≈3% (~10%) in final fluxes, which is far below the overall level of accuracy of our model.

The DM density profile equation (13) is completely defined for a specific halo by two parameters—scaling radius r_s and scaling density ρ_s. Thus, we needed to estimate them for M31. These two parameters are unambiguously linked to another two halo parameters, which are more meaningful—the halo mass M_Δ and its concentration c_Δ. Δ here denotes an overdensity: halo mass M_Δ by definition means the DM halo mass enclosed in the sphere, the average density inside which is equal to $\Delta\rho_{\mathrm{crit}}$ with $\rho_{\mathrm{crit}} = \frac{3H_0^2}{8\pi G} = 9.5 \times 10^{-30}\ \mathrm{g \cdot cm^{-3}}$ being the current critical density of the Universe. In our article we used $\Delta = 100$ due to some practical circumstances. However, the parameters of the actual DM density distribution (13) do not depend indeed on a Δ choice. Halo mass and concentration are connected with the NFW profile parameters through the following relations:

$$r_\Delta = \left(\frac{3M_\Delta}{4\pi\Delta\rho_{\mathrm{crit}}}\right)^{1/3}, \qquad c_\Delta \equiv \frac{r_\Delta}{r_s}, \qquad M_\Delta = \int_0^{r_\Delta} \rho_{\mathrm{DM}}(r) 4\pi r^2 dr. \quad (14)$$

As for the determination of the relevant parameters for M31, we used the results of M_{100} and c_{100} from [8,19]. While these are in a good agreement with each other in determination of M_{100} [$(1.2 \pm 0.3) \times 10^{12} M_\odot$ vs $(0.91 \pm 0.16) \times 10^{12} M_\odot$, respectively], they show a rather big discrepancy in the estimation of c_{100} (the most probable values cited being ≈12 and ≈28, respectively). The expected radiation fluxes from these two concentration values differ by about 1 order of magnitude. This is why we decided to treat these two cases separately. They can be considered as two limiting cases yielding the most conservative constraints for $c_{100} = 12$ and the most optimistic constraints for $c_{100} = 28$.

At this point we were ready to specify the NFW profile by estimation of its two parameters ρ_s, r_s. For the first case $c_{100} = 12$ we took $M_{100} = 1.2 \times 10^{12} M_\odot$ from [8] and obtained ρ_s, r_s by Eq. (14). For the second case $c_{100} = 28$ we did not need to calculate ρ_s, r_s—they were taken directly from Table 2 in [19] as the best-fitting values.

Another potentially relevant question in this subsection is the substructures' contribution in our flux. It is well known that any DM halo contains a lot of small subhalos inside it (see, e.g., [1]). These subhalos are very dense and numerous; that is why they are able to substantially increase the total flux due to DM annihilation from a whole halo—by 10–100 times (see, e.g., [20]). But in our case we can neglect the substructure contribution, because the main part of our expected flux comes from a very central region with a size of about 1 kpc. As can be seen, e.g., in [20], substructures do not survive so close to the center due to tidal disruption, and their contribution to the total expected flux would be negligible at so small radii. Thus, we did not need to include subhalos in our analysis. Moreover, subhalos' presence would only increase the overall flux, so that the constraints obtained here are to be considered conservative.

Thus, at this point we have completely specified the DM density distribution in the M31 halo. Now we can move to the next step—specifying the magnetic field distribution.

C. Magnetic field

The emission due to DM annihilation, which we hope to detect, is generated through the synchrotron mechanism. For synchrotron emission modeling it is crucially important to know the magnetic field strength distribution in our emitting volume. A global axis symmetry of the large spiral galaxy M31 naturally suggests the assumption of a two-parametric magnetic field distribution $B(\rho', z')$, where B depends on the radial distance from the center ρ' in the galactic plane and the vertical height z' above the galactic plane.

As for B dependence on the vertical coordinate z', it's plausible to assume exponential dependence $B \sim \exp(-|z'|/z_0')$ with some scale height z_0'. Such a dependence is commonly used for large spiral galaxies—see, e.g., [21]. In order to consider a reasonable radial dependence of B in the galactic plane we used the findings of [22,23]. In [22], a large-scale magnetic field in the disk plane was measured between radial distances of 6 and 14 kpc. These measurements yielded almost a constant magnetic field over the whole mentioned annular region

of $\approx 7\ \mu$G, which is the expected value for galactic discs (see, e.g., [24]). As for the magnetic field strength in the inner region $\rho' < 6$ kpc, we were unable to find reliable data. Some measurements for this region were reported only in [25] and only for two trial locations with poor justification. Besides this information on the central field properties, we can reliably assume probably only one thing—that the field grows toward the center. In such situation we made a decision to introduce the following field distribution (including the vertical dependence part):

$$B(\rho', z') = \left(B_{10} + B_s \exp\left(-\frac{\rho'}{\rho'_0}\right)\right) \exp\left(-\frac{|z'|}{z'_0}\right). \quad (15)$$

Here $B_{10} = 7\ \mu$G—the plateau value observed on $\rho' \approx$ 6–14 kpc. The term $B_s \exp(-\frac{\rho'}{\rho'_0})$ presents an exponentially decreasing central spike with the characteristic radial extent ρ'_0. Of course, such a distribution has a nonphysical plateau extending to infinity $B(\rho' = \infty, z' = 0) = 7\ \mu$G. But this plateau does not matter for our calculations: at distances of tens of kpc DM density becomes very small, and a contribution of these regions to the overall flux is tiny. The distribution in Eq. (15) can be completely specified by two free parameters: the vertical scale height z'_0 and the central field value $B(0, 0) = B_{10} + B_s$. After specifying these two parameters, the radial scale length ρ'_0 becomes automatically set by a smooth connection of the central exponential spike $B_s \exp(-\frac{\rho'}{\rho'_0})$ to the plateau $B(\rho' > 6$ kpc, $z' = 0) \approx 7\ \mu$G.

Now let us discuss the specification of the values of z'_0 and $B(0, 0)$. We estimated the scale height z'_0 using [22,26]. The first mentioned article outlines such a general property of galactic magnetic fields: the scale height z'_0 is typically about 4 times greater than the scale height of a synchrotron emission, which arises from cosmic rays in a whole galaxy volume. The last mentioned synchrotron scale height was reported in [22] for M31 with a value ≈ 0.3 kpc. This would yield $z'_0 \approx 0.3$ kpc $\cdot\, 4 = 1.2$ kpc. Moreover, such a value for z'_0 is confirmed by the authors of [22] on the basis of other independent considerations: they conclude that the minimal expected z'_0 value is not less than ≈ 1 kpc. We therefore chose $z'_0 = 1.2$ kpc for all our calculations. This estimate reflects a conservative choice, since lower values seem to be unrealistic and possible greater values can only increase the final expected flux and, hence, strengthen the final constraints.

As for the second necessary parameter, $B(0, 0)$, the situation is much less certain. As we already mentioned, we found in the literature only one attempt to measure the central field values in M31, [25]. This work reports the total field strengths for the two locations: $B(\rho' \approx 0.3\,\text{kpc}, z' \approx 0) = 15 \pm 3\ \mu$G and $B(\rho' \approx 0.9$ kpc, $z' \approx 0) = 19 \pm 3\ \mu$G. These values were obtained assuming energy equipartition between cosmic ray particles and magnetic fields. Such an assumption, however, has been shown to lead to an underestimation of the magnetic field in similar setting. For example, the authors of [23] explored the central field properties of the MW and derived the stringent lower limit of 50 μG on the field strength based on multiwavelength studies of a cosmic ray emission. At the same time, they mentioned that a simple equipartition assumption implies a central field strength of only $\sim 10\ \mu$G. As for the upper bound on a central field strength, [23] demonstrates that there is no certainly known value for it. Values of few hundreds μG are mentioned to be absolutely possible.

Considering the possible underestimation of the M31 magnetic field due to the equipartition assumption [25], and the similarity between MW and M31, we chose $B(0, 0) = 50\ \mu$G as the most probable value. However, we performed all our calculations for alternative field values as well (which are considered as less probable) in order to study the dependence of our final results on this model parameter. These alternative less realistic values were chosen to be $B(0, 0) = 15\ \mu$G and $B(0, 0) = 300\ \mu$G. They can be considered as approximate boundaries of the interval where the actual field value lies. The detailed discussion of the final results variation due to uncertainties in $B(0, 0)$ will be done in Sec. III B.

At this point we have completely specified magnetic field distribution. For illustration purposes we showed the density plot of our distribution in Eq. (15) in Fig. 3 for the case of $B(0, 0) = 50\ \mu$G.

The magnetic field distribution in Eq. (15) is written in a cylindrical coordinate system attached to M31. Axes $x'y'$ lie in the M31 disk plane. Another nontrivial step is to

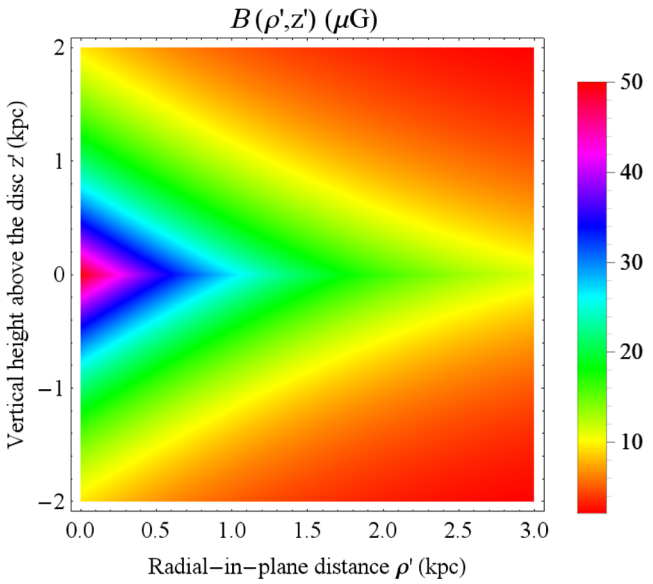


FIG. 3 (color online). Density plot of the magnetic field distribution (15), which was chosen for our computations. Parameter values here correspond to the most probable case with the central field strength $B(0, 0) = 50\ \mu$G. For more details see Sec. II C.

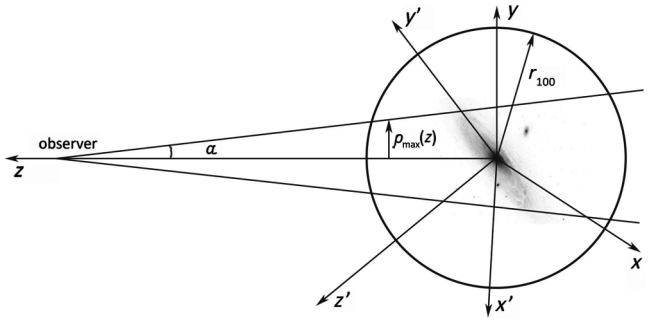


FIG. 4. Two coordinate systems (x, y, z) and (x', y', z'). The plane $x'y'$ is coincident with the M31 disc plane. Integration over the emitting volume is performed in (x, y, z). More details are in Sec. II C.

make a transformation between the coordinate system attached to M31 and the "laboratory" system with the Oz axis pointing from the M31 center to the observer. This is necessary for the flux computation because we are going to perform a numerical integration over the emitting volume along our line of sight, which is coincident with the Oz axis and not coincident with Oz'. The two coordinate systems are shown in Fig. 4. We performed the coordinate transformation $(\rho, \varphi, z) \leftrightarrow (\rho', \varphi', z')$ using the formulas below, which were derived in [27] [formula (6)] for Cartesian coordinates $(x, y, z) \leftrightarrow (x', y', z')$:

$$\begin{cases} x' = -x\sin P + y\cos P, \\ y' = -x\cos P\cos i - y\sin P\cos i - z\sin i, \\ z' = -x\cos P\sin i - y\sin P\sin i + z\cos i, \end{cases} \tag{16}$$

where P and i represent the position angle and axis inclination, respectively, and define the orientation of the M31 disc plane with respect to the sky plane. Following [8], we assumed $P = 38°$, $i = 78°$. From Eq. (16), using relations between cylindrical and Cartesian coordinates it's easy to obtain the one-to-one correspondence $(\rho, \varphi, z) \leftrightarrow (\rho', \varphi', z')$:

$$\begin{cases} \rho' = ((-\rho\cos\varphi\sin P + \rho\sin\varphi\cos P)^2 \\ \qquad + (\rho\cos\varphi\cos P\cos i + \rho\sin\varphi\sin P\cos i + z\sin i)^2)^{\frac{1}{2}}, \\ z' = -\rho\cos\varphi\cos P\sin i - \rho\sin\varphi\sin P\sin i + z\cos i. \end{cases} \tag{17}$$

Finally, we substituted Eq. (17) into Eq. (15) obtaining therefore B as a function of (ρ, φ, z), which allowed us to compute the final flux.

D. Estimated fluxes

A final expected radio flux due to DM annihilation in M31 halo is defined by Eq. (1). In order to compute it we combined all relevant relations (2)–(4), (6)–(15), and (17) and substituted them in Eq. (1). The integration limits for spatial coordinates can be easily figured out from Fig. 4:

$$\begin{cases} 0 \le \rho \le (d - z)\tan\alpha, \\ 0 \le \varphi \le 2\pi, \\ -r_{100} \le z \le r_{100}, \end{cases} \tag{18}$$

where α is the angular radius of our ROI. Figure 5 presents the dependence of the total expected radio flux at $\nu = 74$ MHz on the angular radius of ROI for both selected annihilation channels and three trial WIMP masses: $m_\chi = 10$, 100, and 1000 GeV. Boundaries of every shaded region correspond to the two limiting cases of DM density distribution in the halo, which were discussed in Sec. II B: $c_{100} = 12$ and $c_{100} = 28$. Thus, the actual flux is expected to lie somewhere inside shaded regions. The thick central lines present the algebraic averages between the corresponding boundary curves (fluxes). The flux saturates around $\alpha \approx 5'$ and does not grow significantly at larger radii. We also computed the expected signal-to-noise ratio (SNR) for the same set of parameters and presented it in Fig. 6. Details about noise level computations can be found in Sec. III A. These plots justify our choice of α. Basically, in this choice we are governed by two counteracting effects. On the one hand, Fig. 6 clearly suggests that we use the smallest α possible in order to achieve the best SNR. On the other hand, as discussed in Secs. II B and II C, the accuracy of DM density and magnetic field strength estimates decreases when approaching the central point of the halo. As a matter of fact, we know almost nothing about real distributions of these quantities inside the region of size $\alpha \approx 0.25'$. Hence, our ROI should be much larger than $\approx 0.25'$ in radius in order to encompass a volume where our overall knowledge of the parameters' distribution is precise enough. Based on these considerations, we chose $\alpha = 5'$ as the optimal ROI radius. With such a choice we lose little in SNR; however, we gain in overall reliability of calculations. Also, we cannot increase α any higher than $\sim 5'$ because it will lead to nondesirable capturing of projected point sources.

As an intermediate step of calculations, we decided to study also the contribution of leptons with different energies into the total flux. For this purpose we computed the part of the total flux produced by the leptons with initial energies at production below different thresholds E_m. We spanned the whole possible range of E_m values from the lepton's rest energy to the WIMP's rest energy. The results are presented in Fig. 7 for all four frequencies used. These plots are generated for the most relevant magnetic field model, WIMP mass $m_\chi = 100$ GeV (relevance of this mass scale will be seen in the results section), and the $c_{100} = 12$ halo model. Essentially, we can see in Fig. 7 that the main contribution to the total flux ($\gtrsim 50\%$) for the all frequencies and annihilation channels comes from a relatively narrow window of initial lepton energies between $\sim 0.01 m_\chi c^2$ and $0.1 m_\chi c^2$, or 1 and 10 GeV. This energy window of 1 order of magnitude width is

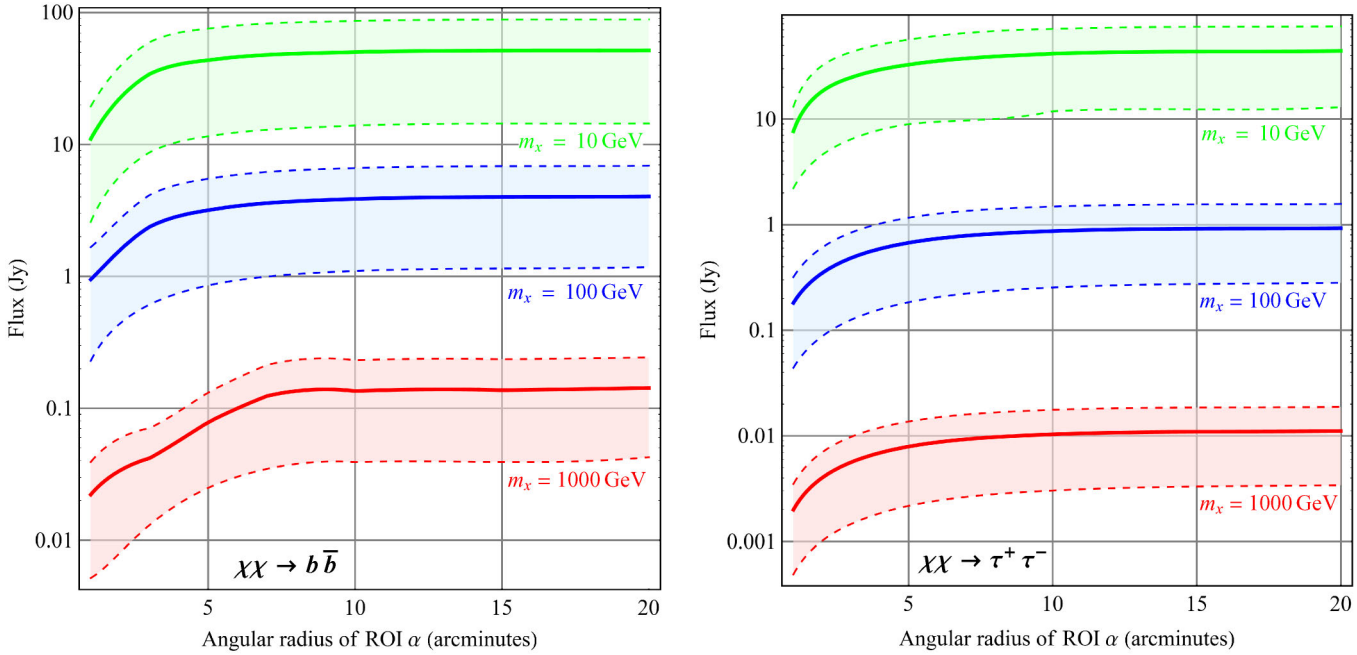


FIG. 5 (color online). The expected radio flux dependence on the angular radius of the ROI. The expected flux lies inside shaded regions. Upper and lower boundaries of these regions correspond to the different halo concentration values $c_{100} = 28$ and $c_{100} = 12$, respectively. Thick central lines present algebraic averages between corresponding limiting cases. Curves are shown for the two annihilation channels $\chi\chi \to b\bar{b}$, $\tau^+\tau^-$, three WIMP masses $m_\chi = 10$, 100, 1000 GeV, and the most probable magnetic field distribution with the central value of 50 μG. The annihilation cross section is $\langle\sigma v\rangle = 3 \times 10^{-26}$ cm^3/s; the observational frequency is $\nu = 74$ MHz. For more details see Sec. II D.

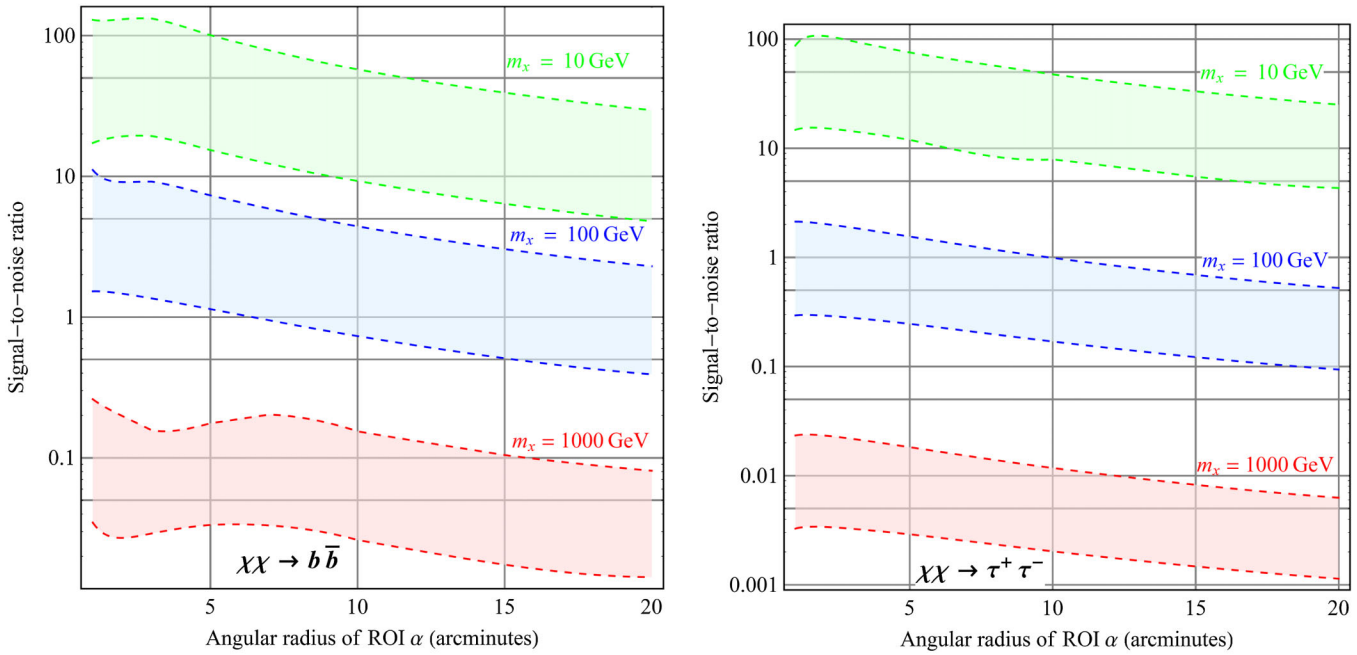


FIG. 6 (color online). The expected SNR dependence on the angular radius of ROI. The expected SNR lies inside shaded regions. Upper and lower boundaries of these regions correspond to different halo concentration values $c_{100} = 28$ and $c_{100} = 12$, respectively. Curves are shown for the two annihilation channels $\chi\chi \to b\bar{b}$, $\tau^+\tau^-$, three WIMP masses $m_\chi = 10$, 100, 1000 GeV, and the most probable magnetic field distribution with the central value of 50 μG. The annihilation cross section is $\langle\sigma v\rangle = 3 \times 10^{-26}$ cm^3/s, the observational frequency is $\nu = 74$ MHz. For more details see Sec. II D.

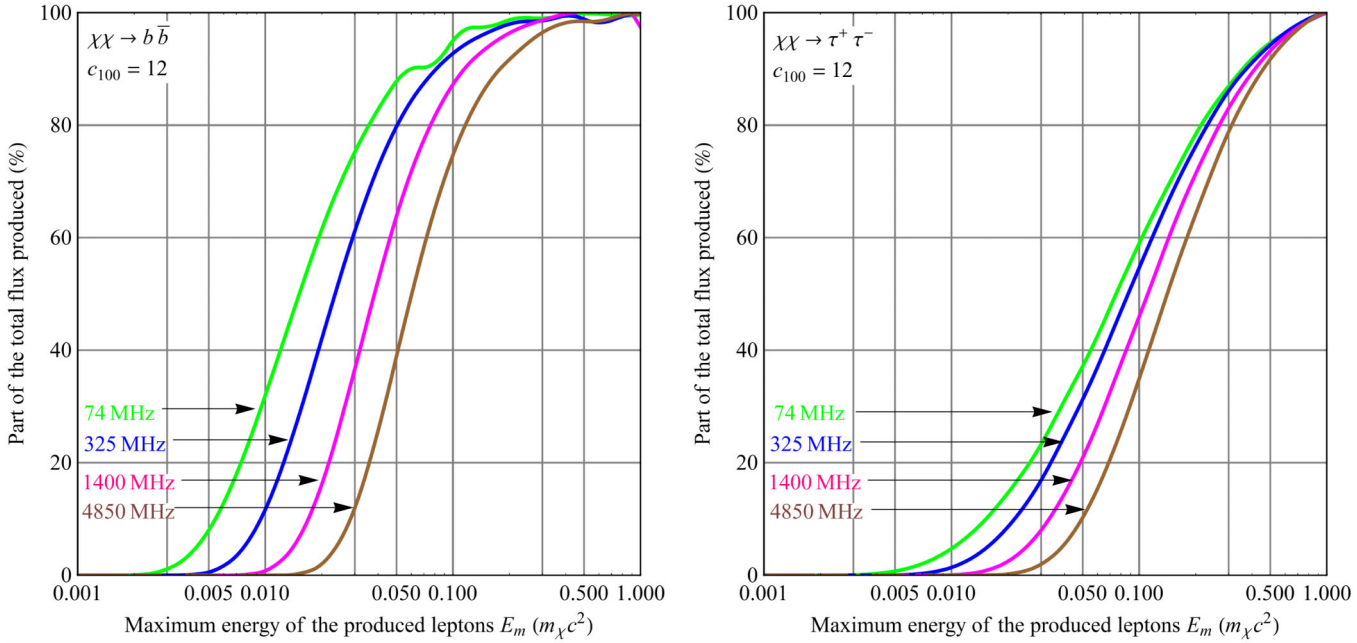


FIG. 7 (color online). The part of total radio flux produced by leptons with energies at production below different thresholds. These illustrations are generated for the following set of parameters: $c_{100} = 12$, $\langle\sigma v\rangle = 3 \times 10^{-26}$ cm^3/s, $B(0, 0) = 50$ μG. The WIMP mass is chosen to be $m_\chi = 100$ GeV, which reflects the most relevant mass scale with respect to the final results, as will be seen below. We can note that the majority of the total flux are produced by leptons with initial energies above $\sim 0.01 m_\chi c^2$. More details are in Sec. II D.

considered to be narrow with respect to the whole energy range of produced leptons between $\sim 10^{-5} m_\chi c^2$ and $1 m_\chi c^2$, which spans more than 5 orders of magnitude. This implies that the most important fraction of the lepton population for our considerations has an energy above ~ 1 GeV. This fact, in turn, means that according to Fig. 2 the main energy loss mechanisms for such a population would be synchrotron and ICS emission. Thus, these

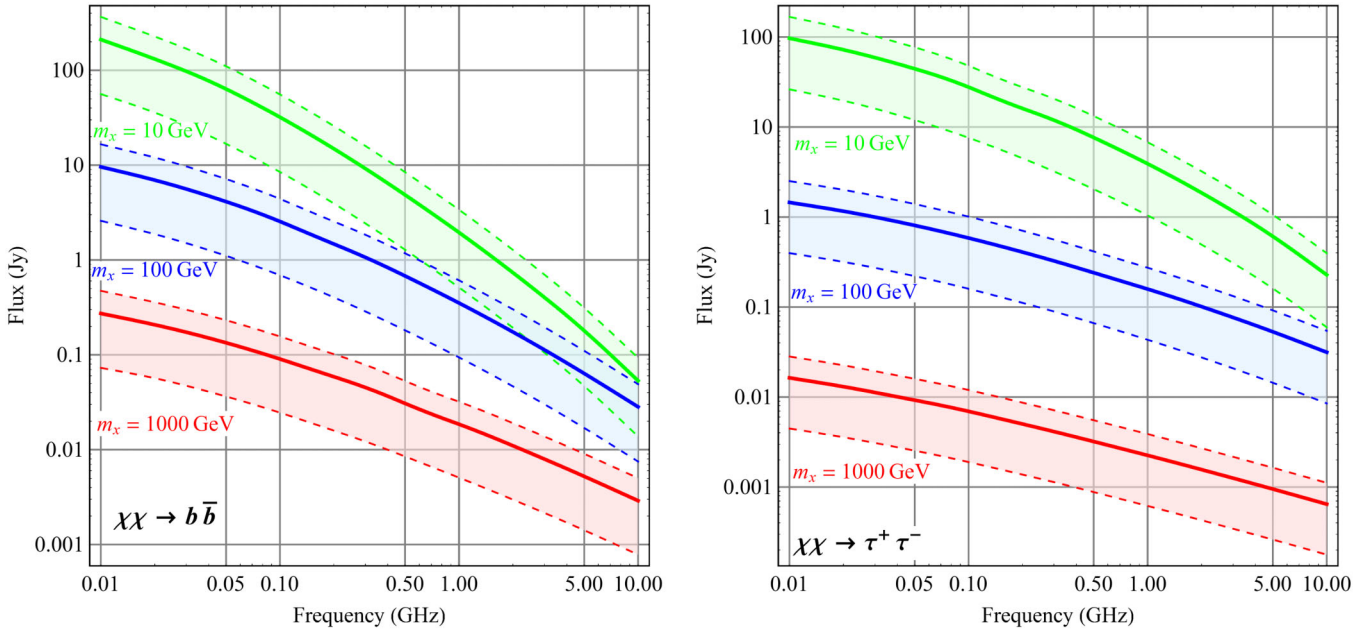


FIG. 8 (color online). The frequency dependence of the expected radio flux for three different WIMP masses and two annihilation channels. ROI radius $\alpha = 5'$; shaded regions reflect uncertainty in the DM density distribution as on the previous plots, $B(0, 0) = 50$ μG, $\langle\sigma v\rangle = 3 \times 10^{-26}$ cm^3/s. More details are in Sec. II D.

kinds of losses dominate in comparison with the other two, bremsstrahlung and Coloumb losses, and play a main role for final results. Meanwhile, it's also useful to note that in the case of the $\tau^+\tau^-$ channel, the total flux is constituted by more energetic leptons than the flux for the $b\bar{b}$ channel, which is in complete agreement with the difference between these two channels mentioned in the Introduction—the $\tau^+\tau^-$ channel produces a harder lepton energy spectrum.

Another important result of our computations is the frequency dependence of radio flux from the M31 halo. These dependencies are shown in Fig. 8 for three different WIMP masses, both annihilation channels, both limiting halo models, and the chosen ROI with $\alpha = 5'$. As a general feature we see, for all cases, a decrease of the radio flux as the frequency increases. The steepness of this decrease is, however, more pronounced for lower WIMP masses. This behavior suggests that we primarily leverage on low frequency observations for obtaining DM constraints. However, the sensitivity of radio surveys typically increases with frequency, partially compensating the effect of the lower signal. There is, therefore, no obvious optimal frequency to be used and that would lead to the strongest constraints possible. For this reason, we opted for radio observations at very different frequencies for actual constraints derivation. This procedure and its results will be described in the next section.

III. OBTAINING CONSTRAINTS ON DM ANNIHILATION

A. Comparison with radio surveys

In order to make a next step on the way to final constraints, we needed to obtain the upper limits on the actually observed radio fluxes from our ROI. A comparison of these upper limits with the expected fluxes computed above immediately provides the upper limits on the annihilation cross section for different values of WIMP masses, since the expected fluxes is directly proportional to $\langle\sigma v\rangle$. For this purpose, we studied many major radio surveys conducted in the past and chose four of them (corresponding frequencies and detailed descriptions are provided in brackets): VLSS (74 MHz [28]), WENSS (325 MHz [29]), NVSS (1400 MHz [30]), and GB6 (4850 MHz [31]). All other surveys were rejected due to either one of the following two reasons: too low resolution of a survey (i.e., the telescope beam size is larger than the ROI size) or not covering the M31 area of the sky. In Table I we outlined the main surveys' parameters, which were collected from [28–31] and then used in calculations. The uncertainties of survey frequencies, caused by finite bandwidth, do not exceed the level of ~4%, and do not affect final results significantly.

Real sky images were viewed and analyzed by the Aladin software, which is described in [32]. The images of our ROI from all four radio surveys are shown in Fig. 9. First, we notice that our ROI does not capture any contaminating point sources. On the last three images (325, 1400, and 4850 MHz) some signal from the M31 center is clearly visible. The 74 MHz image presents essentially noise. For the precise flux upper limit derivations we needed to obtain the measured signal values c_i ($i = 1$–4 denotes different observational frequencies) and the rms (root of mean square or root of dispersion) noise values σ_i for our ROI for all images (we assume Gaussian distributions of noise levels inside a radio telescope beam and inside the ROI). The measured signal values were easily read by the Aladin. As for the rms noise values, we derived from basic principles that they can be estimated as $\sigma_i = \sigma_i^{(b)}\sqrt{N_i} = \sigma_i^{(b)}\frac{\alpha}{\beta_i}$, where N_i are the numbers of beams contained in the ROI, β_i are the angular radii of beams (or half of the FWHM for each survey) and $\sigma_i^{(b)}$ are the rms noises inside a beam for each survey (cited in Table I). Thus, we have obtained both necessary ingredients for a flux upper limit estimation from the ROI—the measured signal values and the rms noise values.

TABLE I. Main parameters of all radio surveys used.

Survey	Frequency (MHz)	Beam diameter or FWHM $2\beta_i$ (arcseconds)	RMS noise level inside the beam $\sigma_i^{(b)}$ (mJy)
VLSS	74	80	100
WENSS	325	82	4.0
NVSS	1400	46	0.5
GB6	4850	240	4.0

Having all the necessary information, we obtained the limiting cross section values for cases of different parameter sets using the following formula for the probability density of the noise values inside our ROI:

$$p_i(n_i = c_i - w_i(\langle\sigma v\rangle)) = \frac{1}{\sqrt{2\pi}\sigma_i}\exp\left(-\frac{(c_i - w_i(\langle\sigma v\rangle))^2}{2\sigma_i^2}\right), \tag{19}$$

where n_i are the noise values inside the ROI, c_i are the measured signal values from the ROI, and $w_i(\langle\sigma v\rangle)$ are the expected signals from WIMP annihilation, which is linearly proportional to an unknown annihilation cross section $\langle\sigma v\rangle$. Here we do not include any background radiation (this question will be further developed in the next section). For our final constraints onto $\langle\sigma v\rangle$ we decided to use 99.73% confidence level, which corresponds to 3σ Gaussian confidence level.

In order to guide intuition on which experiment is the most constraining for a given particle mass, in Fig. 10 we showed our results on the cross section when each frequency is considered individually. There we plotted the constraints obtained at 99.7% confidence level by four different surveys used, for two halo models (described in Sec. II B), two annihilation channels selected $\chi\chi \to b\bar{b}$,

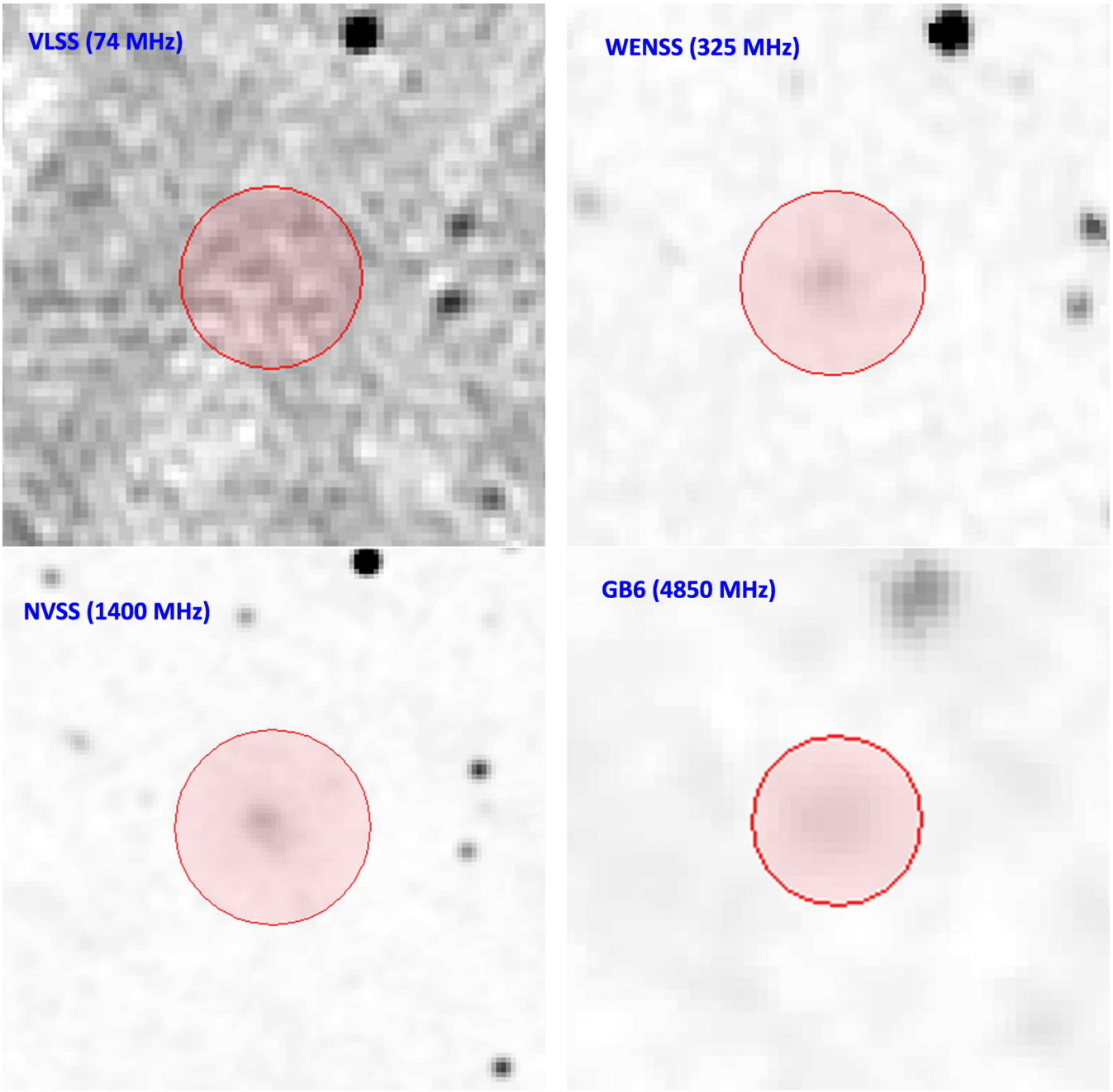


FIG. 9 (color online). Radio images of the M31 central region. Our ROI of 5′ radius is marked by the red circle. Corresponding surveys are commented on each image. We can find noise only on the 74 MHz and significant signals on the other frequencies.

$\tau^+\tau^-$, and the most probable magnetic field distribution with $B(0, 0) = 50\ \mu$G. We spanned the range of WIMP masses between 6 and 1000 GeV and computed the limiting $\langle\sigma v\rangle$ values for a subset of WIMP masses inside this range, interpolating results for mass values in between. The general key properties of our results can be summarized as follows: first of all, different halo models yield very different limiting annihilation cross sections (by about 1 order of magnitude) for all WIMP masses. This reflects the high sensitivity of our results to the halo model assumed. Another noticeable fact is that $\tau^+\tau^-$ annihilation channel appears to be less constrained than the $b\bar{b}$ channel, in complete agreement with the mentioned expectation that harder secondary spectra channels produce a generally lower final radiation flux. It is also interesting to notice that, for different WIMP masses and annihilation channels, the most constraining survey among all the ones considered varies. Therefore, we cannot isolate a specific key frequency or experiment for each plot bearing the role of the most constraining for all WIMP masses—we need to use all experiments together to get the best constraints. And final constraints from the joint analysis will be

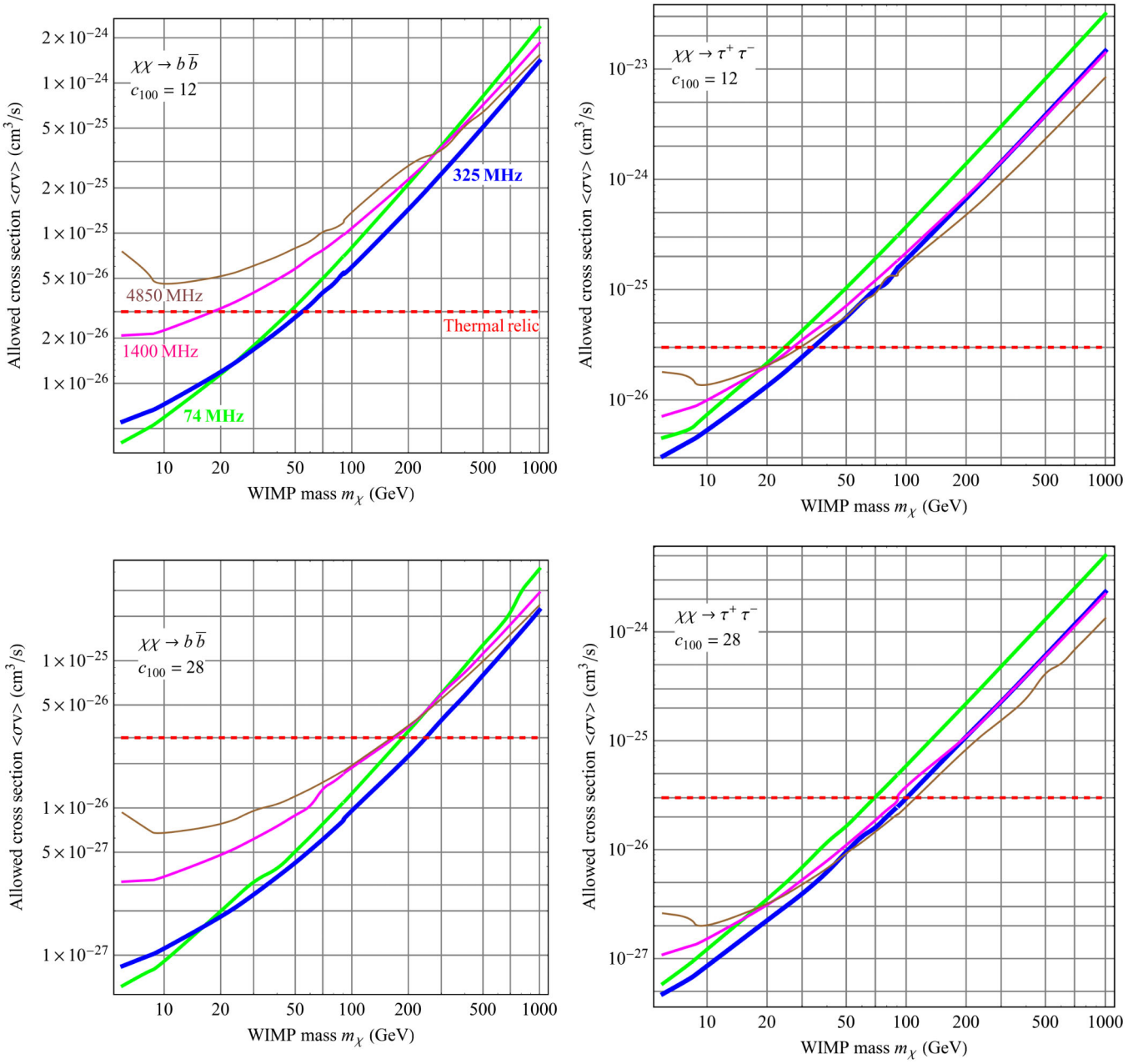


FIG. 10 (color online). All the computed constraints: the WIMP annihilation cross section values above the contours are excluded at 99.7% confidence level. Constraints from different surveys are marked by different colors and thicknesses, which are explained on one of the plots and same for all other plots. Standard thermal relic value $\langle\sigma v\rangle = 3 \times 10^{-26}$ cm^3/s is also shown by the red dashed line. The corresponding halo model and annihilation channel are commented on each plot. No emission sources besides DM are assumed. The magnetic field has the most probable distribution with $B(0, 0) = 50$ μG. For more details see Sec. III A.

gathered in the next section together with analysis of the role of magnetic field uncertainties.

B. Joint analysis and final constraints

Constraints shown in Fig. 10 present exclusion contours from four independent observations. As we can see, these contours lie rather close to each other on each diagram at least for some WIMP masses. Such a situation suggests that we apply a joint likelihood analysis in order to infer combined constraints from all four independent measurements, which we can expect to be better than the constraints taken just considering the exclusion curves in Fig. 10.

Signals other than DM are expected at each frequency. An appropriate modeling of all other astrophysical signals, with their frequency dependence, is necessary in the joint analysis of various frequency maps. We decided to make no assumptions on astrophysical processes other than DM

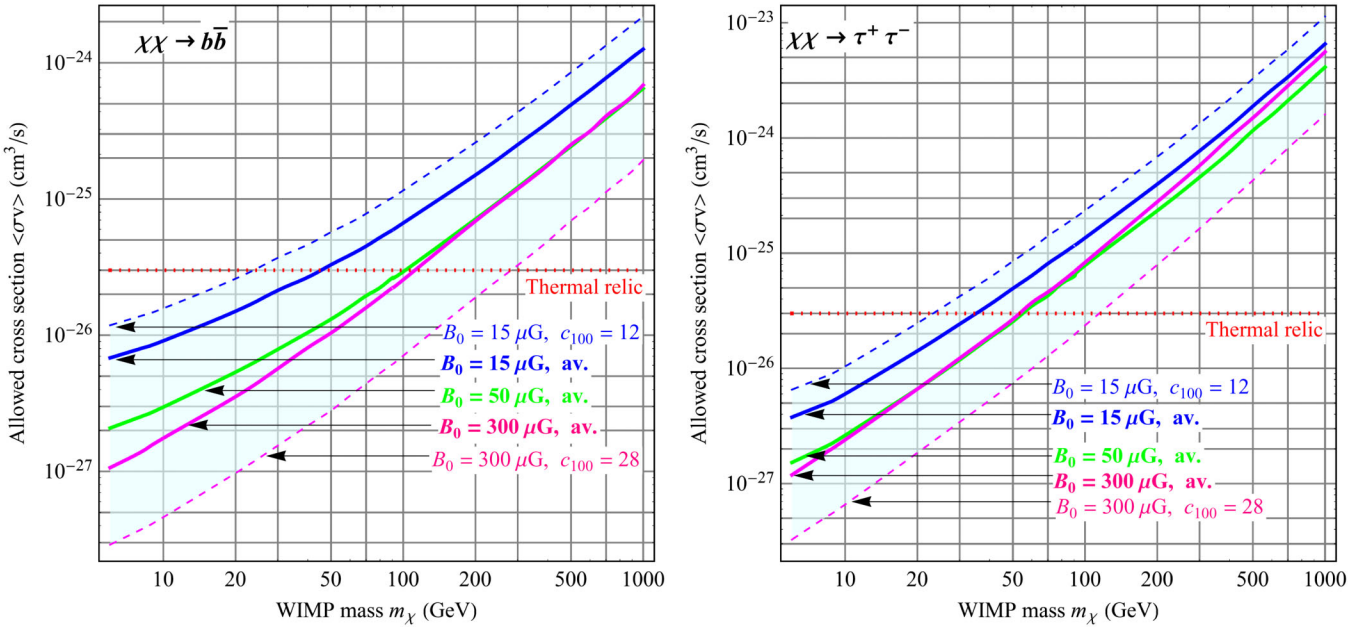


FIG. 11 (color online). Joint constraints including all radio surveys and backgrounds. These plots show all potential uncertainties of both distributions of DM density and magnetic field strength. The dashed contours reflect specific halo models discussed in the text (lines represent 99.7% confidence level). The continuous lines present averages between the exclusions for the corresponding limiting halo models. Different continuous contours illustrate the variation of exclusions due to magnetic field uncertainties. The upper and lower exclusions enclose the shaded regions of all other possible exclusions from the most conservative to the most optimistic ones. More details are in Sec. III B.

annihilation, and simply modeled the total contribution of all other background signals as an *a priori* unconstrained offset uncorrelated between frequency bands. We then performed a standard Bayesian analysis of our data. Following the Bayes theorem (for more details see [33]),

$$p(\vec{\Theta}|\vec{c}) = \frac{p(\vec{c}|\vec{\Theta})p(\vec{\Theta})}{p(\vec{c})}, \tag{20}$$

where the lhs is the desirable probability density distribution for an unknown set of parameters $\vec{\Theta}$ in the case of the observation of data $\vec{c}$, $p(\vec{c}|\vec{\Theta}) \equiv L(\vec{\Theta})$ is the probability density of our observed data $\vec{c}$ for fixed parameters $\vec{\Theta}$ (or likelihood function), $p(\vec{\Theta})$ is the prior probability density of $\vec{\Theta}$, and $p(\vec{c})$ is the marginal likelihood. In our case $\vec{\Theta} = (\langle\sigma v\rangle, s_i)$ is the set of unknown parameters, which we are aiming to infer—annihilation cross section and background radiation fluxes s_i on all four frequencies involved. $\vec{c} = (c_i)$ is the data measured. Then the likelihood function L will have the form

$$p(\vec{c}|\vec{\Theta}) = L(\vec{\Theta}) \sim \prod_{i=1}^{4} \exp\left(-\frac{(c_i - s_i - w_i(\langle\sigma v\rangle))^2}{2\sigma_i^2}\right). \tag{21}$$

This likelihood function presents essentially the product of the independent noise level Gaussian distributions on all frequencies written in terms of the measured and expected fluxes (taking into account that $c_i = s_i + w_i + n_i$). As for $p(\vec{\Theta})$, we made no specific assumptions and chose a constant (flat) prior. The function $p(\vec{c})$ in Eq. (20) does not require specification, since it does not depend on $\vec{\Theta}$ and, hence, plays a role of a normalization constant. After we constructed the five-dimensional density distribution (20) for all five unknown quantities, we needed to integrate Eq. (20) over all possible ranges of noninteresting parameters (marginalization). In our case, we were not interested in background values, so we obtained the distribution for the desired quantity $\langle\sigma v\rangle$ by marginalizing over the background values:

$$\begin{aligned} p(\langle\sigma v\rangle|\vec{c}) &\sim \int L(\vec{\Theta})p(\vec{\Theta})d\vec{s} \\ &= \iint_0^\infty \iint \prod_{i=1}^{4} \exp\left(-\frac{(c_i - s_i - w_i(\langle\sigma v\rangle))^2}{2\sigma_i^2}\right) \\ &\quad \times ds_1 \ldots ds_4, \end{aligned} \tag{22}$$

where we took into account the flat prior. Thus, formula (22) gives us the final probability density distribution for an annihilation cross section combined from all four observations with possible unknown backgrounds included. From this distribution, we easily constructed the final exclusion contours. We presented them for the case of 99.73% confidence level in Figs. 11 and 12, where the allowed area is below the exclusion contours for the corresponding models.

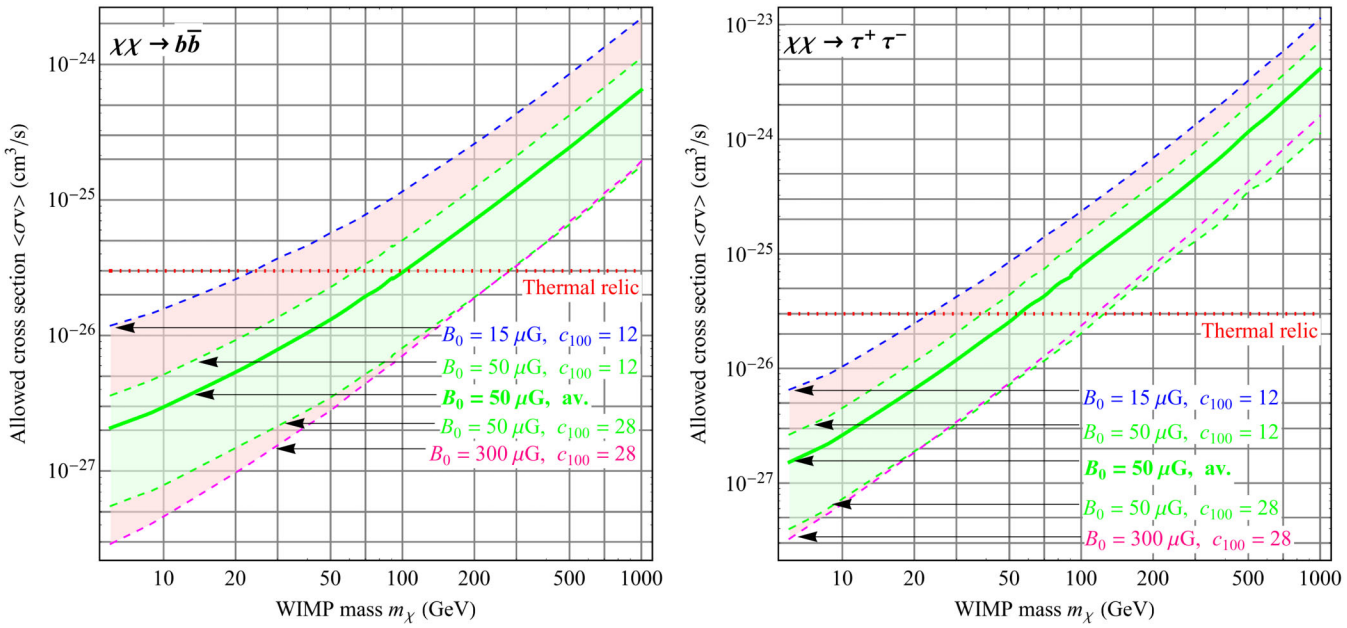


FIG. 12 (color online). Joint constraints obtained. These plots incorporate potential uncertainties of both distributions of DM density and magnetic field strength. The continuous line presents the most realistic exclusion contour, which corresponds to the result of our work on the fiducial case we assumed [average exclusion between those which correspond to the two limiting halo cases and the most realistic magnetic field distribution with $B(0, 0) = 50\ \mu$G]. The shaded area around the continuous contour, which is constrained by the dashed green lines marked as $B_0 = 50\ \mu$G, corresponds to dark halo model uncertainties only. The largest possible shaded region enclosed into the dashed lines, which are the outermost with respect to the continuous contour on each plot, incorporates both uncertainties of the dark halo and magnetic field. For more details see Sec. III B.

We included in our final results possible uncertainties in the magnetic field distribution discussed in Sec. II C. As we outlined there, this distribution is uncertain in two aspects—its vertical scale height z_0' and the central field strength $B(0, 0)$. As for the z_0', our trial runs showed that z_0' variation over all possible values is able to change the final exclusion values of $\langle\sigma v\rangle$ by no more than $\langle\sigma v\rangle^{+5\%}_{-20\%}$ for all possible sets of model parameters. This variation is considerably smaller than the one induced by, e.g., halo model uncertainties, and would suggest less conservative limits. For these reasons, we do not consider it in our final results. However, we cannot treat in this way the second important parameter—$B(0, 0)$, because practice showed significant variation of the final exclusions due to uncertainties in $B(0, 0)$ discussed in Sec. II C. According to this discussion, we expect $B(0, 0) = 50\ \mu$G to be the most probable, but we also consider here $B(0, 0)$ values of $\sim$15 and $\sim$300 μG as limiting cases. We obtained all our final exclusions for these three different magnetic field distributions.

Our results are presented in Figs. 11 and 12. In these figures, the dashed lines represent the specific halo models (either $c_{100} = 12$ or $c_{100} = 28$), while the solid lines correspond to the algebraic averages between the two limiting halo models, for fixed magnetic field values. The two figures show limiting curves for different combinations of the (three) possible magnetic field models and (two) possible halo models. Figure 11 shows more explicitly the dependence on the field strength, while Fig. 12 shows the dependence on the halo model for the reference field strength $B(0, 0) = 50\ \mu$G, and allows us to compare these uncertainties with the ones caused by variation in the magnetic field.

As we can see, annihilation with the standard thermal relic cross section $\langle\sigma v\rangle = 3 \times 10^{-26}$ cm^3/s is excluded

TABLE II. WIMP masses in GeV, below which annihilation with the canonical cross section is excluded, for the different halo and magnetic field models. The most realistic cutoff values are emphasized.

Central field $B(0, 0)$	$c_{100} = 12$, $\chi\chi \to b\bar{b}$	Averaged flux, $\chi\chi \to b\bar{b}$	$c_{100} = 28$, $\chi\chi \to b\bar{b}$	$c_{100} = 12$, $\chi\chi \to \tau^+\tau^-$	Averaged flux, $\chi\chi \to \tau^+\tau^-$	$c_{100} = 28$, $\chi\chi \to \tau^+\tau^-$
15 μG	23	45	160	23	35	88
50 μG	63	*100*	280	39	*55*	130
300 μG	75	110	280	38	53	110

for a significant part of the WIMP mass range. We listed in Table II the precise WIMP mass values for all models considered, below which $\langle\sigma v\rangle$ is less than 3×10^{-26} cm^3/s. These masses were obtained as the contact points between the corresponding exclusions and the thermal relic threshold in Figs. 11 and 12. We can see a significant spread in limiting masses around those which correspond to our preferred model with $B(0, 0) = 50$ μG and the averaged flux between two limiting halo cases. For this most realistic model the WIMP masses that do not allow the standard relic cross section are the ones smaller than 100 and 55 GeV for $b\bar{b}$ and $\tau^+\tau^-$ channels, respectively. In general, these limits were derived with rather conservative assumptions. A discussion of our results and comparison with other studies will be done in the next section.

IV. SUMMARY AND DISCUSSION

In this work, we derived constraints on the WIMP mass and annihilation cross section from radio observations of M31. Annihilating DM in M31 halo produces highly energetic secondary leptons, which, in turn, emit synchrotron radiation due to Andromeda magnetic field. We computed the expected characteristics of this radiation. We first modeled the DM density distribution in M31, using the standard NFW density profile. Previous studies ([8,19], see also [34]) of the M31 halo provide a mass determination, as well as parameters for the fit to the density distribution.

While they agree on the halo mass determination ($M_{100} \approx 10^{12} M_\odot$), they significantly differ in the quoted halo concentration parameter—$c_{100} \approx 12$ vs $c_{100} \approx 28$. We therefore treated these two cases separately and considered them as limiting cases of possible halo models for M31.

As for the modeling of the magnetic field distribution within M31, we used measured values for M31 whenever available, and some extrapolations of MW properties. This is justified by the high similarity between M31 and MW, and also by the much more detailed knowledge we have about the MW. Our reference field distribution is characterized by the 50 μG value of the central field strength and an exponential decline both in vertical and radial-in-plane directions. Then we computed the secondary particle yields from WIMP annihilation using the results of the DarkSUSY package. We neglected the spatial diffusion of the injected leptons, and we calculated expected final fluxes in optically transparent media approximation. We compared these fluxes with available radio observations of M31 spanning a wide range of frequencies: VLSS (74 MHz), WENSS (325 MHz), NVSS (1400 MHz), and GB6 (4850 MHz). This allowed us to derive limits on the cross section $\langle\sigma v\rangle$ as a function of particle mass (ranging from 6 to 1000 GeV). Our analysis is conservative in the sense of the absence of any specific assumptions about a possible radiation other than from DM. The final results are presented in Sec. III in Figs. 11 and 12. We also computed our results for the alternative less probable magnetic field models with the central field values of 15 and 300 μG in order to study the dependence of our final constraints on this model parameter.

Our main result is the exclusion of the possibility of WIMP annihilation with the thermal cross section $\langle\sigma v\rangle = 3 \times 10^{-26}$ cm^3/s or higher for WIMP masses below $\approx$100 GeV ($\approx$55 GeV) for the $b\bar{b}$ ($\tau^+\tau^-$) annihilation channel. However, these estimations are affected by significant uncertainties. Taking into account potential uncertainties in DM density and magnetic field distributions, these limits could be as low as 23 GeV and as high as 280 GeV for the $b\bar{b}$ channel. For annihilation into $\tau^+\tau^-$ these limits, respectively, are 23 and 130 GeV (see Table II).

Our results are comparable with other constraints on WIMP masses derived through other observations. The current best constraints in indirect DM searches were obtained by an analysis of Fermi observations of MW satellites [3]. The reported lowest allowed WIMP masses are 40 and 19 GeV for $b\bar{b}$ and $\tau^+\tau^-$ channels, respectively, for the case of the thermal cross section. When considering 95% systematic errors in the DM distribution within the dwarves, the derived WIMP mass lower limits vary over the ranges 19–240 GeV ($b\bar{b}$) and 13–80 GeV ($\tau^+\tau^-$).

The constraints derived in this work, implying masses above 100 and 55 GeV in order to obtain a relic cross section, are within the range of uncertainties of the current Fermi results. This shows the power of a multifrequency approach in indirect detection: all wavelength ranges may make valuable contributions toward final determinations of allowed parameter ranges. As for other studies dedicated to indirect searches at radio frequencies, we can compare our results with the similar studies for MW [10] and M33 [21]. Our constraints are significantly stronger than the last cited, since the exclusion contours obtained by the authors of [10,21] lie well above the thermal relic value $\langle\sigma v\rangle = 3 \times 10^{-26}$ cm^3/s on the WIMP mass-annihilation cross section plane for any possible WIMP masses ($\langle\sigma v\rangle \lesssim 10^{-24}$ cm^3/s there). Also we can compare our results with the slightly newer work [35] dedicated to the MW gamma and radio constraints. This work reported the relatively stronger exclusions in comparison with, e.g., [10]: $\langle\sigma v\rangle \lesssim 3 \times 10^{-26}$ cm^3/s for the best combinations of parameters (including WIMP mass). However, [35] exclusions are still weaker than ours for M31, as can be seen from Figs. 11 and 12.

We show here, for the first time, that it is possible to constrain the WIMP parameter space significantly employing radio observations of M31. Specifically, while making conservative assumptions, we were able to exclude small WIMP masses for conventional, thermally produced DM. However, the range of higher masses of hundreds GeV is still absolutely allowed and unexplored. This paper presents only the first relatively simple step in a comprehensive analysis of M31, and does not yet include all

potential uncertainties and relevant effects. Particularly, in order to increase an overall level of precision and reliability of our model, it would be necessary to properly introduce the spatial diffusion of annihilation products in our calculations, as this may play some non-negligible role (see Appendix B for an initial estimate). The advantage of the current diffusion-free model resides in its simplicity: our semianalytical results are not affected by large uncertainties related to lepton propagation. This simple model revealed a high constraining potential of M31 in indirect searches. Thus, this first step can be a motivation for a DM community for much more extended investigations of M31. Overall, this work may be expanded in two main directions. First, astrophysical uncertainties can be treated with a more general approach, including further studies of the lepton propagation, magnetic field uncertainties, interstellar radiation field distribution, and others. In addition, while encouraged by current findings, the potential to study this object with other current and upcoming radio telescopes may be explored.

ACKNOWLEDGMENTS

We would like to thank Wendy Lane, the Principal Investigator of the VLSS radio survey, for valuable discussions regarding observational aspects. Also, we are grateful to Jennifer Siegal-Gaskins for generally useful feedback. E. P. acknowledges support from JPL-Planck Subcontract No. 1290790. E. P. and A. E. E. were partially supported by NASA Grant No. NNX07AH59G. We acknowledge the use of the Legacy Archive for Microwave Background Data Analysis (LAMBDA), part of the High Energy Astrophysics Science Archive Center (HEASARC). HEASARC/LAMBDA is a service of the Astrophysics Science Division at the NASA Goddard Space Flight Center [7].

Note added in proof.—While our work was in preparation, the newer study [34] of the M31 dark halo was published. This study reported a quite similar value for the M_{100} and $c_{100} \approx 17$ for the NFW profile. Since the value quoted for the concentration is in between the ones we considered, the implied constraints would lie within our current uncertainty regions for the case of the NFW profile.

APPENDIX A: ABSORPTION ANALYSIS

Here we discuss all potentially relevant mechanisms of absorption of radio emission during its propagation from the M31 center to the observer. We focused only on a potential absorption inside M31 and did not consider possible absorption in MW, because the Andromeda galaxy lies far enough from the galactic plane, and we do not expect any significant absorption in this direction on the sky. In general, inside the Andromeda there are two main agents of interstellar medium relevant for our purposes: a dust and an ionized gas. Among them a dust can be excluded as an absorber rather easily: typically a dust grain size does not exceed 10^{-4} cm (see, e.g., [36]). And the wavelengths of radio emission involved are 10–1000 cm, which is many orders of magnitude larger than grain sizes. In such a case, when a wavelength is much greater than an obstacle size, it is well known that radiation does not interact with obstacles. Thus, we can conclude that a dust does not affect radiation in the considered frequency range.

A situation with the absorption by interstellar plasma is more tricky. Here we can distinguish several possible ways of absorption. First of all, let us check the Langmuir frequency of plasma involved. As is well known, a radiation cannot propagate through plasma if its frequency is less than the Langmuir frequency of the propagation medium. The Langmuir frequency is defined as

$$\nu_{\rm pl} = \frac{\omega_{\rm pl}}{2\pi} = \sqrt{\frac{e^2 n}{\pi m_e}}, \tag{A1}$$

where n is the concentration of plasma electrons which needs to be estimated. For this purpose we used the results of [12], where the gas density distribution was obtained for the central region of MW. Taking into account that MW and M31 are very similar galaxies, we can extrapolate results for MW on M31 staying at the necessary level of accuracy. From [12] we can easily see that the plasma concentration in a Galactic center cannot exceed $n \lesssim 10\ {\rm cm}^{-3}$ in the worst case, which yields $\nu_{\rm pl} \lesssim 30$ kHz. Thus, the Langmuir frequency is much smaller than the observational frequencies of MHz-GHz, which means that the interstellar plasma is transparent with respect to this absorption mechanism.

Another potentially relevant mechanism is a synchrotron self-absorption. Synchrotron emission, generated by relativistic leptons from DM annihilation, can be absorbed by neighbor emitting leptons. In order to estimate the level of this absorption quantitatively we computed the corresponding optical depth along our line of sight, which goes through the M31 center:

$$\tau_{ss} = \int_{\rm los} \alpha_{ss} dl, \tag{A2}$$

where α_{ss} is the synchrotron self-absorption coefficient. We used the derived expression for α_{ss} from [37] [formula (6.50) there]:

$$\alpha_{ss} = -\frac{c^2}{8\pi\nu^2} \int_{m_e c^2}^{m_\chi c^2} dE P_e(E, \nu, \vec{r}) \cdot E^2 \frac{\partial}{\partial E} \times \left(E^{-2} \cdot 2 \frac{dn_e}{dE}(E, \vec{r}) \right), \tag{A3}$$

where $P_e(E, \nu, \vec{r})$ is the synchrotron power of one lepton defined by Eqs. (3) and (4), $\frac{dn_e}{dE}(E, \vec{r})$ is the stationary energy spectrum of emitting leptons of one kind derived by Eq. (6). Then we substituted all relevant values of

the parameters involved. Particularly, for WIMP mass and frequency of observations we used as an example $m_\chi = 100$ GeV and $\nu = 74$ MHz. Such a combination of all parameters yields $\tau_{ss} \sim 10^{-3}$, which means that we can neglect by synchrotron, self-absorption completely and reliably. And this conclusion is valid for all other frequencies used in our work, because α_{ss} decreases with frequency and 74 MHz is the lowest frequency of observations. In general, this conclusion agrees with the results of [6], where the authors solved a similar DM annihilation problem with an application to MW. And they also showed an irrelevance of synchrotron self-absorption on all frequencies.

And the last potential absorption mechanism, which has to be checked, is a free-free absorption by plasma. Here we also estimated the corresponding optical depth:

$$\tau_{ff} = \int_{\text{los}} \alpha_{ff} dl, \tag{A4}$$

where the absorption coefficient α_{ff} was also taken from [37] [formula (5.18b) there]:

$$\alpha_{ff} = 3.7 \times 10^8 T^{-1/2} Z^2 n^2 \nu^{-3} \left(1 - \exp\left(-\frac{h\nu}{kT}\right)\right) g_{ff}, \tag{A5}$$

where n and T are the plasma concentration and temperature, respectively. As for the spatial distribution $n(\vec{r})$, it does not appear to be obtained in the literature for M31. That is why we decided to use such distribution for MW again as an approximation. Taking all relevant information from [12] and assuming $g_{ff} \approx 1$ and $Z = 1$ (hydrogen plasma) we estimated $\tau_{ff} \lesssim 0.01$ in the worst case scenario. Thus, we can see that the free-free absorption is not relevant for our work as well in the first approximation.

Summarizing, in this section we have conducted the detailed analysis of all potentially relevant absorption mechanisms of radio emission generated by DM annihilation. None of these mechanisms achieves a significant level. This conclusion is in agreement with similar studies [6,10] for the MW. Thus, we can ignore any absorption in our analysis without significant loss of accuracy.

APPENDIX B: SPATIAL DIFFUSION OF ANNIHILATION PRODUCTS

Here we study the role of the spatial diffusion of annihilation products in our problem. In order to understand the importance of the spatial diffusion for our final results, we should compare the characteristic distance, which annihilation products travel while they are emitting relevant radiation, with the characteristic size of the emitting region. According to, e.g., [10], the diffusion path traveled by leptons can be calculated as $l_D = \sqrt{D(E)\tau_{\text{loss}}(E)}$, where $D(E)$ is the diffusion coefficient for leptons participating in

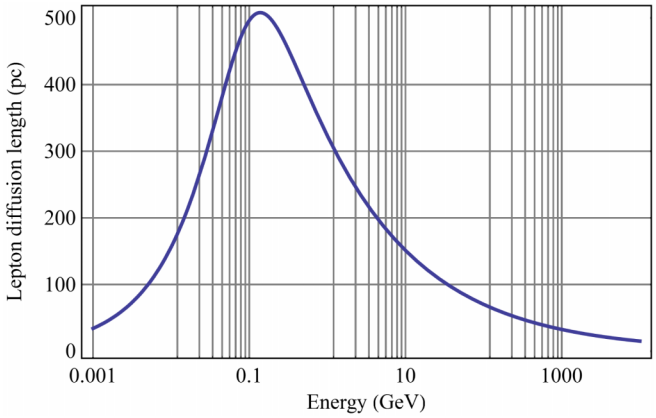


FIG. 13 (color online). The dependence of the lepton diffusion length l_D on the energy E. The magnetic field used is $B = 50\ \mu$G; the concentration is $n = 0.1$ cm^{-3}.

Eq. (5); $\tau_{\text{loss}}(E)$ is the cooling time of leptons, during which they are emitting the expected radiation and losing their energy until escaping the relevant energy domain. We took the diffusion coefficient $D(E)$ from [10], where it is provided for the MW, and expected to work roughly for the Andromeda galaxy as well:

$$D(E) = D_0 \left(\frac{E}{E_0}\right)^\delta, \tag{B1}$$

with $D_0 = 10^{28}$ cm^2/s, $E_0 = 3$ GeV, and a Kolmogorov spectrum $\delta = 1/3$. The cooling time for leptons can be estimated as

$$\tau_{\text{loss}}(E) \sim \frac{E}{\dot{E}} = \frac{E}{b(E, \vec{r})}, \tag{B2}$$

where $b(E, \vec{r}) = b_{\text{ICS}} + b_{\text{sync}} + b_{\text{brem}} + b_{\text{Col}}$ [see Eqs. (8)–(11)]. After all necessary substitutions we obtained l_D dependence on the lepton energy E, which is shown in Fig. 13. For the magnetic field B and the concentration n we used the expected values for the M31 center, $\sim 50\ \mu$G and ~ 0.1 cm^{-3}, respectively. These parameter values were justified the Sec. II. As we can see in Fig. 13, the lepton diffusion path over the relevant range of energies does not exceed ~ 500 pc. Our emitting region, which we capture by our ROI with angular radius $\alpha \approx 5'$, would have the form of the cylinder with the radius $\rho_{\max} \approx \alpha d \approx 1100$ pc. Thus, the smallest size of the emitting region is about 2 times larger than the diffusion length of leptons in the M31 center. It means, in turn, that the leptons do not have enough time to migrate significantly and escape from the emitting volume before they cool down and discontinue radiation. Also taking into account the fact that the majority of total radiation flux due to DM annihilation is formed in the very central region, we can conclude that inclusion of the spatial diffusion in our calculations should not affect our results significantly. And neglecting by the diffusion is an acceptable approximation in our

computation procedure. Such a conclusion is in general agreement with the work [10] where the similar procedure of constraints derivation was conducted for the MW. However, since the spatial scale of the emitting volume and the lepton diffusion path do not differ drastically, we will allow an opportunity to include the diffusion in our calculations in a future work in order to improve the accuracy of our results.

[1] G. Bertone, *Particle Dark Matter: Observations, Models and Searches* (Cambridge University Press, Cambridge, England, 2010).
[2] J. L. Feng, M. Kaplinghat, and H.-B. Yu, Phys. Rev. D **82**, 083525 (2010).
[3] A. Geringer-Sameth and S. M. Koushiappas, Phys. Rev. Lett. **107**, 241303 (2011).
[4] J. Lavalle *et al.*, Astron. Astrophys. **450**, 1 (2006).
[5] M. Fornasa, M. Taoso, and G. Bertone, Phys. Rev. D **76**, 043517 (2007).
[6] M. Regis and P. Ullio, Phys. Rev. D **78**, 043505 (2008).
[7] http://lambda.gsfc.nasa.gov/.
[8] E. Corbelli, S. Lorenzoni, R. Walterbos, R. Braun, and D. Thilker, Astron. Astrophys. **511**, A89 (2010).
[9] S. Colafrancesco, S. Profumo, and P. Ullio, Astron. Astrophys. **455**, 21 (2006).
[10] E. Borriello, A. Cuoco, and G. Miele, Phys. Rev. D **79**, 023518 (2009).
[11] M. Longair, *High Energy Astrophysics* (Cambridge University Press, Cambridge, England, 2011).
[12] K. Ferrière, W. Gillard, and P. Jean, Astron. Astrophys. **467**, 611 (2007).
[13] http://www.marcocirelli.net/PPPC4DMID.html.
[14] M. Cirelli, G. Corcella, A. Hektor, G. Hütsi, M. Kadastik, P. Panci, M. Raidal, F. Sala, and A. Strumia, J. Cosmol. Astropart. Phys. 03 (2011) 051.
[15] P. Ciafaloni, D. Comelli, A. Riotto, F. Sala, A. Strumia, and A. Urbano, J. Cosmol. Astropart. Phys. 03 (2011) 019.
[16] J. F. Navarro, C. S. Frenk, and S. D. M. White, Astrophys. J. **490**, 493 (1997).
[17] A. W. Graham, D. Merritt, B. Moore, J. Diemand, and B. Terzić, Astron. J. **132**, 2701 (2006).
[18] V. Springel, J. Wang, M. Vogelsberger, A. Ludlow, A. Jenkins, A. Helmi, J. F. Navarro, C. S. Frenk, and S. D. M. White, Mon. Not. R. Astron. Soc. **391**, 1685 (2008).
[19] J. J. Geehan, M. A. Fardal, A. Babul, and P. Guhathakurta, Mon. Not. R. Astron. Soc. **366**, 996 (2006).
[20] M. Kamionkowski, S. M. Koushiappas, and M. Kuhlen, Phys. Rev. D **81**, 043532 (2010).
[21] E. Borriello, G. Longo, G. Miele, M. Paolillo, B. B. Siffert, F. S. Tabatabaei, and R. Beck, Astrophys. J. Lett. **709**, L32 (2010).
[22] A. Fletcher, E. M. Berkhuijsen, R. Beck, and A. Shukurov, Astron. Astrophys. **414**, 53 (2004).
[23] R. M. Crocker, D. I. Jones, F. Melia, J. Ott, and R. J. Protheroe, Nature (London) **463**, 65 (2010).
[24] R. Beck, Space Sci. Rev. **166**, 215 (2012).
[25] P. Hoernes, R. Beck, and E. M. Berkhuijsen, in *The Central Regions of the Galaxy and Galaxies*, edited by Y. Sofue, Proceedings of the 184th Symposium of the International Astronomical Union, Kyoto, Japan, 1997 (Kluwer, Dordrecht, 1998), Vol. 184, p. 351.
[26] M. Haverkorn and V. Heesen, Space Sci. Rev. **166**, 133 (2012).
[27] R. P. van der Marel and M.-R. L. Cioni, Astron. J. **122**, 1807 (2001).
[28] A. S. Cohen, W. M. Lane, W. D. Cotton, N. E. Kassim, T. J. W. Lazio, R. A. Perley, J. J. Condon, and W. C. Erickson, Astron. J. **134**, 1245 (2007).
[29] R. B. Rengelink, Y. Tang, A. G. de Bruyn, G. K. Miley, M. N. Bremer, H. J. A. Röttgering, and M. A. R. Bremer, Astron. Astrophys. Suppl. Ser. **124**, 259 (1997).
[30] J. J. Condon, W. D. Cotton, E. W. Greisen, Q. F. Yin, R. A. Perley, G. B. Taylor, and J. J. Broderick, Astron. J. **115**, 1693 (1998).
[31] J. J. Condon, J. J. Broderick, G. A. Seielstad, K. Douglas, and P. C. Gregory, Astron. J. **107**, 1829 (1994).
[32] F. Bonnarel, P. Fernique, O. Bienaymé, D. Egret, F. Genova, M. Louys, F. Ochsenbein, M. Wenger, and J. G. Bartlett, Astron. Astrophys. Suppl. Ser. **143**, 33 (2000).
[33] R. Trotta, Contemp. Phys. **49**, 71 (2008).
[34] A. Tamm, E. Tempel, P. Tenjes, O. Tihhonova, and T. Tuvikene, Astron. Astrophys. **546**, A4 (2012).
[35] R. M. Crocker, N. F. Bell, C. Balázs, and D. I. Jones, Phys. Rev. D **81**, 063516 (2010).
[36] E. Casuso and J. E. Beckman, Astron. J. **139**, 1406 (2010).
[37] G. Rybicki and A. Lightman, *Radiative Processes in Astrophysics* (WILEY-VCH Verlag GmbH, Weinheim, 2004).

Available online at www.sciencedirect.com

ScienceDirect

Advances in Space Research 63 (2019) 3420–3427

ADVANCES IN SPACE RESEARCH (a COSPAR publication)

www.elsevier.com/locate/asr

Multiple Coulomb scattering method to reconstruct low-energy gamma–ray direction in the GAMMA-400 space-based gamma–ray telescope

A.A. Leonov [a,b,*], A.M. Galper [a,b], N.P. Topchiev [a], A.V. Bakaldin [a,c], O.D. Dalkarov [a], E.A. Dzhivelikyan [b], A.E. Egorov [a], M.D. Kheymits [b], V.V. Mikhailov [b], P. Picozza [d,e], R. Sparvoli [d,e], S.I. Suchkov [a], Yu.T. Yurkin [b], V.G. Zverev [a]

[a] Lebedev Physical Institute, Russian Academy of Sciences, Moscow 119991, Russia
[b] National Research Nuclear University MEPhI, Moscow 115409, Russia
[c] Scientific Research Institute for System Analysis, 117218 Moscow, Russia
[d] Istituto Nazionale di Fisica Nucleare, Sezione di Roma 2, Rome, Italy
[e] Physics Department of University of Rome Tor Vergata, Rome, Italy

Received 9 November 2018; received in revised form 16 January 2019; accepted 24 January 2019
Available online 1 February 2019

Abstract

The GAMMA-400 currently developing space-based gamma-ray telescope is designed to measure the gamma-ray fluxes in the energy range from ~20 MeV to several TeV in the highly elliptic orbit (without shadowing the telescope by the Earth) continuously for a long time. The physical characteristics of the GAMMA-400 gamma-ray telescope, especially the angular and energy resolutions (at 100-GeV gamma rays they are ~0.01° and ~1%, respectively), allow us to consider this space-based experiment as the next step in the development of extraterrestrial high-energy gamma-ray astronomy. In this paper, a method to improve the reconstruction accuracy of incident angle for low-energy gamma rays in the GAMMA-400 space-based gamma-ray telescope is presented. The special analysis of topology of pair-conversion events in thin layers of converter was performed. Applying the energy dependence of multiple Coulomb scattering for pair components, it is possible to estimate the energies for each particle, and to use these energies as weight in the angle reconstruction procedure. To identify the unique track in each projection the imaginary curvature method is applied. It allows us to obtain significantly better angular resolution in comparison with other methods applied in current space-based experiments. When using this method for 50-MeV gamma rays the GAMMA-400 gamma-ray telescope angular resolution is about 4°.
© 2019 COSPAR. Published by Elsevier Ltd. All rights reserved.

Keywords: Gamma-ray; Converter-tracker; Angular resolution; GEANT4 simulation toolkit; Coulomb scattering

1. Introduction

The GAMMA-400 instrument was developed to solve a broad range of scientific goals, such as sensitive searching for high-energy gamma-ray emission when annihilating or decaying dark matter particles and searching for new and studying known Galactic and extragalactic discrete high-energy gamma-ray sources (supernova remnants, pulsars, accreting objects, microquasars, active galactic nuclei, blazars, quasars, etc.) (Topchiev et al., 2016a, 2016b). The major advantage of the GAMMA-400 instrument is excellent angular and energy resolutions for gamma rays above 10 GeV. The gamma-ray telescope angular and energy

* Corresponding author.
E-mail address: leon@ibrae.ac.ru (A.A. Leonov).

https://doi.org/10.1016/j.asr.2019.01.039
0273-1177/© 2019 COSPAR. Published by Elsevier Ltd. All rights reserved.

resolutions for the main aperture at 100-GeV gamma rays are ~0.01° and ~1%, respectively. Thus, it will be possible to study the structure of astrophysical objects with high angular resolution, measuring their energy spectra and luminosity with high-energy resolution and identifying discrete gamma-ray sources with known sources of electromagnetic emission in other energy ranges.

The motivation of presented results is to provide the methodical approaches improving physical characteristics of the GAMMA-400 gamma-ray telescope in the energy range of ~20–100 MeV, most unexplored range today (De Angelis et al., 2018). Gamma-ray observations in this energy range are crucial today for a number of high-priority problems faced by modern astrophysics and fundamental physics, including the origin of chemical elements and cosmic rays, the nature of dark matter, and the applicability range of the fundamental laws of physics.

The location of the high-energy gamma-ray sources in the Universe is determined through the reconstruction of the directions of gamma rays. In the GAMMA-400 gamma-ray telescope, this direction is measured via the conversion of gamma rays in thin tungsten foils in the converter-tracker and the subsequent reconstruction of the electron/positron pair with a precise silicon tracker. The energy measurement is provided by calorimeter. The converter introduces, however, an unavoidable error in the direction determination due to the multiple Coulomb scattering of the trajectory of particles. It is crucial to understand how the multiple scattering affects the reconstruction of angular resolution. The detector layers of the GAMMA-400 converter-tracker will provide the measurements of electron/positron tracks (with measurement errors). Depending on the energy of electrons, the effects of multiple scattering can be larger, the same, or smaller than the effects of measurement error. Large uncertainties in the arrival directions of gamma rays hamper the analysis of point sources at energies below 100 MeV. As a result, the confusion among point sources, difficulties in separating point sources from diffuse emission and high contamination from the Earth limb are arisen. The attempt to close a gap of point source analysis between the COMPTEL (<30 MeV) (Schonfelder et al., 2000) and the Fermi-LAT catalogs (>100 MeV) (Acero et al., 2015; Ackermann et al., 2013) was recently provided through the construction of first Fermi Large Area Telescope low-energy catalog (1FLE) (Principe et al., 2018). The accuracy of angle and energy reconstructions is insufficient, and special wavelet transform procedure was used to extract the point sources.

Usually, in the track reconstruction methods, like Kalman filter (Giuliani et al., 2006), multiple scattering is considered as a noise, which contaminates the main signal. In this paper, to determine incident gamma-ray direction in the telescope, we propose to use the energy dependence of multiple scattering for pair components induced by gamma-ray conversion with energy less than 100 MeV. Such approach is the further development of the procedure proposed previously in (Leonov et al., 2017). In this way, we consider only three first planes of pair components in each projection that is enough to evaluate the energy weights for the electron/positron angles. These energy weights are further used to calculate incident gamma-ray direction. The calculation considers several approximations, such as the assumption of a Gaussian distribution of the multiple scattering (ignoring the important non-Gaussian tails) or neglecting the effects of the recoil of nucleus. There are other instrumental problems not considered here, like the pattern recognition, inefficiencies, and dead areas. However, this calculation provides a quantitative improvement of angular resolution at energies below 100 MeV.

2. The GAMMA-400 physical scheme

The GAMMA-400 physical scheme is shown in Fig. 1. GAMMA-400 consists of plastic scintillation top and lateral detectors (ACtop and AClat) forming anticoincidence system, a converter-tracker (C), plastic scintillation detectors (S1 and S2) for a time-of-flight system (ToF), a two-part calorimeter (CC1 and CC2), plastic scintillation detectors (S3 and S4) forming additional trigger.

The anticoincidence detectors surrounding the converter-tracker are used to distinguish gamma rays from significantly larger number of charged particles (in the energy range of 10–100 GeV, the flux ratios for gamma rays to electrons and protons are $\sim 1{:}10^2{:}10^5$ (Moiseev et al., 2007)).

All scintillation detectors consist of two independent layers, with thickness of 1 cm for each layer. The time-of-flight system, where detectors S1 and S2 are separated by approximately 500 mm, determines the top-down direction of arriving particles. The dimensions and location of detectors S1 and S2 determines gamma-ray telescope field of view (FoV), which is about ±45°.The additional scintillation detectors S3 and S4 improve hadrons and electromagnetic showers separation.

The converter-tracker consists of 13 layers of double (x, y) silicon strip coordinate detectors (pitch of 0.08 mm). The first seven layers are interleaved with tungsten conversion foils with 0.1 X_0 (where X_0 is the radiation length), next four layers are interleaved with tungsten conversion foils with 0.025 X_0 and final two layers have no tungsten. Using the four 0.025 X_0 layers allows us to measure gamma rays down to 20 MeV. In this case, the gamma-ray trigger for the energy range of 20–100 MeV and 100 MeV – 1000 GeV is the same: $\overline{AC} \times$ ToF. The total converter-tracker thickness is ~1 X_0. The converter-tracker information is used to precisely determine the direction of each incident particle. The accuracy of the determination of incident particle direction is the goal for the studying in this paper.

The two-part calorimeter measures the particle energy. The CC1 imaging calorimeter consists of 2 layers of double (x, y) silicon strip coordinate detectors (pitch of 0.08 mm)

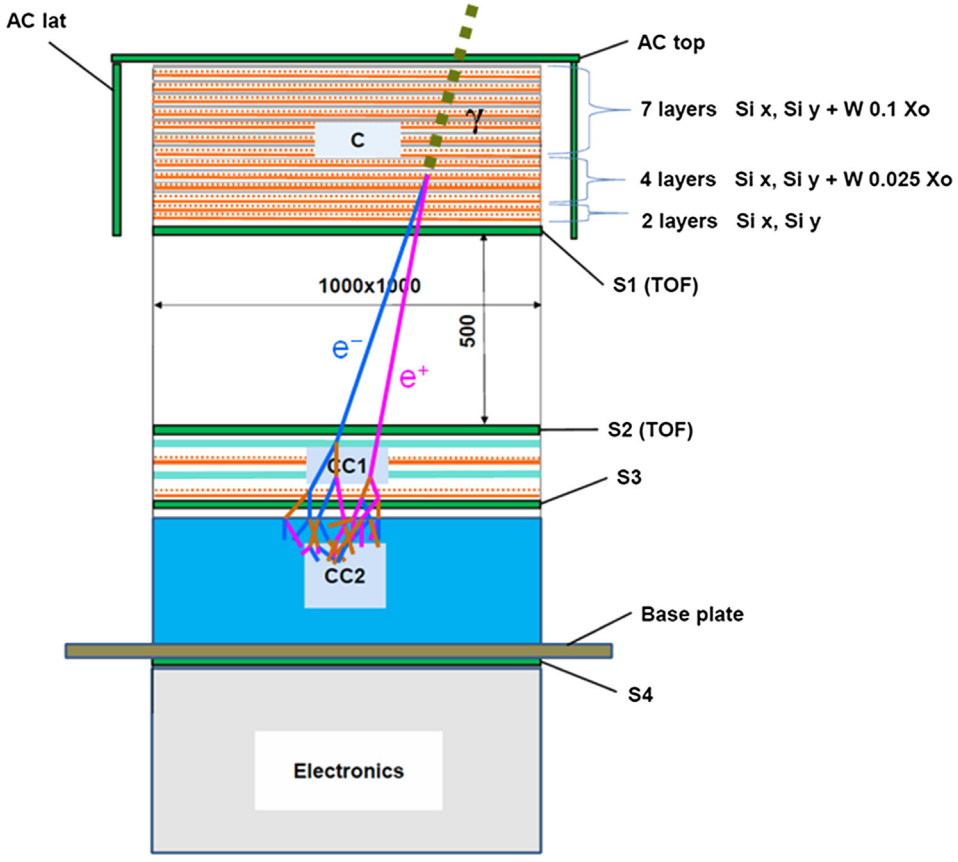


Fig. 1. The GAMMA-400 physical scheme.

interleaved with planes from CsI(Tl) crystals, and the CC2 electromagnetic calorimeter consists of CsI(Tl) crystals. The thickness of CC1 and CC2 is 2 X_0 and 20 X_0, respectively. The total calorimeter thickness is ~22 X_0 or ~1 λ_0 (where λ_0 is the nuclear interaction length). Using the deep calorimeter allows us to extend the energy range up to several TeV for gamma rays and ~10 TeV for electrons + positrons and to reach an energy resolution about ~1% at 100 GeV.

3. Simulation environment and data for the calculations

For simulating the passage of gamma rays through the GAMMA-400 matter, the GEANT4 toolkit (Allison et al., 2016) was used. Angular resolution was calculated for vertical gamma rays with energies from 10 to 150 MeV, which were converted into the electron/positron pair at first or any following tungsten conversion foil with 0.025 X_0. For such events the information about the strip numbers with signal from energy release of charged particles and the values of energy release are retained. Gamma rays can also convert in the rest of the converter-tracker tray containing support matter, but these events are not considered here. The detailed description of material composition of this tray and the methodology to identify the tungsten conversion events are presented in (Leonov et al., 2017).

To calculate the energy dependence of multiple Coulomb scattering for pair components vertical and declined (30^0) electrons with different energies were also generated.

4. Reconstruction of low-energy gamma-ray direction

Electron/positron passing through the converter-tracker matter suffers multiple elastic Coulomb scattering on nuclei. Since mass of nuclei is greater than incoming electron/positron, the energy transfer is negligible, but each scattering center adds a small deviation to the incoming particle trajectory. Even if this deviation is small the sum of all contributions adds a random component to the particle track. As a result, the initial direction of incoming electron/positron is changed. When the thickness of matter increases and the number of interactions becomes high, the angular dispersion can be modelled as Gaussian.

When the energy of the incident gamma rays is less than 150 MeV, each component of e^+/e^- pair produced after conversion in tungsten layer can be readily tracked individually.

The information from double (x, y) silicon strip coordinate detectors provides the possibility to split the total space development of conversion event in two perpendicular plane projections. Each projection, called as X or Y, is considered independently.

For the next analysis, gamma rays converted in thin (0.025 X_0) tungsten layers are only considered. In the converter-trackers, even if there is only one hit, due to capacitive coupling between adjacent strips, multiple strip segments are fired. But, taking into account the possibility of analog readout, the evaluation of the cluster position by means of the center of gravity method allows us to improve significantly the spatial resolution of strip sample and tracking accuracy (Berra et al., 2015). In the following for the sake of simplicity the tracks, consisting from single points (calculated as center of cluster position, if necessary) are considered.

For each event, presented by two tracks of e^+/e^- pair, the information about hit strips in first three X planes and in first three Y planes is used. The left strips with hits in each projection make "left" track (for electron, as example) and the right strips with hits make "right" track (for positron, as example). It is necessary to mention that strictly speaking, the two tracks cannot be surely identified, as pair components can cross and alter their relative position to the opposite one from one layer to another, but with low probability in the GAMMA-400 converter-tracker (Kheymits et al., 2015).

Fig. 2 shows red and purple piecewise lines for electron and positron tracks, respectively. Thus, each track contains six points: three points in the X projection and three points in the Y projection. The first point in the X projection, which is closest to the conversion point in tungsten, is common for both tracks ($x_0^- = x_0^+$). In this interpretation, one delicate point is arisen. How is it possible to determine the correspondence between the "left" and "right" tracks in different projections?

To resolve the problem the following procedure is applied.

For given projection each track of electron or positron due to multiple Coulomb scattering can be represented as three points in successive layers of converter-tracker, through which a circle can be uniquely drawn with the imaginary curvature radius. In this way, for the X projection in left part of Fig. 2, there are two values: R_x^L and R_x^R, corresponding to the "left" X electron track and the "right" X positron track, respectively. In the same manner, the values R_y^L and R_y^R for the Y projection correspond to the "left" Y positron and "right" Y electron tracks, respectively. The reasonable assumption is that the track of more energetic particle has higher imaginary curvature radius in both projections. For the case, shown in Fig. 2 ($R_x^L > R_x^R$, $R_y^L < R_y^R$), the left track in the projection X and the right track in the projection Y belong to the electron track, while the right track in the projection X and the left track in the projection Y belong to the positron track.

Using the value of strip size and the value of vertical distance between the planes with silicon strip coordinate detectors it is straight forward to calculate plane angles with vertical for e^+/e^- pair: α_x^-, α_x^+ and α_y^-, α_y^+ (Fig. 3). From these plane angles for e^+/e^- pair and using the conservation of initial gamma-ray transverse momentum through relativistic e^+/e^- components the plane angles of initial gamma are derived as following:

$$\alpha_x = \frac{\alpha_x^- \times E^- + \alpha_x^+ \times E^+}{E^- + E^+} \quad (1)$$

$$\alpha_y = \frac{\alpha_y^- \times E^- + \alpha_y^+ \times E^+}{E^- + E^+}, \quad (2)$$

where E^-, E^+ are the energies of electron and positron, respectively.

Unlike the previous approach (Leonov et al., 2017), in which the energies of electron and positron were calculated for each projection independently using the dependence of imaginary curvature radius from energy, here, we determine the energies of electron and positron using the direct dependence of multiple Coulomb scattering from the energy, as ~1/E.

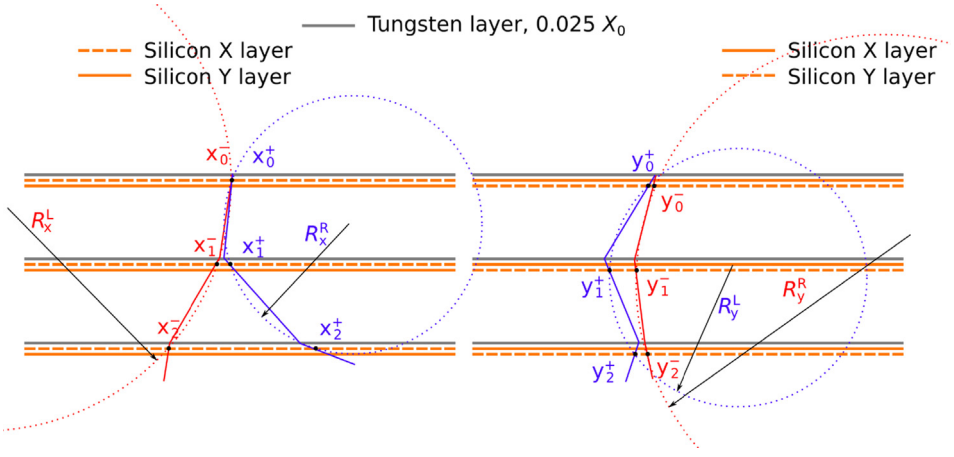


Fig. 2. Two tracks of e^+/e^- pair in X (left) and Y (right) projections. Gray lines are tungsten layers with thickness 0.025 X_0. Orange lines are double (x, y) silicon strip coordinate detectors. (For interpretation of the references to colour in this figure legend, the reader is referred to the web version of this article.)

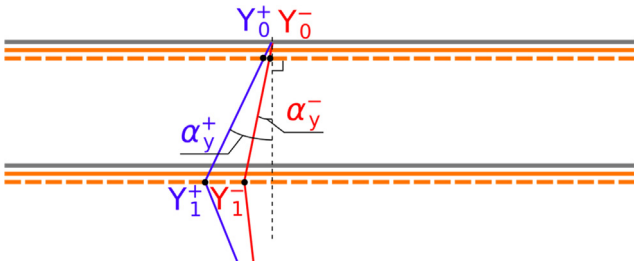


Fig. 3. Plane angles with vertical for e^+/e^- pair in the Y projection.

To obtain the dependence of multiple Coulomb scattering from energy of electron/positron in the GAMMA-400 converter-tracker the simulation of electron beam along vertical direction at first thin tungsten foil (0.025 X_0) was performed for energy range from 10 to 500 MeV. Two plane angles of electron trajectory were determined and retained for the *X* projection and also for the *Y* projection. The number of plane angles (two in the *X* projection and two in the *Y* projection) is an optimal value due to the track length of low energy particles in converter-tracker and in view of the generation of multiple tracks in several converter layers.

Fig. 4 shows an example of electron trajectory in the GAMMA-400 converter-tracker, which is marked by blue line. Three scattering points in tungsten layers are shown by black points. Magenta broken line corresponds to the trajectory restored using information from silicon strip detectors due to the converter-tracker granularity.

Plane angle $\alpha_{x1}^{strip} = \alpha_{x1}$ is the estimation of the electron trajectory deviation after the multiple Coulomb scattering in first and second tungsten layers. It is calculated using the information from first and second planes of silicon strip coordinate detectors. Plane angle α_{x2}^{strip} is the estimation of the electron trajectory deviation after the multiple Coulomb scattering in first, second, and third tungsten layers. It is calculated using the information from second and third planes of silicon strip coordinate detectors. Plane angle α_{x2} is the estimation of the electron trajectory deviation after the multiple Coulomb scattering in third tungsten layer. It is calculated subtracting electron trajectory deviation in first and second tungsten layers: $\alpha_{x2} = \alpha_{x2}^{strip} - \alpha_{1x}$. Plane angles α_{y1} and α_{y2} are calculated in the same manner.

Fig. 5a and b show the couple of distributions for plane angles α_{x1}, α_{y1} and α_{x2}, α_{y2} resulting from vertical electron beam with energy of 10 MeV, respectively. All these distributions are very similar and have approximately the same shape and width. Fig. 5c shows the total distribution including for each event the values: α_{x1}, α_{y1}, α_{x2}, and α_{y2}. Combining the Gaussians of these angles into one quantity assumes that there is negligible energy lost in each tracker-converter layer, thus causing the scattered angle distribution to be similar. The distributions in Fig. 5 are centered at 0^0 angle, as each elementary act of scattering has equal probability for any direction. Each distribution can be approximated by Gaussian due to the Central Limit Theorem, because each elementary act of scattering is statistically independent. Mean squared angle of multiple scattering has dependence 1/E, which is the main point for the next analysis. The Gaussian approximation for total distribution has the standard deviation:

$$\sigma = 12.70^0 \pm 0.07^0$$

The dependence of standard deviation for the Gauss approximation of total distribution (like shown in Fig. 5c) from the energy of electron is shown in Fig. 6. There are two lines: first one is for vertical beam (black line) and another one is for initial beam inclination of 30° (red line). The value of the standard deviation estimated for 10 MeV is also marked.

The curve from Fig. 6 is used to evaluate the energies of electron (E^-) and positron (E^+) using the estimation of standard deviation for the values α_{x1}, α_{y1}, α_{x2}, α_{y2} for each component of the pair:

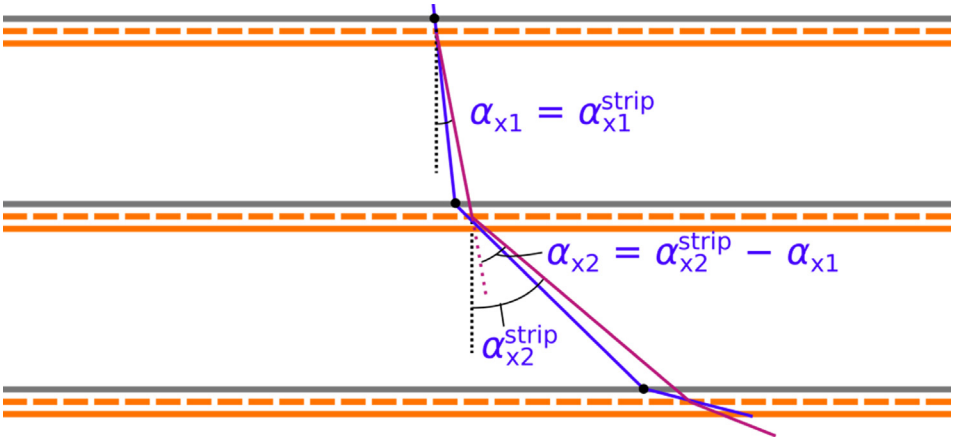


Fig. 4. An example of electron trajectory in the GAMMA-400 converter-tracker (blue line). The trajectory of electron restored using information from silicon strip detectors (magenta line). The estimation of the electron trajectory deviation after the multiple Coulomb scattering in first and second tungsten layers (α_{x1}). The estimation of the electron trajectory deviation after the multiple Coulomb scattering in third tungsten layer (α_{x2}). (For interpretation of the references to colour in this figure legend, the reader is referred to the web version of this article.)

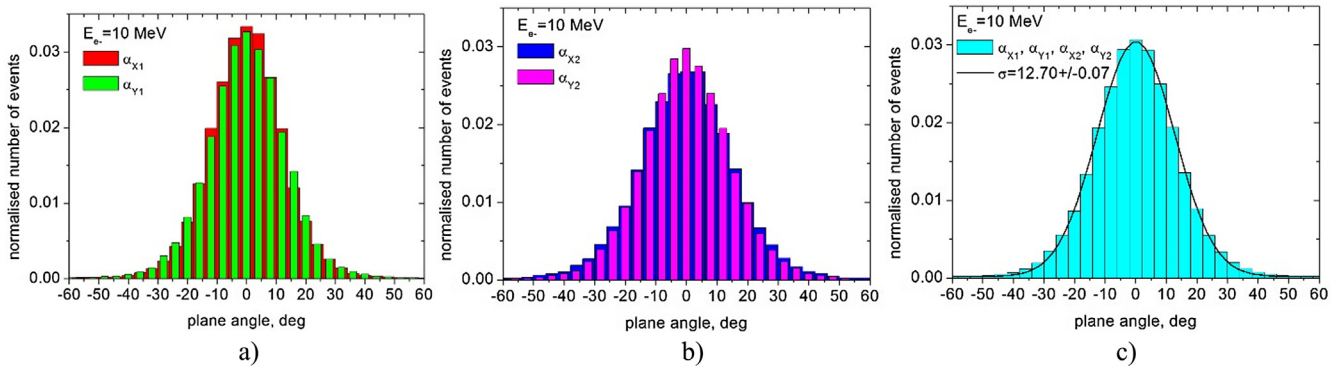


Fig. 5. The couple of distributions for plane angles α_{x1}, α_{y1} (a) and α_{x2}, α_{y2} (b). The total distribution including for each event the values: α_{x1}, α_{y1}, α_{x2}, α_{y2}(c).

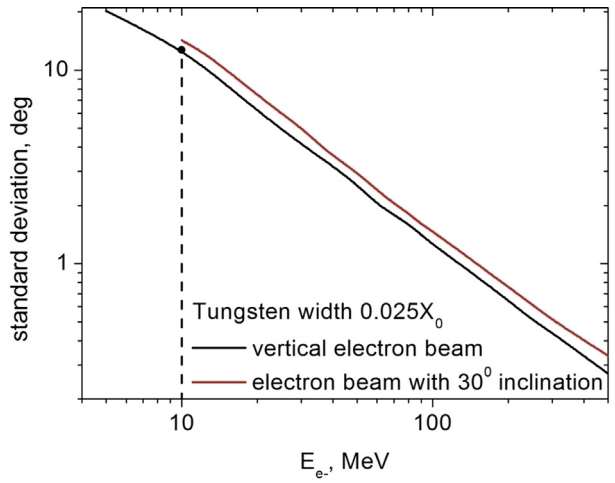


Fig. 6. The dependence of standard deviation for Gauss approximation of total distribution (Fig. 5c) from the energy of electron beam. Black line corresponds to the vertical beam, red line to the beam with inclination 30^0. The value of the standard deviation estimated for 10 MeV is marked by black point. (For interpretation of the references to colour in this figure legend, the reader is referred to the web version of this article.)

$$< \sqrt{\theta^2} >= \sqrt{\frac{(\alpha_{x1}-\bar{\alpha})^2+(\alpha_{y1}-\bar{\alpha})^2+(\alpha_{x2}-\bar{\alpha})^2+(\alpha_{y2}-\bar{\alpha})^2}{4}}, \tag{3}$$

where $\bar{\alpha}=\frac{\alpha_{x1}+\alpha_{y1}+\alpha_{x2}+\alpha_{y2}}{4}$.

Such energy estimation should be considered only as procedure to evaluate relative energy contributions in (1), (2). The initial energy of pair components is not the same, therefore, it is possible for some electron/positron having low energy (< 5 MeV). For this low-energy range the linear extrapolation procedure is used applying the data for higher energy. The restored energy distribution for some initial energy of electron beam has long arm high-energy tail, but the average value of the distribution is well estimated. Fig. 7a shows the calibration dependence of the average value of restored energy for vertical electron beam. It is evident that this dependence is practically linear. The energy resolution, estimated as 68% containment, for the restored energies is shown in Fig. 7b. It is approximately constant in the considered energy range up to 150 MeV.

Considered methods allow us to calculate the plane angles α_x and α_y of initial gamma from plane angles of e^+/e^- pair, using (1) and (2). In the spherical coordinate system, zenith and polar angles (θ and φ) of initial gamma are calculated from the following relations:

$$tan^2(\theta) = tan^2(\alpha_x) + tan^2(\alpha_y), \tag{4}$$

$$tan(\varphi) = \frac{tan(\alpha_x)}{tan(\alpha_y)}. \tag{5}$$

The angle δ of deviation of reconstructed direction (θ, φ) from true direction (θ_0, φ_0) of initial gamma is calculated as:

$$\delta = acos\left(\begin{array}{c} sin\theta\times cos\varphi\times sin\theta_0\times cos\varphi_0 + sin\theta\times sin\varphi\times sin\theta_0\times sin\varphi_0 + \\ cos\theta_0\times cos\theta \end{array}\right). \tag{6}$$

Fig. 8 shows four distributions of deviation angles for initial gamma-ray energies 20, 50, 100, and 150 MeV are shown. Angular resolution is determined as a location of vertical line on the distribution contained 68% of events from the left side. Such estimation is marked as $psf_{68\%}$.

The energy dependence of the GAMMA-400 angular resolution for thin layers of tungsten calculated with proposed methods is shown in Fig. 9 by red line. The results of previous calculations from (Leonov et al., 2017) are also shown using green line. Improved energy weights estimation in (1), (2) allows us to have ~25% better angular resolution. The theoretical limitation for GAMMA-400, based on multiple scattering in couple of thin tungsten layers, is shown in Fig. 9 by blue dashed line. This limitation was calculated using the following relation (Highland, 1975; Lynch and Dahl, 1991):

$$\theta = \frac{13.6MeV}{\beta cp} z\sqrt{\frac{X}{X_0}}\times\left[1+0.038\times ln\frac{X}{X_0}\right], \tag{7}$$

where z is particle charge, β is particle velocity, pc is particle energy in MeV, X_0 is radiation length of the matter, X is thickness of the matter.

As the efficiency and quality of track reconstruction is not considered in the calculations, the comparison with angular resolution (68% containment) of Fermi-LAT

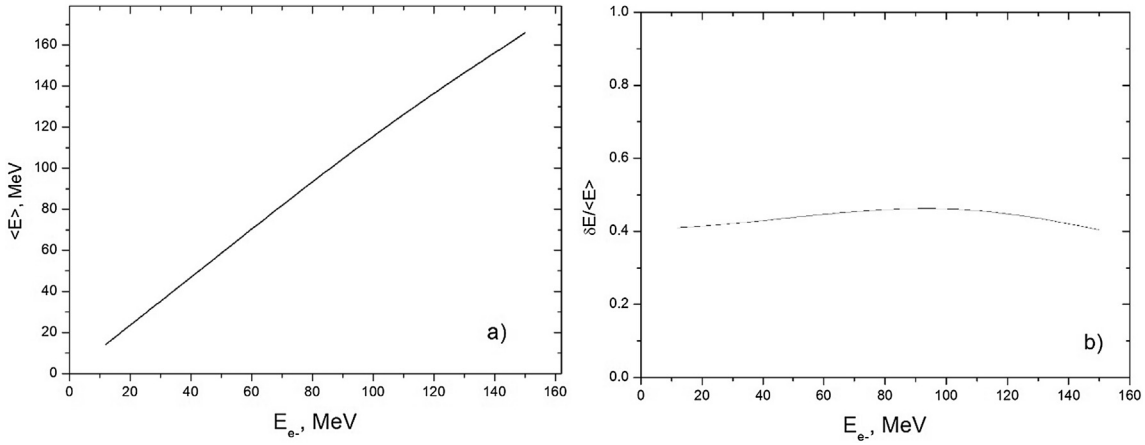


Fig. 7. The calibration dependence of the average value of restored energy for vertical electron beam (a). The energy resolution was estimated as 68% containment (b).

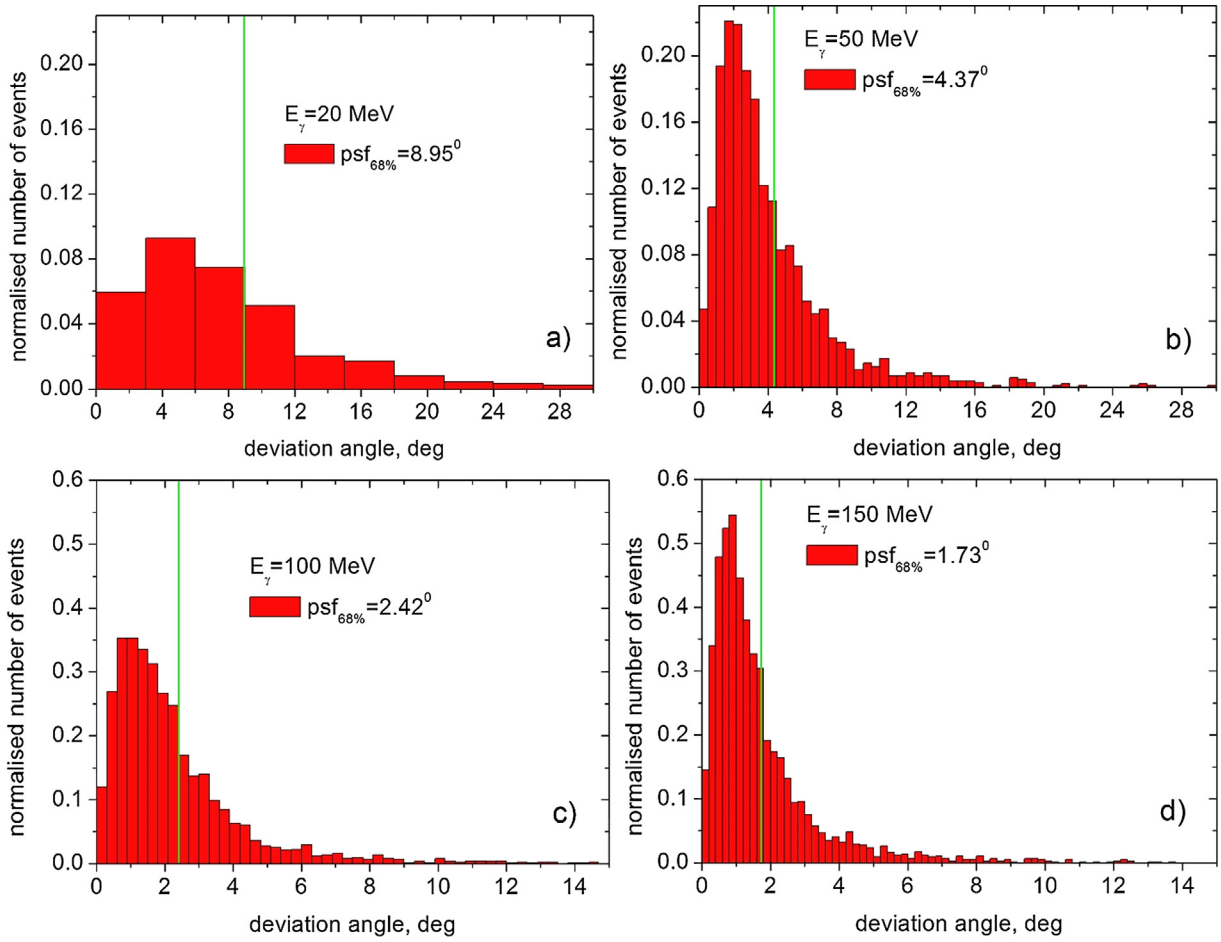


Fig. 8. The distributions of deviation angles for initial gamma-ray energies 20 (a), 50 (b), 100 (c), and 150 MeV (d).

(http://www.slac.stanford.edu/exp/glast/groups/canda/lat_Performance.htm) in front configuration with thin tungsten layers is also shown in Fig. 9. In energy range from 20 to 50 MeV, the estimated angular resolution of GAMMA-400 is 40% better than angular resolution of Fermi-LAT in configuration with thin tungsten foils.

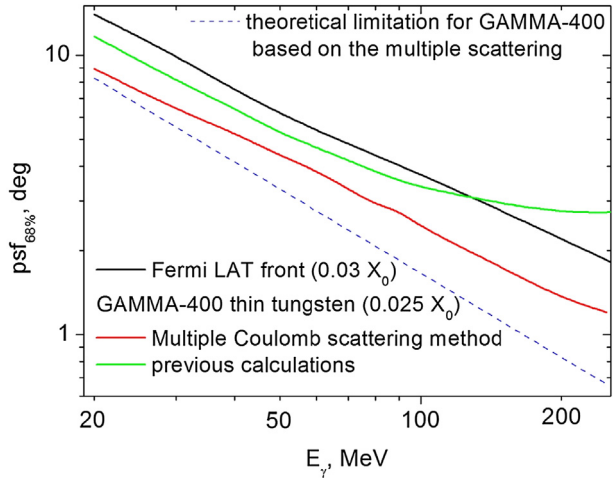


Fig. 9. The energy dependence of GAMMA-400 angular resolution for thin layers of tungsten in converter-tracker is presented by red line. The results of previous calculations from (Leonov et al., 2017) are also shown by green line. The theoretical limitation for GAMMA-400, based on multiple scattering in couple of thin tungsten layers, is shown by blue dashed line. The angular resolution of Fermi-LAT in front configuration with thin tungsten layers is shown by black line. (For interpretation of the references to colour in this figure legend, the reader is referred to the web version of this article.)

5. Conclusions

The method to improve the reconstruction accuracy of incident angle for low-energy gamma rays in the GAMMA-400 space-based gamma-ray telescope is presented. Applying the energy dependence of multiple Coulomb scattering for pair components generated in converter-tracker, it is possible to estimate the energies for each particle, and to use those energies as weight in angle reconstruction procedure. To identify the unique track in different projections imaginary curvature method is applied. Such approach is the further development of the procedure proposed in (Kheymits et al., 2015) and (Leonov et al., 2017) and it allows us to have ~25% better angular resolution in the energy range from 20 to 150 MeV. Comparing presented results with the performance of Fermi-LAT in the configuration with thin tungsten foils, there is ~40% improvement for the energy range from 20 to 50 MeV.

Acknowledgements

This study was supported by the Russian State Space Corporation ROSCOSMOS (contract no. 024-5004/16/224).

References

Acero, F., Ackermann, M., Ajello, M., et al., 2015. Fermi large area telescope third source catalog. Astrophys. J. Suppl. Ser. 218 (2), 23, 1-41.

Ackermann, M., Ajello, M., Allafort, A., et al., 2013. The first Fermi-LAT catalog of sources above 10 GeV. Astrophys. J. Suppl. Ser. 209, 1–34.

Allison, J., Apostolakis, J., Lee, S.B., et al., 2016. Recent developments in Geant4. Nucl. Instrum. Meth. A 835, 186–225.

Berra, A., Bonvicini, V., Lietti, D., et al., 2015. Study of the readout configuration of the GAMMA-400 silicon tracker sensors. Nucl. Instrum. Meth. Phys. Res. A 798, 80–87.

De Angelis, A., Tatischeff, V., Grenier, I.A., et al., 2018. Science with e-ASTROGAM: a space mission for MeV-GeV gamma-ray astrophysics. J. High Energy Astrophys. 19, 1–106.

Giuliani, A., Cocco, V., Mereghetti, S., et al., 2006. The AGILE on-board Kalman filter. Nucl. Instrum. Meth. Phys. Res. A 568, 692–699.

Highland, V.L., 1975. Some practical remarks on multiple scattering. Nucl. Instrum. Meth. 129 (2), 497–499.

Kheymits, M.D., Arkhangelskaja, I.V., Arkhangelskiy, A.I., et al., 2015. Method of incident low-energy gamma-ray direction reconstruction in GAMMA-400 gamma-ray space telescope. Phys. Procedia 74, 368–371.

Leonov, A.A., Galper, A.M., Topchiev, N.P., et al., 2017. Modifications of a method for low energy gamma-ray incident angle reconstruction in the GAMMA-400 gamma-ray telescope. IOP Conf. Ser.: Journal of Physics: Conf. Ser. 798, 012012, 1–5.

Lynch, G.R., Dahl, O.I., 1991. Approximations to multiple Coulomb scattering. Nucl. Instrum. Meth., Section B 58 (1), 6–10.

Moiseev, A.A., Hartman, R.C., Ormes, J.F., et al., 2007. The anticoincidence detector for the GLAST large area telescope. Astroparticle Phys. 27, 339–358.

Principe, G., Malyshev, D., Ballet, J., Funk, S., 2018. The first catalog of Fermi-LAT sources below 100. MeV. Astron. Astrophys. 618 (A22), 1–13.

Schonfelder, V., Bennett, K., Blom, J.J., et al., 2000. The first COMTEL source catalogue. Astron. Astrophys.Suppl. Ser. 143, 145–179.

Topchiev, N.P., Galper, A.M., Bonvicini, V., et al., 2016b. Perspectives of the GAMMA-400 space observatory for high-energy gamma rays and cosmic rays measurements. IOP Conf. Ser.: J. Phys.: Conf. Series 675, 032010.

Topchiev, N.P., Galper, A.M., Bonvicini, V., et al., 2016a. The GAMMA-400 gamma-ray telescope for precision gamma-ray emission investigations. IOP Conf. Ser.: J. Phys.: Conf. Ser. 675, 032009.

http://www.slac.stanford.edu/exp/glast/groups/canda/lat_Performance.htm (the data were accessed on May, 2018).

Available online at www.sciencedirect.com

ScienceDirect

Advances in Space Research 69 (2022) 514–530

ADVANCES IN SPACE RESEARCH (a COSPAR publication)

www.elsevier.com/locate/asr

Capabilities of the GAMMA-400 gamma-ray telescope to detect gamma-ray bursts from lateral directions

A.A. Leonov [a,b,*,1], A.M. Galper [a,b,1], N.P. Topchiev [a,2], I.V. Arkhangelskaja [b,1], A.I. Arkhangelskiy [b,1], A.V. Bakaldin [a,c,3], I.V. Chernysheva [b,1], O.D. Dalkarov [a,2], A.E. Egorov [a,2], M.D. Kheymits [b,1], M.G. Korotkov [b,1], A.G. Malinin [b,1], A.G. Mayorov [b,1], V.V. Mikhailov [b,1], A.V. Mikhailova [b,1], P. Yu Minaev [a,d,4], N. Yu Pappe [a,2], P. Picozza [e,f,5], R. Sparvoli [e,f,5], Yu.I. Stozhkov [a,2], S.I. Suchkov [a,2], Yu.T. Yurkin [b,1]

[a] *Lebedev Physical Institute, Moscow 119991, Russia*
[b] *National Research Nuclear University ûMEPhIý, Moscow 115409, Russia*
[c] *Scientific Research Institute for System Analysis, Moscow 117218, Russia*
[d] *Space Research Institute, Moscow 117997, Russia*
[e] *Istituto Nazionale di Fisica Nucleare, Sezione di Roma 2, Rome, Italy*
[f] *Physics Department of University of Rome Tor Vergata, Rome, Italy*

Received 2 April 2021; received in revised form 15 October 2021; accepted 18 October 2021
Available online 22 October 2021

Abstract

The currently developing space-based gamma-ray telescope GAMMA-400 will measure the gamma-ray and electron + positron fluxes using the main top-down aperture in the energy range from ~ 20 MeV to several TeV in a highly elliptic orbit (without shading the telescope by the Earth and outside the radiation belts) continuously for a long time. The instrument will provide fundamentally new data on discrete gamma-ray sources, gamma-ray bursts (GRBs), sources and propagation of Galactic cosmic rays and signatures of dark matter due to its unique angular and energy resolutions in the wide energy range. The gamma-ray telescope consists of the anticoincidence system (AC), the converter-tracker (C), the time-of-flight system (S1 and S2), the position-sensitive and electromagnetic calorimeters (CC1 and CC2), scintillation detectors (S3 and S4) located above and behind the CC2 calorimeter and lateral detectors (LD) located around the CC2 calorimeter.

In this paper, the capabilities of the GAMMA-400 gamma-ray telescope to measure fluxes of GRBs from lateral directions of CC2 are analyzed using Monte-Carlo simulations. The analysis is based on off-line second-level trigger construction using signals from S3, CC2,

* Corresponding author.
E-mail addresses: AALeonov@mephi.ru, leon@ibrae.ac.ru (A.A. Leonov), AMGalper@mephi.ru (A.M. Galper), tnp51@yandex.ru (N.P. Topchiev), IVArkhangelskaya@mephi.ru (I.V. Arkhangelskaja), AIArkhangelskij@mephi.ru (A.I. Arkhangelskiy), bakaldin71@mail.ru (A.V. Bakaldin), IVChernysheva@mephi.ru (I.V. Chernysheva), dalkarovod@lebedev.ru (O.D. Dalkarov), eae14@yandex.ru (A.E. Egorov), mcsaksik@gmail.com (M.D. Kheymits), mikhail.g.korotkov@gmail.com (M.G. Korotkov), alexander.malinin@cern.ch (A.G. Malinin), mayorov_a_87@mail.ru (A.G. Mayorov), vvmikhajlov@gmail.com (V.V. Mikhailov), ann_mikhailova@mail.ru (A.V. Mikhailova), minaevp@mail.ru (P. Yu Minaev), nikolay-pappe@mail.ru (N. Yu Pappe), piergiorgio.picozza@roma2.infn.it (P. Picozza), roberta.sparvoli@roma2.infn.it (R. Sparvoli), stozhkovyi@lebedev.ru (Y.I. Stozhkov), soutch@mail.ru (S.I. Suchkov), YTYurkin@mephi.ru (Y.T. Yurkin).
[1] 31, Kashirskoe shosse, Moscow, 115409.
[2] 53, Leninskiy prospekt, Moscow, 119991.
[3] 36/1, Nakhimovskiy prospekt, Moscow, 117218.
[4] 84/32, Profsoyuznaya str, Moscow, 117997.
[5] Via della Ricerca Scientifica,1, Rome, 00133.

https://doi.org/10.1016/j.asr.2021.10.031
0273-1177/© 2021 COSPAR. Published by Elsevier B.V. All rights reserved.

S4 and LD detectors. For checking the numerical algorithm the data from space-based GBM and LAT instruments of the Fermi experiment are used, namely, three long bursts: GRB 080916C, GRB 090902B, GRB 090926A and one short burst GRB 090510A. The obtained results allow us to conclude that from lateral directions the GAMMA-400 space-based gamma-ray telescope will reliably measure the spectra of bright GRBs in the energy range from ~ 10 to ~ 100 MeV with the on-axis effective area of about 0.13 m^2 for each of the four sides of CC2 and total field of view of about 6 sr.
© 2021 COSPAR. Published by Elsevier B.V. All rights reserved.

Keywords: Gamma-ray telescope performance for lateral aperture; Space experiments; GEANT4 simulation toolkit; Gamma-Ray Bursts detection; Hadron and electromagnetic showers

1. Introduction

The GAMMA-400 gamma-ray telescope (Galper et al., 2018; Topchiev et al. 2019a,b; Topchiev et al., 2016; Topchiev et al., 2016a) is being designed to achieve a broad range of scientific goals. These scientific goals are the following: precise searching for high-energy gamma-ray emission from annihilation or decay of dark matter particles; searching for new and studying known Galactic and extragalactic point and extended sources of high-energy gamma rays (supernova remnants, pulsars, binaries, microquasars, active galactic nuclei, blazars, quasars, etc.); studying isotropic and Galactic diffuse backgrounds; detection of gamma-ray bursts (GRBs) and other transients, as well as precise measuring electron + positron cosmic-ray fluxes (Leonov et al., 2019a,b).

The key experimental goal of the GAMMA-400 gamma-ray telescope is to measure gamma-ray fluxes in the energy range from ~ 20 MeV to ~ 1 TeV with high angular and energy resolutions. The main top-down aperture of the instrument is about ± 45° (Topchiev et al., 2019a).

The main preliminary planned targets for continuous long time (up to 100 days) source observation mode with GAMMA-400 are sources of the Galactic plane and bulge in contrast to the uniform scanning mode of Fermi-LAT, when the observation time of sources is only ~ 15% of the Fermi-LAT operation time (Abdollahi, et al., 2020). With this observation mode the main aperture covers solid angle ~ 0.3π. Taking into account that GRBs are isotropically detected using lateral aperture allows us to increase the field of view for GRB detection up to 2π. In this paper, the additional capabilities of the GAMMA-400 gamma-ray telescope for GRB detection using the lateral aperture in the energy range from ~ 10 MeV to several hundred MeV are analyzed using Monte-Carlo simulations with GEANT4 software.

"Classical" high variable prompt emission of GRBs is seen mostly in the sub-MeV range as superposition of short FRED-like (Fast Rise and Exponential Decay) pulses. More than 13 000 bursts (http://www.ssl.berkeley.edu/ipn3/masterli.html) were detected and investigated in details in this range, giving the high level of statistics. In the energy range above 100 MeV, emission of GRBs is relatively well studied also (a couple hundreds of detections) by several experiments (e.g. Fermi/LAT and CGRO/EGRET). This high-energy component is presumably associated with the propagation of a relativistic jet, which is observed mainly at high energies above 100 MeV (Joshi and Razzaque, 2021). However, the nature of the high-energy emission and its possible connection with the low-energy classical gamma-ray emission is still debatable. There are several signs of at least bimodal behavior of high-energy emission (separate emission mechanism vs extension of low-energy emission to high energy).

The energy range of 10–100 MeV, being the transition zone between GRB components with energies less than ~ MeV and more than 100 MeV, was weakly studied (Ajello et al., 2019). This is due to both the features of scintillation detectors used to observe GRBs (insufficient efficiency of photon detection in this range), and the shape of the energy spectrum of events in this range (usually described by power-law model with an index of $\alpha \sim -2$ and steeper). At the same time, this range is of particular interest, since, as already mentioned, some GRBs are characterized by a transition from the spectral component, corresponding to the pulses of the burst prompt emission (observed mainly in the sub-MeV range), to the additional high-energy extended duration component. In this view, investigation of GRBs and accumulation of their recording statistics by the GAMMA-400 lateral aperture could shed light on the problem of possible connection between high and low energy gamma-ray emission of GRBs and their physical nature.

The paper is organized as follows. The next section presents the schematic and physical description of the GAMMA-400 gamma-ray telescope. The simulation model is described in the third section. To detect reliably gamma rays from GRBs using the lateral aperture, the special selection algorithm has to be developed decreasing the background of charged particles and diffuse gamma rays. In the fourth section, the construction of such algorithm (off-line second-level trigger) is described, using the results of source and background simulations. Also in this section, the acceptance and on-axis effective area of the instrument for the lateral aperture, taking into account the off-line second-level trigger selection, are provided. Then it is necessary, applying the processed algorithm, to check the possibility of GRB spectra reconstruction. To test this point, the data from space-based GBM and LAT instruments of

Fermi experiment are used. The description of experimental data for three long bursts (GRB 080916C, GRB 090902B, GRB 090926A) and one short burst (GRB 090510A) (Ajello et al., 2019) and the results of GRB spectra reconstruction are reported in the fifth section. Some remarks are placed in the conclusion.

2. The physical scheme of the GAMMA-400 gamma-ray telescope

The GAMMA-400 instrument consists of the anticoincidence system (AC top, AC lat), the converter-tracker (C), the time-of-flight (ToF) system from the detectors S1, S2, the position-sensitive calorimeter (CC1), electromagnetic calorimeter (CC2), the detectors S3 and S4 located above and behind the CC2 calorimeter and lateral detectors (LD) located around the CC2 calorimeter. GAMMA-400 is able to measure high-energy gamma rays on event-by-event basis using main top-down (from the top directions) and additional (from the lateral directions) apertures. The current physical scheme of the GAMMA-400 gamma-ray telescope is shown in Fig. 1. In the future, this scheme can be slightly modified depending on the type of carrier rocket and the final payload mass.

For the main top-down aperture, the dimensions and location of plastic scintillation detectors S1 and S2, which are separated by approximately 500 mm, determine the maximum gamma-ray telescope field of view (FoV), which is about $\pm$ 45°. The converter-tracker consists of 13 layers of double (x, y) coordinate detectors made of scintillation fiber (SciFi) detectors. Each plane contains two groups of scintillating fibers, oriented in orthogonal directions with 4096 SiPM readout channels on each side. The size of pitch is 250 μm. The converter-tracker planes have an active area of $\sim$ 1000 $\times$ 1000 mm^2. The first seven layers are interleaved with tungsten conversion foils with thickness of 0.1 X_0 (X_0 is the radiation length), next four layers are interleaved with tungsten conversion foils with thickness of 0.025 X_0 and final two layers have no tungsten. Using the four layers with thickness of 0.025 X_0 allows us to measure gamma rays down to 20 MeV. In this case, the on-line gamma-ray trigger for the energy range of 20–100 MeV and 100 MeV – 1000 GeV is the same: $\bar{AC} \times ToF$ (the absence of a signal in AC and the presence of ToF time signal from S1 and S2 for top-down directions only). The total converter-tracker thickness is $\sim$ 1 X_0. The two-part calorimeter (CC1 and CC2) measures the particle energy. The CC1 imaging calorimeter consists of the plane from

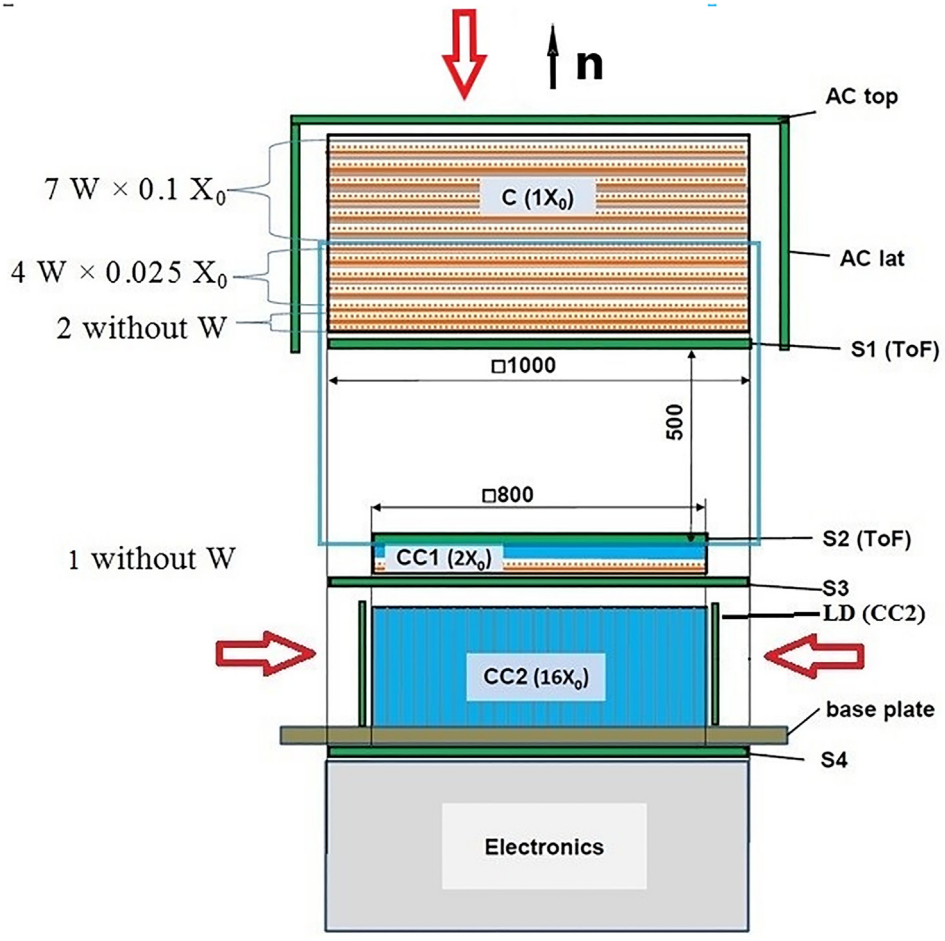


Fig 1. The current physical scheme of the GAMMA-400 gamma-ray telescope.

CsI(Tl) crystals and a layer of double (x, y) SciFi coordinate detector without tungsten the same as final two layers in converter-tracker. The CC2 electromagnetic calorimeter consists of 22 × 22 CsI(Tl) crystals. Each crystal has a dimension of 36 × 36 × 300 mm^3. The thickness of CC1 and CC2 is 2 X_0 and 16 X_0, respectively. The total calorimeter thickness for vertical incidence direction is 18 X_0 or ∼ 0.9 λ_0 (λ_0 is the nuclear interaction length). Using the deep calorimeter allows us to extend the energy range up to several TeV for gamma rays and to reach an energy resolution ∼ 2% at 100 GeV (Topchiev et al., 2019a). The total calorimeter thickness for lateral detection of particles is ∼ 42 X_0 or ∼ 1.95 λ_0, providing the possibility to measure intensities of high-energy electrons and gamma rays up to ∼ 10 TeV.

The structure of SciFi converter-tracker with analog readout, ToF system with large flight distance (500 mm), and an additional layer of SciFi coordinate detector in CC1 allows us to obtain unprecedented angular resolution: ∼0.01° at $E_\gamma = 100$ GeV (Topchiev et al., 2019a).

To detect gamma rays from lateral directions the information from CC2, S3, S4 and LD detectors is used. Each of the scintillation detectors (S3 and S4) consist of two layers of strips. Each strip has dimensions of 1000 × 100 × 10 mm^3 (length/width/thickness). LD detectors have the same structure with the strip dimensions of 380 × 117 × 10 mm^3.

The capabilities of the GAMMA-400 gamma-ray telescope for the lateral aperture are determined by the online special trigger signal to capture such gamma rays:

$$\bar{LD} \times \bar{S_3} \times \bar{S_4} \times CC_2(5MeV < E_{RELEASE} < 350MeV) \qquad (1)$$

where LD, S3, S4 are anticoincidence detectors; lower (5 MeV) and upper (350 MeV) limits for the signal in CC2 are conditioned by lower boundary of calorimeter dynamic range and the limitation of telemetric data volume, respectively.

One of the main problems for applying the GAMMA-400 lateral aperture to detect GRB gamma rays is to provide the effective rejection from all directions of background induced by cosmic-ray particles: protons, electrons, positrons, helium, and additional contribution induced by diffuse gamma rays. Charged particles are excluded by anticoincidence S3, S4, LD detectors and are able to be detected according criterion (1), if penetrate inside CC2 only through the holes between lateral detectors LD and S3, S4 scintillation detectors. At present, this mechanical structure with holes is due to the total mass limitation for the GAMMA-400 scientific payload and will be further modified.

The part of the GAMMA-400 physical scheme, which is using to detect gamma rays from lateral directions, is presented in Fig. 2 in details with the matter of supporting construction. Each of S3 and S4 detectors is installed on the honeycomb panel with average density 0.016 g/cm^3. The electromagnetic calorimeter CC2 is inserted in the supporting structure from aluminum and contains zones for installing electronics. Top part of this structure consists of the layer of aluminum (2.7 g/cm^3) and from the special module of stiffeners and electronics with effective density ∼ 0.4 g/cm^3. The thickness of aluminum is 10 mm and the thickness of the special module is 129 mm. The bottom part of the supporting structure of CC2 contains the same special module of stiffeners and

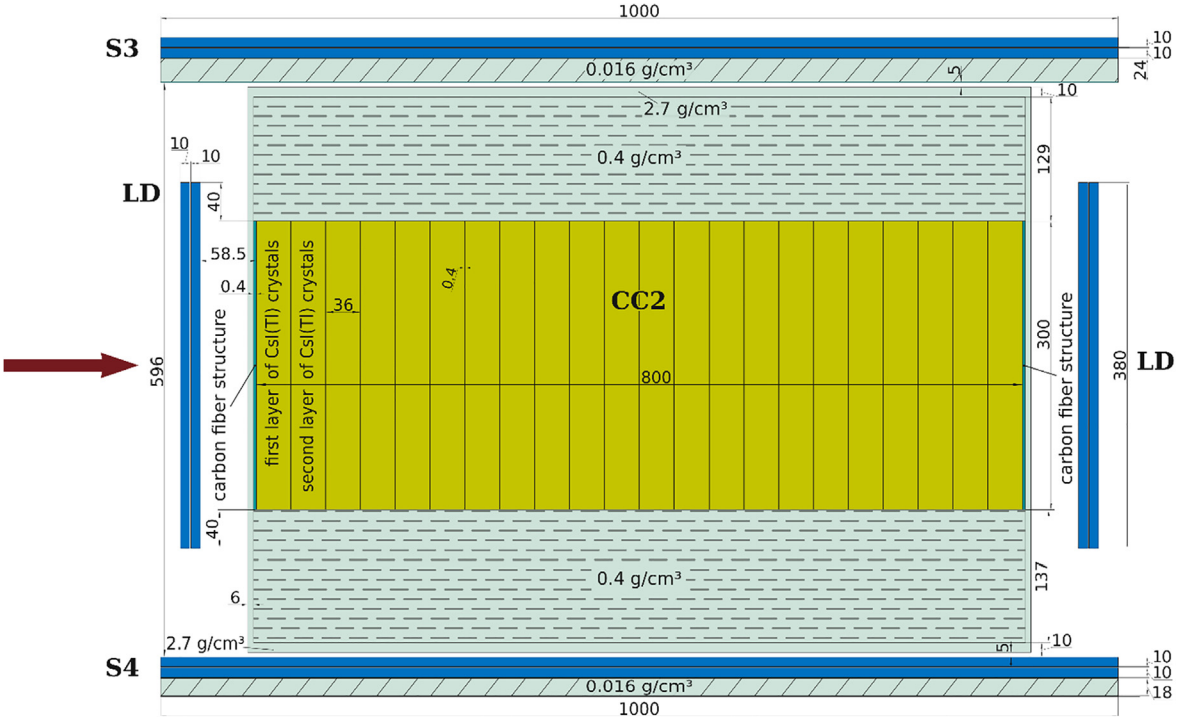


Fig 2. The part of the GAMMA-400 physical scheme, which is using to detect gamma rays from lateral directions.

electronics with thickness of 137 mm and layer of aluminum with thickness 15 mm. Lateral parts from each side contain the layer of aluminum with thickness of 6 mm. CsI (Tl) crystal columns of CC2 are installed inside the cells of the carbon fiber honeycomb structure having thickness of 0.4 mm.

3. The simulation model

Using GEANT4 to evaluate the rejection power, simulations of the differential isotropic fluxes of cosmic-rays protons, electrons/positrons and helium and background of diffuse gamma rays were performed for whole coverage of the GAMMA-400 lateral aperture. The surfaces, over which the simulations were carried out, are shown in Fig. 3 by blue dashed lines.

When simulating, only five (top-down and four lateral) possible directions are considered. From bottom direction, the penetration of particles with logic trigger (1) is not considered due to large amount of satellite platform matter located under the gamma-ray telescope. A lot of shower particles, penetrating from bottom, will be excluded by the veto signal in S4.

To simulate cosmic-ray background, it is necessary to mention that due to the 6-mm thickness of the aluminum box from lateral sides, which surrounds the CC2 calorimeter, only particles with energies above the certain threshold can be captured according condition (1). This threshold is equal to 35 MeV for protons, 140 MeV for helium nuclei and 3.4 MeV for electrons/positrons. Taking into account this point for calculations, we use the experimental data of of the PAMELA experiment during solar minimum for protons (Martucci et al., 2018), electrons/positrons (Adriani et al., 2015) and helium (Adriani et al., 2011) were used. The low energy limits for charged particle detection in this experiment is about 80 MeV (for protons), 50 MeV (for electrons), 120 MeV/n (for helium) (Picozza et al., 2007). In low-energy range, the constant extrapolation for proton spectra is used. Such approach gives some overestimate for the influence of cosmic-ray background (Bisschoff et al., 2019). For electrons and helium in low-energy range, the estimations from (Bisschoff et al., 2019; Ngobeni et al., 2020) were used, respectively. These estimations are accounted for solar modulation effects. The cosmic-ray spectra used in simulations are shown in Fig. 4 by red (protons), green (helium) and blue (electrons) lines.

As a simple estimate of the diffuse gamma-ray background, we took the average intensity of the diffuse Galactic emission inside the disc with 30° radius around the Galactic center according to Fermi-LAT data (Ackermann et al., 2012; https://fermi.gsfc.nasa.gov/ssc/data/access/lat/BackgroundModels.html) and extrapolated such intensity isotropically to the whole sky. Fermi-LAT presents the data down only to 50 MeV, but we extrapolated the intensity linearly below this energy. We use such simple approach with evident overestimation, because the main contribution in the background comes from protons. The accuracy of this estimation does not influence on the result. We also checked that the contributions from point sources and isotropic background are much smaller than the Galactic component estimated this way. Hence, we neglected by these contributions. In general, the simulation results do not depend strongly from the chosen gamma-ray background model. The spectrum of diffuse gamma rays, used in simulations, is shown in Fig. 4 by black line.

For each spectrum $\sim 10^7$ events were simulated over the simulation planes, which are shown in Fig. 3.

4. Off-line second-level trigger for background rejection.

To take into account a realistic description of the full measurement processes involved in a space-based scintillation detector, the results of calibration measurements (Suchkov et al, 2021) were applied into the simulations using approach, described in (Leonov et al., 2015).

Analyzing the results of simulation for the differential isotropic fluxes of cosmic-ray protons, electrons, positrons and helium and for differential flat flux of GRB emission the following estimations for criterion (1) were obtained.

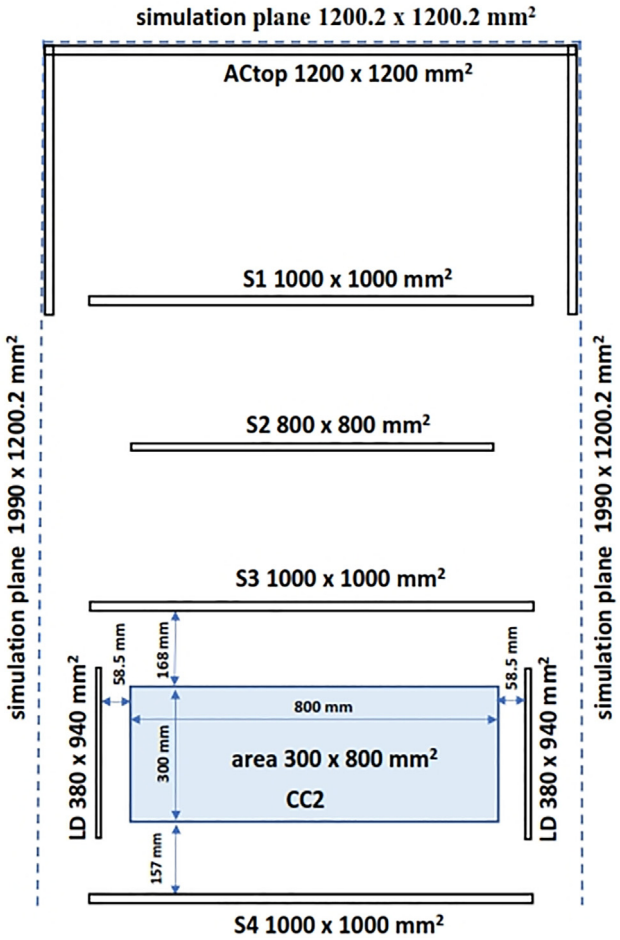


Fig. 3. The scheme of simulations.

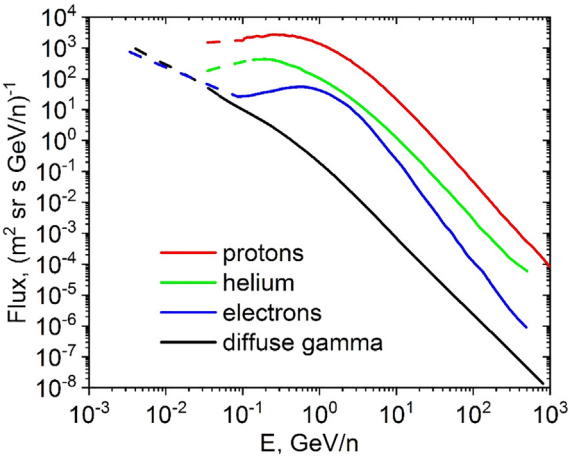


Fig. 4. The cosmic-ray spectra for protons (red) (Martucci et al., 2018), helium (green) (Adriani et al., 2011; Picozza et al., 2007), electrons (blue) (Adriani et al., 2015; Picozza et al., 2007) and of diffuse gamma-rays (black) (Ackermann et al., 2012; https://fermi.gsfc.nasa.gov/ssc/data/access/lat/BackgroundModels.html) used in the background simulations. (For interpretation of the references to colour in this figure legend, the reader is referred to the web version of this article.)

Protons provide count rate ~ 185 Hz; electrons + positrons and helium contribute ~ 5 and ~ 9 Hz, respectively; the contribution of emissions of considered GRBs begins from ~ 21 Hz. It is seen that applying on-board trigger selection (1) for the cosmic-ray particles and gamma-ray emission, which arrive at CC2 from all five directions, the dominant volume of the data, satisfied this selection, will be determined by cosmic-ray particles, in the main, by protons. To extract useful signal from captured gamma rays, additional criterions are needed. Using signals from CsI (Tl) crystals of CC2, it is possible to construct off-line second-level trigger logic to decrease significantly the count rate of cosmic-ray particles (Mikhailova et al., 2020). This logic is based on differences in electromagnetic and hadronic cascades in the CC2 calorimeter.

Considering for definiteness, gamma-ray emission, arriving from left direction of CC2, the significant probability of the conversion arises in first layer of CsI(Tl) crystals (Fig. 2). In this case, the energy is released in the nearest crystals. Then the electromagnetic shower is quickly weakened in calorimeter depth. Low-energy protons survived after applying criterion (1) and arriving to CC2 through the holes between lateral detectors LD and scintillation detectors S3 and S4, with high probability do not give a signals in first layer of CsI(Tl) crystal due to small solid angle of the holes. An energy release distribution on the layers of CsI(Tl) crystals for protons penetrating deeply inside the CC2 will be different in comparison the distribution for gamma rays with the same energy. Besides, protons are able to interact in second or third layers of CsI(Tl) crystals and to provide the location of energy release maximum deeply inside CC2. To take into account these differences gamma-ray and proton responses inside CC2, the following parameters are used:

$E^{tot}_{CC_2}$ is total energy release in all CsI(Tl) crystals of CC2;

$E^{1}_{CC_2}$ is total energy release in first layer of CsI(Tl) crystals of CC2;

$E^{2}_{CC_2}$ is total energy release in second layer of CsI(Tl) crystals of CC2;

N_{hits} is number of CsI(Tl) crystals with energy release over threshold of 5 MeV;

$E^{MAX}_{CC_2}$ is maximum energy release in one of CsI(Tl) crystals;

$N_{layer}\left(E^{MAX}_{CC_2}\right)$ is number of layer, which contains the crystal of CsI(Tl) with maximum energy release in CC2.

As example, the distribution of gamma-ray and proton events in $(E^{2}_{CC_2}, E^{tot}_{CC_2})$ phase space, satisfying condition (1), is presented in Fig. 5a and 5b, respectively. Criterion (1) keeps 3.8×10^4 protons and 4 $.6 \times 10^5$ gamma rays from 6.3×10^6 and 5.5×10^6 events, respectively, if isotropic fluxes from Fig. 4 are simulated on the left simulation plane (Fig. 3). Separation of gamma rays and protons is reached by introducing the linear cut (red line) corresponding to the expression $E^{2}_{CC_2} = \left(0.5 \times E^{tot}_{CC_2} - 50\right)$. It provides the rejection of protons of 85.5% and the efficiency of gamma-ray detection of 51%.

As another example, the distribution of N_{hits} parameter for gamma-ray (green columns) and proton (red columns) events, satisfying condition (1), with energy release $75MeV < E^{tot}_{CC_2} < 120MeV$ is shown in Fig. 6. Introducing a criterion, which is shown by blue dashed line, we obtain the rejection of protons of 74% and efficiency of gamma-ray detection of 89%.

To confirm the possibility to reject protons from gamma rays in the lateral aperture an independent analysis based on machine learning analyses was applied. Usually the particles identification, based on Multivariate analysis (MVA), gives the best performance, because such analysis allows to combine several discriminating variables into one final discriminator, takes into account the correlation between parameters and events, failing a particular criterion, are not ruled out if other criteria could classify them properly. Multivariate analysis of data is easy to understand and interpret with Decision Tree algorithm when consecutive set of questions with only two possible answers are applied to classify events. Final classification corresponds to leaf of the tree with appropriate weighting parameter.

The boosted decision tree (BDT) classifier was used from the toolkit TMVA included in CERN's ROOT package (Brun and Rademakers, 1997). Four parameters: N_{hits} , $E^{2}_{CC_2}$, $E^{MAX}_{CC_2}$ and $E^{1}_{CC_2}$ with a more significant discrimination power between gamma rays and protons together with released energy $E^{tot}_{CC_2}$ were combined into a single discrimination function. Using data of Monte-Carlo simulation both for gamma rays and protons, the BDT algorithm was trained with 10% of data for signals and background. Examples of BDT response distributions are shown in

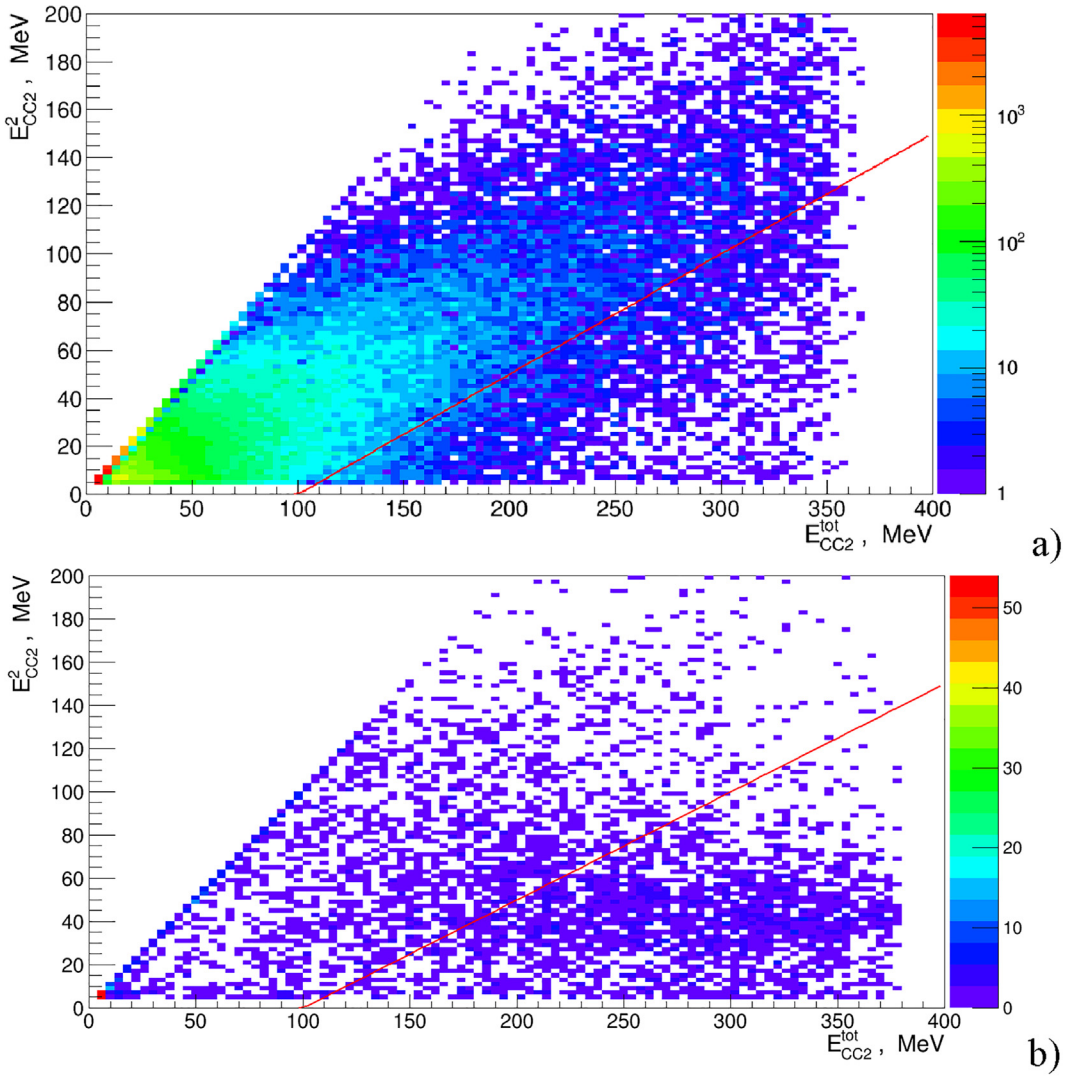


Fig. 5. The distribution of gamma-ray (a) and proton (b) events, satisfying condition (1), in ($E^2_{CC_2}$, $E^{tot}_{CC_2}$) phase space.

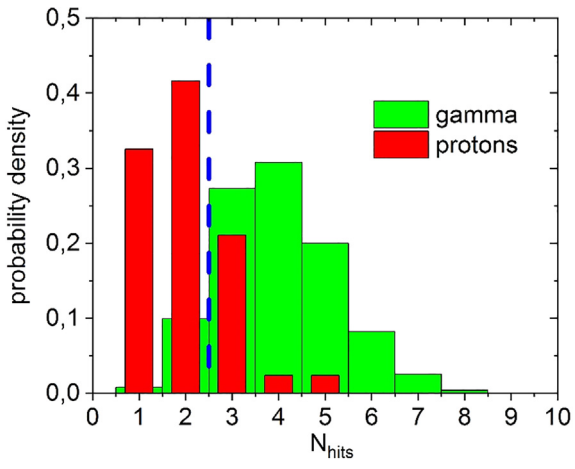


Fig. 6. The distribution of N_{hits} parameter for gamma-rays (green columns) and protons (red columns) with energy release of $75MeV < E^{tot}_{CC_2} < 120MeV$. Blue dashed line denotes a criterion, which provides the rejection of protons with level 74% and efficiency of gamma-rays with level 89%. (For interpretation of the references to colour in this figure legend, the reader is referred to the web version of this article.)

Fig. 7 for samples of gamma-ray and proton data. The data passed the trigger criterion (1). The BDT method provides better selection efficiency, but to achieve necessary energy resolution it has to be accompanied by additional cuts. Nonetheless, even in this simplified case, the location of distributions for gamma rays and protons in Fig. 7 confirms the possibility of rejection. For example, if the value of BDT parameter equal 0, then it provides gamma-ray efficiency of 90% and protons rejection of 87%.

Taking into account the results of the cosmic-ray and diffuse gamma-ray simulations (Fig. 4), the following additional criterions, providing effective rejection of charged particle background and suitable efficiency of gamma rays (~85 % in ~ 40–100 MeV energy interval), were selected:

$E^{tot}_{CC_2} > 7$ is introduced to increase the threshold for excluding indistinguishable events close to low-energy threshold;

$E^1_{CC_2} > 99.21 - 249.5 \times e^{-\frac{E^{tot}_{CC_2}}{88.4}}$ is introduced to take into account that correlation between total energy release in

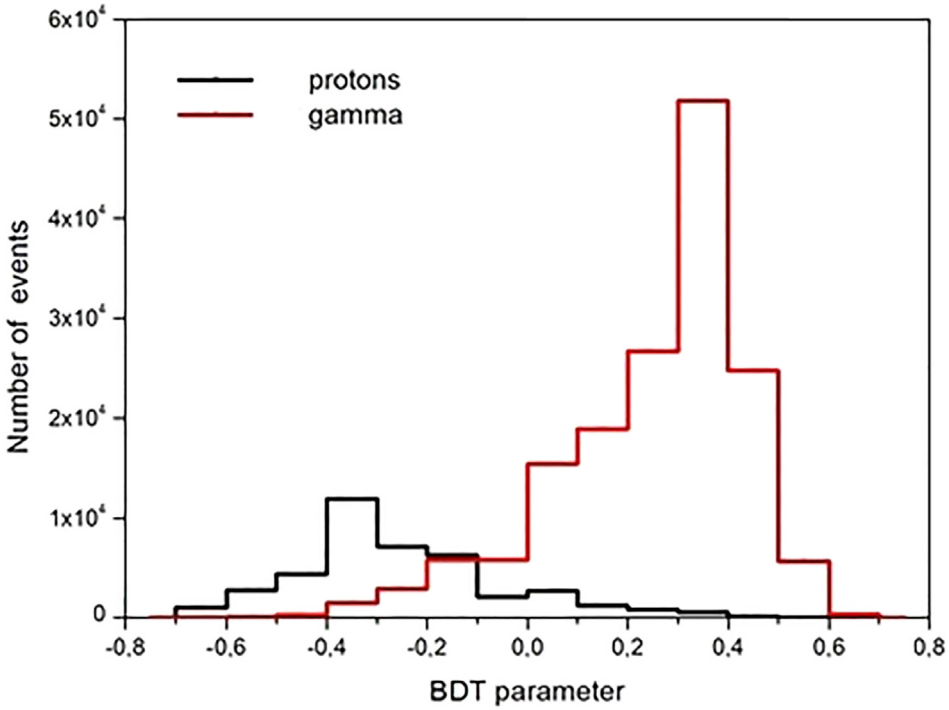


Fig. 7. Example of BDT classifier response distributions for samples of gamma-ray and proton data passed the trigger criterion (1).

first layer of CsI(Tl) crystals and total energy release in all CsI(Tl) crystals differs for proton and gamma-ray induced cascades (it begins from $\sim$ 50 MeV);

$E^1_{CC_2} > 5$ corresponds to lower boundary of calorimeter dynamic range;

$\left[\left((N_{hits}=1)\times\left(E^{tot}_{CC_2}<52\right)\right)\middle|\left((N_{hits}=2)\times\left(E^{tot}_{CC_2}<75\right)\right)\middle|\left((N_{hits}=3)\times\left(E^{tot}_{CC_2}<120\right)\right)\middle|\left((N_{hits}=4)\times\left(E^{tot}_{CC_2}<150\right)\right)\middle|(N_{hits}>4)\right]$ presents the difference of energy releases in CsI (Tl) crystals in proton and gamma-ray induced cascades;

$\left(N_{layer}\left(E^{MAX}_{CC_2}\right)\le 4\right)$ uses the fact that in the considered energy range the position of shower maximum is limited by four layers, if it is initiated by gamma ray;

$E^2_{CC_2} > \left(0.5\times E^{tot}_{CC_2} - 50\right)$ is introduced to take into account that correlation between total energy release in second layer of CsI(Tl) crystals and total energy release in all CsI(Tl) crystals differs for proton and gamma-ray induced cascades;

$E^{MAX}_{CC_2} < 250$ presents the difference of maximum energy release in CsI(Tl) crystals in proton and gamma-ray induced cascades.

The total combination of the developed criterions looks like:

$$\left(E^{tot}_{CC_2}>7\right)\times\left(E^1_{CC_2}>99.21-249.5\times e^{-\frac{E^{tot}_{CC_2}}{88.4}}\right)\times\left(E^1_{CC_2}>5\right)\times\left(E^1_{CC_2}<200\right)\times\left[\begin{array}{c}\left((N_{hits}=1)\times\left(E^{tot}_{CC_2}<52\right)\right)\middle|\left((N_{hits}=2)\times\left(E^{tot}_{CC_2}<75\right)\right)\middle|\\ \left((N_{hits}=3)\times\left(E^{tot}_{CC_2}<120\right)\right)\middle|\left((N_{hits}=4)\times\left(E^{tot}_{CC_2}<150\right)\right)\middle|(N_{hits}>4)\end{array}\right]\times\left(N_{layer}\left(E^{MAX}_{CC_2}\right)\le 4\right)\times\left(E^2_{CC_2}>\left(0.5\times E^{tot}_{CC_2}-50\right)\right)\times\left(E^{MAX}_{CC_2}<250\right) \quad (2)$$

where energy releases are expressed in MeV.

The results of applying criterion (2) to the responses of CC2, when detecting spectra of cosmic rays and diffuse gamma rays according to Fig. 4, are presented in Table 1. In this table the rejection power of this criterion for the candidate events, satisfying conditions (1), is pointed out. It is seen that protons are rejected more than one order of magnitude stronger than gamma rays.

The GAMMA-400 acceptance and on-axis effective area for gamma-ray detection arriving from one lateral direction after applying of criterions (1) and (2) are shown in Fig. 8a and 8b, respectively. The values of on-axis effective area and acceptance reach $\sim$ 0.13 m^2 for each lateral side and $\sim$ 0.42 m^2 $\times$ sr, respectively. The dependence of average total energy release in calorimeter CC2 from initial energy of gamma rays, arriving from one lateral direction and satisfying criterions (1) and (2), is presented in Fig. 9a. From this plot it is seen that appropriate linearity

Table 1
The rejection power of the criterion (2).

Particle type	Number of events (criterion (1) + criterion (2))/ Number of events (criterion (1)), %
Protons	3.1
Electrons/positrons	6.6
Helium	2.1
Gamma rays	37.4

is provided. An example of energy release distribution for 50-MeV gamma rays, satisfying criterions (1) and (2), is shown in Fig. 9b.

5. The results of GRB spectra reconstruction

To restore the initial flux when detecting GRB emission, which arrives from left direction with normal incidence for definiteness, we use the GAMMA-400 performance from Fig. 8b and 9. The initial flux in energy bin $[E_i, E_i + \Delta E_i]$ can be obtained applying unfolding procedure according to the expression (An et al., 2019):

$$F(E_i, E_i + \Delta E_i) = \frac{N_{inc,i}}{S_{eff,i} \times \Delta T \times \Delta E_i}$$
$$N_{dep,j} = \sum_i M_{ji} N_{inc,i} \quad (3)$$

where $N_{inc,i}$ is the number of events in the ith incident energy bin;

$N_{dep,j}$ is the number of events in the jth deposited energy bin;

M_{ji} is the response matrix, i.e., the probability that an event in the ith incident energy bin is detected in the jth deposited energy bin;

$S_{eff,i}$ is the effective area;

ΔE_i is the width of the energy bin;

ΔT is the exposure time.

However, to make a conclusion about the possibility of GAMMA-400 instrument to detect reliably GRB emission through lateral directions, it is necessary to evaluate the background from cosmic rays and diffuse gamma rays. Applying the same algorithm (3), the contribution of background fluxes was calculated. To introduce the real time in the analysis of background simulation results the following expression is used:

$$S \int_{2\pi} \int_{E1}^{E2} I(E) cos(\theta) d\Omega dE = \pi S \int_{E1}^{E2} I(E) dE = \frac{N_0}{\Delta t} \quad (4)$$

where $I(E)$ is the background isotropic intensity of cosmic rays or diffuse gamma rays (Fig. 4);

S is the surface area, over which the initial flux was simulated (left simulation plane in Fig. 3);

E_1 , E_2 are the borders of energy range for given type of particles;

N_0 is number of simulated events;

Δt is real time interval.

After applying of criterions (1) and (2) for N_0 simulated events, only N_{BG} background events are remained. The effective, i.e., virtually flat with normal incidence, background flux in some energy bin ΔE_i is calculated from (3).

The results of calculations of background fluxes, which satisfy criterions (1) and (2), are presented in Fig. 10. In Fig. 10a, background fluxes from separate components are shown. In this figure, the contributions from top and four lateral directions are summed for each component. As already mentioned, the diffuse gamma-ray flux was estimated for direction to Galactic center and can be considered as upper limit. In Fig. 10b, there are background flux from charged particles and total background flux. The dominant contribution of charged particles in background flux is seen.

To check the possibility to measure GRB spectra from lateral directions, the simulation of differential plane flux of gamma-ray emission was fulfilled for the one (for example, left) simulation plane (Fig. 3). For this, we use the data from the GBM and LAT instruments of Fermi experiment: four brightest (in terms of the signal-to-noise ratio) gamma-ray bursts were selected (Ajello et al., 2019). Only for the brightest bursts it is possible to perform the full-band analysis so that the count statistics in the 5–100 MeV range is sufficient (the number of counts from the source significantly exceeds the number of counts from the background signal). Among the investigated GRBs, the sample contains three long bursts (GRB 080916C, GRB 090902B, GRB 090926A) and one short one (GRB 090510A). The analysis used data from the most illuminated detectors (selected individually for each burst) of

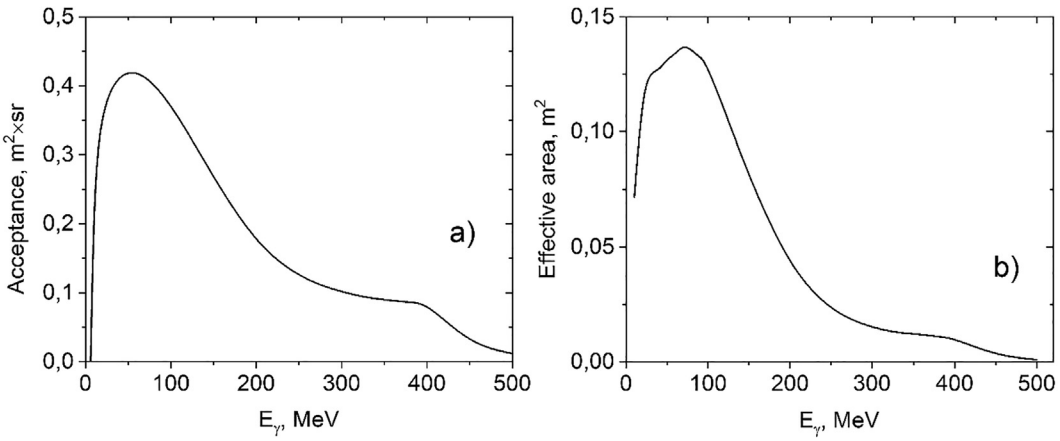


Fig. 8. The GAMMA-400 acceptance (a) and on-axis effective area (b) for gamma-ray detection arriving from one lateral direction after applying criterions (1) and (2).

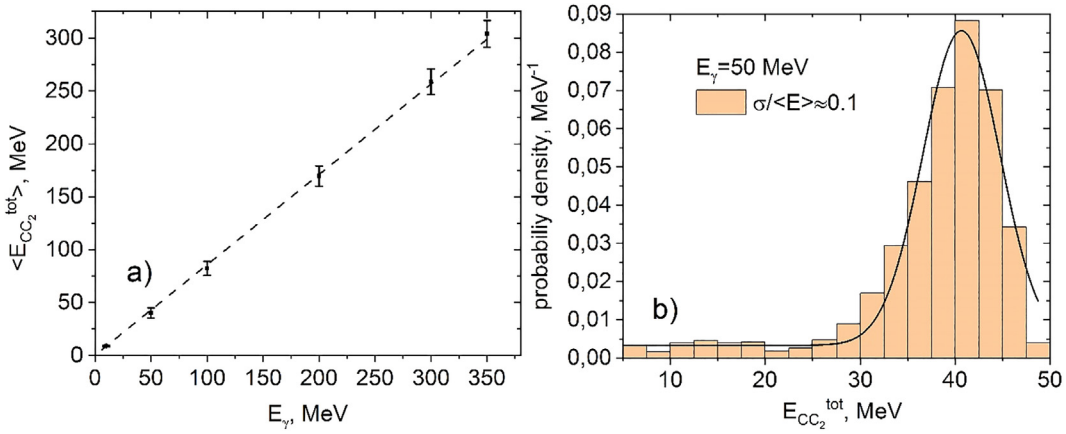


Fig. 9. The dependence of average total energy release in calorimeter CC2 from initial energy of gamma rays, arriving from one lateral direction and satisfying criterions (1) and (2) (a). Energy release distribution for 50-MeV gamma rays, satisfying criterions (1) and (2) (b).

two types: based on NaI (energy range of 7–900 keV) and BGO (energy range of 200 keV – 45 MeV) crystals from the GBM experiment, as well as data from the LAT experiment in the low-energy mode (energy range of 20 MeV – 1 GeV). The procedure of the construction and fitting for the energy spectra of selected GRBs is described in Section 5.

To construct and fit the energy spectra, the RMfit v4.3.2 software package, specially developed for the analysis of GBM and LAT/LLE data from the Fermi observatory (http://fermi.gsfc.nasa.gov/ssc/data/analysis/rmfit/), was used. The spectral analysis method is similar to that proposed in (Gruber et al., 2014), where the RMfit software package was also used. The energy spectra are approximated in the RMfit software package with the highest possible energy resolution, therefore the number of counts in each energy channel is small and, as a consequence, cannot be described by a normal distribution. Therefore, to approximate the energy spectra and to select the optimal spectral model, instead of the χ^2 criterion, modified Cash statistics was used (CSTAT) (Cash, 1979). We used following spectral models (Poolakkil et al., 2021) and their combinations to fit energy spectra and to choose optimal model for each spectrum individually: power law (PL), power law with exponential cutoff (CPL), the Band GRB function, thermal model (BB). The constructing of energy spectra was performed in time intervals, covering the light curve peaks (two peaks for GRB 090926A) and the whole burst. The results of spectral analysis (optimal spectral model for each GRB) are presented in Table 2. It was found that the energy spectrum of GRB 080916C (both integrated and in the peak region of the light curve) is described by Band GRB function in the entire spectrum range (7 keV – 1 GeV), indicating that high-energy emission has the same nature as low energy. A similar behavior was found for the first episode of GRB 090926A. In the remaining cases considered, high-energy emission represents a separate component, which is described by either a simple power-law model (PL) or Band GRB function.

Analyzing the spectrum for the whole burst gave a possibility to verify the sensitivity of GAMMA-400 lateral aperture to detect this burst, and analyzing the peak spectrum allowed to verify the possibility of looking for the details of spectrum using the GAMMA-400 performance.

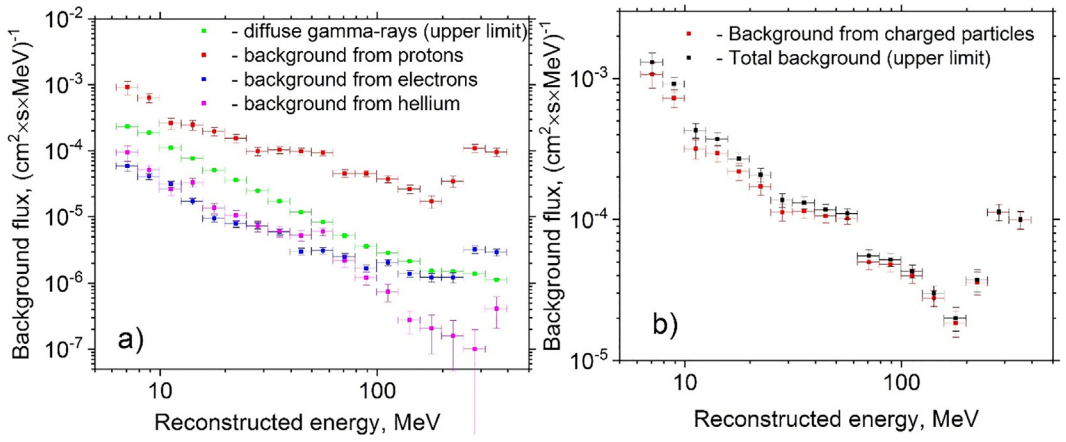


Fig. 10. The results of calculations of the effective background fluxes, which satisfy criterions (1) and (2). Background fluxes from separate components (a); background flux from charged particles and total background flux (b).

We constructed the light curves in energy ranges from 20 MeV to 1 GeV and from 7 keV to 20 MeV for each of considered GRBs using initial data for the GBM and LAT experiments of Fermi available from the public FTP archive (ftp://legacy.gsfc.nasa.gov/fermi/data/). The light curves are shown in Fig. 11. Vertical lines denote time intervals, over which the experimental data were averaged, while constructing spectrum. For GRBs: 080916C, 090902B and 090510A two time ranges were considered, while for GRB 090926A three time ranges were used.

The initial spectrum from GRB 080916C, covered the light peak, averaged over 3-s time interval and used in simulations, is shown in Fig. 12 by red line. The estimated flux from GRB 080916C obtained using (3) is presented in Fig. 12a by red squares. In each logarithmic decade, ten equal energy bins were used. In each energy bin, the number of simulated events was corrected according to real time of 3 s (Fig. 12a) using the following expression:

$$\int_{E1}^{E2} I_{GRB}(E) \times S_{eff}(E) \times dE = \frac{N_0}{\Delta t} \quad (5)$$

where $I_{GRB}(E)$ is flat flux from GRB.

Besides, in Fig. 12a there are total background and observed (background + GRB) fluxes denoted by black squares and blue circles, respectively. The total background flux was constructed from simulation events applying time normalization (4) for 3-s time interval. Finally, the reconstructed flux from GRB was deduced as subtraction of background from the observed flux. The idea is the following. The total background flux is well measured and the observed flux is varied due to the additional contribution from GRB only. The reconstructed GRB flux is presented in Fig. 12b by red squares. From this figure it is seen that GRB 080916C source can be reliably measured with 3-s time bin in the energy range from ~ 10 MeV to 100 MeV using lateral aperture. To avoid uncertainties, concerning sharp profile of effective area (Fig. 8b) and the influence of measurement errors on empirical parameters in criterion (2), the following conclusions are considered for the initial energy of GRB emission > 10 MeV.

The initial spectrum from GRB 080916C, covered the whole burst, averaged over 71-s time interval and used in simulations, is shown in Fig. 13 by red line. The estimated flux from GRB 080916C, obtained by numerical algorithm, is presented in Fig. 13a by red squares. In each energy bin, the number of simulated events was corrected according to real time of 71 s (Fig. 13a).

Also, in Fig. 13a there are total background and observed (background + GRB) fluxes denoted by black squares and blue circles, respectively. The total background flux was constructed from simulation events applying time correction (3) for 71-s time interval. Finally, the reconstructed flux from GRB was deduced as subtraction of background from the observed flux. The reconstructed GRB 080916C flux, covered the whole burst, is presented in Fig. 13b by red squares.

From the Fig. 12b and 13b it is seen that GRB 080916C can be reliably measured as with time interval covered the peak, as with time interval covering the whole burst in the energy range from ~ 10 MeV to 100 MeV using lateral aperture detection.

In Fig. 14, the initial and restored spectra from GRB 090902B are shown by red line and squares, respectively. In Fig. 14a, the spectra covered the peak and averaged over 2-s time interval. In Fig. 14b, the spectra covered the whole burst and averaged over 25-s time interval.

In Fig. 15, the initial and restored spectra from GRB 090926A are shown by red line and squares, respectively. In Fig. 15a, the spectra covered one peak and averaged over 3-s time interval, covering first peak of light curve. In Fig. 15b, the spectra covered another peak and averaged over 2-s time intervals, covering second peak of light curve. In Fig. 16, the initial and restored spectra from GRB 090926A, covered the whole burst and averaged over 22-s time interval, are shown by red line and squares, respectively.

In Fig. 17, the initial and restored spectra from short burst GRB 090510A are shown by red line and squares, respectively. In Fig. 17a, the spectra covered the peak and averaged over 1-s time interval. In Fig. 17b the spectra covered the whole burst and averaged over 8-s time interval.

We also estimated the GRB detection thresholds. For this purpose we took the average value of the spectral index of considered GRBs and calculated two amplitude coefficients A_{MIN} of the minimal detectable flux $J_{MIN} = A_{MIN}\left(\frac{E_0}{E}\right)^{2.2}$ (the pivot energy $E_0 = 1MeV$), integrated over the energy range of 10–100 MeV, applying TS criterion. Specifically, we defined the latter through a typical log-likelihood ratio as (Rolke et al., 2005):

$$TS = 2ln\left(\frac{L_1}{L_0}\right)$$

where $L_{1,0} = \lambda_{1,0}^{n} \frac{e^{-\lambda_{1,0}}}{n!}$ is the Poisson likelihood;

λ_1 is the mean expected number of photons from GRB and background events integrated over our energy range of interest 10–100 MeV;

λ_0 is the number of background events only;

n is the total observed number of events from the simulation.

Substituting $J_{MIN} = A_{MIN}\left(\frac{E_0}{E}\right)^{2.2}$ into λ_1, applying the typical detection criteria TS = 25 (a reference mark to estimate, for example, point source sensitivity in Fermi-LAT experiment, https://www.slac.stanford.edu/exp/glast/groups/canda/lat_Performance.htm) and solving (6) for A_{MIN}, we obtained the following integral detection thresholds. The first amplitude $(A_{MIN})_1 = 0.42[MeV \times cm^2 \times s]^{-1}$ was calculated for 1-s time interval as representative of short GRBs. The second amplitude $(A_{MIN})_{10} = 0.12[MeV \times cm^2 \times s]^{-1}$ was calculated for 10-s time interval as representative of long GRBs. As an exam-

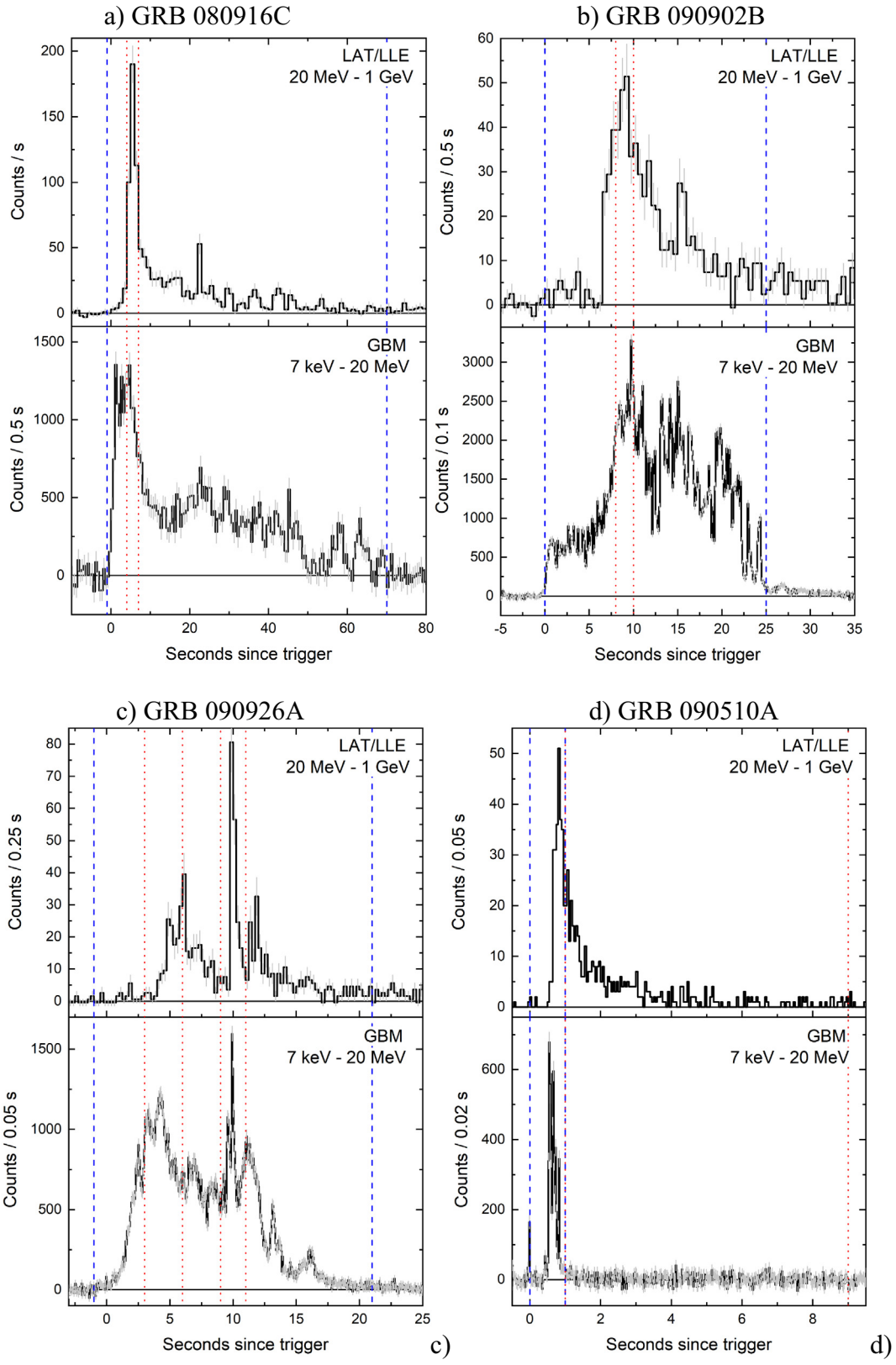


Fig. 11. Light curves for GRB 080916C (a), GRB 090902B (b), GRB 090926A (c), GRB 090510A (d) constructed using initial data for the GBM and LAT experiments of Fermi available from the public FTP archive (ftp://legacy.gsfc.nasa.gov/fermi/data/). Vertical lines denote time intervals, over which the experimental data were averaged.

Table 2
The results of spectral analysis of GRBs based on Fermi/LAT and Fermi/GBM data.

GRB	Time interval, s	Spectral model	Amplitude, $\frac{ph}{cm^2 \times s \times keV}$	alpha	beta	Ep, keV
080916C	(-1, 70)	Band	0.0167+/-0.0003	−1.04+/-0.01	−2.18+/-0.01	498+/-20
	(4, 7)	Band	0.0296+/-0.0006	−1.17+/-0.02	−2.23+/-0.04	2456+/-360
090510A	(0, 1)	Band + PL	0.018/-0.002	−0.66+/-0.06	−3.3+/-0.2	3990+/-290
			0.0039+/-0.0012	−1.56+/-0.04		
	(1, 9)	Band	0.0010+/-0.0002	−1.44+/-0.04	−2.2+/-0.2	(8.5+/-3.0) × 10^4
090902B	(0, 25)	Band + PL	0.0928+/-0.0006	−0.59+/-0.01	−3.51+/-0.11	752 +- 10
			0.0129+/-0.0003	−1.92+/-0.01		
	(8, 10)	CPL + PL	0.073+/-0.002	0.12+/-0.04		947+/-21
			0.052+/-0.001	−1.95+/-0.01		
090926A	(-1, 21)	Band + CPL	0.043+/-0.016	−1.2+/-0.1	−2.15+/-0.02	640+/-270
			0.102+/-0.017	−0.37+/-0.09		288+/-7
	(3, 6)	Band	0.302+/-0.005	−0.58+/-0.01	−2.43+/-0.02	373+/-7
	(9, 11)	Band + CPL	0.032+/-0.003	−1.71+/-0.03	−2.07 +- 0.11	(2.9+/-2.2) × 10^4
			0.278+/-0.008	−0.44+/-0.06		263+/-6

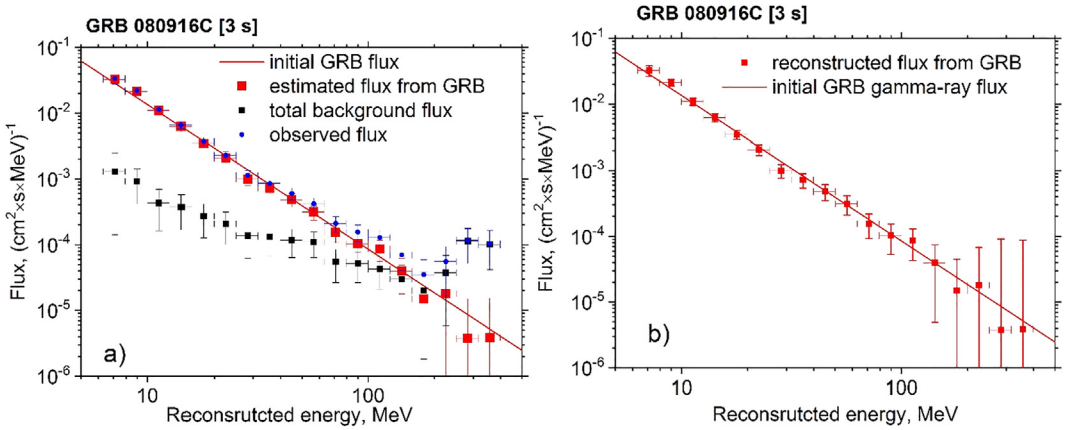


Fig. 12. The initial spectrum from GRB 080916C, averaged over 3-s time interval (red line); the estimated flux from GRB 080916C (red squares); the total background flux (black squares); the observed flux (background + GRB, blue circles) (a). The reconstructed flux from GRB 080916C (red squares) (b). (For interpretation of the references to colour in this figure legend, the reader is referred to the web version of this article.)

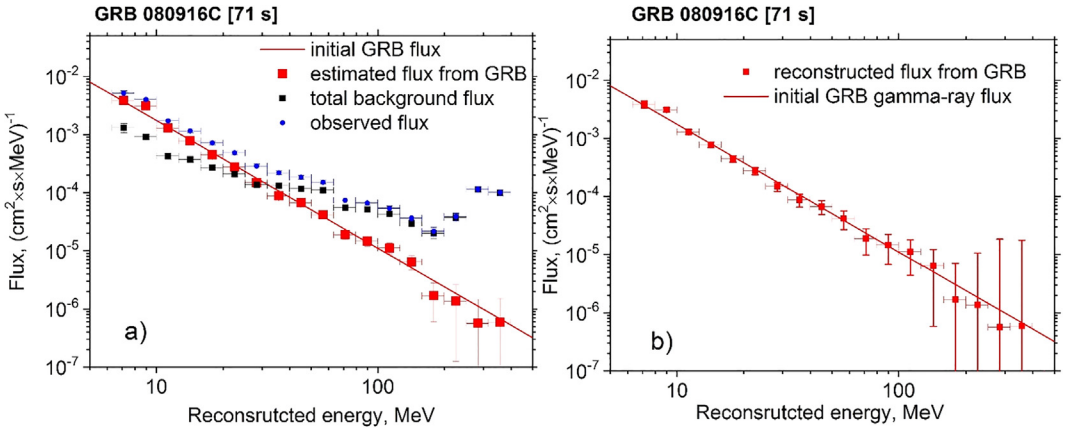


Fig. 13. The initial spectrum from GRB 080916C, averaged over 71-s time interval (red line); the estimated flux from GRB 080916C (red squares); the total background flux (black squares); the observed flux (background + GRB, blue circles) (a). The reconstructed flux from GRB 080916C (red squares) (b). (For interpretation of the references to colour in this figure legend, the reader is referred to the web version of this article.)

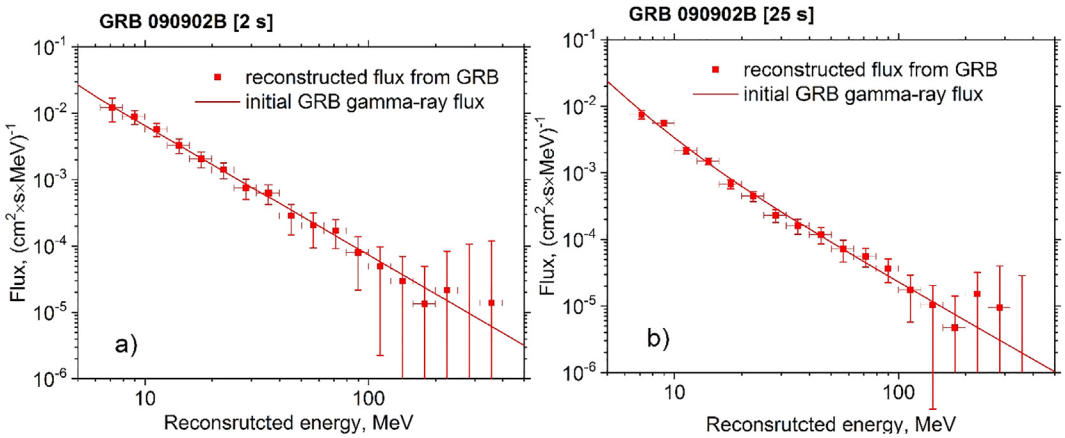


Fig. 14. The initial and reconstructed spectra from GRB 090902B are denoted by red line and squares, respectively. The spectra averaged over 2-s time interval (a). The spectra averaged over 25-s time interval (b). (For interpretation of the references to colour in this figure legend, the reader is referred to the web version of this article.)

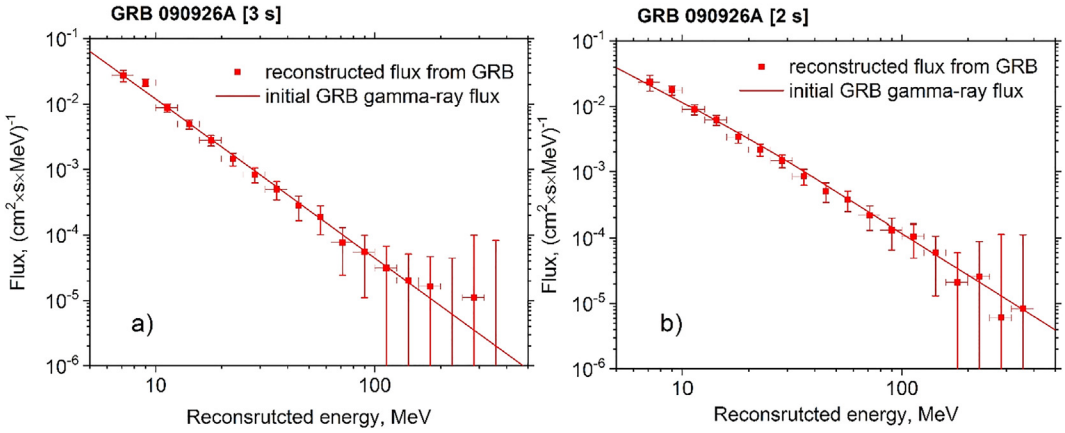


Fig. 15. The initial and reconstructed spectra from GRB 090926A are denoted by red line and squares, respectively. The spectra averaged over 3-s time interval, covering first peak of light curve (a). The spectra averaged over 2-s time interval, covering second peak of light curve (b). (For interpretation of the references to colour in this figure legend, the reader is referred to the web version of this article.)

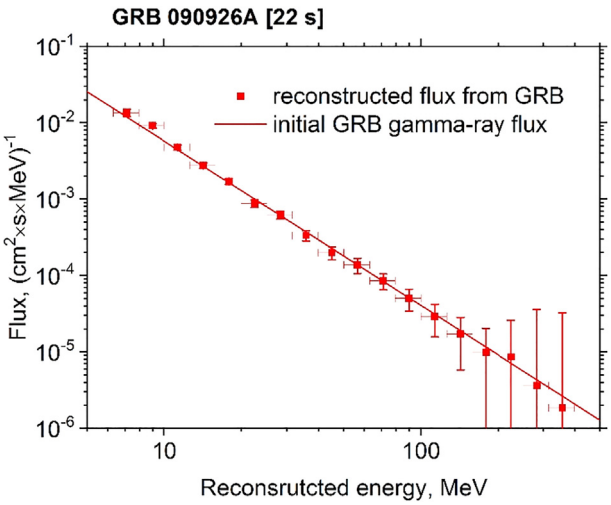


Fig. 16. The initial and reconstructed spectra from GRB 090926A, averaged over 22-s time interval, are denoted by red line and squares, respectively. (For interpretation of the references to colour in this figure legend, the reader is referred to the web version of this article.)

ple of a particular GRB case, we calculated the minimal detectable flux for GRB 090510A for 1-s time interval and presented it in Fig. 17a by the black line.

In above description the capability of the GAMMA-400 instrument to detect GRBs from lateral directions was analyzed for normal incidence. To consider other angles, the special simulations were fulfilled, and results of these simulations are presented in Fig. 18a. In this figure, the effective area for 50-MeV gamma rays versus angle of incidence is presented. The direction Z coincides with the direction of gamma-ray telescope axis for the main aperture. Black line corresponds to flat flux from left direction (left simulation plane, Fig. 3), red line corresponds to flat flux from top direction (top simulation plane, Fig. 3). It is necessary to mention that for both simulations the criterions (1) and (2) were applied in numerical algorithm. It is seen that influence of fluxes from the top direction is insignificant in comparison with impact of fluxes from lateral direction. For gamma rays from the top-down direc-

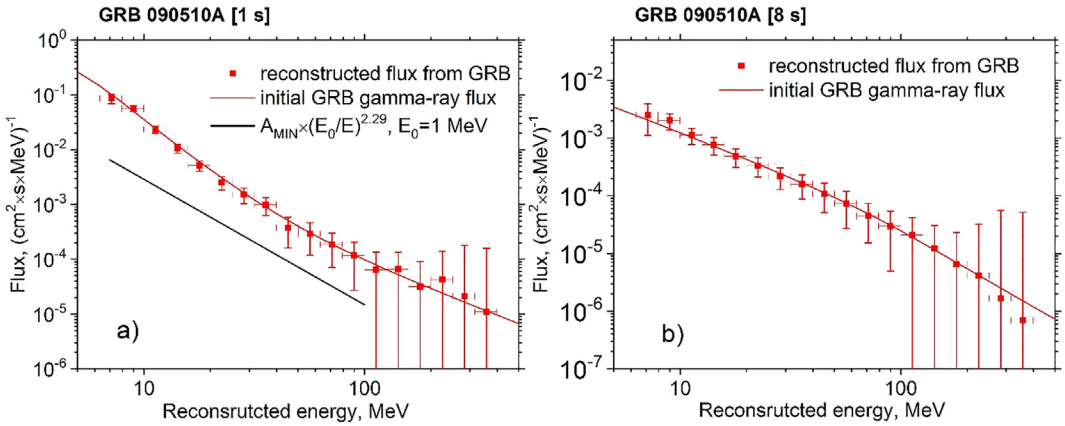


Fig. 17. The initial and reconstructed spectra from short GRB 090510A are denoted by red line and squares, respectively. The spectra are averaged over 1-s time interval. The minimal flux estimated for 1-s time interval with TS = 25 criterion is presented by black line (a). The spectra are averaged over 8-s time interval (b). (For interpretation of the references to colour in this figure legend, the reader is referred to the web version of this article.)

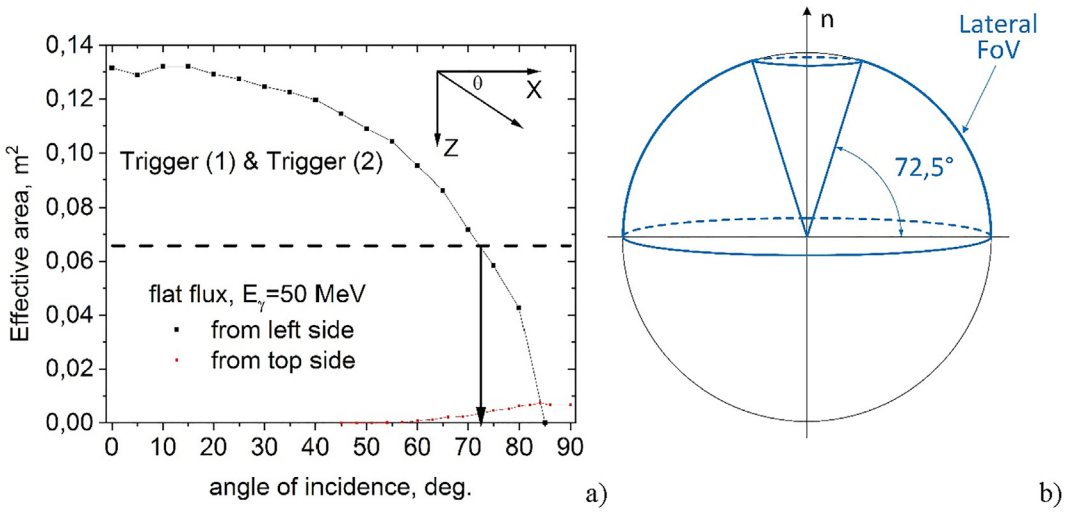


Fig. 18. The effective area for 50-MeV gamma rays versus angle of incidence.

tion, another trigger for the main top-down aperture should be used (Leonov et al., 2019a), but this is not the point to consider in present paper. Fig. 18a shows the dependence of the effective area vs angle of incidence. For the value of the effective area at hail-maximum we obtained an estimation of $\theta_{max} = 72.5°$ deg for opening angle of the cone for the lateral aperture (Fig. 18b). However, as mentioned in Section 3, due to large amount of satellite platform matter located under the gamma-ray telescope, the directions from top hemisphere are allowed only. As a result, the value field of view of lateral aperture of GAMMA-400 can be estimated as $\Omega_{FoV} = 2\pi cos(\pi/2 - \theta_{max}) \approx 6$ sr.

As the structure of CC2 from CsI(Tl) columns provides only 2D projection information, and taking into account that criterion (2) is developed for each of four sides separately, the location is determined only with $\sim \pi/4$ accuracy. Therefore, the GRB optical and X-ray information, which comes from other missions, is required.

Black line corresponds to flat flux from left direction (left simulation plane, Fig. 3), red line corresponds to flat flux from top direction (top simulation plane, Fig. 3). For both lines the criterions (1) and (2) were applied in numerical algorithm. Value of the effective area at half-maximum gives an estimation of 72.5° for opening of a cone for lateral aperture (a). Lateral aperture FoV relative to the gamma-ray telescope axis (b).

In this section, the principle capability of the GAMMA-400 instrument to detect GRBs from lateral directions and measure their spectrum from 10 MeV to 100 MeV, when analyzing time scale of the peak or of the total period of GRBs, is reported. The GRB intensity in given time channel, while analyzing its temporal structure, will determine the possibility of investigations. To study the GRB temporal structure the additional information, concerning the count rate from each of used broad spectral channels, could be provided. The possibility to transmit the GRB temporal profiles (after data compressing) to the ground

station is provided by information quota of 100 GB per day.

6. Conclusion

Currently, the GAMMA-400 launch is scheduled for 2030. In this paper, we showed that the capabilities of the GAMMA-400 gamma-ray telescope allow us to measure GRB spectra from the lateral aperture reliably in the energy range from $\sim$ 10 to $\sim$ 100 MeV. This conclusion was based on the analysis of the results of Monte-Carlo simulations. The test algorithm introduced the sample of data from space-based GBM and LAT instruments of Fermi experiment. This sample contains the brightest three long bursts: GRB 080916C, GRB 090902B, GRB 090926A and one short burst GRB 090510A. To reject background of cosmic rays the off-line additional data processing selection was constructed, providing the on-axis effective area of about 0.13 m^2 for each of four lateral directions. The total effective field of view for the GAMMA-400 lateral aperture is $\sim$ 6 sr.

The nature of the high-energy emission and its possible connection with the low-energy classical gamma-ray emission is still debatable. There are several signs of at least bimodal behavior of high-energy emission (separate emission mechanism vs extension of low-energy emission to high energy). The detailed investigation of GRBs by the GAMMA-400 lateral aperture in energy range 10–100 MeV, being the transition zone between these emission components, could shed light on the problem.

Declaration of Competing Interest

The authors declare that they have no known competing financial interests or personal relationships that could have appeared to influence the work reported in this paper.

Acknowledgements

The authors would like to thank the anonymous referees for their many constructive comments and suggestions that definitely helped to improve the quality of this article. The authors also thank the Editors for their management of the review.

This work was partially supported by the Russian State Space Corporation ROSCOSMOS (contract no. 024-5004/16/224), the Ministry of Science and Higher Education of the Russian Federation under Project "Fundamental problems of cosmic rays and dark matter" (contact no. 0723-2020-0040), NRNU MEPhI Academic Excellence Project (contract 02.a03.21.0005) and was performed using resources of NRNU MEPhI high-performance computing center.

References

Abdollahi, S., Acero, F., Ackermann, M., et al., 2020. Fermi Large Area Telescope Fourth Source Catalog. ApJS 247:33, 37pp.

Ackermann, M., Ajello, M., Atwood, W.B., et al., 2012. Fermi-LAT Observations of the Diffuse γ-Ray Emission: Implications for Cosmic Rays and the Interstellar Medium. Astrophys. J. 750 (3), 1–35.

Adriani, O., Barbarino, G.G., Bazilevskaya, G.A., et al., 2011. PAMELA Measurements of Cosmic-Ray Proton and Helium Spectra. Science 332 (6025), 69–72.

Adriani, O., Barbarino, G.G., Bazilevskaya, G.A., et al., 2015. Time Dependence of the e-Flux Measured by PAMELA During the 2006 July – 2009 December Solar Minimum. Astrophys. J. 810 (142), 1–13.

Ajello, M., Arimoto, M., Axelsson, M., et al., 2019. A Decade of Gamma-Ray Bursts Observed by Fermi-LAT: The Second GRB Catalog. Astrophys. J. 878 (52), 1–61.

An, Q., Asfandiyarov, R., Azzarello, P., et al., 2019. Measurement of the cosmic ray proton spectrum from 40 GeV to 100 TeV with the DAMPE satellite. Sci Adv 5 (eaax3793), 1–10.

Bisschoff, D., Potgieter, M.S., Aslam, O.P.M., 2019. New Very Local Interstellar Spectra for Electrons, Positrons, Protons, and Light Cosmic Ray Nuclei. Astrophys. J. 878 (59), 1–8.

Brun, R., Rademakers, F., 1997. ROOT: An Object Oriented Data Analysis Framework. Nucl. Inst. Meth. A 389, 81–86.

Cash, W., 1979. Parameter Estimation in Astronomy Through Aplication of the Likelihood Ratio. Astrophys. J. 228, 939–947.

Galper, A.M., Topchiev, N.P., Yurkin, Y.T., 2018. GAMMA-400 Project. Astronomy Reports 62 (12), 882–889.

Gruber, D., Goldstein, A., Weller von Achlefeld, V., et al., 2014. The Fermi GBM Gamma-Ray Burst Spectral Catalog: Four Years of Data. Astrophys. J. Suppl. Ser. 211 (12), 1–27.

Joshi, J.C., Razzaque, S., 2021. Modelling synchrotron and synchrotron self-Compton emission of gamma-ray burst afterglows from radio to very-high energies. In: Monthly Notices of the Royal Astronomical Society, p. stab1329..

Martucci, M., Munini, R., Boezio, M., et al., 2018. Proton Fluxes Measured by the PAMELA Experiment from the Minimum to the Maximum Solar Activity for Solar Cycle 24. Astrophys. J. Lett. 854 (L2), 1–8.

Mikhailova, A.V., Bakaldin, A.V., Chernysheva, I.V., et al., 2020. Capabilities of the GAMMA-400 gamma-ray telescope for lateral aperture. IOP Conf. Ser. J. Phys.: Conf. Series 1690 012026.

Ngobeni, M.D., Aslam, O.P.M., Bisschoff, D., et al., 2020. The 3D numerical modeling of the solar modulation of galactic protons and helium nuclei related to observations by PAMELA between 2006 and 2009. Astrophys. Space Sci. 365 (182), 1–18.

Leonov, A.A., Galper, A.M., Bonvicini, V., et al., 2015. Separation of electrons and protons in the GAMMA-400 gamma-ray telescope. Advances in Space Research 56, 1538–1545.

Leonov, A.A., Galper, A.M., Topchiev, N.P., et al., 2019a. Capabilities of the Gamma-400 Gamma-ray Telescope for Observation of Electrons and Positrons in the TeV Energy Range. Physics of Atomic Nuclei 82 (6), 855–858.

Leonov, A.A., Galper, A.M., Topchiev, N.P., et al., 2019b. Multiple Coulomb scattering method to reconstruct low-energy gamma–ray direction in the GAMMA-400 space-based gamma–ray telescope. Adv. Space Res. 63, 3420–3427.

Picozza, P., Galper, A.M., Castellini, G., et al., 2007. PAMELA – A payload for antimatter matter exploration and light-nuclei astrophysics. Astroparticle Physics 27 (4), 296–315.

Poolakkil, S., Preece, R., Fletcher, C., et al., 2021. The Fermi-GBM Gamma-Ray Burst spectral catalog: 10 yr of data. Astrophys. J. 913 (60), 1–20.

Rolke, W.A., Lopez, A.M., Conrad, J., 2005. Limits and confidence intervals in the presence of nuisance parameters. Nucl. Instrum. Methods Phys. Res. A 551, 493–503.

Suchkov, S.I., Galper, A.M., Arkhangelskiy, A.I., et al., 2021. Calibrating the prototype calorimeter for the GAMMA-400 γ-ray telescope on the positron beam at the Pakhra accelerator. Instruments Experim. Tech. 64 (5), 669–675.

Topchiev, N.P., Galper, A.M., Bonvicini, V., et al., 2016. The GAMMA-400 gamma-ray telescope for precision gamma-ray emission investigations. IOP Conf. Ser. J. Phys.: Conf. Series 675 032009.

Topchiev, N.P., Galper, A.M., Bonvicini, V., et al., 2016a. Perspectives of the GAMMA-400 space observatory for high-energy gamma rays and cosmic rays measurements. IOP Conf. Ser.: J. Phys.: Conf. Series 675, 032010.

Topchiev, N.P., Galper, A.M., Arkhangelskaja, I.V., et al., 2019a. Space-based GAMMA-400 mission for direct gamma- and cosmic- ray observations. IOP Conf. Ser. J. Phys. Conf. Series 1181 012041.

Topchiev, N.P., Galper, A.M., Arkhangelskaja, I.V., et al., 2019b. High-energy gamma- and cosmic-ray observations with future space-based GAMMA-400 gamma-ray telescope. EPJ Web of Conferences 208, 14004.

Available online at www.sciencedirect.com

ScienceDirect

Advances in Space Research 70 (2022) 2773–2793

ADVANCES IN SPACE RESEARCH (a COSPAR publication)

www.elsevier.com/locate/asr

Gamma- and Cosmic-Ray observations with the GAMMA-400 Gamma-Ray telescope

N.P. Topchiev [a,*], A.M. Galper [a,b], I.V. Arkhangelskaja [b], A.I. Arkhangelskiy [b], A.V. Bakaldin [c], R.A. Cherniy [a], I.V. Chernysheva [b], E.N. Gudkova [a], Yu.V. Gusakov [a], O.D. Dalkarov [a], A.E. Egorov [a], M.D. Kheymits [b], M.G. Korotkov [b], A.A. Leonov [a,b], A.G. Malinin [b], V.V. Mikhailov [b], A.V. Mikhailova [b], P.Yu. Minaev [a,d], N.Yu. Pappe [a], M.V. Razumeyko [a], M.F. Runtso [b], Yu.I. Stozhkov [a], S.I. Suchkov [a], Yu.T. Yurkin [b]

[a] *Lebedev Physical Institute of the Russian Academy of Sciences, Moscow 119991, Russia*
[b] *National Research Nuclear University "MEPhI" (Moscow Engineering Physics Institute), Moscow 115409, Russia*
[c] *Scientific Research Institute for System Analysis of the Russian Academy of Sciences, Moscow 117218, Russia*
[d] *Space Research Institute, Moscow 117997, Russia*

Received 13 August 2021; received in revised form 20 January 2022; accepted 26 January 2022
Available online 3 February 2022

Abstract

The future space-based GAMMA-400 gamma-ray telescope will operate onboard the Russian astrophysical observatory in a highly elliptic orbit during 7 years to observe Galactic plane, Galactic Center, Fermi Bubbles, Crab, Vela, Cygnus X, Geminga, Sun, and other regions and measure gamma- and cosmic-ray fluxes. Observations will be performed in the point-source mode continuously for a long time (~100 days). GAMMA-400 will measure gamma rays in the energy range from ~ 20 MeV to several TeV and cosmic-ray electrons + positrons up to several tens TeV. GAMMA-400 instrument will have very good angle and energy resolutions, high separation efficiency of gamma rays from cosmic-ray background, as well as electrons + positrons from protons. The main feature of GAMMA-400 is the unprecedented angular resolution for energies > 30 GeV better than the space-based and ground-based gamma-ray telescopes by a factor of 5–10. GAMMA-400 observations will permit to resolve gamma rays from annihilation or decay of dark matter particles, identify many discrete sources, clarify the structure of extended sources, specify the data on cosmic-ray electron + positron spectra.
© 2022 COSPAR. Published by Elsevier B.V. All rights reserved.

Keywords: Gamma rays; Gamma-ray telescope; Gamma-ray burst; Dark matter; Electron + positron fluxes

* Corresponding author.
E-mail addresses: tnp51@yandex.ru (N.P. Topchiev), amgalper@mephi.ru (A.M. Galper), ivarkhangelskaya@mephi.ru (I.V. Arkhangelskaja), aiarkhangelskij@mephi.ru (A.I. Arkhangelskiy), bakaldin71@mail.ru (A.V. Bakaldin), roma.cherny@yandex.ru (R.A. Cherniy), ivchernysheva@mephi.ru (I.V. Chernysheva), elena@gudkoff.ru (E.N. Gudkova), igoussak@yandex.ru (Y.V. Gusakov), odalkarov@rambler.ru (O.D. Dalkarov), eae14@yandex.ru (A.E. Egorov), mcsaksik@gmail.com (M.D. Kheymits), mikhail.g.korotkov@gmail.com (M.G. Korotkov), leon@ibrae.ac.ru (A.A. Leonov), alexander.malinin@cern.ch (A.G. Malinin), vvmikhajlov@gmail.com (V.V. Mikhailov), ann_mikhailova@mail.ru (A.V. Mikhailova), minaevp@mail.ru (P.Yu. Minaev), nikolay-pappe@mail.ru (N.Yu. Pappe), ramv13@yandex.ru (M.V. Razumeyko), mikhail.runtso.45@mail.ru (M.F. Runtso), stozhkov@fian.fiandns.mipt.ru (Y.I. Stozhkov), soutch@mail.ru (S.I. Suchkov), ytyurkin@mephi.ru (Y.T. Yurkin).

https://doi.org/10.1016/j.asr.2022.01.036
0273-1177/© 2022 COSPAR. Published by Elsevier B.V. All rights reserved.

1. Introduction

The last few decades have been marked by a new stage in the development of astronomy, due to active observations in all ranges of the electromagnetic spectrum - from the low-frequency radio emission to the gamma-ray emission of high and ultrahigh energies. The possibility of observation in all wavelength ranges, as well as the use of neutrino and gravitational wave facilities, made it possible to implement an integrated approach in the study of astrophysical objects.

A significant contribution to astrophysical research is made by gamma-ray astronomy. Numerous studies carried out in this area have made it possible to discover galactic diffuse gamma-ray emission, isotropic extragalactic gamma-ray emission, to detect and investigate numerous galactic and extragalactic gamma-ray sources, to study gamma-ray lines, gamma-ray bursts, to study gamma-ray emission from the Sun, as well as to search for dark matter particles.

At present, the Fermi-LAT gamma-ray telescope has continued to observe the gamma-ray emission in space since 2008. The fourth Fermi-LAT catalog (Abdollahi et al., 2020) contains 5065 sources for the energy range from 50 MeV to 1000 GeV, but $\sim$ 30% of gamma-ray sources are still unidentified. It should be noted that Fermi-LAT carries out observations in the scanning mode and the source observation time is only $\sim$ 15% of the telescope operation time (Abdollahi et al., 2020). The ground-based facilities VERITAS, MAGIC, H.E.S.S., HAWC, ARGO-YBJ, LHAASO and others have observed the gamma-ray emission from only $\sim$ 250 gamma-ray sources in the energy range above $\sim$ 100 GeV (http://tevcat.uchicago.edu/). The problem of identifying gamma-ray sources with the best angular resolution in space-based experiments remains one of the central goals.

Another relevant goal is to search for and study gamma-ray bursts (GRBs). Despite the GRB searching with Fermi-LAT (Ajello et al., 2019), Fermi-GBM (von Keinlin et al., 2020), and Swift-BAT (Lien et al., 2016) the complete understanding in the physical processes responsible for high-energy emission from GRBs is not reached.

Attempts to study the properties of dark matter (DM) particles are carried out by direct and indirect detection methods. The indirect detection method consists in recording not DM particles themselves, but the products of their potential annihilation or decay: cosmic-ray (CR) charged particles, antiparticles and gamma rays (the PAMELA, AMS-2, ATIC, Fermi-LAT, DAMPE, CALET, HESS-II, MAGIC, VERITAS, HAWC, AUGER experiments), and neutrinos (the IceCube/DeepCore/PINGU, ANTARES/KM3NET, BAIKAL-GVD, Super-Kamiokande/HyperKamiokande, AUGER experiments).

Weakly interacting massive particles (WIMPs) with mass between several GeV and several TeV are still considered as the most probable candidate (e.g. Leane et al., 2018) for the role of DM. WIMPs can annihilate or decay with the production of gamma rays and electrons + positrons. They can produce both the excess in continuous energy spectrum and narrow gamma-ray lines. Axion-like particles (ALPs) are also proposed as candidate particles for DM (e.g. Calore et al., 2020). Search for and study of the potential emission or particles from DM with the best angular and energy resolutions remains one of the central goals.

ATIC (Chang et al., 2008), Fermi-LAT (Abdollahi et al., 2017), PAMELA (Adriani et al., 2017), AMS-2 (Aguilar et al, 2014), CALET (Adriani et al., 2018), DAMPE (Ambrosi et al., 2017), MAGIC (Tridon et al., 2011), VERITAS (Staszak et al., 2015), H.E.S.S. (Aharonian et al., 2009) measured energy spectra of CR electrons + positrons in the TeV energy range. The data of experiments are not entirely consistent with each other, however, the most of observations show the existence of a remarkable flux suppression at E $\sim$ 1 TeV. The existence of this cut-off has been first reported by the H.E.S.S., confirmed by MAGIC, VERITAS, and also obtained in direct measurements by DAMPE and CALET detectors. At higher energies direct measurements extended only up to $\sim$ 4.8 TeV. The obtained results in the energy range above 100 GeV (e.g. Evoli et al., 2021) require further improvement up to 10 TeV.

Therefore new direct observations of gamma-ray emission in the energy range from $\sim$ 20 MeV up to several TeV, as well as electron + positron fluxes up to several tens TeV are required using the space-based telescope with better angular and energy resolutions, and separation from background, in order to identify many gamma-ray sources, resolve possible gamma-ray lines or clarify an excess in continuous energy spectrum from DM, specify energy spectra of CR electrons + positrons.

2. The GAMMA-400 astrophysical observatory

The Russian GAMMA-400 astrophysical observatory will include the Navigator spacecraft platform (developed by Lavochkin Association, https://www.laspace.ru/projects/astrophysics/gamma-400/), the GAMMA-400 gamma-ray telescope (developed, in the main, by Lebedev Physical Institute, https://gamma400.lebedev.ru/indexeng.html, and National Research Nuclear University "MEPhI") and additional instruments (the ART-XC X-ray telescope with the energy range of 5–30 keV and magnetic plasma detectors developed by Space Research Institute of the Russian Academy of Sciences). The GAMMA-400 gamma-ray telescope is installed on a special truss at a distance of about 2 m from the Navigator space platform. The gamma- and X-ray telescopes are installed coaxially without overlapping fields of view, which are $\pm$ 45° and $\pm$ 0.5°, respectively (Fig. 1).

The GAMMA-400 astrophysical observatory includes the high-data-rate radio complex (HDRRC) with a high-

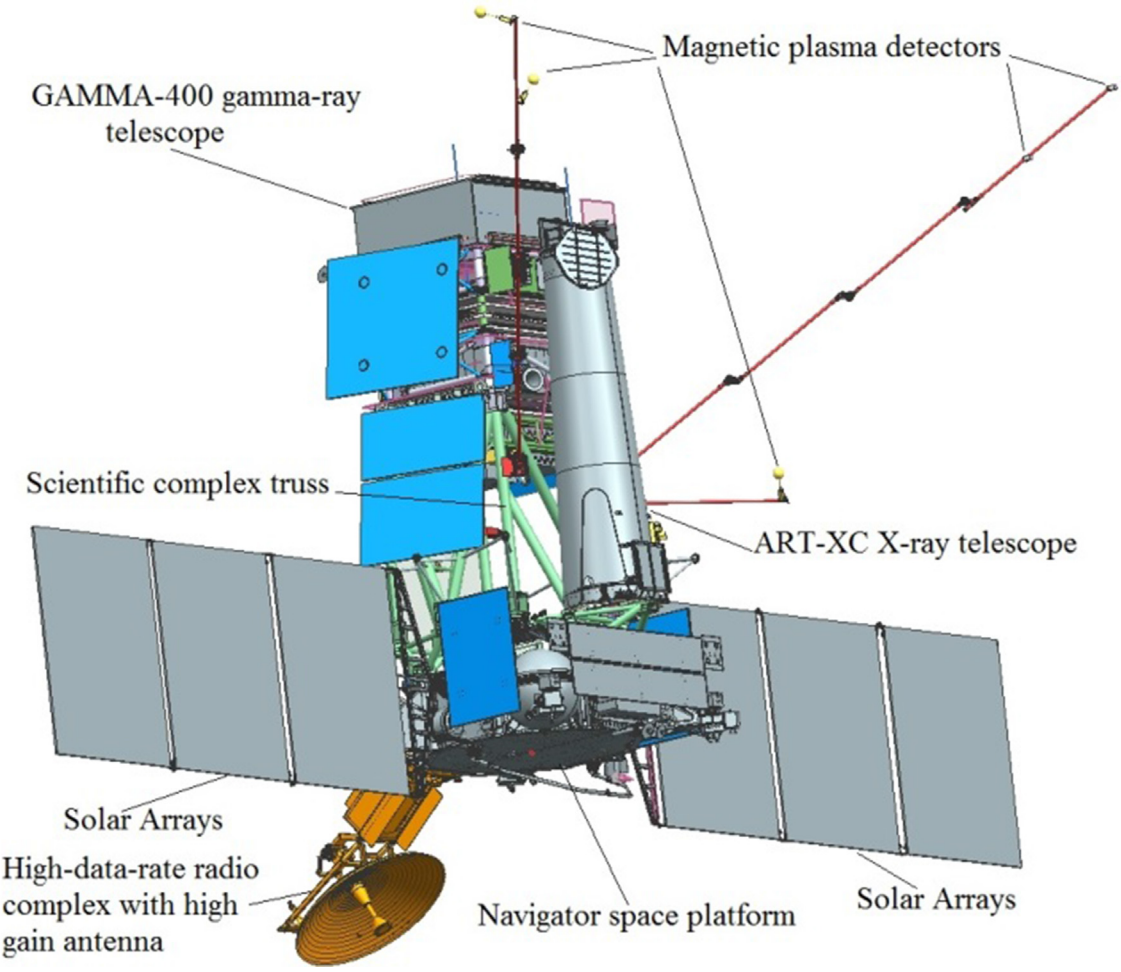


Fig. 1. The Russian GAMMA-400 astrophysical observatory, including the Navigator spacecraft platform, the GAMMA-400 gamma-ray telescope and additional instruments (the ART-XC X-ray telescope and magnetic plasma detectors).

gain antenna (Fig. 2). HDRRC consists of antenna feeder system and on-board (airborne) radio-technical complex.

The antenna feeder system includes:

- two-mirror transmitting high-gain antenna with a diameter of 1.5 m;
- waveguide path and filters.

The on-board (airborne) radio-technical complex contains radio-transmitting device, operating at the frequency of 15 GHz.

HDRRC transmits data with the speed of 160 Mbps, using quadrature phase-shift keying modulation (QPSK) at the frequency of 15 GHz, while due to the use of error-correcting coding, an error probability is no $>10^{-9}$.

HDRRC has two modes of operation:

- operating mode with rated output power (output signal power from 40 to 50 W);
- operating mode with reduced output power (output signal power from 4 to 7 W).

As a ground receiving station (GRS), it is proposed to use the radio-astronomy complex based on the RT-22 radio-telescope (Fig. 3) in Pushchino (Lebedev Physical Institute), the same station as for the RadioAstron mission (Spectr-R) (Kardashev et al., 2013).

GRS functions in cooperation with on-board HDRRC equipment and provides the solution of the following functions:

- tracking the spacecraft in its motion along the sky during the communication session;
- reception and decoding of the scientific data flows at the speed of 2×80 Mbit/s with relative error 10^{-9} and their recording after decoding on special digital recorders (RDR, MARK-5 and others) together with the exact local time information;
- signal selection of the carrier signal frequency of the transmission channel, and the measurement of the frequency of the residual Doppler shift and the current phase difference signal of H-maser GRS, digitization

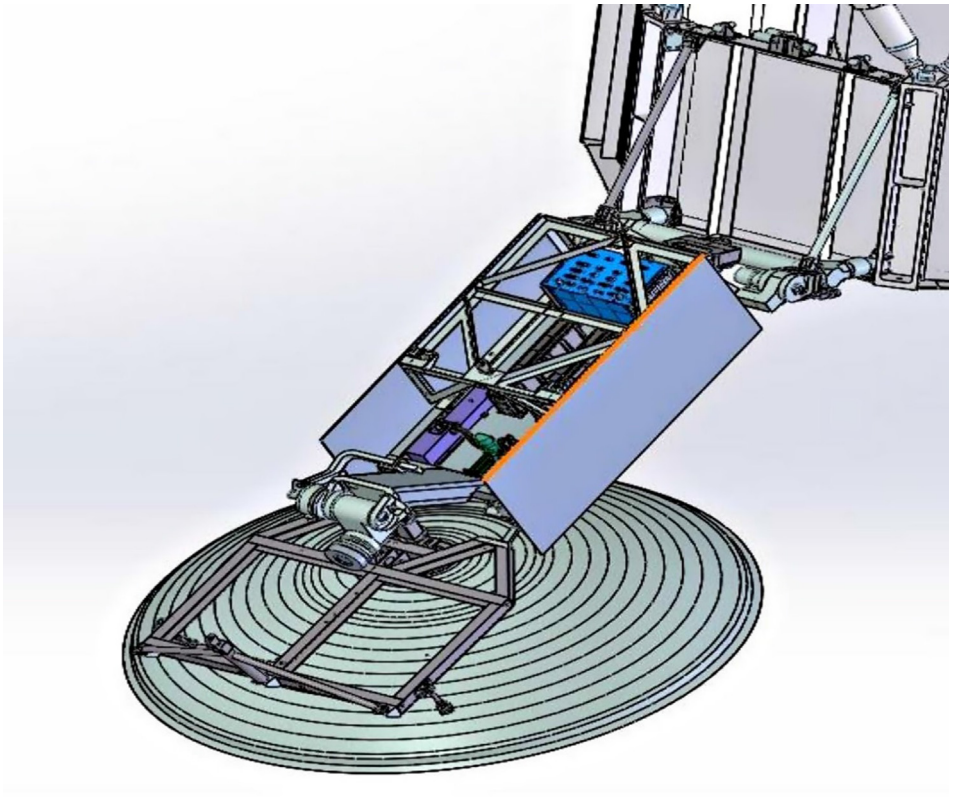


Fig. 2. High-data-rate radio complex with a high-gain antenna.



Fig. 3. The RT-22 radio-telescope in Pushchino as a ground receiving station.

of these data with the specified rate, their recording, which is bound to the current time and the transfer to consumers.

Using the Navigator spacecraft platform gives the GAMMA-400 experiment a highly unique opportunity for the near future gamma- and cosmic-ray science, since it allows us to install the scientific payload (mass of $\sim$ 3000 kg, power consumption of 2000 W, telemetry downlink of 100 GB/day, lifetime >7 years), which will provide the significant contribution of GAMMA-400 as the next generation instrument for gamma-ray astronomy and cosmic-ray physics.

The GAMMA-400 observatory will be initially launched into a highly elliptical orbit (with an apogee of 300 000 km and a perigee of 500 km, with an inclination of 51.4°) with 7 days orbital period. Under the influence of gravitational disturbances of the Sun, Moon, and the Earth after $\sim$ 6 months the orbit will transform to about an approximately circular one with a radius of $\sim$ 200 000 km and will not suffer from the Earth's occultation and be outside the radiation belts. A great advantage of such an orbit is the fact that the many astrophysical objects will always be available for gamma-ray astronomy, since the Earth will not cover a significant fraction of the sky, as in the case for the low-Earth orbit. Moreover, the GAMMA-400 source pointing strategy (continuous point-source observation for a long time $\sim$ 100 days) will be properly defined to maximize the physics outcome of the experiment in contrast to the scanning mode for the current Fermi-LAT, CALET, DAMPE and future HERD, AMS-100 experiments. The launch of the GAMMA-400 space observatory is scheduled for 2030.

3. The GAMMA-400 gamma-ray telescope

3.1. The GAMMA-400 physical scheme

The current physical scheme of the GAMMA-400 gamma-ray telescope (Galper et al., 2013; Topchiev et al., 2017; Galper et al., 2018; Topchiev et al., 2019; Egorov et al., 2020) is shown in Fig. 4.

GAMMA-400 includes:

- anticoincidence AC top and four lateral AC lat detectors;
- converter-tracker C;
- time of flight system ToF from S1 and S2 detectors;
- two-part calorimeter from CC1 and CC2;
- four lateral detectors LD;
- preshower detector S3, shower leakage detector S4.

Electronics includes system of trigger formation (ST), scientific data acquisition system (SDAS) and other electronics units.

Fig. 5 shows view of the GAMMA-400 gamma-ray telescope, where 2 star sensors (SSs) with an accuracy of better than 3″ and thermal control systems (TCSs) are additionally presented.

The construction for installing systems and detectors of the GAMMA-400 gamma-ray telescope and thermal control systems are developed by Lavochkin Association. Many construction elements of the gamma-ray telescope, as well as detectors are made of carbon-filled plastic.

More detailed information about detector systems is presented in Figs. 6 and 7.

AC is anticoincidence system, C is converter-tracker, S1 and S2 are ToF detectors, ST is system of trigger formation, CC1 and CC2 are two parts of calorimeter, SciFi is SciFi detectors in C and CC1, S3 is preshower detector, S4 is shower leakage detector, SS are star sensors, EU are electronic units, and TCS are thermal control systems.

Anticoincidence system. The anticoincidence system AC is used to discriminate incoming charged particles with an efficiency of >0.9995 and time resolution of $\sim$ 200 ps (Arkhangelskiy et al., 2020b). AC (Fig. 6a) includes one top detector AC top and four lateral detectors AC lat (located on honeycomb panels) surrounding converter-tracker C. All anticoincidence detectors are made of two layers of scintillation plastic strips with parallel orientation in both layers, which have dimensions of 10 mm in thickness for each layer and 100 mm in width. The strips of one layer are displaced by 5 mm with respect to the strips of the other layer so that there are no rectilinear slits in the system. AC top with dimensions of 1300 $\times$ 1300 mm^2 includes 2 layers from 22 strips with SiPM readout. AC lat with dimensions of 1300 $\times$ 500 mm^2 includes 2 layers from 21 strips with SiPM readout.

Converter-tracker. The converter-tracker is used to convert incoming gamma rays into electron–positron pair, determine conversion point and reconstruct the electromagnetic shower axis. The converter-tracker consists of 13 detector plane pairs made of scintillating fiber (SciFi) assemblies with SiPM analog readout (Fig. 6b). The SciFi assemblies contain 250 μm diameter scintillating fibers arranged in regular, hexagonal closest packed six-layer structures, with 275 μm pitch. The multichannel SiPM sensors are located at fiber ends, providing signal pulse height measurement for a subsequent light cluster barycenter calculation, resulting in singe plane coordinate resolution better than 50 μm. Scheme of the basic principle of the SciFi tracker is as follows (Fig. 6c, Kirn et al., 2017): charged particle passing through the fiber produces scintillation light, which travels to the end and is detected in a SiPM array. The black dots indicate photons arriving at the SiPM, the yellow squares indicate the pixels that fire. In each pair of planes (1050 $\times$ 1050 mm^2) the adjacent SciFi detectors, located on honeycomb panels, provide measurements in orthogonal directions (x and y coordinates). It is necessary to note that the technology of SciFi detectors is well developed and applied, e.g., in the LHCb tracker at Large Hadron Collider (LHC) (Kirn et al., 2017). The first 7 and next 4 pairs of planes also have tungsten (W) converter foils of 0.1 X_0 and 0.025 X_0 thick in each plane,

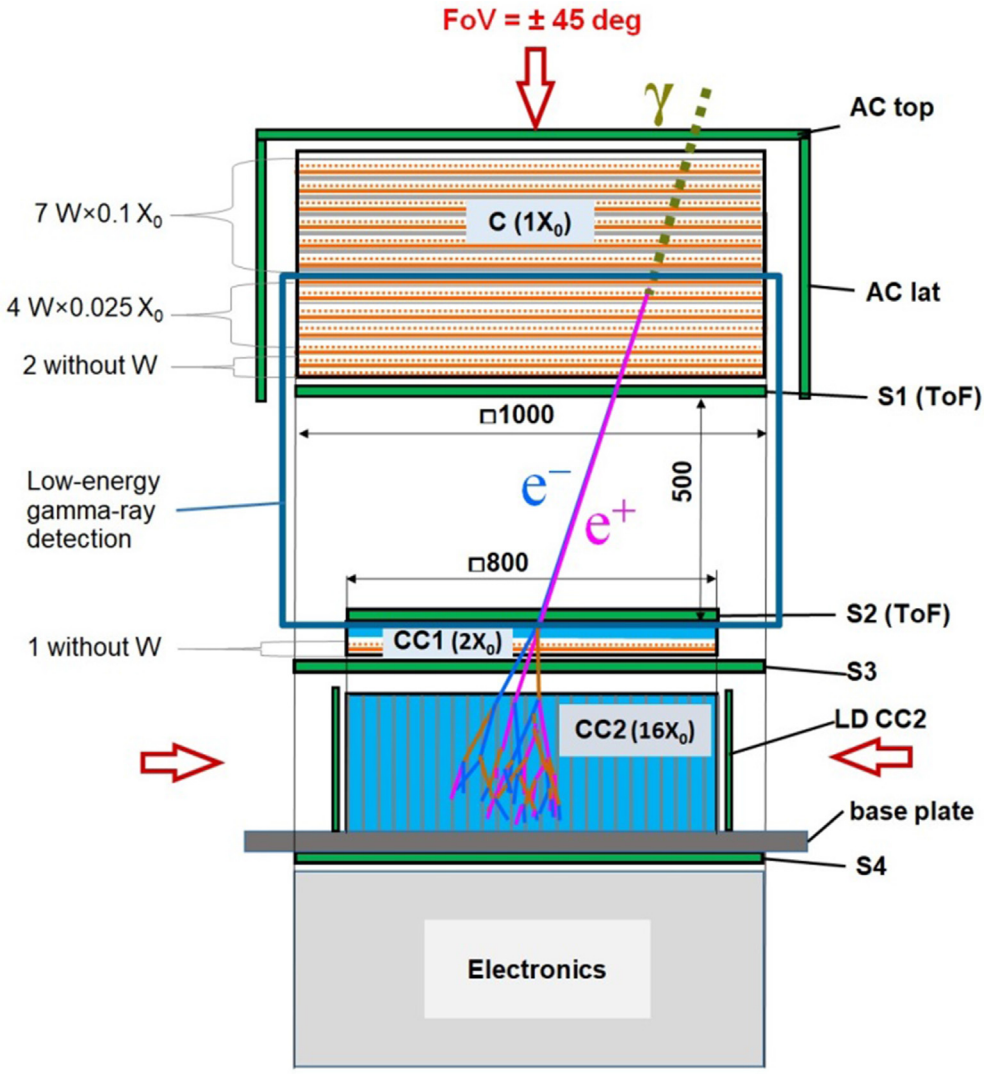


Fig. 4. The GAMMA-400 gamma-ray telescope physical scheme: anticoincidence system AC (top and four lateral detectors), converter-tracker C, time-of-flight system ToF from detectors S1 and S2, two part calorimeter from CC1 and CC2, lateral detectors LDs, preshower detector S3 and shower leakage detector S4.

respectively (X_0 is radiation interaction length) (Fig. 4). The last 2 pairs of planes have no tungsten. The part of converter-tracker with thick layers of tungsten (0.1 X_0) is used to detect high-energy gamma rays (above 300 MeV). The part of the converter-tracker with thin layers of tungsten (0.025 X_0) is used to detect low-energy gamma rays (less than 300 MeV) (Fig. 4). Total thickness of converter-tracker is $\sim$ 1 X_0.

Time of flight system. Under the converter-tracker, there are two scintillation detectors S1 and S2, which form the time-of-flight (ToF) system (Fig. 6d). A distance of 500 mm between these detectors provides a sufficient flight base for effective rejection of particles coming from the lower hemisphere. Detectors S1 and S2 are installed on honeycomb panels and use SiPM readout. The S1 detector with dimensions of 1000 $\times$ 1000 mm^2 consists of two layers of scintillation plastic strips, each having 10 mm in thickness. There are 10 scintillation strips in each layer. The S2 detector with dimensions of 800 $\times$ 800 mm^2 also consists of two layers of scintillation strips, each having 10 mm in thickness. There are 8 scintillation strips in each layer. ToF is used to separate particles moving from top-down directions within the aperture of the gamma-ray telescope (determined by position of S1 and S2 detectors) of down-top directions with coefficient of separation of $\sim$ 1000. The ToF time resolution is $\sim$ 200 ps.

Detectors S3 and S4. Two-layer segmented plastic scintillation detectors S3 and S4 with dimensions of 1000 $\times$ 1000 mm^2 and SiPM readout are located on honeycomb panels. These detectors are necessary for improving hadronic and electromagnetic shower separation (Fig. 6e). S3 detector measures the energy release from secondary particles in shower, which is developed due to the passage of primary gamma- and cosmic-ray particles in the gamma-ray telescope and takes part in the formation of the trigger for detecting high-energy events (Leonov,

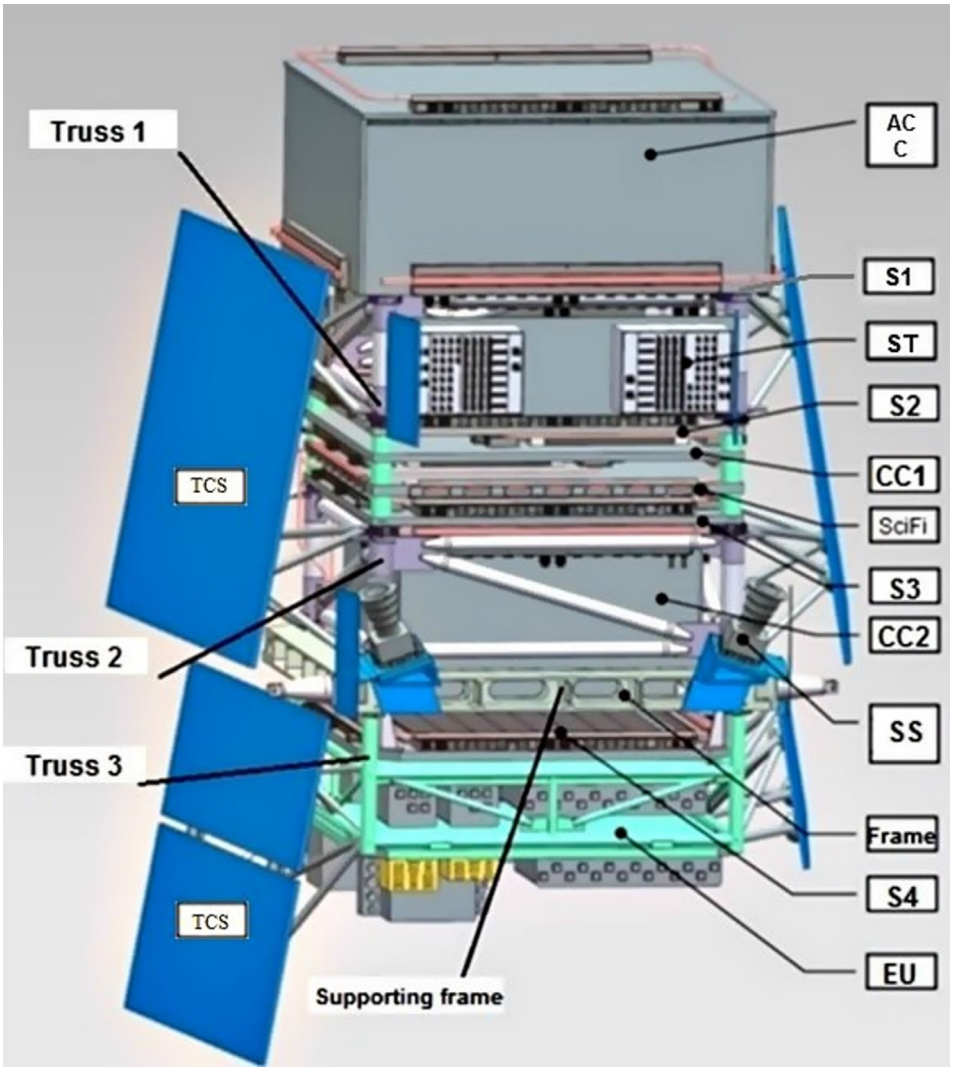


Fig. 5. View of the GAMMA-400 gamma-ray telescope.

et al., 2019). S4 detector measures the energy release of secondary charged particles contained in the shower leakage from the calorimeter.

Calorimeter. The two-part calorimeter consists of CC1 and CC2 detectors with SiPM readout. CC1 (800×800 mm^2) contains two blocks of CsI(Tl) scintillation crystals installed above and under honeycomb panel and the SciFi detector plane without W, providing x and y measurements (Fig. 7a). The SciFi detector plane is the same as last planes in the converter–tracker. CC2 (800×800 mm^2) consists of 22×22 matrix from CsI(Tl) crystals (Fig. 7b). Each crystal has transverse dimensions of 36×36 mm^2. CsI(Tl) crystal columns of CC2 are installed inside the cells of the carbon fiber honeycomb structure, having 0.4 mm in thickness. Total thickness of the CC1 and CC2 calorimeter is $\sim 18\,X_0$ ($\sim 0.9\,\lambda_0$) and $\sim 43\,X_0$ ($\sim 2.0\,\lambda_0$) for vertical and lateral particle detection, respectively (λ_0 is hadronic interaction length).

Lateral detectors. Four lateral scintillation plastic detectors LDs (800×400 mm^2) with SiPM readout located on honeycomb panels around of the CC2 calorimeter are used for detecting particles from lateral directions (Fig. 7c).

System of trigger formation. The system of trigger formation ST generates triggers for detecting various types of events analyzing the output signals of the front-end electronics of the gamma-ray telescope detectors. To improve reliability, the system is designed using a dual redundancy crossover scheme; data exchange highways are also duplicated, with each highway having its own transceiver nodes.

Scientific data acquisition system. The scientific data acquisition system SDAS is intended for collecting scientific data from detectors, temporary storage and transmission of scientific and service information of the gamma-ray telescope to the high-data-rate radio complex for subsequent transmission to a ground receiving station, as well as for direct control of the gamma-ray telescope. SDAS is a monoblock consisting of redundant functional modules. The choice of the configuration of modules is carried out by means of commands coming from the on-board control complex of the Navigator platform.

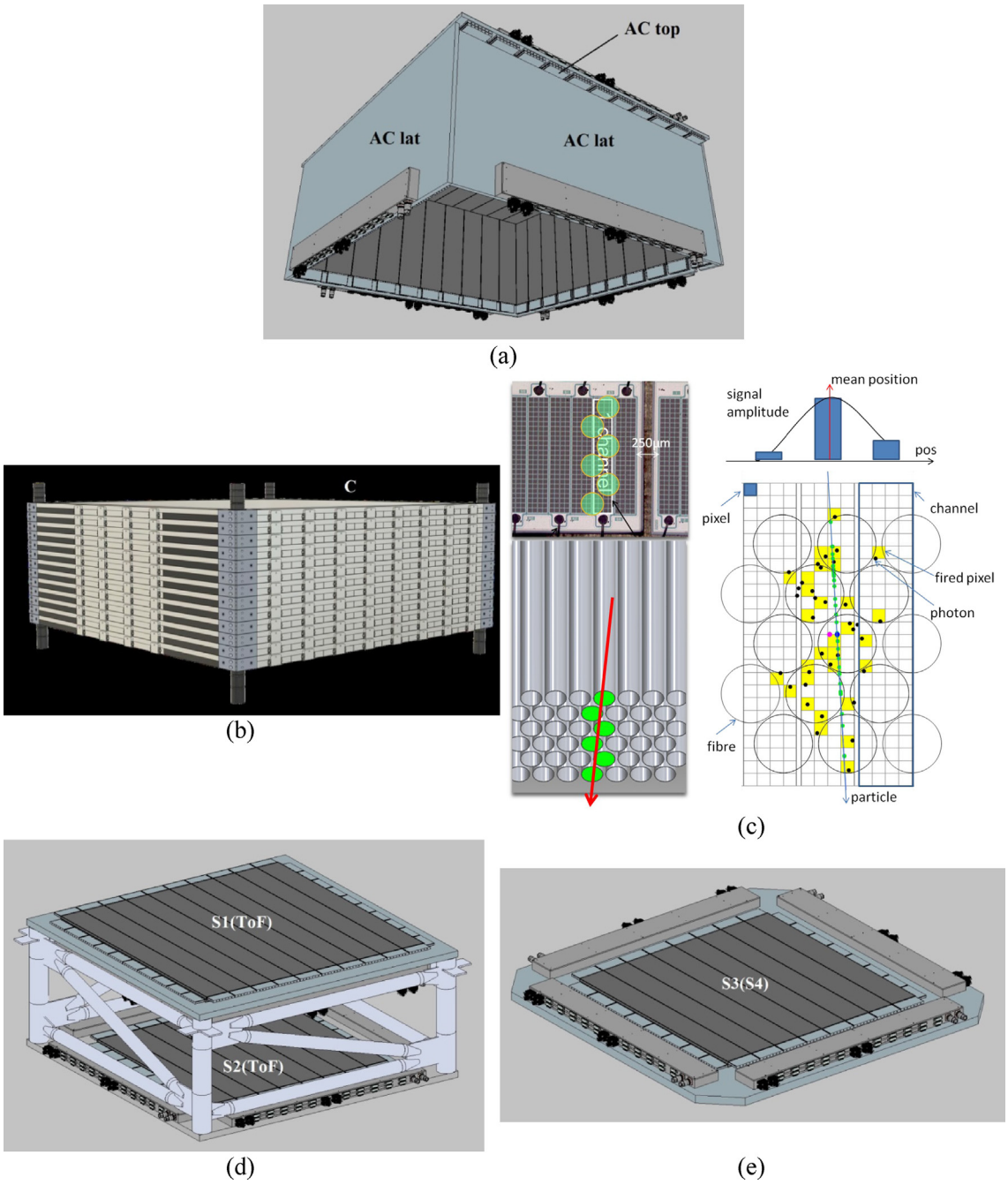


Fig. 6. The GAMMA-400 detector systems: (a) anticoincidence system AC; (b) converter-tracker C; (c) scheme of the basic principle of the SciFi tracker (Kirn et al., 2017); (d) time-of-flight system ToF from S1 and S2; (e) preshower detector S3 and shower leakage detector S4.

Principle of operation. Primary gamma rays pass without interaction the anticoincidence system and are converted into electron–positron pair in the converter-tracker. Further, electron–positron pair passes through the rest part of converter-tracker, time-of-flight system, preshower detector S3 and induces an electromagnetic shower in CC1 and CC2 calorimeter following by shower leakage detector S4. The energy deposits in converter-tracker, S1, S2, CC1, CC2, S3, S4, LD detectors are measured.

The responses of the gamma-ray telescope detectors AC, ToF and S3 contribute to the fast on-board trigger logic in the top-down telescope aperture. The readout electronics for fast on-board trigger and time of flight system of the GAMMA-400 gamma-ray telescope constitutes the multiprocessor structure, which collects data from the gamma-ray telescope detectors and produces the trigger decision for each event. The use of the flexible distributed system provides possibility for adaptive and operational control of the parameters of the gamma-ray telescope recording modes, and the optimization of a search for a specific physics channel according to the observational mode. In order to increase the reliability, the system is crossover and dou-

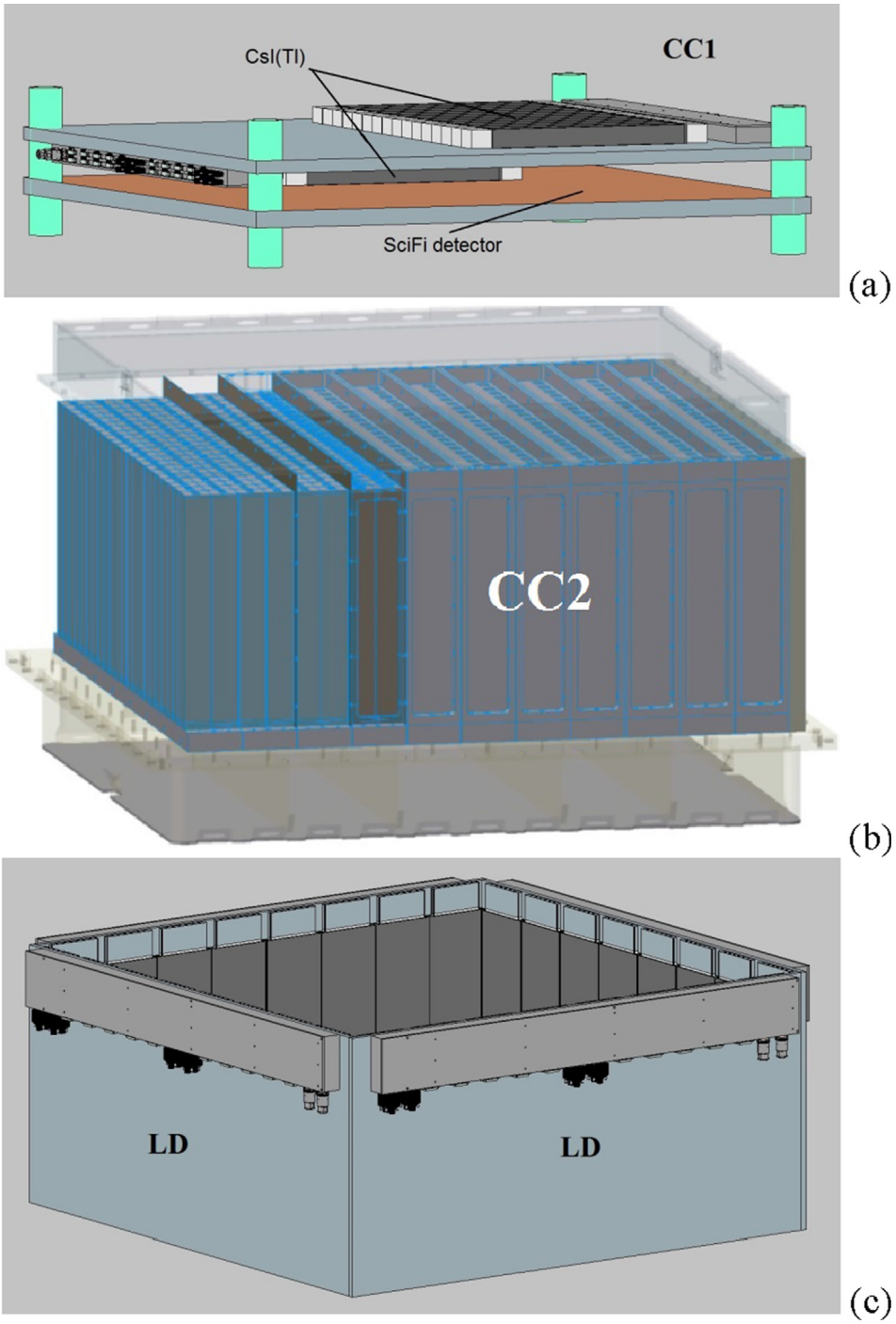


Fig. 7. Two parts of the calorimeter CC1 (a), CC2 (b) and four lateral detectors LDs (c).

ble redundant. Besides, the components of selected electronics components are space qualified and rad-hard or rad-tolerant.

The incidence direction of particles is determined by best determination of conversion point and reconstruction of the electromagnetic shower axis, using SciFi coordinate detectors in the converter-tracker and CC1.

After interaction of incident gamma rays with the GAMMA-400 detector matter backscattering secondary particles (mainly, 1-MeV photons) are arisen. These secondary particles can interact in AC and produce veto signal, excluding primary gamma rays (Fig. 8). To suppress this effect all scintillation detectors are constructed as two-layer segmented layers of strips and additional trigger logic for detecting high-energy particles is organized (Leonov, et al., 2019). Besides, the timing analysis of signals produced in AC, S1 (ToF), S2 (ToF), S3 detectors are used (Arkhangelskiy et al., 2020a).

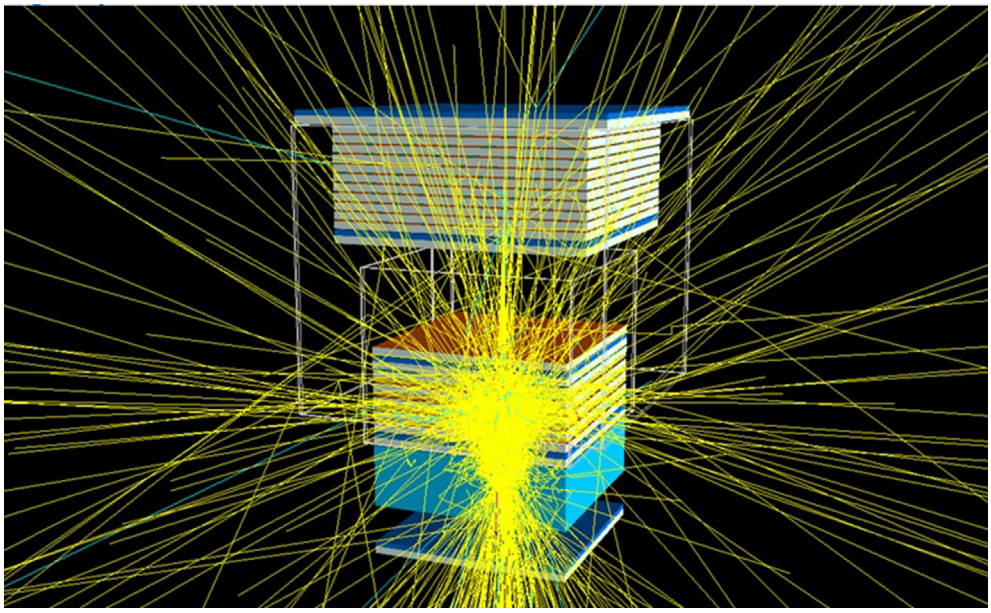


Fig. 8. Backscattering secondary particles (mainly, 1-MeV photons), which can produce veto in AC and exclude primary gamma rays.

The GAMMA-400 energy range for gamma-ray studies is from $\sim$ 20 MeV to several TeV and for CR electrons + positrons is from $\sim$ 1 GeV to several tens TeV. The energy of low-energy gamma rays is measured in the converter-tracker, S1 (ToF), S2 (ToF) after the conversion of gamma rays in the last six planes (Fig. 4, four planes with 0.025 X_0-tungsten and two without tungsten). The maximum field of view (FoV) for detecting particles from top-down directions is $\pm$ 45°.The main trigger of GAMMA-400 is the following:

$$(\bar{AC} \times ToF)|(S3_{THRESHOLD} \times ToF) \quad (1)$$

where $ToF = \mathrm{S1} \times \mathrm{S2} \times [\mathrm{time_{S1}} < \mathrm{time_{S2}}]$, $S3_{THRESHOLD}$ is a special energy threshold (Leonov, et al., 2019).

The value of $S3_{THRESHOLD}$ is determined from the following considerations. For triggered events with gamma rays of energy more than $\sim$ 10 GeV, backscattering secondary particles (mainly, 1-MeV photons) had begun to create a veto signal in AC. To eliminate these events we construct the distributions of energy deposits in S3 detector for 10-GeV gamma rays from vertical direction, which generate veto signal in AC, and for proton spectrum with power index -2.7 with energies >10 GeV and introduce $S3_{THRESHOLD}$ (Fig. 9). The location of the threshold for signal in S3 detector is determined in view of trade-in between proton rejection from gamma channel and recording efficiency for high-energy gamma rays associated with backsplash. When ground processing we will additionally eliminate events with backscattering secondary particles due to reconstructing track and the time consequence of signals produced in AC, S1 (ToF), S2 (ToF).

In Fig. 10, the dependences of recording efficiency for gamma rays and protons from the value of signal in S3 detector are presented. The optimal value for the cutoff of the signal in S3 detector is $\sim$ 60 MeV. For this cutoff, $\sim$20% of gamma rays, which generate veto signal in AC, and $\sim$ 80% of protons are rejected. In Figs. 9 and 10, the location of this energy cut is shown by blue line.

The trigger (1) is used for detecting low- and high-energy gamma rays. For detecting CR electrons + positrons the trigger ($S3_{THRESHOLD} \times ToF$) is used. Moreover, GAMMA-400 can detect gamma and cosmic rays from lateral directions. For this, the trigger $\bar{LD} \times \bar{S_3} \times \bar{S_4} \times CC_2$ and $LD \times CC_2$ are used, respectively.

The functional diagram of the GAMMA-400 gamma-ray telescope is presented in Fig. 11 (Arkhangelskiy et al., 2020a). The module structure of the GAMMA-400

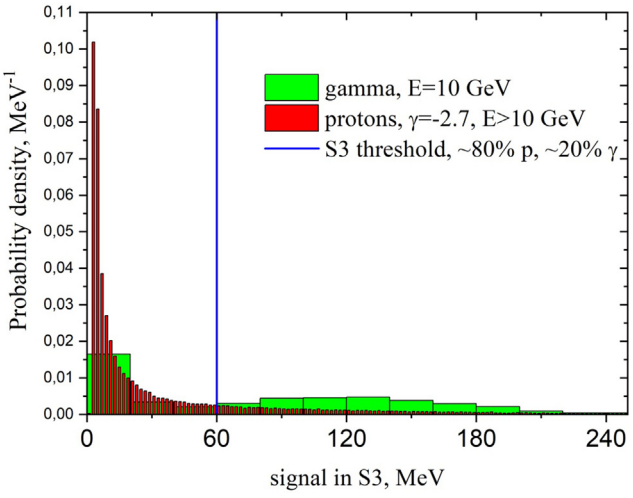


Fig. 9. The distributions of energy deposits in S3 detector for 10-GeV gamma rays from vertical direction, which generate veto signal in AC, and for proton spectrum with power index -2.7 and with energies >10 GeV (Leonov, et al., 2019).

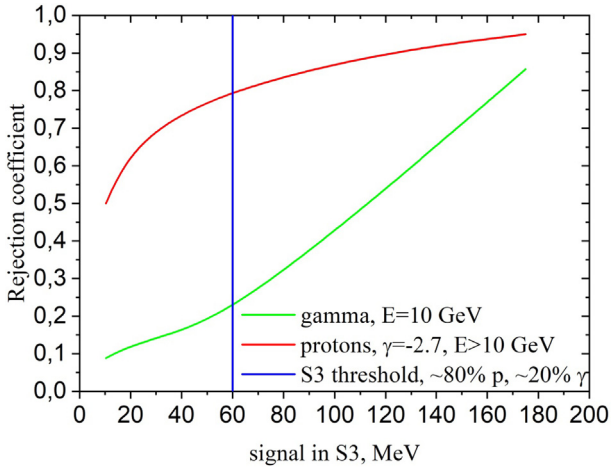


Fig. 10. The dependences of recording efficiency for gamma rays and protons from the value of signal in S3 detector (Leonov, et al., 2019).

gamma-ray telescope includes following subsystems and detecting units:

- scientific measuring subsystems (SMS): converter-tracker C; anticoincidence system AC; calorimeter CC consisting of CC1 and CC2; detectors S3, LD and S4; time-of-flight system ToF consisting of S1 and S2; system of triggers formation ST;
- service subsystem, including two-star sensors and scientific complex telemetry system for cyclic registration up to 65,535 housekeeping parameters of scientific complex;
- scientific data acquisition system SDAS for acquisition and pre-processing data from SMS and service subsystem; storage the data in non-volatile mass memory (1 TByte), scientific data and telemetry transfer into high-speed scientific radio line (up to 400 Mbit/sec) for their transmission to the ground receiving station and control information reception from spacecraft on-board control system via multiplexed channel MIL-STD-1553B; data decoding and transfer into SMS;
- one-time commands and power supply system OCPSS, providing power supply for scientific complex, one-time pulse radio commands sharing and their transmitting to SMS and transit of the most important telemetry parameters directly to the satellite on-board telemetry system.

3.2. The GAMMA-400 performance

Simulations of the GAMMA-400 gamma-ray telescope performance were carried out using the GEANT4.10.01.

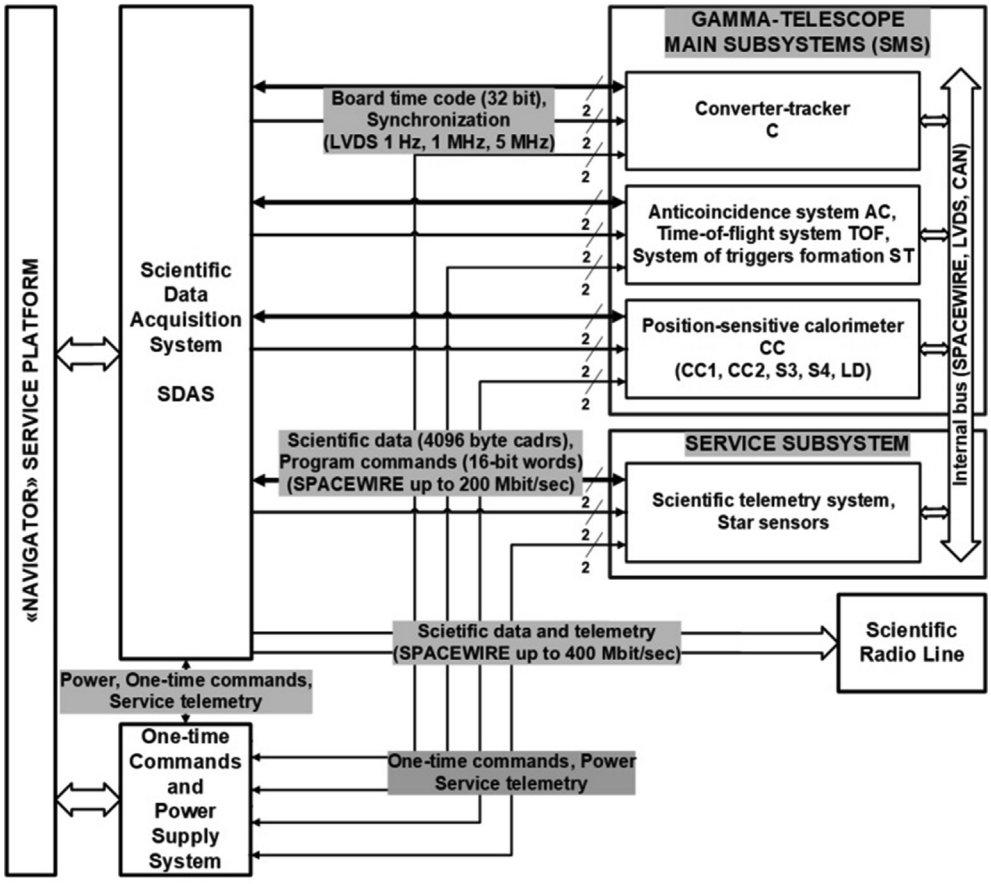


Fig. 11. The functional diagram of the GAMMA-400 gamma-ray telescope.

p02 software package. An example of simulation of 50-GeV gamma-ray energy release in the gamma-ray telescope detectors is shown in Fig. 12, where detectors of the gamma-ray telescope are shown as colored, if the response exists. The incidence of gamma ray is coaxial with the telescope axis. In this figure, two projections of the gamma-ray telescope response are shown at the left and right of the figure. At the center, a view from above CC2 is shown together with anticoincidence system (AC lat) detectors.

As a result of calculations, at which it is necessary to analyze the time consequence of signals produced in S1 (ToF), S2 (ToF) taking into account time resolution obtained from test beam calibration (Arkhangelskiy et al., 2020b) and to be able reconstructing the particle track and restoring the particle energy, we obtained the following dependences:

1) The on-axis effective area vs the energy (Fig. 13). It is seen from Fig. 13 that when using only trigger $(\bar{A}C \times ToF)$ the effective area begins to decrease at the energy >10 GeV due to backscattering particles. Using the trigger $(\bar{A}C \times ToF)|(S3 \times ToF)$ provides the effective area of $\sim$ 4000 cm^2 up to several TeV. If the additional analysis is introduced, providing possibility to reconstruct track and to restore energy, the estimation of effective area (S_{eff}) decreases up to $\sim$ 3200 cm^2.

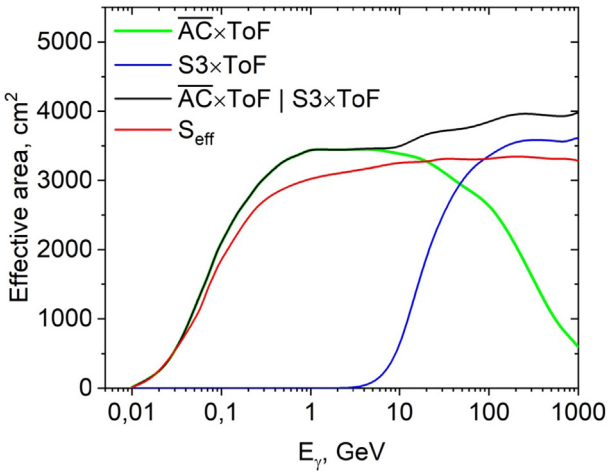


Fig. 13. Dependence of the GAMMA-400 on-axis effective area vs the energy using triggers $\bar{A}C \times ToF$ (green), $\bar{S}3 \times ToF$ (blue), $(\bar{A}C \times ToF)|(S3 \times ToF)$ (black), as well as trigger $(\bar{A}C \times ToF)|(S3 \times ToF)$ and providing possibility to reconstruct track and to restore energy (red).

2) The effective area vs the incident angle for the energies of 1, 10, 100 GeV using the trigger $(\bar{A}C \times ToF)|(S3 \times ToF)$ and providing possibility to reconstruct track and to restore energy (Fig. 14).
3) The differential point-source sensitivity for 1.5 and 10 year observations of the Galactic center (l = 0°, b = 0°) was estimated (Fig. 15). For this purpose we used the typical detection criterion:

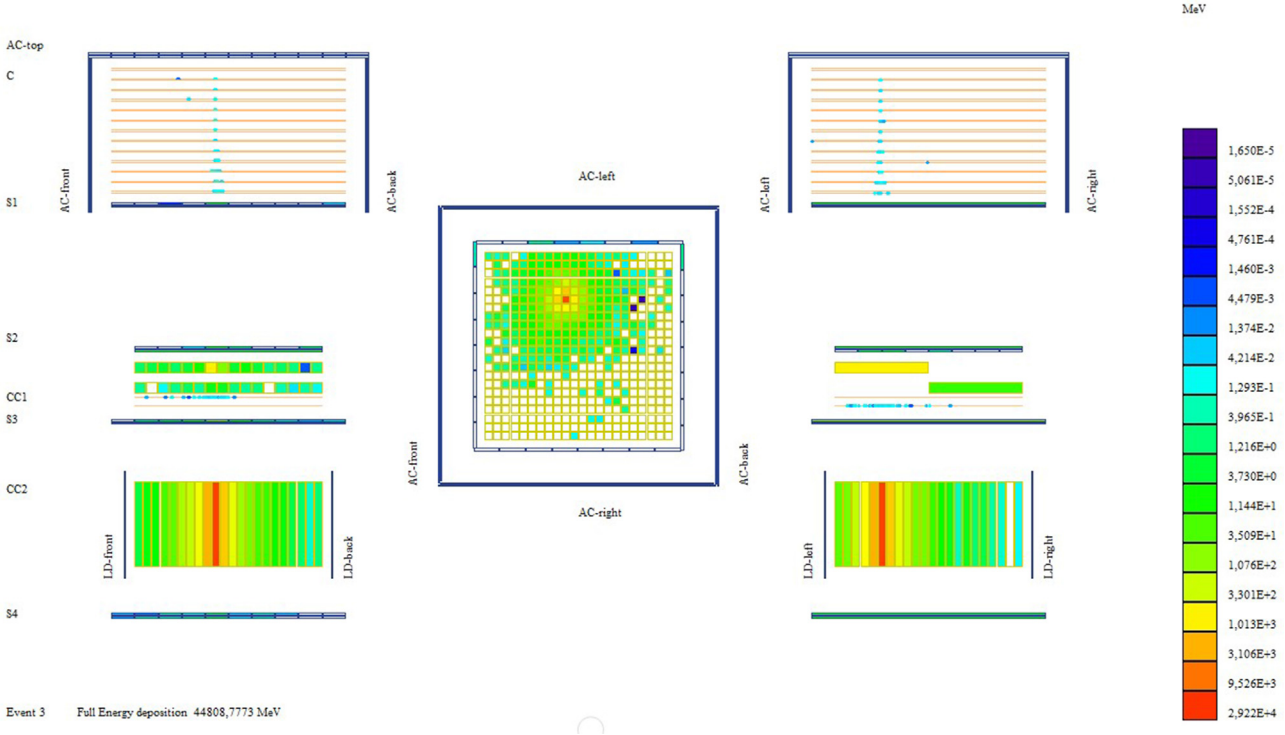


Fig. 12. An example of simulation of energy release in the gamma-ray telescope detectors for 50-GeV gamma ray.

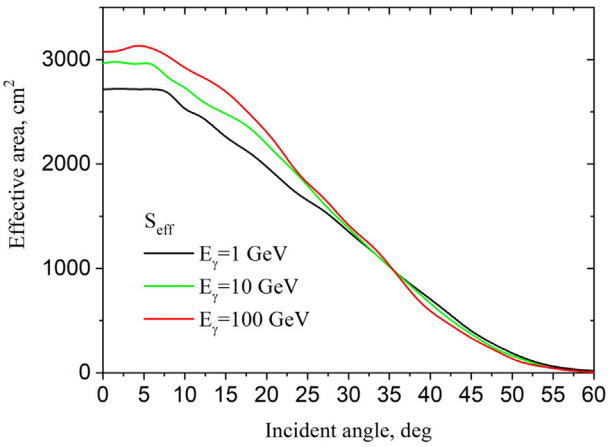


Fig. 14. Dependence of the GAMMA-400 effective area vs the incident angle for the energies of 1 (black), 10 (green), 100 (red) GeV using trigger $(AC \times ToF)|(S3 \times ToF)$ and providing possibility to reconstruct track and to restore energy.

$$TS = 2ln(L_1/L_0) = 25, \quad (2)$$

where L_1 is the likelihood function assuming the source presence on top of background inside PSF and L_0 contains only the background. Similarly to the approach used by Fermi-LAT collaboration we also implied the additional detection criterion that each energy bin must have at least 10 photons from the source. Substituting the Poisson likelihood in (2) we would have:

$$TS = 2(nln(\lambda_1/\lambda_0) - \lambda_1 + \lambda_0), \quad (3)$$

where λ_1 is the mean expected number of photons from source + background, λ_0 is that from the background only and n is the measured number of photons assumed to be $n \equiv \lambda_1$. The expected photon numbers were calculated through the following way:

$$\lambda_{0i} = \int_{E_{il}}^{E_{iu}} \int_{E'-3\sigma_E(E')}^{E'+3\sigma_E(E')} \int_{\Omega_{PSF}(E)} \varepsilon(E) I_b(E) \frac{1}{\sqrt{2\pi}\sigma_E(E)} exp\left(-\frac{(E'-E)^2}{2\sigma_E(E)^2}\right) cos(\theta) d\Omega dE dE', \quad (4)$$

$$\lambda_{1i} = \int_{E_{il}}^{E_{iu}} \int_{E'-3\sigma_E(E')}^{E'+3\sigma_E(E')} \varepsilon(E) \left(k\frac{c_i}{E^2} + \int_{\Omega_{PSF}(E)} I_b(E) cos(\theta) d\Omega\right) \frac{1}{\sqrt{2\pi}\sigma_E(E)} exp\left(-\frac{(E'-E)^2}{2\sigma_E(E)^2}\right) dE dE'. \quad (5)$$

In the equations above, E_{il} and E_{iu} denotes lower and upper margins of the ith energy bin (we choose 4 energy bins per decade, see Fig. 13); $\varepsilon(E) = \int A(E, \Theta(t))dt$ is the exposure of the relevant point in the sky; $I_b(E)$ is the background intensity in that point, which include both the diffuse Galactic component and isotropic background. The spectra of these backgrounds were taken from Fermi-LAT data at https://fermi.gsfc.nasa.gov/ssc/data/access/lat/BackgroundModels.html using Aladin software (https://aladin.u-strasbg.fr/aladin.gml). The Galactic background was averaged in the square 0.5°x0.5° around the relevant point and then assumed isotropic inside our PSF. Indeed this is a simplified methodology, which may introduce some uncertainties. $\Omega_{PSF}(E)$ is the solid angle size of PSF. We choose this size to have 68% containment of the source photons. This is taken into account by the coefficient $k = 0.68$ in (5). The Gaussian function in (4)-(5) reflects the effect of finite energy resolution of the telescope, i.e., the energy dispersion. However, overall dependence of the sensitivity on k and energy resolution is weak. We neglected by the effect of source confusion and assumed a typical inverse square spectral shape for point sources.

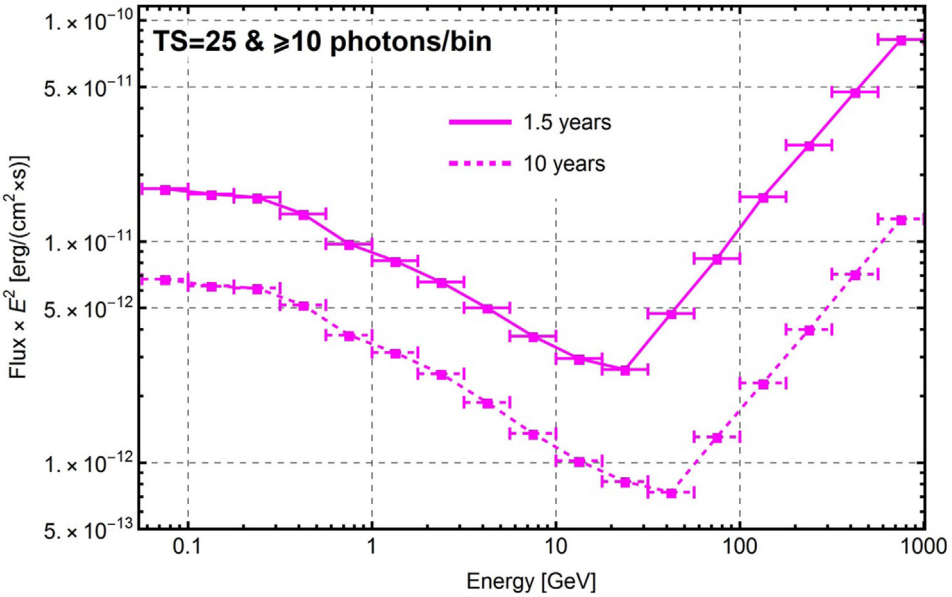


Fig. 15. The GAMMA-400 differential point-source sensitivity for 1.5 and 10 year observations of the Galactic center (l = 0°, b = 0°). The horizontal lines reflect the chosen energy bins for flux density integration.

Then we substituted (4)-(5) into (2)-(3) and solved for c_i. We defined the minimal detectable differential flux m_i as follows:

$$m_i = \int_{E_{il}}^{E_{iu}} \frac{c_i}{E^2} E dE. \quad (6)$$

This quantity physically means the energy flux from the source inside ith energy bins. The result of calculation is presented in Fig. 15 for the Galactic Center and two exposure times of 1.5 and 10 years (continuous exposure in the center of FoV). The curves reach their minima, where the transition happens from TS = 25 to > 10 photons/bin conditions as driving criteria. In other words, above ~ 10 GeV the backgrounds gradually cease, and the scarcity of photons from source becomes the key factor, which limits sensitivity.

4) The angular resolution vs the energy in comparison with Fermi-LAT, HERD, DAMPE, and CTA (https://www.cta-observatory.org/science/ctao-performance/#1472563318157-d0191bc5-0280) (Fig. 16). The angular resolution for $E_\gamma = 100$ GeV is ~ 0.01°.
5) The on-axis energy resolution vs the energy in comparison with Fermi-LAT, HERD, DAMPE, and CTA (https://www.cta-observatory.org/science/ctao-performance/#1472563318157-d0191bc5-0280) (Fig. 17). The energy resolution for $E_\gamma = 100$ GeV is ~ 2%.

Separation of gamma rays against background is carried out using high-efficiency AC system (>0.9995, Arkhangelskiy et al., 2020b), high coefficient of separation of events coming from top-down and down-top directions of ~ 1000 in the time-of-flight system, as well as separation of electromagnetic and hadronic showers in calorimeters and S4 (~10^4) (Leonov et al., 2015). For gamma rays the rejection is ~10^5 due to the additional analysis of the fired strips of AC detectors located along the restored trajectory of initial particle.

GAMMA-400 will detect CR electron + positron fluxes from top-down directions and from lateral directions around the calorimeter. Examples of energy distribution for 100-GeV electron incident on the center of the gamma-ray telescope along the vertical axis (Fig. 18) and on the center of one of the lateral detectors (Fig. 19). For these cases, the energy resolutions are better than 2% and 1%, respectively. Table 1 shows a comparison of performance for GAMMA-400 (top-down and lateral aperture), Fermi-LAT (Atwood et al., 2009), PAMELA (Adriani et al., 2014), AMS-2 (Aguilar et al., 2013), CALET (Mori et al., 2013), DAMPE (Chang et al., 2017), HERD (Cattaneo et al., 2019). It is seen that due to large calorimeter area (0.7 m^2 for top-down and 1.0 m^2 for lateral aperture) and calorimeter thickness (18 X_0 for top-down and 43 X_0 for lateral aperture) GAMMA-400 can improve electron + positron data statistics.

Fig. 20 shows the GAMMA-400 acceptance vs energy when detecting electrons + positrons for top-down directions with the trigger (S3 × ToF) (black) and in addition with separation criterion of electrons + positrons from protons, which will be performed when ground processing (red). The separation criterion of electrons + positrons from protons allows us to identify events with energy leakage from the calorimeter, especially using response of S4 detector, as described further.

The additional separation provides the possibility to restore the energy and consists of the following. Using the combined information from all GAMMA-400 detector systems, it is possible to reject electrons from protons. The methods to separate electrons from protons presented in (Leonov et al., 2015; Leonov et al., 2019) are based on the difference of the development of hadronic and electromagnetic showers inside the gamma-ray telescope.

To take into account the fact that the hadronic cascade begins to develop deeper inside the gamma-ray telescope than the electromagnetic one, the signals in S1 and S2 are

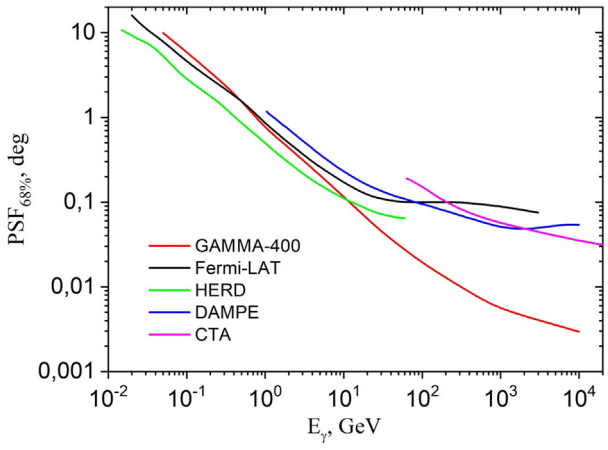


Fig. 16. Dependence of the GAMMA-400 angular resolution vs the energy in comparison with Fermi-LAT, HERD, DAMPE, and CTA.

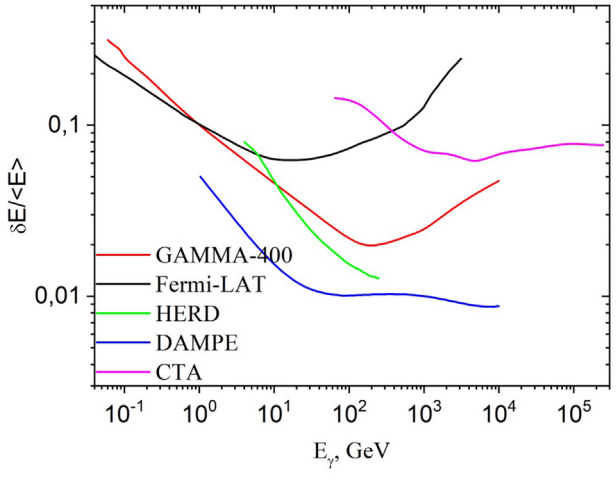


Fig. 17. Dependence of the GAMMA-400 on-axis energy resolution vs the energy in comparison with Fermi-LAT, HERD, DAMPE, and CTA.

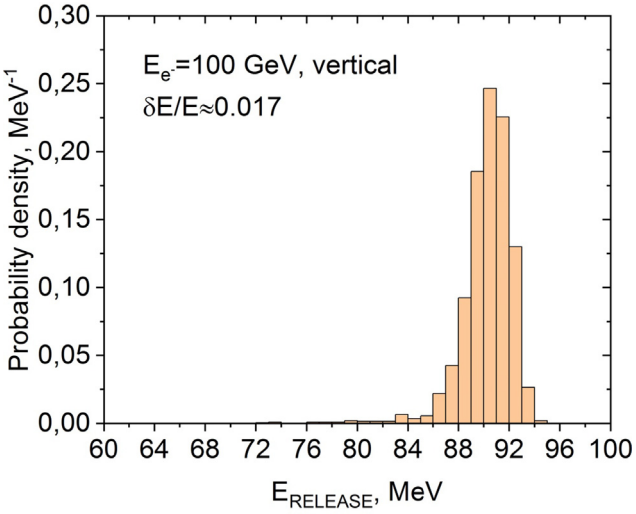


Fig. 18. An example of energy distribution for 100-GeV electron incident on the center of the gamma-ray telescope along the vertical axis. In this case, the energy resolution is better than 2%.

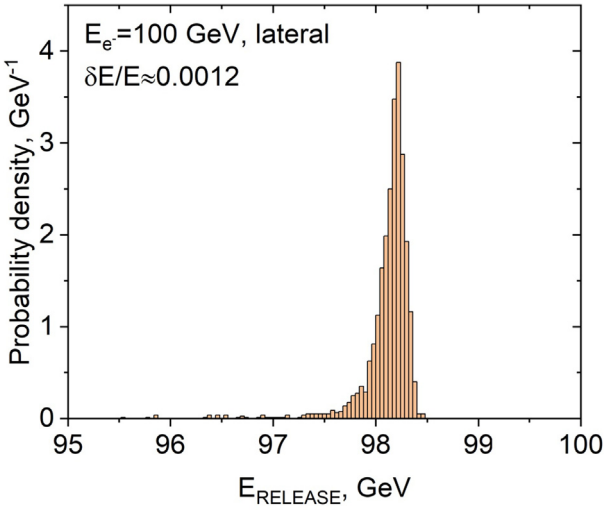


Fig. 19. An example of energy distribution for 100-GeV electron incident on the center of one of the lateral detectors. In this case, the energy resolution is better than 1%.

considered. The difference in electron and proton distributions provides the rejection factor ~ 3.

Additional rejection is obtained when analyzing the CC2 signals. The first criterion is based on the difference of the transversal size for hadronic and electromagnetic showers. Analyzing the distributions of protons and gamma (electrons) for RMS in CC2, it is possible to obtain a rejection factor ~ 15. The second criterion concerns the distribution of energy release in the hadronic and electromagnetic showers. Analyzing the distributions of protons and gamma (electrons) for the ratio between a signal in the crystal containing the axis cascade and the value of the total signal in CC2 for incoming electrons and protons: $E^{CC2}_{MAX}/E^{CC2}_{TOT}$, it is possible to obtain a rejection factor ~ 1.6.

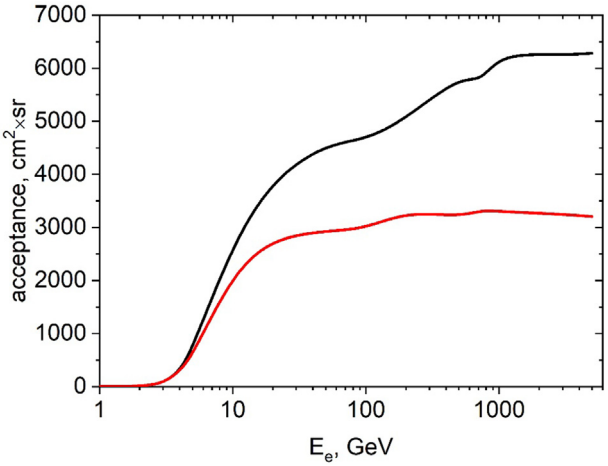


Fig. 20. Dependence of the GAMMA-400 acceptance vs energy when detecting electrons + positrons for top-down directions with the trigger (S3 × ToF) (black) and in addition with separation criteria of electrons + positrons from protons, which will be performed when ground processing (red).

The information from S4 located at the bottom of the calorimeter provides a strong intrinsic rejection factor for protons, due to the difference in attenuation for hadronic and electromagnetic cascades. Electromagnetic showers initiated by gamma (electron) with initial energy up to ~ 100 GeV are fully contained inside a calorimeter with the thickness 16 X_0, while protons leave the calorimeter taking away a considerable part of the energy and produce a signal in S4. By selecting events with signals in S4 less than 40 MeV, it is possible to suppress protons with a factor of ~ 3.1. It turns out that a significantly more powerful criterion can be defined with distributions of the ratio of the signal in S4 to the total signal in CC2. Applying this criterion, the rejection factor ~ 17 is achieved.

Table 1
Comparison of performance when detecting electrons + positrons for GAMMA-400 (top-down and lateral aperture), Fermi-LAT, PAMELA, AMS-2, CALET, DAMPE, HERD.

	GAMMA-400		Fermi-LAT	PAMELA	AMS-2	CALET	DAMPE	HERD
Aperture	top-down	4 sides	top-down	top-down	top-down	top-down	top-down	5 sides
Acceptance, m^2 sr	~0.3 (E$_e$ = 100 GeV)	~0.5 (E$_e$ = 100 GeV)	2.5	0.02	0.4	0.1	0.3	3
Proton rejection factor	~10^4	~5 × 10^3	~10^4	~10^4	~10^4	10^5	10^5	>10^5
Calorimeter area, m^2	0.7	4 × 0.24	0.85	0.06	0.42	0.1	0.36	5x0.4
Calorimeter thickness, X_0	18	43	8.6	16	16	30	32	55

The differences in the proton and electron cascade transverse size are also used, when analyzing information from silicon strips in CC1. The application of this criterion provides a rejection factor of ~ 2.

Using all presented criteria jointly, the total rejection of protons for 100-GeV electrons is $\sim 10^4$.

GAMMA-400 will also measure GRB spectra from lateral directions in the energy range from $\sim$ 10 to $\sim$ 100 MeV. The on-axis effective area is of about 0.13 m^2 for each of four lateral directions. The total effective field of view for the GAMMA-400 lateral aperture, when measuring GRB spectra is $\sim$ 6 sr (Leonov et al., 2022).

Prototypes of some detector systems (Fig. 21) were manufactured, tested in the laboratory (Fig. 22) and calibrated on positron beams at S-25R electron synchrotron (Lebedev Physical Institute, Troitsk) in the energy range of 100–300 MeV. As a result, we obtained time resolution of $\sim$ 200 ps for AC and ToF systems (Arkhangelskiy et al., 2020b) and energy resolution of 10% for CC2 at the energy of positrons of 300 MeV (Suchkov et al., 2021).

GAMMA-400 performance calculations and calibrating detectors at different accelerators will be continued to improve the performance and the event selection methods, as well as to optimize the GAMMA-400 physical scheme.

3.3. Comparison of GAMMA-400 with Fermi-LAT and ground-based facilities

The GAMMA-400 gamma-ray telescope has numerous advantages in comparison with Fermi-LAT:

- highly elliptical orbit (without the Earth's occultation and away from the radiation belts) allows us to observe with the aperture of $\pm$ 45° different gamma-ray sources continuously over a long period of time with 100% efficiency in contrast to 15% efficiency for Fermi-LAT operating in the scanning mode;
- thanks to use scintillating fibers and analog readout providing the best coordinate resolution in the SciFi coordinate detectors of converter-tracker and CC1, as well as time-of-flight system, GAMMA-400 has an excellent angular resolution;
- due to the deep ($\sim$18 X_0) calorimeter, GAMMA-400 has very good energy resolution and can provide more reliable the detection of gamma rays up to several TeV for vertically incident events;
- owing to the significant gamma-ray separation from cosmic rays (the presence of a special trigger with event timing, time-of-flight system, preshower detector S3, separation of electromagnetic and hadronic showers in shower leakage detector S4, two-layer scintillation detectors), GAMMA-400 is significantly well equipped to separate gamma rays from the background of cosmic rays and backscattering events.

GAMMA-400 will have also the unprecedented angular resolution for energy $>$ 30 GeV and very good energy resolution in the energy region 10–1000 GeV in comparison with current and future space- and ground-based instruments: VERITAS, MAGIC, H.E.S.S., CTA, and and it allows us to fill the data gap at the energy of $\sim$ 100 GeV between the space- and ground-based instruments.

It is necessary to note that at present some projects of the gamma-ray telescopes are developed for further investigations of the gamma-ray emission after Fermi-LAT: e-ASTROGAM (DeAngelis et al., 2018) and AMEGO (Kierans et al., 2021) in the medium energy and HERD (Cattaneo et al., 2019) and AMS-100 (Schael et al., 2019) in high-energy range. Performance of these telescopes in comparison with GAMMA-400 and Fermi-LAT is presented in Table 2.

4. The preliminary GAMMA-400 scientific program

The GAMMA-400 main scientific goals are: precise continuous up to $\sim$ 100 days measurements of Galactic Center, Fermi Bubbles, Crab, Vela, Cygnus X, Geminga, Sun, and other regions, extended and point gamma-ray sources, GRBs, diffuse gamma rays, dark matter searching, measuring electron + positron fluxes with the angular ($\sim$0.01° at E_γ = 100 GeV) and energy ($\sim$2% at E_γ = 100 GeV) resolutions.

4.1. Investigation of gamma-ray discrete sources in the Galactic plane

Despite the fact that Fermi-LAT detected gamma-ray emission from 5065 sources, approximately 30% of gamma-ray sources (Abdollahi et al., 2020) were not identified due to insufficient angular resolution. About 40% of them are in the Galactic plane. In contrast to the Fermi-LAT scanning observation mode, GAMMA-400 will be able to identify and investigate many discrete sources due to another observation mode: long-term, continuous observations of point gamma-ray sources, as well as significantly better angular and energy resolutions.

According to the Fermi-LAT results, about 80 extended gamma-ray sources (E $>$ 10 GeV) were found (Abdollahi et al., 2020). Thanks to long-term, continuous observations and significantly better angular and energy resolutions, GAMMA-400 will be able to clarify and map these extended sources in detail.

According to the Fermi-LAT results, an excess of gamma-ray emission from the Galactic center was detected. It is believed to be associated either with the presence of dark matter or with the presence of many millisecond pulsars. Due to long-term, continuous observations and significantly better angular and energy resolutions, GAMMA-400 will be able to clarify this problem.

GAMMA-400 will study different regions of Galactic plane, Galactic center, Fermi Bubbles, Crab, Vela,

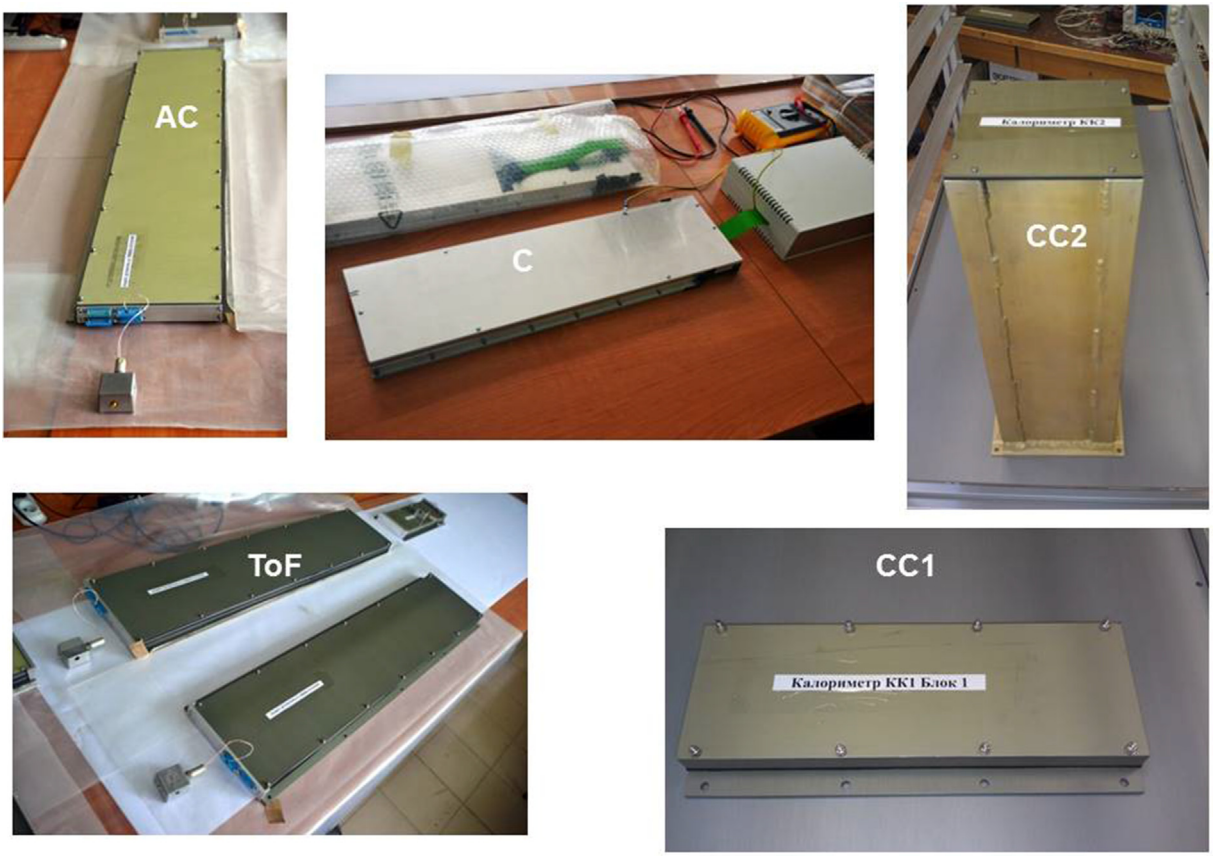


Fig. 21. Prototypes of AC, C, ToF, CC1, CC2 detector systems.

Cygnus X, Geminga and other objects with maximum FoV of ± 45°.

4.2. Dark matter searching

Generally there are two wide classes of DM candidates, which are potentially accessible by GAMMA-400: WIMPs and ALPs.

Galactic Center region historically represents the most favorable target for WIMP annihilation or decay searches due to the biggest J factor. In this context a mysterious gamma-ray excess identified a while ago (e.g. Ackermann et al., 2017) around GC attracts a great interest. It peaks at few GeV, extends up to approximately 10° around GC and can be well-fitted by annihilating WIMPs with the mass of several tens GeV and cross section around the thermal value $\sim 10^{-26}$ cm^3/s. However, alternative explanations for the origin the excess indeed exist. They include the emission from millisecond pulsars (both prompt and secondary), molecular clouds and others. The future high-resolution data from GAMMA-400 will be very important for the ultimate determination of the excess.

Another interesting aspect is the searches for hypothetical narrow spectral lines due to DM annihilation or decay directly into photons. This represents very pristine DM signature, since no other astrophysical processes are expected to produce such lines at the energies above $\sim$ 0.1 GeV. We provided some estimates of GAMMA-400 sensitivity to the diphoton annihilation cross section in (Egorov et al., 2020). However our most recent simulations showed that the sensitivity presented there tends towards slightly optimistic side – realistically we would expect our sensitivity to be comparable with that of Fermi-LAT after 12–15 years of its operation. At the same time DAMPE has comparable sensitivity too (Zun-Lei Xu et al., 2021). Hence, it can be possible in the future to stack together the data from all three telescopes and significantly extend the sensitivity to narrow lines by such joint data analysis.

ALP discovery potential by catching a nearby supernova explosion. Fermi-LAT has not been able to observe any supernova explosion in the Local Group due to rarity of such events. However such observation would be extremely valuable for constraining ALP properties. Since ALPs are converted into photons by the Galactic magnetic field during their propagation, gamma rays from SNe can be a signature of SN ALPs. Thus, in case of such luck, GAMMA-400 will be able to probe ALP-photon coupling constant values down to $g_{a\gamma} \sim 10^{-13}$ GeV^{-1} for ALP masses below $\sim$ 1 neV! The chance to catch such event over the mission lifetime is about 10%. Very high sensitivity of this probe still makes it one of the main GAMMA-400 objectives in the area of DM searches. The detailed calculations on this subject can be seen in (Egorov et al., 2020).



Fig. 22. Testing the GAMMA-400 detector prototypes in the laboratory.

ALP signature searches in the pulsar spectra. Recently the tentative ALP signature in the spectra of pulsars was identified in Fermi-LAT data (Gautham et al., 2020). However this detection is not reliable yet and the future additional GAMMA-400 observational data on those pulsars will be able potentially to confirm or deny robustly this preliminary interpretation of signal.

Other targets include globular clusters, nearby galaxies, dwarf satellites, hypothesized axion clouds around neutron stars, etc.

4.3. Studying the gamma-ray emission from the Sun

The Sun is one of the promising targets for indirect DM searches with gamma rays. The Sun is visible in gamma rays because of the interaction of CRs with the solar environment. The standard gamma-ray emission of the Sun includes two main components: (1) the contribution from the disk, originating from the interactions of hadronic CRs with the solar atmosphere, which yield hadronic cascades with gamma-ray component, and (2) the contribution from diffuse emission, due to the interactions of cosmic-ray electrons and positrons with the optical solar photons in the heliosphere and production of gamma rays by inverse Compton scattering. The standard solar emission mechanisms are expected to yield a smooth gamma-ray spectrum, while both the DM scenarios illustrated above are expected to yield some characteristic features in the spectrum. In particular, if gamma rays are produced through a mediator, the spectrum should exhibit a boxlike feature; on the other hand, if gamma rays are produced directly in DM annihilations, a line-like feature is expected (Mazziotta et al., 2020).

The study of high-energy gamma-ray emission from solar flares is intended to elucidate the role of nuclear processes in a flare, the mechanism of particle acceleration and the interaction of accelerated beams with the solar atmosphere (Ajello et al., 2021). The GAMMA-400 gamma-ray telescope will make it possible to obtain new experimental data on high-energy gamma-ray emission from solar flares, which are necessary to refine the existing models of solar flares, namely:

1) Detailed energy spectra of gamma-ray emission during solar flares in the wide energy range from 20 MeV to several TeV;
2) Precision time profiles of the intensity of gamma-ray emission from solar flares in various energy ranges;
3) Fluxes of high-energy gamma rays from the quiet Sun.

4.4. Searching for GRBs

Gamma-ray bursts (GRBs) are the most violent explosions in the universe with isotropic equivalent energy release in gamma rays up to a few 10^{54} ergs (e.g. Minaev et al., 2020). Observations of GRBs become extremely relevant in the new era of multi-messenger astronomy, which started in 2017 since the first simultaneous detection of a binary neutron star merger GW 170,817 by LIGO-Virgo gravitational wave detectors and short gamma-ray burst GRB 170817A by Fermi and INTEGRAL observatories (Abbott et al., 2017).

GRBs and their different counterparts (prompt emission, afterglow, kilonova, supernova) are successfully observed in the entire range of the electromagnetic spectrum, from radio to high-energy gamma rays. However, a unified model describing all observational features has not been proposed yet. This is largely due to the extremely difficult implementation of simultaneous observations in different ranges of the energy spectrum, especially at the active phase stage (prompt emission), which lasts typically only a few seconds.

Gamma rays with the energy $E_\gamma > 20$ MeV were first detected in the EGRET/CGRO experiment for 28 gamma-ray bursts in the period 1991–2000 (Kaneko et al., 2008). At present, the high-energy component of gamma-ray bursts is recording mainly in the Fermi-LAT experiment, which recorded so far about 200 gamma-ray bursts in the range above 30 MeV (Ajello et al., 2019).

In most GRBs the duration of high-energy emission is significantly (up to tens of times) greater than the duration of low-energy emission and usually has a power-law like decaying light curve. It is also observed as an additional

Table 2
Performance of space- and ground-based telescopes in comparison with GAMMA-400 and Fermi-LAT.

	Space-based gamma-ray telescopes							Ground-based facility
	Medium energy		High-energy					
	e-ASTROGAM	AMEGO	Fermi-LAT	GAMMA-400	HERD	AMS-100	CTA	
Country	Europe	USA	USA/ Europe	Russia	China/ Europe	Europe + USA		
Energy range for gamma rays	0.3 MeV–3 GeV	0.2 MeV–10 GeV	50 MeV–1 TeV	20 MeV–1 TeV	0.5 GeV–10 TeV	1 GeV–10 TeV	> 50 GeV	
Observation mode	Scanning	Scanning	Scanning	Point-source	Scanning	Scanning	Scanning	
Orbit	Circular, ~550 km	Circular, ~550 km	Circular, ~550 km	Highly elliptical, 500–300 000 km	Circular, ~400 km	L2	–	
Angular resolution	0.1° (E_γ = 1 GeV)	1° (E_γ = 1 GeV)	0.1° (E_γ = 100 GeV)	~0.01° (E_γ = 100 GeV)	0.1° (E_γ = 100 GeV)	~0.01° (E_γ = 100 GeV)	0.1° (E_γ = 100 GeV)	
Energy resolution	20% (E_γ = 1 MeV)	10% (E_γ = 1 GeV)	10% (E_γ = 100 GeV)	~2% (E_γ = 100 GeV)	1–2% (E_γ = 100 GeV)	1–2% (E_γ = 100 GeV)	15% (E_γ = 100 GeV)	

component in the energy spectrum, described by a power-law model (Ajello et al., 2019). It indicates the high-energy component in such GRBs represents an additional component to regular gamma-ray emission for these cases. Nevertheless, in some GRBs, the temporal profile of the burst at high energies does indeed repeat the profile at low energies, which implies the same nature of the emission and the absence of an additional component at high energies. Thus, a bimodal behavior of gamma-ray bursts at high energies is presented. The nature of the additional high-energy component and the conditions for its appearance has not been clarified, which makes its study an actual and important task.

An open question is the maximum possible energy of photons emitted in gamma-ray bursts. Recently sub-TeV high-energy emission was confirmed for GRB 180720B by H.E.S.S. in (0.1, 0.44) TeV energy range (Abdalla et al., 2019) and for GRB 190114C by MAGIC in (0.1, 1) TeV energy range (Acciari et al., 2019).

Using top-down and lateral directions of GAMMA-400 will allow us to detect new GRBs with rate of 10–15 GRBs per year to solve problems of GRB science. The most prominent results will be obtained in case of simultaneous GRB registration in a wide energy range of electromagnetic channel (from radio waves to high-energy gamma rays) by different ground-based and space-based facilities, as well as in gravitational wave channel.

4.5. Studying CR electron + positron fluxes

High-energy cosmic-ray electrons provide a unique probe of nearby to the Solar System cosmic sources. Because electrons in the interstellar space fast lose energy via inverse Compton scattering and synchrotron emission their diffusion length is about 1 kpc at energy above 1 TeV. It means that potential sources are located in the vicinity of the Solar System (Kobayashi et al., 2004). A precise measurement of the electron + positron spectrum at high energies above several hundreds of GeV might reveal interesting spectral features and flux anisotropy due to a specific source. Moreover, the anomaly increase of the positron fraction in electron and positron fluxes over 10 GeV established by PAMELA (Adriani et al., 2009) and AMS-02 (Accardo et al., 2014) experiments can require a primary source of the positrons in addition to the commonly accepted secondary origin of the positrons.

Astrophysical objects like pulsars and Super Novae Remnants (SNR) or exotic objects like clumps of hypothetical dark matter are more plausible and investigated candidates for such sources. The electrons and positrons spectrum would exhibit a different spectral features due to origin of the primary source of electrons and positrons, in the energy range above 10 GeV and, especially at about 1 TeV, possible mass of hypothetical DM particles.

It is highly desirable to measure spectrum of electrons + positrons in the TeV region with much more statistics accuracy than it is possible now. Moreover, the data of direct

measurements (DAMPE, CALET) in the TeV region show a suppression of the flux (DAMPE Collaboration, 2017, Adriani et al. 2018). GAMMA-400 with high acceptance both in the main ($\sim 18X_0$) and lateral apertures ($\sim 43X_0$) (see Table 1) will be able to obtain accurate spectral shape above 1 TeV with energy resolution $\sim$ 2% (which will decrease up to $\sim$ 5% at 10 TeV due to leakage from the calorimeter) and, possible, to extend accurate measurements to 20–30 TeV using the lateral aperture, needed to understand origin of local sources.

5. Conclusions

The future space-based GAMMA-400 gamma-ray telescope will operate onboard the Russian astrophysical observatory in a highly elliptic orbit during 7 years to observe Galactic plane, Galactic Center, Fermi Bubbles, Crab, Vela, Cygnus X, Geminga, Sun, and other regions and measure gamma- and cosmic-ray fluxes. Observations will be performed in the point-source mode continuously for a long time ($\sim$100 days) in contrast to the scanning mode for Fermi-LAT. GAMMA-400 will have the unprecedented angular resolution for energies > 30 GeV ($\sim 0.01°$ at $E_\gamma = 100$-GeV) better than the Fermi-LAT and ground-based gamma-ray telescopes by a factor of 5–10, as well as very good energy resolution ($\sim$2% at $E_\gamma = 100$ GeV). Significant separation of gamma rays from cosmic-ray background, as well as electrons + positrons from protons will allow us to measure gamma rays in the energy range from $\sim$ 20 MeV to several TeV and cosmic-ray electrons + positrons up to several tens TeV. GAMMA-400 observations will permit to resolve gamma rays from annihilation or decay of dark matter particles, identify many discrete sources, clarify the structure of extended sources, specify the data on cosmic-ray electron + positron spectra.

After Fermi-LAT the GAMMA-400 mission will greatly improve the direct data on low-energy and high-energy gamma-ray and electron + positron fluxes due to unprecedented angular and very good energy resolutions, large area, and point-source continuous long-term simultaneous coaxial gamma-ray and X-ray telescope observations. The launch of the GAMMA-400 space observatory is scheduled for $\sim$ 2030.

Funding

This study was funded by the Russian State Space Corporation ROSCOSMOS and in part by the Ministry of Science and Higher Education of the Russian Federation under Project "Fundamental problems of cosmic rays and dark matter" (contract no. 0723–2020-0040).

Declaration of Competing Interest

The authors declare that they have no known competing financial interests or personal relationships that could have appeared to influence the work reported in this paper.

References

Abbott, B.P., Abbott, R., Abbott, T.D., et al., 2017. Multi-messenger Observations of a Binary Neutron Star Merger. Astrophys. J. Lett. 848, L12.
Abdalla, H., Adam, R., Aharonian, F., et al., 2019. A very-high-energy component deep in the gamma-ray burst afterglow. Nature 575 (7783), 464–467.
Abdollahi, S., Ackermann, M., Ajello, M., et al., 2017. Cosmic-ray electron-positron spectrum from 7 GeV to 2 TeV with the Fermi Large Area Telescope. Phys. Rev. D 95 082007.
Abdollahi, S., Acero, F., Ackermann, M., Ajello, M., et al., 2020. Fermi large area telescope fourth source catalog. Astrophys. J. Suppl. Ser. 247 (33), 1–37.
Accardo, L., Aguilar, M., Aisa, D., et al., 2014. High statistics measurement of the positron fraction in primary cosmic rays of 0.5–500 GeV with the Alpha Magnetic Spectrometer on the International Space Station. Phys. Rev. Lett. 113, 121101, 1–9.
Acciari, V.A., Ansoldi, S., Antonelli, L.A., et al., 2019. Teraelectronvolt emission from the γ-ray burst GRB 190114C. Nature 575 (7783), 455–458.
Ackermann, M., Ajello, M., Albert, A., et al., 2017. The Fermi galactic center GeV excess and implications for dark matter. Astrophys. J. 840 (43), 1–34.
Adriani, O., Barbarino, G., Bazilevskaya, G., et al., 2009. An anomalous positron abundance in cosmic rays with energies 1.5–100 GeV. Nature 458, 607–609.
Adriani, O., Barbarino, G., Bazilevskaya, G., et al., 2014. The PAMELA mission: heralding a new era in precision cosmic ray physics. Phys. Reports 544, 323–370.
Adriani, O., Barbarino, G., Bazilevskaya, G., et al., 2017. Ten years of PAMELA in space. Nuevo Cimento 10, 473–522.
Adriani, O., Akaike, Y., Asano, K., et al., 2018. Extended measurement of the cosmic-ray electron and positron spectrum from 11 GeV to 4.8 TeV with the calorimetric electron telescope on the International Space Station. Phys. Rev. Lett. 120 261102.
Aguilar, M., Aisa, D., Alpat, B., et al., 2014. Precision Measurement of the (e^++e^-) Flux in Primary Cosmic Rays from 0.5 GeV to 1 TeV with the Alpha Magnetic Spectrometer on the International Space Station. Phys. Rev. Lett. 113 221102.
Aguilar, M., Alberti, G., Alpat, B., et al., 2013. First result from the Alpha Magnetic Spectrometer on the International Space Station: precision measurement of the positron fraction in primary cosmic rays of 0.5–350 GeV. Phys. Rev. Lett. 110, 141102, 1–10.
Aharonian, F., Akhperjanian, A., Anton, G., et al., 2009. Probing the ATIC peak in the cosmic-ray electron spectrum with H.E.S.S. Astron. Astrophys. 508, 561–564.
Ajello, M., Arimoto, M., Axelsson, M., et al., 2019. A decade of gamma-ray bursts observed by Fermi-LAT: The second GRB catalog. Astrophys. J. 878 (52), 1–61.
Ajello, M., Baldini, L., Bastieri, D., et al., 2021. First Fermi-LAT Solar Flare Catalog. Astrophys. J. SS 252 (13), 1–31.
Ambrosi, G., An, Q., Asfandiyarov, R., et al., 2017. Direct detection of a break in the teraelectronvolt cosmic-ray spectrum of electrons and positrons. Nature 552, 63–66.
Arkhangelskiy, A., Galper, A., Arkhangelskaja, I., et al., 2020a. Design of the readout electronics for the fast trigger and time of flight of the GAMMA-400 gamma-ray telescope. J. Phys. Conf. Ser. 1690 (012024), 1–5.
Arkhangelskiy, A., Galper, A., Arkhangelskaja, I., et al., 2020b. The anticoincidence system of space-based gamma-ray telescope GAMMA-400, test beam studies of anticoincidence detector prototype with SiPM readout. Phys. At. Nucl. 83, 252–257.
Atwood, W., Abdo, A., Ackermann, M., et al., 2009. The large area telescope on the Fermi gamma-ray telescope mission. Astrophys. J. 697, 1071–1102.
Calore, F., Carenza, P., Giannotti, M., et al., 2020. Bounds on axionlike particles from the diffuse supernova flux. Phys. Rev. D 102 (123005), 1–12.

Cattaneo, P.W. on behalf of the HERD collaboration, 2019. The space station based detector HERD: precise high energy cosmic rays physics and multimessenger astronomy. Nucl. and Particle Phys. Proc. 306-308, 85-91.

Galper, A., Adriani, O., Aptekar, A., et al., 2013. Status of the GAMMA-400 project. Adv. Space Res. 51, 297–300.

Galper, A., Topchiev, N., Yurkin, Yu., 2018. GAMMA-400 project. Astron. Rep. 62, 882–889.

Gautham, A., Calore, F., Carenza, P., et al., 2020. Reconciling hints on axion-like-particles from high-energy gamma rays with stellar bounds. arXiv:2008.08100.

Chang, J., Adams, J., Ahn, H., et al., 2008. An excess of cosmic ray electrons at energies of 300–800 GeV. Nature 456, 362–365.

Chang, J., Ambrosi, G., An, Q., et al., 2017. The DArk Matter Particle Explorer mission. Astropart. Phys. 95, 6–24.

DAMPE Collaboration, 2017. Direct detection of a break in the teraelectronvolt cosmic-ray spectrum of electrons and positrons. Nature 552, 63–66.

DeAngelis, A., Tatischeff, V., Grenier, I., et al., 2018. Science with e-ASTROGAM. A space mission for MeV–GeV gamma-ray astrophysics. J. High Energy Astroph. 19, 1–106.

Egorov, A., Topchiev, N., Galper, A., et al., 2020. Dark matter searches by the planned gamma-ray telescope GAMMA-400. J. Cosmol. Astropart. Phys. 11 (049), 1–25.

Evoli, C., Amato, E., Blasi, P., Aloisio, R., 2021. Galactic factories of cosmic-ray electrons and positrons. Phys. Rev. D 103 (083010), 1–22.

Kaneko, Y., Magdalena González, M., Preece, R., et al., 2008. Broadband spectral properties of bright high-energy gamma-ray bursts observed with BATSE and EGRET. Astrophys. J. 677, 1168–1183.

Kardashev, N., Khartov, V., Abramov, V., et al., 2013. "RadioAstron"—A Telescope with a Size of 300 000 km: Main Parameters and First Observational Results. Astron. Rep. 57 (3), 153–194.

Kierans, C., Harding, A., Cenko, B., et al., 2021. AMEGO: exploring the extreme multimessenger universe. arXiv:2101.03105.

Kirn, T., on behalf of the LHCb collaboration, 2017. SciFi – A largescintillating fibretrackerforLHCb. Nucl. Instr. Meth. Phys. Res. A 845, 481–485.

Kobayashi, T., Komori, Y., Yoshida, K., Nishimura, J., 2004. The most likely sources of high-energy cosmic-ray electrons in supernova remnants. Astrophys. J. 601, 340–351.

Leane, R., Slatyer, T., Beacom, J., et al., 2018. GeV-scale thermal WIMPs: Not even slightly ruled out. Phys. Rev. D 98 (023016), 1–16.

Leonov, A., Galper, A., Bonvicini, V., et al., 2015. Separation of electrons and protons in the GAMMA-400 gamma-ray telescope. Adv. Space Res. 56, 1538–1545.

Leonov, A., Galper, A., Topchiev, N., et al., 2019. Capabilities of the GAMMA-400 gamma-ray telescope for observation of electrons and positrons in the TeV energy range. Phys. At. Nucl. 82, 855–858.

Leonov, A., Galper, A., Topchiev, N., et al., 2022. Capabilities of the GAMMA-400 gamma-ray telescope to detect gamma-ray bursts from lateral directions. Adv. Space Res., 69, 514–530. https://doi.org/10.1016/j.asr.2021.10.031; arXiv:2103.07161.

Lien, A., Sakamoto, T., Barthelmy, S., et al., 2016. The Third SWIFT Burst Alert Telescope Gamma-Ray Burst Catalog. Astrophys. J. 829, 7.

Mazziotta, M., Loparco, F., Serini, D., et al., 2020. Search for dark matter signatures in the gamma-ray emission towards the Sun with the Fermi Large Area Telescope. Phys. Rev. D 102 (022003), 1–12.

Minaev, P., Pozanenko, A., 2020. The $E_{p,\,i}$-$_{Eis}$o correlation: type I gamma-ray bursts and the new classification method. MNRAS 492, 1919–1936.

Mori, N., on behalf of the CALET collaboration, 2013. CALET: a calorimeter for cosmic-ray measurements in space. Nucl. Phys. B (Proc. Suppl.) 239-240, 199–203.

Schael, S., Atanasyan, A., J. Berdugo, J., et al., 2019. AMS-100: The next generation magnetic spectrometer in space – An international science platform for physics and astrophysics at Lagrange point 2. Nuclear Inst. and Methods in Physics Research A 944, 162561, 1–13.

Staszak, D. for the VERITAS Collaboration, 2015. A Cosmic-ray Electron Spectrum with VERITAS. arXiv:1508.06597.

Suchkov, S., Galper, A., Arkhangelskiy, A., et al., 2021. Calibrating the prototype calorimeter for the GAMMA-400 gamma-ray telescope on the positron beam at the Pakhra accelerator. Instrum. Exp. Tech. 64, 669–675.

Topchiev, N., Galper, A., Bonvicini, V., et al., 2017. High-energy gamma-ray studying with GAMMA-400 after Fermi-LAT. J. Phys. Conf. Ser. 798 (012011), 1–6.

Topchiev, N., Galper, A., Arkhangelskaja, I., et al., 2019. The future space-based GAMMA-400 gamma-ray telescope for studying gamma and cosmic rays. Bull. Russ. Acad. Sci. Phys. 83, 629–631.

Tridon, D., Colin, P., Cossio, L., et al., 2011. Measurement of the cosmic electron plus positron spectrum with the MAGIC telescopes. arXiv:1110.4008.

von Kienlin, A., Meegan, C., Paciesas, et al., 2020. The Fourth Fermi-GBM Gamma-Ray Burst Catalog: A Decade of Data. Astrophys. J. 893, 46.

Zun-Lei Xu, Kai-Kai Duan, Wei Jiang, et al., 2021. Optimal gamma-ray selections for monochromatic line searches with DAMPE. arXiv:2107.13208.

symmetry

IMPACT FACTOR 2.2

CITESCORE 5.4

Article

On a Possible Origin of the Gamma-ray Excess around the Galactic Center

Dmitry O. Chernyshov, Andrei E. Egorov, Vladimir A. Dogiel and Alexei V. Ivlev

Special Issue

Gamma Ray Signals from Dark Matter

Edited by

Dr. Andrea Albert

MDPI

https://doi.org/10.3390/sym13081432

symmetry

MDPI

Article

On a Possible Origin of the Gamma-ray Excess around the Galactic Center

Dmitry O. Chernyshov [1], Andrei E. Egorov [1], Vladimir A. Dogiel [1,*] and Alexei V. Ivlev [2]

[1] Lebedev Physical Institute, Leninskii Prospect 53, 119991 Moscow, Russia; chernyshov@dgap.mipt.ru (D.O.C.); eae14@yandex.ru (A.E.E.)
[2] Max-Planck-Institut für Extraterrestrische Physik, 85748 Garching, Germany; ivlev@mpe.mpg.de
* Correspondence: dogiel@lpi.ru

Abstract: Recent observations of gamma rays with the Fermi Large Area Telescope (LAT) in the direction of the inner galaxy revealed a mysterious excess of GeV. Its intensity is significantly above predictions of the standard model of cosmic rays (CRs) generation and propagation with a peak in the spectrum around a few GeV. Popular interpretations of this excess are that it is due to either spherically distributed annihilating dark matter (DM) or an abnormal population of millisecond pulsars. We suggest an alternative explanation of the excess through the CR interactions with molecular clouds in the Galactic Center (GC) region. We assumed that the excess could be imitated by the emission of molecular clouds with depleted density of CRs with energies below ∼10 GeV inside. A novelty of our work is in detailed elaboration of the depletion mechanism of CRs with the mentioned energies through the "barrier" near the cloud edge formed by the self-excited MHD turbulence. This depletion of CRs inside the clouds may be a reason for the deficit of gamma rays from the Central Molecular Zone (CMZ) at energies below a few GeV. This in turn changes the ratio between various emission components at those energies and may potentially absorb the GeV excess by a simple renormalization of key components.

Keywords: dark matter; gamma-ray excess; galactic center

check for updates

Citation: Chernyshov, D.O.; Egorov, A.E.; Dogiel, V.A.; Ivlev, A.V. On a Possible Origin of the Gamma-ray Excess around the Galactic Center. *Symmetry* **2021**, *13*, 1432. https://doi.org/10.3390/sym13081432

Academic Editor: Floyd W. Stecker

Received: 18 May 2021
Accepted: 12 July 2021
Published: 5 August 2021

Publisher's Note: MDPI stays neutral with regard to jurisdictional claims in published maps and institutional affiliations.

Copyright: © 2021 by the authors. Licensee MDPI, Basel, Switzerland. This article is an open access article distributed under the terms and conditions of the Creative Commons Attribution (CC BY) license (https://creativecommons.org/licenses/by/4.0/).

1. Introduction and Motivation

The physical nature of dark matter (DM) remains one of the biggest puzzles in modern physics despite the extensive searches for DM with colliders, direct detectors and indirect observations. The latter comprises the searches of various CR particles (see, e.g., [1]) and emissions from DM annihilation or decay, particularly in gamma rays (e.g., [2] part V). Possible gamma-ray signals from DM may in turn have two different spectral types: wideband continuum and narrow lines from annihilation directly into photons. The latter would represent a very pristine signature of DM, since such spectral features are not expected from any other astrophysical processes. Searches for narrow lines in the Fermi-LAT data were not successful so far—only upper limits were derived; see, e.g., [3]. This justifies a motivation to develop new gamma-ray telescopes with better spectroscopic capabilities. One such project, GAMMA-400, is being developed in Russia now [4]. It is expected to have better sensitivity to narrow spectral lines around GC in the energy range of ∼(0.1–100) GeV in comparison with Fermi-LAT due to better energy resolution. This and other aspects of DM searches by GAMMA-400 are described in detail in [5].

There is less ignorance when it comes to the searches for continuum signals from DM annihilation or decay: already a while ago, a significant excess of gamma rays around GC was firmly identified (e.g., [6]). It is difficult to explain such diffuse excess by phenomenological models of emission from CRs, described, e.g., in the monographs [7,8] and implemented in sophisticated numerical codes such as GALPROP [9,10].

The excess is spherically symmetric, visible up to ∼10° from GC and peaks around 2 GeV. It can be well fitted by annihilating WIMPs with the mass of several decades of

GeV, the annihilation cross-section around the thermal value, and steep density profile (e.g., [11,12]). However, alternative explanations through various astrophysical mechanisms indeed exist. Thus, the excess can be caused by the unusual population of ∼1000-millisecond pulsars in the Galactic bulge—e.g., [13]. The pulsar interpretation is probably considered to be the most plausible at present. Other astrophysical interpretations include the emission from molecular clouds, the base of Fermi bubbles, a CR burst in the past etc. Furthermore, in our opinion, the secondary emissions from millisecond pulsars, produced by inverse Compton and bremsstrahlung of $e^{\pm}$ ejected by pulsars, also deserve an attention. Thus, the DM interpretation is challenged by both its own systematics (e.g., Calore et al. [14]) and the existence of many competing opportunities.

Almost all of the mentioned opportunities were challenged at some point by a non-trivial observational fact: abnormal excessive emission was identified in other regions of the galactic plane [15]. This may indicate that the excess source is concentrated around the galactic plane rather than around GC. This in turn supports the molecular cloud (MC) origin of the excess originally proposed in [16], since the clouds indeed reside along all the plane. This creates a motivation to investigate this interesting opportunity further, which comprises the subject of our work. The next section describes in detail our model of CR interaction with MCs, which may modify the MC emission spectra through a peculiar way leading to the imitation of some excessive emission at GeV energies.

2. Modeling the CR Interaction with Molecular Clouds

The authors de Boer et al. [16] found that the GC excess is correlated with the distribution of MCs. They tested two hypothesis of the GeV-excess: the real excess hypothesis assuming the excess is caused by DM annihilation, and the seeming excess hypothesis assuming that the "GeV-excess" is related to a hypothetical depletion of gamma rays from MCs below ≈2 GeV, as it is directly observed in the Central Molecular Zone (CMZ). The authors [16] did not model in details the origin of the emission depletion below 2 GeV, however stated that it is most likely caused by a magnetic cutoff of cosmic rays in MCs. We have developed the latter idea further.

Generally speaking (see, e.g., [15,16]) the hadronic gamma-ray emission is presented by the two components: π^0 gamma-ray emission from the diffuse gas around the GC and π^0 gamma-ray emission from MCs. The investigation by [16] showed that the derived spatial distribution of the emission from MCs correlated nicely with the molecular hydrogen (traced by CO) distribution. Moreover, they found that the gamma-ray emission in the direction on the GC is fully determined by the MC component, where a huge mass of $5 \times 10^7 M_{\odot}$ of molecular hydrogen is concentrated, while other components have a minor effect there. de Boer et al. [16] speculated that this 2 GeV spectral bump is formed due to depletion of the density of CRs with certain energies inside the clouds.

Ivlev et al. [17] and Dogiel et al. [18] abandoned the phenomenological model of CR propagation and conducted more realistic non-linear simulations of gamma-ray emission from MCs, which naturally produces the "GeV excess" through the "MHD-barrier", which reflects CRs with energies $\lesssim$10 GeV and does not allow them to penetrate into the clouds. We assumed that the apparent GeV excess does not have a real source but rather can be explained through an unaccounted modification of MC spectra at certain energies and overall renormalization of the spectra of all emission components. MC spectra gets depleted below few GeV due to a self-excited MHD turbulence by CRs, when the density of CRs inside the cloud is depleted by magnetic fluctuations around the MCs. A flux of CRs propagating through the diffuse ionized gas can excite self-generated magnetic fluctuations (MHD waves). As for the required renormalization of the emission components, it is not large, taking into account that the overall intensity of the GC excess does not exceed ≈10% of the total gamma-ray intensity within 10° from GC (see, e.g., [15]). Such renormalization by ≈10% could be made relatively easily accounting for the systematic uncertainties related to the gas emissivity. Let us discuss now in detail our model of the modification of MC spectra.

The following system of nonlinear kinetic equations describes processes of CR penetration into MCs (see details of the equations in [17]) in one-dimensional approximation. The spectrum of CRs $f(z, E, t)$ and the spectrum of magnetic fluctuations W are described by

$$\frac{\partial f}{\partial t} = \frac{\partial}{\partial z}\left(D\frac{\partial f}{\partial z} - v_A f\right) + \frac{\partial}{\partial p}\left(\frac{dp}{dt} f\right) \quad (1)$$

$$\frac{\partial W}{\partial t} = \frac{\partial}{\partial k}\left(\frac{W}{T_{\rm nl}}\right) - \frac{\partial}{\partial z}(v_a W) + \Gamma W - \nu W\,. \quad (2)$$

where p is the particle momentum, the spatial diffusion coefficient

$$D \simeq \frac{vB^2}{6\pi^2 k^2 W}\,, \quad (3)$$

Γ is the frequency of CR collisions with the background gas, v_A is the Alfvenic velocity, the rate of stream instability excited by CR is

$$\Gamma(k, z) \simeq \pi^2 \frac{e^2 v_A}{m_p c^2 \Omega} pvD\frac{\partial f}{\partial z}\,, \quad (4)$$

$(\partial/\partial k)(W/T_{\rm nl}(k))$ describes the nonlinear cascade of magnetic fluctuations and ν describes waves damping due to ion-neutral friction.

The flux of CRs $S(E) = v_A f - D\frac{\partial f}{\partial z}$ propagating through the envelope and entering the dense interior of the cloud is derived as (see Equations (1) and (2))

$$S(E) = \frac{v_A f_{IS}(E)}{1 - \delta e^{-\eta_0(E)}} \quad (5)$$

where

$$\eta_0(E) = v_A \int_0^H \frac{dz}{D(E, z)}\,, \quad (6)$$

H is the size of the envelope, and f_{IS} is the CR spectrum in the the interstellar medium. Coordinate $z = 0$ corresponds to the boundary between ISM and the envelope, while $z = H$ corresponds to the conditional boundary between the envelope and the dense interior. The parameter $\delta < 1$ in Equation (5) describes opacity of the cloud and depends on its column density N_H (see [18] for details).

The expression for η_0 can be estimated from a balance of the growth rate between MHD wave excitation and damping rates due to ion-neutral collisions, $\Gamma = \nu$, which leads to the following equation for η_0:

$$1 - \delta e^{-\eta_0(E)} \propto \delta v p f_{IS}(E)\,. \quad (7)$$

Since $\delta < 1$ and $f_{IS}(E)$ decreases with energy quite steeply, there is a certain value of $E = E_{ex}$, where $\eta_0(E_{ex}) = 0$. Furthermore, at higher energies the balance can no longer be maintained. This threshold energy, E_{ex}, is a boundary between range of free penetration into the cloud core and the range of self modulated CRs. At sufficiently high energies, $E > E_{ex}$, the CR flux is not affected by MHD-turbulence and converges to the regime of the free-streaming (since $\eta_0 = 0$ and $D \to \infty$).

Within the range of wave excitation by CRs, $E < E_{ex}$, the spectrum of MHD fluctuations is provided by excitation-damping balance described by Equation (7). As a result, below $\sim E_{ex}$, a universal spectrum of CRs $f_p(E) \propto E^{-1}$ is formed inside the dense regions

of MCs. This spectrum is independent of external parameters outside the cloud. Above $\sim E_{ex}$, the spectrum in the core is the same as in the intercloud medium:

$$f_p(E) \propto \begin{cases} E^{-1}, & \text{if } E \lesssim E_{ex}, \\ E^{-\gamma_p}, & \text{if } E \gtrsim E_{ex}, \end{cases} \tag{8}$$

where γ_p is the spectral index of the CRs spectrum in the intercloud medium of the CMZ.

Self-excited MHD turbulence may also impact the gamma-ray emission produced by relativistic electrons, since relativistic protons and electrons interact with turbulence in the same way. This is also very relevant for GeV excess interpretations, since the bremsstrahlung and inverse Compton emission from relativistic electrons may comprise a significant part of the total emission intensity in the GC region (see, e.g., [15,19]). Hence any minor modifications of those emission components may have a big impact on the GC excess amplitude and spectrum.

Even if the intensity of bremsstrahlung from electrons is lower as compared to the emission from proton–proton collisions, the energy break in the spectrum of bremsstrahlung emission is expected to be located at higher energies. Therefore visible effect of CRs self-modulation on bremsstrahlung emission should appear at much lower column densities.

To illustrate the potential influence of self-generated MHD turbulence on the observed spectra of gamma-ray emission we showed in Figure 1 spectra of proton–proton emission $\left(\frac{dN}{dE}\right)_{pp}$ and electron bremsstrahlung emission $\left(\frac{dN}{dE}\right)_{br}$ from the particles inside the cloud. For comparison, we displayed the experimental data points of the GeV excess taken from Ackermann et al. [15].

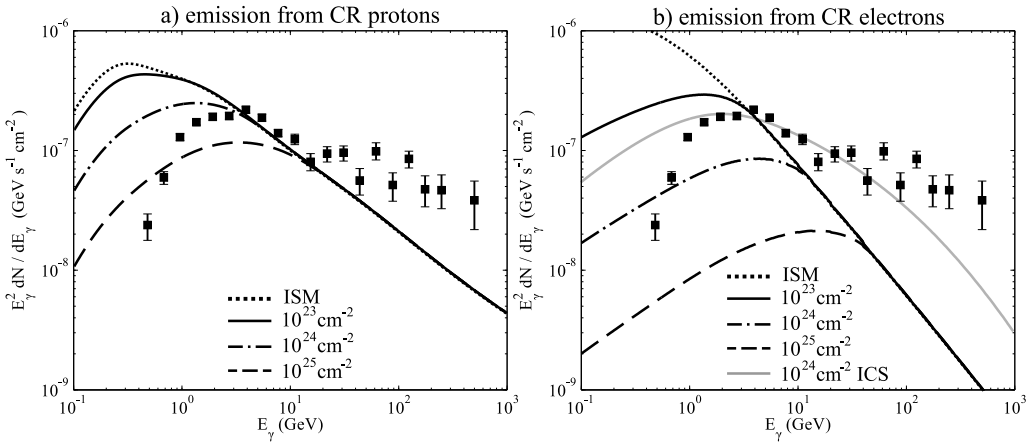


Figure 1. Gamma-ray emission from particles inside the clouds for different values of the cloud column density. (**a**) Emission from relativistic protons. (**b**) Bremsstrahlung emission from relativistic electrons. ICS emission due to scattering of optical photons is also displayed for comparison. The data points represent the GC excess spectrum according to Ackermann et al. [15].

We used the following expressions to calculate the gamma-ray emission spectra:

$$\left(\frac{dN}{dE_\gamma}\right)_i = \frac{M_i c}{4\pi R_{GC}^2 m_p} \int dE\, f_j(E) \left(\frac{d\sigma(E, E_\gamma)}{dE_\gamma}\right)_i, \tag{9}$$

where i stands for either pp or br and j is either p in the case of proton–proton interactions or e in the case of electron bremsstrahlung. M is the total mass of of clouds emitting gamma rays, $R_{GC} = 8$ kpc is the distance to the galactic center, and m_p is the mass of the proton. The differential cross section of the photon production in proton–proton interactions is taken from Kafexhiu et al. [20], and the bremsstrahlung cross section is from Blumenthal and Gould [21].

Equation (9) assumes that the CR spectrum does not change significantly throughout the cloud. This assumption is based on the fact that clouds absorb only a small portion

of the penetrating relativistic protons and electrons and that their density is therefore almost constant in the dense regions of the clouds. CR spectra experience significant spatial variations in the diffuse envelope, where the modulation process takes place. However, the mass of that envelope is negligible as compared to the total mass of the cloud, and gamma-ray emission from this envelope can be ignored.

We did not implement any spatial modeling of the gamma rays in the current work. The main reason was that, to produce a correct spatial distribution of the gamma-ray emission, we need to know how clouds with different masses and different column densities are distributed in the galaxy. Indeed, for each cloud, there should be a specific value of E_{ex}, and therefore, to get a correct spectral shape, we need to integrate over the distribution of all values of E_{ex}. We intend to do this in the future; however, here we only want to show possible effects of the CR modulation on the gamma-ray spectrum.

We assumed that the CR density in the GC is the same as local CR density [22] and took the analytical forms of CR spectra from Ivlev et al. [23]. We considered four representative values of the cloud column density: 0 (marked in Figure 1 as ISM), 10^{23}, 10^{24}, and 10^{25} cm^{-2}, which, according to Dogiel et al. [18], correspond to the following values of E_{ex}: 0, 3.4, 12, and 43 GeV. These column densities can be observed in the following clouds. $N_{H_2} = 10^{23}$ cm^{-2} corresponds to the average column density of CMZ [24] or to the envelope of Sgr B2 [25]. $N_{H_2} = 10^{24}$ cm^{-2} and $N_{H_2} = 10^{25}$ cm^{-2} correspond to the moderate-density region and core of Sgr B2, accordingly [25]. One should notice, however, that Sgr B2 is one of the most massive molecular clouds in the galaxy; therefore, column density as high as 10^{24}–10^{25} cm^{-2} should be considered as a rare occurrence.

The parameters of the ISM were taken as follows: magnetic field strength is $B = 10$ μG, and the diffuse gas density is $n = 10$ cm^{-3} [24,26]. We note that exact value of the magnetic field strength is uncertain, especially in the central regions of the galaxy; however, its value does not affect the value of E_{ex} significantly. Similarly to Ivlev et al. [17], we assumed that the most abundant ion in the envelope is C^+, with density of 3×10^{-3} cm^{-3}. The corresponding value of the Alfven velocity in the envelope is $v_A = 10^7$ cm/s.

To reproduce the curves shown in Figure 1 we need the following values of the total mass. For proton–proton collisions it is equal to $M_{pp} = 2 \times 10^8 M_\odot$ and for the electron bremsstrahlung it equals $M_{br} = 2 \times 10^9 M_\odot$. These values exceed the total mass of CMZ and even the mass of the galactic circumnuclear disk (CND) [24]. The reason for this discrepancy may be due to the influence of the local clouds along the line of sight. Indeed, we assumed that all molecular clouds are located at the distance of $R = 8$ kpc and ignored the contribution of clouds that are located in the vicinity. In the case of electrons, we can also argue that their density in the galactic center is much higher than their local density [19].

We also plotted the ICS emission from the modulated spectrum of electrons due to the scattering of soft photons with energy of 1 eV. To calculate this, we used Equation (9), where we replaced factor $\frac{M}{m_p}$ with εV. Here, ε is the average energy density of soft photons in the galaxy and V is the total volume involved in the emission. The differential cross section of the ICS emission is taken from Blumenthal and Gould [21].

If we assume that $\varepsilon = 10$ eV·cm^{-3} [27], we need the volume to be equal to $V = 7 \times 10^{65}$ cm^3 to match the data points and assuming that the region is spherical with a radius of about $r = 2$ kpc. This is larger than the size of the the CMZ and CND; however, we can argue that soft photon density is much higher in the central regions of the galaxy.

As one can see from Figure 1, modulation of CR flux due to self-generated turbulence indeed produces the deficit of gamma-ray photons at the required energies below several GeV. Thus, our model is able to justify the explanation of GC excess (see [16]).

One can assume that the analysis performed by, e.g., Ackermann et al. [15] used standard assumptions (incorporated by GALPROP) to calculate the emissivity of MCs and did not take into account self-modulation of the CRs. Therefore, they overestimated the intensity of all the key emission components coming from MCs: hadronic due to proton–proton interactions, and bremsstrahlung and ICS from electrons at energies below several GeV.

Although the intercloud diffuse gas emissivity in our model is not modified, the modification of the part of total emission coming from MCs is potentially able to change the ratio of all components significantly. The deficit of gamma-ray intensity from MCs below several GeV would require in turn an increase in the GC excess intensity at those energies in order to preserve the whole balance. The GC excess brightening at low energies in turn would make its spectrum more monotonous, i.e., less bumpy. Furthermore, this kind of power-law spectrum is then relatively easy to "absorb" into the overall diffuse gas or point sources (both resolved and unresolved) spectra, which have the similar shape close to a power law, by their slight renormalization towards higher levels. Such procedure would remove the GC excess as a separate emission component merging the former with the known components.

Finally, we would like to notice that our model curves in Figure 1 are not intended to fit the GC excess directly. They only illustrate that reasonable parameter values for MCs and ISM are able to produce the spectral break in intensity of MCs at an energy near the GC excess peak, allowing the excess below this energy to "brighten" up to the state (ideally) where the whole excess spectrum is close to a monotonous power law.

3. Conclusions and Discussion

We elaborated the mechanism of the modification of emission spectra of MCs, which, according to [16], can fit the mysterious GeV excess around GC. Our mechanism represents a viable alternative to other possible excess explanations such as annihilating DM, millisecond pulsars, etc. In order to investigate the nature of the GC excess further and finally establish its exact source, the astrophysical community needs in new high-quality gamma-ray data. Thus, we crucially need to increase angular and energy resolutions of our instruments around the energies $E_\gamma \sim 1$ GeV with respect to capabilities of Fermi-LAT. This will allow us to conduct the resolved imaging of the CMZ region [18] and better discriminate the spectra of various emission components there. At the same time, we still cannot exclude the DM origin of the excess. Hence, further investigations may eventually lead to DM discovery. This is why we have great expectations from the currently planned new gamma-ray telescopes: *GAMMA-400* [5], *e-ASTROGAM* [28], *AMEGO* [29], and others.

Author Contributions: Conceptualization, D.O.C., V.A.D. and A.V.I.; investigation, D.O.C. and A.E.E.; writing—original draft preparation, D.O.C., V.A.D. and A.E.E.; writing—review and editing, D.O.C., A.E.E. and A.V.I.; supervision, V.A.D. All authors have read and agreed to the published version of the manuscript.

Funding: This research was supported by Russian Science Foundation via the Project 20-12-00047.

Conflicts of Interest: The authors declare no conflict of interest.

References

1. Adriani, O.; Barbarino, G.C.; Bazilevskaya, G.A.; Bellotti, R.; Boezio, M.; Bogomolov, E.A.; Bonechi, L.; Bongi, M.; Bonvicini, V.; Bottai, S.; et al. An anomalous positron abundance in cosmic rays with energies 1.5–100 GeV. *Nature* **2009**, *458*, 607–609. [CrossRef]
2. Bertone, G.; Silk, J. Particle dark matter. In *Particle Dark Matter: Observations, Models and Searches*; Bertone, G., Ed.; Cambridge University Press, The Edinburgh Building: Cambridge, UK, 2010; p. 3.
3. Ackermann, M.; Ajello, M.; Albert, A.; Anderson, B.; Atwood, W.B.; Baldini, L.; Barbiellini, G.; Bastieri, D.; Bellazzini, R.; Bissaldi, E.; et al. Updated search for spectral lines from Galactic dark matter interactions with pass 8 data from the Fermi Large Area Telescope. *Phys. Rev. D* **2015**, *91*, 122002. [CrossRef]
4. Galper, A.M.; Suchkov, S.I.; Topchiev, N.P.; Arkhangelskaja, I.V.; Arkhangelskiy, A.I.; Bakaldin, A.V.; Gusakov, Y.V.; Dalkarov, O.D.; Egorov, A.E.; Zverev, V.G.; et al. Precision Measurements of High-Energy Cosmic Gamma-ray Emission with the GAMMA-400 Gamma-ray Telescope. *Phys. Atom. Nuclei* **2017**, *80*, 1141–1145. [CrossRef]
5. Egorov, A.E.; Topchiev, N.P.; Galper, A.M.; Dalkarov, O.D.; Leonov, A.A.; Suchkov, S.I.; Yurkin, Y.T. Dark matter searches by the planned gamma-ray telescope GAMMA-400. *J. Cosmol. Astropart. Phys.* **2020**, *11*, 049. [CrossRef]
6. Abazajian, K.N.; Kaplinghat, M. Detection of a gamma-ray source in the Galactic Center consistent with extended emission from dark matter annihilation and concentrated astrophysical emission. *Phys. Rev. D* **2012**, *86*, 083511. [CrossRef]
7. Ginzburg, V.L.; Syrovatskii, S.I. *The Origin of Cosmic Rays*; Macmillan: New York, NY, USA, 1964.

8. Berezinskii, V.S.; Bulanov, S.V.; Dogiel, V.A.; Ginzburg, V.L.; Ptuskin, V.S. *Astrophysics of Cosmic Rays*; North Holland: Amsterdam, The Netherlands, 1990.
9. Moskalenko, I.V.; Strong, A.W. Production and Propagation of Cosmic-Ray Positrons and Electrons. *Astrophys. J.* **1998**, *493*, 694–707. [CrossRef]
10. Jóhannesson, G.; Porter, T.A.; Moskalenko, I.V. The Three-dimensional Spatial Distribution of Interstellar Gas in the Milky Way: Implications for Cosmic Rays and High-energy Gamma-ray Emissions. *Astrophys. J.* **2018**, *856*, 45. [CrossRef]
11. Di Mauro, M.; Winkler, M.W. Multimessenger constraints on the dark matter interpretation of the Fermi-LAT Galactic center excess. *arXiv* **2021**, arXiv:2101.11027.
12. Hooper, D.; Goodenough, L. Dark matter annihilation in the Galactic Center as seen by the Fermi Gamma Ray Space Telescope. *Phys. Lett. B* **2011**, *697*, 412–428. [CrossRef]
13. Macias, O.; Horiuchi, S.; Kaplinghat, M.; Gordon, C.; Crocker, R.M.; Nataf, D.M. Strong evidence that the galactic bulge is shining in gamma rays. *J. Cosmol. Astropart. Phys.* **2019**, *2019*, 042. [CrossRef]
14. Calore, F.; Cholis, I.; Weniger, C. Background model systematics for the Fermi GeV excess. *J. Cosmol. Astropart. Phys.* **2015**, *2015*, 038. [CrossRef]
15. Ackermann, M.; Ajello, M.; Albert, A.; Atwood, W.B.; Baldini, L.; Ballet, J.; Barbiellini, G.; Bastieri, D.; Bellazzini, R.; Bissaldi, E.; et al. The Fermi Galactic Center GeV Excess and Implications for Dark Matter. *Astrophys. J.* **2017**, *840*, 43. [CrossRef]
16. de Boer, W.; Bosse, L.; Gebauer, I.; Neumann, A.; Biermann, P.L. Molecular clouds as origin of the Fermi gamma-ray GeV excess. *Phys. Rev. D* **2017**, *96*, 043012. [CrossRef]
17. Ivlev, A.V.; Dogiel, V.A.; Chernyshov, D.O.; Caselli, P.; Ko, C.M.; Cheng, K.S. Penetration of Cosmic Rays into Dense Molecular Clouds: Role of Diffuse Envelopes. *Astrophys. J.* **2018**, *855*, 23. [CrossRef]
18. Dogiel, V.A.; Chernyshov, D.O.; Ivlev, A.V.; Malyshev, D.; Strong, A.W.; Cheng, K.S. Gamma-ray Emission from Molecular Clouds Generated by Penetrating Cosmic Rays. *Astrophys. J.* **2018**, *868*, 114. [CrossRef]
19. Yusef-Zadeh, F.; Hewitt, J.W.; Wardle, M.; Tatischeff, V.; Roberts, D.A.; Cotton, W.; Uchiyama, H.; Nobukawa, M.; Tsuru, T.G.; Heinke, C.; et al. Interacting Cosmic Rays with Molecular Clouds: A Bremsstrahlung Origin of Diffuse High-energy Emission from the Inner $2^\circ \times 1^\circ$ of the Galactic Center. *Astrophys. J.* **2013**, *762*, 33. [CrossRef]
20. Kafexhiu, E.; Aharonian, F.; Taylor, A.M.; Vila, G.S. Parametrization of gamma-ray production cross sections for p p interactions in a broad proton energy range from the kinematic threshold to PeV energies. *Phys. Rev. D* **2014**, *90*, 123014. [CrossRef]
21. Blumenthal, G.R.; Gould, R.J. Bremsstrahlung, Synchrotron Radiation, and Compton Scattering of High-Energy Electrons Traversing Dilute Gases. *Rev. Mod. Phys.* **1970**, *42*, 237–271. [CrossRef]
22. Acero, F.; Ackermann, M.; Ajello, M.; Albert, A.; Baldini, L.; Ballet, J.; Barbiellini, G.; Bastieri, D.; Bellazzini, R.; Bissaldi, E.; et al. Development of the Model of Galactic Interstellar Emission for Standard Point-source Analysis of Fermi Large Area Telescope Data. *Astrophys. J. Suppl. Ser.* **2016**, *223*, 26. [CrossRef]
23. Ivlev, A.V.; Padovani, M.; Galli, D.; Caselli, P. Interstellar Dust Charging in Dense Molecular Clouds: Cosmic Ray Effects. *Astrophys. J.* **2015**, *812*, 135. [CrossRef]
24. Ferrière, K.; Gillard, W.; Jean, P. Spatial distribution of interstellar gas in the innermost 3 kpc of our galaxy. *Astron. Astrophys.* **2007**, *467*, 611–627. [CrossRef]
25. Huettemeister, S.; Wilson, T.L.; Mauersberger, R.; Lemme, C.; Dahmen, G.; Henkel, C. A multilevel study of ammonia in star-forming regions. VI. The envelope of Sagittarius B2. *Astron. Astrophys.* **1995**, *294*, 667–676.
26. Ferrière, K. Interstellar magnetic fields in the Galactic center region. *Astron. Astrophys.* **2009**, *505*, 1183–1198. [CrossRef]
27. Porter, T.A.; Jóhannesson, G.; Moskalenko, I.V. High-energy Gamma Rays from the Milky Way: Three-dimensional Spatial Models for the Cosmic-Ray and Radiation Field Densities in the Interstellar Medium. *Astrophys. J.* **2017**, *846*, 67. [CrossRef]
28. De Angelis, A.; Tatischeff, V.; Argan, A.; Brandt, S.; Bulgarelli, A.; Bykov, A.; Costantini, E.; Curado da Silva, R.; Grenier, I.A.; Hanlon, L.; et al. Gamma-ray Astrophysics in the MeV Range: The ASTROGAM Concept and Beyond. *arXiv* **2021**, arXiv:2102.02460.
29. McEnery, J.; van der Horst, A.; Dominguez, A.; Moiseev, A.; Marcowith, A.; Harding, A.; Lien, A.; Giuliani, A.; Inglis, A.; Ansoldi, S.; et al. All-sky Medium Energy Gamma-ray Observatory: Exploring the Extreme Multimessenger Universe. *Bull. Am. Astron. Soc.* **2019**, *51*, 245.

ISSN 1063-7737, Astronomy Letters, 2009, Vol. 35, No. 4, pp. 241–246. © Pleiades Publishing, Inc., 2009.
Original Russian Text © A.E. Egorov, K.A. Postnov, 2009, published in Pis'ma v Astronomicheskiĭ Zhurnal, 2009, Vol. 35, No. 4, pp. 272–278.

On the Possible Observational Manifestation of the Impact of a Supernova Shock on the Neutron Star Magnetosphere

A. E. Egorov* **and K. A. Postnov****

Sternberg Astronomical Institute, Universitetskii pr. 13, Moscow, 119992 Russia

Received September 2, 2008

Abstract—The impact of a supernova explosion on the magnetosphere of a neutron star in a massive binary system is considered. The supernova shock impact on a plasma-filled neutron star magnetosphere can give rise to a long magnetospheric tail with a considerable store of magnetic energy. Magnetic reconnection in the formed current sheet can transform the magnetic energy stored in the tail into the kinetic energy of charged particles. The plasma instabilities excited by beams of accelerated relativistic particles can lead to the formation of a short pulse of coherent radio emission with parameters similar to those measured for the bright extragalactic millisecond radio burst detected in 2007.

PACS numbers : 97.60.Bw; 97.60.Gb; 95.30.Gv
DOI: 10.1134/S1063773709040033

Key words: *supernovae, pulsars, radiation mechanisms.*

INTRODUCTION

A supernova (SN) explosion in a binary system with a neutron star (NS) is not a rare event. Since the binary system can be disrupted as a result of the second SN explosion, the lower limit for the rate of "impacts" on the NSs can be estimated, for example, as the formation rate of binary NSs in the Galaxy. This rate inferred from the binary pulsar statistics and population synthesis calculations is $\sim 10^{-4}$–10^{-5} yr^{-1} (Postnov and Yungelson 2006), i.e., the spatial rate is ~ 10 day^{-1}Gpc^{-3}.

The impact of a SN shock on the NS magnetosphere can be accompanied by interesting observational manifestations. For example, Istomin and Komberg (2002) argue that this process can generate a highly collimated beam of hard radiation that can be observed as a gamma-ray burst (GRB). In their opinion, this radiation has the following generation mechanism: the cumulative effect of the SN shock impact on the NS magnetosphere gives rise to a long magnetospheric tail. Subsequently, magnetic reconnection takes place in this tail, which causes particle acceleration. The accelerated particles emit hard X-ray synchrophotons that can be observed as a GRB. However, this physical problem on the conversion of magnetic energy in the tail into hard radiation is very complex and it is not yet completely clear whether all of the known GRB properties can be described by this mechanism. However, the acceleration of particles to high energies during magnetic reconnection is beyond question (see, e.g., the recent numerical calculations by Zenitani and Hoshino (2007)) and a wide range of plasma phenomena can arise when the accelerated particles interact with the ambient medium.

Here, we will show that the plasma instabilities that develop during magnetic reconnection in the magnetospheric tail can generate a powerful short pulse of nonthermal radio emission. A very short powerful radio burst with unusual properties has recently been discovered by Lorimer et al. (2007): the radio flux at 1.4 GHz was 30 ± 10 Jy, the duration of the event was less than 5 ms, and the dispersion measure was 375 pc cm^{-3}. The latter may be indicative of an extragalactic nature of the source at a distance of ~ 1 Gpc. There is no host galaxy at the location of the source down to 18^m in B, which places a lower limit on the distance of 600 Mpc for a Milky-Way-like host. At such a distance, the total energy release in the observed radio burst is $\sim 10^{40}$ erg with a brightness temperature of $\sim 10^{34}$ K for isotropic radiation. The total spatial rate of such events was estimated by Lorimer et al. (2007) to be ~ 90 day^{-1}Gpc^{-3}, which is much lower than the core-collapse SN rate, ~ 1000 day^{-1}Gpc^{-3}, but is considerably higher than the observed GRB rate, ~ 4 day^{-1}Gpc^{-3}, and the expected binary NS merger rate: ~ 2 day^{-1}Gpc^{-3}. Of

*E-mail: astrotula@gmail.com
**E-mail: kpostnov@gmail.com

course, this estimate of the radio burst rate is very uncertain due to poor statistics based only on one event.

It should be immediately noted that the short-duration radio emission detected by Lorimer et al. (2007) is very similar in its properties to the pulsar one: coherence, a very high brightness temperature at 1.4 GHz, and a steeply decreasing power-law spectrum ($\sim\nu^{-4}$). Lorimer et al. (2007) considered several known sources of strong millisecond radio bursts (rotating radio transients (RRATs) and giant pulses from radio pulsars) and concluded that their energy release is not enough for the detected radio burst to be explained. Based only on statistical arguments, Popov and Postnov (2007) suggested that this burst could be generated by a hyperflare of an extragalactic magnetar.

Assuming the radio emission to be as efficient as that from the Crab pulsar, a magnetar ($B \sim 10^{15}$ G) with a millisecond rotation period would be required to explain the observed radio burst by the generation mechanism of giant radio pulses (like those emitted by the Crab pulsar with a peak flux of ~1000 Jy). However, the observed magnetars rotate slowly ($P = 1$–10 s) due to their rapid spin-down. If a newly born millisecond magnetar is considered, then, according to the models by Usov (1992, 1994), its characteristic spin-down time is several seconds. In this time, it will emit a sequence of weakening pulses and, thus, a single burst cannot be plausibly explained by this mechanism.

On the other hand, magnetic reconnection during the relaxation of the NS magnetosphere after its interaction with the SN shock naturally gives rise to beams of accelerated particles. Plasma instabilities in such flows contribute to the conversion of the kinetic energy of accelerated particles into the energy of transverse electromagnetic waves, which can be observed as short powerful bursts of nonthermal radio emission. Lyubarsky (2008) showed that such radio pulses could propagate through the stellar wind without decaying due to the induced Compton and Raman scattering if they are emitted at a distance $>10^{15}$ cm from the exploding massive star, with the relativistic motion of the source being required. Such a distance between the components of the massive binary system is quite possible, while the relativistic motion of the emitting region is nontrivial. In our model, the relativistic motion of the emitting region can also be achieved when the beam of electrons accelerates as a result of nonstationary magnetic reconnection.

THE IMPACT OF A SN SHOCK ON THE NS MAGNETOSPHERE

Following Istomin and Komberg (2002), we will take typical SN shock parameters at the post-explosion stage of free expansion (Imshennik and Nadyozhin 1989): a total kinetic energy $E_{\rm kin} \approx 10^{47}$ erg, a velocity $u \approx 4 \times 10^9$ cm s^{-1}, a density $\rho \approx 10^{-8}$ g cm^{-3}, and a shock width $h \approx 10^9$ cm.

We assume that the already existing NS was a pulsar before the SN explosion in the binary system, i.e., a relativistic plasma was generated near its surface. The pulsar stage can last for the first $\sim 10^7$ yr of the NS lifetime. The probability that the second component explodes as a SN during this stage is high, especially if the binary components initially had close masses. The characteristic size of the pulsar magnetosphere (neglecting its possible distortions by the stellar wind from the SN progenitor) is of the order of the light cylinder size $R_l \sim c/\Omega = cP/2\pi$. A stationary pulsar magnetosphere must be filled with an electron–positron plasma with the Goldreich–Julian number density (Goldreich and Julian 1969):

$$n_{\rm GJ} = \frac{|\rho_{\rm GJ}|\,k}{e} = \frac{|\mathbf{\Omega B}|k}{2\pi ce}, \qquad (1)$$

where $k = 10^4$–10^5 is the particle multiplication factor and e is the electron charge.

The kinetic energy of the SN shock that is geometrically intercepted by the NS magnetosphere can be estimated as

$$E' = E_{\rm kin}\frac{\pi R_l^2}{4\pi a^2} \qquad (2)$$
$$= 10^{39}\left(\frac{\Omega}{10\ {\rm rad\ s^{-1}}}\right)^{-2}\left(\frac{a}{1\ {\rm AU}}\right)^{-2}\ {\rm erg},$$

where a is the distance between the stars. Istomin and Komberg (2002) argue that such a perturbation can give rise to a magnetospheric tail with a considerable store of magnetic energy. This tail is unstable against magnetic reconnection, which causes particle acceleration to high energies. Below, we will show that the disruption of the magnetospheric tail can be accompanied by the formation of two colliding relativistic electron and positron beams. The beam collision leads to the development of plasma instabilities that generate plasma waves. These can be converted into transverse electromagnetic waves that can be observed as a highly collimated beam of nonthermal radio emission. This situation is in many ways similar to the most likely pulsar radio emission generation mechanism described by Lyubarsky (1992).

Istomin and Komberg (2002) argue that the front part of the NS magnetosphere is compressed as a result of the SN shock passage and a long narrow

magnetospheric tail is formed on the opposite side (a clear analogy is the Earth's magnetosphere blown by the solar wind). The dependences of the tail magnetic field strength and diameter on the distance l from the NS can be obtained by using the conditions for the magnetic field being frozen into the shock plasma and for the magnetic flux conservation in the tail (for more detail, see Istomin and Komberg 2002):

$$B_\mathrm{t} = B^* \left(\frac{l}{r^*}\right)^{1/2}, \quad (3)$$

$$d_\mathrm{t} = 2r^* \left(\frac{l}{r^*}\right)^{-1/4}, \quad (4)$$

respectively. Here,

$$B^* = (4\pi\rho u^2)^{1/2}$$
$$\approx 10^6 \left(\frac{\rho}{10^{-8}\mathrm{g\,cm^{-3}}}\right)^{1/2} \left(\frac{u}{4\times10^9\ \mathrm{cm\ s^{-1}}}\right)\ \mathrm{G}$$

is the magnetic field strength at the Alfvénic radius r^*, where the magnetic field pressure is balanced by the shock ram pressure. In the case of a a dipole magnetic field for the assumed shock parameters,

$$r^* = R\left(\frac{B}{B^*}\right)^{1/3} = R\left(\frac{B^2}{4\pi\rho u^2}\right)^{1/6} \quad (5)$$
$$\approx 10^8 \left(\frac{R}{10\ \mathrm{km}}\right)\left(\frac{B}{10^{12}\ \mathrm{G}}\right)^{1/3}\ \mathrm{cm},$$

where B is the NS surface magnetic field, and R is the NS radius.

The store of magnetic energy in this narrow ($d_\mathrm{t} \ll L \simeq h$, where L is the tail length), magnetized ($B^* \approx 10^6$ G) tail will then be

$$\epsilon_B = \int \frac{B_\mathrm{t}^2}{8\pi}\frac{\pi d_\mathrm{t}^2}{4}dl = \frac{1}{12}B^{*2}r^{*3/2}h^{3/2} \quad (6)$$
$$= 3\times10^{36}\left(\frac{B^*}{10^6\ \mathrm{G}}\right)^2$$
$$\times \left(\frac{r^*}{10^8\ \mathrm{cm}}\right)^{3/2}\left(\frac{h}{10^9\mathrm{cm}}\right)^{3/2}\ \mathrm{erg}.$$

Clearly, such a tail can be unstable against magnetic reconnection in the current sheet. The symmetry of the problem corresponds to a plane geometry of the current sheet in the orbital plane. An electric field perpendicular to the tail axis in the orbital plane is generated during magnetic reconnection. This field can accelerate plasma electrons with a broad energy distribution to high Lorentz factors (see, e.g., the recent numerical calculations by Zenitani and Hoshino (2007)). An important thing is that some amount of electron–positron plasma with a number density lower than the Goldreich–Julian value (1) could be initially expected in the tail, since the magnetosphere can open up during the tail formation and the pairs will flow out along open magnetic field lines. Thus, the upper limit on the number density of pairs in the tail is estimated as

$$n_\mathrm{pairs} \le n_\mathrm{GJ}(l) \quad (7)$$
$$\approx 10^7\left(\frac{\Omega}{10\ \mathrm{rad\ s^{-1}}}\right)$$
$$\times \left(\frac{B}{10^{12}\ \mathrm{G}}\right)\left(\frac{k}{10^4}\right)\left(\frac{l}{5r^*}\right)^{-3}\ \mathrm{cm^{-3}}.$$

At the same time, some amount of electron–ion plasma can penetrate from the shock into the magnetospheric tail during its formation. The number density of this plasma can exceed significantly that of the pairs.

THE GENERATION OF RADIO EMISSION

At the beginning of magnetic reconnection, the tail is filled with plasma with an admixture of pairs. During reconnection, several X-points can be formed along the entire tail (tearing instability) and a strong electric field transverse to the tail axis appears and accelerates particles. The electrons and positions are accelerated in opposite directions. Thus, the positron beam can begin to move against the relativistic electron beam. This situation is similar to the pulsar wind flowing along the open field lines of the NS magnetosphere (Lyubarsky 1992), where the electric field appears due to the leak of the Goldreich charge density (the total field screening condition is violated in the quasi-stationary regime). In this case, part of the kinetic energy of accelerated particles can be transformed by plasma instabilities into the energy of plasma oscillations at the comoving plasma frequency. These oscillations can then be nonlinearly converted into transverse electromagnetic waves observable as pulsar radio emission.

In our case, the duration of the radio emission generated during magnetic reconnection (fast reconnection with an Alfvén velocity is assumed) can be roughly estimated from the diameter of the emitting tail: $\tau \approx r^*/v_\mathrm{a} \approx r^*/c \approx 3$ ms. This duration is of the order of that measured for the extragalactic radio burst by Lorimer et al. (2007).

The sequential picture of the phenomenon can be as follows. A flow of relativistic electron plasma moving perpendicularly to the tail with some effective Lorentz factor Γ can emerge as the magnetic field topology changes. The reverse flow of positron plasma is accelerated by the same electric field in the reconnecting current sheet and, as a result, moves with a similar Lorentz factor toward the electrons. Due to

the development of various instabilities (beam instability etc.), a significant fraction of the kinetic energy of the positron beam can dissipate in the electron plasma by exciting plasma waves. This energy conversion is efficient at a low positron number density compared to the electron one ($n^+ \ll n^-$), which is expected in our case. These plasma oscillations are nonlinearly converted into transverse electromagnetic waves that can be observed as a short radio pulse at appropriate relative positions of the tail and the observer. Relativistic aberration confines the radio emission within a narrow cone with an opening angle $\theta \sim \Gamma^{-1}$. The oscillations are excited at the comoving plasma frequency

$$\tilde{\omega} = \sqrt{\frac{4\pi e^2 \tilde{n_e^-}}{m}}. \quad (8)$$

The conversion rate of plasma waves into transverse ones can be expressed as (see, e.g., Lyubarsky 1992)

$$\frac{\partial \tilde{W}_\mathrm{t}}{\partial t} = \tilde{\alpha} \tilde{W}_\mathrm{t} \tilde{W}_\mathrm{l}, \quad (9)$$

where

$$\tilde{\alpha} = \frac{\tilde{\omega}}{\tilde{n}^- mc^2}, \quad (10)$$

$\tilde{W}_\mathrm{t}$ and $\tilde{W}_\mathrm{l}$ are the energy densities of the transverse and longitudinal waves, respectively, in the comoving plasma frame. The observed emission frequency is Doppler shifted (the emitting electrons move toward the observer with a Lorentz factor Γ):

$$\nu \cong 2\Gamma\tilde{\nu} = 2\Gamma\frac{\tilde{\omega}}{2\pi} = 2\Gamma e\sqrt{\frac{\tilde{n}_e^-}{\pi m}}, \quad (11)$$

where $\tilde{n}_e^-$ is the electron number density at the time of emission. It can be slightly lower than the initial number density in the tail, since the volume of the emitting current sheet can increase during magnetic reconnection due to a number of instabilities (for more detail, see Zenitani and Hoshino 2007). Therefore, below, we assume that $\tilde{n}_e^- = \alpha\tilde{n}^-$, where $\alpha < 1$ is the ratio of the particle number densities in the current sheet and the tail. The total energy of the radio emission E can be estimated as the kinetic energy of positrons enhanced by a factor $(2\Gamma)^2$. One power of the factor (2Γ) is related to the Doppler effect and its other power is related to the transformation of the positron kinetic energy to the frame comoving with the emitting electron plasma. Here, we assume the Lorentz factors of the electrons and positrons to be identical. Thus,

$$E = \zeta\Gamma N^+ mc^2 (2\Gamma)^2 \approx 4\zeta\Gamma^3 \tilde{n}^+ \pi r^{*2} hmc^2, \quad (12)$$

where the factor $\zeta < 1$ takes into account the conversion efficiency of the positron kinetic energy into the energy of electromagnetic radiation, the particle acceleration efficiency, etc.; N^+ is the total number of positrons; and h is the tail length. The observed flux is then

$$S = \frac{E}{\tau\Delta_\nu \pi (0.5\theta r)^2} = \frac{16\zeta\Gamma^5 \tilde{n}^+ r^{*2} hmc^2}{\tau\Delta_\nu r^2}, \quad (13)$$

where $\theta = 1/\Gamma$ is the relativistic aberration angle, Δ_ν is the frequency bandwidth of the receiver, and r is the distance to the source.

For millisecond radio burst parameters $\nu \approx 1.4$ GHz, $S \approx 30$ Jy, $r \approx 500$ Mpc, and $\Delta_\nu \approx 300$ MHz (Lorimer et al. 2007) and assuming that $\tilde{n}^+ = \beta\tilde{n}^-$, $\beta < 1$, and $\tau \approx r^*/c$, we find from Eqs. (11)–(13) that

$$\Gamma \approx 2000 \left(\frac{S}{30\ \mathrm{Jy}}\right)^{1/3} \left(\frac{h}{10^9\ \mathrm{cm}}\right)^{-1/3} \times \left(\frac{r}{500\ \mathrm{Mpc}}\right)^{2/3} \left(\frac{r^*}{10^8\ \mathrm{cm}}\right)^{-1/3} \left(\frac{\nu}{1.4\ \mathrm{GHz}}\right)^{-2/3} \times \left(\frac{\alpha}{0.1}\right)^{1/3} \left(\frac{\beta}{0.1}\right)^{-1/3} \left(\frac{\zeta}{0.1}\right)^{-1/3}, \quad (14)$$

$$\tilde{n}^+ \approx 3\times 10^3 \left(\frac{\nu}{1.4\ \mathrm{GHz}}\right)^{10/3} \times \left(\frac{S}{30\ \mathrm{Jy}}\right)^{-2/3} \left(\frac{h}{10^9\ \mathrm{cm}}\right)^{2/3} \times \left(\frac{r}{500\ \mathrm{Mpc}}\right)^{-4/3} \left(\frac{r^*}{10^8\ \mathrm{cm}}\right)^{2/3} \times \left(\frac{\alpha}{0.1}\right)^{-5/3} \left(\frac{\beta}{0.1}\right)^{5/3} \left(\frac{\zeta}{0.1}\right)^{2/3} \mathrm{cm}^{-3}, \quad (15)$$

$$\tilde{n}^- \approx 3\times 10^4 \left(\frac{\nu}{1.4\ \mathrm{GHz}}\right)^{10/3} \times \left(\frac{S}{30\ \mathrm{Jy}}\right)^{-2/3} \left(\frac{h}{10^9\ \mathrm{cm}}\right)^{2/3} \times \left(\frac{r}{500\ \mathrm{Mpc}}\right)^{-4/3} \left(\frac{r^*}{10^8\ \mathrm{cm}}\right)^{2/3} \times \left(\frac{\alpha}{0.1}\right)^{-5/3} \left(\frac{\beta}{0.1}\right)^{2/3} \left(\frac{\zeta}{0.1}\right)^{2/3} \mathrm{cm}^{-3}, \quad (16)$$

$$E \approx 5\times 10^{32} \left(\frac{S}{30\ \mathrm{Jy}}\right)^{1/3} \times \left(\frac{h}{10^9\ \mathrm{cm}}\right)^{2/3} \left(\frac{r}{500\ \mathrm{Mpc}}\right)^{2/3} \times \left(\frac{r^*}{10^8\mathrm{cm}}\right)^{5/3} \left(\frac{\alpha}{0.1}\right)^{-2/3} \quad (17)$$

$$\times \left(\frac{\beta}{0.1}\right)^{2/3} \left(\frac{\zeta}{0.1}\right)^{5/3} \text{ erg} \approx 10^{-4}\epsilon_B.$$

The Lorentz factor obtained is admitted by the constraints imposed by the induced scattering on the source's plasma transparency (Lyubarsky 2008). The positron number density and the total energy of the radio emission are consistent with estimates (7) and (6), respectively, as their upper limits.

The radio burst spectrum is also known, $dS/d\nu \sim \nu^{-4\pm1}$. As has been noted above, the generation mechanism of the radio burst is similar to that of the pulsar radio emission. Therefore, as would be expected, this spectrum is similar the pulsar one (in the range of high frequencies; the Crab pulsar has almost the same spectrum). There are many factors affecting the spectral shape: the wide spectrum of plasma waves ($\Delta\tilde{\omega} \sim \tilde{\omega}$), the wide energy spectrum of accelerated particles, plasma inhomogeneities, the scattering of emission by the plasma surrounding the source, the absorption of emission in the host galaxy, etc. We can attempt to partly explain this spectrum by assuming a power-law energy distribution of accelerated electrons $d\tilde{n}^-/d\gamma \sim \gamma^{-p}$. The contribution from the emitting electrons with Lorentz factors $[\gamma, \gamma + d\gamma]$ to the observed emission in the linear approximation will then be

$$dS \sim \gamma d\tilde{n}^- \sim \gamma^{1-p} d\gamma. \qquad (18)$$

The additional Lorentz factor results from the Doppler effect. Next, taking into account (11) and (18), we obtain

$$\frac{dS}{d\nu} = \frac{dS}{d\gamma}\Big/\frac{d\nu}{d\gamma} \sim \gamma^{1-p} \sim \nu^{1-p}.$$

This spectrum agrees with observations at $p = 4$–6, which is generally consistent with the numerical simulations of the energy spectrum for nonthermal particles during relativistic magnetic reconnection (Zenitani and Hoshino 2007).

The problem of the passage of the generated radio emission through the shock can arise. However, the shock can be very inhomogeneous and can have regions with considerably lower densities (holes) transparent to radio emission. The upper limit on the density of the shock plasma transparent to radio emission can be estimated from the condition that the plasma frequency of the (completely ionized) shock matter be lower than the radio wave frequency:

$$\rho' \lesssim m_p n'_e = \frac{\pi m_p m_e \nu^2}{e^2} \approx 10^{-14}\ \text{g cm}^{-3} \ll \rho,$$

where n'_e is the electron number density corresponding to the maximum admissible plasma frequency. Previously, the appearance of X-ray emission from the remnant of SN 1987a suggested that such strong inhomogeneities could be present in the expanding shell (Grebenev and Sunyaev 1987). The radio emission can also pass through these inhomogeneities; the observed flux and duration can differ from the above estimates due to the absorption effects in the shell.

THE GENERATION OF HARD RADIATION

Let us roughly estimate the upper limits for the parameters of the hard synchrotron radiation that can accompany magnetic reconnection in the magnetospheric tail. The characteristic synchrophoton energy is

$$\epsilon_\gamma = \hbar\omega_\gamma \sim \hbar\frac{eB_\mathrm{t}}{mc}\Gamma^2 \approx 40\left(\frac{B_\mathrm{t}}{10^6\ \text{G}}\right)\left(\frac{\Gamma}{2000}\right)^2 \text{ keV};$$

this is the soft gamma-ray energy range. The upper limits on the total gamma-ray energy E_γ and flux S_γ can be obtained using Eqs. (3), (14), (16), and the expression for the synchrotron intensity from one particle $I = (2/3)(e^4 B_\mathrm{t}^2)/(m^2c^3)\Gamma^2$:

$$E_\gamma = IN^-\tau = \frac{2e^4 B_\mathrm{t}^2\Gamma^2}{3m^2c^3}\tilde{n}^-\pi r^{*2}h\tau \qquad (19)$$
$$\approx 4\times10^{30}\left(\frac{B_\mathrm{t}}{10^6\ \text{G}}\right)^2\left(\frac{\Gamma}{2000}\right)^2$$
$$\times\left(\frac{\tilde{n^-}}{3\times10^4\ \text{cm}^{-3}}\right)\left(\frac{r^*}{10^8\ \text{cm}}\right)^2$$
$$\times\left(\frac{h}{10^9\ \text{cm}}\right)\left(\frac{\tau}{3\ \text{ms}}\right)\ \text{erg},$$

$$S_\gamma = \frac{E_\gamma}{\pi(0.5\theta r)^2\tau} \approx 10^{-14}\left(\frac{B_\mathrm{t}}{10^6\ \text{G}}\right)^2 \qquad (20)$$
$$\times\left(\frac{\Gamma}{2000}\right)^4\left(\frac{\tilde{n^-}}{3\times10^4\ \text{cm}^{-3}}\right)\left(\frac{r^*}{10^8\ \text{cm}}\right)^2$$
$$\times\left(\frac{h}{10^9\ \text{cm}}\right)\left(\frac{r}{500\ \text{Mpc}}\right)^{-2}\frac{\text{erg}}{\text{s cm}^2}.$$

We see that the total energy of the hard nonthermal radiation is comparable to that of the radio emission (17) but the flux is below the sensitivity threshold of modern detectors. Therefore, no "GRB" is expected in the case under consideration, as confirmed by the absence of any gamma-ray event at the time when the radio burst was detected by Lorimer et al. (2007). Naturally, if such an event occurred in our Galaxy or in the Local Group, then both radio and gamma-ray emissions could be detected. The SN must also be seen.

DISCUSSION

We showed that a bright millisecond burst of nonthermal radio emission with parameters similar to those measured when Lorimer et al. (2007) discovered the radio burst could be generated during the impact of a SN shock on the magnetosphere of a NS in a massive binary system. The shock passage gives rise to a long magnetospheric tail in the NS (Istomin and Komberg 2002). The magnetic energy stored in the tail can be transformed into the kinetic energy of nonthermal particles during magnetic reconnection. If positrons are present in the magnetospheric tail (which is quite likely if the NS before the SN explosion was at the pulsar stage), then plasma instabilities can transform the kinetic energy of the accelerated positron beam into the energy of plasma oscillations in the denser electron counterflow. These plasma oscillations can then be nonlinearly converted into transverse electromagnetic waves just as in pulsar magnetospheres (Lyubarsky 1992), producing a short pulse of nonthermal radio emission. The magnetic fields of young NSs vary over a wide range, from 10^{11} to 10^{15} G, causing the same variations in magnetospheric sizes, pair plasma densities in the magnetosphere, etc. The situation can be complicated by the presence of a strong stellar wind from the SN progenitor. On the other hand, the SN shock density and velocity can vary significantly. Therefore, all parameters of our model ($r^*, \tilde{n}^+, \tau, \Gamma$, and $\tilde{n}^-$) can vary over a wide range, which naturally entails significant variations in the properties (frequency, flux, duration) of radio bursts that can accompany the NS magnetosphere topology restructuring during magnetic reconnection.

Magnetic reconnection can also take place in the region of the toroidal magnetic field behind the pulsar light cylinder. In this case, the current sheet is located at the NS rotation equator. The magnetic field strength at the light cylinder B_l can be significant:

$$B_l \approx B\left(\frac{R}{R_l}\right)^3 \approx 4\times 10^5 \times \left(\frac{B}{10^{13}\ \mathrm{G}}\right)\left(\frac{\Omega}{100\ \mathrm{rad\ s^{-1}}}\right)^3\ \mathrm{G}.$$

Consequently, there is a large store of magnetic energy, $\epsilon_B \sim (B_l^2/8\pi)R_l^3 \sim 10^{35}$ erg, in the region of the toroidal field (the toroidal magnetic field decreases slowly with distance as $1/r$). A stationary reconnection of the toroidal magnetic field was already invoked by Lyubarsky (1996) to explain the hard radiation from pulsars. In our case, compression of the NS magnetosphere by the SN shock can result in a nonstationary large-scale reconnection of the toroidal magnetic field behind the light cylinder. Estimates similar to those given in Section 3 indicate that a short radio burst can be generated in principle (in the approximation of a two-dimensional current sheet). The radio burst characteristics will be similar to those measured by Lorimer et al. (2007) at model parameters close to those given by Eqs. (14)–(17) (the positrons that excite plasma waves are assumed to be collected from a large volume $\sim R_l^3$). Since such parameters are consistent with the existing constraints, this approach may be considered as an alternative model for the millisecond radio burst. An advantage of this model is that there is no problem of the passage of the generated radio emission through the shock: it can emerge before the shock "engulfs" the entire magnetosphere and screens the source from the observer.

The search for new short radio transients goes on (Lorimer et al. 2007) and the suggested model can be tested as the statistics increases.

ACKNOWLEDGMENTS

We wish to thank B.V. Somov, V.V. Kocharovsky, and Yu.E. Lyubarsky for helpful discussions. This work was supported in part by the Russian Foundation for Basic Research (project no. 07-02-00961).

REFERENCES

1. P. Goldreich and W. H. Julian, Astrophys. J. **157**, 869 (1969).
2. S. A. Grebenev and R. A. Sunyaev, Pis'ma Astron. Zh. **13**, 1024 (1987) [Sov. Astron. Lett. **13**, 431 (1987)].
3. V. S. Imshennik and D. K. Nadyozhin, Sov. Sci. Sect. E **8**, 1 (1989).
4. Ya. N. Istomin and B. V. Komberg, Astron. Zh. **46**, 908 (2002) [Astron. Rep. **46**, 908 (2002)].
5. D. R. Lorimer, M. Bailes, M. A. McLaughlin, et al., Science **318**, 777 (2007).
6. Yu. E. Lyubarsky, Astron. Astrophys. Lett. **33**, 265 (1992).
7. Yu. E. Lyubarsky, Astron. Astrophys. **311**, 172 (1996).
8. Yu. E. Lyubarsky, Astrophys. J. **682**, 1443 (2008).
9. S. B. Popov and K. A. Postnov, arXiv:0710.2006 (2007).
10. K. A. Postnov and L. R. Yungelson, Living Rev. Relativ. (2006).
11. V. Usov, Nature **357**, 472 (1992).
12. V. Usov, Mon. Not. R. Astron. Soc. **267**, 1035 (1994).
13. S. Zenitani and M. Hoshino, Astrophys. J. **670**, 702 (2007).

Translated by V. Astakhov

universe

IMPACT FACTOR 2.6

CITESCORE 5.2

Article

The Upcoming GAMMA-400 Experiment

Sergey I. Suchkov, Irina V. Arkhangelskaja, Andrey I. Arkhangelskiy, Aleksey V. Bakaldin, Irina V. Chernysheva, Arkady M. Galper, Oleg D. Dalkarov, Andrey E. Egorov, Maxim D. Kheymits, Mikhail G. Korotkov et al.

Special Issue

Astrophysics of Cosmic Rays from Space

Edited by

Dr. Vera Georgievna Sinitsyna

MDPI

https://doi.org/10.3390/universe9080369

universe

MDPI

Article

The Upcoming GAMMA-400 Experiment

Sergey I. Suchkov [1,*], Irina V. Arkhangelskaja [2], Andrey I. Arkhangelskiy [2], Aleksey V. Bakaldin [3], Irina V. Chernysheva [2], Arkady M. Galper [1,2], Oleg D. Dalkarov [2], Andrey E. Egorov [1], Maxim D. Kheymits [2], Mikhail G. Korotkov [2], Aleksey A. Leonov [1,2], Svetlana A. Leonova [4], Alexandr G. Malinin [2], Vladimir V. Mikhailov [2], Pavel Yu Minaev [1,5], Nikolay Yu. Pappe [1], Mikhail V. Razumeyko [1], Nikolay P. Topchiev [1] and Yuri T. Yurkin [2]

1 Lebedev Physical Institute of the Russian Academy of Sciences, Moscow 119991, Russia
2 Moscow Engineering Physics Institute, National Research Nuclear University "MEPhI", Moscow 115409, Russia
3 Scientific Research Institute for System Analysis of the Russian Academy of Sciences, Moscow 117218, Russia
4 The Department of General Subjects, Dubna State University, Branch "Protvino", Moscow Region, Protvino 142281, Russia
5 Space Research Institute, Moscow 117997, Russia
* Correspondence: soutch@mail.ru

Abstract: The upcoming GAMMA-400 experiment will be implemented aboard the Russian astrophysical space observatory, which will be operating in a highly elliptical orbit over a period of 7 years to provide new data on gamma-ray emissions and cosmic-ray electron + positron fluxes, mainly from the galactic plane, the Galactic Center, and the Sun. The main observation mode will be a continuous point-source mode, with a duration of up to ~100 days. The GAMMA-400 gamma-ray telescope will study high-energy gamma-ray emissions of up to several TeV and cosmic-ray electrons + positrons up to 20 TeV. The GAMMA-400 telescope will have a high angular resolution, high energy and time resolutions, and a very good separation efficiency for separating gamma rays from the cosmic-ray background and the electrons + positrons from protons. A distinctive feature of the GAMMA-400 gamma-ray telescope is its wonderful angular resolution for energies of >30 GeV (0.01° for E_γ = 100 GeV), which exceeds the resolutions of space-based and ground-based gamma-ray telescopes by a factor of 5–10. GAMMA-400 studies can reveal gamma-ray emissions from dark matter particles' annihilation or decay, identify many unassociated, discrete sources, explore the extended sources' structures, and improve the cosmic-ray electron + positron spectra data for energies of >30 GeV.

Keywords: gamma-ray emission; gamma-ray telescope; gamma-ray bursts; dark matter particles; cosmic-ray electron + positron fluxes

check for updates

Citation: Suchkov, S.I.; Arkhangelskaja, I.V.; Arkhangelskiy, A.I.; Bakaldin, A.V.; Chernysheva, I.V.; Galper, A.M.; Dalkarov, O.D.; Egorov, A.E.; Kheymits, M.D.; Korotkov, M.G.; et al. The Upcoming GAMMA-400 Experiment. *Universe* **2023**, *9*, 369. https://doi.org/10.3390/universe9080369

Academic Editors: Alexandre Marcowith and Vera Georgievna Sinitsyna

Received: 7 June 2023
Revised: 14 July 2023
Accepted: 25 July 2023
Published: 14 August 2023

Copyright: © 2023 by the authors. Licensee MDPI, Basel, Switzerland. This article is an open access article distributed under the terms and conditions of the Creative Commons Attribution (CC BY) license (https://creativecommons.org/licenses/by/4.0/).

1. Introduction

A significant contribution to astrophysical research has been made with gamma-ray astronomy in recent decades. Since 2008, the Fermi-LAT gamma-ray telescope has been continually used to observe high-energy gamma-ray emissions in space. The fourth Fermi-LAT catalog [1] contains 6658 sources, including various classes of objects in the energy range of 50 MeV to 1000 GeV. In spite of great progress, many problems have not yet been solved; ~30% of gamma-ray sources in the fourth catalog are still unidentified. Fermi-LAT operates in scanning mode, and the source observation time is only ~15% of the operation time [2]. The ground-based facilities H.E.S.S., MAGIC, VERITAS, and others have observed emissions from only ~250 gamma-ray sources in the energy range of above ~100 GeV (http://tevcat.uchicago.edu/, accessed on 2 August 2023). In order to identify many unassociated gamma-ray sources, it is necessary to perform long-term, continuous observations with better angular and energy resolutions than the existing telescopes.

The high-energy gamma sky consists of Milky Way galactic sources like pulsars and SNRs and extragalactic sources, mainly galactic gamma rays, which constitute roughly half of the identified emitters at energies of more than E > 100 MeV [1]. Most of the weak γ-ray emissions of numerous galactic cosmic rays powered by stellar explosions are produced in the nuclear collisions of pions or in pulsars and pulsar wind nebulae. Fermi_LAT was able to detect Andromeda (M31) using HE (high-energy) rays. It is still not clear whether M31 is an extended source or composed of two point sources, as proposed in [3]. The possible presence of dark matter in M31 could lead to the production of an additional gamma-ray flux. Because of the specifics of the Andromeda galaxy's disk orientation (slightly inclined to the line of sight), the difference in energies could arise from photons from the two hemispheres of Andromeda's halo. It was reported in [4] that such an asymmetry could be at the level of several tens of percents. The better spatial resolution of Fermi_LAT's successor would be useful in achieving a clear understanding of the origin of M31's emission.

Active galactic nuclei (AGNs) are black holes which are powered by infalling gas. AGNs are the most powerful astrophysical sources, with known luminosities of up to 10^{41} W. Radio-loud AGNs with jets represent the majority of known extragalactic gamma-ray sources in the Fermi_LAT catalog [1]. As reported in [5], the combination of radio-band antennas, optical telescopes, X-ray telescopes, Fermi_LAT, and the current generation of ground Cherenkov telescopes, provide the opportunity to characterize the spectral energy distributions of blazars of over 15 or more decades in energy. The most remarked-upon feature of this distribution is its two-hump shape, with the second peak in the ~10 MeV region. But the Fermi_LAT tracker is sensitive enough above ~100 MeV that the lack of spectral observations in the ~1–100 MeV range has surely hampered blazar studies [5].

Searching for and studying gamma-ray bursts (GRBs) are of great interest [6–8]. High-level GRB statistics in the sub-Mev range with more than 13,000 bursts are provided at http://www.ssl.berkeley.edu/ipn3/masterli.html (accessed on 2 August 2023). In this energy range, "classical", highly variable prompt emission is seen as a superposition of short, FRED (fast rise and exponential decay)-like pulses. The sub-MeV emission is usually associated with the internal shocks of a GRB's central engine, but a detailed physical model has not been developed yet. High-energy (above 100 MeV) emissions of GRBs were detected in a couple hundred bursts in Fermi-LAT and CGRO/EGRET experiments [6]. Recently, sub-TeV emission was also been detected in a few bursts in the HESS and MAGIC experiments. Neither the nature of the high-energy component nor whether the maximum photon energy could be generated by a GRB central engine is clear. This high-energy component could be connected with an afterglow—the propagation of a relativistic jet (external shocks). This is confirmed by the temporal behavior of the high-energy component and its spectral shape for several bursts (e.g., GRB 130427A and GRB 190114C). However, in some cases, the temporal and spectral characteristics of the high-energy emission point to its connection with a sub-MeV emission. Therefore, there is at least bimodal behavior demonstrated by the high-energy emission: a separate emission mechanism vs. the extension of the low-energy emission to high energies. Observations with high signal-to-noise ratios are important in the intermediate energy range of (10, 100) MeV to investigate the connection of regular, sub-MeV emissions to high-energy emissions. GAMMA-400 shows a higher level of sensitivity in this range (in simulations) and could shed light on the problem.

The next problem is to study dark matter (DM) particles via indirect gamma-ray detection. Indirect detection consists of recording th annihilation or decay of gamma-ray products. Weakly interacting massive particles (WIMPs) with masses between several GeV and several TeV are still considered to be the most probable candidates (e.g., [9]) responsible for DM. WIMPs can annihilate or decay with gamma-ray production. They can produce both excess in a continuous energy spectrum and narrow gamma-ray lines. Axion-like particles (ALPs) are also proposed as candidate particles for DM (e.g., [10]). Searching for and studying the emission of gamma rays from DM particles with better angular and energy resolutions remain some of the central goals.

The high-precision measurement of CR electron + positron fluxes of energies up to ~4.8-TeV is an important problem in the light of data obtained from many experiments such as ATIC [11], Fermi-LAT [12], PAMELA [13], AMS-2 [14], CALET [15], DAMPE [16], MAGIC [17], VERITAS [18], and H.E.S.S. [19]. These experiments have revealed several features of the spectral shapes of their fluxes, and they sometimes do not agree. It is necessary to improve the electron + positron flux data for energies up to 20 TeV.

Therefore, new space-based experiments to study gamma-ray emissions in the energy range of up to several TeV, as well as CR electron + positron fluxes of up to several tens of TeV, with better angular and energy resolutions are required.

2. The GAMMA-400 Gamma-Ray Telescope

The GAMMA-400 (Gamma Astronomical Multifunctional Modular Apparatus) gamma-ray telescope, with an initial upper energy limit of 400 GeV, was first proposed in 1988 [20] and has been developed further since then [21–23]. Its current physical scheme is shown in Figure 1.

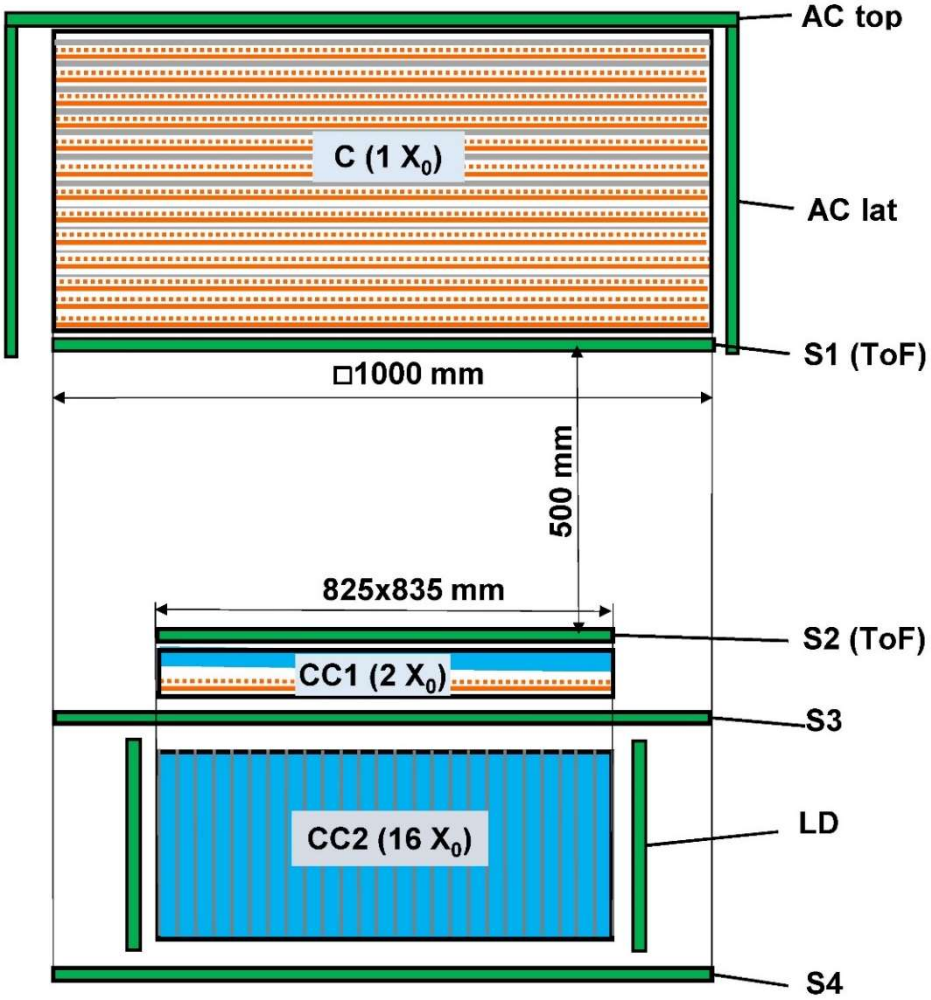


Figure 1. The GAMMA-400 gamma-ray telescope's physical scheme: an anticoincidence system, AC top, and four AC lat detectors, a converter–tracker, C, a time-of-flight system, ToF, from the S1 and S2 detectors, a two-part calorimeter, CC1 and CC2, lateral detectors, LDs, a detector, S3, and a shower leakage detector, S4.

The GAMMA-400 gamma-ray telescope consists of the following:

- A scintillation anticoincidence system, AC top, and four lateral AC detectors, AC lat. All anticoincidence detectors are made of two layers of scintillation plastic strips. The

anticoincidence system has an efficiency of ~0.9999 for detecting incoming charged particles and a time resolution of ~200 ps;

- The converter–tracker, C (~1 X_0, X_0 is the radiation interaction length), made from scintillating fibers (SciFi). The converter–tracker consists of 13 detector plane pairs made of SciFi assemblies. The top seven pairs of planes have tungsten (W) converter foils of 0.1 X_0. The next four pairs of planes contain tungsten converter foils that are 0.025 X_0 thick in each plane. The bottom two pairs of planes have no tungsten;
- Time-of-flight system, ToF, comprising the scintillation detectors S1 and S2 (the ToF signal means that the time of the S1 response must be earlier than the time of the S2 response). A distance of 500 mm between these detectors provides a sufficient flight base for the effective rejection of particles coming from the lower hemisphere with a separation coefficient of ~1000. The ToF time resolution is ~200 ps;
- A two-part electromagnetic calorimeter, comprising CC1 (2 X_0) and CC2 (~16 X_0). The pre-shower CC1 contains two blocks of CsI(Tl) scintillation crystals and the SciFi detector plane. CC2 consists of CsI(Tl) crystal columns. The total thickness of the CC1 and CC2 calorimeter is ~18 X_0 (~0.9 λ_0) and ~43 X_0 (~2.0 λ_0) for vertical and lateral particle detection, respectively (λ_0 is the hadronic interaction length);
- Four lateral scintillation detectors, LDs, located around the CC2 calorimeter for detecting particles from lateral directions;
- Scintillation detectors, S3, and shower leakage, S4. These detectors are necessary for improving hadronic and electromagnetic shower separation.

The electronic units include the system of trigger formation (ST), the scientific data acquisition system (SDAS), and other electronic units. Two-star sensors with an accuracy greater than 3″ and thermal control systems are also presented.

Incident gamma rays pass without interaction with AC and are converted into electron–positron pairs in C. The electron–positron pairs pass through the C and ToF and produce an electromagnetic shower in CC1, S3, CC2, and S4. In all the layers of the C, S1, S2, CC1, S3, CC2, S4, and LD, the energy deposits are measured.

The direction of the incidence particles is determined by reconstructing the conversion point and the electromagnetic shower axis using the SciFi coordinate detectors in the C and CC1.

High-energy (E_γ > 5 GeV) gamma rays interact with the GAMMA-400 gamma-ray telescope's detector matter and create a backscattering of secondary particles (mainly 1-MeV photons). These secondary particles can interact in the AC and produce a veto signal, excluding the primary gamma rays. To exclude this effect, all scintillation detectors are constructed as two-layer segmented strips, additional trigger logic for detecting high-energy particles is organized, and time analyses of signals in the AC, S1 (ToF), S2 (ToF), and S3 detectors are conducted.

The GAMMA-400 gamma-ray telescope's energy range is from ~20 MeV to several TeV and from ~1 GeV to several tens of TeV for gamma rays and CR electrons + positrons, respectively. The maximum field of view (FoV) for incident particles from the top-down direction is ±45°. The energy of low-energy gamma rays in the C, S1 and S2 is measured after the conversion of gamma rays in the last six planes (Figure 1, four planes with 0.025 X_0-tungsten and two without tungsten).

In contrast to previous calculations [23], in this study, a trigger based on the scintillation detector response times was used due to the very good time resolutions of the detectors. The basic characteristics were re-calculated, but they remained practically the same, confirming the correctness of the new method.

The main trigger of the GAMMA-400 telescope (with no signal in the AC and with the presence of a ToF signal) is as follows:

$$\overline{AC_{SP1}} \times ToF, \quad (1)$$

where

$$\overline{\mathrm{AC}_{\mathrm{SP1}}} = \overline{\mathrm{AC}(\mathrm{thesamepositionstrip})}\Big|[\mathrm{timeAC} > \mathrm{timeS1}]; \quad (2)$$

$$\begin{aligned}&\mathrm{AC}(\text{the same position strip})\\&= \mathrm{AC}_{\mathrm{TOP}}(\text{the same position strip})|\mathrm{AC}_{\mathrm{LAT}}(\text{the same position strip})\end{aligned} \quad (3)$$

means that in both layers of any AC detector, the strips located one above the other have a signal [timeAC > timeS1], meaning that the AC response time is later than the S1 response time, ToF = S1 × S2 × [timeS1 < timeS2].

The $\mathrm{AC}_{\mathrm{SP1}}$ logic construction takes into account the possible influence of backscattering particles (which are mainly generated in calorimeter CC2). These backscattering particles have an energy distribution peak of ~1 MeV. Analyzing each layer of the AC detectors separately and taking into account that the electronic threshold in each 1 cm thick plastic scintillator strip is ~0.5 MeV, it is possible to retain useful events against backscattering particles. For this purpose, the relative location of the impacted scintillation plastic strip in the neighboring layers of each AC detector is checked. Then, only the events involving a scintillation plastic strip hit in each layer in the same position (one directly against another) are marked by veto. Other events accompanied by backscattering particles in the AC detectors not having hit the scintillation plastic strip in each layer in the same position are retained for subsequent analysis.

2.1. Gamma-Ray Detection

Gamma-400 simulations were performed using GEANT4. An example of a 100 GeV gamma-ray energy release simulation in the gamma-ray telescope's detectors is shown in Figure 2. The gamma-ray telescope's detectors are shown in color if the response exists. In this figure, the GAMMA-400 telescope's two projection responses are shown on the left and on the right of Figure 2. In the center, the CC2 view from above is demonstrated together with the AC lat detector. It is shown that a vertical gamma-ray quantum is converted into an electron–positron pair in the upper converter layer, the track goes through the whole converter, the hits are presented in S1, S2, S3, and S4, and the shower in CC1 and the shower in CC2 begin.

Some calculations were performed in which it was necessary to analyze the time consequence of the signals produced in S1(ToF) and S2(ToF), taking into account the time resolution obtained from the test beam calibration and the ability to reconstruct the particle's track and restore the particle's energy. As a result, some dependences are presented as follows:

(1) The on-axis effective area, depending on the energy (Figure 3) using triggers, is as follows:

$$\overline{\mathrm{AC}} \times \mathrm{ToF}\ (\mathrm{black}), \quad (4)$$

$$\overline{\mathrm{AC}_{\mathrm{SP}}} = \overline{\mathrm{AC}(\text{the same position strip})}\ (\mathrm{red}), \quad (5)$$

$$\overline{\mathrm{AC}_{\mathrm{SP1}}} = \overline{\mathrm{AC}(\text{the same position strip})}\Big|[\mathrm{timeAC}_{\mathrm{SP1}} > \mathrm{timeS1}]\ (\mathrm{green}), \quad (6)$$

$$\overline{\mathrm{AC}_{\mathrm{SP2}}} = \overline{\mathrm{AC}(\text{the same position strip})}\Big|[\mathrm{timeAC}_{\mathrm{SP1}} > \mathrm{timeS2}]\ (\mathrm{blue}). \quad (7)$$

As can be seen from Figure 3, when using only the trigger $(\overline{\mathrm{AC}} \times \mathrm{ToF})$, the effective area begins to decrease at an energy of more than 10 GeV due to backscattering particles. Using the triggers with $\overline{\mathrm{AC}_{\mathrm{SP1}}}$ or $\overline{\mathrm{AC}_{\mathrm{SP2}}}$ provides an effective area of ~4000 cm^2 and up to several TeV. If an additional analysis is used, providing the possibility to reconstruct the particle's track and to restore its energy, the effective area estimation ($\mathrm{S}_{\mathrm{eff}}$) provides ~3200 cm^2.

(2) The GAMMA-400 telescope's angular resolution, depending on energy, in comparison with Fermi-LAT and CTA (https://www.cta-observatory.org/science/ctao-performance/#1472563157648-91558872-faf1, accessed on 2 August 2023) (Figure 4). The angular resolution for E_γ = 100 GeV is ~0.01°. The improvement in angular resolution was achieved via analog readout in the coordinate detectors, in addition to the long arm between the coordinate detectors in the C and CC1.

(3) The on-axis energy resolution, depending on the energy, in comparison with Fermi-LAT and CTA (https://www.cta-observatory.org/science/ctao-performance/#1472563318157-d0191bc5-0280, accessed on 2 August 2023) (Figure 5). The energy resolution for E_γ = 100 GeV is ~2%.

The CC2 prototype was manufactured and calibrated on a positron beam using an S-25R electron synchrotron (Lebedev Physical Institute, Troitsk), and an energy resolution of ~10% at an energy of 300 MeV was obtained [22].

The separation of gamma rays from the background of charged particles and gamma rays emerging from the GAMMA-400 aperture plays an important role. The AC and ToF prototypes were manufactured and calibrated on a positron beam on an S-25R electron synchrotron in the energy range of 100-300 MeV. A high efficiency of charged particle detection equal to ~0.9999 for the AC system and a high coefficient of event separation coming from the top-down and down-top directions of ~1000 for the ToF system were obtained. Taking into account the separation of the electromagnetic and hadronic showers in CC1, CC2, and S4 and the additional analysis of the hit strips of the AC detectors located along the trajectory of the initial particle, a rejection of ~10^5 was obtained.

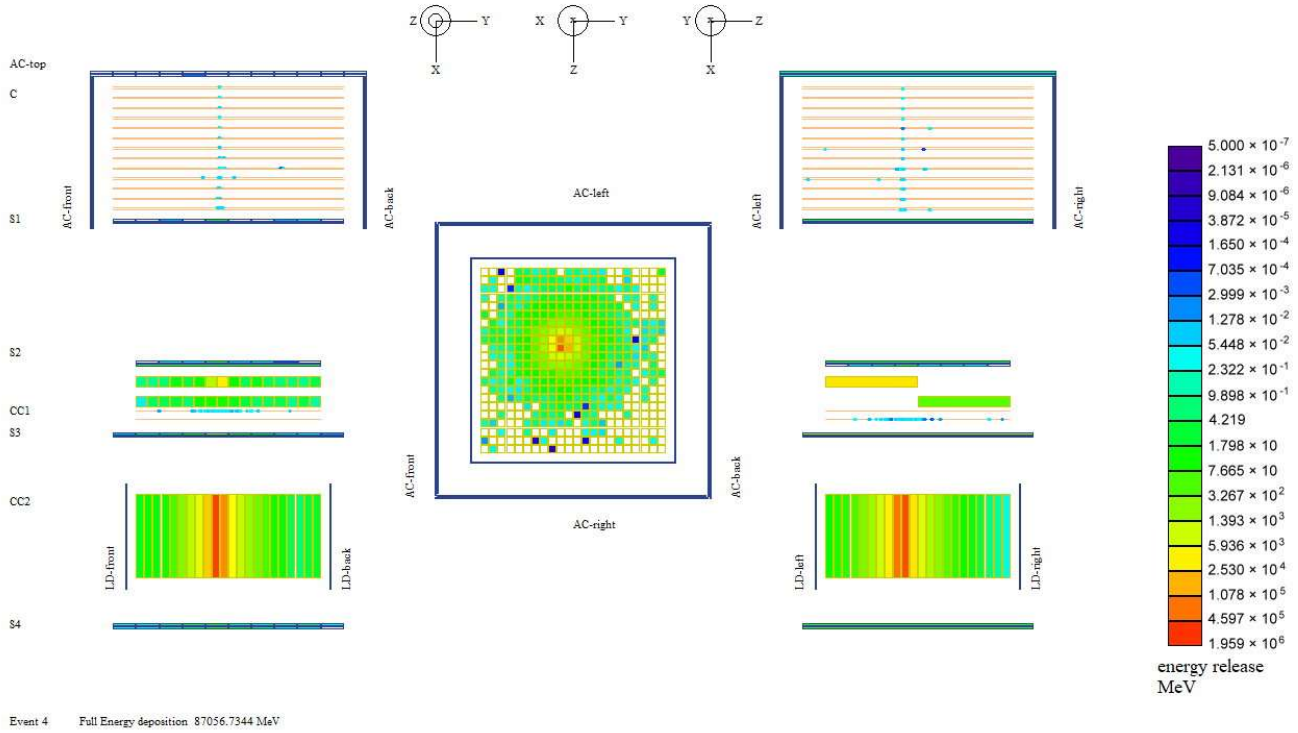


Figure 2. An example of an energy release simulation in the gamma-ray telescope's detectors. (the color scale of the energy release in MeV is shown in the right column).

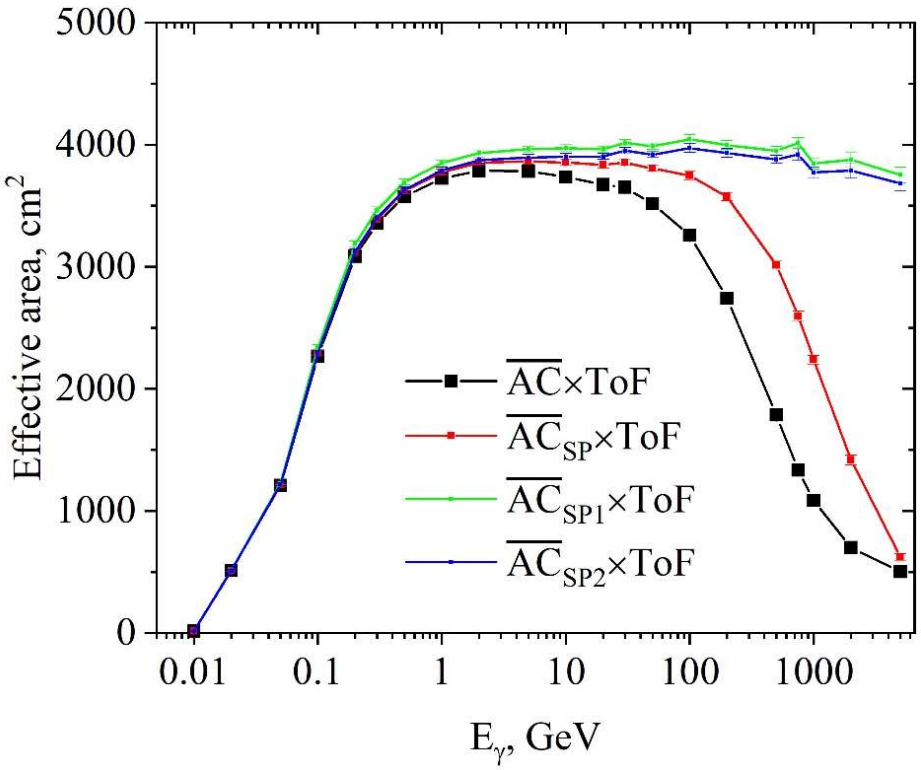


Figure 3. Dependence of the GAMMA-400 telescope's on-axis effective area on energy, using the triggers $\overline{AC} \times$ ToF (black), $\overline{AC_{SP}} \times$ ToF (red), $\overline{AC_{SP1}} \times$ ToF (green), and $\overline{AC_{SP2}} \times$ ToF (blue).

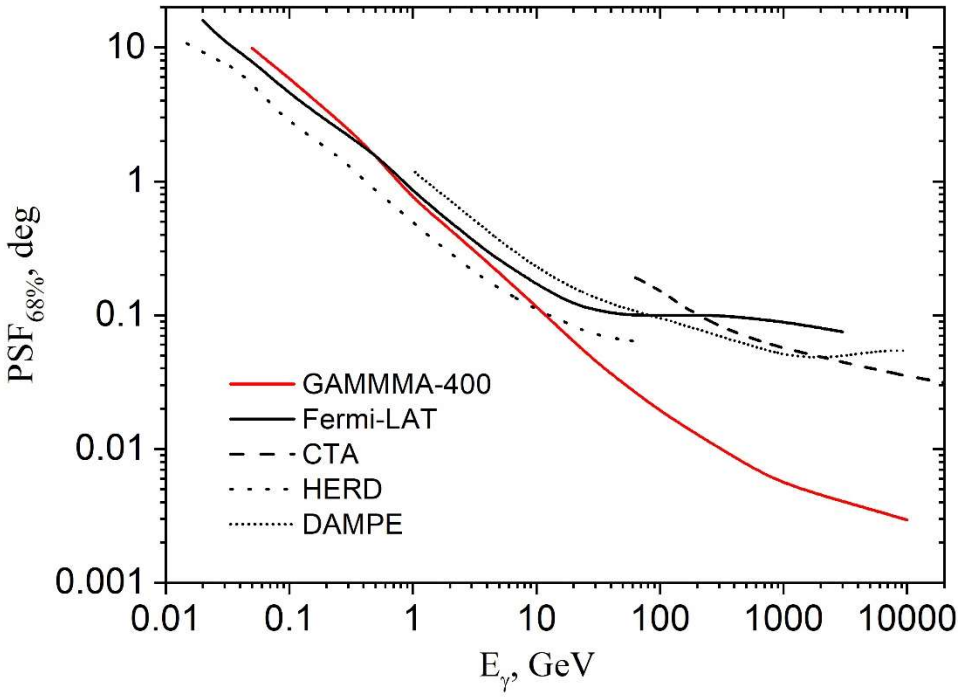


Figure 4. Dependence of the GAMMA-400 telescope's angular resolution on energy, in comparison with Fermi-LAT, CTA, HERD, and DAMPE.

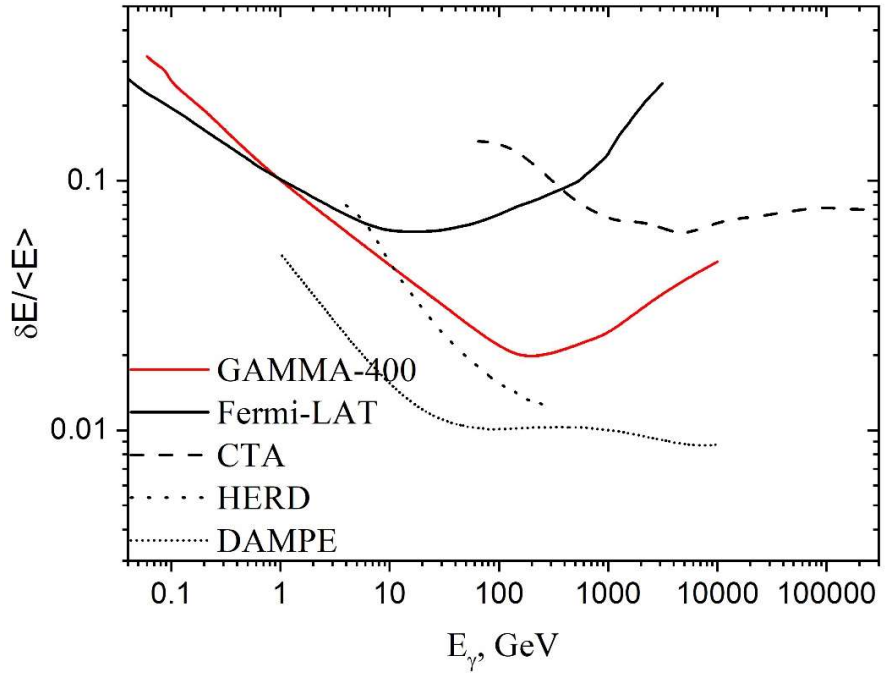


Figure 5. Dependence of the GAMMA-400 telescope's on-axis energy resolution on energy, in comparison with Fermi-LAT, CTA, HERD, and DAMPE.

2.2. Gamma-Ray Bursts

The GAMMA-400 telescope can also record GRBs from the top-down and lateral directions. When recording GRBs using the lateral aperture, the GAMMA-400 telescope's total effective field of view is ~6 sr. The GAMMA-400 telescope will allow us to detect ~15 GRBs per year.

2.3. Electron + Positron Detection

The GAMMA-400 telescope will also measure CR electron + positron fluxes from the top-down and lateral directions around the calorimeter. For these directions, the energy resolutions are ~2% and <1%, respectively. Figure 6 shows an example of a simulation of the energy release in the GAMMA-400 detectors for a 1-TeV electron coming from the left lateral direction. It is shown that for an electron from the left lateral direction, a significant amount of of backsplash hits the AC, converter, S1, S2, S3, and S4, and produces a deep shower in CC2; only the track continues in CC2.

Table 1 shows a performance comparison for the GAMMA-400 (top-down and lateral aperture) and Fermi-LAT [24] telescopes. It can be seen that due to the large area of the calorimeter (0.7 m^2 for the top-down and 1.0 m^2 for the lateral aperture) and the thickness of the calorimeter (18 X_0 for the top-down and 43 X_0 for the lateral aperture), the GAMMA-400 telescope can improve the electron + positron data statistics.

Table 1. Comparison of performance when detecting electrons + positrons for the GAMMA-400 (top-down and lateral aperture) and Fermi-LAT telescopes.

	GAMMA-400		**Fermi-LAT**
Aperture	**Top–Down**	**Four Lateral Sides**	**Top–Down**
Acceptance, m^2 sr	~0.3 (E_e = 100 GeV)	~0.5 (E_e = 100 GeV)	2.5
Proton rejection factor	~10^4	~10^4	~10^4
Calorimeter area, m^2	0.7	4 × 0.24	0.85
Calorimeter thickness, X_0	18	43	8.6

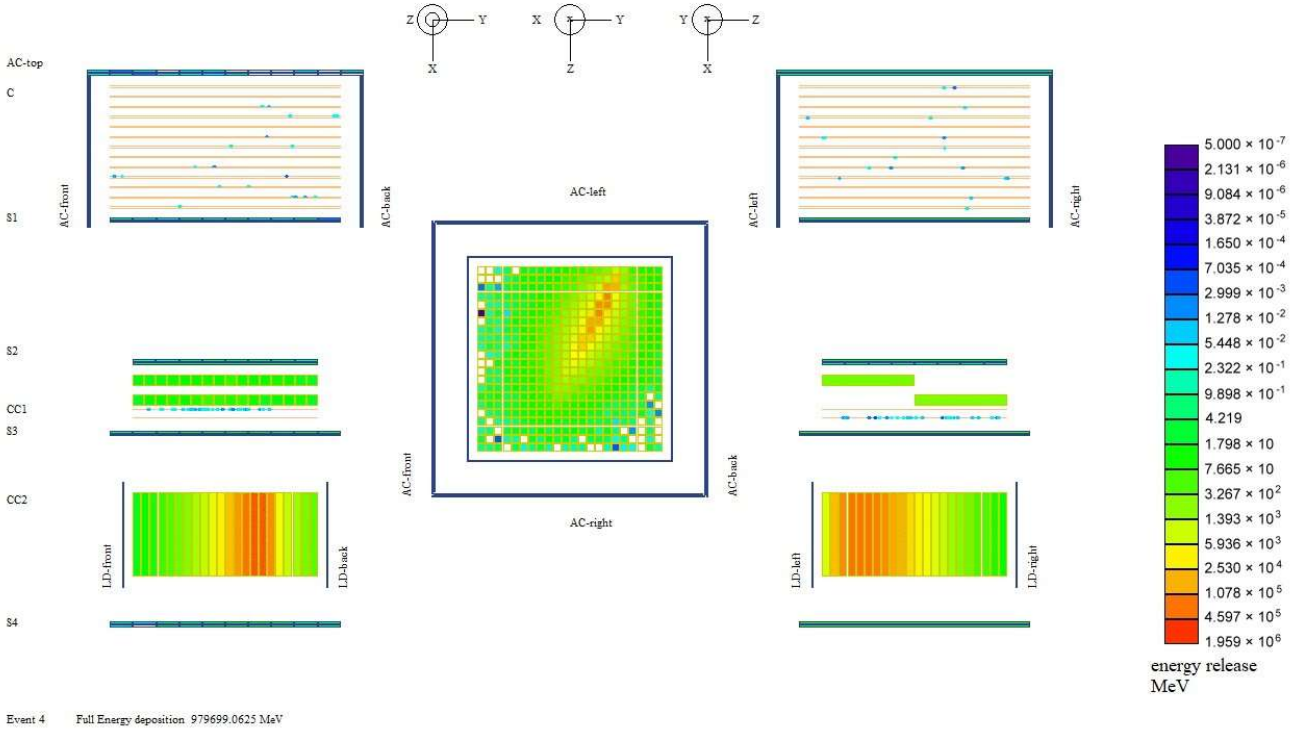


Figure 6. The example of an energy release simulation in the GAMMA-400 detectors (the color scale of the energy release is shown in MeV in the right column).

2.4. The Preliminary GAMMA-400 Scientific Program

The GAMMA-400 gamma-ray telescope has the following several advantages in comparison with current and future space-based and ground-based instruments:

(1) The GAMMA-400 gamma-ray telescope will continuously operate in a high orbit with a radius of ~200,000 km (after 6 months from its launch) in point-source mode with 100% efficiency over a long period of time (~100 days), with an aperture of ±45° in contrast to the scanning mode of other instruments;

(2) The GAMMA-400 gamma-ray telescope has a high angular resolution of ~0.01° (E_γ = 100 GeV) due to the high coordinate resolution in the SciFi coordinate detectors in the C and CC1 and the long arm between the coordinate detectors in the C and CC1;

(3) The GAMMA-400 gamma-ray telescope has a high energy resolution of ~2% (E_γ = 100 GeV) and the ability to detect incident particles from the top-down and lateral directions;

(4) The GAMMA-400 gamma-ray telescope is very good at separating gamma rays from the background of cosmic rays and backscattering events, as well as for the electrons + positrons from protons.

2.5. The GAMMA-400 Experiment Addresses Important Scientific Problems Remaining Relevant to Date

(1) The high-energy resolution provides the possibility of searching for features in the energy spectra of high-energy gamma-ray emissions up to energies of 1000 GeV, which can be associated with the annihilation or decay of dark matter particles (the most popular DM candidates are WIMPs and ALPs);

(2) The high angular resolution provides the possibility of studying discrete gamma-ray sources and identifying them (according to the fourth Fermi-LAT catalog, gamma-ray emissions from ~6500 sources were recorded, and ~30% of them were not identified);

(3) The high angular resolution also provides the possibility of studying the extended discrete sources' spatial structures in detail;
(4) The high angular resolution makes it possible to significantly reduce the influence of the background within the potential detection of gamma rays from pair halos around AGNs;
(5) The highly accurate event timing of several μs (due to the AC and ToF time resolutions of ~200 ps and the instrument timing interface accuracy of several μs) provides the possibility to study the source variability, including recording gamma-ray emissions from millisecond pulsars, and to explain the excess of gamma-ray emissions from the Galactic center;
(6) Searching for and studying GRBs will be carried out when a gamma-ray emission is detected from both top-down along the axis of the gamma-ray telescope and from four lateral directions;
(7) Simultaneous observations of discrete gamma-ray sources will be carried out jointly with X-ray telescopes, ground-based facilities, and optical, radio, and neutrino telescopes. Even if the GAMMA-400 telescope is anticipated to have a slightly lower degree of sensitivity to point sources in comparison with the Fermi-LAT telescope, it will be able to detect nearby extragalactic sources, including AGNs, in a wider energy range, beginning from about 20 MeV. Moreover, simultaneous observations with ART-XC could be more valuable given that both detectors will be co-directional;
(8) CR electron + positron fluxes will be recorded from top-down directions along the axis of the gamma-ray telescope at energies of up to several TeV (with a calorimeter thickness of 18 X_0) and from four lateral directions at energies of up to ~20 TeV (with a calorimeter thickness of 43 X_0) and will obtain significantly better measurement statistics.

The observations made using the Fermi-LAT gamma ray telescope have revealed many new types of flare sources: the so-called transients. Among them are quasi-periodic sources and sources that flare up only once. The study of their nature is declared one of the main goals of MeV-range telescopes and ground-based TeV-range gamma-ray telescopes. The absence of an instrument operating in the range of ~0.1–1000 GeV significantly impairs their capabilities.

The GAMMA-400 experiment will help solve the main problems that currently exist when measuring the spectrum of cosmic-ray electrons and positrons at high energies (100 GeV and above). The main advantages of the GAMMA-400 experiment are associated, firstly, with the good basic parameters of the instrument—its energy resolution and geometric factors—and secondly with the high reliability of the methodological measurement results. In fact, this is related to the implementation of two independent methods of electron recording (recording from the top-down direction, along the telescope axis, and recording from lateral directions) in one telescope.

3. Astrophysical Observatory

The new GAMMA-400 astrophysical observatory is being developed in Russia. It will consist of the Navigator spacecraft platform (being developed by the Lavochkin Association, https://www.laspace.ru/ru/activities/projects/gamma-400/, accessed on 2 August 2023), the GAMMA-400 gamma-ray telescope (being developed mainly by the Lebedev Physical Institute (https://gamma400.lebedev.ru/indexeng.html, accessed on 2 August 2023), and the National Research Nuclear University "MEPhI") and additional instruments (the ART-XC X-ray telescope with an energy range of 5–30 keV and magnetic plasma detectors that are being developed by the Space Research Institute of the Russian Academy of Sciences).

The Navigator spacecraft platform will have a possibility of pointing to any astrophysical source with an accuracy of 30″. The scientific payload will have the following characteristics: a mass of ~3000 kg, a power consumption of 2000 W, and a telemetry downlink of 100 GB/day.

The GAMMA-400 astrophysical observatory will be initially launched into a highly elliptical orbit with the following preliminary parameters: an apogee of 300,000 km, a perigee of 500 km, an inclination of 51.4°, a 7-day orbital period, and a lifetime of more than 7 years. After ~6 months, the orbit will be transformed into an approximately circular orbit with a radius of ~200,000 km due to the influence of the gravitational disturbances of the Sun, Moon, and Earth. Therefore, the observatory will not suffer from the Earth's occultation and will be outside the radiation belts. This is a great advantage in comparison with low-Earth orbit. The GAMMA-400 gamma-ray telescope will run continuously in a point-source operating mode for a long time, ~100 days, in contrast to the scanning modes for the current Fermi-LAT and future HERD [25] and AMS-100 [26] experiments. The launch of the GAMMA-400 space observatory is scheduled for ~2030.

4. Conclusions

The upcoming GAMMA-400 experiment will be implemented aboard the Russian astrophysical space observatory, which will be operating in a highly elliptical orbit for a period of 7 years to provide new data on gamma-ray emissions and cosmic-ray electron + positron fluxes that mainly originate from the galactic plane, the Galactic Center, and the Sun. A continuous point-source mode with an experimental duration of up to ~100 days will be the main operating mode. The GAMMA-400 gamma ray telescope will study high-energy emissions of gamma rays of up to several TeV and cosmic-ray electrons + positrons of up to ~20 TeV. The GAMMA-400 gamma-ray telescope will have a never—before-seen angular resolution, high energy and time resolutions, and a very good separation efficiency for separating gamma rays from the cosmic-ray background and the electrons + positrons from protons. A distinctive feature of the GAMMA-400 gamma-ray telescope is its wonderful angular resolution for energies of >30 GeV (0.01° for E_γ = 100 GeV), which exceeds the resolutions of current space-based and ground-based gamma ray telescopes by a factor of 5–10. The GAMMA-400 studies can reveal gamma-ray emissions from the annihilation or decay of dark matter particles, identify many unassociated discrete sources, explore the extended sources' structures, and improve the data on cosmic-ray electron + positron spectra for energies of >30 GeV. The Gamma-400 space observatory launch is scheduled for ~2030.

Author Contributions: Investigation, S.I.S., I.V.A., A.I.A., A.G.M., M.V.R. and N.Y.P.; formal analysis, A.V.B., V.V.M. and Y.T.Y.; software, I.V.C. and M.D.K.; conceptualization, A.M.G.; project administration, O.D.D.; methodology, A.E.E. and P.Y.M.; data curation, M.G.K. and A.A.L.; writing—review and editing, S.A.L.; supervision writing—original draft, N.P.T. All authors have read and agreed to the published version of the manuscript.

Funding: This study was supported by the Russian State Space Corporation ROSCOSMOS, in part by the Ministry of Science and Higher Education of the Russian Federation under the Project "Fundamental and applied research of cosmic rays" (contract no. FSWU–2023-0068).

Data Availability Statement: http://gamma400.lebedev.ru/index.html accessed on 2 August 2023.

Conflicts of Interest: The authors declare no conflict of interest.

References

1. Abdollahi, S.; Acero, F.; Baldini, L.; Ballet, J.; Bastieri, D.; Bellazzini, R.; Berenji, B.; Berretta, A.; Bissaldi, E.; Blandford, R.D.; et al. Incremental Fermi large area telescope fourth source catalog. *Astrophys. J. Suppl. Ser.* **2022**, *260*, 53. [CrossRef]
2. Abdollahi, S.; Acero, F.; Ackermann, M.; Ajello, M.; Atwood, W.B.; Axelsson, M.; Baldini, L.; Ballet, J.; Barbiellini, G.; Bastieri, D.; et al. Fermi large area telescope fourth source catalog. *Astrophys. J. Suppl. Ser.* **2020**, *247*, 33. [CrossRef]
3. Xing, Y.; Wang, Z.; Zheng, D.; Li, J. On the Gamma-Ray Emission of the Andromeda Galaxy M31. *Astrophys. J. Lett.* **2023**, *945*, L22. [CrossRef]
4. Belotsky, K.; Shlepkina, E.; Soloviev, M. Theoretical indication of a possible asymmetry in gamma-radiation between Andromeda halo hemispheres due to Compton scattering on electrons from their hypothetical sources in the halo. *arXiv* **2020**, arXiv:2011.04689.
5. Dermer, C.; Giebels, B. Active galactic nuclei at gamma-ray energiesNoyaux actifs de galaxie dans le domaine des rayons gamma. *C. R. Phys.* **2016**, *17*, 594–616. [CrossRef]

6. Ajello, M.; Arimoto, M.; Axelsson, M.; Baldini, L.; Barbiellini, G.; Bastieri, D.; Bellazzini, R.; Bhat, P.N.; Bissaldi, E.; Blandford, R.D.; et al. A decade of gamma-ray bursts observed by Fermi-LAT: The second GRB catalog. *Astrophys. J.* **2019**, *878*, 52. [CrossRef]
7. Von Kienlin, A.; Meegan, C.A.; Paciesas, W.S.; Bhat, P.N.; Bissaldi, E.; Briggs, M.S.; Burns, E.; Cleveland, W.H.; Gibby, M.H.; Giles, M.M.; et al. The Fourth Fermi-GBM Gamma-Ray Burst Catalog: A Decade of Data. *Astrophys. J.* **2020**, *893*, 46. [CrossRef]
8. Lien, A.; Sakamoto, T.; Barthelmy, S.D.; Baumgartner, W.; Chen, K.; Collins, N.R.; Cummings, J.; Gehrels, N.; Krimm, H.A.; Markwardt, C.B.; et al. The Third SWIFT Burst Alert Telescope Gamma-Ray Burst Catalog. *Astrophys. J.* **2016**, *829*, 7. [CrossRef]
9. Leane, R.K.; Slatyer, T.R.; Beacom, J.F.; Ng, K.C. GeV-scale thermal WIMPs: Not even slightly ruled out. *Phys. Rev. D* **2018**, *98*, 023016. [CrossRef]
10. Calore, F.; Carenza, P.; Giannotti, M.; Jaeckel, J.; Mirizzi, A. Bounds on axionlike particles from the diffuse supernova flux. *Phys. Rev. D* **2020**, *102*, 123005. [CrossRef]
11. Chang, J.; Adams, J.H.; Ahn, H.S.; Bashindzhagyan, G.L.; Christl, M.; Ganel, O.; Guzik, T.G.; Isbert, J.; Kim, K.C.; Kuznetsov, E.N.; et al. An excess of cosmic ray electrons at energies of 300–800 GeV. *Nature* **2008**, *456*, 362–365. [CrossRef]
12. Abdollahi, S.; Ackermann, M.; Ajello, M.; Atwood, W.B.; Baldini, L.; Barbiellini, G.; Bastieri, D.; Bellazzini, R.; Bloom, E.D.; Bonino, R.; et al. Cosmic-ray electron-positron spectrum from 7 GeV to 2 TeV with the Fermi Large Area Telescope. *Phys. Rev. D* **2017**, *95*, 082007. [CrossRef]
13. Adriani, O. et al. [Pamela Collaboration]); Adriani, O.; Barbarino, G.C.; Bazilevskaya, G.A.; Bellotti, R.; Boezio, M.; Bogomolov, E.V.; Bongi, M.; Bonvicini, V.; Bottai, S.; et al. Ten years of PAMELA in space. *Nuevo C* **2017**, *10*, 473–522.
14. Aguilar, M.; Aisa, D.; Alpat, B.; Alvino, A.; Ambrosi, G.; Andeen, K.; Arruda, L.; Attig, N.; Azzarello, P.; Bachlechner, A.; et al. Precision Measurement of the (e^+ + e^-) Flux in Primary Cosmic Rays from 0.5 GeV to 1 TeV with the Alpha Magnetic Spectrometer on the International Space Station. *Phys. Rev. Lett.* **2014**, *113*, 221102. [CrossRef]
15. Adriani, O.; Akaike, Y.; Asano, K.; Asaoka, Y.; Bagliesi, M.G.; Berti, E.; Bigongiari, G.; Binns, W.R.; Bonechi, S.; Bongi, M.; et al. Extended measurement of the cosmic-ray electron and positron spectrum from 11 GeV to 4.8 TeV with the calorimetric electron telescope on the International Space Station. *Phys. Rev. Lett.* **2018**, *120*, 261102. [CrossRef] [PubMed]
16. Ambrosi, G. et al. [DAMPE Collaboration] Direct detection of a break in the teraelectronvolt cosmic-ray spectrum of electrons and positrons. *Nature* **2017**, *552*, 63–66. [CrossRef]
17. Tridon, D.B.; Colin, P.; Cossio, L.; Doro, M.; Scalzotto, V. Measurement of the cosmic electron plus positron spectrum with the MAGIC telescopes. *arXiv* **2011**, arXiv:1110.4008.
18. Staszak, D. et al. [for the VERITAS Collaboration] A Cosmic-ray Electron Spectrum with VERITAS. *arXiv* **2015**, arXiv:1508.06597.
19. Aharonian, F.; Akhperjanian, A.G.; Anton, G.; de Almeida, U.B.; Bazer-Bachi, A.R.; Becherini, Y.; Behera, B.; Bernlöhr, K.; Bochow, A.; Boisson, C.; et al. Probing the ATIC peak in the cosmic-ray electron spectrum with H.E.S.S. *Astron. Astrophys.* **2009**, *508*, 561–564. [CrossRef]
20. Dogiel, V.; Fradkin, M.; Kurnosova, L.; Razorenov, L.; Rusakovich, M.; Topchiev, N. Some tasks of observational gamma-ray astronomy in the energy range 5-400 GeV. *Space Sci. Rev.* **1988**, *49*, 215–226. [CrossRef]
21. Ginzburg, V.L.; Kaplin, V.A.; Karakash, A.I.; Kurnosova, L.V.; Labenskii, A.G.; Runtso, M.F.; Soldatov, A.P.; Topchiev, N.P.; Fradkin, M.I.; Chernichenko, S.K.; et al. Development of the GAMMA-400 gamma-ray telescope to record cosmic gamma rays with energies up to 1 TeV. *Cos. Res.* **2007**, *45*, 449–451. [CrossRef]
22. Suchkov, S.I.; Arkhangelskiy, A.I.; Baskov, V.A.; Galper, A.M.; Dalkarov, O.D.; L'vov, A.I.; Pappe, N.Y.; Polyansky, V.V.; Topchiev, N.P.; Chernysheva, I.V. Calibrating the prototype calorimeter for the GAMMA-400 gamma-ray telescope on the positron beam at the Pakhra accelerator. *Instrum. Exp. Tech.* **2021**, *64*, 669–675. [CrossRef]
23. Topchiev, N.; Galper, A.; Arkhangelskaja, I.; Arkhangelskiy, A.; Bakaldin, A.; Cherniy, R.; Chernysheva, I.; Gudkova, E.; Gusakov, Y.; Dalkarov, O.; et al. Gamma- and Cosmic-Ray Observations with the GAMMA-400 Gamma-Ray Telescope. *Adv. Space Res.* **2022**, *70*, 2773–2793. [CrossRef]
24. Atwood, W.B.; Abdo, A.A.; Ackermann, M.; Althouse, W.; Anderson, B.; Axelsson, M.; Baldini, L.; Ballet, J.; Band, D.L.; Barbiellini, G.; et al. The large area telescope on the Fermi gamma-ray telescope mission. *Astrophys. J.* **2009**, *697*, 1071–1102. [CrossRef]
25. Cattaneo, P.W. et al. [on behalf of the HERD Collaboration] The space station based detector HERD: Precise high energy cosmic rays physics and multimessenger astronomy. *Nucl. Part. Phys. Proc.* **2019**, *306–308*, 85–91.
26. Schael, S.; Atanasyan, A.; Berdugo, J.; Bretz, T.; Czupalla, M.; Dachwald, B.; von Doetinchem, P.; Duranti, M.; Gast, H.; Karpinski, W.; et al. AMS-100: The next generation magnetic spectrometer in space—An international science platform for physics and astrophysics at Lagrange point 2. *Nucl. Instrum. Methods Phys. Res. Sect. A* **2019**, *944*, 162561.

Disclaimer/Publisher's Note: The statements, opinions and data contained in all publications are solely those of the individual author(s) and contributor(s) and not of MDPI and/or the editor(s). MDPI and/or the editor(s) disclaim responsibility for any injury to people or property resulting from any ideas, methods, instructions or products referred to in the content.

Nucl. Phys. B 1013 (2025) 116846

Contents lists available at ScienceDirect

Nuclear Physics, Section B

journal homepage: www.elsevier.com/locate/nuclphysb

Particle Cosmology

Independent check of sporadic beta decay anomalies reported earlier by Parkhomov

Andrei E. Egorov [a,*], Aleksey A. Alekseev [b,c,d]

[a] Nuclear Physics and Astrophysics Division, Lebedev Physical Institute, Leninskii prospect – 53, Moscow, 119333, Russia
[b] Physics Department, Lomonosov Moscow State University, Leninskiye Gory – 1, Moscow, 119991, Russia
[c] Kulakov National Medical Research Center For Obstetrics, Gynecology And Perinatology, Oparina street – 4, Moscow, 117997, Russia
[d] Russian Research Institute of Health, Dobrolyubova street – 11, Moscow, 127254, Russia

ARTICLE INFO

Editor: Yasaman Farzan

Keywords:
Beta decay
Exponential law
Neutrino
Dark matter

ABSTRACT

A. Parkhomov reported in the past the detection of strong, short, sporadic, nearly everyday decay rate increases in β-isotopes placed at the focus of a concave mirror directed at a clear sky. He interpreted this effect as neutrino-induced decay. These neutrinos were assumed to be slow and arrive from space in the form of gravitationally collimated beams. We precisely replicated this experiment for the purpose of independent verification. We recorded about 50 days of data employing Geiger-counter-based signal and control detectors, ^{40}K and ^{90}Sr/^{90}Y isotopes as β-sources. We did not detect any significant difference between the data from signal and control detectors, both datasets obeyed the standard Poissonian process. Thus, we robustly excluded the hypothesized new effect. We suspect that A. Parkhomov was just misled by a trivial electromagnetic instability of his setup.

1. Introduction and motivation

Dr. Alexander Parkhomov (AP) reported in the past the discovery of a new physical effect: β-decaying isotopes, which are placed at the focal point of a concave parabolic mirror pointed at the clear sky, manifest frequent and strong increases in their decay rates. This anomaly was described in [1–6]. When we refer to AP through our paper, we mean these publications, where AP presented in detail both his empirical findings and original theoretical explanation of the observed effect. However, no one has yet reported any attempts to replicate independently the anomalies claimed by AP. And the authors of this work conducted such replication, the results of which are reported here.

In this section we *briefly* expound the whole AP's concept (to the best of our understanding) *without* any substantial critical assessment. For more details we refer readers to the publications cited above. Then in section 2 we describe our precise replication of the original AP's experiment. Section 3 reports the results. Section 4 discusses the experiment in a broad context. And the last section 5 summarizes our work.

A while ago, AP suspected that some yet-unknown cosmic agent manifests itself by influencing the decay rate of β-radioactive substances. AP conducted a series of experiments, which led him to the following conclusions about the hypothesized agent: this should be a neutrino-resembling elementary particle (let us denote it by ν_x), which comes from space (sometimes in the form of collimated flows), interacts with matter through (at least) the weak force and possesses wave properties. The former property obviously follows

* Corresponding author.
E-mail addresses: aegorov@runbox.com (A.E. Egorov), regulred25@gmail.com (A.A. Alekseev).

https://doi.org/10.1016/j.nuclphysb.2025.116846
Received 28 October 2024; Received in revised form 13 February 2025; Accepted 14 February 2025

Available online 17 February 2025
0550-3213/© 2025 The Author(s). Published by Elsevier B.V. Funded by SCOAP³. This is an open access article under the CC BY license (http://creativecommons.org/licenses/by/4.0/).

from the fact of influence on β-radioactivity, and the latter one was deduced from observation of the phenomenon of ν_x diffraction on periodic structures. This observation motivated AP to make the next step in his experimentation – he created a series of telescopes designed for ν_x detection. These telescopes utilized the assumed wave behavior of ν_x: they contain a concave reflecting mirror, which is supposed to focus the plane-parallel ν_x wavefront analogously to how optical astronomical telescopes focus photons, and the detector in the form of β-decaying source paired with Geiger counter (GC). The reflection of ν_x from the mirror surface is assumed to happen through elastic scattering process. The detection of ν_x is assumed to happen through the capture process by β-decaying nuclei with subsequent emission of $e^{\pm}$, which are detected in turn by GC:

$$\nu_x | \bar{\nu_x} + N(A, Z) \rightarrow N(A, Z \mp 1) + e^{\pm}. \tag{1}$$

Such inverse β-decay reaction does not have any ν_x energy threshold in the case of spontaneously decaying $N(A, Z)$. Produced $e^{\pm}$ have the fixed distinct kinetic energy: it is easy to show that their kinetic energy exceeds the β-decay spectrum endpoint by $2m_{\nu_x}c^2$ (e.g., [7]). Thus, according to AP, β-decaying isotopes, which were placed at the mirror focus point, manifested frequent and strong activity increases, which were distributed quasi-randomly in time and mirror direction on the sky. AP reported positive results with ^{40}K, ^{60}Co, ^{90}Sr/^{90}Y and even with a bare GC. The latter case was interpreted as decay rate bursts of trace β-active nuclides in the body of GC and ambient air (e.g., radon). One may naturally suspect the presence of trivial electrical noises in this situation instead of the actual activity increases. AP excluded such possibility by claiming two following facts. One is the classical controlling scheme, when the second identical detector works in parallel with the main one but is placed aside from the mirror. The control detector did not show any anomalies. The second reported fact is absence of the anomalies during cloudy weather. Local electrical interferences are not expected to have such anticorrelation. These facts convinced AP of the realness of anomaly, as well as led him to the conclusion, that atmospheric clouds attenuate cosmic ν_x flows.

Let us now write out AP's findings more quantitatively. His most efficient telescope has the steel mirror with parabolic surface ($\sim$ 10 μm surface quality), diameter of 22 cm, focal length of 10 cm and thickness of $\sim$ 1 cm. The characteristic size of β-decaying targets is $\sim$ 0.1 cm. For electron detection, AP *mainly* used the miniature industrial GC called "SBM-12" (GC-12 hereafter for simplicity) with $\sim$ 0.1 cm^2 sensitive zone covered by a metal with $\approx$ 0.005 cm thickness, but other detectors were occasionally employed too. The mirror with attached detector was situated on a simplistic equatorial mount with an electric motor, which can swing the mirror along the declination sky coordinate in the range $0° \lesssim \delta \lesssim 40°$ for efficient sky surveying. Thus, employing Earth's rotation, such telescope is able to sweep rather large portion of the sky during a day. After doing such sky scanning for several years, AP revealed the following key properties of the purported signals. The rate of statistically significant signals was $\sim$ 1 day^{-1} (meaning clear days). The typical signal duration is $\sim$ 1 s, though signals lasting minutes to hours and having fine temporal structure were detected too. The signal amplitude was up to $\sim$ 1000 times (!) with respect to the steady count rate; which was $\sim$ 1 s^{-1}, and was composed of a minor contribution from external background and the main contribution from the normal decay rate of the β-source.

After decades of his research, AP arrived to the following theoretical explanation of the observed effect: it is caused by the electron neutrinos with the mass $m_{\nu_e} \sim 10$ eV, which float in the space like the cosmic neutrino background (CνB) with typical speeds of hundreds km/s. Such large value of m_{ν_e} was considered; since its limits from direct measurements back to the times, when AP was conducting his research in 1990–2010, were not so stringent [8] as nowadays. The possibility of ν_e significant interactions with matter was justified by AP through the fact of very large de-Brogile wavelength $\lambda_{dB} \equiv 2\pi\hbar/p$ of such particles – λ_{dB} values fall into μm–mm range for ν_e parameter values mentioned above. He assumed that the typical weak interaction cross section is enhanced in this situation proportionally to the number of target nucleons in the volume $\sim \lambda_{dB}^3$, which is rather macroscopic. Moreover, AP drew the analogy between ν_e and photons with wavelengths λ_{dB}, and treated ν_e by laws of wave optics. Such treatment was initially motivated by the mentioned diffraction observation and then justified ν_e focusing by the concave mirrors. Another essential element of AP's concept is dense and narrowly collimated ν_e beams, which are absent "by default" in CνB. AP invented such beams through the mechanism of local gravitational focusing of globally uniform and isotropic ν_e background by the Sun and nearby stars. An example of modeling of such focusing can be seen in e.g. [9]. Essentially, this mechanism creates dense and anisotropic structures like streams and caustics (meanwhile, similar mechanism was also considered in [10]). AP suggested that an ambient uniform ν_e background is not dense enough in order to cause a detectable reaction of his telescope. But sometimes the Sun and nearby stars create short-lived, non-stationary, narrowly-directed ν_e flows with the density by many orders of magnitude larger than that of background. Such flows strike the telescope, get focused by its mirror and cause β-radioactivity bursts at the detector. According to AP, the gravitational focusing works especially efficiently; when the Earth, Sun and some nearby star get aligned along the straight line. At such moments we see the Sun conjunction with that star in our sky. AP reported certain reproducibility of the signals recorded at the days of some of such conjunctions in different years. Finally, based on estimates of ν_e spatial concentration, AP suggested that these particles can account for all dark matter (DM) (at least in our Galaxy) rather than just CνB.

AP's concept, which we expounded above, is indeed crude and vague in a multitude of aspects. First of all, the modern constraints on m_{ν_e} from both direct measurements and cosmological observations yield $m_{\nu_e} \lesssim 0.1$ eV [11], thus excluding the value estimated by AP. Eliminating the usual, i.e. active, electron neutrinos from consideration, one may in principle hypothesize a manifestation of sterile neutrinos [7] here; which are assumed to be heavier than ν_e, may have a small mixing with ν_e and represent the viable DM candidate. Having such perspective in mind, the authors of the present work got inspired to *check only the empirical part* of AP's work *fully agnostically* of theoretical possibilities. Saying by another way, we aimed to check independently whether the claimed β-radioactivity anomaly is reproducible and real.

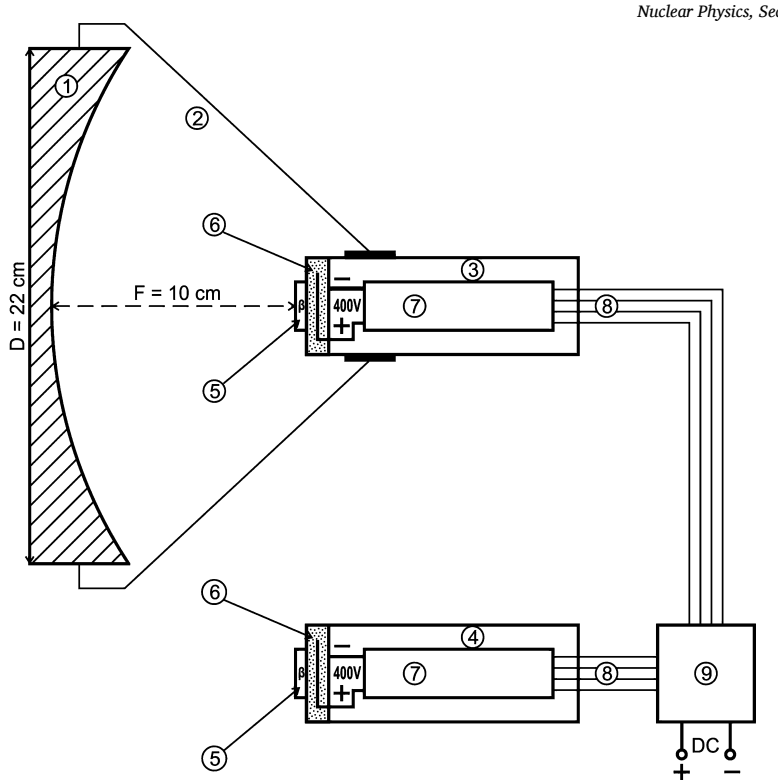


Fig. 1. The principal scheme (side view) of our experimental setup: 1 – the steel mirror with parabolic surface; 2 – four supports; 3 – the main (signal) detector; 4 – the control detector; 5 – β-sources; 6 – Geiger counters; 7 – powering and linking electronic boards; 8 – I2C bus; 9 – the main electronic unit containing CPU, display, memory card etc. The relative sizes in the figure are close to reality.

2. Our replication of Parkhomov's experiment

Our practical goal was to replicate AP's setup as identically as possible. We were communicating directly with AP during our experimentation, and he kindly gave us his mirror with mount described in the previous section. We created new detectors telic for our purposes. We conducted our measurements during the summer seasons of 2023 and 2024. The first season was preparatory to some degree: we were testing various detector configurations, and understanding their noises and backgrounds. Thus, we drew our final conclusion based majorly on the measurements made in 2024, when our setup was firmly established. This setup is depicted in Fig. 1. Two nearly identical detectors were always working: the signal detector with β-decaying source fixed at the mirror focal spot and the control detector (with the same source) put aside from the mirror. For β-sources we employed two (enveloped) isotopes: ^{40}K in the form of natural potassium chloride and ^{90}Sr/^{90}Y with the activity $\approx$ 40 Bq (measured by GC). Both sources have the cylindrical (coin-like) shape with diameter $\approx$ 2 cm and height $\approx$ 0.2 cm. These coin-shaped sources were positioned orthogonally to the mirror's "optical" axis in order to efficiently intercept the hypothetical focused ν_x beam. The source thickness along the axis was chosen as a compromise between sufficient source activity and smallness of electron absorption (we aimed to detect only electrons from the reaction (1) as AP did it). These sources were fixed in front of the thin mica window of GC with diameter $\approx$ 4 cm. We employed mainly GCs called "Beta-1" [12]. Following AP's recipe, we inserted the additional $\approx$ 0.5 cm layer of plastic between the source and GC window in the case of ^{90}Sr/^{90}Y in order to filter out the majority of "normal" electrons (including all the electrons from ^{90}Sr) and thus increase sensitivity, since all the target electrons are expected to have the same (high) energy near the β-spectrum endpoint. ^{40}K source is relatively weak, hence no additional attenuation was used. GCs were powered by 400 V potential with several layers of voltage stabilization. This setup yielded the following steady mean count rates: 2.3 s^{-1} for ^{40}K and 1.5 s^{-1} for ^{90}Sr/^{90}Y. These rates are dominated by counts from the sources, the external background rate is $\lesssim$ 0.5 s^{-1}.

The data from both detectors, i.e. the number of accumulated counts, were recorded on the memory card simultaneously at 1 and 10 Hz rates in order to have the opportunity to analyze data with various temporal resolutions. Two different sky survey methods were utilized. The ordinary method was rather trivial: the telescope mount was just fixed to the stationary position, and the motor was swinging the mirror back and forth with the speed $\approx 7°$/min and amplitude $\approx 40°$. The second survey mode was used during the days of Sun conjunction with nearby stars or clusters in the sky. As was mentioned in section 1, AP stated that on such days, especially strong signals are expected. Quantitatively, the angular separation between the solar disk center and the star must not exceed several arcmin, and the gravitationally collimated ν_x beams are anticipated to arrive from the region with $\approx 15°$ radius around the Sun. We were scanning this region around the Sun semi-manually at such days. Specifically, we picked those conjunctions, when the stars with visual magnitudes brighter than 6^m went behind the solar disk, i.e. the angular separation was $\leqslant 15'$.

Table 1
An estimate of our recorded exposure, i.e. the number of clear days, when the telescope was working. Numbers in brackets mean the number of days, when the exposure intervals were intersecting in time with conjunctions of Sun with nearby stars. More details are in section 2.

Year	^{40}K	^{90}Sr/^{90}Y	GC-12
2023	2.0 with NaI, 13 with GC (3)	0	0
2024	12 (3)	24 (7)	0.50 (3)

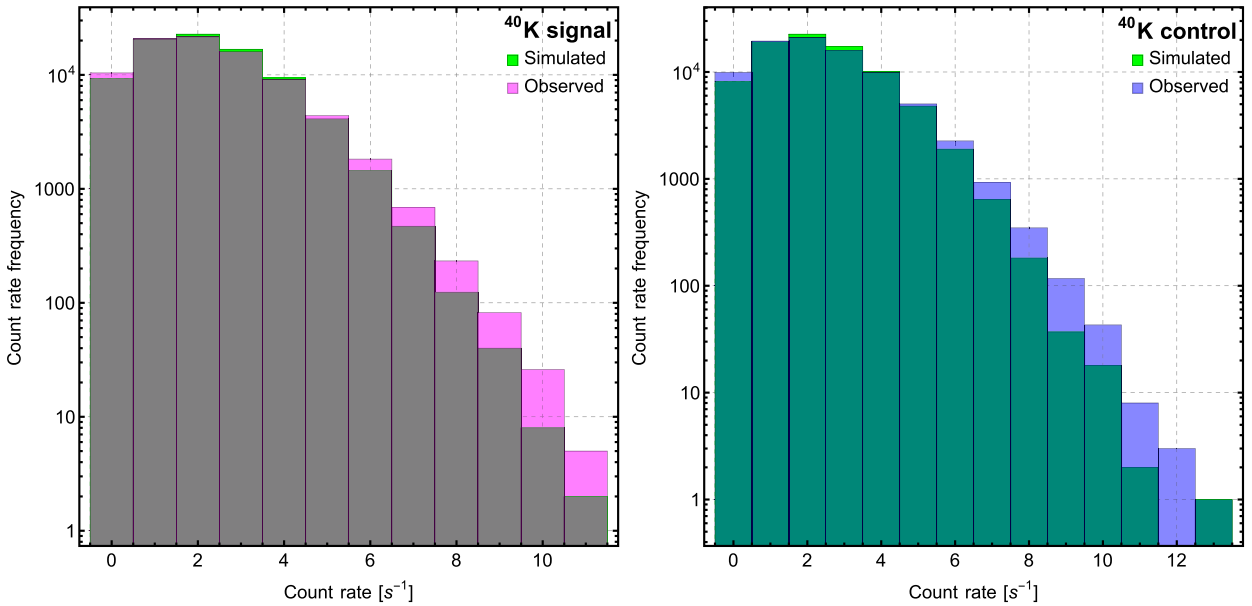


Fig. 2. The measured and simulated count rate distributions (count integration time is 1 s) for the case of ^{40}K source. The measured data was gathered during the whole clear day of 8th June 2024. The left panel reflects the signal detector at the mirror focus, the right panel reflects the control detector aside. The darker (bottom) bar sections represent the overlap of two datasets.

Besides the main detector configurations described above, we also occasionally used others. Thus, in 2023, we recorded several days using miniature NaI-based dosimeters paired with ^{40}K targets. Then in 2024 we recorded a small dataset employing bare GC-12 during the Sun conjunction with Messier 44 open star cluster. Table 1 summarizes our accumulated recording times in various modes under reasonably clear sky. We can see that, including preliminary 2023 data, we recorded in total about 27 days with ^{40}K and 24 days with ^{90}Sr/^{90}Y. The conjunctions, which satisfy the criteria above, were happening during 16 days, which intersected in time with our recordings. As we mentioned in section 1, AP observed significant signals nearly every clear day. Thus, our exposure in every mode is absolutely sufficient in order to draw a firm conclusion on the hypothesized effect. The former follows in the next sections.

3. The results of our measurements

Let us start here from the note on what kind of signals we were aiming to reveal. AP did not elaborate very well on the event occurrence rate, and their distribution by duration and intensity. But roughly, to the best of our understanding, we expected the following minimal occurrence rates in terms of orders of magnitude normalized to the steady β-source activity: one 10-fold event (i.e., increase or burst) every day, one 100-fold event every 10 days and one 1000-fold event every 100 days (meaning clear days). These signals are expected to have duration $\gtrsim 1$ s and to be rather insensitive to the β-isotope. As we outlined in the previous section, our GC mean count rate, which reflects the steady/normal β-source activity, is ~ 1 s^{-1}. Thus, taking into account our total exposure, we may anticipate tens of $\gtrsim 10$ s^{-1} events and even several ~ 100 s^{-1} events above the normal Poissonian background in our data even with the modest 1 Hz time resolution.

Examples of our daily data for both β-isotopes are shown in Fig. 2-3. These histograms represent the numbers of occurrences of various observed counts integrated over 1 s during the whole day. We also plotted there the corresponding computer-simulated random realizations of Poisson distribution for comparison. These particular examples can be considered as representative, since the data from all other days do not differ significantly from these trial days. We can see at first a good accordance between the signal and control count rate distributions. At second, they both agree well with the simulated Poissonian count rate distributions. We can notice just a mild heavy tail in the observed distribution of both signal and control counts. We attribute such tail to an imperfectness of insulation of our detectors from nuisance electromagnetic interference, which may create a relatively small number of false counts.

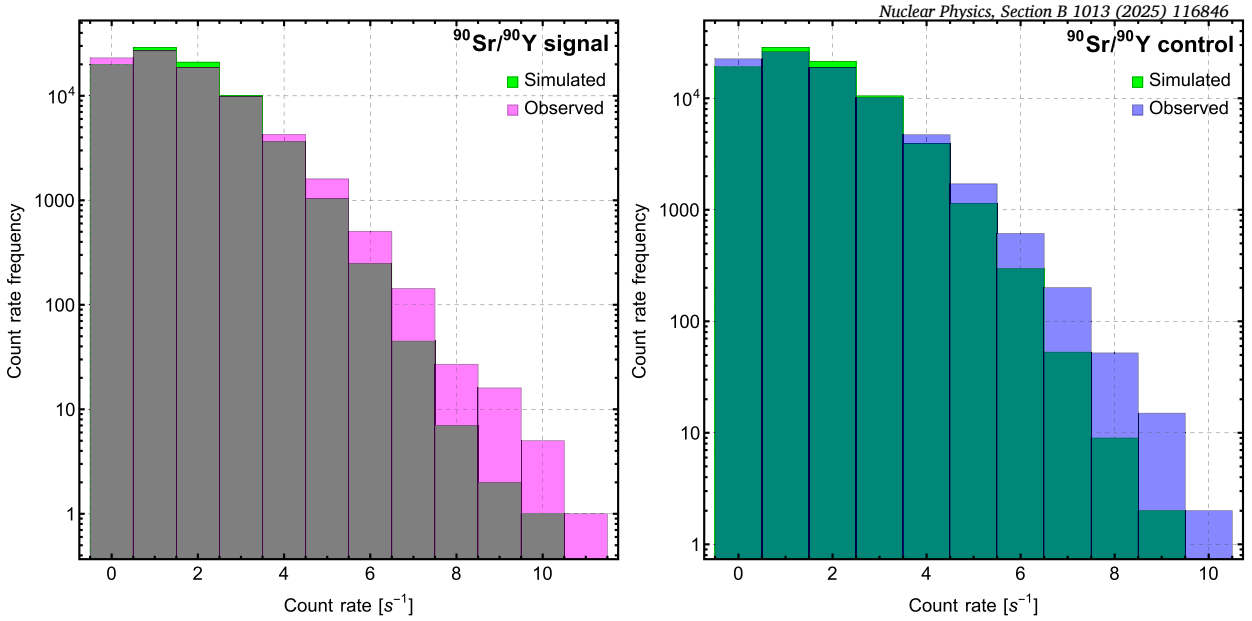


Fig. 3. Same as Fig. 2, but for ^{90}Sr/^{90}Y source measured on 28th June 2024.

Over all ≈ 50 days of our exposure, we saw something abnormal only once. This happened on 17th August 2023, when ^{40}K count rate jumped up by ∼ 100 times for 1–2 s. However, we attributed this candidate event to the bogus signal rather than real, since at that time we had not yet achieved full understanding of possible electrical noises in our relatively simple setup. Once we eliminated all possible electromagnetic interference, no significant signals were observed above the steady rate. Also, if we assume that burst to be real, then it must not be so alone. As we outlined above, according to AP we should have tens of events with amplitudes above 10 s^{-1}. But nothing significant was seen beyond the steady Poissonian decay rate over all the robust data gathered in 2024 for both tested isotopes at the signal detector.

AP in fact was recording his data in a different way due to various reasons. He was recording not the number of counts during fixed time intervals, but instead the time interval durations with the fixed number of accumulated counts (usually $N = 256$). Then he was deriving the count rate through division of N by the accumulation duration. Such method yields a bit integrated signal and erases weak features. Thus, for example, AP was recording ^{40}K with $N = 128$ during 4 calendar months and detected 34 bursts with amplitudes of ⩾ 2-fold with respect to the steady count rate. We processed our data through this method too for a comprehensive comparison. This algorithm yielded at most ≈ 1.5 times increases, which were the same on the signal and control detectors. Therefore, the absence of anomalies was confirmed. Indeed, the signal amplitudes are not equivalent in two registration methods.

Finally, we also tested AP's claim about strong signals obtained with bare GC-12 near the Sun, when it passes nearby M44 open star cluster in the sky. This was happening on 29–31st July 2024. The weather was not very good, but we were able to record ≈ 12 hours of data under sunshine, which should be sufficient to see at least something. But absolutely no hints of anomalies were found again. The corresponding count rate distributions are depicted in Fig. 4. We can see nearly perfect agreement between the measured and simulated distributions.

4. Discussion

We suppose that we replicated AP's experimental setup identically enough and gathered sufficient amount of data in order to draw the reliable verdict for the effect being tested. We suspect that AP was observing just trivial electromagnetic interference/noise during his work. The presence of anomalies on his signal detector only and their absence on the control detector could be due to a physical/electrical contact between the signal detector mounted on the mirror and the whole telescope, which includes electrical motor etc. The claimed anticorrelation between the signals and atmospheric clouds might be a result of psychological bias. Thus, for example, in-depth analysis of AP's data revealed strong and unphysically looking signals during the night on 3-4 August 2007, when a strong rain with thunderstorm was going on in Moscow (where AP was working), according to the weather archive. This example supports the above reasoning. Additional suspicion arises from the absence of specific inherent characteristic timescale in hypothesized signals: they were reported to last from seconds to hours, which resembles just everyday human activity timescales.

Speaking more about experimental weaknesses, AP almost solely relied on just one detector type – i.e. GC, which is known to be a primitive and noise-vulnerable particle detector [13]. Another possible weakness is that AP powered his setup by a usual city electrical network and never tried autonomous power supply.

On the theoretical side, AP did not analyze enough unavoidable manifestations of the hypothesized particle and its effects beyond his narrow concept. Thus, the following simple thought experiment severely challenges the concept. AP estimated the coefficient of reflection of ν_x from the telescope mirror surface to be $k \sim 0.01$. In the absolute units, this corresponds to a tiny area of ≈ 4 cm^2.

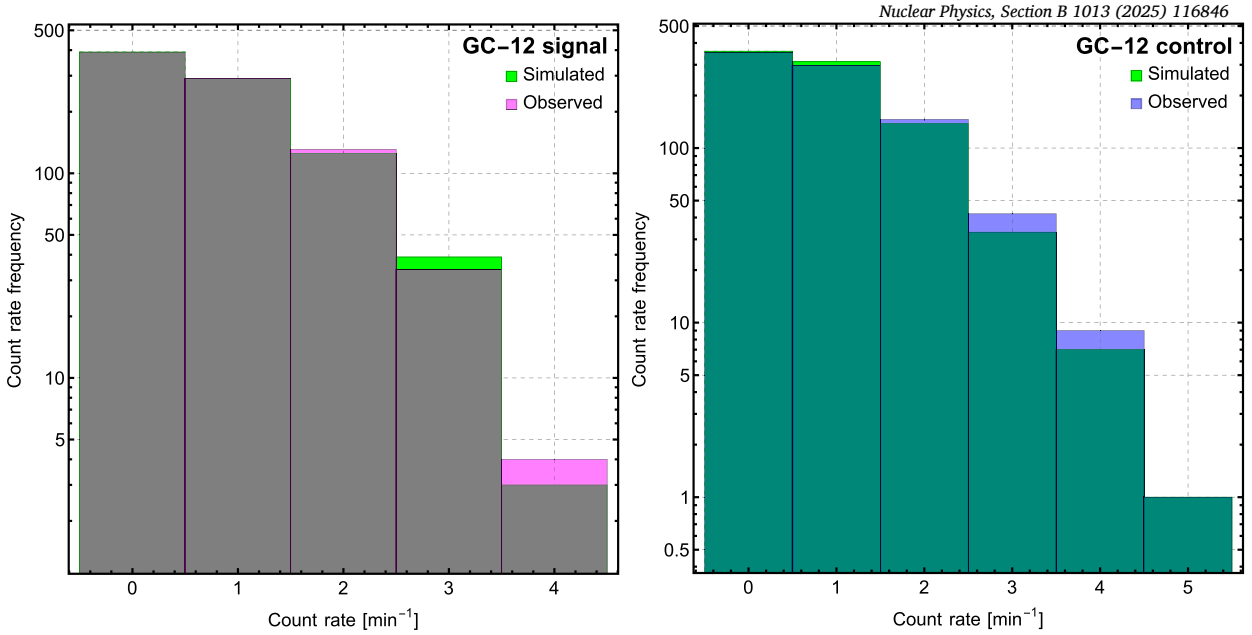


Fig. 4. The measured and simulated count rate distributions (count integration time is 1 min) for the whole exposure (≈ 12 hours) recorded with bare GC-12 on 29–31st July 2024 during the Sun passage near M44 star cluster on the sky.

This essentially represents the effective area of his detector. This implies that any β-source alone with such size under the clear sky inevitably must demonstrate similar activity bursts with even larger occurrence rate, since the mirror collects ν_x flows from a small portion of sky. But such bursts do not exist in reality, obviously; and even if $k = 1$, this effect can not stay unnoticed nowadays. Thus, for example, the experiment [14] watched ≈ 6.2 kg of the natural potassium during about 500 days above ground and found no decay rate anomalies down to the relative amplitude $\sim 10^{-5}$. In this respect, the mirror seems to play a crucial role only for the purpose of fine sky imaging, but not for just detection/revelation of hypothesized ν_x. In order to overcome this challenge, one needs to make unusual assumptions: e.g., collective effects in ν_x beam, when its efficiency of β-decay induction depends on the flux non-linearly, and the beam compression by the mirror provides non-linear induction enhancement.

Besides sporadic bursts, AP also reported in [1–5] the detection of small annual oscillation of β-decay rate with relative amplitude $\sim 0.1\%$ by watching various isotopes by various GCs for over 10 years. He attributed this modulation to β-decay induction modulation due to minor annual changes in the smooth background flux of hypothetical ν_x. In our work, we did not aim to test this minor slow oscillation. However, the work [15] was dedicated to analysis of the former. These authors found out a strong anticorrelation between the ambient air humidity in Moscow shifted forward in time by ∼ one month and the decay rate in AP's data. Thus, they concluded that the claimed abnormal oscillation can be likely due to just instability of measurement conditions, which often causes such false detections [16]. This conclusion can be ambiguous; because the air humidity outside, i.e. at some city weather monitor, can differ significantly from the air humidity in immediate vicinity of the experimental setup. But if the conclusion is valid, our work neatly complements [15]: we can exclude all the β-decay anomalies claimed by AP! In general, S. Pomme et al. conducted very extensive and valuable work on the critical assessment of the claims about the influence of cosmic neutrinos on β-decay [13].

5. Conclusions

We conducted independent and precise replication of AP's experiment, when β-decaying sources are being placed at the focus of steel concave mirror pointed at a clear sky. AP reported in the past an observation of sporadic and strong activity increases in this setup. We recorded about 27 days of data with ^{40}K and 24 days with ^{90}Sr/^{90}Y employing GCs "Beta-1". We did not observe any significant differences between the data from signal and control detectors. The count rate in both datasets follows well the standard Poisson distribution. Thus we robustly excluded the hypothesized effect and related necessity of new physics. Nevertheless, such brave AP's attempt to attack one of the biggest puzzles in modern science – i.e., the physical nature of DM – being worked alone with very scarce resources definitely deserves respect!

Based on [13,16], we can probably state the global conclusion, that currently no sufficiently justified deviations from the standard exponential law of radioactive decay have been found.

Declaration of competing interest

The authors declare that they have no known competing financial interests or personal relationships that could have appeared to influence the work reported in this paper.

Acknowledgements

We acknowledge helpful usage of the following software in our work: R programming language, RStudio, Wolfram Mathematica, Stellarium and TeXstudio.

Data availability

Data will be made available on request.

References

[1] A.G. Parkhomov, Rhythmic and sporadic changes in the rate of beta decays: possible reasons, J. Mod. Phys. 9 (8) (2018) 1617–1632, https://doi.org/10.4236/jmp.2018.98101.
[2] A.G. Parkhomov, Deviations from beta radioactivity exponential drop, J. Mod. Phys. 2 (11) (2011) 1310–1317, https://doi.org/10.4236/jmp.2011.211162.
[3] A. Parkhomov, Space. Earth. Human. New Views on Science, 2nd edition, ISBN 978-5-519-70031-3, 2020, Moscow (in Russian).
[4] A. Parkhomov, Space. Earth. Human. New Views on Science, ISBN 978-1711221212, 2019, https://www.amazon.com/dp/171122121x.
[5] A.G. Parkhomov, Influence of relic neutrinos on beta radioactivity, arXiv:1010.1591, Oct. 2010, https://doi.org/10.48550/arXiv.1010.1591.
[6] A.G. Parkhomov, Bursts of count rate of beta-radioactive sources during long-term measurements, Int J. Pure Appl. Phys 1 (2) (2005) 119–128, https://www.researchgate.net/profile/A-Parkhomov/publication/287232436_Bursts_of_count_rate_of_beta-radioactive_sources_during_long-term_measurements/links/637cacc32f4bca7fd080914b/Bursts-of-count-rate-of-beta-radioactive-sources-during-long-term-measurements.pdf.
[7] K.-Y. Choi, E. Lkhagvadorj, S.M. Yoo, Probing sterile neutrino dark matter in the Ptolemy-like experiment, J. Cosmol. Astropart. Phys. 2023 (6) (2023) 021, https://doi.org/10.1088/1475-7516/2023/06/021, arXiv:2212.14192.
[8] V.M. Lobashev, V.N. Aseev, A.I. Belesev, A.I. Berlev, E.V. Geraskin, A.A. Golubev, O.V. Kazachenko, Y.E. Kuznetsov, R.P. Ostroumov, L.A. Rivkis, B.E. Stern, N.A. Titov, C.V. Zadoroghny, Y.I. Zakharov, Direct search for neutrino mass and anomaly in the tritium beta-spectrum: status of “Troitsk neutrino mass” experiment, Nucl. Phys. B, Proc. Suppl. 91 (1) (2001) 280–286, https://doi.org/10.1016/S0920-5632(00)00952-X.
[9] B.R. Patla, R.J. Nemiroff, D.H.H. Hoffmann, K. Zioutas, Flux enhancement of slow-moving particles by Sun or Jupiter: Can they be detected on Earth?, Astrophys. J. 780 (2) (2014) 158, https://doi.org/10.1088/0004-637X/780/2/158, arXiv:1305.2454.
[10] S. Bertolucci, K. Zioutas, S. Hofmann, M. Maroudas, The Sun and its planets as detectors for invisible matter, Phys. Dark Universe 17 (2017) 13–21, https://doi.org/10.1016/j.dark.2017.06.001, arXiv:1602.03666.
[11] M. Aker, D. Batzler, A. Beglarian, J. Behrens, J. Beisenkötter, M. Biassoni, B. Bieringer, Y. Biondi, F. Block, S. Bobien, M. Böttcher, B. Bornschein, L. Bornschein, T.S. Caldwell, M. Carminati, A. Chatrabhuti, S. Chilingaryan, B.A. Daniel, K. Debowski, M. Descher, D. Díaz Barrero, P.J. Doe, O. Dragoun, G. Drexlin, F. Edzards, K. Eitel, E. Ellinger, R. Engel, S. Enomoto, A. Felden, C. Fengler, C. Fiorini, J.A. Formaggio, C. Forstner, F.M. Fränkle, K. Gauda, A.S. Gavin, W. Gil, F. Glück, S. Grohmann, R. Grössle, R. Gumbsheimer, N. Gutknecht, V. Hannen, L. Hasselmann, N. Haußmann, K. Helbing, H. Henke, S. Heyns, S. Hickford, R. Hiller, D. Hillesheimer, D. Hinz, T. Höhn, A. Huber, A. Jansen, C. Karl, J. Kellerer, K. Khosonthongkee, M. Kleifges, M. Klein, J. Kohpeiß, C. Köhler, L. Köllenberger, A. Kopmann, N. Kovač, A. Kovalík, H. Krause, L. La Cascio, T. Lasserre, J. Lauer, T. Le, O. Lebeda, B. Lehnert, G. Li, A. Lokhov, M. Machatschek, M. Mark, A. Marsteller, E.L. Martin, C. Melzer, S. Mertens, S. Mohanty, J. Mostafa, K. Müller, A. Nava, H. Neumann, S. Niemes, A. Onillon, D.S. Parno, M. Pavan, U. Pinsook, A.W.P. Poon, J.M. Lopez Poyato, S. Pozzi, F. Priester, J. Ráliš, S. Ramachandran, R.G.H. Robertson, C. Rodenbeck, M. Röllig, C. Röttele, M. Ryšavý, R. Sack, A. Saenz, R. Salomon, P. Schäfer, M. Schlösser, K. Schlösser, L. Schlüter, S. Schneidewind, U. Schnurr, M. Schrank, J. Schürmann, A. Schütz, A. Schwemmer, A. Schwenck, M. Šefčík, D. Siegmann, F. Simon, F. Spanier, D. Spreng, W. Sreethawong, M. Steidl, J. Štorek, X. Stribl, M. Sturm, N. Suwonjandee, N. Tan Jerome, H.H. Telle, L.A. Thorne, T. Thümmler, S. Tirolf, N. Titov, I. Tkachev, K. Urban, K. Valerius, D. Vénos, C. Weinheimer, S. Welte, J. Wendel, C. Wiesinger, J.F. Wilkerson, J. Wolf, S. Wüstling, J. Wydra, W. Xu, S. Zadorozhny, G. Zeller, Direct neutrino-mass measurement based on 259 days of KATRIN data, arXiv:2406.13516, Jun. 2024, https://doi.org/10.48550/arXiv.2406.13516.
[12] https://consensus-group.ru/radiation-counters/alpha-beta-gamma-radiation/106-beta-1-1.
[13] S. Pommé, K. Pelczar, Neutrino-induced decay: a critical review of the arguments, Space Sci. Rev. 218 (8) (2022) 64, https://doi.org/10.1007/s11214-022-00932-0.
[14] E. Bellotti, C. Broggini, G. Di Carlo, M. Laubenstein, R. Menegazzo, M. Pietroni, Search for time modulations in the decay rate of ^{40}K and ^{232}Th, Astropart. Phys. 61 (2015) 82–87, https://doi.org/10.1016/j.astropartphys.2014.05.006.
[15] S. Pommé, K. Pelczar, I. Kajan, Air humidity and annual oscillations in ^{90}Sr/^{90}Y and ^{60}Co decay rate measurements, Sci. Rep. 12 (2022) 9535, https://doi.org/10.1038/s41598-022-13841-7.
[16] S. Pommé, H. Stroh, T. Altzitzoglou, J. Paepen, R. Van Ammel, M. Marouli, L. Verheyen, M. Unterweger, R. Fitzgerald, D.E. Bergeron, L. Pibida, O. Nähle, K. Kossert, N. Ramirez, E. Bendall, A. Fenwick, K. Ferreira, J. Keightley, M. Baker, S. Collins, C. Michotte, S. Courte, R. Coulon, T.W. Jackson, W.M. Van Wyngaardt, A. Fazio, P. De Felice, B. Vodenik, M. Korun, F. Juget, C. Bailat, Y. Nedjadi, F. Bochud, T. Buchillier, T. Roy, R. Galea, I. Kajan, M.W. Van Rooy, P. McGinnity, I. Tucakovic, I. Osvath, K. Pelczar, Ambient humidity, the overlooked influencer of radioactivity measurements, Metrologia 61 (1) (2024) 015001, https://doi.org/10.1088/1681-7575/ad0c9f.

ISSN 1063-7788, Physics of Atomic Nuclei, 2017, Vol. 80, No. 6, pp. 1141–1145. © Pleiades Publishing, Ltd., 2017.
Original Russian Text © A.M. Galper, S.I. Suchkov, N.P. Topchiev, I.V. Arkhangelskaja, A.I. Arkhangelskiy, A.V. Bakaldin, Yu.V. Gusakov, O.D. Dalkarov, A.E. Egorov, V.G. Zverev, V.V. Kadilin, A.A. Leonov, P.Yu. Naumov, M.F. Runtso, M.D. Kheymits, Yu.T. Yurkin, 2017, published in Yadernaya Fizika, 2017, Vol. 80, No. 6, pp. 660–664.

ELEMENTARY PARTICLES AND FIELDS
Experiment

Precision Measurements of High-Energy Cosmic Gamma-Ray Emission with the GAMMA-400 Gamma-Ray Telescope

A. M. Galper[1),2)], S. I. Suchkov[1)*], N. P. Topchiev[1)], I. V. Arkhangelskaja[2)], A. I. Arkhangelskiy[2)], A. V. Bakaldin[3)], Yu. V. Gusakov[1)], O. D. Dalkarov[1)], A. E. Egorov[1)], V. G. Zverev[1)], V. V. Kadilin[2)], A. A. Leonov[1),2)], P. Yu. Naumov[2)], M. F. Runtso[2)], M. D. Kheymits[2)], and Yu. T. Yurkin[2)]

Received March 22, 2017

Abstract—The GAMMA-400 γ-ray telescope installed at the Russian space observatory is intended for precision measurements in the energy range of 20 MeV–1000 GeV of γ-ray emission (with the angular and energy resolutions several times better than that of current γ-ray telescopes) from discrete sources; measurement of the energy spectra of Galactic and extragalactic diffuse γ-ray emission; studies of γ-ray emission from the active Sun; and measurements of fluxes of γ-ray emission and electron–positron cosmic-ray component, which are probably associated with the annihilation or decay of dark-matter particles.

DOI: 10.1134/S1063778817060096

INTRODUCTION

In accordance with the Federal Space Programs of Russia for 2009–2015 and 2016–2025, the activities are continuing at present to create the GAMMA-400 γ-ray telescope (gamma-astronomical multifunctional modular apparatus) [1, 2].

GAMMA-400, which will be installed at the Russian space observatory, is intended for studying γ-ray emission in the energy range of 20 MeV–1000 GeV, obtaining data for solving the problem of the nature of dark matter in the Universe, and developing the theory of the origin of high-energy cosmic rays.

GAMMA-400 will provide information about (i) the features in the energy spectra of high-energy γ-ray emission from discrete and extended sources and the electron–positron component that can be associated with dark-matter particles; (ii) the variability of high-energy γ-ray emission from discrete sources in order to clarify the nature of processes involving the acceleration of elementary particles in these sources; (iii) diffuse Galactic and extragalactic γ-ray emission; and (iv) high-energy γ-ray emission arising in solar flares.

The goals of the GAMMA-400 experiment are continuous long-term (up to 100 days) observations of high-energy γ-ray emission from the Galactic center; Fermi bubbles; the Crab nebula; and the constellations Vela, Geminga, and Cygnus, as well as the Sun, etc., with unprecedented angular ($\sim$0.01° for $E_\gamma > 100$ GeV) and energy ($\sim$1% for $E_\gamma > 100$ GeV) resolutions, which are significantly better than those of the Fermi-LAT [3] and AGILE [4] γ-ray telescopes currently operated in orbit, as well as those of the operated and projected ground-based γ-ray telescopes VERITAS [5], MAGIC [6], H.E.S.S. [7], and CTA [8].

GAMMA-400 GAMMA-RAY TELESCOPE

GAMMA-400 is a satellite γ-ray telescope that uses, for recording γ-ray emission, the conversion of gamma rays propagating in a converter into electron–positron pairs. The conversion electron and positron move in the direction of photon motion and are recorded by detector systems. The basic mode of GAMMA-400 is precision measurements of individual regions of the celestial sphere, e.g., the region of the Galactic center, with the duration of the continuous observation of up to 100 days in a highly elliptical orbit, where the passages through the radiation belts and the shadowing of the field of view of the γ-ray telescope by the Earth are virtually absent, for the following initial parameters: an apogee of 300 000 km, a perigee of 500 km, and an inclination of 51.4°.

[1)]Lebedev Physical Institute, Russian Academy of Sciences, Leninskii pr. 53, Moscow, 119991 Russia.
[2)]National Research Nuclear University MEPhI, Kashirskoe sh. 31, Moscow, 115409 Russia.
[3)]Scientific Research Institute for System Analysis, Russian Academy of Sciences, Moscow, 117218 Russia.
[*]E-mail: soutch@mail.ru

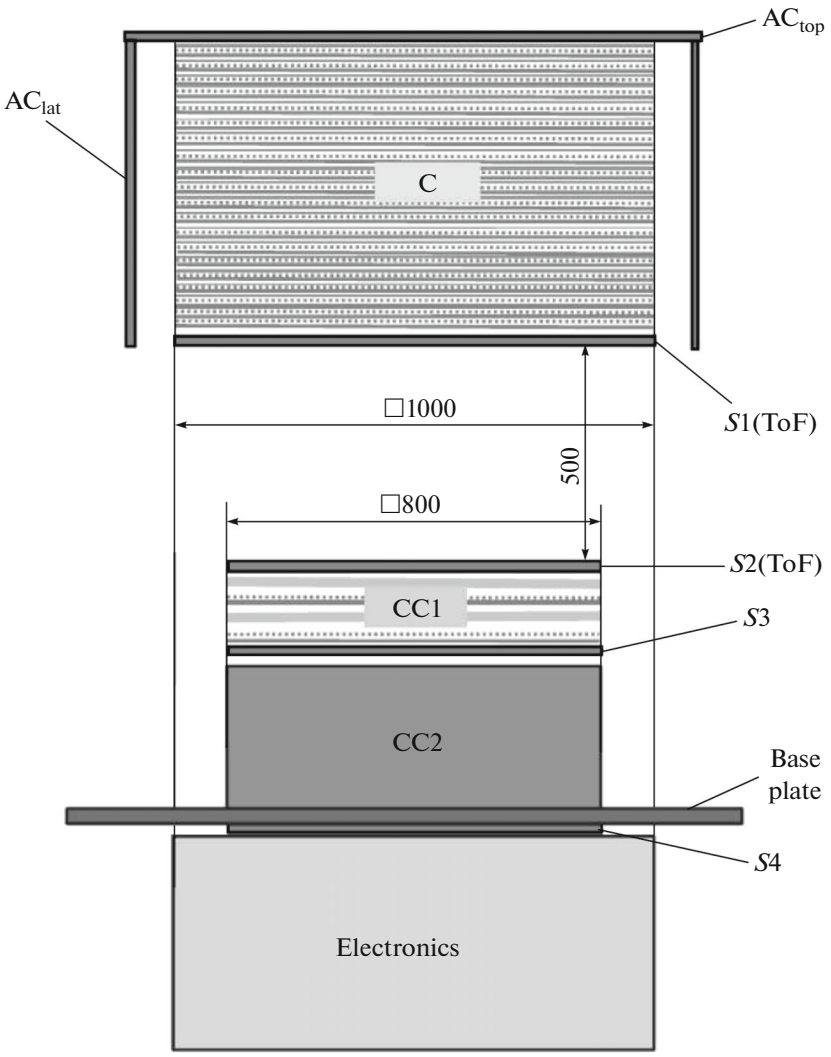


Fig. 1. Layout of the GAMMA-400 γ-ray telescope: anticoincidence system (AC) (top and lateral detectors), converter-tracker (C), time-of-flight system (ToF), parts of coordinate-sensitive calorimeter (CC1 and CC2), and scintillation detectors of the calorimeter ($S3$ and $S4$).

The basic detector systems of the GAMMA-400 γ-ray telescope are an anticoincidence system, a converter-tracker, a time-of-flight system, a calorimeter, and scintillation detectors of the calorimeter (Fig. 1). For manufacturing detectors, technologies well-tested in space experiments and high-energy physics were selected.

The anticoincidence system (AC) provides the separation of cosmic gamma rays against the background of a significantly higher flux of protons and electrons of primary cosmic rays with an efficiency of separation of gamma rays against the background of charged particles better than 0.999995. The detector system of AC surrounds the converter from five sides (top detector AC_{top} and four lateral detectors AC_{lat}).

The top detector AC_{top} is a two-layer detector from plastic scintillator BC-408. The upper layer consists of ten strips; the bottom layer consists of 11 strips parallel to the upper layer; the slits between the strips of one layer are shifted relative to the strips of the other, which ensures the overlap of the slits. Four lateral anticoincidence detectors AC_{lat1}–AC_{lat4}, which are similar in design to AC_{top}, are oriented perpendicularly to the plane of the top detector AC_{top} on the four sides of the tracker-converter. The use of the two-layer construction with overlapping slits allows us to achieve the value of 0.999995 for the separation of γ-ray events against the charged-particle background.

The converter-tracker (C) is intended for (i) converting gamma rays into electron—positron pairs and recording them and (ii) determining the gamma-ray arrival direction with a high accuracy, which allows us to obtain a high angular resolution of the GAMMA-400 γ-ray telescope.

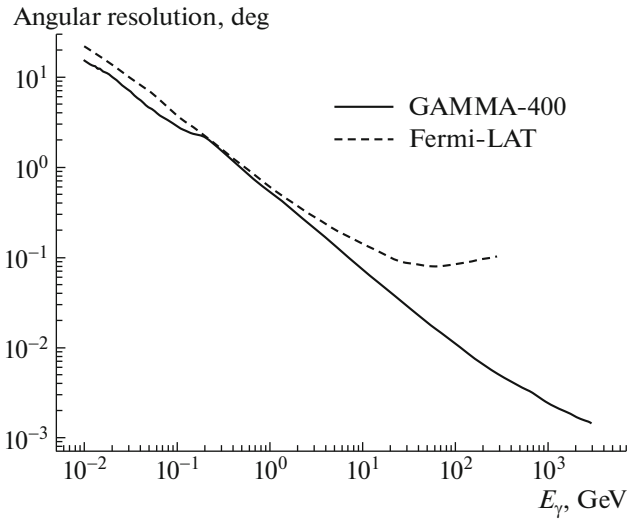


Fig. 2. Energy dependence of the angular resolution of the GAMMA-400 γ-ray telescope. The analogous dependence for Fermi-LAT is shown for the sake of comparison.

The converter-tracker C consists of 22 pairs of planes of silicon strip detectors (X and Y coordinates) located on 23 honeycombs with a strip pitch of 80 μm and a analog readout, which greatly improves a spatial accuracy. On the top 20 panels, there are tungsten converters of thickness 0.025 r.l. (radiation length unit). The total thickness of the converter-tracker for vertical incidence of particles is about 1 r.l.

The chosen design of the converter-tracker (and of the γ-ray telescope as a whole) provides a significant improvement in the angular resolution in comparison with Fermi-LAT in over almost the whole energy range from about 20 MeV to about 1000 GeV, especially from 10 GeV, and is about 0.01° at the energy of 100 GeV (Fig. 2). This is achieved by (i) improving the spatial resolution of silicon strip detectors (use of strip detectors with a pitch of 80 μm versus 225 μm in Fermi-LAT and of an analog readout instead of a binary one in Fermi-LAT); (ii) employing a long flight base from the strip detectors of the converter to the strip detectors of the calorimeter; (iii) significantly reducing the background level from the backscattered flux owing to the large distance from the converter to the calorimeter, about 100 cm versus about 10 cm in Fermi-LAT; and (iii) additionally using a fast trigger, which provides the reduction of the background from cosmic radiation, about 50 ns versus about 1.5 μs in Fermi-LAT.

The time-of-flight system (ToF) is intended for separating events caused by converted gamma rays moving in the telescope's aperture from the upper detector ($S1$) to the lower one ($S2$) against background events caused by gamma rays and particles moving in the opposite direction.

ToF consists of the upper $S1$ and lower $S2$ scintillation detectors. Each detector consists of two layers of plastic scintillator BC-408.

The coordinate-sensitive calorimeter is intended for measuring the energy of γ-ray emission. It consists of two parts: a position-sensitive calorimeter (CC1) and an electromagnetic calorimeter (CC2).

CC1 is intended for determining the spatial position of the axis of the electromagnetic shower from the recorded gamma rays and for measuring the electromagnetic-shower energy released in it from the recorded gamma rays.

CC1 consists of two groups. Each group consists of two detectors: a scintillation detector of CsI(Tl) crystals overlapping the sensitive area and a two-layer (X, Y) silicon strip detector with a strip pitch of 80 μm and an analog readout. The thickness of CC1 is about 2 r.l. The use of CC1 allows us to determine the position of the axis of the electromagnetic shower with a high accuracy.

CC2 is intended for measuring the released energy of the electromagnetic shower from recorded gamma rays with a high energy resolution, determining the shower profile, and rejecting protons.

CC2 consists of CsI(Tl) scintillation crystals. The thickness of CC2 for the normal incidence of particles is 20 r.l.

The calorimeter (CC1 and CC2) of total thickness about 22 r.l. for the normal incidence of particles (about 8.5 r.l. in Fermi-LAT) will allow us to obtain an energy resolution significantly better than that of Fermi-LAT beginning from the energy of 10 GeV; it will be about 1% at the energy of 100 GeV (Fig. 3).

The scintillation detectors of the calorimeter (SDC), which consist of plastic scintillation detectors $S3$ and $S4$, are intended for determining the energy release from the recorded particles and generating signals for the formation of a trigger; separating single-particle events for a calibration; and determining, with detector $S4$, the leakage of electromagnetic-shower particles escaping from the calorimeter.

The design of the SDC detectors is similar to the design of the ToF detectors.

When recording gamma rays of energy more than a few tens of GeV units, there arises a flux of backscattered (BS) particles, (mainly gamma rays of energy about 1 MeV) formed during the development of the electromagnetic shower in the calorimeter, which move in the direction opposite to the anticoincidence detector. This flux causes false actuations of the AC system, creating an imitation of the passage of charged particles, as well as imaginary signals in the strip detectors of the converter-tracker. The flux of BS particles can significantly reduce the

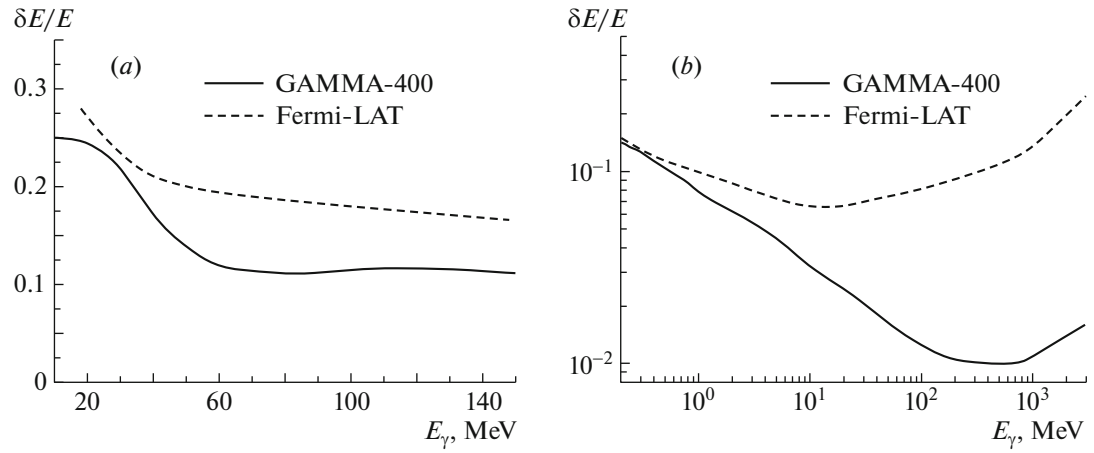


Fig. 3. The energy resolution of the GAMMA-400 γ-ray telescope as a function of the gamma-ray energy in the ranges of (*a*) 20–140 MeV and (*b*) 0.2–1000 GeV. The analogous dependences for Fermi-LAT are shown for the sake of comparison.

efficiency of the γ-ray telescope in recording gamma rays of energy higher than several tens of GeV units.

The following design features used in GAMMA-400 significantly reduce the effect of BS particles on recording high-energy γ-ray emission: (i) the segmentation (including the two-layer structure) of AC detectors, which reduces the probability of triggering AC segments from BS particles; (ii) the use of CC1, which significantly reduces the flux of BS particles formed in CC2; and (iii) an increased distance from CC2 to the converter-tracker (it is equal to 100 cm).

Calculations showed that, for the chosen design of the γ-ray telescope, the number of events that are associated with the flux of BS particles and which could be interpreted as charged particles and should be excluded from detection is not more than a few percent even for gamma rays of energy 1000 GeV.

Moreover, a time method based on measuring the time of particle flight between the detectors of these systems is used to reduce the flux of BS particles. Its signal in AC appears later than the event occurring in ToF $S1$ and triggering the beginning of detection, and this makes it possible to separate events induced by BS particles [9].

The triggers for recording gamma rays in GAMMA-400 are the actuation of ToF $S1$ earlier than $S2$ and the absence of the AC signal.

The delay between triggering and readout of information from the detectors is about 50 ns.

The use of a faster trigger allows us to reduce significantly the influence of the cosmic-radiation background in GAMMA-400.

CONCLUSIONS

The unprecedented characteristics of GAMMA-400 (an angular resolution of about 0.01° for $E_\gamma >$ 100 GeV and an energy resolution of about 1% for $E_\gamma > 100$ GeV), along with a continuous long-term (up to 100 days) observation of individual regions of the celestial sphere, the Galactic center, etc., will allow us to make significant advances in precision studies of discrete sources of γ-ray emission; measurements of the energy spectra of Galactic and extragalactic diffuse γ-ray emission; and measurements of fluxes of gamma rays and the electron–positron cosmic-ray component, which can be associated with the annihilation or decay of dark-matter particles. The launch of the space observatory with the GAMMA-400 γ-ray telescope is scheduled for 2025–2026.

ACKNOWLEDGMENTS

This work was supported by the Space Council of the Russian Academy of Sciences and by Roscosmos.

REFERENCES

1. A. M. Galper, O. Adriani, R. L. Aptekar, I. V. Arkhangelskaja, A. I. Arkhangelskiy, M. Boezio, V. Bonvicini, K. A. Boyarchuk, Yu.V. Gusakov, M. O. Farber, M. I. Fradkin, V. A. Kachanov, V. A. Kaplin, M. D. Kheymits, A. A. Leonov, F. Longo, et al., Adv. Space Res. **51**, 297 (2013).
2. N. P. Topchiev, A. M. Galper, V. Bonvicini, O. Adriani, R. L. Aptekar, I. V. Arkhangelskaja, A. I. Arkhangelskiy, A. V. Bakaldin, L. Bergstrom, E. Berti, G. Bigongiari, S. G. Bobkov, M. Boezio, E. A. Bogomolov, L. Bonechi, M. Bongi, et al., J. Phys.: Conf. Ser. **675**, 032009 (2016).

3. W. B. Atwood, A. A. Abdo, M. Ackermann, W. Althouse, B. Anderson, M. Axelsson, L. Baldini, J. Ballet, D. L. Band, G. Barbiellini, J. Bartelt, D. Bastieri, B. M. Baughman, K. Bechtol, D. Bédérède, F. Bellardi, et al., Astrophys. J. **697**, 1071 (2009).
4. M. Tavani, G. Barbiellini, A. Argan, F. Boffelli, A. Bulgarelli, P. Caraveo, P. W. Cattaneo, A. W. Chen, V. Cocco, E. Costa, F. D'Ammando, E. del Monte, G. de Paris, G. di Cocco, G. di Persio, I. Donnarumma, et al., arXiv: 0807.4254.
5. R. E. Ong (for the VERITAS Collab.), Adv. Space. Res. **53**, 1483 (2014).
6. D. Mazin, D. Tescaro, M. Garczarczyk, G. Giavitto, and J. Sitarek (for the MAGIC Collab.), arXiv: 1410.5073.
7. A. Balzer, M. Füßling, M. Gajdus, D. Göring, A. Lopatin, M. de Naurois, S. Schlenker, U. Schwanke, and C. Stegmannar, arXiv: 1311.3486.
8. M. Actis, G. Agnetta, F. Aharonian, A. Akhperjanian, J. Aleksi', E. Aliu, D. Allan, I. Allekotte, F. Antico, L. A. Antonelli, P. Antoranz, A. Aravantinos, T. Arlen, H. Arnaldi, S. Artmann, K. Asano, et al., Exp. Astron. **32**, 193 (2011).
9. M. D. Kheimits, A. M. Galper, I. V. Arkhangel'skaya, A. I. Arkhangel'skii, Yu. V. Gusakov, V. G. Zverev, V. V. Kadilin, V. A. Kaplin, A. A. Leonov, P. Yu. Naumov, M. F. Runtso, S. I. Suchkov, N. P. Topchiev, and Yu. T. Yurkin, Instrum. Exp. Tech. **59**, 508 (2016).

Translated by N. Topchiev

ISSN 1063-7788, Physics of Atomic Nuclei, 2018, Vol. 81, No. 3, pp. 373–378. © Pleiades Publishing, Ltd., 2018.
Original Russian Text © A.E. Egorov, A.M. Galper, N.P. Topchiev, A.A. Leonov, S.I. Suchkov, M.D. Kheymits, Yu.T. Yurkin, 2018, published in Yadernaya Fizika, 2018, Vol. 81, No. 3, pp. 360–365.

ELEMENTARY PARTICLES AND FIELDS
Experiment

Detactability of Dark Matter Subhalos by Means of the GAMMA-400 Telescope

A. E. Egorov[1)*], A. M. Galper[1),2)], N. P. Topchiev[1)], A. A. Leonov[1),2)], S. I. Suchkov[1)], M. D. Kheymits[2)], and Yu. T. Yurkin[2)]

Received November 14, 2017

Abstract—The potential of the planned GAMMA-400 gamma-ray telescope for detecting subhalos of mass between 10^6 $M_\odot$ and 10^9 $M_\odot$ in the Milky Way Galaxy that consist of annihilating dark matter in the form of weakly interacting massive particles (WIMPs) is studied. The inner structure of dark matter subhalos and their distribution in the Milky Way Galaxy are obtained on the basis of respective theoretical models. Our present analysis shows that the expected gamma-ray flux from subhalos depends strongly on the WIMP mass and on the subhalo concentration, but that it depends less strongly on the subhalo mass. Optimistically, a flux of 10 to 100 ph per year in the energy range above 100 MeV can be expected from the closest and most massive subhalos, which can therefore be thought to be detectable sources for GAMMA-400. Because of the smallness of fluxes, however, only via a joint analysis of future GAMMA-400 data and data from other telescopes would it become possible to resolve the inner structure of the subhalos. Also, the recent subhalo candidates 3FGL J2212.5+0703 and J1924.8−1034 are considered within our model. Our conclusion is that these sources hardly belong to the subhalo population.

DOI: 10.1134/S1063778818030110

1. INTRODUCTION AND MOTIVATION

Although dark matter (DM) in the Universe was discovered more than 80 years ago, its physical nature remains one of the most fundamental unresolved problems in modern astrophysics. There are many DM candidates but weakly interacting massive particles (WIMPs) in the form of neutralinos still remain the most probable and natural candidate (see, for example, [1]). As well known, these supersymmetric particles may undergo self-annihilation, producing highly energetic Standard Model particles, such as photons, electrons, and protons [1]. This process proceeds vigorously in regions where the DM concentration is high and could manifest itself via the emission of annihilation products. This is quite a promising approach to discovering WIMP and its physical parameters or, at least, to setting limits on these parameters. Such indirect DM searches are being vigorously performed in all astrophysical objects that could in principle contain DM: from the Sun to galaxy clusters. Such objects of interest include DM subhalos in the dark halo of the Milky Way Galaxy. An N-body simulation of DM halos reliably predicts the presence of a hierarchical substructure within them in the form of subhalos having masses in a very broad range extending down to about 10^{-6} $M_\odot$ [1]. Specifically, modern N-body models (see, for example, [2]) are able to resolve several tens of thousand subhalos within a Milky Way–sized halo. The most massive subhalos are expected to be dwarf satellites of the Milky Way (MW). A simulation also shows [3] that less massive subhalos of mass below 10^7 or 10^8 $M_\odot$ do not contain a luminous gas or a stellar component. However, such halos could be rather close and be bright gamma sources because of DM annihilation. At the same time, one-third of gamma sources in the 3FGL Fermi-LAT catalog have not been associated with any sources in different ranges of the spectrum [4]. These unidentified sources could in fact be DM subhalos. In summary, one can expect the following valuable subhalo properties making it possible to identify unambiguously subhalo radiation as photons from annihilating dark matter: (i) Subhalos emit virtually no radiation other than that from DM annihilation. (ii) This emission is absolutely stable, featuring no variability in time. (iii) All subhalos have the same predictable spectrum. (iv) They have a nearly isotropic distribution on the sky. (v) In contrast to typical astrophysical objects, such as blazars, they can be resolved as extended sources.

Thus, DM subhalos is an object of great interest for DM searches. A profound investigation of sub-

[1)]Lebedev Physical Institute, Russian Academy of Sciences, Leninskii pr. 53, Moscow, 119991 Russia.
[2)]National Research Nuclear University MEPhI, Kashirskoe sh. 31, Moscow, 115409 Russia.
[*]E-mail: eae14@yandex.ru

halo detectability by means of gamma-ray telescopes, such as Fermi-LAT, has been performed earlier (for example, [3]). However, the conclusion at which the authors of that investigation arrived is not optimistic: Fermi-LAT is able to detect about one subhalo over the whole sky and to resolve spatially less than one subhalo as an extended object. At the same time, several research groups have already studied catalogs of pointlike gamma-radiation sources for the presence of subhalo candidates in them (see, for example, [5]). This resulted in revealing two interesting candidates, J2212.5+0703 and J1924.8−1034, in the 3FGL Fermi-LAT catalog [5–7]. Their exact nature is still the subject of lively discussions. Section 4 of our present article is devoted to this issue.

Also, the problem of assessing the potential of future gamma-ray telescopes for the detection of DM subhalos is urgent at the present time (see, for example, [8]). The main objective of our present study is to explore the detectability of subhalos with GAMMA-400, which is a new gamma-ray telescope currently being designed and which is planned to be launched around 2025 [9, 10]. This telescope will possess unique energy and angular resolutions. They are expected to be at a level of 1% and 0.01°, respectively, at an energy of about 100 GeV. These features are substantially better than those characteristic of Fermi-LAT. Thus, GAMMA-400 would possibly possess a high potential for detecting subhalos and for resolving their inner structure. In turn, this would pave the way toward obtaining deeper insight into DM nature. Also, we may expect interesting results from a joint analysis of GAMMA-400 data and data from other telescopes, including Fermi-LAT and proposed e-ASTROGAM [11]. In the present analysis, it is assumed that DM is constituted by neutralinos exclusively.

2. SIMULATION OF THE SUBHALO POPULATION

Here, we make use of the elaborate model of the subhalo population in the MW Galaxy from [3]. The authors of [3] performed an N-body simulation of MW halos of two types—that which contains only cold DM (CDM) and that which contains CDM together a baryon component. They did not reveal any significant difference between the results in these two cases. The mass range of subhalos that are resolvable in this simulation is $\sim(10^6-10^{11})\ M_\odot$. Here, we focus on the subhalo-mass range of $(10^6-10^9)\ M_\odot$, since, according to [3], all heavier subhalos contain stars; therefore, they are formally dwarf satellites. Of course, the boundary between subhalos and dwarfs involves a substantial degree of arbitrariness since these are objects of the same nature. Here, however, we do not dwell on signals from dwarfs—that is, the most massive subhalos—postponing their analysis to our future studies. As for subhalos of mass in the range of $10^6-10^9\ M_\odot$, the analysis reported in [3] predicts about 4000 such objects in MW under the assumption of a typical mass distribution, $dN/dM \sim M^{-1.9}$.

Relying on the results obtained in [3], we will now describe briefly basic properties of subhalos and the DM distribution in them. The DM density distribution within a subhalo is approximated by the Einasto profile

$$\rho(r) = \rho_s \exp\left(-\frac{2}{\alpha}\left(\left(\frac{r}{r_s}\right)^\alpha - 1\right)\right), \qquad (1)$$

where r is the distance from the subhalo center; r_s and ρ_s are the characteristic scales of the subhalo radius and density, respectively; and $\alpha = 0.16$. Figures 2 and 10 in [3] illustrate the resulting dependence of the radius r_s on the subhalo mass. One can see that these radii exhibit a rather broad spread of values for each mass. It is important to study this uncertainty in detail since, as will be seen below, gamma-ray fluxes from subhalos depend strongly on r_s. In this context, we decided to compare the results of the simulation with real data on the mass distribution within dwarf MW satellites. For this purpose, we used the results obtained in [12, 13], where the authors reproduced the mass (that is, DM, since one can disregard the stellar and gas masses) distributions in known dwarfs on the basis of observations of their kinematics. This comparison revealed that, by and large, the results reported in [3] reproduce dwarfs to a reasonable degree of precision. However, we noticed the following systematic trend: on average, the dwarfs have r_s values smaller than those predicted by the simulation—upon plotting the dwarfs in Fig. 2 from [3], one can see that they lie near the lower boundary of the cloud of points from the simulation. In this situation, we took the M_{SH} dependence of r_s in the form exhibited by real dwarfs as a realistic mean expectation—it corresponds to minimum values of r_s from the simulation in [3]. This dependence was approximated in the form

$$\log(r_s/\mathrm{kpc}) = 0.441\log(M_{200}/M_\odot) - 4.10, \qquad (2)$$

where M_{200} is the virial subhalo mass—that is, the mass within the sphere with average density $200\rho_{\mathrm{crit}}$. As a matter of fact, r_s specifies the subhalo-concentration parameter $c_{200} \approx r_{200}/r_s$, which affects strongly the gamma-ray flux from DM of the whole subhalo. The higher the concentration, the higher the flux, which depends quadratically on the DM density. Therefore, it is important to study the dependence of the gamma-ray flux on the uncertainty in the concentration model. For this purpose, we have considered, in addition to mean model specified

by Eq. (2), the extreme cases of the maximum and minimum possible fluxes: these are the maximum possible r_s in the form of the middle (blue) line in Fig. 2 [3], which are approximately twice as great as mean r_s (2), and the minimum possible ones, which are one-half as large as mean r_s. The maximum values of r_s are approximated by the equation

$$\log(r_s/\text{kpc}) = -0.111\log^2(M_{200}/M_\odot) + 2.11\log(M_{200}/M_\odot) - 10.0. \quad (3)$$

This choice of range for the possible values of r_s is not accidental: it approximately corresponds to the range of measurement uncertainties in r_s for real dwarfs according to [12].

In order to calculate the gamma-ray flux, it is also necessary to specify the distance to subhalos. This is done with the aid of Fig. 10 in [3]. Naturally, we have considered subhalos closest to the observer—they are so close that their number over the whole sky is about unity in each mass interval of width about one order of magnitude. We deduced the following approximation of the distance as a function of the mass of such subhalos:

$$\log(d_{\min}/\text{kpc}) = 0.0505\log^2(M_{200}/M_\odot) - 0.556\log(M_{200}/M_\odot) + 2.76. \quad (4)$$

This monotonic dependence yields $d_{\min}(10^6\ M_\odot) = 17$ kpc and $d_{\min}(10^9\ M_\odot) = 70$ kpc.

3. RESULTS—FLUXES AND ANGULAR SIZE OF SUBHALOS

The gamma-ray flux in the energy range $[E_{\min}...E_{\max}]$ within the solid angle $\Delta\Omega$ can be calculated by the well-known formula

$$F_\gamma(\Delta\Omega) = \frac{1}{4\pi}\frac{\langle\sigma v\rangle}{2m_\chi^2}\int\limits_{E_{\min}}^{E_{\max}}\frac{dN_\gamma}{dE_\gamma}dE_\gamma \times \int\limits_{\Delta\Omega}\int_{\text{l.o.s.}}\rho^2(\mathbf{r})dld\Omega', \quad (5)$$

where m_χ is the neutralino mass, $\langle\sigma v\rangle$ is the annihilation cross section, and dN_γ/dE_γ is the spectrum of photons produced in one annihilation event (according to calculations based on the studies reported in [14–16]). The double integral on the right of the multiplication sign in expression (5) is the so-called J factor. The spectrum of the gamma rays being considered depends substantially on the annihilation channel (that is, on primary annihilation products), which is a priori unknown. In view of this, we follow common practice, examining two representative channels: $\chi\chi \to b\bar{b}$ and $\chi\chi \to \tau^+\tau^-$. It is noteworthy that, in the most general case, the DM density $\rho(r)$ in expression (5) should include the contribution of the substructure within a subhalo in addition to the smooth component in (1). However, the substructure effect can increase the total signal from subhalos by not more than 10% (see Fig. 7 in [17]), which is beyond the accuracy of our estimations. Therefore, we disregard this effect.

Table 1. Annihilation cross sections chosen according to [18] for calculating gamma-ray fluxes from subhalos

m_χ, GeV	$\langle\sigma v\rangle(b\bar{b})$, cm^3/s	$\langle\sigma v\rangle(\tau^+\tau^-)$, cm^3/s
10	5×10^{-27}	4×10^{-27}
100	3×10^{-26}	3×10^{-26}
1000	2×10^{-25}	8×10^{-25}

By substituting the dependences in (1)–(4) into expression (5), we have calculated the expected fluxes of gamma rays for representative neutralino masses and neutralino-annihilation channels. The results are given in Fig. 1 ($E_\gamma > 100$ MeV). The annihilation cross section for each mass value was taken to be maximum possible with allowance for the current constraints obtained by the Fermi-LAT Collaboration on the basis of observations of 15 dwarf MW satellites [18] (see Table 1). We have also calculated the fluxes for the various subhalo-concentration models described in Section 2. Figure 1 shows that the flux depends rather weakly on the subhalo mass, decreasing as the mass decreases. Thus, the highest mass subhalos are the brightest, even though they are the most remote. The probability for detecting subhalos of mass below $10^6\ M_\odot$ (which are not resolvable individually within the model considered in [3]) is low. As might have been expected, the dependence on the concentration is substantially stronger—upon going over from one concentration model to another, fluxes change by about one order of magnitude. The mass of the DM particle also plays a significant role: as the mass increases, fluxes decrease very fast despite the growth of the annihilation cross section (see Table 1). It is also noteworthy that the tau-leptonic annihilation channel provides substantially lower fluxes in relation to the hadronic channel. For specific combinations of model parameters, the flux may reach 10 to 100 photons per year (we assume a normal incidence of photons to the detector), in which case this class of objects is potentially detectable with the GAMMA-400 telescope. The expected effective area of the detector was taken to be $A = 4000$ cm^2.

Figure 2*a* shows the spectrum of gamma rays from a massive subhalo for various masses of the DM particle and various annihilation channels. It

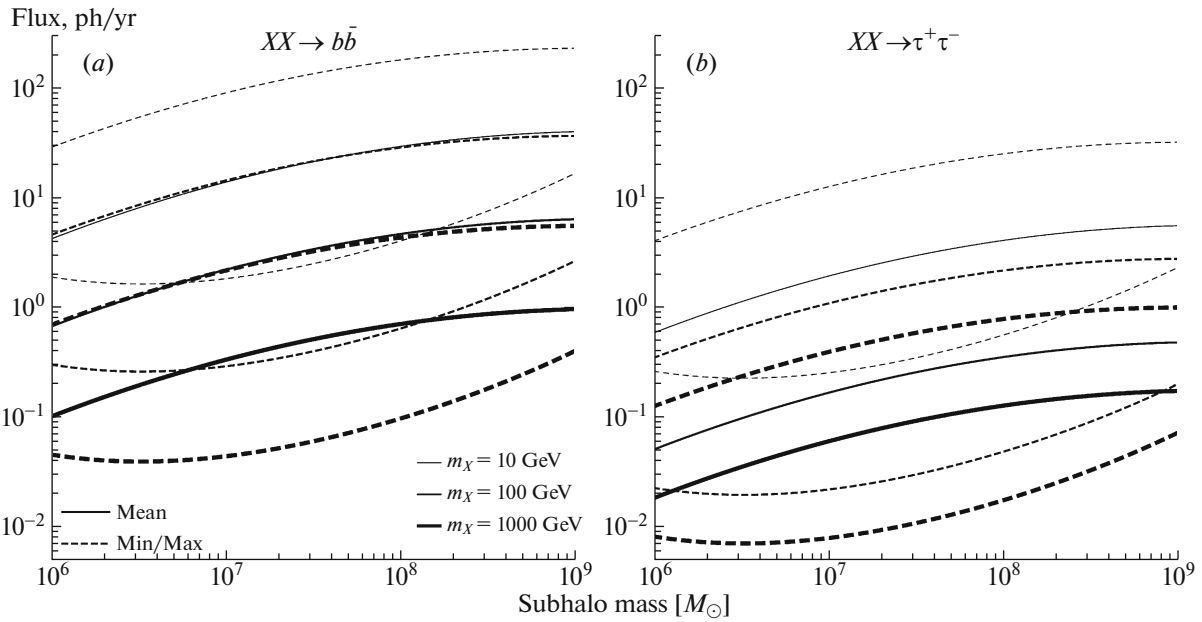


Fig. 1. Flux of gamma rays with energy above 100 MeV from the closest subhalos as a function of their mass for two representative annihilation channels. The lines of different thickness correspond to different values of the neutralino mass: 10, 100, and 1000 GeV. The solid lines represent the results obtained on the basis of the mean realistic subhalo-concentration model, while the dashed lines stand for their counterparts in the extreme cases of the minimum and maximum possible concentrations. For each mass, the annihilation cross section was set to the maximum possible value compatible with the Fermi-LAT limits from the observations of dwarfs [18] (see Table 1). The effective detector area is 4000 cm^2 (for more details, see Sections 2 and 3).

is noteworthy that the $b\bar{b}$ channel dominates over the $\tau^+\tau^-$ channel at low energies and vice versa at high energies ($E_\gamma \gtrsim 0.1 m_\chi$). That example of the distribution of the subhalo surface brightness in the range between 10 and 100 GeV which is optimal for detection is given in Fig. 2*b* along with the respective point spread function (PSF) for our instrument. We see that the subhalo brightness curve goes well above PSF within some angular-distance range before undergoing fusion with the isotropic sky background (we consider the case that is optimistic for detection and in which the subhalo being considered lies at high galactic latitudes). Thus, the convolution of the subhalo brightness distribution with PSF would be substantially different from that for a pointlike source, making it possible in principle to resolve the inner structure of the subhalo being considered and to discriminate it reliably from objects of a different class. However, the flux of photons from the whole subhalo in the above energy range is as low as about one photon per year, and this will prevent the accumulation of a sufficiently vast data sample for photons. A change in the energy range would not be helpful either, since the GAMMA-400 angular resolution decreases sharply at lower energies [10]. This problem could possibly be solved by combining future data from GAMMA-400 with data from other telescopes, such as Fermi-LAT and e-ASTROGAM, and by performing a joint analysis of these data. This would permit synthesizing the spatial image of a subhalo.

4. J2212.5+0703 AND J1924.8−1034 CANDIDATES FOR DM SUBHALOS FROM THE 3FGL CATALOG

As was mentioned in Section 1, the authors of [5–7] asserted that, in the 3FGL catalog of sources, there are two subhalo candidates—J2212.5+0703 and J1924.8−1034. They are likely to be extended objects of angular radius about 0.1°. Their spectrum is well described in terms of DM annihilation through the channel $\chi\chi \to b\bar{b}$ at a neutralino mass in the range of $m_\chi \approx 20$–40 GeV. The authors of [6, 7] assumed a thermal annihilation cross section of $\langle\sigma v\rangle \approx 3 \times 10^{-26}$ cm^3/s in their fits to the spectrum of signals from the candidates. We would like to indicate that this cross-section value is overly large for the above masses of the DM particle—Fermi-LAT limits [18] allow cross sections that are severalfold smaller. We rescaled the required J-factor values reproducing the measured fluxes from these objects by employing realistic values for the annihilation cross section and found that $J \geqslant 5 \times 10^{20}$ GeV^2 cm^{-5}. All known dwarf satellites have $J \lesssim 10^{20}$ GeV^2 cm^{-5} [20]. Thus, we see that the subhalo candidates require

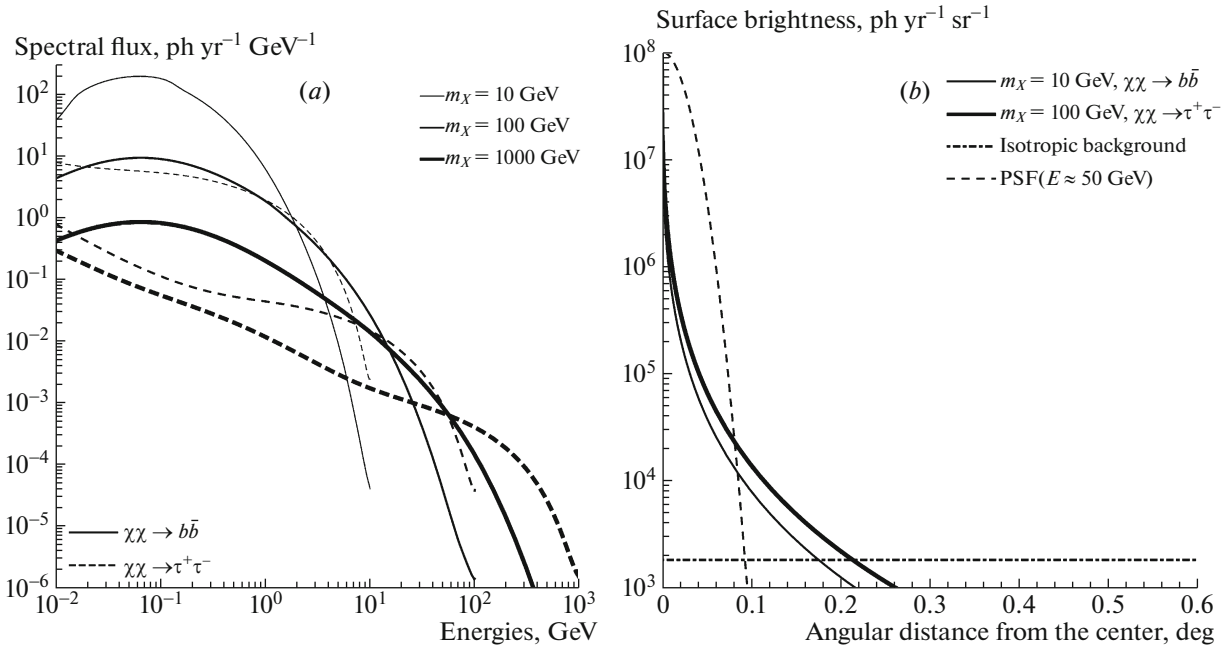


Fig. 2. (*a*) Spectra of a nearby subhalo with mass $10^9\ M_\odot$ for various neutralino masses and various annihilation channels. The annihilation cross section was chosen in just the same way as for Fig. 1, and the mean realistic model was assumed for the DM subhalo concentration. (*b*) Example of the surface-brightness distribution for the case of a nearby subhalo with mass $10^9\ M_\odot$ in the energy range from 10 to 100 GeV. The model of the high subhalo concentration was chosen. This model provides a flux of approximately one photon per year in the above energy range. The dashed line stands for an approximate telescope point spread function. The horizontal line represents the brightness of the isotropic sky background according to Fermi-LAT data from [19]. The right boundary of the graph (at about 0.6°) corresponds to the distance $r = r_s$ for the subhalo being considered.

anomalously high values of J. The absence of a substantial stellar population in such objects seems highly improbable. The only possibility for them to be dark is that they are light subhalos situated extremely close to the observer. We fitted the distances to such subhalos to the measured gamma-ray flux from them. In doing this, we took two representative mass values for the subhalo candidates—$10^6\ M_\odot$ and $10^9\ M_\odot$. For these values, we obtained distances of, respectively, about 1 and 10 kpc (which are approximately identical for the two objects being considered). These distances contradict sharply the dependence in (4). Also, this contradiction can be seen more clearly from Fig. 10 in [3]: in 100 simulations of MW, no subhalo was discovered at distances smaller than about 12 kpc. Thus, the candidates under discussion do not pass either of the two simple tests—that in the J factor and that in the distance to them. On this basis, we are inclined to think that the candidates in question are typical astrophysical sources, each consisting of two sources on very close lines of sight. This possibility was also admitted in [5–7]. It is indirectly confirmed by the fact that the analysis of observational data revealed a slight deviation of the object images from a circular shape.

5. CONCLUSIONS AND DISCUSSION

We have assessed the detectability of DM subhalos in MW Galaxy with the planned GAMMA-400 gamma-ray telescope. For this purpose, we first developed a model of DM density distributions within subhalos and spatial subhalo distributions in the MW Galaxy for subhalos in the mass range of 10^6–$10^9\ M_\odot$, relying on the results reported in [3]. This made it possible to calculate gamma-ray fluxes from subhalos and the morphology of subhalos for various values of DM and subhalo parameters (see Figs. 1 and 2). We can formulate the following brief conclusions: (i) The integrated gamma-ray flux from subhalos depends rather weakly on the subhalo mass, but it depends rather strongly on the DM concentration and on the mass of the DM particle. The most massive subhalos are the brightest. (ii) For the neutralino mass that is the most realistic at the present time (about 100 GeV) and the thermal annihilation cross section, we can expect the existence of several objects on the whole sky that produce a gamma-ray flux of about 10 photons per year, with the result that such subhalos are detectable in principle with the GAMMA-400 gamma-ray telescope even in the case of rather heavy DM particles. (iii) Because of the smallness of gamma-ray fluxes, it is hardly possible to resolve the inner structure of subhalos. However, this

obstacle could possibly be sidestepped by combining and jointly processing future data from GAMMA-400 with data from other telescopes. (iv) In our opinion, the J2212.5+0703 and J1924.8−1034 candidates for DM subhalos in the 3FGL catalog are likely to be classical binary astrophysical sources.

Thus, DM subhalos are an interesting object from the point of view of DM searches by means of the GAMMA-400 gamma-ray telescope. A further study of this class of objects and an analysis of the possibilities for detecting DM in dwarf MW satellites and for setting limits on the properties of DM on this basis are planned.

ACKNOWLEDGMENTS

This work was supported by the Space Research Council of Russian Academy of Sciences and by the Roscosmos State Corporation for Space Activities.

REFERENCES

1. *Particle Dark Matter: Observations, Models and Searches,* Ed. by G. Bertone (Cambridge Univ. Press, Cambridge, 2010).
2. E. Charles, M. Sánchez-Conde, B. Anderson, R. Caputo, A. Cuoco, M. di Mauro, A. Drlica-Wagner, G. A. Gomez-Vargas, M. Meyer, L. Tibaldo, M. Wood, G. Zaharijas, S. Zimmer, M. Ajello, A. Albert, L. Baldini, et al., Phys. Rep. **636**, 1 (2016); arXiv: 1605.02016.
3. F. Calore, V. de Romeri, M. Di Mauro, F. Donato, and F. Marinacci, Phys. Rev. D **96**, 063009 (2017); arXiv: 1611.03503.
4. F. Acero, M. Ackermann, M. Ajello, A. Albert, W. B. Atwood, M. Axelsson, L. Baldini, J. Ballet, G. Barbiellini, D. Bastieri, A. Belfiore, R. Bellazzini, E. Bissaldi, R. D. Blandford, E. D. Bloom, J. R. Bogart, et al., Astrophys. J. Suppl. Ser. **218**, 23 (2015); arXiv: 1501.02003.
5. B. Bertoni, D. Hooper, and T. Linden, J. Cosmol. Astropart. Phys. **5**, 049 (2016); arXiv: 1602.07303.
6. Y.-P. Wang, K.-K. Duan, P.-X. Ma, Y.-F. Liang, Z.-Q. Shen, S. Li, C. Yue, Q. Yuan, J.-J. Zang, Y.-Z. Fan, and J. Chang, Phys. Rev. D **94**, 123002 (2016); arXiv: 1611.05135.
7. Z.-Q. Xia, K.-K. Duan, S. Li, Y.-F. Liang, Z.-Q. Shen, C. Yue, Y.-P. Wang, Q. Yuan, Y.-Z. Fan, J. Wu, and J. Chang, Phys. Rev. D **95**, 102001 (2017); arXiv: 1611.05565.
8. T.-L. Chou, D. Tanoglidis, and D. Hooper, arXiv: 1709.08562.
9. A. M. Galper, O. Adriani, R. L. Aptekar, I. V. Arkhangelskaja, A. I. Arkhangelskiy, M. Boezio, V. Bonvicini, K. A. Boyarchuk, Yu. V. Gusakov, M. O. Farber, M. I. Fradkin, V. A. Kachanov, V. A. Kaplin, M. D. Kheymits, A. A. Leonov, F. Longo, et al., Adv. Space Res. **51**, 297 (2013); arXiv: 1201.2490.
10. N. P. Topchiev, A. M. Galper, V. Bonvicini, O. Adriani, I. V. Arkhangelskaja, A. I. Arkhangelskiy, A. V. Bakaldin, S. G. Bobkov, M. Boezio, O. D. Dalkarov, A. E. Egorov, M. S. Gorbunov, Y. V. Gusakov, B. I. Hnatyk, V. V. Kadilin, V. A. Kaplin, et al., EPJ Web. Conf. **145**, 06001 (2017).
11. A. De Angelis, V. Tatischeff, M. Tavani, U. Oberlack, I. Grenier, L. Hanlon, R. Walter, A. Argan, P. von Ballmoos, A. Bulgarelli, I. Donnarumma, M. Hernanz, I. Kuvvetli, M. Pearce, A. Zdziarski, A. Aboudan, et al., Exp. Astron. **44**, 25 (2017); arXiv: 1611.02232.
12. G. D. Martinez, Mon. Not. R. Astron. Soc. **451**, 2524 (2015); arXiv: 1309.2641.
13. A. Geringer-Sameth, S. M. Koushiappas, and M. Walker, Astrophys. J. **801**, 74 (2015), 1408.0002.
14. http://www.marcocirelli.net/PPPC4DMID.html.
15. M. Cirelli, G. Corcella, A. Hektor, G. Hütsi, M. Kadastik, P. Panci, M. Raidal, F. Sala, and A. Strumia, J. Cosmol. Astropart. Phys. **3**, 051 (2011); arXiv: 1012.4515.
16. P. Ciafaloni, D. Comelli, A. Riotto, F. Sala, A. Strumia, and A. Urbano, J. Cosmol. Astropart. Phys. **3**, 019 (2011); arXiv:1009.0224.
17. Á. Moliné, M. A. Sánchez-Conde, S. Palomares-Ruiz, and F. Prada, Mon. Not. R. Astron. Soc. **466**, 4974 (2017); arXiv:1603.04057.
18. M. Ackermann, A. Albert, B. Anderson, W. B. Atwood, L. Baldini, G. Barbiellini, D. Bastieri, K. Bechtol, R. Bellazzini, E. Bissaldi, R. D. Blandford, E. D. Bloom, R. Bonino, E. Bottacini, T. J. Brandt, J. Bregeon, et al., Phys. Rev. Lett. **115**, 231301 (2015); arXiv:1503.02641.
19. https://fermi.gsfc.nasa.gov/ssc/data/access/.
20. A. Albert, B. Anderson, K. Bechtol, A. Drlica-Wagner, M. Meyer, M. Sánchez-Conde, L. Strigari, M. Wood, T. M. C. Abbott, F. B. Abdalla, A. Benoit-Lévy, G. M. Bernstein, R. A. Bernstein, E. Bertin, D. Brooks, D. L. Burke, et al., Astrophys. J. **834**, 110 (2017); arXiv: 1611.03184.

ISSN 1063-7788, Physics of Atomic Nuclei, 2019, Vol. 82, No. 6, pp. 845–854. © Pleiades Publishing, Ltd., 2019.

ELEMENTARY PARTICLES AND FIELDS
Experiment

Gammas and Charged Particles Identification in Lateral and Additional Apertures of GAMMA-400

I. V. Arkhangelskaja[1)*], A. I. Arkhangelskiy[1),2)], A. M. Galper[1),2)], A. V. Bakaldin[3)], I. V. Chernysheva[1)], E. N. Chasovikov[1)], O. D. Dalkarov[2)], A. E. Egorov[2)], Yu. V. Gusakov[2)], M. D. Kheymits[1)], A. A. Leonov[1),2)], N. Yu. Pappe[2)], M. F. Runtso[1)], Yu. I. Stozhkov[2)], S. I. Suchkov[2)], N. P. Topchiev[2)], and Yu. T. Yurkin[1)]

Received July 19, 2019; revised July 19, 2019; accepted July 19, 2019

Abstract—The GAMMA-400 (Gamma Astronomical Multifunctional Modular Apparatus) will be a new generation satellite gamma-observatory. The gamma-ray telescope GAMMA-400 consists of the anticoincidence system (top and lateral sections—ACtop and AClat), the converter-tracker (C), the time-of-flight system TOF (two sections $S1$ and $S2$), the position-sensitive and electromagnetic calorimeters (CC1 and CC2), the scintillation detectors of the calorimeter ($S3$ and $S4$) and lateral anticoincidence detectors of the calorimeter LD. Two apertures used for observation of transient events do not require the best angular resolution as for the gamma-ray bursts and solar flares from both upper and lateral directions. Additional aperture allows the particle registering from upper direction, which do not interact with converter-tracker and do not form a TOF signal. The lateral aperture allows registering of γ-quanta in perpendicular direction with respect to main axis of GAMMA-400 due to CC2, LD, $S3$, and $S4$. The thickness of CC2 in this direction is $\sim 44\ X_0$ and this allows detection of gammas, electrons and positrons with energies up to 10 TeV. The results of calculation of the fractal dimension of temporal profiles of additional aperture prototype of GAMMA-400 during its calibration using secondary positron beam of the synchrotron C-25P "PAKHRA" of Lebedev Physical Institute confirm the absence of any correlation between the AC and CC1 characteristics and correspondence of additional aperture background to Poisson statistics or Erlang one with shape parameter up to 10.

DOI: 10.1134/S1063778819660049

1. SHORT DESCRIPTION OF GAMMA-400 APERTURES

The gamma-ray telescope GAMMA-400 (Gamma Astronomical Multifunctional Modular Apparatus) consists of the anticoincidence system (top and lateral sections—ACtop and AClat), the converter-tracker (C), the time-of-flight system TOF (two sections $S1$ and $S2$), the position-sensitive calorimeter CC1, the electromagnetic calorimeter CC2, the scintillation detectors of the calorimeter ($S3$ and $S4$), and the lateral anticoincidence detectors of the calorimeter LD. A sketch of the under consideration variant of the gamma-ray telescope GAMMA-400 and its three apertures are shown in Fig. 1. Three sensor types are used in these systems: tracking coordinate detectors, plastic and inorganic scintillators [1, 2]. Double (X, Y) tracking coordinate detectors (marked as CSD in Fig. 1) are used in the converter-tracker (C) and position-sensitive calorimeter CC1. The following detectors are based on BC-408 plastics: the time-of-flight system TOF (two sections $S1$ and $S2$), top (ACtop) and lateral (AClat) sections of anticoincidence system, the scintillation detectors of the calorimeter ($S3$ and $S4$) and the lateral detectors of the calorimeter (LD) (its installation is required for particle registration from lateral directions). All detector systems ACtop, AClat, $S1-S4$, and LD consist of two sensitive layers of 1-cm thickness each [3]. Two calorimeters are made of CsI(Tl): the position-sensitive (CC1) and the electromagnetic (CC2) ones. The thickness of CC1 and CC2 is $\sim 2\ X_0$ ($\sim 0.1\ \lambda_0$) and $\sim 16\ X_0$ ($\sim 0.74\ \lambda_0$), respectively (where X_0 is the radiation length and λ_0 is the nuclear interaction length).

2. THE GAMMA-QUANTA REGISTRATION IN DIFFERENT GAMMA-400 APERTURES

The total calorimeter thickness for vertical incident particles is $\sim 18\ X_0 (\sim 0.8\ \lambda_0)$ [3] (both CC1

[1)]National Research Nuclear University MEPhI (Moscow Engineering Physics Institute), Moscow, Russia.
[2)]P.N. Lebedev Physical Institute of the Russian Academy of Sciences, Moscow, Russia.
[3)]Scientific Research Institute of System Analysis of the Russian Academy of Sciences, Moscow, Russia.
[*]E-mail: irene.belousova@usa.net

and CC2). Laterally incident particles registered by CC2 and for such events calorimeter thickness is $\sim 44\ X_0$ ($\sim 2\ \lambda_0$) [3]. There are two opportunities of particle registration using GAMMA-400: event-by-event mode and spectral one.

The GAMMA-400 is optimized for registration of γ-quanta and charged particles with energy $\sim$100 GeV with the best performance parameters achieved using the main aperture for upper incidents. The size of the main aperture is defined by the geometry of the converter-tracker (C): the gammas converted in tungsten foils are registered. The triggers in the main aperture will be formed using information about the particle direction provided by the TOF system and one about the presence of charged particles or backsplash obtained from the ACtop and AClat anticoincidence detectors in the energy band of $E > 20$ MeV for gammas and $E > 100$ MeV for electrons [4]. The gamma-ray telescope operates in event-by-event registration mode in this aperture.

The other two apertures are used for observation of transient events (gamma-ray bursts—GRBs, soft gamma repeaters (SGR), pulsars, solar flares, etc.) do not require the best angular resolution both from upper and lateral directions.

The additional aperture allows registering particles from upper direction which do not interact with the converter-tracker and do not form a TOF signal. In the additional aperture the gamma-telescope also operates in event-by-event registration mode (see panel (a) in Fig. 2). Particle detection in the additional aperture is triggered by signals from fast discriminators of CC1 individual strips in anticoincidence with TOF [4]. Up–down particle direction can be reconstructed using fast signals from individual strips of detectors CC1 and $S3$, anticoincidence in this aperture is provided by $S2$, LD, and $S4$. In this case, $S2$ and LD are used as anticoincidence detectors, with a larger energy deposition possibly signifying not only the shower propagating beyond the calorimeter, but a particle entering laterally outside of this aperture (and said particle's backsplash). These kinds of events would be undistinguishable within the margin of error. Therefore, only $S4$ is used as a leakage detector in this case, with energy deposition it signifies that the shower propagated beyond CC2. In this case, only a lower limit of the particle energy can be obtained. The analysis of the $S3$ energy deposition shows whether the shower starts propagating in CC1 or not. In this case it is an electromagnetic cascade, because a nuclear cascade starts propagating deeper due to the small CC1 thickness being only $\sim 2\ X_0$ ($\sim 0.1\ \lambda_0$). Moreover, it also gives a rough estimate of the primary particle energy.

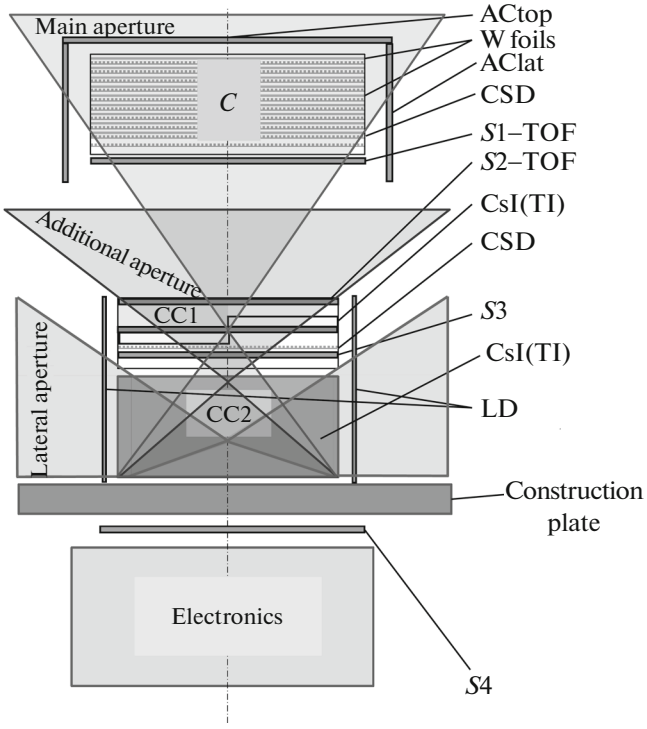


Fig. 1. The sketch of the under-consideration variant of GAMMA-400 telescope [1–3] and its three apertures [4]: main, additional, and lateral. The following detectors are based on BC-408 plastics: the time-of-flight system TOF, the anticoincidence system AC, the scintillation detectors of the calorimeter ($S3$ and $S4$) and the lateral detectors of the calorimeter (LD). The top section of the anticoincidence system ACtop consisst of two layers; each contains 13 strips with dimensions of $128 \times 10 \times 1$ cm^3. The lateral one AClat consists of four detectors and also includes two layers; each contains 13 strips but with size of $60 \times 10 \times 1$ cm^3. The time-of-flight system TOF consists of two detectors $S1$ and $S2$; each includes two layers. The layers of $S1$ contain 10 strips with dimensions of $100 \times 10 \times 1$ cm^3 every, but the ones of $S2$ include 8 strips with dimensions of $80 \times 10 \times 1$ cm^3 each. The scintillation detectors of the calorimeter ($S3$ and $S4$) are similar to $S2$. The lateral detectors of the calorimeter LD are similar to AClat. The position-sensitive calorimeter CC1 consists of two parts, each contains 16 crystals based on CsI(Tl) with dimensions of $40 \times 5 \times 4$ cm^3 ($\sim 2\ X_0$ and $\sim 0.1\ \lambda_0$). The electromagnetic calorimeter CC2 includes 23×23 crystals based on CsI(Tl) with dimensions of $29 \times 3.6 \times 3.6$ cm^3 ($\sim 16\ X_0$ and $\sim 0.74\ \lambda_0$). Double (X, Y) tracking coordinate detectors CSD consist of combination of layers using 100-cm-long scintillating fibres in converter-tracker C and 80-cm-long ones in CC1. Fibres are similar to those used in Scintillating Fibre tracker (SciFi) of upgraded LHCb experiment in CERN [5, 6].

A positron beam with energy of 300 MeV [7] was used for the calibration of prototypes of GAMMA-400 detectors at the synchrotron "PAKHRA". The prototype of the additional aperture of GAMMA-400

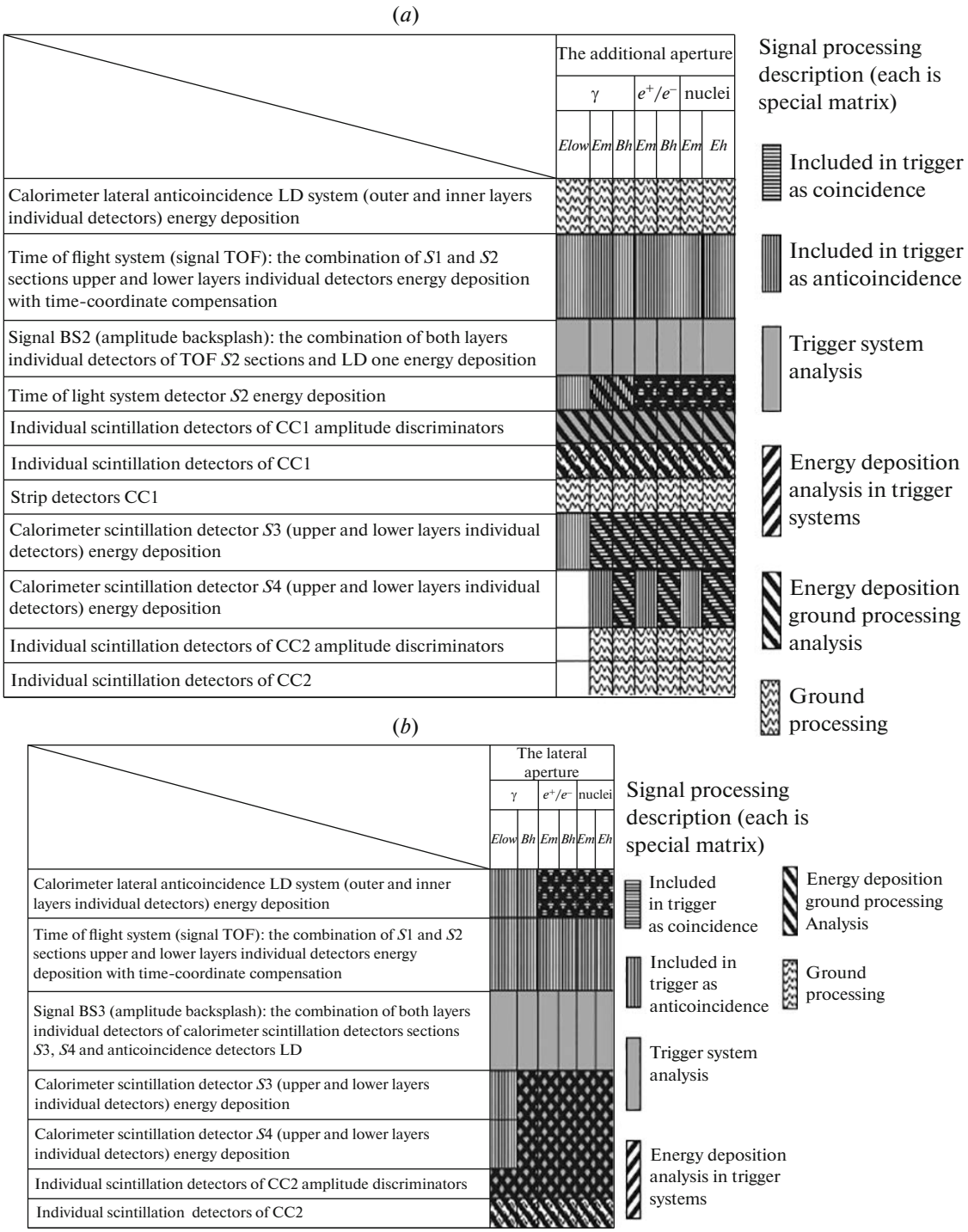


Fig. 2. The detector response analysis matrix for triggers and trigger markers signals formation matrixes for the additional (*a*) and lateral (*b*) apertures (adopted from [4]).

consists of two detectors. One of them is the BC-408-based one with dimensions of $128 \times 10 \times 1$ cm^3 (one detecting strip from the AC prototype) and the other is composed of a CsI(Tl) crystal with dimensions of $33 \times 5 \times 2$ cm^3 (one block of CC1 prototype) [8, 9]. We calculated the fractal dimension of temporal profiles measured during calibrations of the AC/LD and CC1 prototypes. The preliminary results are 1.50 ± 0.05 and 1.48 ± 0.08, respectively [9]. These results confirm the absence of any correlation between these detectors' characteristics and that the background of this aperture obeys Poisson statistics or Erlang one with shape parameter up to 10.

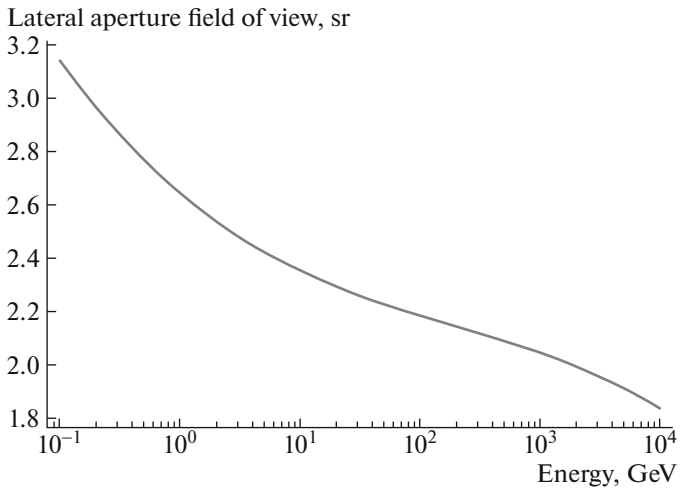


Fig. 3. The dependence of lateral aperture field of view on initial γ-quantum energy.

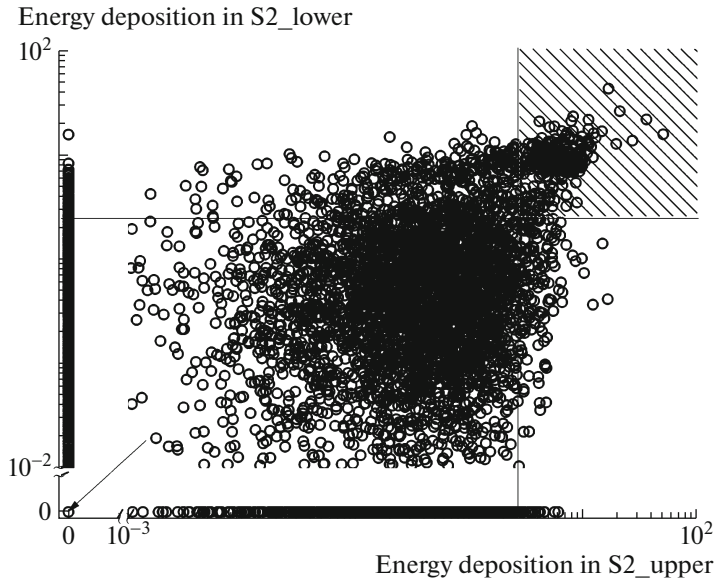


Fig. 4. The results of simulation of total energy deposition distributions in $S2$ (both upper and lower layers) for subsets of 7500 gammas with $E = 3$ GeV. Vertical and horizontal lines together with dashed area represent energy threshold for charged particles registration 2.8 MeV. Approximately 15% of gammas are in this area and be recognized as electrons, but ~85% of γ-quanta can be detected. Arrow marked area contains events with energy deposition less than 1 keV in both $S2$ layers constituted ~70%.

For particle identification only signals from each individual detecting unit of detectors system without any summation are analyzed. Thus, we used individual signals from an ADS placed from two sides of long scintillators. However, backsplash should be taken into account. This effect occurs when low-energy charged particles (mostly electrons from electromagnetic shower) and gammas moved backward relatively to the incident particle due to particle production in their interactions with the detectors and construction materials and reverse scattering of secondary particles. Because of these particles interact with detectors working in anticoincidence mode, the γ quantum could be identified as a charged particle [10]. But backsplash for the γ quantum starts only 1 X_0 after it first interaction. Therefore, even without using the converter, showers for electrons and gammas have different signature. Thus, if gammas were converted at the end of the first 1 X_0, its backsplash was formed only during the second X_0 and should move back through the material of detector and be absorbed. The results of 3-GeV γ-quanta interaction inside $S2$ are presented in Fig. 4. It was confirmed that ~85% of gammas can be detected in additional

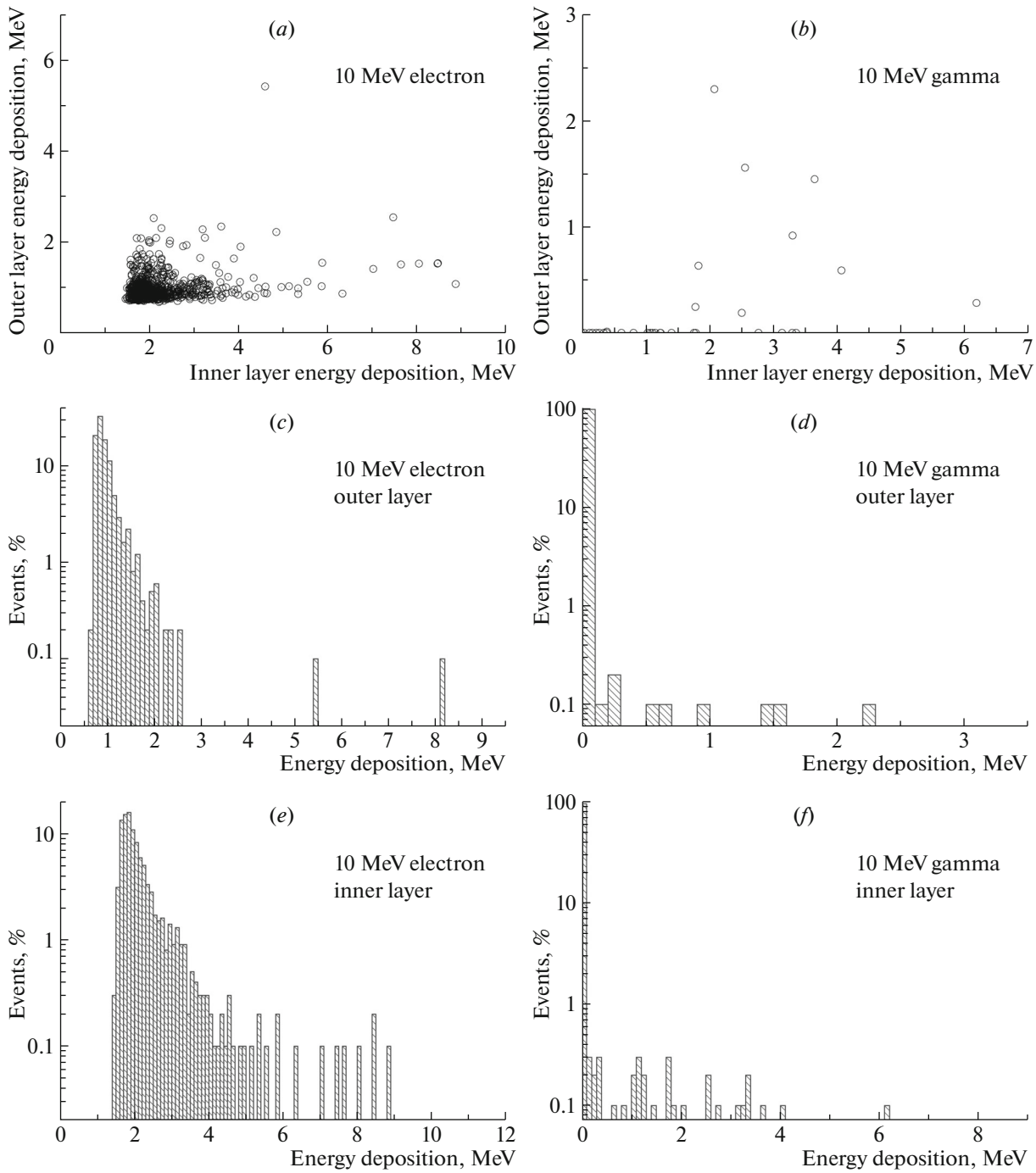


Fig. 5. The comparison of the results from simulations of 10 MeV gammas and electrons energy deposition inside both layers of individual detector of LD which particle incident.

aperture and the backsplash can be effectively rejected using the energy deposition analysis in both layers of $S2$.

The energy band for gamma registration in this aperture in the event-by-event mode is similar to the main one. The angular resolution is provided by the layer of double (X, Y) tracking coordinate detectors in the CC1. The reconstruction of the starting point position of the electromagnetic shower is realized due to the methods analogous to the technique used in accelerator (so-called "center-of-gravity technique") allowing accuracy $\sim$1 mm for electrons (positrons) with $E \sim 8$ GeV—for example, in experiments BTeV [11] and PANDA [12]. The additional aperture can be used in the spectral mode for the study and correction (in addition to main scientific purposes) of the energy

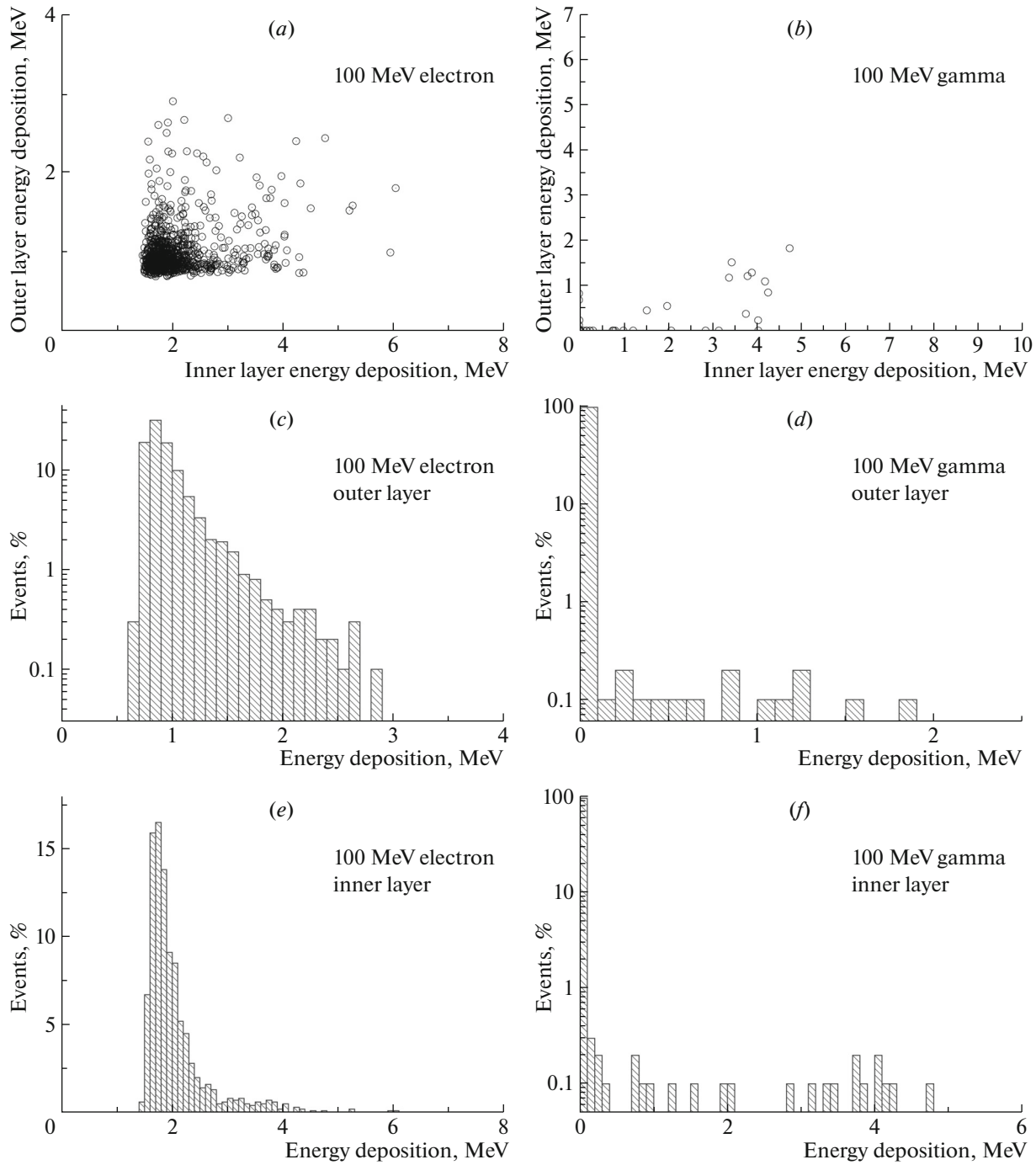


Fig. 6. The comparison of the results from simulations of 100 MeV gammas and electrons energy deposition inside both layers of individual detector of LD which particle incident.

spectra of known source and non-stationary events, such as solar flares, GRBs, SGR, pulsars, etc. in the energy band $E > 1$ MeV. At the same time, the particles' direction determining is possible for low-energy events (the energy range is defined for each event depending on the flux, so the count speed during the count spike length would be at least several standard deviations higher than the background) by comparing count speeds of separate detectors in CC1 similar to BATSE (Burst And Transient Source Experiment onboard Compton Gamma Rays Observatory) algorithm for transient sources (see [13] and references therein) and KONUS detectors [14].

In the cases, where the event entry direction is known and the determination of the position of the high-energy source is not necessary (solar flares,

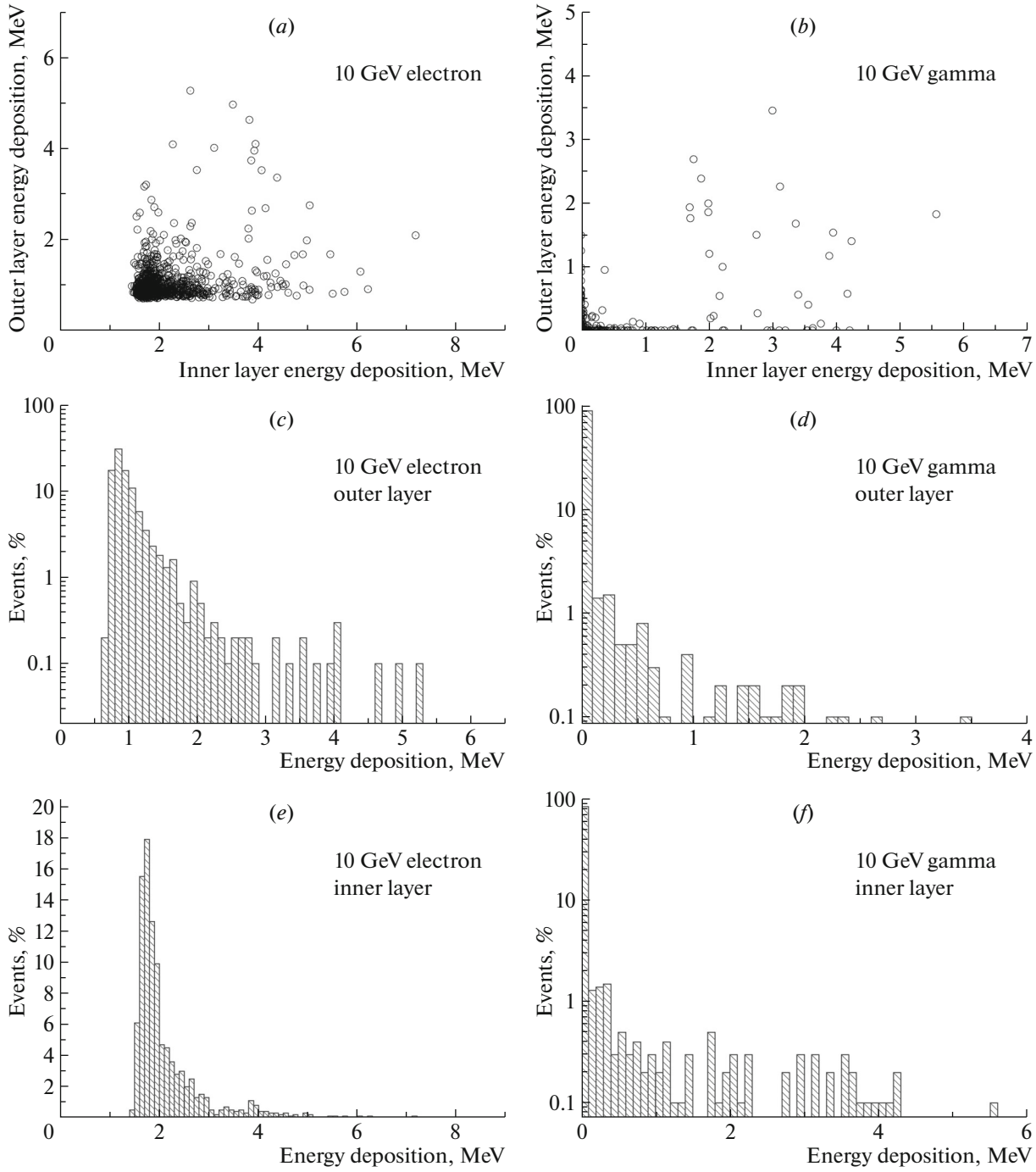


Fig. 7. The comparison of the results from simulations of 10 GeV gammas and electrons energy deposition inside both layers of individual detector of LD which particle incident.

GRBs, SGRs, bright pulsars, etc.), the CC2 lateral aperture can be used to register γ-quanta. The event detection in this aperture is triggered with a signal from fast discriminators of CC2 individual strips in anticoincidence with TOF pulse and CC1 individual strips fast discriminators. The γ-quanta of higher energies can be identified using energy deposition in the individual strips of LD, $S3$, $S4$ and fast signals from discriminators of CC2 individual detectors (see panel (*b*) on Figs. 2). For this aperture, the energy resolution is determined only by CC2 calorimeter, with full effective depth for lateral aperture being $\sim$44 X_0 or $\sim$2.0 λ_0. It allows to increase maximal detectable γ-quanta energy up to several TeV—see lateral aperture field of view dependence on initial γ-quantum energy presented in Fig. 3. The $S2$, $S3$,

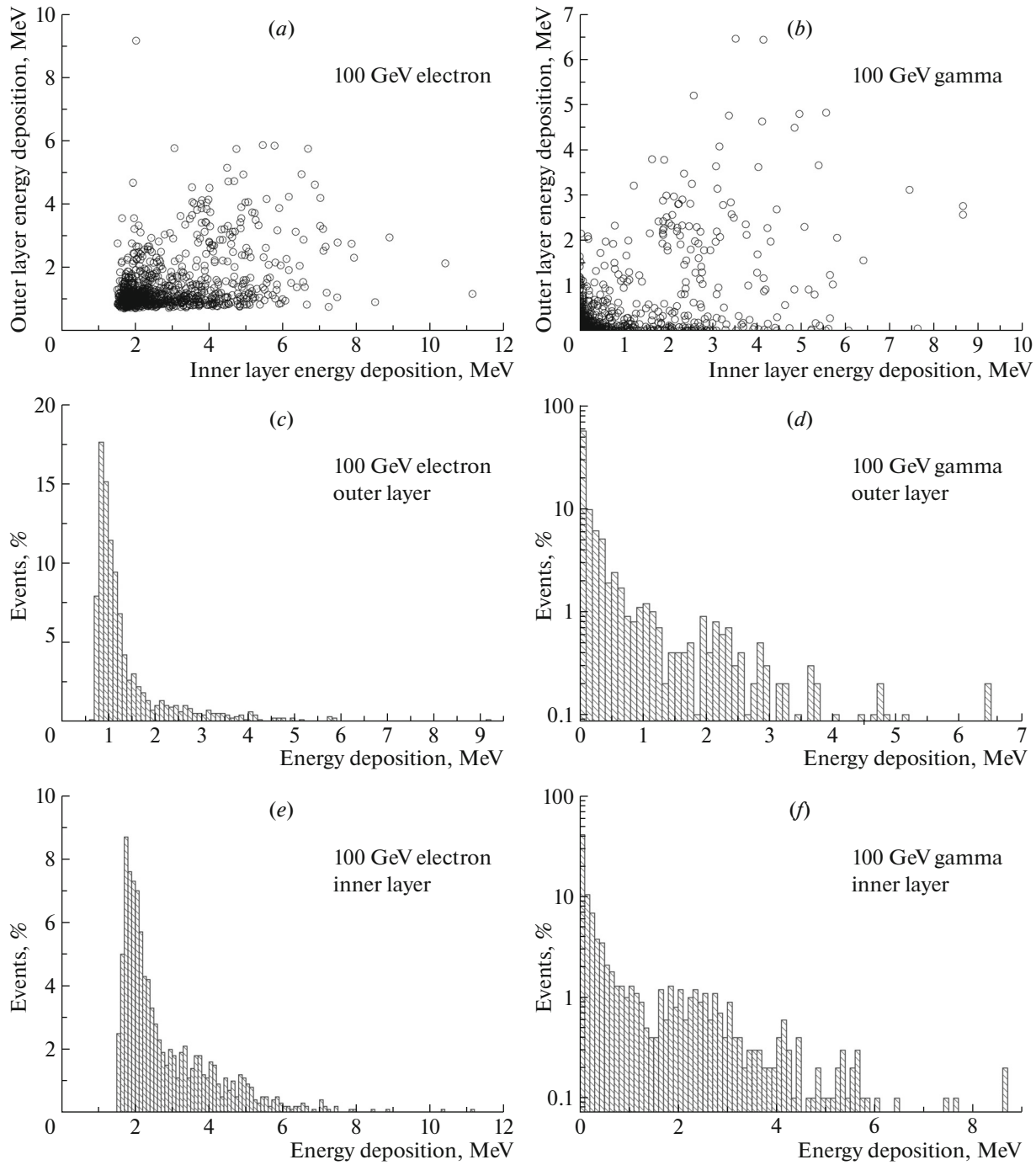


Fig. 8. The comparison of the results from simulations of 100 GeV gammas and electrons energy deposition inside both layers of individual detector of LD which particle incident.

$S4$, and LD detectors are used as anticoincidence detectors, with high-energy deposition in $S2$ indicating primary particle entry from above the aperture. In this case, $S3$ and $S4$ are used as leakage detectors, with high-energy deposition signaling shower egress beyond CC2. The backsplash effect mostly rejected due double layered LD. The results from simulations of gammas and electrons passing through lateral aperture in each layer of individual detector LD which particle incident are shown in Figs. 5–8 for energies of 10 MeV, 100 MeV, 10 GeV, and 100 GeV, respectively. The results of these figures' analysis are presented in Table 1. Using combination of energy thresholds with values of 0.5 and 1.0 MeV it is possible to provide a detector efficiency of ~96% for gammas in the energy band of 10–100 MeV and

Table 1. Trigger activation probability for γ-quanta in lateral aperture

Energy deposition threshold		Trigger activation probability for γ-quantum of a given energy			
Outer layer, MeV	Inner layer, MeV	10 MeV	100 MeV	10 GeV	100 GeV
0.5	0.5	96%	96%	90%	60%
0.5	1.0	96%	97%	92%	66%
1.0	0.5	96%	96%	92%	64%
1.0	1.0	96%	97%	93%	71%

$\sim$92% at $E \sim 10$ GeV. Only 60% of γ-quanta will be registered at $E \sim 100$ GeV but it is possible to increase this value up to $\sim$70% due to LD energy resolution improvement.

Low-energy photons are recognized by simple anticoincidence signals from the individual detectors of LD and registered in the spectral mode with acquisition time scaled depending on the count rate of the detectors. The angular resolution will be $\sim 5^\circ$ vertical segments only for the γ-quanta with energies of 0.2–10 MeV in the lateral aperture obtained from the CC2 individual detectors count rate analysis for non-stationary events only (GRB and so on). The applied method looks like the KONUS [11] and the BATSE algorithm for transient sources (see [11] and references therein). One side of the calorimeter will be solar oriented to support solar panels functioning and cooling radiator located from its other three sides. It allows to use a part of lateral aperture for solar flares investigation.

3. CONCLUSION

The gamma-ray telescope GAMMA-400 consists of an anticoincidence system (top and lateral sections—ACtop and AClat), the converter-tracker (C), the time-of-flight system (two sections $S1$ and $S2$), the position-sensitive calorimeter CC1, the electromagnetic calorimeter CC2, the scintillation detectors of the calorimeter ($S3$ and $S4$) and the lateral anticoincidence detectors of the calorimeter LD. The two apertures used for observation of the transient events do not require best angular resolution as gamma-ray bursts and solar flares from both upper and lateral directions. The additional aperture allows particle detection from upper directions, which do not interact with converter-tracker and do not form a TOF signal. The results of simulation of 3 GeV γ-quanta interaction inside the double-layered $S2$ confirm that $\sim$85% of gammas can be registered in the additional aperture and backsplash is effectively rejected using energy deposition analysis in both layers of $S2$.

The lateral aperture allows registering γ-quanta incident in perpendicular direction with respect to the main axis of GAMMA-400 due to CC2, LD, $S3$ and $S4$. The thickness of CC2 in this direction is $\sim 44\ X_0$ and it allows the detection of gammas, positrons and electrons with energies up to 10 TeV. The field of view of the gamma-ray telescope varies from 3.1 sr (at $E \sim 0.1$ GeV) down to 1.8 sr (at $E \sim 10$ TeV). Using combination of LD energy thresholds with values of 0.5 and 1.0 MeV it is possible to provide backsplash rejection and a detector efficiency of $\sim$96% for gammas in the energy band of 10–100 MeV and $\sim$92% at $E \sim 10$ GeV. Only 60% of γ-quanta will be registered at energy $\sim$100 GeV but it is possible to increase this value up to $\sim$70% due to LD energy resolution improvement.

We have calculated the fractal dimension of temporal profiles measured during calibrations of the AC/LD and CC1 prototypes using positron beam of the synchrotron C-25P "PAKHRA" of Lebedev Physical Institute. Preliminary results confirm the absence of any correlation between these detectors' characteristics and correspondence of the additional aperture background to the Poisson statistics or Erlang one with shape parameter up to 10.

ACKNOWLEDGMENTS

Authors thank for the support from National Research Nuclear University MEPhI in the framework of the Russian Academic Excellence Project (contract no. 02.a03.21.0005, 27.08.2013).

REFERENCES

1. N. P. Topchiev, A. M. Galper, V. Bonvicini, O. Adriani, R. L. Aptekar, I. V. Arkhangelskaja, A. I. Arkhangelskiy, L. Bergstrom, E. Berti, G. Bigongiari, S. G. Bobkov, E. A. Bogomolov, M. Boezio, M. Bongi, S. Bonechi, S. Bottai, et al., Bull. Russ. Acad. Sci. Phys. **79**, 417 (2015).
2. A. M. Galper, O. Adriani, R. L. Aptekar, I. V. Arkhangelskaja, A. I. Arkhangelskiy, M. Boezio, V. Bonvicini, K. A. Boyarchuk, Yu. V. Gusakov, M. O. Farber, M. I. Fradkin, V. A. Kachanov,

V. A. Kaplin, M. D. Kheymits, A. A. Leonov, F. Longo, et al., Adv. Space Res. **51**, 297 (2013).
3. A. A. Leonov, A. M. Galper, N. P. Topchiev, A. V. Bakaldin, O. D. Dalkarov, E. A. Dzhivelikyan, A. E. Egorov, M. D. Kheymits, V. V. Mikhailov, P. Picozza, R. Sparvoli, S. I. Suchkov, Yu. T. Yurkin, and V. G. Zverev, Adv. Space Res. **63**, 3420 (2018).
4. I. V. Arkhangelskaja, A. I. Arkhangelskiy, E. N. Chasovikov, A. M. Galper, M. D. Kheymits, A. E. Murchenko, and Y. T. Yurkin, J. Phys.: Conf. Ser. **675**, 032015 (2016).
5. P. Hopchev, in *Proceedings of the Fifth Annual LHCP* (Shanghai, China, 2017), arXiv: 1710.08325v1 (2017).
6. A. Obłąkowska-Mucha and T. Szumlak, Nucl. Instrum. Methods A **824**, 62 (2016).
7. G. A. Sokol, T. A. Aibergenov, A. V. Koltsov, A. V. Kravtsov, Yu. I. Krutov, A. I. L'vov, L. N. Pavlyuchenko, V. P. Pavlyuchenko, and S. S. Sidorin, AIP Conf. Proc. **549**, 411 (2000).
8. A. I. Arkhangelskiy, A. M. Galper, I. V. Arkhangelskaja, A. V. Bakaldin, E. N. Chasovikov, I. V. Chernysheva, O. D. Dalkarov, A. E. Egorov, Yu. V. Gusakov, M. D. Kheymits, A. A. Leonov, N. Yu. Pappe, M. F. Runtso, Yu. I. Stozhkov, S. I. Suchkov, et al., J. Phys.: Conf. Ser. (2019) (in press).
9. I. V. Arkhangelskaja, A. I. Arkhangelskiy, E. N. Chasovikov, S. I. Suchkov, M. F. Runtso, Y. T. Yurkin, A. M. Galper, N. P. Topchiev, A. A. Leonov, and A. E. Egorov, J. Phys.: Conf. Ser. **1181**, 012083 (2019).
10. W. B. Atwood, A. A. Abdo, M. Ackermann, W. Althouse, B. Anderson, M. Axelsson, L. Baldini, J. Ballet, D. L. Band, G. Barbiellini, J. Bartelt, D. Bastieri, B. M. Baughman, K. Bechtol, D. Bédérède, F. Bellardi, et al., Astrophys. J. **697**, 1071 (2009).
11. V. A. Batarin, J. Butler, A. A. Derevschikov, Y. M. Goncharenko, V. N. Grishin, V. A. Kachanov, V. Y. Khodyrev, A. S. Konstantinov, V. I. Kravtsov, Y. Kubota, Y. A. Matulenko, Y. M. Melnick, A. P. Meschanin, N. E. Mikhalin, N. G. Minaev, V. V. Mochalov, et al., Nucl. Phys. B Proc. Suppl. **150**, 262 (2006).
12. P. A. Semenov, Yu. V. Kharlov, A. V. Uzunian, S. K. Chernichenko, A. A. Derevschikov, A. M. Davidenko, Y. M. Goncharenko, V. A. Kachanov, A. S. Konstantinov, V. A. Kormilitsin, Yu. A. Matulenko, A. P. Meschanin, Y. M. Melnick, N. G. Minaev, V. V. Mochalov, D. A. Morozov, et al., Nucl. Instrum. Methods A **598**, 224 (2009).
13. J. Hakkila, Research Reports: NASA/ASEE Summer Faculty Fellowship Program, SEE N91–18967 10-99 (Alabama Univ., 1990).
14. E. P. Mazets and S. V. Golenetskii, Astrophys. Space Sci. **75**, 47 (1981).

ISSN 1063-7788, Physics of Atomic Nuclei, 2020, Vol. 83, No. 2, pp. 252–257. © Pleiades Publishing, Ltd., 2020.

ELEMENTARY PARTICLES AND FIELDS
Experiment

The Anticoincidence System of Space-Based Gamma-Ray Telescope GAMMA-400, Test Beam Studies of Anticoincidence Detector Prototype with SiPM Readout

A. I. Arkhangelskiy[1),2)*], A. M. Galper[1),2)], I. V. Arkhangelskaja[2)], A. V. Bakaldin[3)], I. V. Chernysheva[2)], O. D. Dalkarov[1)], A. E. Egorov[1)], Yu. V. Gusakov[1)], M. D. Kheymits[2)], A. A. Leonov[1),2)], N. Yu. Pappe[1)], M. F. Runtso[2)], Yu. I. Stozhkov[1)], S. I. Suchkov[1)], N. P. Topchiev[1)], and Yu. T. Yurkin[2)]

Received July 11, 2019; revised July 11, 2019; accepted July 11, 2019

Abstract—The GAMMA-400 gamma-ray telescope is planned for the launch at the end of 2026 on the Navigator service platform designed by Lavochkin Association on an elliptical orbit with following initial parameters: an apogee ∼300 000, a perigee ∼500 km, a rotation period ∼7 days and inclination of 51.4°. The apparatus is expected to operate for more than 5 years, reaching an unprecedented sensitivity for the search of dark matter signatures and the study of the unresolved and so far unidentified gamma-ray sources. The segmented anticoincidence counters surround the converter-tracker and calorimeter of the telescope with the purpose of vetoing to assure a clean track reconstruction and charged particle background suppression. The anticoincidence detector prototype based on long BC-408 scintillator with silicon photomultipliers readout was tested using 300-MeV positron beam of synchrotron C-25P "PAKHRA" of Lebedev Physical Institute. The measurement setup, design concepts for the prototype detector together with test results are discussed.

DOI: 10.1134/S1063778820020039

1. INTRODUCTION

The scientific project GAMMA-400 [1, 2] is one of the new generation of space observatories intended for an indirect search for signatures of dark matter in the cosmic-ray fluxes, precision investigation of the characteristics of diffuse gamma-ray emission and gamma-rays from the Sun during periods of solar activity, gamma-ray bursts, extended and point gamma-ray sources in the wide energy range from several tens of MeV up to the TeV region, electron/positron and cosmic-ray nuclei fluxes with energies up to $\sim 10^{15}$ eV by means of the GAMMA-400 gamma-ray telescope that represents the core of the scientific complex, installed on the Navigator service platform [3] designed by Lavochkin Association. For gamma rays with the energy ∼100 GeV the expected energy and angular resolution are ∼2% and ∼0.01° respectively and the electron/proton rejection factor is $\sim 5 \times 10^5$. In Fig. 1 the physical model of the gamma-ray telescope is presented. The C designates the converter-tracker consisting of 13 layers of double (x, y) tracking coordinate detectors with total thickness about $1X_0$ (radiation length). The first 11 layers are interleaved with tungsten conversion foils (first 7 layers of $0.1X_0$ and next 4 layers of $0.025X_0$). The last two layers have no tungsten. The data from the converter-tracker is used for high precision determination of the gamma-quanta conversion point and reconstruction of the trajectory of the primary and secondary charged particles. The ACS is segmented anticoincidence system (135 scintillator strips) which includes one top detector $\mathrm{AC}_{\mathrm{top}}$ and four lateral detectors $\mathrm{AC1}_{\mathrm{lat}}$–$\mathrm{AC4}_{\mathrm{lat}}$ surrounding convertor-tracker for discrimination between incoming charged particles and gamma-quanta with an efficiency of $\geqslant$99.95%. All anticoincidence counters, as well as LD, $S3$, and $S4$ are made of two oriented in parallel layers of 1-cm thickness, 10-cm width BC-408 polyvinyltoluene scintillator strips with different length. The strips of one layer are displaced with respect to the strips of the other layer so that there are no rectilinear slits in the system. The TOFS—time-of-flight system, consists of hodoscope of four oriented perpendicularly layers of 1-cm thickness, 10-

[1)]Lebedev Physical Institute, Russian Academy of Sciences, Moscow, Russia.
[2)]National Research Nuclear University MEPhI (Moscow Engineering Physics Institute), Moscow, Russia.
[3)]Scientific Research Institute of System Analysis, Russian Academy of Sciences, Moscow, Russia.
[*]E-mail: AIArkhangelskij@mephi.ru

cm width, 100-cm (top) and 80-cm (bottom) length BC-408 plastic scintillation counters combined in two detector planes $S1$ and $S2$ located at the distance of 50 cm between the convertor-tracker C and calorimeter CC. The TOFS provides a fast trigger to gamma-ray telescope readout electronics by measuring the particles charge, crossing time and position, and separates upward from downward going particles within 10^{-3} level. The CC is an 80×80 cm^2, $\sim 16X_0$ thick coordinate-sensitive calorimeter to measure the incoming particles energy with resolution of $\sim 2\%$ for gamma-rays with $E_\gamma \geqslant 100$ GeV and separate $e^\pm$ and photons from hadrons at $\sim 5 \times 10^{-5}$ level. The CC includes preshower CC1 (consists of two CsI(Tl) planes with total thickness of $\sim 2X_0$, two layers of double (x, y) tracking coordinate detectors and fast plastic scintillation detector $S3$), the total-absorption calorimeter CC2, based on the set of CsI(Tl) crystals $\sim 16X_0$ thick, the anticoincidence LD and leakage $S4$ plastic detectors. Four fast plastic detectors ACS, TOFS, $S3$ and $S4$ are included in fast trigger logic in the main telescope aperture.

The space-based gamma-ray telescope must effectively separate photons from charged particles of instrumental background and cosmic rays. The anticoincidence system (ACS) of gamma-ray telescopes is suffered from the self-veto (backsplash) effect when the products of the high-energy photon interactions in the instrument's calorimeter, mainly low-energy electromagnetic shower particles moving in the direction opposite to the direction of the detected photons, cause a veto signal in the ACS, resulting in the degradation of the efficiency for high-energy (>5 GeV) gamma rays. One method of this self-veto effect reduction is segmenting the ACS into tiles and vetoing an event only if the pulse appears in the tile through which the reconstructed event trajectory passes [4]. Further improvement is time-based backsplash rejection technique [5] based on ignoring the veto signals in appropriate segments of ACS within the time interval in which backsplash particles hit the ACS. This time interval start moment and duration depend on the detector geometry and for the GAMMA-400 telescope averages out from 3 ns to 12 ns after TOFS triggering. It requires the intrinsic time resolution of TOFS and ACS segments better than 500 ps for effective self-vetoing suppression. In this case the proton impurity in the selected gamma rays and the loss of useful events do not exceed 10^{-5} and 10% respectively [6].

2. EXPERIMENTAL SETUP

The tested detector presents two strips of polyvinyltoluene scintillator BC-408 with dimensions of $1280 \times 100 \times 10$ mm^3, wrapped with one layer of Tyvek

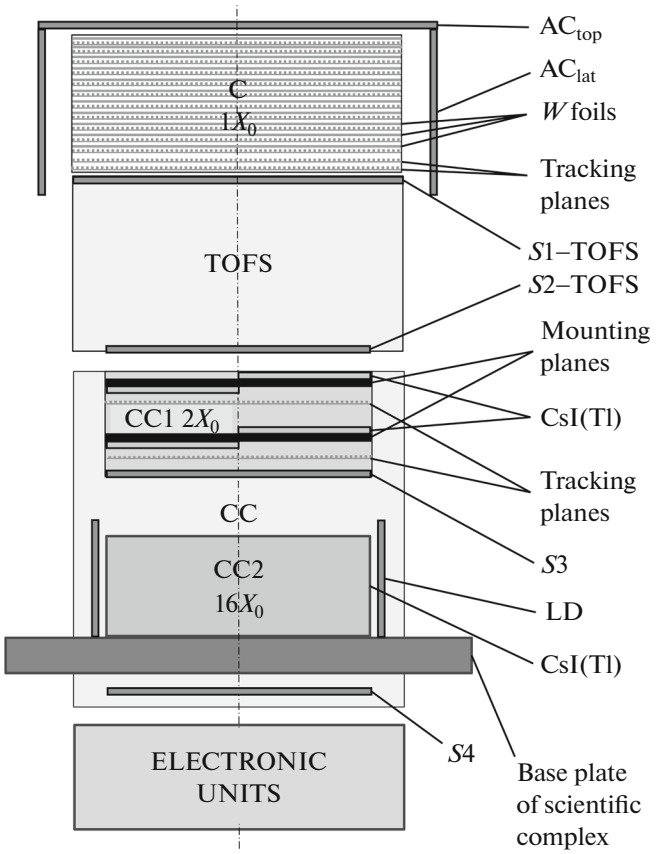


Fig. 1. Sketch of the GAMMA-400 gammaray telescope.

reflective material and placed into 1.5-mm thick aluminum cover. At the middle of each strip the FC-type fiber optic adapters are situated for optic cables' connection from laser monitoring system. Each strip is viewed at the opposite shortest ends by two photo-sensor blocks which consist of four 6×6 mm^2 silicon photomultipliers (SiPM) of the type SensL MicroFC-60035-SMT [7] connected in parallel and frontend electronics. Only "slow" SiPM outputs were used in this prototype variant. The amplified and shaped signals from both sides of the detector are split into two paths: the first signal goes directly to the LeCroy WaveRunner 6Zi digital oscilloscope, for amplitude and charge analysis, and the second signal goes through the constant fraction discriminator (CFD) ORTEC Model 935 for timing analysis. Threshold of CFD was set at about 25% of the most probable energy deposited by minimum-ionizing particles crossing the whole thickness of the scintillator (10 mm). The bias voltage for SiPMs was set at 29.5 V level (~5 V above SiPM breakdown voltage).

The primary beam of the synchrotron C-25P "PAKHRA" of Lebedev Physical Institute consists

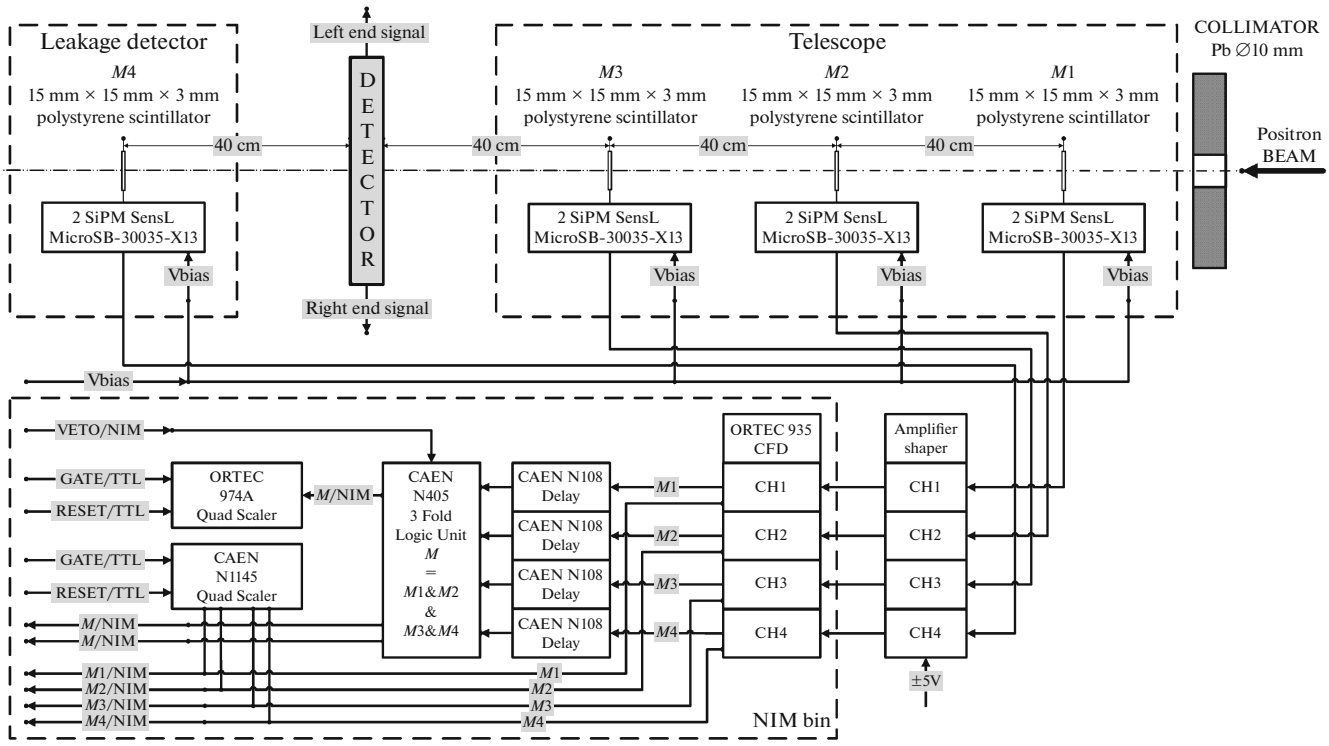


Fig. 2. The functional diagram of experimental setup. The dash–dotted line represents the positron beam line. The NIM and TTL signatures mark type of logical signals.

of 300–850 MeV electrons with particle intensity up to 2×10^{12} s^{-1} and repetition frequency of 50 Hz. Bremsstrahlung photon beam is formed by the interaction of accelerated electrons with an internal tungsten target with a thickness of $0.22X_0$ (X_0—radiation length) placed inside the accelerator vacuum chamber. This beam is used to create a secondary positron beam by $e\pm$ pair production on copper converter with 0.1–5 mm thickness. Secondary positrons with particle momentum of 300 MeV/c and intensity up to $\sim$100 s^{-1} cm^{-2} are selected using dipole magnet. The studied detector was installed on a remote controlling platform which allows horizontally and vertically moves of the detector with respect to the beam position in the range of $\pm$40 cm with the accuracy of 1 mm. A beam monitor for secondary positrons' selection installed behind the 10-mm diameter lead collimator consists of four $15 \times 15 \times 3$ mm^3 polystyrene (IHEP_SC-301) scintillation counters $M1$-$M4$ wrapped with aluminized mylar film and coupled with silicon grease BC-630 from one side with two 3×3 mm^2 SensL MicroSB-30035-X13 SiPMs connected in parallel. These counters are installed on high-precision horizontal and vertical slide positioners for finely positioning of the monitor counters with respect to the positron beam (range $\pm$6.5 mm with 10-μm accuracy). The signals from each SiPM pair are amplified by two-stage broad-band shaper-amplifiers with pole-zero cancellation circuits based on fast AD8000 operational amplifiers, produced output signals with rise-time of $\sim$3.5 ns and width of $T_{90} \sim 10$ ns. The

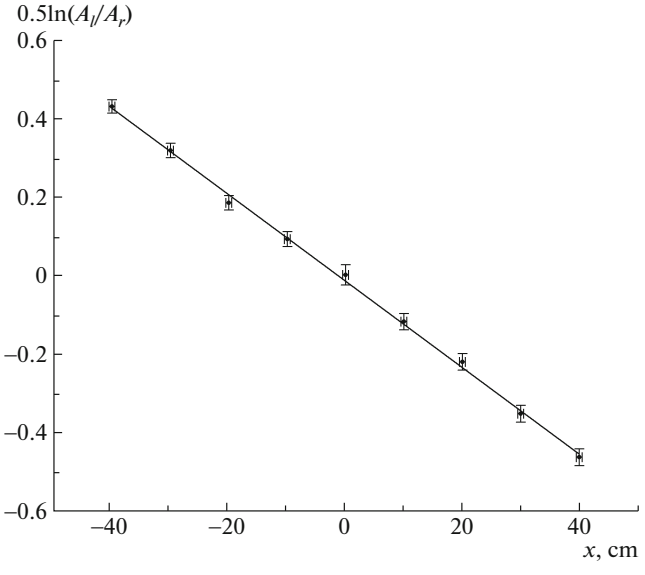


Fig. 3. Logarithmic ratio of amplitude of signals from the left and right ends of prototype detector. The inverse slope of the linear fit indicates the attenuation length $\lambda = 91 \pm 1$ cm of scintillation light in the scintillator strip.

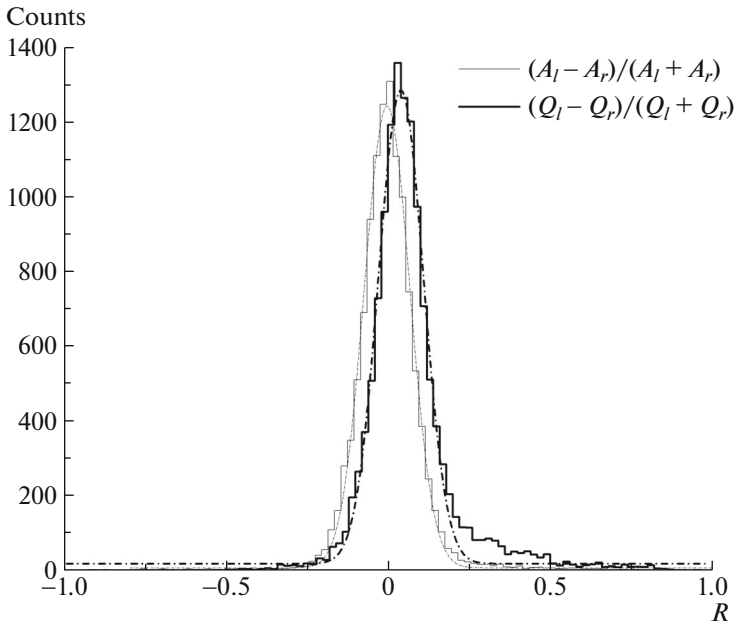


Fig. 4. The distributions of the ratio R for positron beam position in the center of tested prototype detector. Full thin and thick lines match the amplitude and charge measurements respectively, dash–dot lines—to corresponding Gaussian approximations.

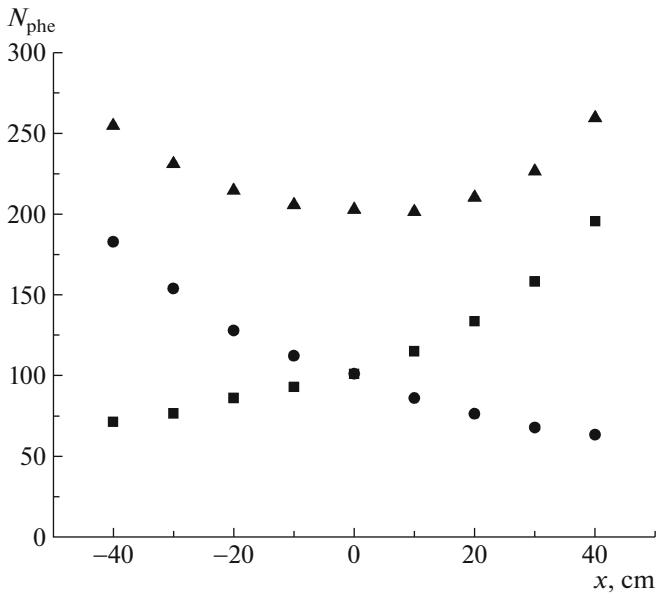


Fig. 5. Average total number of photoelectrons registered per incident positron at each end of the prototype detector strip as a function of the beam impact position relative to the detector centre. The squares present data for the left strip end, circles—for the right end, triangles—for left and right end sum. Error bars are smaller than the points on the plot.

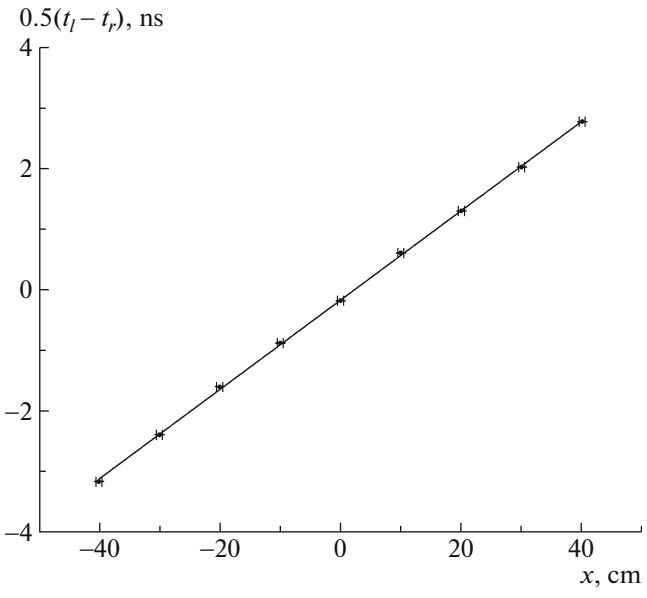


Fig. 6. Straight line fit to the semi-resultant of times of scintillation light arriving at the strip ends at different beam positions relative to the detector centre. The inverse slope of the fit gives the effective scintillation light velocity $v = 13.1 \pm 0.1$ cm ns^{-1} in the prototype detector strip.

amplified and shaped signals are fed into the four-channel CFD (ORTEC Model 935). The CFD outputs are connected through the set of delay lines to the coincidence the logic unit (CAEN Model N405) which generates the reference start time pulse $M = M1 \wedge M2 \wedge M3 \wedge M4$ for the positrons' registration. Two quad scalers are used for counting $M1$–$M4$ and M pulses. The beam monitor time resolution

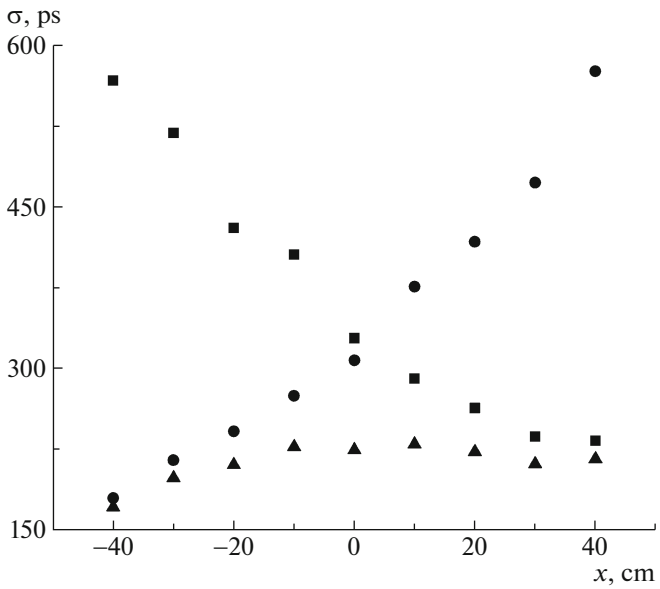


Fig. 7. The time resolution measured at each end of the prototype detector strip as a function of the beam impact position relative to the detector centre. The squares are data for the left strip end, circles—for the right end, triangles—combined time resolution σ_{lr} at both ends obtained as $1/1\sigma_{lr}^2 = 1/\sigma_l^2 + 1/\sigma_r^2$. Error bars are smaller than the points on the plot.

was measured as 104 ± 2 ps. The beam monitor functional diagram is shown in Fig. 2.

3. STUDIES OF THE PROTOTYPE DETECTOR

To characterize the prototype detector, the measurements of the following parameters defined its time resolution were carried out: attenuation length, photostatistics, effective light velocity and intrinsic time resolution. The statistics at each data point is about 10^4 for all results presented. The measurements of the absolute detection efficiency require much greater beam intensity to reach suitable accuracy in a reasonable accelerator time than the defined above secondary positron beam intensity and are in preparation now at the primary beam of synchrotron C-25P "PAKHRA".

3.1. Attenuation Length

Assuming that the light attenuation can be approximated by a single exponential function, we can formulate the following relations for light attenuation in the scintillator:

$$A_l(x) = C_l \exp\left(-\frac{\frac{L}{2} - x}{\lambda}\right), \qquad (1)$$

$$A_r(x) = C_r \exp\left(-\frac{\frac{L}{2} + x}{\lambda}\right).$$

Here, L and λ represent the length and attenuation length of the scintillator; x denotes the hit position from the center of the scintillator; A_l and A_r are measured signal amplitudes from the left and right scintillator ends. Appropriate proportionality constants C_l and C_r depend on the stopping power of charged particles, light attenuation due to optical couplings between the scintillator and photosensor block, etc. Taking the ratio of the above two equations, the attenuation length λ can be expressed as:

$$0.5 \ln \frac{A_l}{A_r} = \frac{1}{\lambda} x + 0.5 \ln \frac{C_l}{C_r}, \qquad (2)$$

which is a straight-line equation of the variable $y(x) = 0.5 \ln (A_l/A_r)$ with the inverse slope parameter of λ. The measured A_l/A_r distributions for different x positions were fitted with a Gaussian. The mean values of the Gaussian distributions for the prototype detector are plotted in Fig. 3. A least-square ?t to a straight line gives $\lambda = 91 \pm 1$ cm, which is approximately one fourth of the attenuation length for a bulk scintillator [8].

3.2. Photostatistics

The measurement of charge or amplitude of the detector output signals allows estimating the lower limit of the total number of photoelectrons produced by the particles into the scintillator. Assuming g_i—gain and ε_i—efficiency of the photosensor blocks ($i = l$, r—left and right counter sides' indexes) are equalized, i.e. $g_i \times \varepsilon_i = \text{const}$; $N_{\text{phe}} = N_{\text{phe}}^l + N_{\text{phe}}^r$ is the total number of photoelectrons collected at both sides of the counter; Q_i and A_i are the measured charge and amplitude of signals and $Q_i = \text{const} \times A_i = g_i \varepsilon_i N_{\text{phe}}^i$ one can write:

$$R = \frac{Q_l - Q_r}{Q_l + Q_r} = \frac{A_l - A_r}{A_l + A_r} = \frac{N_{\text{phe}}^l - N_{\text{phe}}^r}{N_{\text{phe}}^l + N_{\text{phe}}^r} \qquad (3)$$
$$= \frac{N_{\text{phe}}^l - N_{\text{phe}}^r}{N_{\text{phe}}} = \frac{2N_{\text{phe}}^l}{N_{\text{phe}}} - 1.$$

Supposing that N_{phe}^l follows a binomial distribution, N_{phe} and standard deviation on R are given by:

$$\sigma_R = \frac{2}{N_{\text{phe}}} \sqrt{N_{\text{phe}} p (1-p)} = \frac{1}{\sqrt{N_{\text{phe}}}}, \qquad (4)$$
$$p = \frac{1}{2}, \quad \text{and} \quad N_{\text{phe}} = \frac{1}{\sigma_R^2}.$$

In Fig. 4 the distributions of the ratio R for the positron beam impact in the center of the tested prototype detector are shown. The corresponding total photoelectron numbers 203 ± 3 for amplitude measurements and 209 ± 6 for charge measurements match the statistical errors. In Fig. 5 the average photoelectron yield per incident positron is presented as a function of the beam position.

3.3. Timing Measurements

For studying the prototype detector timing properties the distributions of three time intervals for the set of positron beam positions along the strip were analyzed: $(t_l - t_M)$, $(t_r - t_M)$, and $(t_l - t_r)$. Here t_l and t_r are the measured signal arriving times from each end of the strip and t_M is the trigger reference signal M moment from the positron beam monitor. The measured distributions were fitted by the Gaussian function and the resulting mean values and standard deviations were used for further analysis.

The positron position x along the strip is determined as $x = 0.5v\,(t_l - t_r)$. The effective speed of scintillation light propagation v along the strip is calculated by linear fitting of expression $0.5\,(t_l - t_r) = x/v$ as inverse value of the fit slope. The corresponding result is presented in Fig. 6. The time resolutions σ_l and σ_r for each end of the scintillator strip are shown in Fig. 7 together with combined resolution $\sigma_{lr} = \sigma_l\sigma_r/\sqrt{\sigma_l^2 + \sigma_r^2}$ as a function of the beam position along the strip relative to the strip centre. All resolutions shown represent the fitted Gaussian standard deviation of the corresponding distributions, corrected for the resolution of the beam monitor and uncertainty due to finite size of the positron beam ($\sim$1 cm). As expected, the time resolutions σ_l and σ_r worsen with the increase in distance of the beam position from respective SiPMs block. The combined time resolution is the worst ($\sim$230 ps) at the centre of the strip due to the less light collected by SiPMs.

4. CONCLUSION

The prototype detector on the base of $1280 \times 100 \times 10$ mm^3 BC-408 polyvinyltoluene scintillator strips with readout at both ends by photosensor blocks consisting of four SiPMs of the type SensL MicroFC60035-SMT was developed for carrying out a series of experiments in order to study amplitude, triggering and timing characteristics of the anticoincidence system of the GAMMA-400 gamma-ray telescope. The properties of the prototype are measured using 300-MeV/c secondary positron beam of the synchrotron C-25P "PAKHRA" of Lebedev Physical Institute. The intrinsic time resolution of the prototype detector is found to be not worse than 230 ps which is enough for reliable suppression of the backsplash events. The measured effective scintillation light velocity is 13.1 ± 0.1 cm ns^{-1}. The measured attenuation length is 91 ± 1 cm, which is one quarter of the corresponding length of a bulk scintillator. This value is about 1.5 times less than the one expected and can be explained by degradation of the scintillator strip (the microcracks net was disclosed on the scintillator surface after thorough inspection). For further improvement of the prototype parameters the defective strip was replaced, the number of SiPMs at each detector end was increased up to 8 instead of currently used 4 SiPMs and the new type of silicon photomultipliers SensL MicroFJ-60035-TSV with enhanced photon detection efficiency and lower dark count rate were employed for obtaining the better photoelectron statistics and time resolution. The "fast" SiPM outputs were used as a source of signal for timing measurements too.

ACKNOWLEDGMENTS

The authors thank for the support from National Research Nuclear University MEPhI in the framework of the Russian Academic Excellence Project (contract no. 02.a03.21.0005, 27.08.2013).

REFERENCES

1. N. P. Topchiev, A. M. Galper, V. Bonvicini, O. Adriani, R. L. Aptekar, I. V. Arkhangelskaja, A. I. Arkhangelskiy, L. Bergstrom, E. Berti, G. Bigongiari, S. G. Bobkov, E. A. Bogomolov, M. Boezio, M. Bongi, S. Bonechi, S. Bottai, et al., Bull. Russ. Acad. Sci. Phys. **79**, 417 (2015).
2. A. M. Galper, N. P. Topchiev, and Yu. T. Yurkin, Astron. Rep. **62**, 882 (2018).
3. A. S. Syrov, V. V. Smirnov, V. N. Sokolov, G. S. Iodko, V. V. Mischihin, V. N. Kosobokov, M. A. Shatsky, and D. A. Dobrynin, Cosmonaut. Rocket Engin. **3**, 58 (2015).
4. A. A. Moiseev, R. C. Hartman, J. F. Ormes, D. J. Thompson, M. J. Amato, T. E. Johnson, K. N. Segal, and D. A. Sheppard, Astropart. Phys. **27**, 339 (2007).
5. M. D. Kheymits, A. M. Galper, I. V. Arkhangelskaja, A. I. Arkhangelskiy, Yu. V. Gusakov, V. G. Zverev, V. V. Kadilin, V. A. Kaplin, A. A. Leonov, P. Yu. Naumov, M. F. Runtso, S. I. Suchkov, N. P. Topchiev, and Yu. T. Yurkin, Instrum. Exp. Tech. **59**, 508 (2016).
6. I. V. Arkhangelskaja, A. I. Arkhangelskiy, E. N. Chasovikov, A. M. Galper, M. D. Kheymits, A. E. Murchenko, and Y. T. Yurkin, J. Phys.: Conf. Ser. **675**, 032015 (2016).
7. K. O'Neill and C. Jackson, Nucl. Instrum. Methods A **787**, 169 (2015).
8. Organic Scintillation Materials and Assemblies, Saint Gobain Crystals (Web document accessed June 2019). https://www.crystals.saint-gobain.com/sites/imdf.crystals.com/files/documents/organics-plastic-scintillators.pdf.

ISSN 1063-7788, Physics of Atomic Nuclei, 2021, Vol. 84, No. 6, pp. 1053–1058. © Pleiades Publishing, Ltd., 2021.

ELEMENTARY PARTICLES AND FIELDS
Experiment

GAMMA-400 Gamma-Ray Observations in the GeV and TeV Energy Range

N. P. Topchiev[1)*], A. M. Galper[1),2)], I. V. Arkhangelskaja[2)], A. I. Arkhangelskiy[2)], A. V. Bakaldin[3)], R. A. Cherniy[1)], I. V. Chernysheva[2)], O. D. Dalkarov[1)], A. E. Egorov[1)], M. D. Kheymits[2)], M. G. Korotkov[2)], A. A. Leonov[1),2)], A. G. Malinin[2)], V. V. Mikhailov[2)], P. Yu. Minaev[1),4)], N. Yu. Pappe[1)], M. F. Runtso[2)], A. I. Smirnov[1)], Yu. I. Stozhkov[1)], S. I. Suchkov[1)], and Yu. T. Yurkin[2)]

Received July 22, 2021; revised July 22, 2021; accepted July 22, 2021

Abstract—The future space-based GAMMA-400 γ-ray telescope will operate onboard the Russian astrophysical observatory in a highly elliptic orbit during 7 years. Observing γ-ray sources from Galactic plane, γ-ray bursts, γ-ray diffuse emission, γ rays from the Sun, and γ rays from dark matter particles will be performed uninterruptedly for a long time ($\sim$100 days) in point-source mode in contrast to scanning mode for Fermi-LAT and other space- and ground-based instruments. GAMMA-400 will measure γ rays in the energy range from $\sim$20 MeV to several TeV units, have the unprecedented angular ($\sim$0.01° at $E_\gamma = 100$ GeV) and energy ($\sim$2% at $E_\gamma = 100$ GeV) resolutions better than for Fermi-LAT, as well as ground-based γ-ray facilities, by a factor of 5–10, and perfectly separate γ rays from cosmic-ray background.

DOI: 10.1134/S106377882113038X

1. INTRODUCTION

At present Fermi-LAT performs observations of γ-ray emission in space. The fourth Fermi-LAT catalog (4FGL) contains 5065 sources for the energy range from 50 MeV to 1000 GeV, but $\sim$30% of γ-ray sources are unidentified [1]. The ground-based facilities VERITAS, MAGIC, H.E.S.S., HAWC and others observe only 243 γ-ray sources in the energy range above 100 GeV (http://tevcat.uchicago.edu/).

A very interesting and important goal in the studies of γ-ray sky is to search for dark matter (DM). WIMPs with mass between several GeV units and several TeV units are still considered as the most probable candidate. WIMPs can annihilate or decay with the production of γ rays. This emission can have both a continuous energy spectrum or monoenergetic narrow lines. Up to now, there are no data on DM γ-ray lines from space- and ground-based instruments. Other DM candidates are ALPs from nearby supernova explosion.

Another urgent problem is to search for and study γ-ray bursts (GRBs). Despite the discovery of 186 GRBs with Fermi-LAT and GBM [2] it represents an initial step in understanding the processes behind high-energy emission from γ-ray bursts.

2. THE GAMMA-400 GAMMA-RAY TELESCOPE

The GAMMA-400 γ-ray telescope [3–6] and additional instruments (ART-XC X-ray telescope and magnetic plasma detectors) will be installed onboard the Russian space astrophysical observatory (Fig. 1). Gamma- and X-ray telescopes are installed coaxially without overlapping fields of view.

GAMMA-400 includes high data transmission radio complex with high gain antenna. As a ground receiving station, it is proposed to use the radio-astronomy complex based on the RT-22 radio-telescope in Pushchino (Lebedev Physical Institute), the same station as for Radioastron mission (Spectr-R) (Fig. 2).

The GAMMA-400 main scientific goals are: precise uninterrupted up to $\sim$100 days measurements of Galactic Center, Fermi Bubbles, Crab, Vela, Cygnus, Geminga, Sun, and other regions, extended and point γ-ray sources, GRBs, diffuse γ rays, dark matter searching with unprecedented angular ($\sim$0.01° at

[1)] P. N. Lebedev Physical Institute of the Russian Academy of Sciences, Moscow, Russia.
[2)] National Research Nuclear University MEPhI (Moscow Engineering Physics Institute), Moscow, Russia.
[3)] Scientific Research Institute for System Analysis of the Russian Academy of Sciences (SRISA), Moscow, Russia.
[4)] Space Research Institute, Moscow, Russia.
[*] E-mail: tnp51@yandex.ru

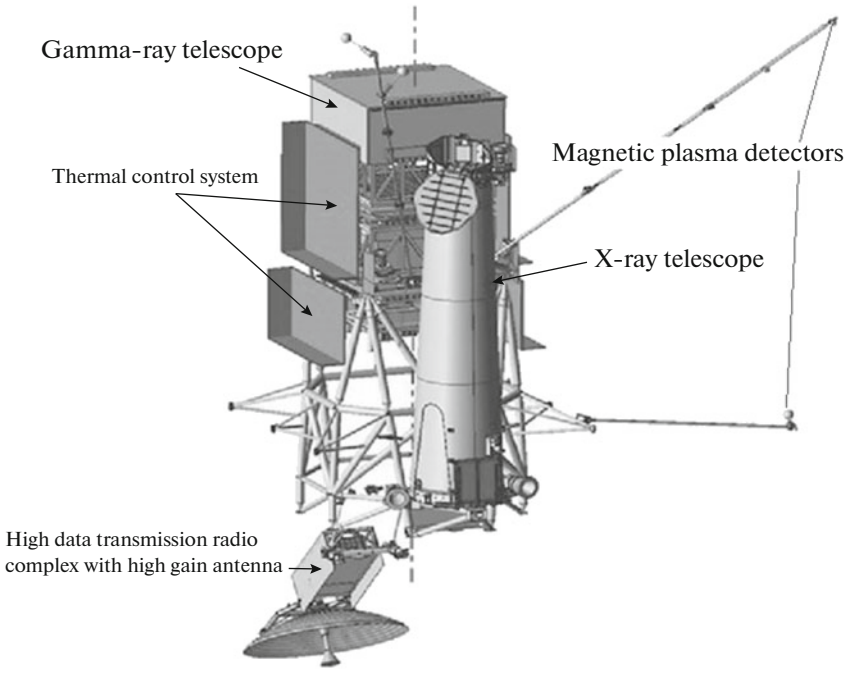


Fig. 1. GAMMA-400 scientific complex including GAMMA-400 γ-ray telescope and additional instruments: ART-XC X-ray telescope, magnetic plasma detectors, high data transmission radio complex with high gain antenna, thermal control system.

$E_\gamma = 100$ GeV) and energy ($\sim$2% at $E_\gamma = 100$ GeV) resolutions.

2.1. The GAMMA-400 Physical Scheme

The physical scheme of the GAMMA-400 γ-ray telescope is shown in Fig. 3.

GAMMA-400 includes:

—plastic scintillation anticoincidence top AC top (1280 $\times$ 1280 mm) and four lateral AC lat (1280 $\times$ 600 mm) detectors with efficiency of 0.99995 and time resolution of 200 ps;

—converter-tracker (C), consisting of 13 pairs of planes of scintillating fiber detectors (X and Y coordinates, 1000 $\times$ 1000 mm) and analog readout. The first 7 and 4 pairs have W converter foils of 0.1 X_0 and 0.025 X_0 thick each, respectively. The last 2 pairs have no W;

—time-of-flight system (ToF) consisting of plastic scintillation detectors (S1 and S2, 1000 $\times$ 1000 mm) spaced by 500 mm with coefficient of separation for top/down moving particles of 1000 and time resolution of 200 ps;

—the calorimeter (CC1 and CC2). CC1 (800 $\times$ 800 mm) consists of CsI(Tl) scintillation crystals and scintillating fiber detectors (X and Y coordinates) without W. CC2 (800 $\times$ 800 mm) consists of 22 $\times$ 22 CsI(Tl) crystals. Total thickness of calorimeter is $\sim$18 X_0 ($\sim$0.9 λ_0) and $\sim$42 X_0 ($\sim$2.0 λ_0) for vertical and lateral particle detection, respectively;

—four lateral scintillation detectors (LD) for detecting lateral particles;

—plastic scintillation detectors (S3 and S4, 800 $\times$ 800 mm) for improving hadronic and electromagnetic shower separation.

After interaction of incident γ rays with the GAMMA-400 detector matter the backscattering omnidirectional particles (mainly, 1-MeV photons) are arisen. In order to exclude backscattering particles, all scintillation detectors consist of two independent 10-mm layers and fast timing methods are used.

The GAMMA-400 energy range for γ-ray studies is from $\sim$20 MeV to several TeV. The field of view (FoV) for detecting particles from top-down directions is $\pm 45^\circ$. In GAMMA-400, the common trigger $(\overline{\mathrm{AC}} \times \mathrm{ToF})|(\mathrm{S3} \times \mathrm{ToF})$ is used for detecting low- and high-energy particles.

Moreover, GAMMA-400 can detect γ rays from lateral directions using trigger $\overline{\mathrm{LD}} \times \overline{\mathrm{S_3}} \times \overline{\mathrm{S_4}} \times \mathrm{CC_2}$.

2.2. The GAMMA-400 Performance

Model calculations of the GAMMA-400 γ-ray telescope performance were carried out using the "GEANT4.10.01.p02" software package. As a result of calculations, we obtained the following dependences:



Fig. 2. RT-22 radio-telescope in Pushchino as a ground receiving station.

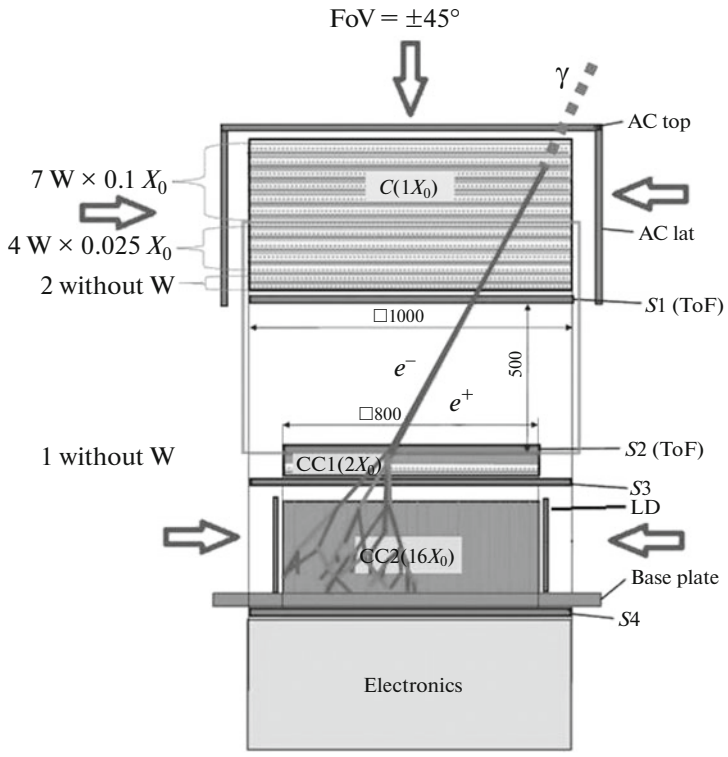


Fig. 3. GAMMA-400 γ-ray telescope physical scheme. GAMMA-400 consists of anticoincidence system AC (top and lateral detectors), converter-tracker C, time-of-flight system ToF from scintillation detectors $S1$ and $S2$, two parts of calorimeter CC1 and CC2, lateral detectors LD, scintillation detectors of the calorimeter $S3$ and $S4$.

—the angular resolution vs the energy (Fig. 4). The angular resolution for $E_\gamma = 100$ GeV is $\sim 0.01°$;

—the energy resolution vs the energy (Fig. 5). The energy resolution for $E_\gamma = 100$ GeV is $\sim 2\%$.

Using the combined information from all GAMMA-400 detector systems, it is possible to reach an effective rejection of protons from electrons. The methods to separate electrons from protons presented in [7] are based on the difference of the

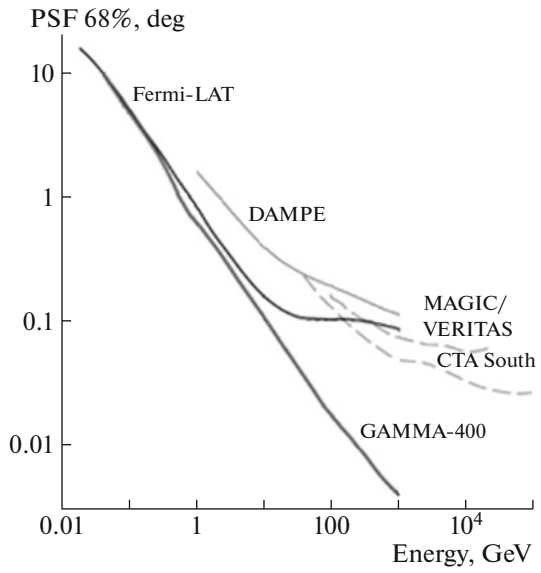


Fig. 4. The angular resolution vs the energy for GAMMA-400, Fermi-LAT, DAMPE, MAGIC, VERITAS, CTA.

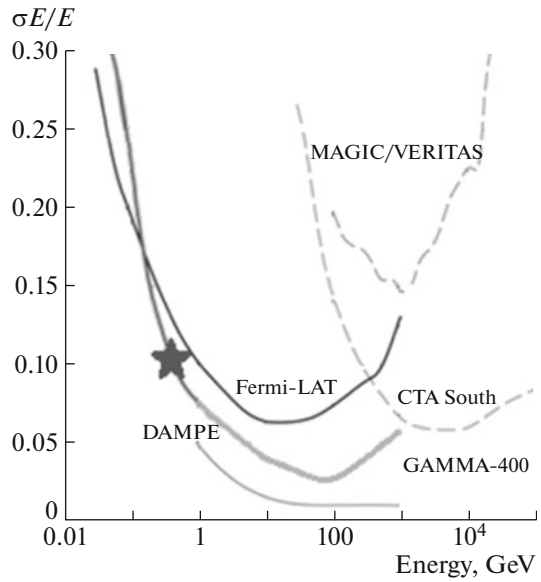


Fig. 5. The energy resolution vs the energy for GAMMA-400, Fermi-LAT, DAMPE, MAGIC, VERITAS, CTA. GAMMA-400 experimental energy resolution of 10% for the energy of 300 MeV obtained at LPI electron synchrotron in Troitsk is marked with an asterisk.

development of hadronic and electromagnetic showers inside the instrument. For the current physical scheme the rejection factor for vertical protons is about 3×10^5.

For testing and calibrating, prototypes from some detector systems were manufactured and calibrated on positron beams at the S-25R electron synchrotron (Lebedev Physical Institute, Troitsk) in the energy range of 100–300 MeV.

2.3. The GAMMA-400 Astrophysical Observatory

The GAMMA-400 scientific payload will be installed onboard of the Navigator space platform, which is designed and manufactured by the Lavochkin Association and includes the γ-ray telescope, an X-ray telescope, and magnetic plasma detectors.

Using the Navigator space platform gives the GAMMA-400 experiment a highly unique opportunity for the near future γ- and cosmic-ray science, since it allows us to install the scientific payload (mass of ~3000 kg, power consumption of 2000 W, and telemetry downlink of 100 GB/day, with lifetime more than 7 years), which will provide the significant contribution of GAMMA-400 as the next generation instrument for γ-ray astronomy and cosmic-ray physics.

The GAMMA-400 experiment will be initially launched into a highly elliptical orbit (with an apogee of 300 000 km and a perigee of 500 km, with an inclination of 51.4°), with 7 days orbital period. Under the influence of gravitational disturbances of the Sun, Moon, and the Earth after ~6 months the orbit will transform to about an approximately circular one with a radius of ~200 000 km and will not suffer from the Earth's occultation and be outside the radiation belts. A great advantage of such an orbit is the fact that the full sky coverage will always be available for γ-ray astronomy, since the Earth will not cover a significant fraction of the sky, as is usually the case for low-Earth orbit. Therefore, the GAMMA-400 source pointing strategy will be properly defined to maximize the physics outcome of the experiment. The launch of the GAMMA-400 space observatory is planned for 2030.

2.4. Comparison of GAMMA-400 with Fermi-LAT and Ground-Based Facilities

The GAMMA-400 γ-ray telescope has numerous advantages in comparison with the Fermi-LAT:

- highly elliptical orbit (without the Earth's occultation and away from the radiation belts) allows us to observe with the aperture of $\pm 45°$ different γ-ray sources continuously over a long period of time with the exposition greater by a factor of 8 than for Fermi-LAT operating in the sky-survey mode;

- thanks to using scintillating fibers and analog readout in the coordinate detectors, as well as time-of-flight system, GAMMA-400 has an excellent angular resolution;

- due to the deep ($\sim$18 X) calorimeter, GAMMA-400 has an excellent energy resolution and can provide more reliably the detection of γ rays up to several TeV for vertically incident events;

- owing to the better γ-ray separation from cosmic rays (in contrast to Fermi-LAT, the presence of a special trigger with event timing, time-of-flight system, two-layer scintillation detectors), GAMMA-400 is significantly well equipped to separate γ rays from the background of cosmic rays and backscattering events.

GAMMA-400 will have also the better angular and energy resolutions in the energy region 10–1000 GeV in comparison with current and future space- and ground-based instruments: VERITAS, MAGIC, H.E.S.S., CTA, and HAWC and it allows us to fill the data gap at the energy of $\sim$100 GeV between the space- and ground-based instruments.

It is necessary to note that at present various γ-ray telescopes are developed to study γ-ray emission in the medium energy (e-ASTROGAM [8] and AMEGO [9]) and high energy (HERD [10] and AMS-100 [11]) range. Performance of these telescopes in comparison with GAMMA-400 and Fermi-LAT is presented in Table 1.

3. THE PRELIMINARY GAMMA-400 SCIENTIFIC PROGRAM

3.1. Galactic Plane

GAMMA-400 will study continuously over a long period of time different regions of Galatic plane, Galactic center, Fermi Bubbles, Crab, Vela, Cygnus, Geminga with FoV of $\pm 45^\circ$.

3.2. Dark Matter Searching

Generally there are two wide classes of DM candidates, which are potentially accessible by GAMMA-400—WIMPs and ALPs. Below we briefly describe the main targets for searches of both candidates.

Galactic Center region historically represents the most favorable target for WIMP annihilation (decay) searches due to the biggest $J(D)$-factor. In this context a mysterious γ-ray excess identified a while ago (e.g. [12]) around the GC attracts a great interest. It peaks at few GeV, extends up to $\approx 10^\circ$ around the GC and can be well-fitted by annihilating WIMPs with the mass of several tens of GeV and cross section around the thermal value $\sim 10^{-26}$ cm^3/s. However alternative explanations of the excess origin indeed exist. They include the emission from millisecond pulsars (both prompt and secondary), molecular clouds and others. The future high-resolution data from GAMMA-400 will be very important for the ultimate determination of the excess origin.

Another interesting aspect is the searches for hypothetical narrow spectral lines due to DM annihilation or decay directly into photons. This represents very pristine DM signature, since no other astrophysical processes are expected to produce such lines at the energies above $\sim$0.1 GeV. We provided some estimates of GAMMA-400 sensitivity to the diphoton annihilation cross section in [6]. However our most recent simulations showed that the sensitivity presented in [6] tends towards slightly optimistic side—realistically we would expect our sensitivity to be comparable with that of Fermi-LAT after 12–15 years of its operation. At the same time DAMPE has comparable sensitivity too [13]. Hence, it can be possible in the future to stack together the data from all three telescopes and significantly extend the sensitivity to narrow lines by such joint data analysis.

ALP discovery potential by catching a nearby supernova explosion. Fermi-LAT has not been able to observe any supernova explosion in the Local Group due to rarity of such events. However such observation would be extremely valuable for constraining ALP properties. Thus in case of such luck GAMMA-400 will be able to probe ALP-photon coupling constant values down to $g_{a\gamma} \sim 10^{-13}$ GeV^{-1} for ALP masses below $\sim$1 neV! The chance to catch such event over the mission lifetime is about 10%. But the very high sensitivity of this probe still makes it one of the main GAMMA-400 objectives in the area of DM searches. The detailed calculations on this subject can be seen in [6].

ALP signature searches in the pulsar spectra. Recently the tentative ALP signature in the spectra of pulsars was identified in Fermi-LAT data [14]. However this detection is not reliable yet, and the future additional GAMMA-400 observational data on those pulsars will be able potentially to confirm or deny robustly this preliminary signal.

Other targets include globular clusters, nearby galaxies, dwarf satellites, hypothesized axion clouds around neutron stars, etc.

3.3. Searching for GRBs

Using detection of GRBs from top-down and lateral directions GAMMA-400 will discover many new GRBs ($\sim$10 GRBs per year).

Table 1

	Space-based γ-ray telescopes						Ground-based facility
	medium energy			high-energy			
	e-ASTROGAM	AMEGO	Fermi-LAT	GAMMA-400	HERD	AMS-100	CTA
Country	Europe	USA	USA	Russia	China	Europe + USA	
Energy range	0.3 MeV–3 GeV	0.2 MeV–10 GeV	50 MeV–1 TeV	20 MeV–1 TeV	0.5 GeV–10 TeV	1 GeV–10 TeV	>50 GeV
Observation mode	Scanning	Scanning	Scanning	Point-source	Scanning	Scanning	Scanning
Orbit	Circular, ~550 km	Circular, ~550 km	Circular, ~550 km	Highly elliptical, 500–300 000 km	Circular, ~400 km	*L2*	
Angular resolution	0.1°	1°	0.1°	~0.01°	0.1°	~0.01°	0.1°
Energy resolution	20%	10%	10%	~2%	1–2%	1–2%	15%

4. CONCLUSIONS

After Fermi-LAT the GAMMA-400 mission will greatly improve the direct data of low-energy and high-energy γ rays due to unprecedented angular and energy resolutions, large area, and continuous long-term simultaneous coaxial gamma-ray and X-ray telescope observations. GAMMA-400 space observatory is scheduled to launch for ~2030.

FUNDING

This study was funded by the Russian State Space Corporation ROSCOSMOS.

REFERENCES

1. S. Abdollahi, F. Acero, M. Ackermann, M. Ajello, W. B. Atwood, M. Axelsson, L. Baldini, J. Ballet, G. Barbiellini, D. Bastieri, J. Becerra Gonzalez, R. Bellazzini, A. Berretta, E. Bissaldi, R. D. Blandford, E. D. Bloom, et al., Astrophys. J. Suppl. Ser. **247**, 33 (2020).
2. M. Ajello, M. Arimoto, M. Axelsson, L. Baldini, G. Barbiellini, D. Bastieri, R. Bellazzini, P. N. Bhat, E. Bissaldi, R. D. Blandford, R. Bonino, J. Bonnell, E. Bottacini, J. Bregeon, P. Bruel, R. Buehler, et al., Astrophys. J. **878**, 52 (2019).
3. A. M. Galper, O. Adriani, R. L. Aptekar, I. V. Arkhangelskaja, A. I. Arkhangelskiy, M. Boezio, V. Bonvicini, K. A. Boyarchuk, Yu. V. Gusakov, M. O. Farber, M. I. Fradkin, V. A. Kachanov, V. A. Kaplin, M. D. Kheymits, A. A. Leonov, F. Longo, et al., Adv. Space Res. **51**, 297 (2013).
4. A. M. Galper, N. P. Topchiev, and Yu. T. Yurkin, Astron. Rep. **62**, 882 (2018).
5. N. P. Topchiev, A. M. Galper, I. V. Arkhangelskaja, A. I. Arkhangelskiy, A. V. Bakaldin, Yu. V. Gusakov, O. D. Dalkarov, A. E. Egorov, V. G. Zverev, A. A. Leonov, P. Yu. Naumov, N. Yu. Pappe, M. F. Runtso, Yu. I. Stozhkov, S. I. Suchkov, M. D. Kheimitz, et al., Bull. Russ. Acad. Sci.: Phys. **83**, 629 (2019).
6. A. E. Egorov, N. P. Topchiev, A. M. Galper, O. D. Dalkarov, A. A. Leonov, S. I. Suchkov, and Yu. T. Yurkin, J. Cosmol. Astropart. Phys. **049**, 11 (2020).
7. A. A. Leonov, A. M. Galper, V. Bonvicini, N. P. Topchiev, O. Adriaini, R. L. Aptekar, I. V. Arkhangelskaja, A. I. Arkhangelskiy, L. Bergstrom, E. Berti, G. Bigongiari, S. G. Bobkov, M. Boezio, E. A. Bogomolov, S. Bonechi, M. Bongi, et al., Adv. Space Res. **56**, 1538 (2015).
8. A. DeAngelis, V. Tatischeff, I. A. Grenier, J. McEnery, M. Mallamaci, M. Tavani, U. Oberlack, L. Hanlon, R. Walter, A. Argan, P. VonBallmoos, A. Bulgarelli, A. Bykov, M. Hernanz, G. Kanbach, I. Kuvvetli, et al., J. High Energy Astrophys. **19**, 1 (2018).
9. C. A. Kierans, A. Harding, B. Cenko, D. Thompson, G. De Nolfo, J. Perkins, J. Mitchell, J. Racusin, J. McEnery, L. Hays, T. Venters, A. Moiseev, A. Lien, B. Rani, C. Shrader, E. Ferrara, et al., arXiv: 2101.03105 (2021).
10. P. W. Cattaneo, O. Adriani, G. Ambrosi, Y. Bai, B. Bertucci, X. Bi, J. Casaus, I. De Mitri, M. Dong, Y. Dong, I. Donnarumma, F. Gargano, E. Liang, H. Liu, C. Lyu, G. Marsella, et al., Nucl. Part. Phys. Proc. **306–308**, 53 (2019).
11. S. Schael, A. Atanasyan, J. Berdugo, T. Bretz, M. Czupalla, B. Dachwald, P. von Doetinchem, M. Duranti, H. Gast, W. Karpinski, T. Kirn, K. Lübelsmeyer, C. Маба, P. S. Marrocchesi, P. Mertsch, I. V. Moskalenko, et al., Nucl. Instrum. Methods Phys. Res., Sect. A **944**, 162561 (2019).
12. M. Ackermann, M. Ajello, A. Albert, W. B. Atwood, L. Baldini, J. Ballet, G. Barbiellini, D. Bastieri, R. Bellazzini, E. Bissaldi, R. D. Blandford, E. D. Bloom, R. Bonino, E. Bottacini, T. J. Brandt, J. Bregeon, et al., Astrophys. J. **840**, 43 (2017).
13. P. Fusco (on behalf of the DAMPE Collab.), Int. J. Mod. Phys. A **35**, 2044024 (2020).
14. G. A. Pallathadka, F. Calore, P. Carenza, M. Giannotti, D. Horns, J. Majumdar, A. Mirizzi, A. Ringwald, A. Sokolov, and F. Stief, arXiv: 2008.08100.

ResearchGate

See discussions, stats, and author profiles for this publication at: https://www.researchgate.net/publication/373614627

Cosmophysical Research with GAMMA-400

Article *in* Physics of Atomic Nuclei · September 2023

DOI: 10.1134/S1063778823040361

CITATIONS
0

READS
74

18 authors, including:



Nikolay Topchiev
Russian Academy of Sciences
117 PUBLICATIONS **641** CITATIONS
SEE PROFILE



Irene Arkhangelskaja
National Research Nuclear University MEPhI
158 PUBLICATIONS **616** CITATIONS
SEE PROFILE



Andrey Arkhangelskiy
National Research Nuclear University MEPhI
128 PUBLICATIONS **623** CITATIONS
SEE PROFILE



A. V. Bakaldin
National Research Nuclear University MEPhI
95 PUBLICATIONS **443** CITATIONS
SEE PROFILE

All content following this page was uploaded by A. A. Leonov on 22 September 2023.

The user has requested enhancement of the downloaded file.

ISSN 1063-7788, Physics of Atomic Nuclei, 2023, Vol. 86, No. 4, pp. 489–499. © Pleiades Publishing, Ltd., 2023.

ELEMENTARY PARTICLES AND FIELDS
Experiment

Cosmophysical Research with GAMMA-400

N. P. Topchiev[1)], A. M. Galper[1),2)], I. V. Arkhangelskaja[2)], A. I. Arkhangelskiy[2)], A. V. Bakaldin[3)], I. V. Chernysheva[4)], O. D. Dalkarov[2)], A. E. Egorov[1)], M. D. Kheymits[2)], M. G. Korotkov[2)], A. A. Leonov[1),2)], S. A. Leonova[4)], A. G. Malinin[2)], V. V. Mikhailov[2)], P. Yu. Minaev[1),5)], N. Yu. Pappe[1)], S. I. Suchkov[1)*], and Yu. T. Yurkin[2)]

Received March 2, 2023; revised March 2, 2023; accepted March 2, 2023

Abstract—The GAMMA-400 gamma-ray telescope is the successor of Soviet and Russian gamma-ray telescopes. GAMMA-400 is being developed for cosmophysical research in accordance with the Russian Federal Space Program 2016–2025. The GAMMA-400 experiment will be implemented aboard the Russian astrophysical space observatory in a highly elliptic orbit during 7 years to provide new data on gamma-ray emission mainly from the Galactic plane, Galactic Center, the Sun and cosmic-ray electron + positron fluxes. The main mode of observations will be the continuous point-source mode with the duration of up to ~100 days. The GAMMA-400 gamma-ray telescope will study high-energy gamma-ray emission up to several TeV and cosmic-ray electrons + positrons up to 20 TeV. GAMMA-400 will have the never-achieved angular resolution, the high-energy and time resolutions, as well as very good separation efficiency of gamma rays from cosmic-ray background and of electrons + positrons from protons. The distinctive features of GAMMA-400 are the excellent angular resolution of ~0.01° at $E_\gamma = 100$ GeV that exceeds resolutions of the space-based and ground-based gamma-ray telescopes by a factor of 5–10, as well as high-energy resolution of ~2% at $E_\gamma = 100$ GeV. GAMMA-400 studies can discover gamma-ray emission from annihilation or decay of dark matter particles, identify many unassociated discrete sources, explore the structure of extended sources, search for gamma-ray bursts and solar gamma-ray flares, improve the data on cosmic-ray electron + positron spectra for energies of >50 GeV.

DOI: 10.1134/S1063778823040361

1. INTRODUCTION

First of all, it is necessary to give a short review of the development of gamma-ray astronomy in the Soviet Union and Russia. The fundamental basis of gamma-ray astronomy in the Soviet Union and Russia was laid by Academician V. L. Ginzburg in his mid-twentieth century papers [1, 2]. Remarkable reviews on experimental gamma-ray astronomy and the requirements for developing gamma-ray telescopes were set out by Professor A. M. Galper et al. from Moscow Engineering Physics Institute (MEPhI) in [3–7].

In connection with the 80th anniversary of the founding of NRNU MEPhI (https://eng.mephi.ru/), its significant contribution to the development of experimental space gamma-ray astronomy in the Soviet Union and Russia should be mentioned. Almost all space-based gamma-ray telescopes were developed with the leading role of MEPhI. The first experimental studies in space on gamma-ray astronomy in the Soviet Union were carried out in 1968–1969 on the satellites Cosmos-251 and Cosmos-264 [8, 9]. The satellites were equipped with a gamma-ray telescope consisting of two scintillation detectors, a directed Cherenkov counter, a converter, and a spark chamber with the effective area of ~80 cm^2. The telescope measured gamma-ray emission in the energy range of 100–1500 MeV. During the flight, the telescope recorded gamma-ray emission from parts of the sky in the region of the constellations of Ophiuchus, Virgo, Leo, Hercules, etc.

A significant contribution to the development of the methodology for cosmic gamma-ray emission studying was made by the GAMMA-1 gamma-ray telescope with the energy range of 50–5000 MeV

[1)]Lebedev Physical Institute of the Russian Academy of Sciences, Moscow, Russia.
[2)]National Research Nuclear University MEPhI, Moscow, Russia.
[3)]Scientific Research Institute for System Analysis of the Russian Academy of Sciences, Moscow, Russia.
[4)]Dubna State University, Branch "Protvino", Moscow region, Protvino, Russia.
[5)]Space Research Institute of the Russian Academy of Sciences, Moscow, Russia.
[*]E-mail: soutch@mail.ru

and the effective area of 320 cm^2. Its development methods made it possible to significantly increase the angular resolution up to $\sim 1^\circ$ and improve the energy resolution up to $\sim$35% [10, 11]. The characteristics of GAMMA-1 were significantly better than those of the previous gamma-ray telescopes SAS-2 [12] and COS-B [13]. In this space experiment, great importance was attached to the gamma rays' release against the background of a cosmic ray (CR) charged particles' flux, which exceeds the gamma-ray flux by 4–5 orders of magnitude. For the effective observation of gamma-ray sources, for the first time in world practice, reorientation of the spacecraft with the GAMMA-1 gamma-ray telescope was used. According to the forecast of pre-flare activity of the Sun, the spacecraft was also reoriented to the Sun to observe solar flares. Gamma-ray emission was observed from the following sources: the pulsar PSR 0833-45 (Vela), the pulsar Geminga, the binary system Cyg X-3, double system Hercules X-1, as well as the Sun. In 1991, during the period of maximum solar activity, GAMMA-1 first detected high-energy (up to several GeV) gamma-ray emission from the Sun during powerful flares on March 26, 1991 (3B/X4.7) and June 15, 1991 (3B/X12+) [14] (before EGRET [15]).

Among other experiments, the NATALYA-2M spectrometer on board the CORONAS-PHOTON satellite in 2009 should be noted [16]. The instrument intended for recording gamma-ray emission of solar flares in the broad energy range of 0.2–1600 MeV as well as neutrons of solar origin with energies of 20–300 MeV was itself as a scintillation spectrometer based on CsI(Tl) crystals with a total area of 32×38 cm^2 and the thickness of 18 cm. The spectrometer recorded several powerful gamma-ray bursts.

At present, since 2008 the Fermi-LAT gamma-ray telescope has kept space gamma-ray emission observing. The fourth Fermi-LAT catalog [17] contains $\sim$6700 sources for the energy range from 50 MeV to 1000 GeV, but $\sim$30% of gamma-ray sources are still unidentified. Fermi-LAT operates in the scanning mode and the source observation time is only $\sim$15% of the operation time [18]. The ground-based facilities H.E.S.S., MAGIC, VERITAS and others have observed the emission from only $\sim$250 gamma-ray sources in the energy range above $\sim$100 GeV (http://tevcat.uchicago.edu/). In order to identify many unassociated gamma-ray sources it is necessary to observe with better angular and energy resolutions.

Gamma-ray bursts (GRBs) search and study are of great interest. GRB study was performed by Fermi-LAT [19], Fermi-GBM [20], and Swift-BAT [21]. The high level of GRB statistics in the sub-Mev range with more than 13 000 bursts is provided in http://www.ssl.berkeley.edu/ipn3/masterli.html. For such energies, "classical" high variable prompt emission of GRBs is seen as a superposition of short FRED-like (Fast Rise and Exponential Decay) pulses. For energies above 100 MeV also there are a couple of hundred of detections by Fermi-LAT and EGRET [22] experiments. This high-energy component is presumably associated with the propagation of a relativistic jet. However, at present time the clarification about the nature of the high-energy emission and its possible connection with the low-energy classical gamma-ray emission is needed. This could be at least bimodal behavior of high-energy emission: separate emission mechanism vs extension of low-energy emission to high energy.

The next issue is to study dark matter (DM) particles by indirect gamma-ray detection. The indirect detection consists of recording the gamma rays of their annihilation or decay. Weakly interacting massive particles (WIMPs) with the mass between several GeV and several TeV are still considered to be the most probable candidate (e.g. [23]) for the role of DM. WIMPs can annihilate or decay with gamma-ray production. They can produce both the excess in continuous energy spectrum and narrow gamma-ray lines. Axion-like particles (ALPs) are also proposed as candidate particles for DM (e.g. [24]). Search for and study of gamma-ray emission or from DM particles with the better angular and energy resolutions remain one of the central goals.

High-precision measurements of CR electron + positron fluxes up to the $\sim$4.8-TeV energy have been made by many experiments ATIC [25], Fermi-LAT [26], PAMELA [27], AMS-2 [28], CALET [29], DAMPE [30], MAGIC [31], VERITAS [32], and H.E.S.S. [33]. These results found several features in the spectral shape of their flux and sometimes they do not correspond to each other. It is necessary to improve electron + positron flux data for energies up to 20 TeV.

Therefore, new space-based experiments to study gamma-ray emission in the energy range up to several TeV, as well as CR electron + positron fluxes up to several tens TeV with better angular and energy resolutions are required.

2. THE GAMMA-400 GAMMA-RAY TELESCOPE

The GAMMA-400 (Gamma Astronomical Multifunctional Modular Apparatus) gamma-ray telescope with an initial upper energy limit of 400 GeV was first proposed in 1988 [34] and has been developed further

since then [35–47]. The current physical scheme is shown in Fig. 1.

GAMMA-400 consists of:

—scintillation anticoincidence AC top and four lateral AC lat detectors. All anticoincidence detectors are made of two layers of scintillation plastic strips. The anticoincidence system AC has an efficiency of $\sim$0.9996 for detecting incoming charged particles and time resolution of $\sim$200 ps;

—converter-tracker C ($\sim 1X_0$, X_0 is radiation interaction length) from scintillating fibers (SciFi). The converter-tracker consists of 13 detector plane pairs made of SciFi assemblies. The top seven pairs of planes have tungsten (W) converter foils of $0.1X_0$. Next four pairs of planes also contain tungsten converter foils of $0.025X_0$ thick in each plane. The bottom two pairs of planes have no tungsten;

—time of flight system (ToF) from scintillation $S1$ and $S2$ detectors (the ToF signal means that the time of the $S1$ response must be earlier than the time of the $S2$ response, ToF $= S1 \times S2 \times [\text{time}S1 < \text{time}S2]$). The distance of 500 mm between these detectors provides a sufficient flight base for effective rejection of particles coming from the lower hemisphere with the coefficient of separation of $\sim$1000. The ToF time resolution is $\sim$200 ps;

—two-part calorimeter from $CC1$ ($2X_0$) and $CC2$ ($\sim 16X_0$). Preshower $CC1$ contains two blocks of CsI(Tl) scintillation crystals and the SciFi detector plane without W. $CC2$ consists of CsI(Tl) crystal columns. Total thickness of the $CC1$ and $CC2$ calorimeter is $\sim 18X_0$ ($\sim 0.9\lambda_0$) for vertical and $\sim 43X_0$ ($\sim 2.0\lambda_0$) for lateral particle detection, respectively (λ_0 is hadronic interaction length);

—four lateral scintillation detectors LDs located around the $CC2$ calorimeter for detecting particles from lateral directions;

—$S3$ and shower leakage $S4$ scintillation detectors. These detectors are necessary for improving hadronic and electromagnetic shower separation.

Electronic units include system of trigger formation (ST), scientific data acquisition system (SDAS) and other electronics units. Two star sensors with an accuracy of better than $3''$ and thermal control systems are additionally presented.

Incident gamma rays pass without interaction AC and are converted into electron–positron pairs in C. Electron–positron pair passes through C and ToF and produces an electromagnetic shower in $CC1$, $S3$, $CC2$, and $S4$. In all layers of C, $S1$, $S2$, $CC1$, $S3$, $CC2$, $S4$, and LD, the energy deposits are measured.

Reconstructing conversion point and the electromagnetic shower axis using SciFi coordinate detectors in C and $CC1$ the incidence direction of particles is determined with high precision.

High-energy ($E_\gamma > 5$ GeV) gamma rays interact with the GAMMA-400 detector matter and create backscattering secondary particles (mainly, 1-MeV photons). These secondary particles can interact in AC and produce veto signal, excluding primary gamma rays. To exclude this effect we construct all scintillation detectors as two-layer segmented strips, organize additional trigger logic for high-energy particle detecting, and use the signal time analysis in AC, $S1$ (ToF), $S2$ (ToF), $S3$ detectors.

The GAMMA-400 energy range is from $\sim$20 MeV to several TeV and from $\sim$1 GeV to several tens TeV for gamma rays and CR electrons + positrons, respectively. The maximum field of view (FoV) for incident particles from top–down directions is $\pm 45^\circ$. We measure the energy of low-energy gamma rays in C, $S1$, and $S2$ after the conversion of gamma rays in the last six planes (Fig. 1, four planes with $0.025X_0$-tungsten and two without tungsten).

In contrast to the previous calculations [46], in this study we use the new trigger based on the times of scintillation detector responses due to the high time detector resolutions. The basic characteristics were recalculated, but they remained practically the same to confirm the correctness of the new method.

The new main trigger of GAMMA-400 (no signal in AC and the presence of ToF signal) is the following:

$$\overline{\text{AC}_{\text{SP1}}} \times \text{ToF},$$

where

$$\overline{\text{AC}_{\text{SP1}}} = \overline{\text{AC(the same position strip)}}|[\text{time AC} > \text{time}S1];$$

$$\text{AC(the same position strip)} = \text{AC}_{\text{TOP}}(\text{the same position strip})|\text{AC}_{\text{LAT}}(\text{the same position strip})$$

means that in both layers of any AC detectors the strips located one above the other have a signal; [time AC $>$ time$S1$] means that time of AC response is later than the time of $S1$ response; ToF $= S1 \times S2 \times [\text{time}S1 < \text{time}S2]$.

The AC_{SP1} logic construction takes into account the possible influence of backscattering particles (mainly generated in calorimeter $CC2$). These backscattering particles have the energy distribution peaked $\sim$1 MeV. Analyzing each layer of AC detectors separately and taking into account, that the electronic threshold in each scintillation plastic strip of 1 cm thickness is $\sim$0.5 MeV, it is possible to retain useful events against backscattering particles. For this purpose, the relative location of the hit scintillation plastic strip in neighboring layers of each AC detectors is checked. Then only the events having hit scintillation plastic strip in each layer in

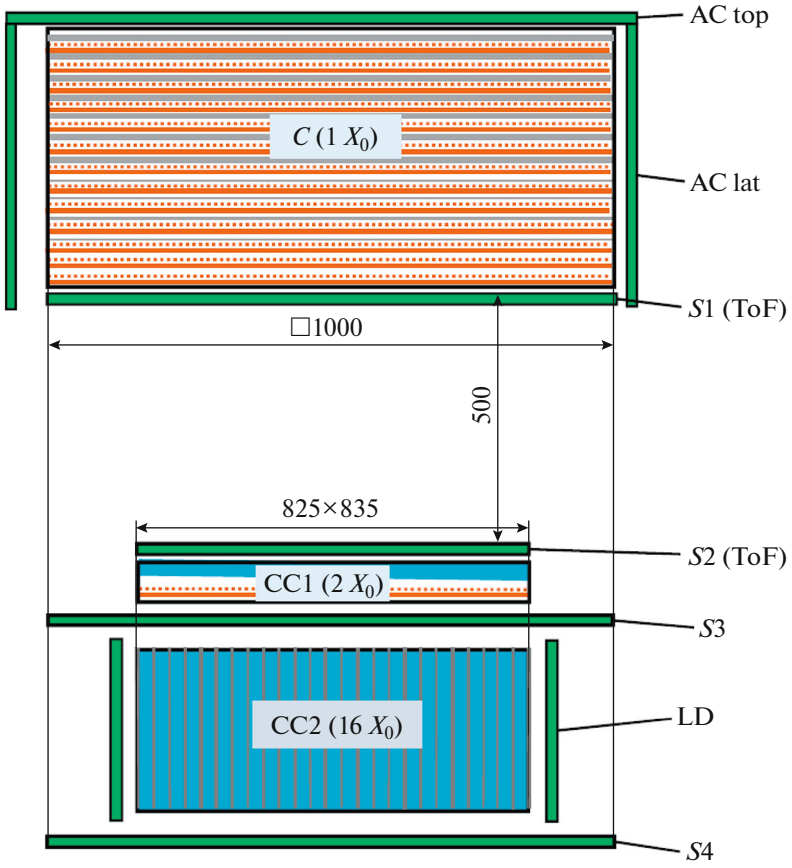


Fig. 1. The GAMMA-400 gamma-ray telescope physical scheme: anticoincidence system from AC top and four AC lat detectors, converter-tracker C, time-of-flight system ToF from $S1$ and $S2$ detectors, two-part calorimeter from $CC1$ and $CC2$, lateral detectors LDs, detector $S3$ and shower leakage detector $S4$.

the same position (one just against other) are marked by veto. Other events accompanied by backscattering particles in AC detectors which do not hit scintillation plastic strip in each layer in the same position are retained for subsequent analysis [42].

3. GAMMA-RAY DETECTION

Simulations of the GAMMA-400 performance were conducted using GEANT4. An example of simulation of 100-GeV gamma-ray energy release in the gamma-ray telescope detectors is shown in Fig. 2. Detectors of the gamma-ray telescope are shown as colored, if the response exists. In this figure, the GAMMA-400 two projection responses are shown at the left and right of Fig. 2. At the center, the $CC2$ view from above is shown together with AC lat.

Some calculations were performed within which it is necessary to analyze the time consequence of signals produced in $S1$(ToF), $S2$(ToF) taking into account time resolution obtained from test beam calibration and to be able to reconstruct the particle track and to restore the particle energy. As a result, some dependences are presented:

(1) The on-axis effective area depending on the energy (Fig. 3) using triggers

$$\overline{\text{AC}} \times \text{ToF (black)},$$

$$\overline{\text{AC}_{\text{SP1}}} = \overline{\text{AC(the same position strip)}}|[\text{time}\text{AC}_{\text{SP1}} > \text{time}S1] \text{ (green)},$$

$$\overline{\text{AC}_{\text{SP2}}} = \overline{\text{AC(the same`position strip)}}|[\text{time}\text{AC}_{\text{SP1}} > \text{time}S2] \text{ (blue)}.$$

As can be seen from Fig. 3, when using only trigger ($\overline{\text{AC}} \times$ ToF) the effective area begins to decrease at the energy of more than 10 GeV due to backscattering particles. Using the trigger with $\overline{\text{AC}_{\text{SP1}}}$ or $\overline{\text{AC}_{\text{SP2}}}$ provides the effective area of $\sim$4000 cm^2 up to several TeV. If the additional analysis is used providing possibility to reconstruct track and to restore energy the estimation of the effective area (S_{eff}) decreases up to $\sim$3200 cm^2

(2) The GAMMA-400 angular resolution depending on the energy in comparison with Fermi-

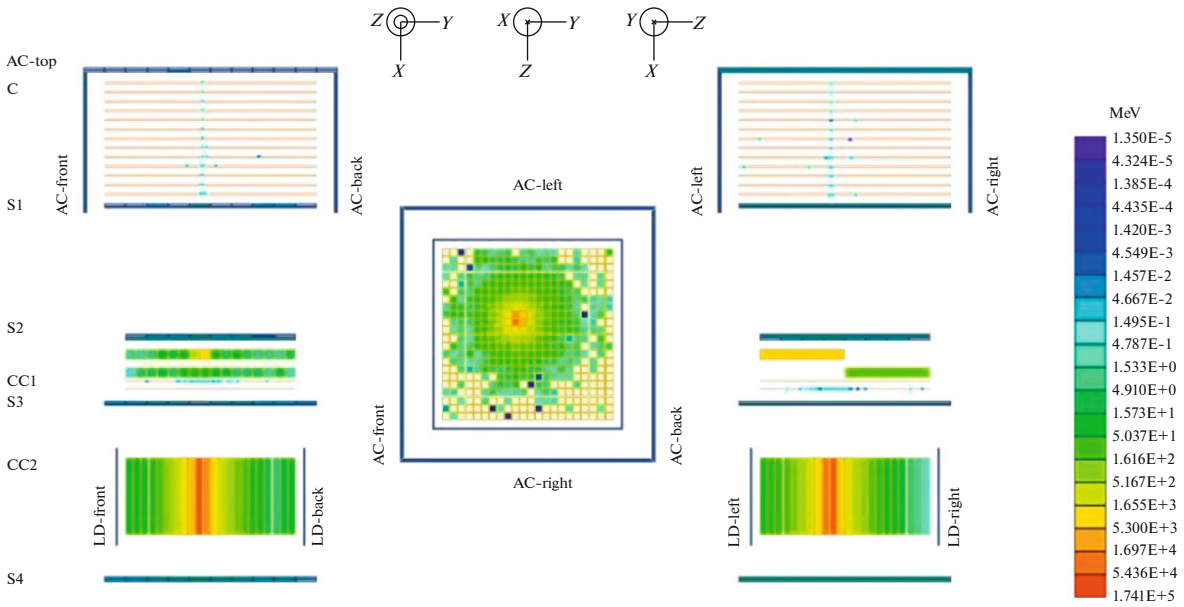


Fig. 2. An example of energy release simulation in the gamma-ray telescope detectors for 100-GeV gamma ray.

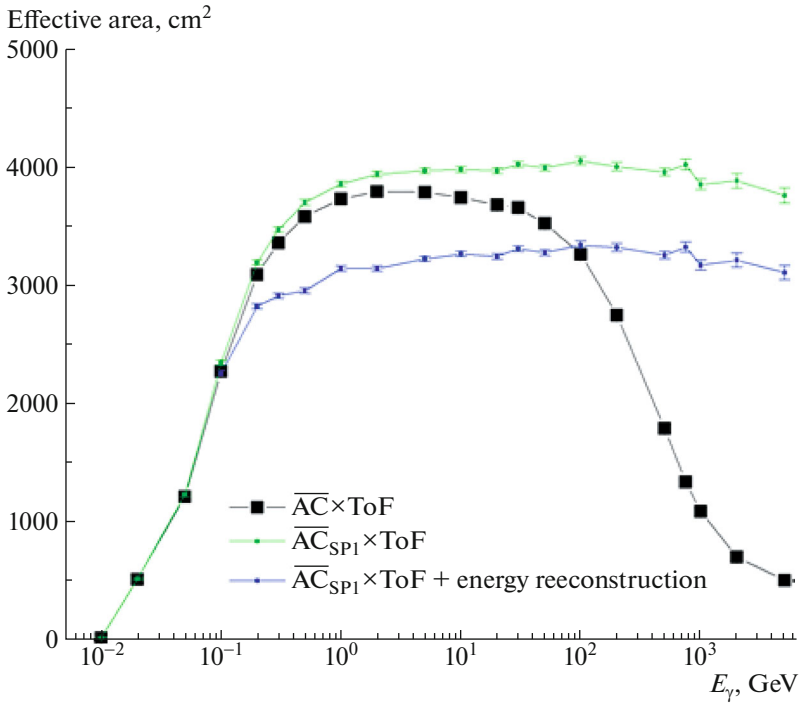


Fig. 3. Dependence of the GAMMA-400 on-axis effective area on the energy using triggers $\overline{\text{AC}}$ × ToF (black), $\overline{\text{AC}_{\text{SP1}}}$ × ToF (green), $\overline{\text{AC}_{\text{SP1}}}$ × ToF + energy reconstruction (blue).

LAT and CTA (https://www.cta-observatory.org/science/ctao-performance/#1472563157648—91558872-faf1) (Fig. 4). The angular resolution for $E_\gamma = 100$ GeV is $\sim 0.01^\circ$.

(3) The on-axis energy resolution depending on the energy in comparison with Fermi-LAT and CTA (https://www.cta-observatory.org/science/ctao-performance/#1472563318157-d0191bc5-0280) (Fig. 5). The energy resolution for $E_\gamma = 100$ GeV is $\sim 2\%$.

The *CC*2 prototype was manufactured and calibrated on a positron beam at S-25R electron synchrotron (Lebedev Physical Institute, Troitsk) and the

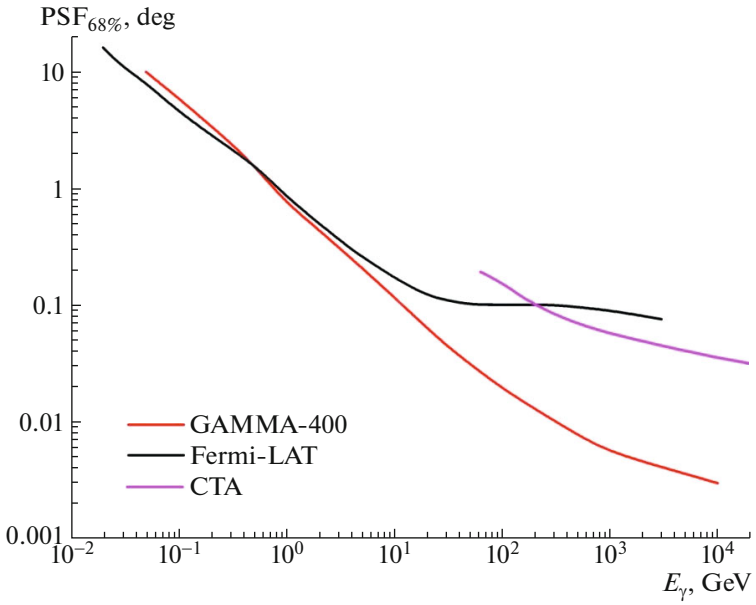


Fig. 4. Dependence of the GAMMA-400 angular resolution on the energy in comparison with Fermi-LAT and CTA.

energy resolution of ~10% at the energy of 300 MeV was obtained [43, 45].

The separation of gamma rays from the background of charged particles and gamma rays coming out of the GAMMA-400 aperture plays an important role. The AC and ToF prototypes were manufactured and calibrated on a positron beam at S-25R electron synchrotron in the energy range of 100–300 MeV. The high efficiency of charged particle detection equal to ~0.9996 for the AC system and high coefficient of separation of events coming from top–down and down–top directions of ~1000 for the ToF system were obtained. Taking into account the separation of electromagnetic and hadronic showers in $CC1$, $CC2$, $S4$ and the additional analysis of the hit strips of AC detectors located along the initial particle trajectory the rejection of $\sim 10^5$ was obtained.

4. GAMMA-RAY BURSTS

GAMMA-400 can also record GRBs from top–down and lateral directions. When recording GRBs using the lateral aperture, the GAMMA-400 total effective field of view is ~6 sr [46]. GAMMA-400 will allow us to detect ~15 GRBs per year.

5. ELECTRON + POSITRON DETECTION

GAMMA-400 will also measure CR electron + positron fluxes from top–down and lateral directions around the calorimeter. For these directions, the energy resolutions are ~2% and < 1%, respectively. Figure 6 shows an example of energy release simulation in the GAMMA-400 detectors for 1-TeV electron from left lateral direction.

Table 1 shows the comparison of performance for GAMMA-400 (top–down and lateral aperture) and Fermi-LAT [48]. It is obvious that due to the large calorimeter area (0.7 m^2 for top–down and 1.0 m^2 for lateral aperture) and calorimeter thickness ($18X$ for top–down and $43X$ for lateral aperture) GAMMA-400 can improve electron + positron data statistics.

6. THE PRELIMINARY GAMMA-400 SCIENTIFIC PROGRAM

The GAMMA-400 gamma-ray telescope has several advantages in comparison with current and future space-based and ground-based instruments:

(1) GAMMA-400 will operate in a highly elliptical orbit in the point-source mode with 100% efficiency continuously over a long period of time (~100 days) with the aperture of ±45° in contrast to the scanning mode for others instruments;

(2) GAMMA-400 has an excellent angular resolution due to the high coordinate resolution in the SciFi coordinate detectors in C and $CC1$, as well as ToF system;

(3) GAMMA-400 has a highenergy resolution and possibility to detect incident particles from top–down and lateral directions;

(4) GAMMA-400 has a very good separation for gamma rays from the background of cosmic rays and backscattering events, as well as for electrons + positrons from protons.

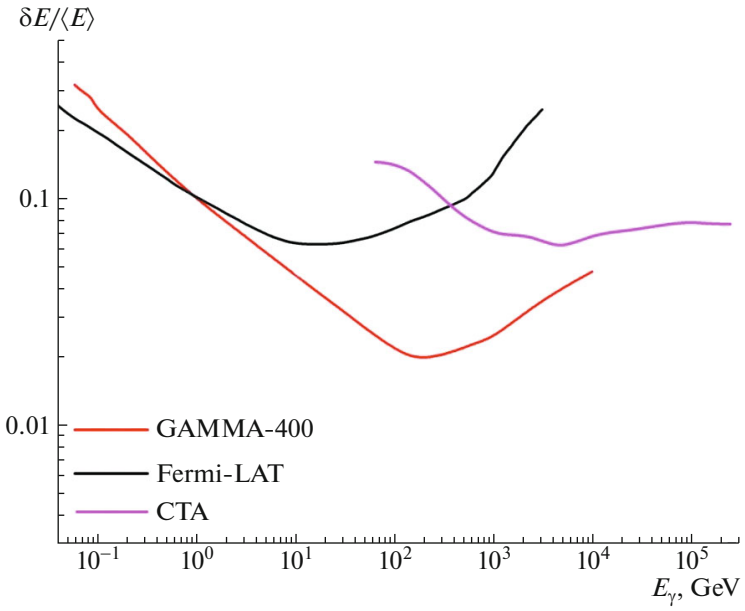


Fig. 5. Dependence of the GAMMA-400 on-axis energy resolution on the energy in comparison with Fermi-LAT and CTA.

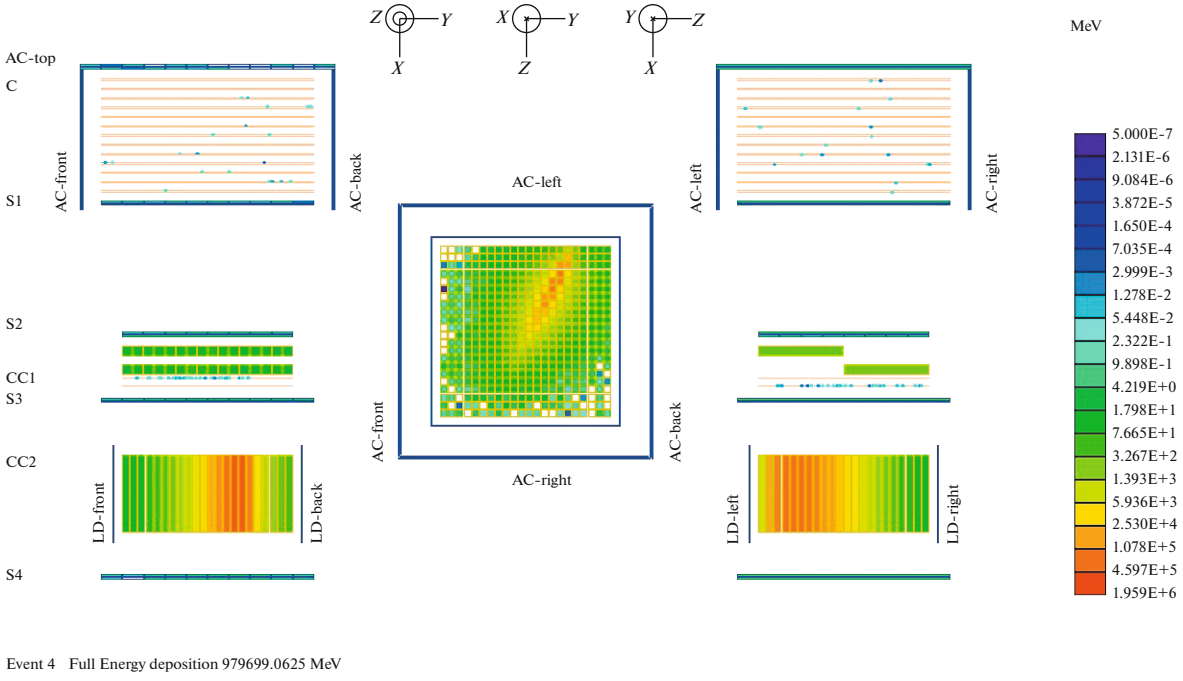


Fig. 6. An example of energy release simulation in the GAMMA-400 detectors for 1-TeV electron from left lateral direction.

The GAMMA-400 main scientific problems remaining relevant today are:

(1) to search for features in the energy spectra of high-energy gamma-ray emission up to energies of ~1000 GeV, which can be associated with the annihilation or decay of dark matter particles (most popular DM candidates are WIMPs and ALPs) due to the high-energy resolution of ~2% ($E_\gamma = 100$ GeV);

(2) to study discrete gamma-ray sources and identify them (according to the fourth Fermi-LAT catalog the gamma-ray emission from ~6500 sources was recorded, ~30% of them were not identified) due to the high angular resolution of ~0.01° ($E_\gamma = 100$ GeV);

(3) to study the spatial structure of extended discrete sources in detail due to the high angular resolution of ~0.01° ($E_\gamma = 100$ GeV);

(4) to study source variability, including gamma-

Table 1. Comparison of performance when detecting CR electrons + positrons for GAMMA-400 (top–down and lateral aperture) and Fermi-LAT

Aperture	GAMMA-400		Fermi-LAT
	Top–down	4 lateral sides	Top–down
Acceptance, m^2 sr	~ 0.3 ($E_e = 100$ GeV)	~ 0.5 ($E_e = 100$ GeV)	2.5
Proton rejection factor	$\sim 10^4$	$\sim 10^4$	$\sim 10^4$
Calorimeter area, m^2	0.7	4×0.24	0.85
Calorimeter thickness, X_0	18	43	8.6

ray emission from millisecond pulsars recording in order to explain the gamma-ray emission excess from the Galactic center due to the high event timing accuracy of several μs (due to the AC and ToF time resolutions of $\sim$200 ps and the instrument timing interface accuracy of several μs);

(5) to search for and study GRBs when gamma-ray emission is detected both from top–down along the axis of the gamma-ray telescope and from four lateral directions;

(6) to carry out simultaneous observations of discrete gamma-ray sources jointly with X-ray telescopes, ground-based facilities (especially with the Russian TAYGA [49]), optical, radio and neutrino telescopes;

(7) to detect CR electron + positron fluxes from both top–down directions along the axis of the gamma-ray telescope up to energies of several TeV (with a calorimeter thickness of $18X_0$) and from four lateral directions up to energies of $\sim$20 TeV (with a calorimeter thickness of $43X_0$) and obtain significantly better measurement statistics.

Observations by the Fermi-LAT gamma-ray telescope have revealed many new types of flare sources, the so-called transients. Among them there are quasi-periodic sources and sources that flare up only once. The study of their nature is declared as one of the main goals of MeV-range telescopes and ground-based TeV-range gamma-ray telescopes. The absence of an instrument operating in the range of $\sim$0.1–1000 GeV significantly impairs their capabilities.

The GAMMA-400 experiment will help solve the main problems that currently exist when measuring the spectrum of CR electrons and positrons at high energies (100 GeV and above). The main advantages of the GAMMA-400 are associated firstly with the good basic instrument parameters (i.e. the energy resolution and the geometric factor), and secondly with the measurement results' high methodological reliability. This is related with two actually independent electron recording methods (recording from top–down along the telescope axis and recording from lateral directions) implemented in one telescope.

7. ASTROPHYSICAL OBSERVATORY

The new GAMMA-400 astrophysical observatory is being developed in Russia. It will consist of the Navigator spacecraft platform (being developed by Lavochkin Association, https://www.laspace.ru/projects/astrophysics/gamma-400/), the GAMMA-400 gamma-ray telescope (being developed mainly by Lebedev Physical Institute (https://gamma400.lebedev.ru/indexeng.html), and National Research Nuclear University "MEPhI") and additional instruments (the ART-XC X-ray telescope with the energy range of 5–30 keV and magnetic plasma detectors being developed by Space Research Institute of the Russian Academy of Sciences).

The Navigator spacecraft platform will have the possibility of pointing to any astrophysical source with accuracy of 30″. The scientific payload will have the following characteristics: mass of $\sim$3000 kg, power consumption of 2000 W, telemetry downlink of 100 GB/day.

The GAMMA-400 astrophysical observatory will be initially launched into a highly elliptical orbit with preliminary parameters: an apogee of 300 000 km, a perigee of 500 km, an inclination of 51.4° , a 7-day orbital period, and a lifetime of more than 7 years. After $\sim$6 months the orbit will transform to about an approximately circular one with a radius of $\sim$200 000 km due to the influence of gravitational disturbances of the Sun, the Moon, and the Earth. Therefore the observatory will not suffer from the Earth's occultation and will be outside the radiation belts. This is a great advantage compared to the low-Earth orbit. The GAMMA-400 will function in a point-source operating mode continuously for a long time for $\sim$100 days in contrast to the scanning mode for the current Fermi-LAT and future HERD [50], AMS-100 [51] experiments. The launch of the GAMMA-400 space observatory is scheduled for $\sim$2030.

8. CONCLUSIONS

The upcoming GAMMA-400 experiment will be implemented aboard the Russian astrophysical space observatory, which will be operating in a highly elliptic orbit during 7 years to provide new data on gamma-ray emission mainly from the Galactic plane, Galactic Center, the Sun and CR electron + positron fluxes. The continuous point-source mode with duration up to ~100 days will be the main mode. The GAMMA-400 gamma-ray telescope will study high-energy gamma-ray emission up to several TeV and CR electrons + positrons up to ~20 TeV. GAMMA-400 will have the never-achieved angular resolution, the high-energy and time resolutions, as well as very good separation efficiency of gamma rays from CR background and electrons + positrons from protons. The distinctive feature of GAMMA-400 is the wonderful angular resolution for energies >30 GeV (~0.01° for $E_\gamma = 100$ GeV) that exceeds resolutions of the space-based and ground-based gamma-ray telescopes by the factor of 5-10. GAMMA-400 studies can reveal gamma-ray emission from dark matter particles annihilation or decay, identify many unassociated discrete sources, explore the extended sources structure, improve the data on CR electron + positron

the GAMMA-400 space observatory is scheduled for ~2030.

FUNDING

This study was supported by the Russian State Space Corporation ROSCOSMOS, in part by the Russian Ministry of Science and Higher Education, project "Fundamental and applied research of cosmic rays," no. FSWU-2023-0068, and in part by the MEPhI Program Priority 2030.

CONFLICT OF INTEREST

The authors declare that they have no conflicts of interest.

REFERENCES

1. V. L. Ginzburg and S. I. Syrovatskii, Sov. Phys. Usp. **7**, 696 (1965).
2. V L. Ginzburg and S. I. Syrovatskii, Sov. Phys. Usp. **9**, 223 (1966).
3. A. M. Gal'per, V. G. Kirillov-Ugryumov, B. I. Luchkov, and O. F. Prilutskii, Sov. Phys. Usp **14**, 630 (1972).
4. A. M. Gal'per, V. G. Kirillov-Ugryumov, and B. I. Luchkov, Sov. Phys. Usp. **17**, 186 (1974).
5. A. M. Gal'per, V. G. Kirillov-Ugryumov, and B. I. Luchkov, Sov. Phys. Usp. **20**, 350 (1977).
6. A. M. Gal'per, B. I. Luchkov, and O. F. Prilutskii, Sov. Phys. Usp. **22**, 456 (1979).
7. A. M. Gal'per, Yu. D. Kotov, and B. I. Luchkov, Sov. Phys. Usp. **23**, 873 (1980).
8. S. A. Volobuev, A. M. Galper, V. G. Kirillov-Ugryumov, B. I. Luchkov, Yu. V. Ozerov, I. L. Rozental, E. M. Shermanzon, N. L. Grigorov, L. F. Kalinkin, A. S. Melioranskii, I. A. Savenko, and T. A. Shashko, Izv. Akad. Nauk SSSR, Ser. Fiz. **34**, 2259 (1970).
9. S. A. Volobuev, A. M. Galper, V. G. Kirillov-Ugryumov, B. I. Luchkov, and Yu. V. Ozerov, Sov. Phys. JETP Lett. **13**, 28 (1971).
10. V. V. Akimov, V. M. Balebanov, A. S. Belaousov, I. D. Blochintsev, G. V. Veselova, M. B. Dobriyan, L. F. Kalinkin, S. V. Kovalenko, V. D. Kozlov, N. G. Leikov, N. K. Mordvov, Y. I. Nagornih, V. E. Nesterov, O. F. Prilutskiy, V. L. Prohin, V. G. Rodin, et al., Space Sci. Rev. **49**, 111 (1988).
11. V. V. Akimov, V. M. Balebanov, A. S. Belaousov, I. D. Blohintsev, V. A. Volzhenskaya, I. A. Gerasimov, M. B. Dobriyan, L. F. Kalinkin, V. D. Kozlov, V. B. Kotova, N. G. Leikov, N. K. Mordvov, Yu. I. Nagornih, V. E. Nesterov, V. P. Poluektov, O. F. Prilutskiy, et al., Space Sci. Rev. **49**, 125 (1988).
12. C. E. Fichtel, R. C. Hartman, D. A. Kniffen, D. J. Thompson, G. F. Bignami, H. Ögelman, M. E. Özel, and T. Tümer, Astrophys. J. **198**, 163 (1975).
13. B. N. Swanenburg, K. Bennett, G. F. Bignami, R. Buccheri, P. Caraveo, W. Hermsen, G. Kanbach, G. G. Lichti, J. L. Masnou, H. A. Mayer-Hasselwander, J. A. Paul, B. Sacco, L. Scarsi, and R. D. Wills, Astrophys. J. **243**, L69 (1981).
14. A. R. Bazer-Bachi, J. M. Lavigne, J. F. Olive, M. Gros, I. Grenier, N. G. Leikov, V. V. Akimov, V. A. Volsenskaya, L. F. Kalinkin, V. E. Nesterov, A. M. Galper, V. M. Zemskov, Y. V. Oserov, N. P. Topchiev, M. I. Fradkin, E. I. Chuikin, et al., Nucl. Phys. B Suppl. **33**, 208 (1993).
15. E. J. Schneid, D. L. Bertsch, B. L. Dingus, J. A. Esposito, S. E. Fichte, R. C. Hartman, S. D. Hunter, G. Kanbach, D. A. Kniffen, Y. S. Lin, N. A. Mayer-Hasselwander, P. F. Michelson, S. von Montigny, R. Mukherjee, P. L. Nolan, R. Sreekumar, and D. J. Thompson, Astron. Astrophys. Suppl. Ser. **120**, 299 (1996).
16. Yu. D. Kotov, V. N. Yurov, E. E. Lupar, K. F. Vlasik, A. I. Arkhangelsky, A. S. Glyanenko, I. V. Rubtsov, V. V. Kadilin, and V. G. Tyshkevich, Solar Syst. Res. **45**, 97 (2011).
17. S. Abdollahi, F. Acero, L. Baldini, J. Ballet, D. Bastieri, R. Bellazzini, B. Berenji, A. Berretta, E. Bissaldi, R. D. Blandford, E. Bloom, R. Bonino, A. Brill, R. J. Britto, P. Bruel, T. H. Burnett, et al., Astrophys. J. Suppl. Ser. **260**, 53 (2022).
18. S. Abdollahi, F. Acero, M. Ackermann, M. Ajello, W. B. Atwood, M. Axelsson, L. Baldini, J. Ballet, G. Barbiellini, D. Bastieri, J. Becerra Gonzalez,

R. Bellazzini, A. Berretta, E. Bissaldi, R. D. Blandford, E. D. Bloom, et al., Astrophys. J. Suppl. Ser. **247**, 33 (2020).

19. M. Ajello, M. Arimoto, M. Axelsson, L. Baldini, G. Barbiellini, D. Bastieri, R. Bellazzini, P. N. Bhat, E. Bissaldi, R. D. Blandford, R. Bonino, J. Bonnell, E. Bottacini, J. Bregeon, P. Bruel, R. Buehler, et al., Astrophys. J. **878**, 52 (2019).
20. A. von Kienlin, C. A. Meegan, W. S. Paciesas, P. N. Bhat, E. Bissaldi, M. S. Briggs, E. Burns, W. H. Cleveland, M. H. Gibby, M. M. Giles, A. Goldstein, R. Hamburg, C. M. Hui, D. Kocevski, B. Mailyan, C. Malacaria, et al., Astrophys. J. **893**, 46 (2020).
21. A. Lien, T. Sakamoto, S. D. Barthelmy, W. H. Baumgartner, J. K. Cannizzo, K. Chen, N. R. Collins, J. R. Cummings, N. Gehrels, H. A. Krimm, C. B. Markwardt, D. M. Palmer, M. Stamatikos, E. Troja, and T. N. Ukwatta, Astrophys. J. **829**, 7 (2016).
22. D. J. Thompson, Rep. Prog. Phys. **71**, 116901 (2008).
23. R. K. Leane, T. R. Slatyer, J. F. Beacom, and K. C. Y. Ng, Phys. Rev. D **98**, 023016 (2018).
24. F. Calore, P. Carenza, M. Giannotti, J. Jaeckel, and A. Mirizz, Phys. Rev. D **102**, 123005 (2020).
25. J. Chang, J. H. Adams, H. S. Ahn, G. L. Bashindzhagyan, M. Christl, O. Ganel, T. G. Guzik, J. Isbert, K. C. Kim, E. N. Kuznetsov, M. I. Panasyuk, A. D. Panov, W. K. H. Schmidt, E. S. Seo, N. V. Sokolskaya, J. W. Watts, et al., Nature (London, U.K.) **456**, 362 (2008).
26. S. Abdollahi et al. (Fermi-LAT Collab.), Phys. Rev. D **95**, 082007 (2017).
27. PAMELA Collab., Riv. Nuovo Cim. **40**, 473 (2017).
28. M. Aguilar et al. (AMS Collab.), Phys. Rev. Lett. **113**, 221102 (2014).
29. O. Adriani et al. (CALET Collab.), Phys. Rev. Lett. **120**, 261102 (2018).
30. DAMPE Collab., Nature (London, U.K.) **552**, 63 (2017).
31. D. B. Tridoni, P. Colin, L. Cossio, M. Doro, and V. Scalzotto, arXiv: 1110.4008.
32. D. Staszak, arXiv: 1508.06597.
33. F. Aharonian, A. G. Akhperjanian, G. Anton, U. Barres de Almeida, A. R. Bazer-Bachi, Y. Becherini, B. Behera, K. Bernlöhr, A. Bochow, C. Boisson, J. Bolmont, V. Borrel, J. Brucker, F. Brun, P. Brun, R. Bühler, et al., Astron. Astrophys. **508**, 561 (2009).
34. V. A. Dogiel, M. I. Fradkin, L. V. Kurnosova, L. A. Razorenov, M. A. Rusakovich, and N. P. Topchiev, Space Sci. Rev. **49**, 215 (1989).
35. V. L. Ginzburg, V. A. Kaplin, A. I. Karakash, L. V. Kurnosova, A. G. Labenskii, M. F. Runtso, A. P. Soldatov, N. P. Topchiev, M. I. Fradkin, S. K. Chernichenko, and I. V. Shein, Cosmic Res. **45**, 449 (2007).
36. A. M. Galper, O. Adriani, R. L. Aptekar, I. V. Arkhangelskaja, A. I. Arkhangelskiy, M. Boezio, V. Bonvicini, K. A. Boyarchuk, Yu. V. Gusakov, M. O. Farber, M. I. Fradkin, V. A. Kachanov, V. A. Kaplin, M. D. Kheymits, A. A. Leonov, F. Longo, et al., Adv. Space Res. **51**, 297 (2013).
37. A. A. Leonov, A. M. Galper, V. Bonvicini, N. P. Topchiev, O. Adriaini, R. L. Aptekar, I. V. Arkhangelskaja, A. I. Arkhangelskiy, L. Bergstrom, E. Berti, G. Bigongiari, S. G. Bobkov, M. Boezio, E. A. Bogomolov, S. Bonechi, M. Bongi, et al., Adv. Space Res. **56**, 1538 (2015).
38. N. P. Topchiev, A. M. Galper, V. Bonvicini, O. Adriani, I. V. Arkhangelskaja, A. I. Arkhangelskiy, A. V. Bakaldin, S. G. Bobkov, M. Boezio, O. D. Dalkarov, A. E. Egorov, M. S. Gorbunov, Yu. V. Gusakov, B. I. Hnatyk, V. V. Kadilin, V. A. Kaplin, et al., J. Phys.: Conf. Ser. **798**, 012011 (2017).
39. A. M. Galper, N. P. Topchiev, and Yu. T. Yurkin, Astron. Rep. **62**, 882 (2018).
40. A. A. Leonov, A. M. Galper, N. P. Topchiev, A. V. Bakaldin, M. D. Kheimits, A. V. Mikhailova, V. V. Mikhailov, and S. I. Suchkov, Phys. At. Nucl. **82**, 855 (2019).
41. N. P. Topchiev, A. M. Galper, I. V. Arkhangelskaja, A. I. Arkhangelskiy, A. V. Bakaldin, Yu. V. Gusakov, O. D. Dalkarov, A. E. Egorov, V. G. Zverev, A. A. Leonov, P. Yu. Naumov, N. Yu. Pappe, M. F. Runtso, Yu. I. Stozhkov, S. I. Suchkov, M. D. Kheimitz, et al., Bull. Russ. Acad. Sci.: Phys. **83**, 629 (2019).
42. A. I. Arkhangelskiy, A. M. Galper, I. V. Arkhangelskaja, A. V. Bakaldin, E. N. Chasovikov, I. V. Chernysheva, O. D. Dalkarov, A. E. Egorov, Yu. V. Gusakov, M. D. Kheymits, A. A. Leonov, N. Yu. Pappe, M. F. Runtso, Yu. I. Stozhkov, S. I. Suchkov, N. P. Topchiev, et al., J. Phys.: Conf. Ser. **1690**, 012024 (2020).
43. A. I. Arkhangelskiy, A. M. Galper, I. V. Arkhangelskaja, A. V. Bakaldin, I. V. Chernysheva, O. D. Dalkarov, A. E. Egorov, Yu. V.Gusakov, M. D. Kheymits, A. A. Leonov, N. Yu. Pappe, M. F. Runtso, Yu. I. Stozhkov, S. I. Suchkov, N. P. Topchiev, and Yu. T. Yurkin, Phys. At. Nucl. **83**, 252 (2020).
44. A. E. Egorov, N. P. Topchiev, A. M. Galper, O. D. Dalkarov, A. A. Leonov, S. I. Suchkov, and Yu. T. Yurkin, J. Cosmol. Astropart. Phys. **2020**, 049 (2020).
45. S. I. Suchkov, A. I. Arkhangelskiy, V. A. Baskov, A. M. Galper, O. D. Dalkarov, A. I. L'vov, N. Yu. Pappe, V. V. Polyansky, N. P. Topchiev, and I. V. Chernysheva, Instrum. Exp. Tech. **64**, 669 (2021).
46. A. A. Leonov, A. M. Galper, N. P. Topchiev, I. V. Arkhangelskaja, A. I. Arkhangelskiy, A. V. Bakaldin, I. V. Chernysheva, O. D. Dalkarov, A. E. Egorov, M. D. Kheymits, M. G. Korotkov,

A. G. Malinin, A. G. Mayorov, V. V. Mikhailov, A. V. Mikhailova, P. Yu. Minaev, et al., Adv. Space Res. **69**, 514 (2022).

47. N. P. Topchiev, A. M. Galper, I. V. Arkhangelskaja, A. I. Arkhangelskiy, A. V. Bakaldin, R. A. Cherniy, I. V. Chernysheva, E. N. Gudkova, Yu. V. Gusakov, O. D. Dalkarov, A. E. Egorov, M. D. Kheymits, M. G. Korotkov, A. A. Leonov, A. G. Malinin, V. V. Mikhailov, et al., Adv. Space Res. **70**, 2773 (2022).
48. W. B. Atwood, A. A. Abdo, M. Ackermann, W. Althouse, B. Anderson, M. Axelsson, L. Baldini, J. Ballet, D. L. Band, G. Barbiellini, J. Bartelt, D. Bastieri, B. M. Baughman, K. Bechtol, D. Bédérède, F. Bellardi, et al., Astrophys. J. **697**, 1071 (2009).
49. N. Budnev, I. Astapov, P. Bezyazeekov, E. Bonvech, A. Borodin, A. Bulan, A. Chiavassa, D. Chernov, A. Dyachok, A. Gafarov, A. Garmash, V. Grebenyuk, O. Gress, E. Gress, T. Gress, A. Grinyuk, et al., Nucl. Instrum. Methods Phys. Res., Sect. A **1039**, 167047 (2022).
50. P. W. Cattaneo, HERD Collab., Nucl. Part. Phys. Proc. **306–308**, 85 (2019).
51. S. Schael, A. Atanasyan, J. Berdugo, T. Bretz, M. Czupalla, B. Dachwald, P. von Doetinchem, M. Duranti, H. Gast, W. Karpinski, T. Kirn, K. Lübelsmeyer, C. Mana, P. S. Marrocchesi, P. Mertsch, I. V. Moskalenko, et al., Nucl. Instrum. Methods Phys. Res., Sect. A **944**, 162561 (2019).

View publication stats

Journal of Physics:
Conference Series

PURPOSE-LED PUBLISHING™

PAPER • OPEN ACCESS

High-energy gamma-ray studying with GAMMA-400 after Fermi-LAT

To cite this article: N P Topchiev *et al* 2017 *J. Phys.: Conf. Ser.* **798** 012011

View the article online for updates and enhancements.

You may also like

- A nine-pixel matched collimator for low- and medium-energy SPECT imaging
Atsuro Suzuki, Wataru Takeuchi, Yuichi Morimoto et al.
- THE FIRST DETECTION OF GeV EMISSION FROM AN ULTRALUMINOUS INFRARED GALAXY: Arp 220 AS SEEN WITH THE *FERMI* LARGE AREA TELESCOPE
Fang-Kun Peng, Xiang-Yu Wang, Ruo-Yu Liu et al.
- Imaging of gamma photons from activated gold wire using a high-energy gamma camera after irradiation of neutrons from boron neutron capture therapy (BNCT) system
Seiichi Yamamoto, Naonori Hu, Jun Kataoka et al.



This content was downloaded from IP address 95.24.161.63 on 28/07/2025 at 09:44

IOP Conf. Series: Journal of Physics: Conf. Series **798** (2017) 012011 doi:10.1088/1742-6596/798/1/012011

High-energy gamma-ray studying with GAMMA-400 after Fermi-LAT

N P Topchiev[1,*], A M Galper[1,2], V Bonvicini[3], O Adriani[4], I V Arkhangelskaja[2], A I Arkhangelskiy[2], A V Bakaldin[5], S G Bobkov[5], M Boezio[3], O D Dalkarov[1], A E Egorov[1], M S Gorbunov[5], Yu V Gusakov[1], B I Hnatyk[6], V V Kadilin[2], V A Kaplin[2], M D Kheymits[2], V E Korepanov[7], A A Leonov[1,2], F Longo[3], V V Mikhailov[2], E Mocchiutti[3], A A Moiseev[8], I V Moskalenko[9], P Yu Naumov[2], P Picozza[10], M F Runtso[2], O V Serdin[5], R Sparvoli[10], P Spillantini[4], Yu I Stozhkov[1], S I Suchkov[1], A A Taraskin[2], M Tavani[11], Yu T Yurkin[2] and V G Zverev[1]

[1] Lebedev Physical Institute, Russian Academy of Sciences, Leninskiy pr. 53, 119991 Moscow, Russia
[2] National Research Nuclear University MEPhI (Moscow Engineering Physics Institute), Kashirskoe highway 31, Moscow, 115409, Russia
[3] Istituto Nazionale di Fisica Nucleare, Sezione di Trieste, Via Valerio 2, Trieste, 34127, Italy
[4] Istituto Nazionale di Fisica Nucleare, Sezione di Firenze, Via G. Sansone 1, Firenze, 50019, Italy
[5] Federal State Institution "Scientific Research Institute for System Analysis of the Russian Academy of Sciences", Nakhimovskiy pr. 36, Moscow, 117218, Russia
[6] Taras Shevchenko National University, Volodymyrska street 64/13, 01601, Kyiv, Ukraine
[7] Lviv Center of Institute of Space Research, Naukova street 5-A, Lviv, Ukraine
[8] CRESST and Astroparticle Physics Laboratory NASA/GSFC, Greenbelt, MD 20771, USA
[9] Hansen Experimental Physics Laboratory, Kavli Institute for Particle Astrophysics and Cosmology, Department of Physics and SLAC National Accelerator Laboratory, Stanford University, Stanford, CA 94305, USA
[10] Istituto Nazionale di Fisica Nucleare, Sezione di Roma 2 and Physics Department of University of Rome Tor Vergata, Via della Ricerca Scientifica 1, Rome, 00133, Italy
[11] Istituto Nazionale di Astrofisica and Physics Department of University of Rome Tor Vergata, Via della Ricerca Scientifica 1, Rome, 00133, Italy

E-mail: *tnp51@yandex.ru

Abstract. Fermi-LAT has made a significant contribution to the study of high-energy gamma-ray diffuse emission and the observation of ~3000 discrete sources. However, one third of all gamma-ray sources (both galactic and extragalactic) are unidentified, the data on the diffuse gamma-ray emission should be clarified, and signatures of dark matter particles in the high-energy gamma-ray range are not observed up to now. GAMMA-400, currently developing gamma-ray telescope, will have the angular (~0.01° at 100 GeV) and energy (~1% at 100 GeV) resolutions in the energy range of 10-1000 GeV better than the Fermi-LAT (as well as ground gamma-ray telescopes) by a factor of 5-10 and observe some regions of the Universe (such as Galactic Center, Fermi Bubbles, Crab, Cygnus, etc.) in the highly elliptic orbit (without shading the telescope by the Earth) continuously for a long time. It will permit to identify many discrete sources, to clarify the structure of extended sources, to specify the data on the diffuse emission, and to resolve gamma rays from dark matter particles.

Content from this work may be used under the terms of the Creative Commons Attribution 3.0 licence. Any further distribution of this work must maintain attribution to the author(s) and the title of the work, journal citation and DOI.
Published under licence by IOP Publishing Ltd

1. Current gamma-ray study challenges

1.1. Analysis of the Fermi-LAT and ground-based telescope gamma-ray results

Since 2008 Fermi-LAT is operating in a near-Earth orbit in the scanning mode and surveying full sky every three hours. Up to now, three catalogs of gamma-ray sources have been published based on the Fermi-LAT observational results: 1FGL [1] and 2FGL [2] for the energy range of 0.1-100 GeV, 3FGL [3] for the energy range of 0.1-300 GeV. Moreover two catalogs of high-energy gamma-ray sources were published: 1FHL [4] for the energy above 10 GeV and 2FHL [5] for the energy range of 50-2000 GeV. From these catalogs, it is seen that 33% of gamma-ray sources are unidentified. The exposition of the source observations presented in [3] shows that during four years of the operation Fermi-LAT observed, e.g., the Galactic center during only ~12% or 1/8 of total operation time.

Based on results of gamma-ray observations at energies above 100 GeV by ground-based facilities VERITAS [6], MAGIC [7], H.E.S.S. [8] and others the TeVCat catalog of discrete gamma-ray sources [9] was created, which contains about 180 sources and mainly matches with 3FGL.

It is important to note that the observational data from Fermi-LAT and ground-based facilities were obtained for the energy ranges, which overlap insufficiently for many gamma-ray sources. Sometimes they don't overlap at all. Hence, the frontier range around 100 GeV is still very interesting for investigations from space. In addition, the angular resolution of Fermi-LAT, existing ground-based telescopes, and even planned CTA [10] in the region of around 10-300 GeV is only ~0.1°. Therefore a much better angular resolution is required in order to identify many gamma-ray sources.

1.2. Indirect searches of dark matter

Another very interesting and important goal in the studies of gamma-ray sky is indirect searches of dark matter (DM). In general, an exact physical nature of DM is a top puzzle in the modern astrophysics. There are many candidates on the DM role being proposed. However, WIMPs with mass between several GeV and several TeV are still considered as the most probable candidate [11]. WIMPs can annihilate or decay with the production of gamma rays. This emission can have both continuum energy spectrum or monoenergetic lines. This depends on which annihilation channel realizes in the nature. The continuum spectrum would come in the case of annihilation into particle pairs like

$$\chi\chi \to b\bar{b}, \tau^+\tau^-, W^+W^-, \mu^+\mu^-, q\bar{q}, ZZ$$

or others and gamma-ray lines would be produced in the case of direct annihilation into photons $\chi\chi \to \gamma\gamma, \gamma Z, \gamma H$ [12]).

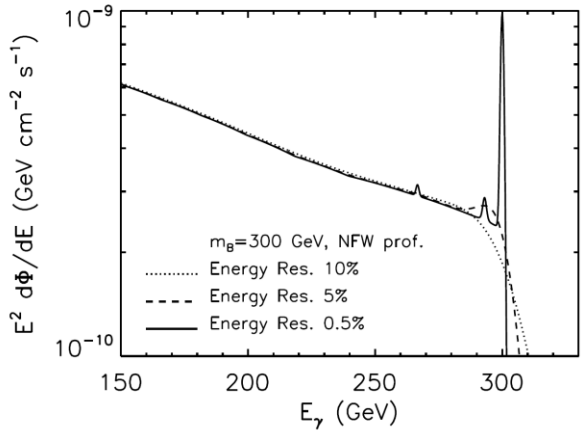


Figure 1. Expected energy spectrum for the annihilation of 300-GeV WIMP producing gamma rays ($\gamma\gamma$, γZ, and γH lines), which can be resolved from background by various telescopes with the energy resolutions of 10%, 5%, and 0.5% [13].

To resolve gamma-ray lines from background it is necessary to have a high-energy resolution. Figure 1 shows expected energy spectrum for the annihilation of 300-GeV WIMP producing gamma rays ($\gamma\gamma$, γZ, and γH lines), which can be resolved from background by various telescopes with the energy resolutions of 10%, 5%, and 0,5% [13]. Note that the energy resolution of Fermi-LAT and ground-based telescopes is only 10-15% for the energy of 10-300 GeV. Thus, as seen from figure 1, the future telescopes need to have 1-2% energy resolution.

2. The GAMMA-400 gamma-ray telescope

Thus, to resolve unidentified gamma-ray sources and search for the potential gamma-ray lines from DM we need in a gamma-ray telescope with the angular resolution of several hundredth degrees and the energy resolution of few percent for the energy of ~100 GeV. This is going to be GAMMA-400, which will be installed onboard the Russian space observatory [14-18].

The GAMMA-400 main scientific goals are: dark matter searching by means of gamma-ray astronomy; precise measurements of Galactic Center, Fermi Bubbles, Crab, Vela, Cygnus, Geminga, Sun, and other regions, extended and point gamma-ray sources, diffuse gamma rays with unprecedented angular (~0.01° at $E_\gamma > 100$ GeV) and energy (~1% at $E_\gamma > 100$ GeV) resolutions.

2.1. The GAMMA-400 physical scheme

The physical scheme of the GAMMA-400 gamma-ray telescope is shown in figure 2. The GAMMA-400 energy range for gamma-ray studies is from ~20 MeV to ~1000 GeV. The GAMMA-400 field of view (FoV) is ±45°.

GAMMA-400 consists of plastic scintillation anticoincidence top and lateral detectors (AC top and AC lat), converter-tracker (C), plastic scintillation detectors (S1 and S2) for the time-of-flight system (TOF), calorimeter (CC), plastic scintillation detector (S3).

The anticoincidence detectors surrounding the converter-tracker are used to distinguish gamma rays from significantly larger number of charged particles (e.g., in the region of 10-100 GeV, the flux ratios for gamma rays to electrons and protons are ~ $1:10^2:10^5$.

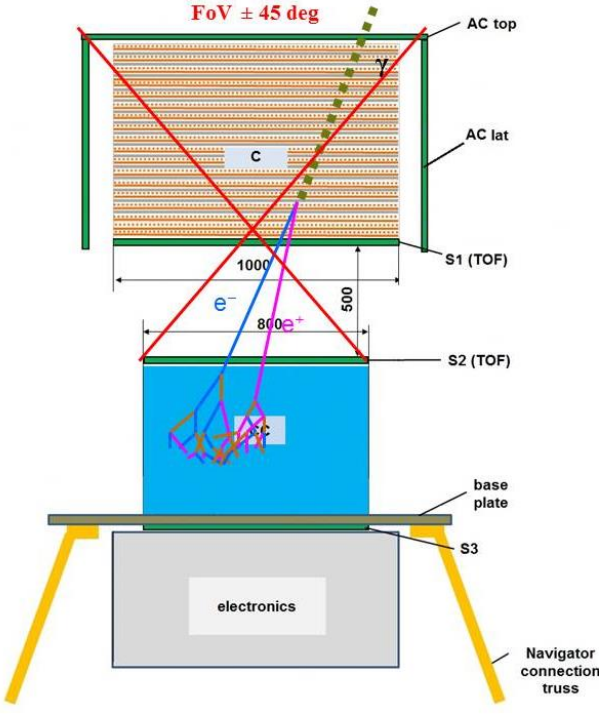


Figure 2. The GAMMA-400 physical scheme.

All scintillation detectors consist from two independent 1-cm layers. The time-of-flight system, where detectors S1 and S2 are separated by approximately 500 mm, determines the top-down direction of arriving particles. The additional scintillation detector S3 improves hadron and electromagnetic shower separation.

The converter-tracker consists of 22 layers of double (x, y) silicon strip coordinate detectors (pitch of 0.08 mm). Twenty layers are interleaved with tungsten conversion foils and final two layers have no tungsten. This configuration allows us to measure gamma rays down to ~20 MeV. The total converter-tracker thickness is ~1 X_0. The converter-tracker information is used to precisely determine the conversion point and the direction of each incident particle.

The calorimeter CC measures particle energy and consists of CsI(Tl) crystals. The total calorimeter thickness is ~21 X_0 or ~1.0 λ_0 when detecting vertical incident particles and ~43 X_0 or ~2.0 λ_0 when detecting laterally incident particles. Using the deep calorimeter allows us to extend the energy range up to several TeV for gamma rays, and to reach the energy resolution of ~1% above 100 GeV.

2.2. The GAMMA-400 gamma-ray observatory

The GAMMA-400 gamma-ray observatory will be installed onboard of the Navigator space platform, which is designed and manufactured by the Lavochkin Association.

Using the Navigator space platform gives the GAMMA-400 experiment a highly unique opportunity for the near future gamma- and cosmic-ray science, since it allows us to install a scientific payload (mass of 2500 kg, power consumption of 2000 W, and telemetry downlink of 100 GB/day, with lifetime more than 7 years), which will provide GAMMA-400 with the means to significantly contribute as the next generation instrument for gamma-ray astronomy and cosmic-ray physics.

The GAMMA-400 experiment will be initially launched into a highly elliptical orbit (with an apogee of 300,000 km and a perigee of 500 km, with an inclination of 51.4°), with 7 days orbital period. Under the action of gravitational disturbances of the Sun, Moon, and the Earth after ~6 months the orbit will transform to about an approximately circular one with a radius of ~200 000 km and will not suffer from the Earth's occultation and shielding by the radiation belts. The launch of the GAMMA-400 space observatory is planned for the middle of the 2020s.

2.3. Comparison of GAMMA-400 with Fermi-LAT and ground-based telescopes

GAMMA-400 has numerous advantages in comparison with the Fermi-LAT:

- highly elliptical orbit (without the Earth's occultation and away from the radiation belts) allows us to observe with the full aperture of ±45° different gamma-ray sources continuously over a long period of time with the exposition greater by a factor of 8 than for Fermi-LAT operating in the sky-survey mode;
- thanks to a smaller pitch (by a factor of 3) and analog readout in the coordinate silicon strip detectors, GAMMA-400 has an excellent angular resolution above ~20 MeV;
- due to the deep (~21 X_0) calorimeter, GAMMA-400 has an excellent energy resolution and can more reliably to detect gamma rays up to several TeV for vertically incident events;
- owing to the better gamma-ray separation from cosmic rays (in contrast to Fermi-LAT, the presence of a special trigger with event timing, time-of-flight system, two-layer scintillation detectors), GAMMA-400 is significantly well equipped to separate gamma rays from the background of cosmic rays and backscattering events.

GAMMA-400 will have also the better angular and energy resolutions in the energy region 10-1000 GeV in comparison with current and future ground-based instruments: VERITAS [6], MAGIC [7], H.E.S.S. [8], CTA [10], and HAWC [19] (figure 3) and it allows us to fill the gap at the energy of ~100 GeV between the space- and ground-based instruments.

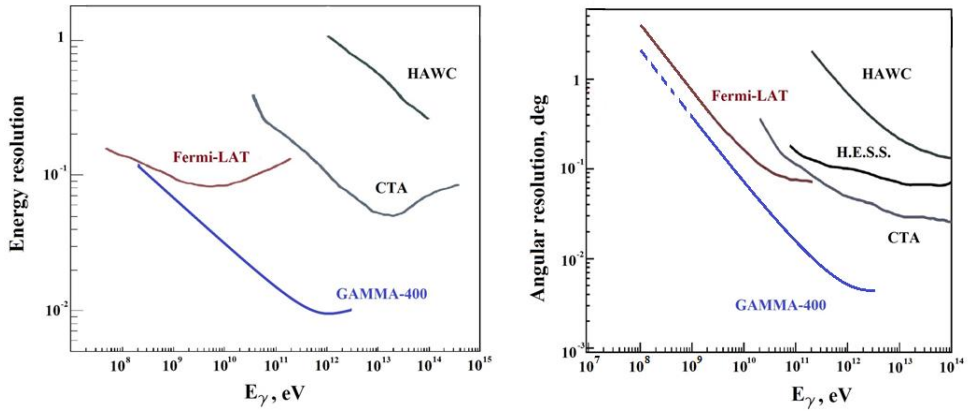


Figure 3. Comparison of energy and angular resolutions for GAMMA-400, Fermi-LAT, H.E.S.S., HAWC, and CTA.

3. The anticipated GAMMA-400 scientific output

3.1. Galactic plane

GAMMA-400 will study continuously over a long period of time different regions of Galactic plane (figure 4), for example, Galactic center, Fermi Bubbles, Crab, Vela, Cygnus, Geminga with FoV of ±45°. In particular, using the gamma-ray fluxes obtained by Fermi-LAT, we can expect that GAMMA-400 when observing the Galactic center with aperture of ±45°during 1 year will detect: 57400 photons for E_γ > 10 GeV; 5240 photons for E_γ > 50 GeV; 1280 photons for E_γ > 100 GeV; 535 photons for E_γ > 200 GeV.

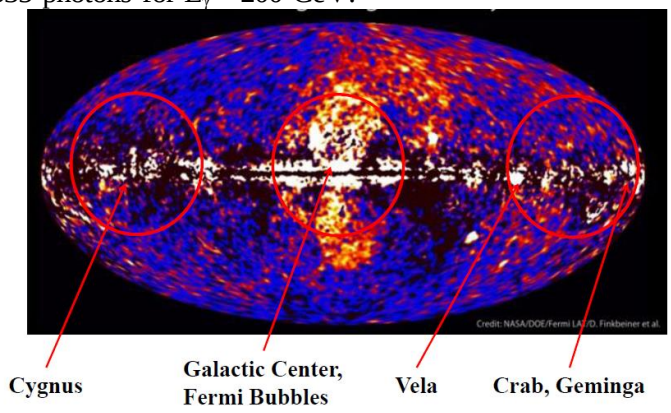


Figure 4. Galactic center, Fermi Bubbles, Crab, Cygnus, Vela, Geminga, and other regions will be observed with the GAMMA-400 FoV of ±45°.

3.2. Dark matter searching

When detecting gamma rays from DM, the intensity from gamma rays is calculated by

$$\frac{d\Phi}{d\Omega dE} = \frac{1}{2}\frac{\langle\sigma v\rangle}{m_\chi^2}\frac{dN_\gamma}{dE} \times \frac{J}{4\pi}\ [\text{erg s}^{-1}\,\text{cm}^{-2}\,\text{GeV}^{-1}\,\text{sr}^{-1}], J = \int_{l.o.s.} \rho^2(\vec{r})dl.$$

Here, $\langle\sigma v\rangle$ is particle annihilation cross section, m_χ is particle mass, dN_γ/dE is the spectrum of gamma rays from annihilation, $\rho(\vec{r})$ is the DM density of investigated object [20].

The Galactic center is, apparently, the best potential source of DM emission possessing the largest *J*-factor [11]. Moreover, recently, the anomaly excess of gamma-ray emission in the GeV energy range was revealed near the Galactic center (the region of about one degree) [21], which can be well described by DM with mass of several tens of GeV and annihilation cross section of about standard thermal 10^{-26} cm^3/s. However, this observed excess can have another interpretation - the presence a population of millisecond pulsars [22]. Therefore, the new GAMMA-400 observational data can help to solve this problem.

Dwarf galaxies are considered for a long time as the strongest sources of constraints for DM, because they have sufficiently large *J*-factors and at the same time have considerably less gamma-ray background in comparison with the Galactic center. Current and predicted constraints for DM parameters according to observations of 15 known dwarf galaxies are shown in figure 5 (for the typical quark-antiquark channel [23]). GAMMA-400 will able to specify the constrain area.

Potentially interesting objects are other galaxies and their clusters, where DM presents and can emit gamma rays. GAMMA-400 with the highest energy resolution of ~1% will have unique sensitivity for detecting DM.

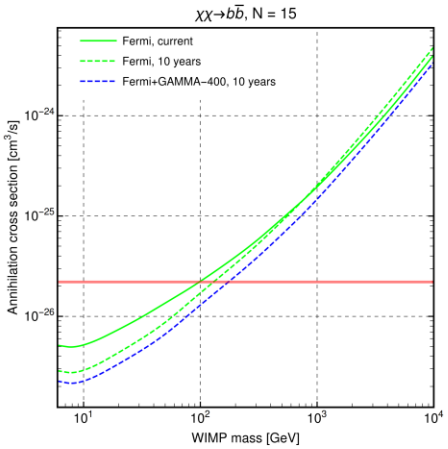


Figure 5. Current and predicted constraints for DM parameters according to observations of 15 known dwarf galaxies.

References

[1] Abdo A *et al.* 2010 *ApJ* **188** 405
[2] Nolan P *et al.* 2012 *ApJS* **199** 31
[3] Acero F. *et al.* 2015 *ApJS* **218** 23
[4] Ackermann M *et al.* 2013 *ApJS* **209** 1
[5] Ackermann M *et al.* 2016 *ApJS* **222** 1
[6] Ong R E *et al.* 2014 *Adv. Space Res.* **53** 1483
[7] Mazin D *et al.* 2014 *arXiv*:1410.5073
[8] Balzer A *et al.* 2013 *arXiv*:1311.3486
[9] URL: http://tevcat.uchicago.edu/
[10] CTA Consortium. 2011 *Exp. Astron.* **32** 193
[11] Bertone G 2010 *Particle Dark Matter: Observations, Models and Searches* (Cambridge Univ. Press)
[12] Bertone G *et al.* 2010 *arXiv*:1009.5107
[13] Nekrassov D *et al.* 2011 *arXiv*:1106.2752
[14] Dogiel V *et al.* 1988 *Space Sci. Rev.* **49** 215
[15] Galper A *et al.* 2013 *Adv. Space Res.* **51** 297
[16] Galper A *et al.* 2013 *AIP Conf. Proc.* **1516** 288
[17] Topchiev N *et al.* 2015 *Bull. Russ. Acad. Sci. Phys.* **79** 417
[18] Topchiev N *et al.* 2016 *J. of Phys.: Conf. Ser.* **675** 032009
[19] Westerhoff S *et al.* 2014 *Adv. Space Res.* **53** 1492
[20] Cirelli M *et al.* 2011 *JCAP* **03** 051
[21] Abazajian K and Kaplinghat M 2012 *Phys. Rev.* **D86** (2012) 083511
[22] Bartels R, Krishnamurthy S and Weniger C 2015 *arXiv*:1506.05104
[23] Charles E *et al.* 2016 *arXiv*:1605.02016

PROCEEDINGS OF SCIENCE

Updated constraints on WIMP dark matter annihilation by radio observations of M31 – all annihilation channels

Andrei E. Egorov*

Nuclear Physics and Astrophysics Division, Lebedev Physical Institute,
Leninskii prospect - 53, Moscow, Russia

E-mail: aegorov@runbox.com

The present work derived the robust constraints on annihilating WIMP parameters utilizing new radio observations of M31, as well as new studies of its DM distribution and other properties. The characteristics of emission due to DM annihilation were computed in the frame of 2D galactic model employing GALPROP code adapted specifically for M31. This enabled us to refine various inaccuracies of previous studies on the subject. DM constraints were obtained for all possible annihilation channels except $\chi\chi \to \gamma\gamma, \nu\bar{\nu}$. A wide variety of radio data was utilized in the frequency range ≈(0.1–10) GHz. As the result the thermal WIMP lighter than fiducially ≈(40–70) GeV was excluded in the case of light primary annihilation products $\chi\chi \to \tau^+\tau^-, \mu^+\mu^-, gg, c\bar{c}, u\bar{u}, d\bar{d}, s\bar{s}, e^+e^-, b\bar{b}$ (and an arbitrary combination of them). Heavier WIMP, which can annihilate to $W^+W^-, Z^0Z^0, t\bar{t}, hh$; can not be probed at the level of thermal cross section, unless one assumes the optimistic cases of DM density and magnetic field distributions in M31. In summary, $m_x \gtrsim 40$ GeV represents the fiducial channel-independent mass limit for the thermal WIMP with the full uncertainty range estimated to be ≈(20–90) GeV. The obtained exclusions are competitive to those from Fermi-LAT observations of dwarfs and AMS-02 measurements of antiprotons. Our constraints significantly restrict the opportunity to explain the gamma-ray outer halo of M31 by annihilating DM. And, finally, we questioned the possibility claimed in other studies to robustly constrain heavy thermal WIMP with $m_x > 100$ GeV by radio data on M31.

*** 27th European Cosmic Ray Symposium - ECRS ***
*** 25-29 July 2022 ***
*** Nijmegen, the Netherlands ***

*Speaker

© Copyright owned by the author(s) under the terms of the Creative Commons Attribution-NonCommercial-NoDerivatives 4.0 International License (CC BY-NC-ND 4.0).

PoS(ECRS)120

1. Introduction and motivation

The physical nature of dark matter (DM) remains to be one of the biggest puzzles in modern physics and astronomy. Currently, we may outline three most popular candidates for the role of DM: weakly interacting massive particles (WIMPs), axionlike particles (ALPs) and sterile neutrinos (see e.g. [1] for a review). This work is dedicated to indirect searches of WIMPs, which traditionally have been the most anticipated. In our case we consider DM halo of the big neighbor galaxy M31 (Andromeda galaxy). Annihilating WIMPs in its halo would produce relativistic electrons and positrons ($e^{\pm}$), which in turn would generate synchrotron emission in the galactic magnetic field (MF) at radio frequencies. Hence, radio observations of the galaxy may infer some constraints on annihilating DM or even hints of its signal. Meanwhile, historically, the first attempt (known to the author) to constrain DM particle properties by radio observations was made in [2].

Traditionally the gamma-ray band has been the most promising for WIMP indirect searches: space-based gamma-ray telescopes, particularly Fermi-LAT, are able to probe the thermal WIMPs up to $m_x \approx 100$ GeV by observations of Milky Way (MW) dwarf satellites [3]; and ground-based facilities, particularly CTA, will be able to probe the thermal WIMPs above this mass scale by observations of the Galactic halo [4]. However, the mass range around $m_x \approx 100$ GeV is poorly reachable by both techniques. And here it is very relevant to employ alternative methodologies – particularly, radio observations – in order to complement the gamma-ray window and explore the whole WIMP mass range evenly.

M31 is one of the best targets in the sky for DM searches in radio due to its proximity, which allows detailed imaging and studies of the galactic medium. Also the central region of M31 is relatively faint in radio, which implies higher sensitivity to the potential DM signal due to lower hindering by usual astrophysical emissions. Being motivated by these advantages we started our work on the subject by [5]. The current work refined and updated the former (and also the works by other authors) in a variety of aspects. All the details are thoroughly described in [6] (sec. II there detailizes inaccuracies of the previous works on the subject). This letter provides a brief summary and generalization for all possible annihilation channels (in [6] only popular $\chi\chi \rightarrow b\bar{b}, \tau^+\tau^-$ channels were computed).

At first we modeled theoretically the characteristics of anticipated emission due to DM annihilation, i.e. the emission intensity dependence on all the parameters. This modeling procedure is described in the next sec. 2. Then the relevant observational data were collected and compared with the theoretically calculated DM emission intensities in order to derive DM constraints of interest – this is described in sec. 3. And sec. 4 provides a summary and relation with the gamma-ray band.

2. Modeling the emission due to DM annihilation by GALPROP

For this purpose one has to solve the transport equation for $e^{\pm}$ produced by DM annihilation (DM $e^{\pm}$ hereafter) and then to calculate the synchrotron emission from them assuming certain MF distribution. This task was fully solved by employment of GALPROP package [7] (v56, specifically adapted for M31) together with my addition [8], which precisely calculates DM source term for the transport equation. The former has the following form (in general case of an arbitrary combination

PoS(ECRS)120

of the annihilation channels):

$$q(R,E) = \frac{1}{2}\langle\sigma v\rangle \left(\frac{\rho(R)}{m_x}\right)^2 \xi(R) \sum_i BR_i \frac{dN_{e,i}}{dE}(E, m_x), \quad (1)$$

where $\langle\sigma v\rangle$ denotes WIMP annihilation cross section, $\rho(R)$ is DM density distribution, m_x is WIMP mass, $\xi(R)$ is the DM annihilation rate boost factor due to substructures, BR_i is the branching ratio to the i-th channel (summation goes over all channels and $\sum_i BR_i = 1$) and $\frac{dN_{e,i}}{dE}(E, m_x)$ represents the energy spectra of $e^{\pm}$ per annihilation. These spectra were taken from PPPC 4 DM ID resource [9]. The transport equation for DM $e^{\pm}$ was solved in 2D, which is a proper approximation for a spiral galaxy. All the previous works employed a deficient 1D (i.e. spherical symmetry) approximation.

Indeed there are significant uncertainties in the emission modeling procedure. The main sources of uncertainties are DM density and MF distributions. $e^{\pm}$ propagation parameters are uncertain too, but they play a secondary role. In order to quantify the uncertainties thoroughly I employed the quite traditional MIN-MED-MAX paradigm, when MIN and MAX model setups provide respectively the lowest and highest DM emission intensities and, hence, the weakest and strongest possible constraints. And MED setup represents some middle or "average expectation" scenario (but not necessarily the average intensity). MIN-MED-MAX models were built separately for DM density profile and MF distribution together with the propagation parameters (MF/prop. with "/" meaning "and") – i.e. three independent density profiles and three independent MF/prop. configurations were tested. MF and propagation parameters were treated jointly in order to reduce a computational heaviness of the task taking into account a subdominant role of the propagation uncertainties. Thus, for each discrete WIMP mass and annihilation channel 3 DM density profiles $\times$ 3 MF/prop. configurations = 9 independent models were computed, providing a good coverage of the parameter space. 1161 separate GALPROP runs were made in order to explore all the relevant WIMP masses and annihilation channels.

In order to set MIN-MED-MAX DM density profiles I conducted a comprehensive analysis of various profile determinations available in the literature with especial emphasis to newer works, which emerged in recent years. Several papers on the subject agree that very cuspy or cored profiles are not favored for M31. Finally I chose Einasto density profiles from [10] and [11] for MIN and MAX cases respectively, and NFW profile from [10] for MED. I refer readers to [6] for the fully-detailed description. Here the description is very brief due to a paper length limit. Regarding the MF distribution model, it is 2D and comprises piecewise-linear dependence on the radius r multiplied by the exponential dependence on the vertical coordinate z. MED and MAX MF models have additional central cusps, which were motivated by MF determination in MW central region [12] and possible similarity between two galaxies. MF strength in the central region of M31 has the biggest importance for our work, since the potential DM signal is very concentrated around the galactic center. I set the central field values based mainly on the results of [12, 13]. These values are the following: for MIN – 14 μG, for MED – 50 μG and for MAX – 100 μG. $e^{\pm}$ propagation parameters were modeled based on CR diffusion studies for both M31 and MW. One important peculiarity in M31 nucleus is that $e^{\pm}$ there have much faster cooling rate through the inverse Compton scattering losses due to denser (by $\approx$2 times) radiation field in comparison with MW nucleus. And the free-free absorption of the synchrotron emission of interest (at $\nu \gtrsim 0.1$ GHz) was proved to be negligible.

PoS(ECRS)120

Putting together all the ingredients described above, DM emission maps and spectra were computed. Their examples and parameter dependencies can be seen in [6, sec. IV].

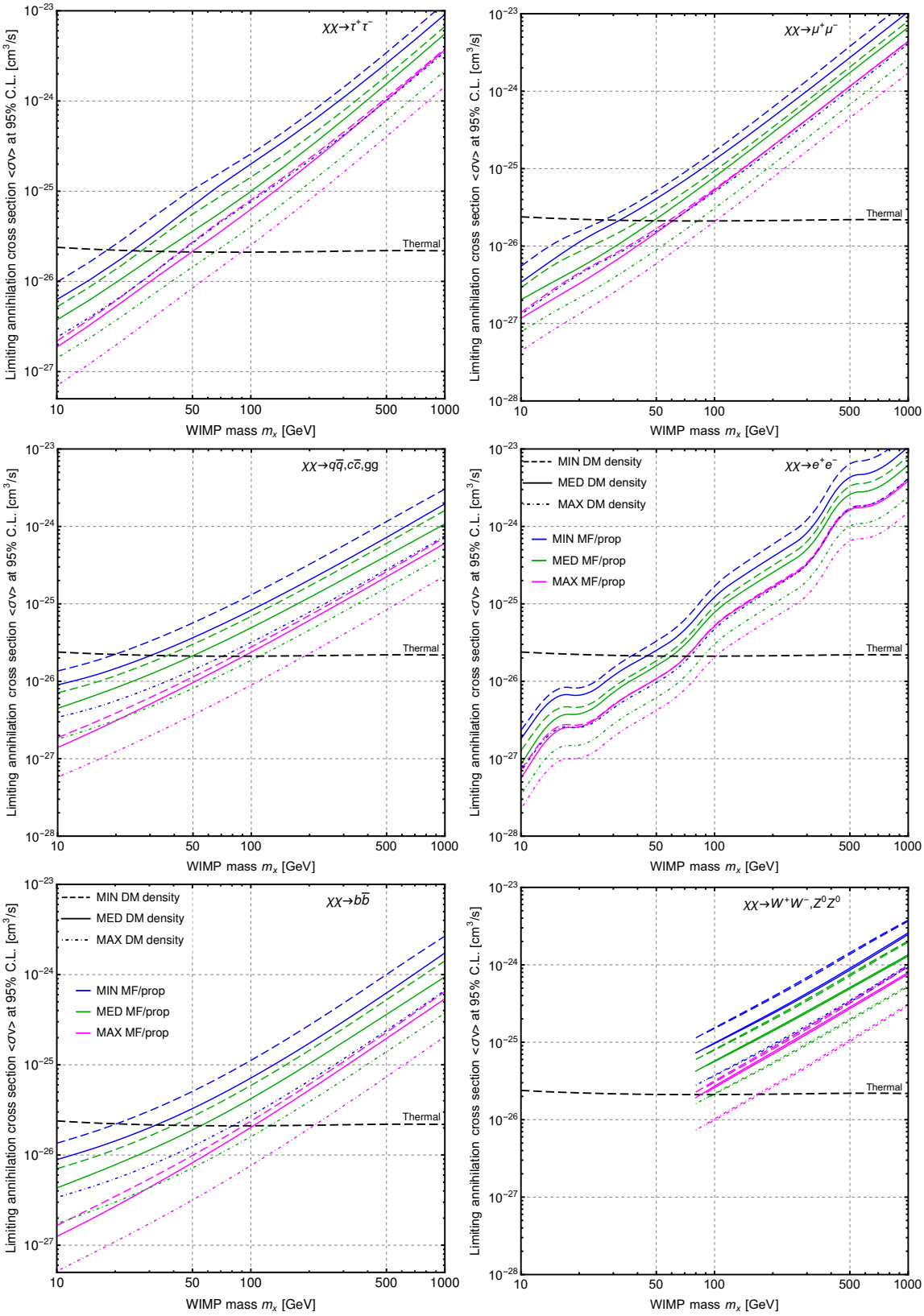
3. Derivation of DM constraints from various radio data

M31 images at eight frequencies in the range ≈(0.1–10) GHz were employed for the derivation of constraints. These maps are mainly clean of the projected discrete sources. On some images even the diffuse thermal emission was subtracted. The main role (by constraining power) belongs to very new and sensitive data from LOFAR Two-meter Sky Survey (LoTSS) [14]. Regarding a choice of the region of interest (ROI) on the sky for derivation of constraints, the central (i.e. bulge) region with $R \lesssim 3$ kpc was employed, since it comprises a vast majority of the emission flux due to DM. Outside of this radius DM emission intensity becomes too low w.r.t. the usual astrophysical backgrounds. Intrinsically this bulge region was divided to concentric annuli individually at each frequency according to the corresponding image resolution. And the observed emission intensity in each annulus at each frequency entered the likelihood function individually and independently. Thus the latter has 33 components/multipliers in total. An important aspect in our model is an absence of any specific assumptions about the intensity of standard astrophysical emission, i.e. the flat independent priors were set for it at all frequencies. This essentially means that the upper limit of the total observed intensity defines the limit for DM emission. This makes our DM constraints quite robust and model-independent. And our likelihood function includes also the systematic uncertainties for the observed intensity besides the statistical uncertainties in the form of map noise.

After construction of the likelihood, which is a function of DM parameters and the observed intensities with their uncertainties, it was marginalized over nuisance parameters in order to get the probability density for DM annihilation cross section. DM emission intensity is linearly proportional to the cross section, if other DM parameters are fixed. Thus the limiting $\langle\sigma v\rangle$ values were numerically calculated for each of 1161 DM models. The results are presented in fig. 1. Overall, we do not see any drastic differences between the exclusion bands for various channels. A general trend is that the exclusion lines for the hadronic channels have smaller slope (i.e. $\langle\sigma v\rangle_{\rm lim}$ increases with the mass slower) and wider uncertainty range w.r.t. the leptonic channels. Considering heavier thermal WIMP annihilating to $W^+W^-, Z^0Z^0, t\bar{t}, hh$, it might manifest itself only in the case of optimistic configurations of DM density and MF/prop. A typical width of the whole uncertainty bands in fig. 1 in the vertical direction (i.e., over $\langle\sigma v\rangle$) slightly exceeds one order of magnitude.

We also naturally would like to have some representative constraints, which are averaged over the uncertainties. For this purpose the geometric mean of all nine DM density and MF/prop. models was calculated for each channel as the fiducial or effective average constraint. The result is shown in fig. 2 for all the channels. We see that the exclusions for all channels form a relatively narrow band – narrower than one order of magnitude over the cross section at any WIMP mass. For $m_x \gtrsim 60$ GeV the exclusions for all channels are mainly confined between those for $b\bar{b}$ and $\tau^+\tau^-$. And $\tau^+\tau^-$ appears to be the least constrained channel over almost the whole mass range considered. Table 1 lists WIMP mass limits and their uncertainty ranges for the thermal cross section. The "..." symbol in the table means that the corresponding exclusion curve does not reach the thermal level at any WIMP mass; i.e. our setup is not sensitive enough to probe the corresponding channel, and any WIMP mass is allowed.

PoS(ECRS)120


χχ→τ⁺τ⁻
χχ→μ⁺μ⁻
χχ→qq̄,cc̄,gg
χχ→e⁺e⁻
χχ→bb̄
χχ→W⁺W⁻,Z⁰Z⁰
MIN DM density
MED DM density
MAX DM density
MIN MF/prop
MED MF/prop
MAX MF/prop
Thermal
Limiting annihilation cross section <σv> at 95% C.L. [cm³/s]
WIMP mass m_x [GeV]

PoS(ECRS)120

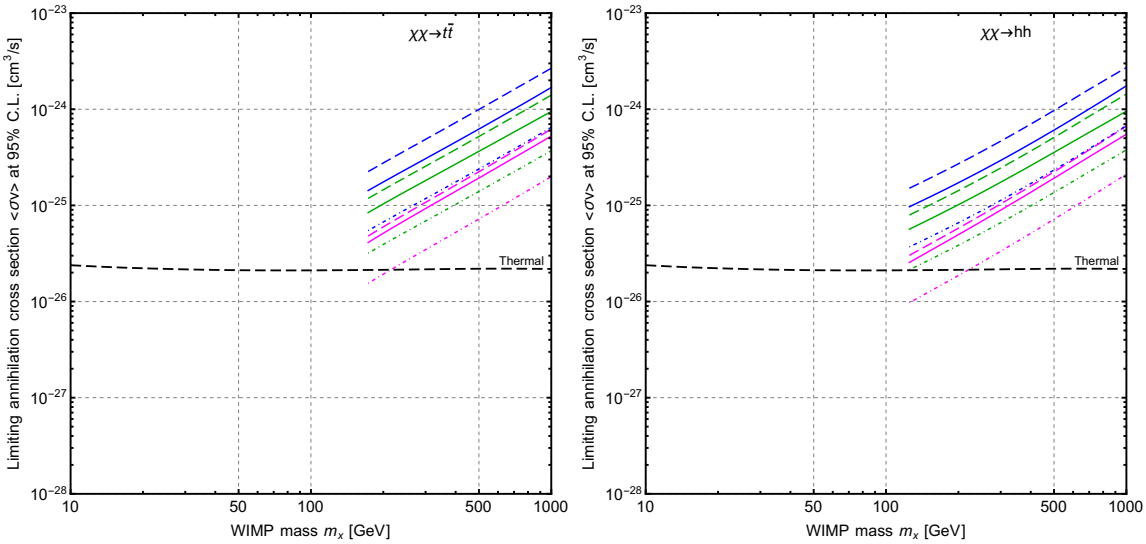


Figure 1: The limits on annihilation cross section vs. WIMP mass for various annihilation channels marked at each panel ($q \equiv u, d, s$). Each panel shows all nine computed configurations of DM density profiles and MF/prop. The (almost) horizontal dashed line shows the thermal relic cross section value (taken from [15]).

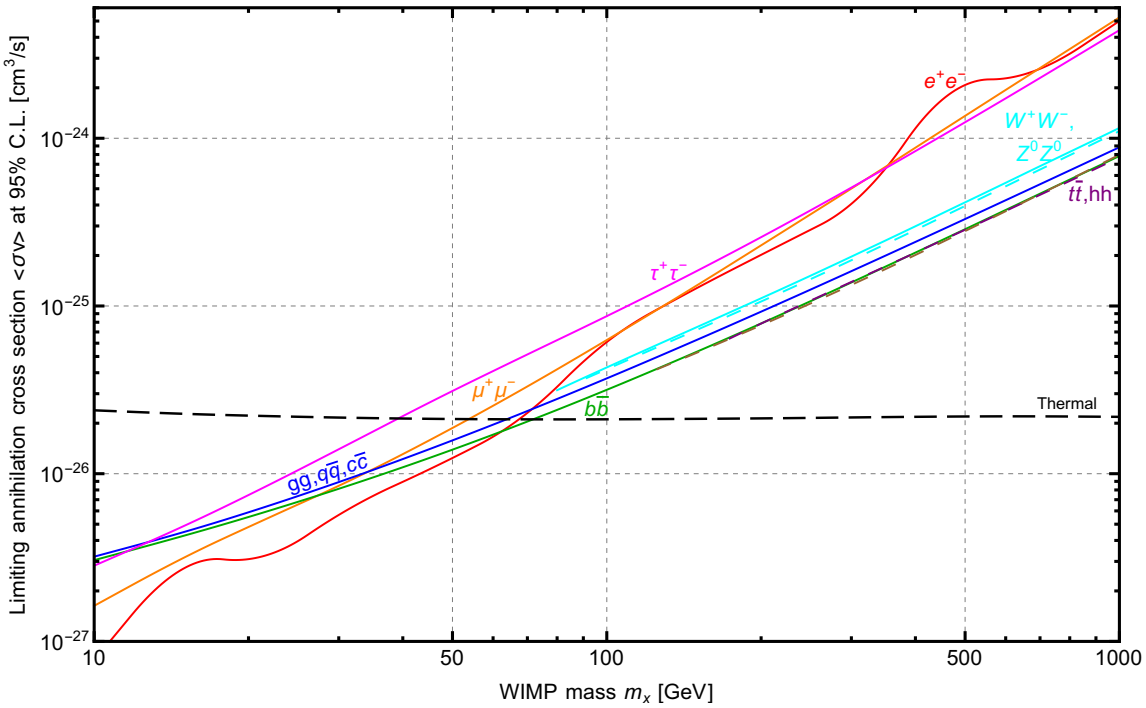


Figure 2: The fiducial or effective average exclusions for all the channels together. These exclusions represent the geometric averages of all nine DM density and MF/prop. models.

Another natural opportunity, which should be taken into account, is the annihilation through several channels simultaneously. It is easy to prove algebraically, that in the case of an arbitrary mixture of channels the limit for cross section is confined between the limits for the least and most constrained channels in the mixture, when the latter channels are considered alone. In general,

PoS(ECRS)120

Table 1: The obtained lower limits on the thermal WIMP mass (in GeV) and their uncertainty ranges.

Annihilation channel	Fiducial (geometric) average	Range due to DM density uncertainties (MED MF/prop.)	Range due to DM density and MF/prop. uncertainties
$\chi\chi \to \tau^+\tau^-$	**39**	27–65	18–89
$\chi\chi \to \mu^+\mu^-$	**54**	41–81	27–100
$\chi\chi \to gg$	**62**	36–110	19–190
$\chi\chi \to c\bar{c}$	**63**	36–110	19–190
$\chi\chi \to u\bar{u}, d\bar{d}, s\bar{s}$	**64**	37–110	20–190
$\chi\chi \to e^+e^-$	**67**	54–89	37–100
$\chi\chi \to b\bar{b}$	**72**	40–120	20–210
$\chi\chi \to W^+W^-$	**...**	...–98	...–170
$\chi\chi \to Z^0Z^0$	**...**	...–99	...–170
$\chi\chi \to t\bar{t}$	**...**	...	...–210
$\chi\chi \to hh$	**...**	...	...–220

WIMPs may also annihilate directly to photons or neutrinos, although these channels are highly suppressed in many models [9]. $\chi\chi \to \gamma\gamma$ channel is probed effectively by gamma-ray observations [16], which severely exclude the thermal WIMP, up to $m_x \sim 10$ TeV!

4. Conclusions and discussion

The robust WIMP annihilation constraints were derived here based on radio observations of the central (bulge) region of M31 in the wide frequency range ≈(0.1–10) GHz. Our model does not assume anything specific about the intensities of usual astrophysical emissions in M31. Table 1 summarizes the thermal WIMP mass lower limits for all annihilation channels. Thus, we may finally conclude that $m_x \gtrsim 20$ GeV represents the *hard and channel-independent* limit for the thermal WIMP; i.e. the former holds under *any* reasonable assumptions about DM density and MF distributions, and propagation parameters. $m_x \gtrsim 40$ GeV is the fiducial (effective average over the uncertainties) limit, and $m_x \gtrsim 90$ GeV is the most optimistic limit.

It was reported recently in [17], that M31 possess the extended gamma-ray outer halo, which may originate from annihilating WIMPs with $m_x \approx (45-72)$ GeV ($\chi\chi \to b\bar{b}$ channel). Our limits severely constrain this interpretation. The latter requires $\langle\sigma v\rangle \sim (10^{-26} - 10^{-23})$ cm^3/s depending on the assumed DM density distribution. One can see from the corresponding panel of fig. 1 above, that such high cross section values are majorly excluded even for MIN configuration of MF/prop.

References

[1] V.A. Rubakov, *Cosmology and Dark Matter*, *arXiv* (2019) arXiv:1912.04727 [1912.04727].

[2] V.S. Berezinsky, A.V. Gurevich and K.P. Zybin, *Distribution of dark matter in the galaxy and the lower limits for the masses of supersymmetric particles*, *Phys. Lett. B* **294** (1992) 221.

PoS(ECRS)120

[3] S. Hoof, A. Geringer-Sameth and R. Trotta, *A global analysis of dark matter signals from 27 dwarf spheroidal galaxies using 11 years of Fermi-LAT observations*, *J. Cosmol. Astropart. Phys.* **02** (2020) 012 [1812.06986].

[4] A. Acharyya, R. Adam, C. Adams, I. Agudo, A. Aguirre-Santaella, R. Alfaro et al., *Sensitivity of the Cherenkov Telescope Array to a dark matter signal from the Galactic centre*, *J. Cosmol. Astropart. Phys.* **01** (2021) 057 [2007.16129].

[5] A.E. Egorov and E. Pierpaoli, *Constraints on dark matter annihilation by radio observations of M31*, *Phys. Rev. D* **88** (2013) 023504 [1304.0517].

[6] A.E. Egorov, *Updated constraints on WIMP dark matter annihilation by radio observations of M31*, *Phys. Rev. D* **106** (2022) 023023 [2205.01033].

[7] http://galprop.stanford.edu/.

[8] https://github.com/a-e-egorov/GALPROP_DM.

[9] http://www.marcocirelli.net/PPPC4DMID.html.

[10] M. Blaña Díaz, O. Gerhard, C. Wegg, M. Portail, M. Opitsch, R. Saglia et al., *Sculpting Andromeda - made-to-measure models for M31's bar and composite bulge: dynamics, stellar and dark matter mass*, *Mon. Not. R. Astron. Soc.* **481** (2018) 3210 [1808.07494].

[11] A. Tamm, E. Tempel, P. Tenjes, O. Tihhonova and T. Tuvikene, *Stellar mass map and dark matter distribution in M 31*, *Astron. Astrophys.* **546** (2012) A4 [1208.5712].

[12] R.M. Crocker, D.I. Jones, F. Melia, J. Ott and R.J. Protheroe, *A lower limit of 50 microgauss for the magnetic field near the Galactic Centre*, *Nature (London)* **463** (2010) 65 [1001.1275].

[13] P. Hoernes, R. Beck and E.M. Berkhuijsen, *Properties of synchrotron emission and magnetic fields in the central region of M31*, in *The Central Regions of the Galaxy and Galaxies*, Y. Sofue, ed., vol. 184, p. 351, Jan., 1998.

[14] T.W. Shimwell, M.J. Hardcastle, C. Tasse, P.N. Best, H.J.A. Röttgering, W.L. Williams et al., *The LOFAR Two-metre Sky Survey. V. Second data release*, *Astron. Astrophys.* **659** (2022) A1 [2202.11733].

[15] K. Saikawa and S. Shirai, *Precise WIMP dark matter abundance and Standard Model thermodynamics*, *J. Cosmol. Astropart. Phys.* **08** (2020) 011 [2005.03544].

[16] A.E. Egorov, N.P. Topchiev, A.M. Galper, O.D. Dalkarov, A.A. Leonov, S.I. Suchkov et al., *Dark matter searches by the planned gamma-ray telescope GAMMA-400*, *J. Cosmol. Astropart. Phys.* **11** (2020) 049 [2005.09032].

[17] C.M. Karwin, S. Murgia, I.V. Moskalenko, S.P. Fillingham, A.-K. Burns and M. Fieg, *Dark matter interpretation of the Fermi-LAT observations toward the outer halo of M31*, *Phys. Rev. D* **103** (2021) 023027 [2010.08563].

PoS(ECRS)120

Dark matter searches in M31 and Milky Way

Andrey Egorov

Degree being conferred: Ph.D. in Physics
University of Southern California
Degree conferral date: May 13, 2016



Contents

1 Introduction and motivation **2**

2 Radio-microwave emission due to DM annihilation **5**

3 M31 at radio frequencies **7**
- 3.1 General aspects 7
- 3.2 Computing the radio flux 8
  - 3.2.1 Solution of the transport equation. 8
  - 3.2.2 DM density distribution 9
  - 3.2.3 Magnetic field distribution 11
  - 3.2.4 Estimated fluxes 13
- 3.3 Obtaining constraints on DM annihilation 17
  - 3.3.1 Comparison with radio surveys 17
  - 3.3.2 Joint analysis and final constraints 19
- 3.4 Summary and discussion 21

4 Milky Way at microwave frequencies **24**
- 4.1 General aspects 24
- 4.2 Computing the microwave emission 25
  - 4.2.1 Solution of the transport equation by GALPROP 25
  - 4.2.2 DM density distribution 26
  - 4.2.3 Magnetic field distribution 27
  - 4.2.4 Diffusion model 28
  - 4.2.5 DM emission maps 29
- 4.3 Regions of interest on the sky 30
- 4.4 DM microwave spectra 31
- 4.5 Conservative constraints on DM annihilation 33
- 4.6 DM constraints from a component separation approach 37
  - 4.6.1 The WMAP-Planck Haze: history 37
  - 4.6.2 Methodology 38
  - 4.6.3 Fitting results 41
  - 4.6.4 DM implications 45
- 4.7 Summary and discussion 48

5 Conclusions and future plans **49**

A Absorption analysis for M31 **56**

B Spatial diffusion of annihilation products in M31 **57**

1 Introduction and motivation

Dark matter (DM) was discovered already about 80 years ago by Fritz Zwicky as some invisible gravitating mass in galaxies and clusters [1]. But its physical nature is continuing to be not understood. The newest cosmological data (e.g. from the Planck mission) indicates the DM abundance in the global energy balance of the Universe at the level $\Omega_{CDM} = 27\%$, which is much larger than for an ordinary baryonic matter $\Omega_b = 4.9\%$. Thus, DM plays a big role in our Universe and its evolution. And, accordingly, an exact nature of DM represents one of the biggest puzzles in a modern basic science. After decades of years of efforts astrophysicists robustly ruled out the baryonic origin of DM (see e.g. [2], Part I). A potential modification of gravity laws at large spatial scales (so-called MOND theories for explanation of the DM phenomenon) looks also unlikely in light of recent observations of merging clusters. Nowadays the most probable candidate for the role of DM gets used to be Weakly Interacting Massive Particle (WIMP). These are massive ($\sim$10 GeV–10 TeV) particles with a typical interaction cross section of the order of the weak scale. The latter fact comprises the so-called WIMP miracle: the weak cross section matches very well the one, which is needed for the simplest thermal production of DM during the pre-BBN era of the Universe to set the correct current abundance Ω_{CDM}. Numerically this cross section is $\langle \sigma v \rangle \approx 3 \cdot 10^{-26}$ cm^3/s. Historically it gets used to be cited as the product with particles' relative velocity with $\langle\rangle$ meaning the averaging over the velocity distribution. The reasons for that are practical to some extent: in this work one usually can measure only the DM annihilation rate, which always depends on the product above (more details will follow below).

From the point of view of particle physics, there are well motivated candidates falling into a wide class of WIMPs. Particularly, one of them are supersymmetric partners (partners by spin) of the Standard Model (SM) particles, which come as a natural extension of SM to e.g. Minimal Supersymmetric SM (for more details, one can see [2], Part II). Specifically, the best proposed candidate is the lightest neutralino (usually denoted as χ), which represents a linear combination of bino (superpartner of the gauge field corresponding to weak hypercharge), wino (superpartner of W boson) and two higgsinos (superpartners of the Higgs field). Such particle satisfies basic requirements of a long term stability, electric neutrality, low level of interaction with SM particles and an expected mass in the range cited above. At the same time, neutralino is the Majorana fermion, which implies an annihilation of any two colliding particles.

In attempts to detect and study WIMPs there are three main undergoing approaches: accelerator, direct and indirect searches. The first approach relies on an opportunity to produce WIMPs on big particle accelerators like LHC and detect them obliquely in a form of missing energy/momentum. Direct searches attempt to catch DM scattering on an ordinary matter in big ultra-sensitive detectors like DAMA/LIBRA, CDMS, XENON, LUX etc. Our work belongs to the last mentioned strategy - indirect searches, which is based on the opportunity of WIMP annihilation (e.g., [2], Part V for a review). Such annihilation is expected to have the cross section value cited above and produce various possible SM particles:

$$\chi\chi \to e^+e^-,\ \mu^+\mu^-,\ \tau^+\tau^-,\ q\bar{q},\ c\bar{c},\ b\bar{b},\ t\bar{t},\ \gamma\gamma,\ W^+W^-,\ Z^0Z^0,\ hh,\ \nu_i\bar{\nu}_i \qquad (1.1)$$

and others. Different opportunities in 1.1 are called annihilation channels. We do not know a-priori which channel (or a combination of channels) works in the real nature. Thus, all the opportunities can be explored on an equal basis. Majority of the channels in 1.1 yields unstable primary products, which then decay sequentially till stable secondary ones:

$e^{\pm}$, $p\bar{p}$, $d\bar{d}$, $\gamma\gamma$, $\nu_i\bar{\nu}_i$. For example, such a cascade for the relevant $\tau^+\tau^-$ channel looks as follows (the most probable modes are taken, e.g. [3] for more details):

$$\chi\chi \to \tau^+\tau^- \to \pi^\pm + 2\pi^0 + \nu_\tau + \bar{\nu_\tau} \to \mu^\pm + \nu_\mu + \bar{\nu_\mu} + 4\gamma + \nu_\tau + \bar{\nu_\tau} \to \\ \to e^\pm + 2\nu_\mu + 2\bar{\nu_\mu} + \nu_e + \bar{\nu_e} + 4\gamma + \nu_\tau + \bar{\nu_\tau}. \quad (1.2)$$

Having quite high energies of a GeV scale, all these products can manifest themselves in any regions with high DM density (e.g. Galactic Center) through various mechanisms. We see above the production of a big bunch of neutrinos, which are potentially detectable directly by neutrino telescopes. The gamma photons are especially promising signature, since at such energies they can stream without absorption over very long distances in the Universe. Relativistic electrons and positrons (hereafter referred as $e^\pm$) can emerge in several ways through: modification of the standard population of the Galactic Cosmic Rays (CRs); Inverse Compton Scattering (ICS) emission of hard radiation on CMB, starlight and others; bremsstrahlung on an ambient gas; medium heating; synchrotron on an ambient magnetic field (MF) etc. Thus, such electromagnetic signatures can be generated at any wavelengths from radio to gamma. A search for the DM annihilation products and their emissions comprises the subject of indirect searches. Studying such DM signatures may allow us to reconstruct DM particle properties or at least put some constraints on them. Many objects have been already widely explored in this context including: CMB (e.g. [4]), dwarf satellite galaxies (e.g. [5]), usual galaxies (including Milky Way (MW) - e.g. [6]) and galaxy clusters (e.g. [7]). Despite such extensive efforts, no robust DM signal has been identified yet. However, each of these works yields constraints on DM parameters. The sensitivity of searches grows with time, shrinking the allowed DM parameter space (which is quite wide from a pure theory) and possibly approaching us to DM discovery. More specifically, indirect searches usually derive constraints on WIMP mass and annihilation cross section for selected representative channels. Although we already cited the expected cross section value above, this thermal relic value represents just a fiducial simple scenario. In more sophisticated cases the cross section can be different (e.g. through Sommerfeld enhancement [8]), which makes it to be essentially a free parameter too. Indirect searches indeed suffer from significant astrophysical uncertainties, since they always require to predict the expected DM signal theoretically for some object and then compare these predictions with observations. And the expected DM signal in turn depends on the DM distribution in this object, MF distribution, propagation properties of a medium etc. These things can not be known precisely, which creates an inevitable model dependence of the results of indirect searches. Also a separation of the potential DM signal from all other astrophysical foregrounds represents a big challenge.

Nowadays the most promising direction of indirect searches seems to be the observations of MW dwarf satellites in gamma rays, particularly by Fermi gamma observatory [5]. We can consider this work as an example. A general idea of this approach is to try to catch the primary gamma radiation from WIMP annihilation in the MW satellites, which are highly DM enriched and lack irrelevant sources of gammas at the same time. Results of this work are summarized in fig. 1. It shows exclusion contours (solid lines) on the WIMP parameter plane $\langle\sigma v\rangle - m_\chi$ (cross section values above the lines are excluded) for the anticipated range of WIMP masses for $b\bar{b}$ and $\tau^+\tau^-$ channels. Since it's hard practically to study all the numerous annihilation channels 1.1, authors usually choose few most important ones. Often these are $b\bar{b}$ and $\tau^+\tau^-$, because they are quite opposite in some sense, and the constraints for others lay more or less between these two boundary cases. The dashed lines in fig. 1 show the

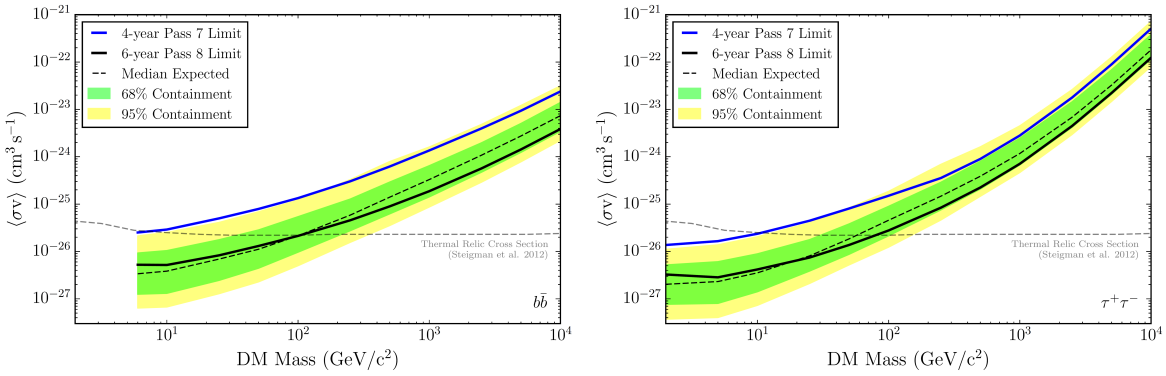


Figure 1. (from [5]) Constraints on the DM annihilation cross section at 95% CL for the $b\bar{b}$ (left) and $\tau^+\tau^-$ (right) channels derived from a combined analysis of 15 MW satellites by Fermi-LAT. The dashed lines with bands around reflect the expected Fermi-LAT sensitivity computed from observations of blank fields at high Galactic latitudes. The blue lines represent the constraints obtained after 4 years of observations, the black lines - the newest constraints after 6 years. More details are in §1.

Fermi sensitivity after 6 years of data collecting with respective uncertainty bands. The solid black lines show DM constraints at 95% confidence level (CL). They are quite strong: WIMP masses below about 100 GeV are excluded for the thermal cross section for both channels. Also we can notice the significant progress in comparison with the previous constraints from 4 years of observations: these are blue lines, which barely reach just 10 GeV mass. Although a progress in the field goes on, one can clearly see a big window of possibilities to discover DM at masses above 100 GeV.

Aiming to proceed the exploration of the DM parameter space, specifically in our work we decided to look for the potential radio-microwave emission due to DM annihilation in the big Local Group galaxies - M31 (Andromeda galaxy, fig. 2) and our own MW. A general idea behind such searches is the following. Any big galaxy is known to host a big DM halo and significant MF in its inner regions. WIMPs in the halo annihilate and produce relativistic $e^{\pm}$, which in turn emit synchrotron photons in galactic MF at radio-microwave frequencies. M31 and MW are close objects, which may allow for this signal to appear strong enough. Also their proximity allows to study them in details with a high resolution, which is especially relevant in the case when one needs to separate different emission components. And indeed MW is probably the most explored galaxy concerning our knowledge of its medium properties like MF/gas distributions, CR diffusion etc. From the point of view of previous studies, M31 appeared quite unexplored in regard to DM annihilation at the time we did our work on it. One could find few rather old papers on it - e.g. [9, 10]. Thus, this object could yield strong DM constraints, which motivated us to study it. This study was published in Phys. Rev. D journal [11].

As for MW, naturally it was studied much more in the DM context - see e.g. [6, 12–14] and others. Moreover, recently several works claimed a detection of some anomalous emission excesses around the Galactic Center (GC), which are hard to explain by conventional astrophysical sources: the gamma excess in the Fermi data (e.g. [15, 16]) and the microwave excess in WMAP-Planck data (e.g. [17, 18]). A possibility of explanation of both excesses by DM was proposed [19]. And we aimed to study this interesting opportunity in details, analyzing an interplay between microwave and gamma data in the context of DM annihilation. This work was published in [20]. For this study we employed the GALPROP code for

modeling of the propagation and emission from DM $e^{\pm}$ in the Galaxy.

Further text is organized through the following way. §2 describes in details the modeling of the expected radio-microwave emission due to DM annihilation from an arbitrary galaxy. §3 describes the application of the results of §2 to M31 and the results on this object. §4 reports DM searches in MW: modeling the $e^{\pm}$ propagation by the GALPROP code, the emission component separation procedure and its results. §5 summarizes the whole work and discusses further perspectives.

2 Radio-microwave emission due to DM annihilation

The first step on the way towards a potential DM detection or at least constraining its properties is to model the theoretically expected synchrotron signal from DM $e^{\pm}$. As was already mentioned above, the general model to be described in this section works for pretty much any DM halo. Specifically in our work it was applied to M31 and MW.

Relativistic $e^{\pm}$ in MF create the synchrotron isotropic emissivity of the galactic halo medium $j(\nu, l, \theta, \phi)$ (measured in e.g. erg/(s cm^3 Hz) in CGS system). Then if an observer is located at the coordinate origin $l = 0$ (either inside or outside the halo) and points his telescope with a field of view $\Delta\Omega$ sr in the direction (θ, ϕ), he would receive the following flux density $S(\nu, \theta, \phi, \Delta\Omega)$ at some frequency ν (in case of a transparent medium):

$$S(\nu, \theta, \phi, \Delta\Omega) = \frac{1}{4\pi} \int\limits_{\Delta\Omega} d\Omega \int\limits_{l.o.s.} j(\nu, l, \theta, \phi) dl, \tag{2.1}$$

where the second integration goes along the line of sight (and here we indeed neglected by any redshift effects, which are irrelevant in our cases). Hence, in order to calculate this flux density one has to derive the emissivity $j(\nu, l, \theta, \phi)$ everywhere in the halo. Moving to the more convenient reference frame with $\vec{r}$ originating at the halo center, we can express the local emissivity as

$$j(\nu, \vec{r}) = \int\limits_{m_e c^2}^{m_\chi c^2} (P_{e^+}(E_{e^+}, \nu, \vec{r}) n_{e^+}(E_{e^+}, \vec{r}) dE_{e^+} + P_{e^-}(E_{e^-}, \nu, \vec{r}) n_{e^-}(E_{e^-}, \vec{r}) dE_{e^-}) = \\ = 2 \int\limits_{m_e c^2}^{m_\chi c^2} P_e(E, \nu, \vec{r}) n(E, \vec{r}) dE, \tag{2.2}$$

where $P_e(E, \nu, \vec{r})$ is the synchrotron emission power of one lepton with an energy E on a frequency ν (measured in erg/(s Hz) in CGS), $n(E, \vec{r})$ is the spectral concentration of $e^{\pm}$. We assumed the electron and positron terms in eq. 2.2 to be equal to each other, because these both species behave similarly in all relevant aspects. According to [7]:

$$P_e(E, \nu, \vec{r}) = \int\limits_0^\pi d\theta' \pi \sqrt{3} \sin^2 \theta' r_e m_e c \nu_0 F\left(\frac{x}{\sin\theta'}\right), \tag{2.3}$$

where

$$\begin{cases} r_e = \frac{e^2}{m_e c^2}, \\ x = \frac{2\nu}{3\nu_0 \gamma^2} \left(1 + \left(\frac{\gamma \nu_{pl}}{\nu}\right)^2\right)^{3/2}, \\ \nu_0(\vec{r}) = \frac{eB(\vec{r})}{2\pi m_e c}, \\ \nu_{pl} = \sqrt{\frac{e^2 n_{pl}}{\pi m_e}} - \text{plasma frequency of an ambient plasma}, \\ F(t) \approx 1.25(648)^{1/12} t^{1/3} \exp(-t) - \text{synchrotron spectrum}, \\ \gamma = \frac{E}{m_e c^2} - \text{lepton Lorentz-factor}. \end{cases} \tag{2.4}$$

This set of formulas describes the synchrotron power of a lepton in a MF $B(\vec{r})$ in the presence of an ambient plasma with concentration n_{pl}. Integration over θ' in eq. 2.3 represents the averaging over all possible random angles between the lepton's velocity and MF. In order to proceed our computation of the flux density we needed to derive the spectral concentration $n(E, \vec{r})$. For this, one has to solve the transport equation for $e^{\pm}$, which has the following form in its most general version:

$$\frac{\partial n}{\partial t} = q + \vec{\nabla}(D_{xx}\vec{\nabla}n - \vec{V}n) + \frac{\partial}{\partial E}E^2 D_{EE}\frac{\partial}{\partial E}\frac{n}{E^2} - \frac{\partial}{\partial E}\left(bn - \frac{E}{3}(\vec{\nabla}\vec{V})n\right), \tag{2.5}$$

where we neglected by the positron annihilation, which does not occur in our case. In general, all the quantities in the eq. above may depend on both $\vec{r}$ and E. However, various simplifying assumptions were made indeed. They are described below together with all the eq. terms.

- $q \equiv q(r, E)$ represents the spherically symmetric source term, which defines the $e^{\pm}$ production rate per unit volume per unit energy range:

$$q(r, E) = \frac{1}{2}\langle \sigma v \rangle \left(\frac{\rho_{\mathrm{DM}}(r)}{m_\chi}\right)^2 \xi_{\mathrm{DM}}(r)\frac{dN_e}{dE}(E), \tag{2.6}$$

  where $\langle \sigma v \rangle$ denotes the WIMP annihilation cross section, $\rho_{\mathrm{DM}}(r)$ is the DM density distribution, m_χ is the WIMP mass, $\xi_{\mathrm{DM}}(r)$ is the DM annihilation rate boost factor due to substructures and $\frac{dN_e}{dE}(E)$ represents the energy spectrum of $e^{\pm}$ per annihilation. The latter was taken from the respective particle physics data - PPPC4DMID package [21–23].

- The term with D_{xx} in eq. 2.5 reflects the spatial diffusion of the annihilation products. Usually it's assumed to have the form:

$$D_{xx} \equiv D_{xx}(E) = D_0 \left(\frac{E}{E_0}\right)^{\delta}, \tag{2.7}$$

  where E_0 is set to the constant value 1 GeV (see e.g. [14]). The choice of D_0 and δ constants will be discussed below in regard to MW.

- $\vec{V}$ above represents the convection velocity of the particles. Although it may be significant, typically it's not included into analysis due to its poor knowledge. We also did not account for it in order to avoid too many weakly-constrained model parameters.

- D_{EE} in the transport eq. is the particle reacceleration coefficient. Particle reacceleration in the interstellar medium happens due to interactions with MHD waves. D_{EE}

is usually defined through the spatial diffusion coefficient (eq. 2.7), see [24] for further details:

$$D_{EE}(E)D_{xx}(E) = \frac{4E^2 v_a^2}{3c^2\delta(4-\delta^2)(4-\delta)w}, \tag{2.8}$$

where v_a is the Alfven speed in the medium and w is the ratio of the MHD waves energy density to the MF energy density, assumed to be 1 typically.

- $b \equiv \frac{dE}{dt}(E)$ term is the total energy loss rate through various mechanisms. Below we itemize the main components of this rate (see e.g. [2, 7, 25, 26]).
  - The energy losses due to ICS:

$$b_{ICS} \approx 0.76 \frac{U_{ph}}{1 \text{ eV}\cdot\text{cm}^{-3}} \left(\frac{E}{1 \text{ GeV}}\right)^2, \tag{2.9}$$

    here and in other loss terms numerical pre-factors like 0.76 come from the exact analytical computation of the corresponding loss rate. U_{ph} denotes the total energy density of an ambient radiation in relevant locations. This is mainly composed by CMB, starlight and dust emission photons. For a central region of MW-like galaxies $U_{ph} \approx 8$ eV·cm^{-3}, for the CMB field $U_{ph} \approx 0.25$ eV·cm^{-3} (see e.g. [2]).
  - The synchrotron radiation losses:

$$b_{sync} \approx 0.025 \left(\frac{B(\vec{r})}{1\ \mu\text{G}}\right)^2 \left(\frac{E}{1 \text{ GeV}}\right)^2. \tag{2.10}$$

  - The bremsstrahlung losses (on an ionized ambient gas):

$$b_{brem} \approx 4.70 \frac{n_{pl}}{1 \text{ cm}^{-3}} \frac{E}{1 \text{ GeV}}, \tag{2.11}$$

    where $n_{pl} \sim 0.1$ cm^{-3} for galactic centers.
  - The Coulomb (collisional) losses:

$$b_{Col} \approx 6.13 \frac{n_{pl}}{1 \text{ cm}^{-3}} \left(1 + \frac{1}{75} \log\left(\frac{E}{m_e c^2 n_{pl}}\right)\right). \tag{2.12}$$

All the loss rates here are measured in the units 10^{-16} GeV/s.

3 M31 at radio frequencies

3.1 General aspects

The general formalism described in the previous section works for any DM halo. In this section we will apply it to M31 in order to derive constraints on WIMP parameters from radio observations. In general, one can see quite easily from eq. 2.1–2.12 that the radio flux density due to DM is linearly proportional to the annihilation cross section. Hence, limits on the emission due to DM from observations can be easily converted into limits on the cross section for any WIMP mass and channel. To perform this task, at first we had to choose a region of interest (ROI), inside which we plan to compare the potential DM emission with the observed one. For this we chose the disc of $\alpha \approx 5'$ radius around the M31 center (fig. 2).

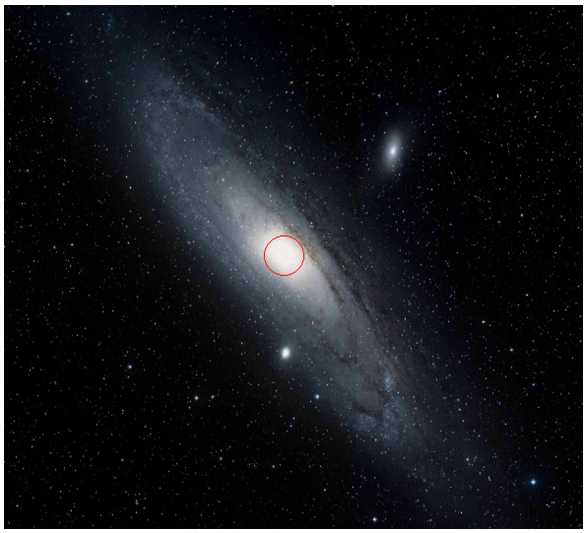


Figure 2. Optical image of M31 with the marked region of interest (ROI) selected for our purposes. The disc radius is $5'$.

Basic reasons for this choice are the following: *i)* a radio quietness of the M31 nucleus, which implies a low contamination by other standard astrophysical emission sources; *ii)* an absence of any projected bright compact sources inside it; *iii)* very central regions of galaxies are expected to have high DM concentrations providing high annihilation rates, larger ROI would capture not much more of the DM emission and much more of nuisance foregrounds (some more quantitative reasoning is also shown in §3.2.4).

The next step was naturally to compute the synchrotron emission from DM $e^{\pm}$ in our ROI (§3.2). One important aspect here was to check a validity of the absorption-free approximation, which was indeed made in §2. Our estimates did not reveal any significant mechanisms of the absorption (all respective details are described in §A). Then we compared the theoretically predicted DM fluxes with real observational data (§3.3). An important aspect in this comparison was what to assume for all other than DM emissions, which exist inevitably from e.g. regular galactic CRs. In our work we chose the most conservative approach, which assumes essentially no a-priori significant other than DM emissions. The constraints from this approach would be relatively weak (i.e. big cross sections would be allowed), but very robust and model-independent. The latter presents an advantage of such an approach. As the observational input we used radio data of four all sky surveys, which captured M31: VLSS (74 MHz), WENSS (325 MHz), NVSS (1400 MHz) and GB6 (4850 MHz).

In this section we adopted the Hubble constant value $H_0 = 71$ km/(s Mpc) taken from the WMAP7 data.

3.2 Computing the radio flux

3.2.1 Solution of the transport equation.

We significantly simplified the full transport eq. 2.5 and neglected (besides the convection) by the particle reacceleration and spatial diffusion. The former represents a second-order effect, which is explored quite poorly. Hence, to avoid too many weakly constrained model parameters we did not include it. Regarding the spatial diffusion, this is usually a more

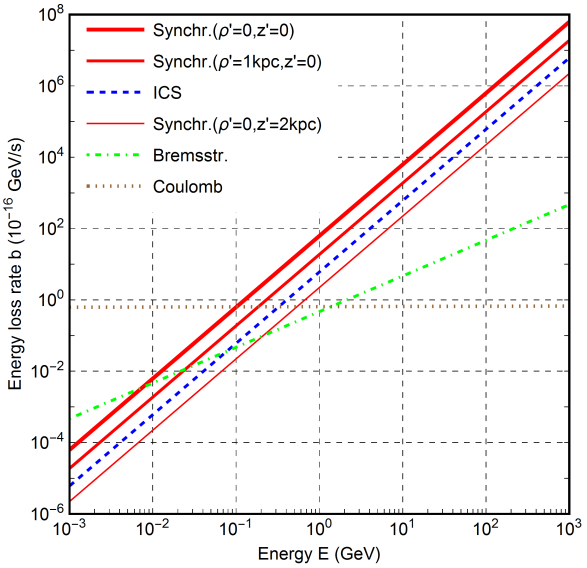


Figure 3. The energy dependence of various types of lepton energy losses. Synchrotron losses are shown for three representative locations around the M31 center. For more details see §3.2.1 and §3.2.3.

relevant effect. However, the majority of our emission of interest is generated in a very small vicinity of the M31 center with a characteristic size $\sim$ 1 kpc. $e^{\pm}$ there cool down relatively fast due to high concentration of ambient photons and MF strength (according to eqs. 2.9–2.12). Hence, they do not have time to move much in space, while they are emitting the relevant synchrotron. A quantitative assessment of this aspect is presented in §B. This assessment showed that one can drop the spatial diffusion term to have reasonable estimates. Also we indeed assumed the stationary case, which is a quite typical approximation. Under these assumptions, the transport eq. can be easily solved analytically:

$$n(E,\vec{r}) = \frac{1}{b(E,\vec{r})} \int_{E}^{m_\chi c^2} q(E',r)dE'. \tag{3.1}$$

For illustrative purposes, we showed in fig. 3 the energy dependencies of each term in the losses $b(E,\vec{r})$ (eqs. 2.9–2.12) over the relevant range of energies. We can clearly see that the synchrotron losses depend on the location through $B(\vec{r})$. For this reason, we presented b_{sync} in fig. 3 for three relevant trial locations, which are away from the M31 center by 0, 1 and 2 kpc. More details about $B(\vec{r})$ distribution will be discussed in §3.2.3. In the most general case, the quantities U_{ph} and n_{pl} depend on $\vec{r}$ as well, indeed. However, at the current level of accuracy of our model we made two simplifying assumptions. First, we assumed constant values for these quantities with conservative choices; and second, we adopted the values for MW relying on high similarity between these two galaxies.

For the next step we needed to specify the DM density distribution $\rho_{DM}(r)$, which enters the source term eq. 2.6. Next subsubsection is dedicated to the DM density profile derivation.

3.2.2 DM density distribution

As a model for $\rho_{DM}(r)$ in the M31 halo we used the standard NFW profile, firstly introduced in [27] as a result of numerical N-body simulations and widely used since that due to its

universality. Some other profiles potentially describe a DM distribution in galactic halos even better than NFW - this was demonstrated e.g. in [28] for the Einasto density profile. However, we did not use any other profiles except NFW further due to the following reasons. First, all available models of the DM density distribution in M31 were made in the frame of NFW profile (at least at the time of our work). The second reason is that among all profiles, NFW yields moderate emission fluxes due to DM annihilation (lower than e.g. Moore profile - see [6]), and this makes our constraints reasonably conservative with respect to the assumptions on the adopted profile. Also, the NFW profile is specified by only two free parameters, while a larger number of parameters is required by other typical profiles. This choice therefore minimizes the overall number of "degrees of freedom" in our model.

Quantitatively the DM density distribution of our choice is the following:

$$\rho_{DM}(r) = \begin{cases} \rho_{DM}(r = 50 \text{ pc}), & \text{if } 0 \leqslant r < 50 \text{ pc}; \\ \frac{\rho_s}{\frac{r}{r_s}\left(1+\frac{r}{r_s}\right)^2}, & \text{if } r \geqslant 50 \text{ pc}. \end{cases} \tag{3.2}$$

It represents the exact NFW profile with a minor modification, which can be called as a flat core: we do not extrapolate the density below the radial distance of $r_t = 50$ pc, inside this central region we leave DM density at the constant level of $\rho_{DM}(r = 50 \text{ pc})$. This choice is motivated by the divergence of the NFW distribution towards the central point of the halo, which prevents to estimate the DM density reliably in the very central region. The NFW profile provides reliable density estimate down to the radius ~ 50 pc for a M31–size halo (see e.g. fig. 4 in [29]). That's why in order to be conservative in our computation of the medium emissivity, which depends quadratically on the local DM density, we truncated the profile at $r = r_t = 50$ pc and left the density at smaller radii on the level of $\rho_{DM}(r = 50 \text{ pc})$. We tested the dependence of our results on the specific arbitrary choice of the truncation radius r_t. This study showed that a decrease (increase) of r_t by a factor two (a factor four) produces an increase (decrease) of $\approx 3\%$ ($\sim 10\%$) in final fluxes, which is far below the overall level of accuracy of our model.

The DM density profile eq. 3.2 is completely defined for a specific halo by two parameters - scaling radius r_s and scaling density ρ_s. Thus, we needed to estimate them for M31. These two parameters are unambiguously linked to another two halo parameters, which are more meaningful - the halo mass M_Δ and its concentration c_Δ. Δ here denotes the overdensity: halo mass M_Δ by definition means the DM halo mass enclosed in the sphere, average density inside which is equal to $\Delta\rho_{crit}$ with $\rho_{crit} = \frac{3H_0^2}{8\pi G} = 9.5 \cdot 10^{-30}$ g·cm^{-3} being the current critical density of the Universe. In our work we used $\Delta = 100$ due to some practical circumstances. However, the parameters of the actual DM density distribution eq. 3.2 do not depend indeed on a Δ choice. Halo mass and concentration are connected with the NFW profile parameters through the following relations:

$$r_\Delta = \left(\frac{3M_\Delta}{4\pi\Delta\rho_{crit}}\right)^{1/3}, \; c_\Delta \equiv \frac{r_\Delta}{r_s}, \; M_\Delta = \int_0^{r_\Delta} \rho_{DM}(r) 4\pi r^2 dr. \tag{3.3}$$

As for the determination of the relevant parameters for M31, we used the results of M_{100} and c_{100} from [30] and [31]. While these are in a good agreement with each other in determination of M_{100} ($(1.2 \pm 0.3) \cdot 10^{12} M_\odot$ vs. $(0.91 \pm 0.16) \cdot 10^{12} M_\odot$ respectively), they show a rather big discrepancy in the estimation of c_{100} (the most probable values cited being ≈ 12 and ≈ 28

respectively). The expected radiation fluxes from these two concentration values differ by about one order of magnitude. This is why we decided to treat these two cases separately. They can be considered as two limiting cases yielding the most conservative constraints for $c_{100} = 12$ and the most optimistic constraints for $c_{100} = 28$.

At this point we were ready to specify the NFW profile by estimation of its two parameters ρ_s, r_s. For the first case $c_{100} = 12$ we took $M_{100} = 1.2 \cdot 10^{12} M_\odot$ from [30] and obtained ρ_s, r_s by eq. 3.3. For the second case $c_{100} = 28$ we did not need to calculate ρ_s, r_s - they were taken directly from the table 2 in [31] as the best-fitting values.

Another potentially relevant question in this subsection is substructures' contribution to our flux (counted by the boost factor $\xi_{\mathrm{DM}}(r)$ in eq. 2.6). It's well known that any DM halo contains a lot of small subhalos inside it (see e.g. [2]). These subhalos are very dense and numerous, that's why they are able to substantially increase the total flux due to DM annihilation from a whole halo - by 10-100 times (see e.g. [32]). But in our case we can neglect substructure contribution, because the main part of our expected flux comes from very central region with a size about 1 kpc. As can be seen e.g. in [32], substructures do not survive so close to the center due to tidal disruption, and their contribution to the total expected flux would be negligible at so small radii. Thus we did not need to include subhalos in our analysis. Moreover, subhalos' presence would only increase the overall flux, so that the constraints obtained here are to be considered conservative.

Thus, at this point we have completely specified the DM density distribution in M31 halo. Now we can move to the next step - specifying the MF distribution.

3.2.3 Magnetic field distribution

The emission due to DM annihilation, which we hope to detect, is generated through the synchrotron mechanism. For synchrotron emission modeling it's crucially important to know the MF strength distribution in our emitting volume. A global axial symmetry of the large spiral galaxy M31 naturally suggests an assumption of two-parametric MF distribution $B(\rho', z')$, where B depends on the radial distance from the center ρ' in the galactic plane and the vertical height z' above the plane.

As for B dependence on the vertical coordinate z', it's plausible to assume exponential dependence $B \sim \exp(-|z'|/z'_0)$ with some scale height z'_0. Such dependence is commonly used for large spiral galaxies - see e.g. [33]. In order to find out a reasonable radial dependence of B in the galactic plane we used the findings of [34, 35]. In [34] the large-scale MF in the disk plane was measured between radial distances of 6 and 14 kpc. These measurements yielded almost constant MF over the whole mentioned annular region of ≈ 7 μG, which is an expected value for galactic discs (see e.g. [36]). As for the MF strength in the inner region $\rho' < 6$ kpc, we were unable to find reliable data. Some measurements for this region were reported only in [37] and only for two trial locations with a poor justification. Besides this information on the central field properties we can reliably assume probably only one thing - that the field grows towards the center. In such situation we made a decision to introduce the following field distribution (including the vertical dependence part):

$$B(\rho', z') = \left(B_{10} + B_s \exp\left(-\frac{\rho'}{\rho'_0} \right) \right) \exp\left(-\frac{|z'|}{z'_0} \right). \tag{3.4}$$

Here $B_{10} = 7$ μG - the plateau value observed on $\rho' \approx 6 - 14$ kpc. The term $B_s \exp\left(-\frac{\rho'}{\rho'_0}\right)$ presents an exponentially decreasing central spike with the characteristic radial extent ρ'_0. Of

course, such distribution has a non–physical plateau extending to infinity $B(\rho' = \infty, z' = 0) = 7\ \mu$G. But this plateau does not matter for our calculations: at distances of tens of kpc DM density becomes very small, and a contribution of these regions to the overall flux is negligible. The distribution in eq. 3.4 can be completely specified by two free parameters: the vertical scale height z'_0 and the central field value $B(0,0) = B_{10} + B_s$. After specifying these two parameters, the radial scale length ρ'_0 becomes automatically set by the smooth connection of the central exponential spike $B_s \exp\left(-\frac{\rho'}{\rho'_0}\right)$ to the plateau $B(\rho' > 6 \text{ kpc}, z' = 0) \approx 7\ \mu$G.

Now let's discuss the specification of the values of z'_0 and $B(0,0)$. We estimated the scale height z'_0 using [38] and [34]. The first mentioned article outlines such a general property of galactic MFs: the scale height z'_0 is typically about 4 times greater than the scale height of a synchrotron emission, which arises from CRs in a whole galaxy volume. The last mentioned synchrotron scale height was reported in [34] for M31 with a value ≈ 0.3 kpc. This would yield $z'_0 \approx 0.3 \text{ kpc} \cdot 4 = 1.2$ kpc. Moreover, such a value for z'_0 is confirmed by the authors of [34] on the basis of other independent considerations: they conclude that the minimal expected z'_0 value is not less than ≈ 1 kpc. We therefore chose $z'_0 = 1.2$ kpc for all our calculations. This estimate reflects a conservative choice, since lower values seem to be unrealistic and possible greater values can only increase the final expected flux and, hence, strengthen the final constraints.

As for the second necessary parameter - $B(0,0)$, the situation is much less certain. As we already mentioned, we found in the literature only one attempt to measure the central field values in M31 - [37]. This work reports the total field strengths for the two locations: $B(\rho' \approx 0.3 \text{ kpc}, z' \approx 0) = 15 \pm 3\ \mu$G and $B(\rho' \approx 0.9 \text{ kpc}, z' \approx 0) = 19 \pm 3\ \mu$G. These values were obtained assuming the energy equipartition between CRs and MF. Such assumption, however, has been shown to lead to an underestimation of the MF in similar setting. For example, the authors of [35] explored the central field properties of MW and derived the stringent lower limit of 50 μG based on multi-wavelength studies of a CR emission. At the same time, they mentioned that a simple equipartition assumption implies a central field strength of only $\sim 10\ \mu$G. As for the upper bound on a central field strength, [35] demonstrates that there is no certainly known value for it. Values of few hundreds μG are mentioned to be absolutely possible.

Considering the possible underestimation of M31 MF due to the equipartition assumption ([37]), and the similarity between MW and M31, we chose $B(0,0) = 50\ \mu$G as the most probable value. However, we performed all our calculations for alternative field values as well (which are considered as less probable) in order to study the dependence of our final results on this model parameter. These alternative less realistic values were chosen to be $B(0,0) = 15\ \mu$G and $B(0,0) = 300\ \mu$G. They can be considered as approximate boundaries of the interval, where the actual field value lies. The detailed discussion of the final results variation due to uncertainties in $B(0,0)$ will be done in §3.3.2.

At this point we have completely specified the MF distribution. For illustration purposes we showed the density plot of our distribution eq. 3.4 in fig. 4 for the case of $B(0,0) = 50\ \mu$G.

The MF distribution eq. 3.4 is written in the cylindrical coordinate system attached to M31. Axes $x'y'$ lie in the M31 disk plane. Another non trivial step was to make the transformation between the coordinate system attached to M31 and the "laboratory" system with Oz axis pointing from the M31 center to the observer. This is necessary for the flux computation, because we are going to perform a numerical integration over the emitting volume along our line of sight, which is coincident with Oz axis and not coincident with Oz'.

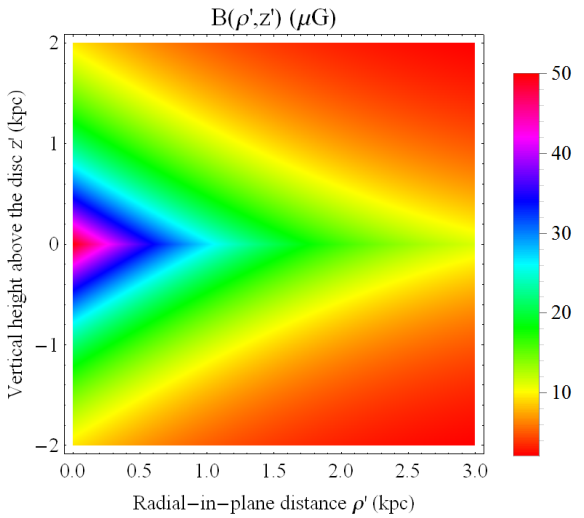


Figure 4. Density plot of the MF distribution eq. 3.4, which was chosen for our computations. Parameter values here correspond to the most probable case with the central field strength $B(0,0) = 50\ \mu$G. For more details see §3.2.3.

The two coordinate systems are shown in fig. 5. We performed the coordinate transformation $(\rho, \varphi, z) \longleftrightarrow (\rho', \varphi', z')$ using the formulas below, which were derived in [39] (eq. 6) for cartesian coordinates $(x, y, z) \longleftrightarrow (x', y', z')$:

$$\begin{cases} x' = -x \sin P + y \cos P, \\ y' = -x \cos P \cos i - y \sin P \cos i - z \sin i, \\ z' = -x \cos P \sin i - y \sin P \sin i + z \cos i, \end{cases} \tag{3.5}$$

where P and i represent the position angle and axis inclination respectively, and define the orientation of the M31 disc plane with respect to the sky plane. Following [30], we assumed: $P = 38°, i = 78°$. From eq. 3.5, using relations between the cylindrical and cartesian coordinates it's easy to obtain the one-to-one correspondence $(\rho, \varphi, z) \longleftrightarrow (\rho', \varphi', z')$:

$$\begin{cases} \rho' = ((-\rho \cos\varphi \sin P + \rho \sin\varphi \cos P)^2 + (\rho \cos\varphi \cos P \cos i + \rho \sin\varphi \sin P \cos i + z \sin i)^2)^{\frac{1}{2}}, \\ z' = -\rho \cos\varphi \cos P \sin i - \rho \sin\varphi \sin P \sin i + z \cos i. \end{cases} \tag{3.6}$$

Finally, we substituted eq. 3.6 into eq. 3.4 obtaining therefore B as a function of (ρ, φ, z), which allowed to compute the final flux.

3.2.4 Estimated fluxes

The final expected radio flux due to DM annihilation in M31 halo is defined by eq. 2.1. In order to compute it we combined all relevant relations eqs. 2.2–2.4, 2.6, 2.9–2.12, 3.1-3.4, 3.6 and substituted them in eq. 2.1. The integration limits for the spatial coordinates can be easily figured out from fig. 5:

$$\begin{cases} 0 \leqslant \rho \leqslant (d - z) \tan\alpha, \\ 0 \leqslant \varphi \leqslant 2\pi, \\ -r_{100} \leqslant z \leqslant r_{100}, \end{cases} \tag{3.7}$$

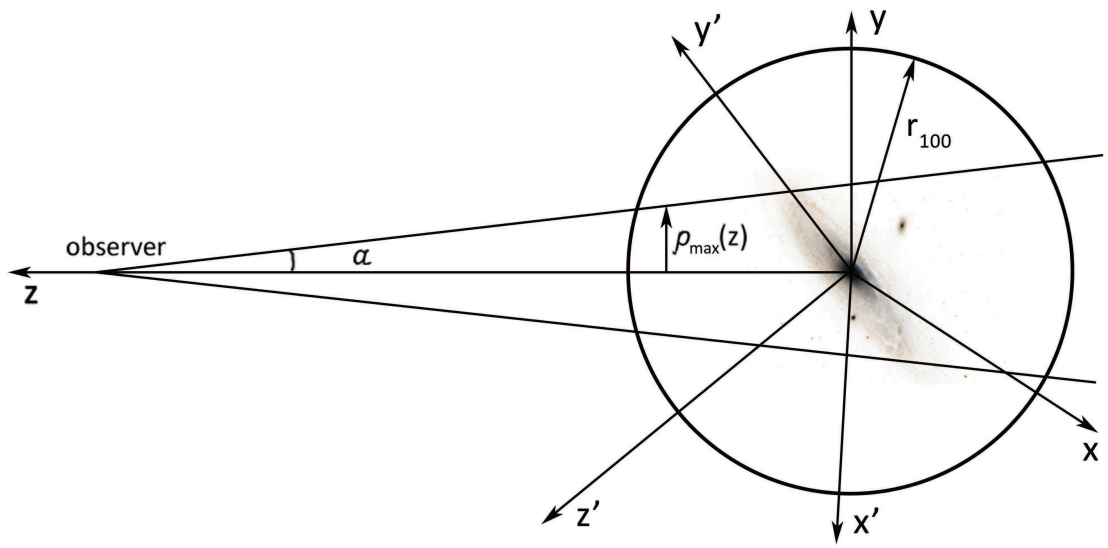


Figure 5. Two coordinate systems (x, y, z) and (x', y', z'). The plane $x'y'$ is coincident with the M31 disc plane. Integration over the emitting volume is performed in (x, y, z). More details are in §3.2.3.

where α is the angular radius of our ROI. Fig. 6 shows the dependence of the computed radio flux at $\nu = 74$ MHz on the angular radius of the ROI for both selected annihilation channels and three trial WIMP masses: $m_\chi = 10, 100$ and 1000 GeV. Boundaries of every shaded region correspond to the two limiting cases of the DM density distribution in the halo, which were discussed in §3.2.2: $c_{100} = 12$ and $c_{100} = 28$. Thus the actual flux is expected to lie somewhere inside the shaded regions. The thick central lines represent the algebraic averages between the corresponding boundary curves (fluxes). The flux saturates around $\alpha \approx 5'$ and does not grow significantly at larger radii. These plots together with the signal-to-noise ratio (SNR) considerations justify our choice of α. Basically, in this choice we were governed by two counteracting effects. On one hand, the SNR was seen to increase with decrease of α. On the other hand, as discussed in §3.2.2–3.2.3, we know very poorly the DM and MF distributions in the very close vicinity of the center $\alpha \sim 1'$. And $\alpha = 5'$ was set as an optimal ROI radius in this situation. With such choice we lose little in SNR, but gain in overall reliability of calculations. Also, we did not want to increase α any higher than $\sim 5'$, because it would lead to non-desirable capturing of projected compact sources.

As an intermediate step of calculations, we decided to study also the contribution of $e^\pm$ with different energies into the total flux. For this purpose we computed the part of the total flux produced by the $e^\pm$ with initial energies at production below different thresholds E_m. We spanned the whole possible range of E_m values from the lepton's rest energy to the WIMP's rest energy. The results are presented in fig. 7 for all four frequencies used. These plots are generated for the most relevant MF model, WIMP mass $m_\chi = 100$ GeV (relevance of this mass scale will be seen in the results section) and the $c_{100} = 12$ halo model. Essentially, we can see in fig. 7 that the main contribution to the total flux ($\gtrsim 50\%$) for all frequencies and annihilation channels comes from a relatively narrow window of initial $e^\pm$ energies between $\sim 0.01 m_\chi c^2$ and $0.1 m_\chi c^2$, or 1 GeV and 10 GeV. This energy window of one order of magnitude width is considered to be narrow with respect to the whole energy range of produced $e^\pm$ between $\sim 10^{-5} m_\chi c^2$ and $1 m_\chi c^2$, which spans more than 5 orders of magnitude.

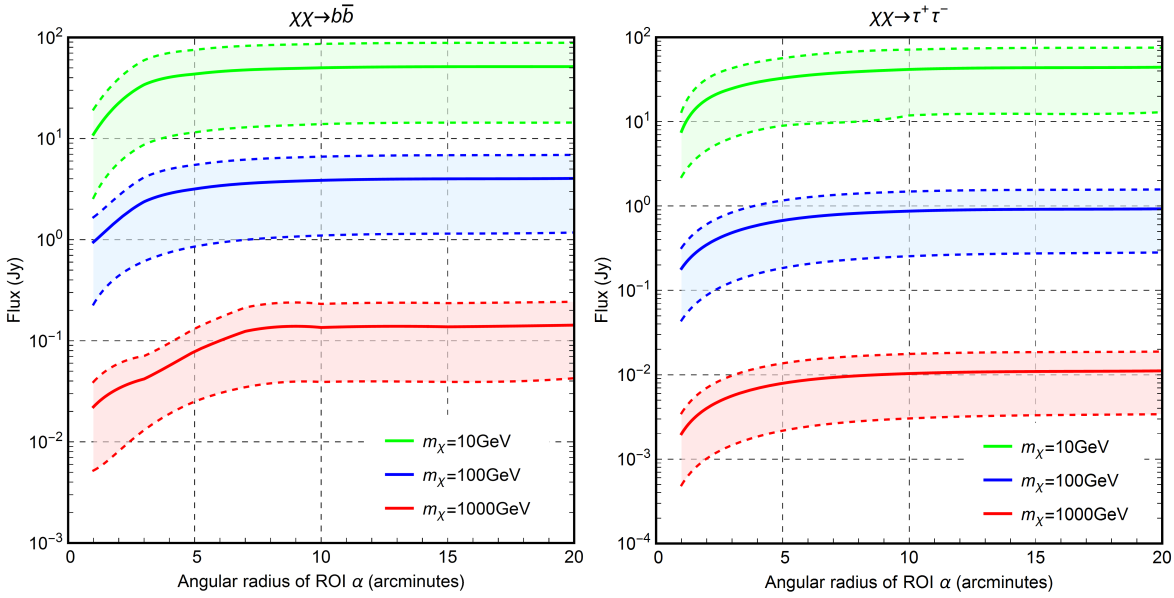


Figure 6. The expected radio flux dependence on the angular radius of the ROI. The expected flux lies inside shaded regions. Upper and lower boundaries of these regions correspond to the different halo concentration values $c_{100} = 28$ and $c_{100} = 12$ respectively. Thick central lines represent algebraic averages between corresponding limiting cases. Curves are shown for the two annihilation channels $\chi\chi \to b\bar{b}$, $\tau^+\tau^-$, three WIMP masses $m_\chi = 10, 100, 1000$ GeV and the most probable MF distribution with the central value of 50 μG. The observational frequency is $\nu = 74$ MHz. By default hereafter $\langle\sigma v\rangle = 3 \cdot 10^{-26}$ cm^3/s. For more details see §3.2.4.

This implies that the most important fraction of the $e^\pm$ population for our considerations has an energy above ~ 1 GeV. This fact, in turn, means that according to fig. 3 the main energy loss mechanisms for such population would be synchrotron and ICS emission. Thus, these kinds of losses dominate in comparison with the other two - bremsstrahlung and Coloumb losses, and play a main role for final results. Meanwhile, it's also useful to note that in the case of $\tau^+\tau^-$ channel the total flux is constituted by more energetic $e^\pm$ than the flux for $b\bar{b}$ channel, which is in complete agreement with the difference between these two channels - $\tau^+\tau^-$ channel produces harder $e^\pm$ energy spectrum.

Another important result of our computations is the frequency dependence of the radio flux from the M31 halo. These dependencies are shown in fig. 8 for three different WIMP masses, both annihilation channels, both limiting halo models and the chosen ROI with $\alpha = 5'$. As a general feature, we see, for all cases, a decrease of the radio flux as the frequency increases. The steepness of this decrease is, however, more pronounced for lower WIMP masses. This behavior suggests to primarily leverage on low frequency observations for obtaining DM constraints. However, the sensitivity of radio surveys typically increases with frequency, partially compensating the effect of the lower signal. There is, therefore, no obvious optimal frequency to be used to get the strongest constraints possible. For this reason, we opted radio observations at very different frequencies for actual constraints derivation. This procedure and its results will be described in the next subsection.

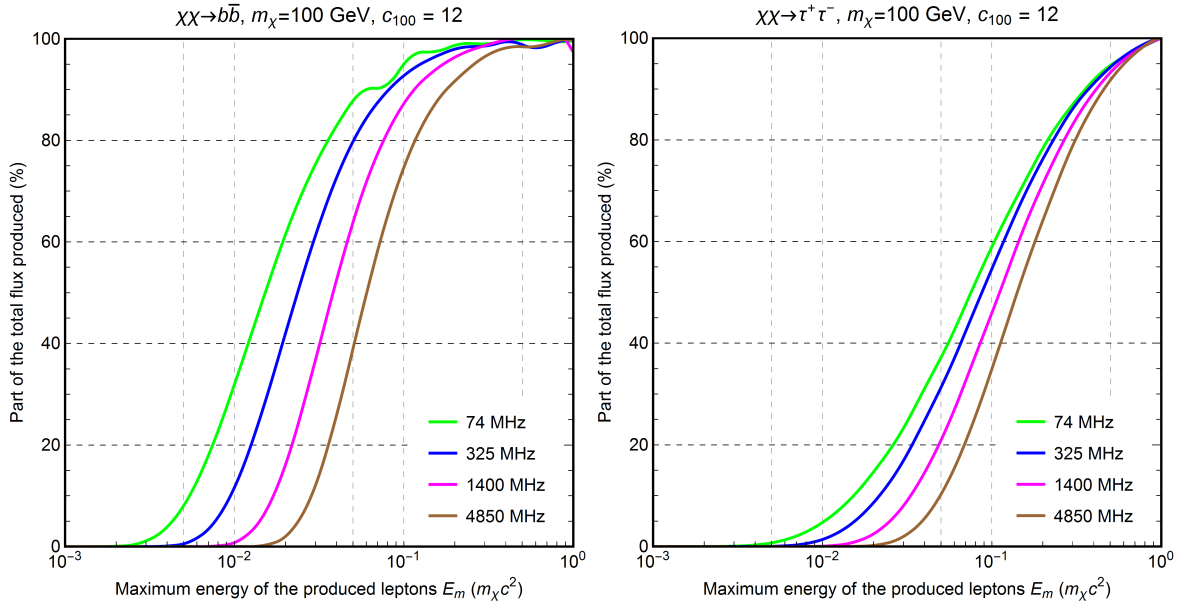


Figure 7. The part of the total radio flux produced by $e^{\pm}$ with energies at production below different thresholds. WIMP mass is chosen to be $m_\chi = 100$ GeV, which reflects the most relevant mass scale with respect to the final results, as will be seen below. $B(0,0) = 50$ μG. We can note that the majority of the total flux are produced by $e^{\pm}$ with initial energies above $\sim 0.01 m_\chi c^2$. More details are in §3.2.4.

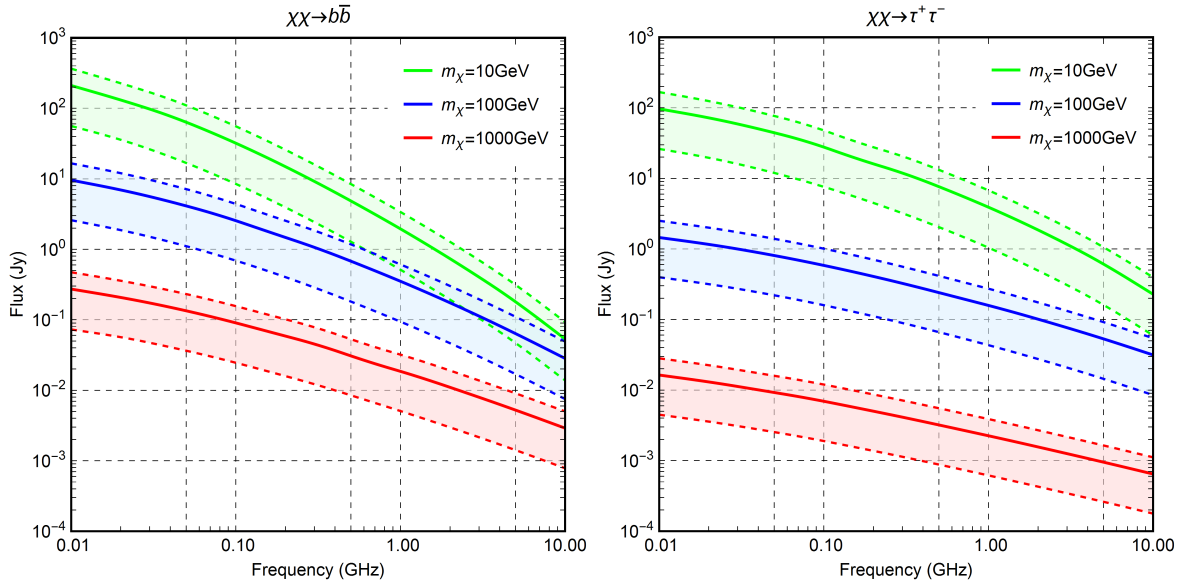


Figure 8. The frequency dependence of the expected radio flux for three different WIMP masses and two annihilation channels. ROI radius $\alpha = 5'$, shaded regions reflect the uncertainty in DM density distribution as on the previous plots, $B(0,0) = 50$ μG. More details are in §3.2.4.

Table 1. Main parameters of all radio surveys used.

Survey	**Frequency, MHz**	**Beam diameter or FWHM $2\beta_i$, arcsec**	**RMS noise level inside the beam $\sigma_i^{(b)}$, mJy**
VLSS	74	80	100
WENSS	325	82	4.0
NVSS	1400	46	0.5
GB6	4850	240	4.0

3.3 Obtaining constraints on DM annihilation

3.3.1 Comparison with radio surveys

In order to make a next step, we needed to obtain the upper limits on the actually observed radio fluxes from our ROI. Comparison of these upper limits with the expected fluxes computed above immediately provides the upper limits on the annihilation cross section for any WIMP masses. For this purpose we studied many major radio surveys conducted in the past and chose four of them (corresponding frequencies and detailed descriptions are provided in brackets): VLSS (74 MHz, [40]), WENSS (325 MHz, [41]), NVSS (1400 MHz, [42]) and GB6 (4850 MHz, [43]). All other surveys were rejected due to either one of the following two reasons: too low resolution of a survey (i.e. the telescope beam size is larger than the ROI size) or not covering the M31 area of the sky. In table 1 we outlined the main surveys' parameters, which were collected from [40]-[43] and then used in calculations. The uncertainties of survey frequencies, caused by a finite bandwidth, do not exceed the level of $\sim 4\%$ and do not affect final results significantly.

Real sky images were viewed and analysed by the Aladin software, which is described in [44]. The images of our ROI from all four radio surveys are shown in fig. 9. Firstly, we notice that our ROI does not capture any contaminating point sources. On the last three images (325, 1400 and 4850 MHz) some signal from M31 center is clearly visible. The 74 MHz image presents essentially noise. For the precise flux upper limit derivations we needed to obtain the measured signal values c_i ($i = 1 - 4$ denotes different observational frequencies) and the rms (root of mean square or root of dispersion) noise values σ_i for our ROI for all images (we assumed the Gaussian distributions of noise levels inside a radio telescope beam and inside the ROI). The measured signal values were easily read by the Aladin. As for the rms noise values, we derived from basic principles that they can be estimated as $\sigma_i = \sigma_i^{(b)}\sqrt{N_i} = \sigma_i^{(b)}\frac{\alpha}{\beta_i}$, where N_i are the numbers of beams contained in the ROI, β_i are the angular radii of beams (or half of the FWHM for each survey) and $\sigma_i^{(b)}$ are the rms noises inside a beam for each survey (cited in table 1). Thus, we have obtained both necessary ingredients for a flux upper

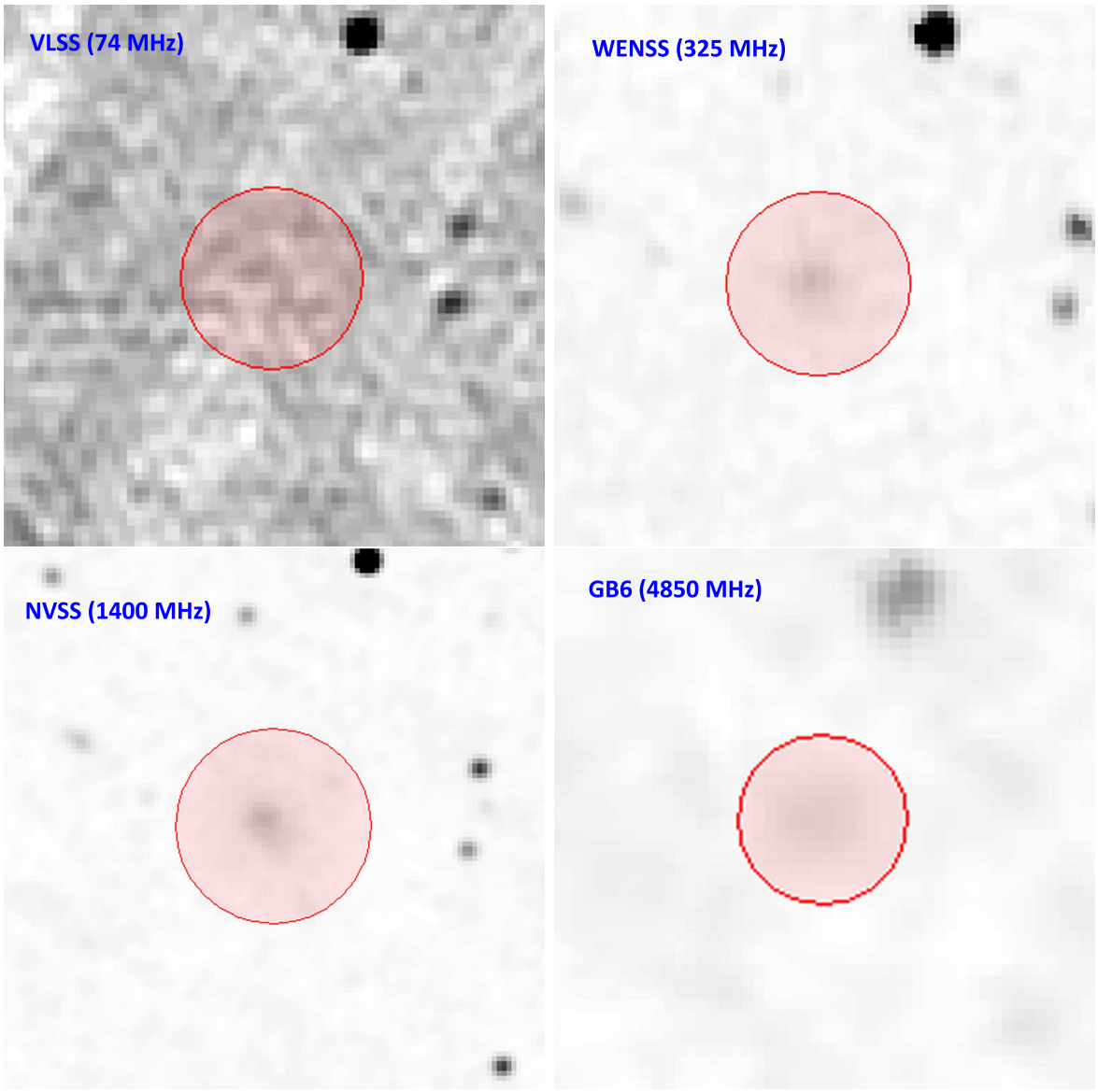


Figure 9. Radio images of the M31 central region. Our ROI of 5′ radius is marked by the red circle. Corresponding surveys are commented on each image. We can find noise only on 74 MHz and significant signals on the other frequencies.

limit estimation from the ROI - the measured signal values and the rms noise values.

Having all the necessary information, we obtained the limiting cross section values for different parameter sets using the following formula for the probability density of the noise values n_i inside our ROI:

$$p_i(n_i = c_i - w_i(\langle\sigma v\rangle)) = \frac{1}{\sqrt{2\pi}\sigma_i} \exp\left(-\frac{(c_i - w_i(\langle\sigma v\rangle))^2}{2\sigma_i^2}\right), \tag{3.8}$$

where $w_i(\langle\sigma v\rangle)$ is the expected signals from WIMP annihilation, which is linearly proportional to $\langle\sigma v\rangle$. Here we do not include any background radiation (this question will be further

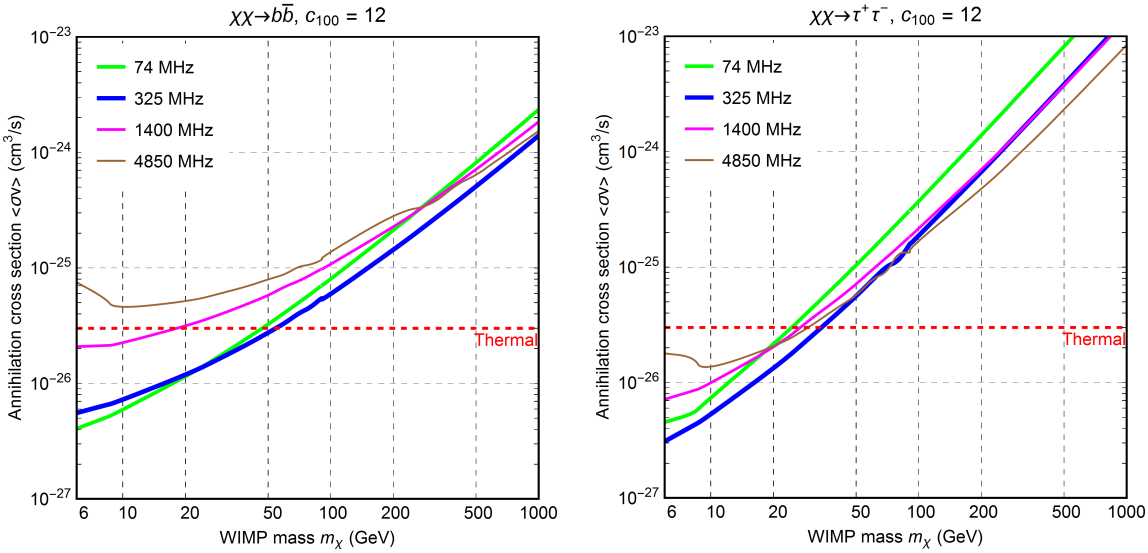


Figure 10. The computed constraints for the $c_{100} = 12$ case: the WIMP annihilation cross section values above the contours are excluded at 99.7% CL. Constraints from different surveys are marked by different colors and thicknesses. Standard thermal relic value $\langle\sigma v\rangle = 3 \cdot 10^{-26}$ cm^3/s is also shown by the red dashed line. No emission sources besides DM are assumed. MF has the most probable distribution with $B(0,0) = 50$ μG. For more details see §3.3.1.

developed in the next subsubsection). For our final constraints onto $\langle\sigma v\rangle$ we decided to use 99.73% CL, which corresponds to 3σ Gaussian deviation.

In order to guide an intuition on which experiment is the most constraining for a given particle mass, in fig. 10 we showed our results on the cross section when each frequency is considered individually. There we plotted the constraints obtained at 99.7% CL by four different surveys used, for $c_{100} = 12$ halo models (described in §3.2.2), two annihilation channels selected $\chi\chi \to b\bar{b}, \tau^+\tau^-$ and the most probable MF distribution with $B(0,0) = 50$ μG. We spanned the range of WIMP masses between 6 GeV and 1000 GeV and computed the limiting $\langle\sigma v\rangle$ values for a subset of masses inside this range, interpolating results for mass values in between. One important feature of the constraints derived is that $\tau^+\tau^-$ channel appears to be less constrained than $b\bar{b}$ channel as expected from the theory. It's also interesting to notice that for different WIMP masses and annihilation channels, the most constraining survey among all the considered varies. Therefore, we can not isolate a specific key frequency/experiment for each plot, which bears the role of the most constraining for all WIMP masses - we need to use all experiments together to get the best constraints. And final constraints from the joint analysis will be gathered in the next subsubsection together with analysis of the role of DM and MF distribution uncertainties.

3.3.2 Joint analysis and final constraints

Constraints shown in fig. 10 represent exclusion contours from four independent observations. As we can see, these contours lie rather close to each other on each diagram at least for some WIMP masses. Such situation suggests to apply a joint likelihood analysis in order to infer combined constraints from all four independent measurements, which we can expect to be better than the constraints taken just considering the exclusion curves in fig. 10.

Signals other than DM are anyway expected to exist in reality at each frequency. An appropriate modeling of all other astrophysical signals, with their frequency dependence, is preferable in the joint analysis. We decided to make no assumptions on astrophysical processes other than DM annihilation, and simply modeled the total contribution of all other background signals as an a-priori unconstrained offset uncorrelated between the frequency bands. We then performed a standard Bayesian analysis of our data. Following the Bayes theorem (for more details see [45]):

$$p(\vec{\Theta}|\vec{c}) = \frac{p(\vec{c}|\vec{\Theta})p(\vec{\Theta})}{p(\vec{c})}, \tag{3.9}$$

where the l.h.s. is the desirable probability density distribution for unknown set of parameters $\vec{\Theta}$ in case of the observation of data $\vec{c}$, $p(\vec{c}|\vec{\Theta}) \equiv L(\vec{\Theta})$ is the probability density of our observed data $\vec{c}$ for fixed parameters $\vec{\Theta}$ (or likelihood function), $p(\vec{\Theta})$ is the prior probability density of $\vec{\Theta}$ and $p(\vec{c})$ is the marginal likelihood. In our case $\vec{\Theta} = (\langle\sigma v\rangle, s_i)$ is the set of unknown parameters, which we are aiming to infer - annihilation cross section and background radiation fluxes s_i on all four frequencies. $\vec{c} = (c_i)$ is the data measured. Then the likelihood function L will have the form:

$$p(\vec{c}|\vec{\Theta}) = L(\vec{\Theta}) \sim \prod_{i=1}^{4} \exp\left(-\frac{(c_i - s_i - w_i(\langle\sigma v\rangle))^2}{2\sigma_i^2}\right). \tag{3.10}$$

This likelihood function represents essentially the product of the independent noise level Gaussian distributions on all frequencies written in terms of the measured and expected fluxes (taking into account that $c_i = s_i + w_i + n_i$). As for $p(\vec{\Theta})$, we made no specific assumptions and chose a constant (flat) prior. The function $p(\vec{c})$ in eq. 3.9 does not require specification, since it does not depend on $\vec{\Theta}$ and, hence, plays a role of a normalization constant. After we constructed the five-dimensional density distribution eq. 3.9 for all five unknown quantities, we needed to integrate eq. 3.9 over all possible ranges of non-interesting parameters (marginalization). In our case we were not interested in the background values, so we obtained the distribution for the desired quantity $\langle\sigma v\rangle$ by marginalizing over the background values:

$$p(\langle\sigma v\rangle|\vec{c}) \sim \int L(\vec{\Theta})p(\vec{\Theta})d\vec{s} = \int_0^\infty\int\int\int \prod_{i=1}^{4} \exp\left(-\frac{(c_i - s_i - w_i(\langle\sigma v\rangle))^2}{2\sigma_i^2}\right) ds_1..ds_4, \tag{3.11}$$

where we took into account the flat prior. Thus eq. 3.11 gives us the final probability density distribution for annihilation cross section combined from all four observations with possible unknown backgrounds included. From this distribution we easily constructed the final exclusion contours. We presented them for the case of 99.73% CL in fig. 11–12, where the allowed area is below the exclusion contours for the corresponding models.

We included in our final results possible uncertainties in both the DM and MF distributions discussed in §3.2.2–§3.2.3. Regarding MF, its distribution is uncertain in two aspects - its vertical scale height z_0' and the central field strength $B(0,0)$. As for the z_0', our trial runs showed that z_0' variation over all possible values is able to change the final exclusion values of $\langle\sigma v\rangle$ by no more than $\langle\sigma v\rangle^{+5\%}_{-20\%}$ for all possible sets of model parameters. This variation is considerably smaller than the one induced by the halo model uncertainties and would suggest less conservative limits. For these reasons, we do not consider it in our final

Table 2. WIMP masses in GeV, below which annihilation with the canonical cross section is excluded, for the different halo and MF models. The most realistic cut off values are emphasized.

Central field B(0, 0)	$c_{100} = 12, \chi\chi \to b\bar{b}$	Averaged flux, $\chi\chi \to b\bar{b}$	$c_{100} = 28, \chi\chi \to b\bar{b}$	$c_{100} = 12, \chi\chi \to \tau^+\tau^-$	Averaged flux, $\chi\chi \to \tau^+\tau^-$	$c_{100} = 28, \chi\chi \to \tau^+\tau^-$
15 μG	23	45	160	23	35	88
50 μG	63	***100***	280	39	***55***	130
300 μG	75	110	280	38	53	110

results. However, we can not treat in this way the second important parameter - $B(0, 0)$, because practice showed a significant variation of the final exclusions due to uncertainties in $B(0, 0)$ discussed in §3.2.3. According to that discussion, we expect $B(0, 0) = 50$ μG to be the most probable, but we also consider here $B(0, 0)$ values of ~ 15 and ~ 300 μG as limiting cases. We obtained all our final exclusions for these three different MF distributions.

In fig. 11–12 with the main results the dashed lines represent the specific halo models (either $c_{100} = 12$ or $c_{100} = 28$), while the solid lines correspond to the algebraic averages between them for the fixed MF values. The two figures show limiting curves for different combinations of the (three) possible MF models and (two) possible halo models. Fig. 11 shows more explicitly the dependence on the field strength, while fig. 12 shows the dependence on the halo model for the reference field strength $B(0, 0) = 50$ μG, and allows to compare these uncertainties with the ones caused by variation in the MF.

As we can see, annihilation with the standard thermal relic cross section $\langle\sigma v\rangle = 3 \cdot 10^{-26}$ cm^3/s is excluded for a significant part of the WIMP mass range. We listed in table 2 the precise WIMP mass values for all models considered, below which $\langle\sigma v\rangle$ is less than $3 \cdot 10^{-26}$ cm^3/s. These masses were obtained as the contact points between the corresponding exclusions and the thermal relic threshold in fig. 11–12. We can see a significant spread in limiting masses around those which correspond to our preferred model with $B(0, 0) = 50$ μG and the averaged flux between two limiting halo cases. For this most realistic model the WIMP masses, which do not allow the standard relic cross section, are the ones smaller than **100 GeV** and **55 GeV** for $b\bar{b}$ and $\tau^+\tau^-$ channels respectively. In general, these limits were derived with rather conservative assumptions. Discussion of our results and comparison with other studies will be done in the next subsection.

3.4 Summary and discussion

In this section we aimed to obtain robust constraints on WIMP–mass/annihilation–cross–section plane by studying radio observations of M31. Annihilating DM in M31 halo produces highly energetic secondary $e^{\pm}$, which, in turn, emit synchrotron radiation due to Andromeda MF. We computed the expected characteristics of this radiation. We first modeled the DM density distribution in M31, using the standard NFW density profile. Parameters of this distribution were found in the previous studies of the M31 halo. These studies appeared to have a good agreement between each other in the halo mass determination ($M_{100} \approx 10^{12} M_\odot$), but they differ significantly in the obtained halo concentration parameter - $c_{100} \approx 12$ vs. $c_{100} \approx 28$. That's why we treated these two cases separately and considered them as limiting cases of the possible halo models for M31. Another important step of the calculations was MF distribution modeling. For this purpose we used available MF measurements in M31. Information, which is not available for M31, was gathered by extrapolating the MW MF

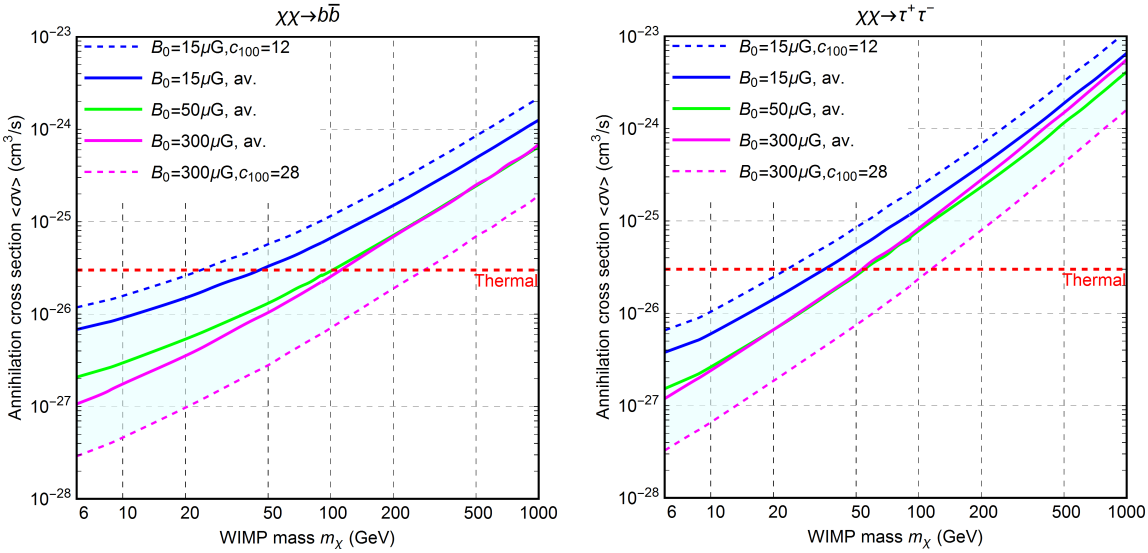


Figure 11. Joint constraints including all radio surveys and backgrounds. These plots show all potential uncertainties of both distributions of DM density and MF strength. The dashed contours reflect specific halo models discussed in the text (lines represent 99.7% CL). The continuous lines represent averages between the exclusions for the corresponding limiting halo models. Different continuous contours illustrate the variation of exclusions due to MF uncertainties. The upper and lower exclusions enclose the shaded regions of all other possible exclusions from the most conservative to the most optimistic ones. More details are in §3.3.2.

distribution properties and general properties of galactic MFs as well. The idea to use the MW MF measurements was motivated by high similarity between M31 and MW, and, also, by the much more detailed knowledge we have about MW. We introduced the realistic field distribution, which is characterized by the 50 μG value of the central field strength and exponential decline both in vertical and radial-in-plane directions. Then we computed the secondary particle yields from WIMP annihilation using [21]. We showed that neglecting the spatial diffusion of the injected $e^{\pm}$ is a reasonable approximation. We calculated final fluxes in the transparent medium approximation. As for the sky area chosen for putting the constraints, we chose the disc with the angular radius $5'$ around the M31 center, and motivated our choice in §3.2.4.

After obtaining the expected radio fluxes due to DM, we compared them with available radio observations of M31. For this purpose we used four radio surveys spanning wide range of frequencies: VLSS (74 MHz), WENSS (325 MHz), NVSS (1400 MHz) and GB6 (4850 MHz). This comparison yielded the limits on the cross section $\langle\sigma v\rangle$ as a function of the particle mass (ranging from 6 GeV to 1000 GeV). Our analysis is conservative in sense of the absence of any specific assumptions about a possible radiation other than from DM. The final results are presented in §3.3 in fig. 11–12. We also computed our results for the alternative less probable MF models with the central field values of 15 and 300 μG in order to study the dependence of our final constraints on this model parameter.

Our main result is the exclusion of the possibility of WIMP annihilation with the thermal cross section $\langle\sigma v\rangle = 3 \cdot 10^{-26}$ cm^3/s or higher for WIMP masses below $\approx$ 100 GeV ($\approx$ 55 GeV) for the $b\bar{b}$ ($\tau^+\tau^-$) annihilation channel. However, these estimations are affected by significant uncertainties. Taking into account potential uncertainties in the DM density and

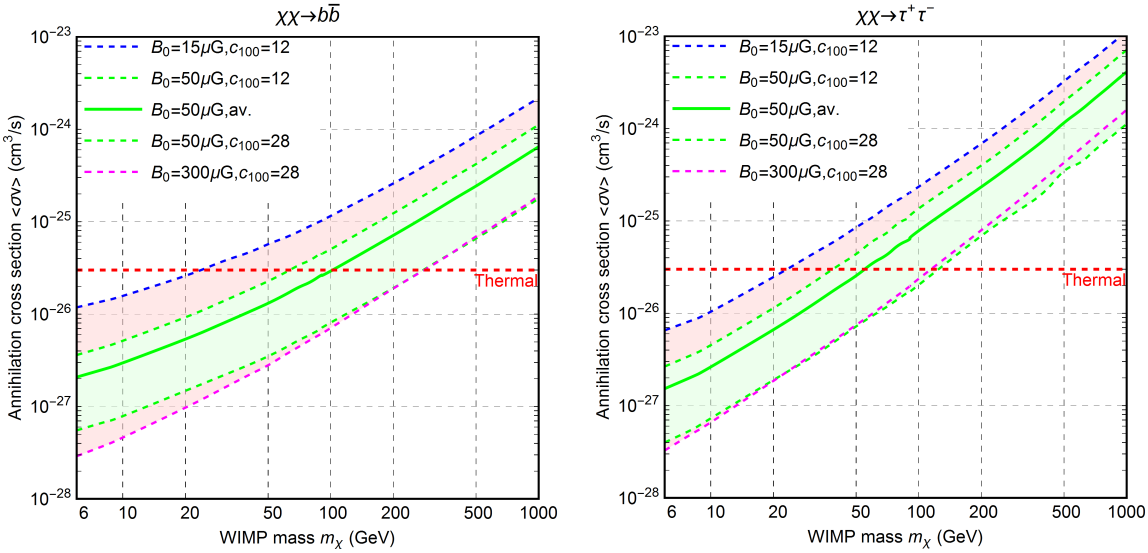


Figure 12. Joint constraints obtained. These plots incorporate potential uncertainties of both distributions of DM density and MF strength. The continuous line represents the most realistic exclusion contour, which corresponds to the result of our work on the fiducial case we assumed (average exclusion between those which correspond to the two limiting halo cases and the most realistic MF distribution with $B(0,0) = 50$ μG). The shaded area around the continuous contour, which is constrained by the inner dashed green lines, corresponds to the dark halo model uncertainties only. Larger shaded region, which is enclosed into the outer dashed lines, incorporates both uncertainties of the dark halo and MF. For more details see §3.3.2.

MF distributions, these limits could be as low as 23 GeV and as high as 280 GeV for the $b\bar{b}$ channel. For annihilation into $\tau^+\tau^-$ these limits respectively are 23 GeV and 130 GeV (see table 2). Also, soon after we submitted our work [11], the new study of the M31 halo came out [46]. This work derived the updated DM distribution parameters for various profiles including NFW. M_{100} estimate in [46] agrees quite well with that used by us. As for the concentration c_{100} for the NFW profile, they derived it to be 17. This is good because this value falls almost exactly in the middle of our used range 12-28. Using $c_{100} = 17$ our fiducial WIMP mass limits 100/55 GeV in table 2 would become respectively 140/73 GeV. Thus, they even further increase. The latter limits might be more representative rather those coming from just averaging of the limiting halo cases. However, we would still like to stick to 100/55 GeV as the final result in order to stay conservative, since some assumptions we made (e.g. no spatial diffusion) might be quite strong and overestimate the constraints.

Our results were comparable with other constraints on WIMP masses derived through other observations at the time we did our work. That time the best constraints were coming from the joint analysis of the MW satellites by Fermi telescope [47]. The latter work excluded WIMP masses below 40 GeV and 19 GeV for $b\bar{b}$ and $\tau^+\tau^-$ channels respectively for the case of the thermal cross section. When considering 95% systematic errors in the DM distribution within the dwarves, their derived limits vary over the ranges 19–240 GeV ($b\bar{b}$) and 13–80 GeV ($\tau^+\tau^-$). Our constraints, suggesting the masses above 100 GeV and 55 GeV, even exceeded those in [47]. This proved the relevance of multi-frequency approach in indirect detection: all wavelength ranges may make valuable contributions into an overall progress.

4 Milky Way at microwave frequencies

4.1 General aspects

MW, in general, represents an object of a great interest for our purposes being probably the closest target for the DM indirect detection. The GC is expected to be the brightest source in the sky of gamma rays from DM annihilation. And as was already mentioned in the Introduction, in recent years an interest to the GC increased dramatically with detections of some mysterious gamma and microwave excesses around it. Thus several independent studies (e.g., [13, 15, 16, 48–51]) confirmed the presence of an excess at GeV energies over the expected astrophysical gamma-ray emission around the GC, which is consistent with expectations for a DM annihilation signal. However, in addition to the DM interpretation, other explanations were also shown to be possible: a population of unresolved gamma-ray millisecond pulsars (MSPs) [15, 16, 52–56], gamma rays from CRs injected in bursts near the GC [57–59] and others. Some very recent works [60, 61], which were published already after our work, tended to claim that MSPs are more likely responsible for the excess than DM. However, a major debate about it still remains in the community, leaving open the exciting possibility that the excess represents a detection of DM annihilation.

On the other hand, a similarly intriguing excess over conventional astrophysical foregrounds at microwave frequencies was identified several years ago: the Haze or WMAP-Planck [17, 62]. The Haze refers to an excess emission in the Inner Galaxy identified in the WMAP mission data (and later confirmed by Planck), observed to be approximately symmetric around the GC, extending tens of degrees away from the GC, and exhibiting a harder spectral index than expected for the synchrotron associated with the Galactic CR population from astrophysical sources. The spectrum of the Haze suggests that it originates from a distinct population of high-energy electrons. And annihilating DM can naturally be the source of this population.

More recently, a new feature in the gamma-ray sky has been identified: the so-called Fermi Bubbles [63, 64]. The Bubbles are a bipolar structure centered on the GC and extending above and below it out to the Galactic latitude $|b| \approx 50^\circ$, and they are clearly visible in the Fermi gamma-ray data. Similar structures had previously been identified in X-ray and 408 MHz radio data [65] as well as in infrared maps [66], and they had been suggested to result from starburst-driven winds in the GC. Refined observations in microwave with Planck revealed a correlated morphology between the Haze and Fermi Bubbles [18]. This indicates a potentially common origin of these two phenomena. In addition, recent observations of polarized radio emission with the S-PASS survey at 2.3 GHz revealed that the radio features are also closely aligned with those observed in gamma rays [67], again pointing to a consistent interpretation (e.g., [68]).

The Bubble-like structures observed over a broad range of energies are now presumed to be multi-wavelength views of the same phenomenon, and compelling non-exotic explanations have been put forth (e.g. reverse shocks in the GC's giant outflows [68]). Moreover, due to the unique morphology of these structures, it is quite unlikely that they are associated with DM annihilation. Thus, a search for a potential DM signal in the WMAP-Planck data requires an understanding of not only "standard" astrophysical foregrounds but also the microwave emission associated with the Fermi Bubbles. Despite the presence of the Bubbles in multi-frequency observations, and its potential manifestation in the microwave band in the form of the Haze, it is still possible that some part of the observed Haze is due to DM annihilation. Throughout this section, the term "Haze" will refer to the microwave emission not accounted

for by common foregrounds (i.e. emission from the Bubbles and DM annihilation), and "Bubbles" will refer to the microwave counterpart of the Fermi Bubbles.

In this work, we revisited the problem of multi-wavelength DM searches in the Galaxy using the WMAP-9 and Planck 2013 data sets, focusing on DM models that could explain the observed GC gamma-ray excess. Thus, we considered WIMP masses in the range 7.0-52 GeV, and two benchmark annihilation channels $b\bar{b}$ and $\tau^+\tau^-$ (similar to those in M31 work above). We calculated the microwave emission associated with WIMP annihilation in the Galaxy, and tested the consistency of that signal with the observations by performing a complete model-fitting analysis of the WMAP-Planck data. The predicted microwave emission due to WIMP annihilation is subject to uncertainties in the modeling of the Galactic environment. In particular, uncertainties in the MF distribution in the Galaxy and in the propagation parameters for $e^{\pm}$ in the interstellar medium can lead to significant variations in the expected emission. We addressed these sources of uncertainty by varying the MF and propagation models in order to understand their impact on our results. We then compared our models with the data in order to assess the potential contribution of DM to the total signal.

We adopted two different approaches for the model-data comparison: first we assumed that the data only contain noise, CMB and DM signal (but no other foregrounds or the Bubbles). This leads to an overestimate of the potential DM contribution which translates to a conservative but very robust upper limits on the DM annihilation cross section. Next, we performed a component separation procedure based on template fitting, this time also considering all relevant foregrounds and the Bubbles. In this case, we presented the best-fit DM parameters obtained. With these analyses we aimed to address the following issues: *i)* the exact nature of the Haze – whether the data favor (and at what significance) a DM component in the Haze emission; and *ii)* the compatibility of WIMP models needed to fit the GC gamma-ray excess with the microwave data.

We present the DM models and the computation of the microwave emission from DM annihilation in §4.2. In §4.3 we define the two ROIs we consider, and in §4.4 we show the predicted DM spectra in the Haze region. §4.5 is dedicated to conservative WIMP model constraints obtained from the data when considering CMB and DM emission as the only contributions, neglecting all other foregrounds. A comprehensive component separation procedure, which includes models of expected foregrounds, is described along with its results in §4.6. We discuss the implications of these findings for DM models and a DM interpretation of the GC gamma-ray excess in §4.7.

4.2 Computing the microwave emission

4.2.1 Solution of the transport equation by GALPROP

Here we could not use a simple solution eq. 3.1 of the transport eq. employed for M31 in the previous section, because for MW we considered a significant part of its halo, and the spatial diffusion of the annihilation products is important. This makes it difficult to find an analytical solution of the transport eq. 2.5. Hence people created a variety of tools for its numerical integration. Among them one of the oldest and most developed is so-called GALPROP code (see [24, 26, 69] for detailed descriptions), which was written in Fortran and C/C++ languages. It's capable to fully model a propagation of CRs of any type and to calculate all sky emission from them at respective frequencies. And we naturally decided to employ GALPROP for our purposes. However, there was a caveat on this way - the current public version of GALPROP does not have a proper DM functionality. That's why at first

we developed this functionality by ourselves. Essentially, that required to implement the DM source term eq. 2.6 into GALPROP. Below we briefly describe important aspects of the implementation of each component of the DM source.

For the DM distribution entering eq. 2.6 we implemented the opportunity for a user to choose between the generalized NFW (eq. 4.1 below), Isothermal, Einasto or Burkert profile. These are several most popular profiles with different levels of cuspinness (see e.g. [22] for more details). Since the transport eq. is being solved on a grid with a finite cell size, and the DM density can change significantly over one spatial cell, we also implemented a proper averaging of the squared density (which enters eq. 2.6) in each cell. This is especially important for the central cell of the grid (located at the MW center), where cuspy profiles like NFW have a divergent spike. Simple averaging algorithms appeared to fail in the central cell. For this reason, we employed there a high precision numerical integration of the profile using respective functions from the GNU Scientific Library (see e.g. [70]). For the local boost factor due to substructures $\xi_{\rm DM}(r)$ we substituted the one derived in [32] for the MW-like halo (see fig. 4 there).

Another important component of the DM source eq. 2.6 is the $e^{\pm}$ spectra from one annihilation $\frac{dN_e}{dE}(E)$. This information were obtained from the same resource as for M31 [21]. For the description one can see [22]. We took the annihilation yields in their latest version, which includes electroweak corrections [23]. We computed the tables of yields for various WIMP masses and annihilation channels by Mathematica package. Then we attached these table to GALPROP.

Besides coding the source term, some other practical upgrades were implemented. Thus, we introduced an opportunity to generate synchrotron emission maps at arbitrary frequencies. Also, we coded a parallelization of some internal routines in GALPROP in order to get an opportunity to compute many runs relatively fast. In total we needed to compute 300 different DM configurations (see below), which respectively required 300 separate runs of the code. But even with the optimized code we needed to employ the USC computing cluster to run all our models (using 240 processor cores simultaneously). After we implemented all the upgrades into GALPROP, it gained a comprehensive DM functionality. At the beginning of the run a user has to specify all DM parameters: WIMP mass, annihilation cross section, channel, density profile and its parameters. And then GALPROP is capable to produce all sky maps of the emission due to DM through all the relevant mechanisms: prompt gammas, secondary gammas/X-rays due to ICS of $e^{\pm}$ from DM, synchrotron etc. Soon we plan to release our upgraded version of GALPROP for a public use by the respective community.

For our purposes we ran GALPROP in 3D version. This is indeed much more computationally expensive than the minimal 2D version. But the former is able to provide more precise and reliable results. Thus, the propagation of annihilation products was done in 5 dimensions: 3 spatial + energy + time. The propagation in time is being done until the stationary solution is achieved $n(\vec{r}, E, t) \to n(\vec{r}, E)$. §4.2.2-§4.2.4 explain the choices of all the parameters, which enter the transport eq. through eqs. 2.6–2.12. And we did not include any other than DM emission sources in the GALPROP runs.

4.2.2 DM density distribution

The exact DM density distribution in our Galaxy is a matter of active debate. A wide range of DM density profiles from cored to very cuspy are in agreement with numerical simulations and observational data (e.g., [71–75]). In this work we restricted our analysis to profile shapes that have been shown to provide a good fit to the GeV excess around the GC [13, 15, 16, 48–

50, 76]. In particular, we adopted for the DM distribution a generalized form of the NFW density profile [27]

$$\rho_{\rm DM}(r) = \frac{\rho_{\rm s}}{\left(\frac{r}{r_{\rm s}}\right)^{\gamma}\left(1+\left(\frac{r}{r_{\rm s}}\right)^{\alpha}\right)^{(\beta-\gamma)/\alpha}}, \tag{4.1}$$

where α, β, and γ are shape parameters. We adopted the common convention to fix $\alpha = 1$ and $\beta = 3$, and allowed only the inner profile slope, parametrized by γ, to vary. Following the results of [13, 15, 16, 48–50, 76], we considered values of γ ranging between 1.1 and 1.3 (considering three discrete values 1.1, 1.2 and 1.3). We adopted $r_{\rm s} = 23$ kpc and fixed the local density at the solar position to $\rho_{\rm DM}(r_\odot = 8.3\ {\rm kpc}) = 0.34\ {\rm GeV/cm^3}$ (which are similar to the values adopted in [13, 15, 16, 48–50, 76]).

The density distribution in eq. 4.1 is technically divergent at the central halo point. We solved this issue by introducing a constant density core within a radius $r_{\rm core}$. Although this is highly unconstrained parameter, from general considerations (including the size of the central black hole and the gamma excess fit requirements) we can set it to be in the range $4.2 \cdot 10^{-7}\ {\rm pc} \lesssim r_{\rm core} \lesssim 10\ {\rm pc}$. We obtained that the DM emission intensities in the relevant ROIs only vary by about $\sim 1\%$ when vary $r_{\rm core}$ over the mentioned range. Hence, our setup in fact is not sensitive to a specific choice of $r_{\rm core}$. For definiteness we adopted $r_{\rm core} = 4.2 \cdot 10^{-7}$ pc for all models.

As already mentioned, substructures are known to play an important role in boosting the luminosity of a DM halo. Thus, we found that substructures increase the signal in our chosen ROI (discussed in §4.3) by $\approx (30 - 35)\%$. This boost is relatively mild due to the fact that the majority of our signal comes from areas close to the GC where, due to tidal disruption, we do not expect a large amount of substructures.

4.2.3 Magnetic field distribution

Synchrotron emission depends crucially on the MF distribution in the Galaxy. Although sophisticated MF configurations are possible (see, e.g., [77]), for the sake of simplicity we modeled the MF with an axisymmetric distribution, as also adopted in earlier works, e.g. [78, 79]:

$$B(R,z) = B_0 \exp(-(R - R_\odot)/R_B - |z|/z_B), \tag{4.2}$$

where R and z represent radial-in-plane and plane-orthogonal distances in the Galaxy, respectively.

The parameter B_0 in eq. 4.2 represents the total MF value at the Solar location and is taken to be 6 μG following [14]. The radial scale R_B in eq. 4.2 naturally sets the central field value and is more uncertain. On this point, we relied on the lower limit $B(0,0) = 50$ μG derived in [35] as our preferred choice. This sets the respective $R_B = 4.0$ kpc, which we consider to be the most realistic value. However, we also computed our results for $B(0,0) = 100$ μG as a limiting case which would produce higher DM emission. Such high central MF values are encountered in the literature [80]. However, the field would reach these values only very close to the GC (within ~ 0.2 kpc), and in that case the field radial dependence in eq. 4.2 might not be steep enough to produce the proper field attenuation at larger radii. For this reason, we consider the $B(0,0) = 100$ μG (with respective $R_B = 3.0$ kpc) configuration to be generally less realistic.

The z_B parameter in eq. 4.2 sets the vertical characteristic scale of the MF, which is also somewhat uncertain. Various studies of the MF distribution in MW and other similar galaxies (e.g. [38, 81, 82]) estimate z_B to be robustly constrained in the range $\approx (1 - 10)$

kpc with a characteristic "average" value of 4-6 kpc. At the same time, z_B is naturally linked to the CR propagation parameters (discussed in §4.2.4), since the MF is the driving reason for the CR diffusion, and where the MF is small or null CRs can freely escape. We therefore expect the MF spatial extent z_B to be comparable to the spatial extent of the diffusion region, parametrized by h below (the vertical half-height of the diffusion zone). Proportionality between these two parameters was employed in multiple earlier works to estimate z_B (e.g. [14, 79]). We followed this approach and, similarly to [14], computed all our results for two values of z_B: $z_B = \delta \cdot h$ and $z_B = 0.5 \cdot h$. The parameter δ denotes the spectral slope of the spatial diffusion coefficient (described below).

4.2.4 Diffusion model

As was already mentioned in §2, we assumed no particle convection and isotropic spatial independent diffusion coefficient eq. 2.7. This simplifies the full transport eq. to the form (with $n \equiv n(\vec{r}, E, t)$):

$$\frac{\partial n}{\partial t} = q(r, E) + D_{xx}(E)\nabla^2 n + \frac{\partial}{\partial E} E^2 D_{EE}(E) \frac{\partial}{\partial E} \frac{n}{E^2} - \frac{\partial}{\partial E}(b(\vec{r}, E)n), \tag{4.3}$$

where the actually used diffusion and reacceleration coefficients were defined by eqs. 2.7–2.8. As for the loss term $b(\vec{r}, E)$, for MW it was automatically modeled by GALPROP employing all its detailed knowledge about our Galaxy.

For the choice of the parameter values in eqs. 2.7–2.8, to begin we followed the canonical MIN/MED/MAX paradigm which has been used extensively in earlier works (see, e.g., [14, 22, 79]). These three diffusion parameter configurations were derived from various CR data sets. MED is an average "best-fit" configuration, while MIN and MAX are intended to represent possible extremes. Because recent CR data seem to reliably exclude the MIN model [83], we discarded this case and included instead a newly proposed model derived in [84], which includes CR reacceleration effects in the fit. Specifically, we used the posterior mean parameter values from Table 2 of [84].

Recalling that we consider two values for the MF vertical scale height z_B (referred to as z_{B1} and z_{B2}), which is related to h, we now define combined MF and propagation models. In principle we would consider both values of z_B with the three propagation models described above, however we discovered empirically that the intensity for the two z_B values is very similar for the MAX propagation configuration, and so we used only the z_{B1} case with the MAX model. This results in five z_B/propagation models. Table 3 summarizes the parameter values for these five configurations.

For each of these five models, we considered the two central MF values mentioned previously, for a total of ten MF/propagation models. These are meant to represent current systematic uncertainties on this aspect of the analysis. For each of these models, we calculated the emission from each of the DM models described in §4.1 and §4.2.2. In §4.2.5 we show the dependence of the DM emission intensity on the MF and propagation configuration.

Table 3 cites the vertical sizes of the rectangular 3D diffusion box h; for the horizontal size, we set the box edges to be $+/-15$ kpc along both x- and y-axes to approximately enclose the Galactic disc (see e.g. [14]). Boundary conditions were set to the free escape mode. For the energy boundaries, we took 0.01 to 200 GeV. The lower boundary is mainly defined by the fact that $e^{\pm}$ with smaller energies have no contribution to the synchrotron radiation at the frequencies of interest. The upper boundary has to contain the most energetic $e^{\pm}$ produced by our DM source. One might naively assume that they would approximately correspond

Table 3. Diffusion parameter values for the electron propagation (which enter eqs. 4.3, 2.7, 2.8) and MF vertical scale heights (which enter eq. 4.2) used in our work.

Parameter	MED	MAX	Reacc
Half-height of the diffusion box h, kpc	4.0	15	5.4
Diffusion coefficient normalization D_0, cm^2/s	$3.4 \cdot 10^{27}$	$2.3 \cdot 10^{28}$	$5.4 \cdot 10^{28}$
Diffusion coefficient energy dependence power δ	0.70	0.46	0.31
Alfven speed in the intragalactic media v_a, km/s	0	0	38
MF vertical scale height, version 1 $z_{B1} = \delta \cdot h$, kpc	2.8	6.9	1.7
MF vertical scale height, version 2 $z_{B2} = 0.5 \cdot h$, kpc	2.0	-	2.7

to the largest DM particle rest mass involved ($\sim$ 50 GeV), however particle reacceleration (as in our Reacc model) can in principle raise the electron energies much beyond $m_\chi c^2$. We empirically found that 200 GeV is an effective upper limit on the energies $e^\pm$ attain in our cases.

Further details on all parameters we adopted in the GALPROP runs can be requested from the authors.

4.2.5 DM emission maps

We implemented the modeling described above and produced multi-frequency maps for all DM models needed to cover the parameter space. In total, we computed 300 parameter configurations, which are constituted by 5 different WIMP masses over the range of interest (we interpolated our results between the computed points), 2 annihilation channels ($b\bar{b}$, $\tau^+\tau^-$), 3 profile slopes (see §4.2.2), and 10 MF/propagation models (see §4.2.3 and §4.2.4). The maps have a resolution of $\approx 0.5^\circ$ (HEALPix [85] resolution $N_{side} = 128$) and are produced at the WMAP and Planck frequencies of 23, 28, 33, 41, 44, 61, and 70 GHz. Similarly to our work on M31 (§3) we also checked here a potential relevance of the free-free absorption. GALPROP is capable to calculate it based on the parameters of the interstellar ionized gas. For any reasonable parameter values we confirmed an absence of any significant free-free absorption at our frequencies.

Fig. 13, top left panel, shows the DM intensity map for a reference model ("REF"); this is also the best-fitting configuration found in §4.6. The figure shows an intensity distribution around the GC that is highly concentrated, spanning six orders of magnitude between the center and anti-center. The other panels of fig. 13 show examples of the dependence of the emission on various parameters in terms of the ratio to the REF case.

We comment now on some general features. The difference between the maps typically grows with distance from the GC. This is seen when changing the DM particle mass (top right), and also interestingly, for the frequency dependence (middle row, left). However the steeper DM density profile map ($\gamma = 1.3$ vs $\gamma = 1.1$ for the REF model) differs noticeably only very close to the GC (middle row, right); this indicates that the profile slope does not have an important impact on the emission at higher Galactic latitudes. The $b\bar{b}$ annihilation channel produces significantly smaller intensities than $\tau^+\tau^-$ one, everywhere on the sky, as expected (bottom left). A more conservative MF/propagation model (bottom right) differs non-trivially from the REF model: the intensity is much smaller around the center and much larger around the anti-center. This can be primarily attributed to an overall smaller MF, which generates weaker synchrotron around the GC and cools $e^\pm$ less efficiently, allowing them to diffuse further while still emitting.

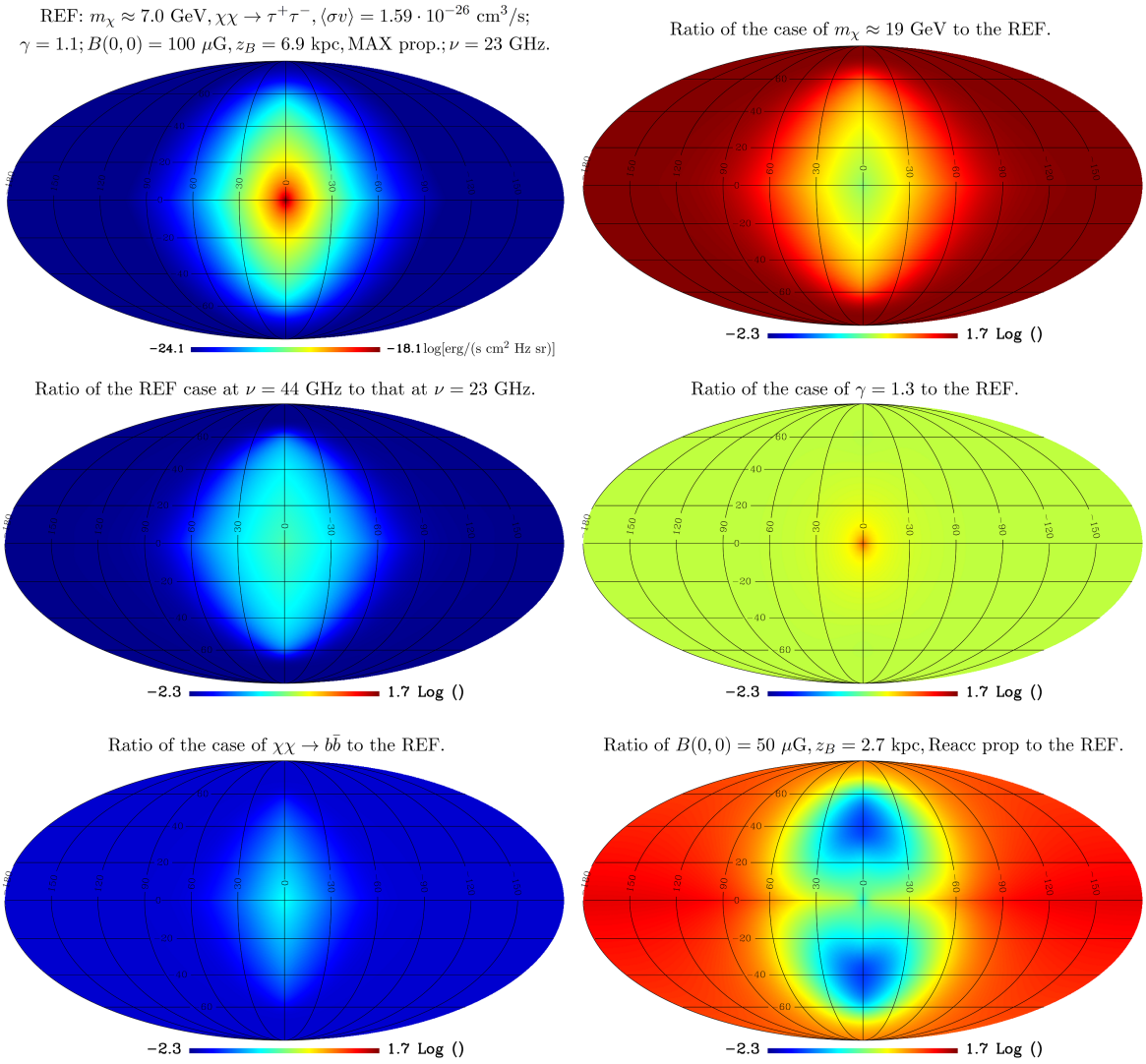


Figure 13. Examples of DM emission intensity maps in Galactic coordinates, at the frequencies indicated. The top left map represents a reference DM parameter configuration ("REF"). Specific parameters of the configuration are given above the map. Other maps show the difference with respect to the REF map when the model parameters are changed as noted. The difference is shown as the ratio $I_x(b,l)/I_{\rm REF}(b,l)$, where I_x is the intensity of the map with one of parameters being changed and $I_{\rm REF}$ is the intensity of the REF map. To illustrate dependence on MF/propagation we changed several relevant parameters. For more details see §4.2.5.

4.3 Regions of interest on the sky

For each of the two approaches to testing a DM contribution to the data, we selected a ROI in the sky on which to perform the analysis. For the first approach, in which we derived conservative limits by assuming the total data is composed of only the CMB and a DM component, the ROI choice was based on the Planck collaboration's study of the Haze [18], and consists of the rectangular area in Galactic coordinates $-35° \leq b \leq -10°$, $|l| \leq 35°$. This choice is well-motivated for a DM search, since that ROI is sufficiently far from the bright

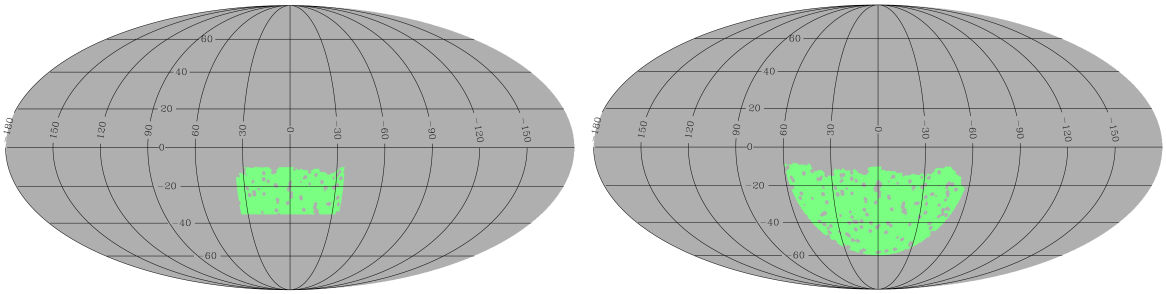


Figure 14. *Left:* Our ROI with masked compact sources chosen to produce the conservative DM constraints with CMB subtraction only. It was constructed as the rectangle $-35^\circ \leq b \leq -10^\circ$, $|l| \leq 35^\circ$. *Right:* Our ROI with masked compact sources chosen for the regional fitting in the component separation procedure (see more in §4.6). Before point source masking it was constructed as a half-disc of 60° radius around GC, with very bright areas around the Galactic plane also masked. This ROI is also used in the presentation of example DM emission spectra in §4.4.

foreground emission in the Galactic plane but still in a region where the DM emission is relatively strong. We also masked bright compact sources inside the ROI using the product of the WMAP and Planck source masks for each channel, smoothed to 1° [86, 87]. Our final ROI for the conservative analysis is shown in fig. 14 (left panel).

For the component separation analysis in which we determined the contribution to the data from DM by modeling Galactic foregrounds and the Bubbles, we adopted a slightly different ROI. The ROI for this analysis is shown in right panel of fig. 14. It is a 60° semi-disc centered on the GC, with bright compact sources masked as in the first ROI, and also strong Galactic plane emission masked [86]. The choice of 60° addresses additional challenges for this approach, namely avoiding strong foreground degeneracies due to using too small an area while still selecting an area in which each foreground has a spatially-uniform frequency dependence and including the relevant Haze emission.

4.4 DM microwave spectra

Considering the ROIs we have defined, it is useful to examine the frequency dependence of the DM component from our simulated maps. For this purpose, we considered the larger ROI used later in the component fitting analysis in §4.6, shown in the right panel of fig. 14. Inside this ROI we averaged the DM intensity and plotted it versus frequency of emission in fig. 15. In general a simple power law is not sufficient to describe the spectra, as a mild spectral index evolution is observed within the frequency range considered. Intensities for the $\tau^+\tau^-$ channel are typically five to ten times larger than those for $b\bar{b}$, for the same WIMP mass, density profile and MF/propagation model.

In addition to the amplitude of the emission, the slope of the spectrum strongly depends on the DM particle mass. Approximating the spectra by a simple power law $I \sim \nu^\beta$, we found that for the $b\bar{b}$ case β grows with mass over the range $-3.3 \lesssim \beta \lesssim -1.6$. For $\tau^+\tau^-$ the variation is even slightly larger: $-3.2 \lesssim \beta \lesssim -1.2$. Essentially no dependence of the intensity or slope on the inner profile slope γ is observed, as expected from inspecting the relevant maps in fig. 13.

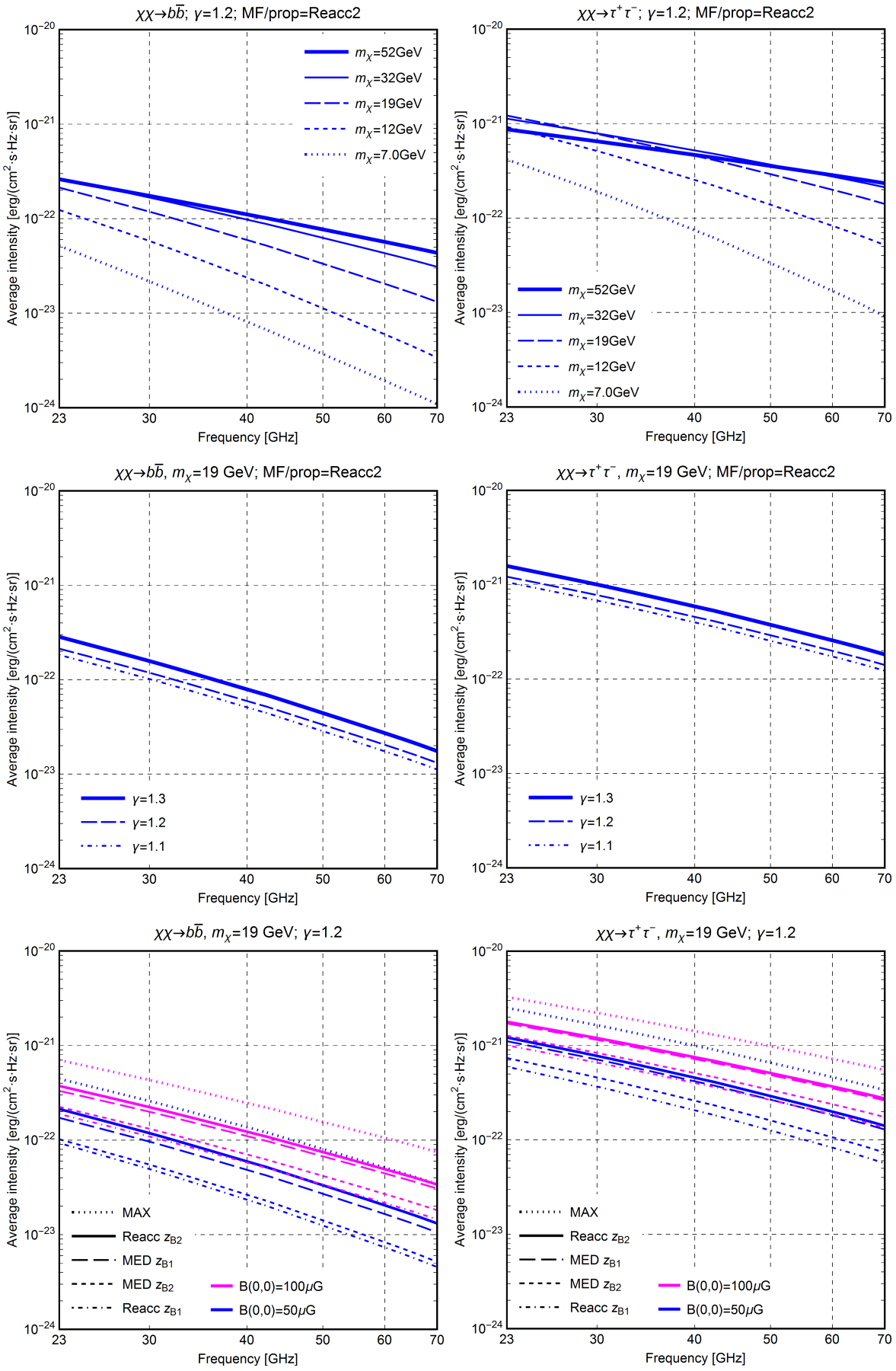

χχ→bb̄; γ=1.2; MF/prop=Reacc2
χχ→τ⁺τ⁻; γ=1.2; MF/prop=Reacc2
χχ→bb̄, m_χ=19 GeV; MF/prop=Reacc2
χχ→τ⁺τ⁻, m_χ=19 GeV; MF/prop=Reacc2
χχ→bb̄, m_χ=19 GeV; γ=1.2
χχ→τ⁺τ⁻, m_χ=19 GeV; γ=1.2
Average intensity [erg/(cm²·s·Hz·sr)]
Frequency [GHz]
m_χ=52GeV
m_χ=32GeV
m_χ=19GeV
m_χ=12GeV
m_χ=7.0GeV
γ=1.3
γ=1.2
γ=1.1
MAX
Reacc z_B2
MED z_B1
MED z_B2
Reacc z_B1
B(0,0)=100μG
B(0,0)=50μG

Figure 15. *(preceding page)* Dependence of the DM emission spectrum on various model parameters. The ROI over which the DM intensity was averaged is shown in the right panel of fig. 14. Left column in this Figure represents the $b\bar{b}$ annihilation channel, while the right column shows results for the $\tau^+\tau^-$ channel. The annihilation cross section $\langle\sigma v\rangle = 3 \cdot 10^{-26}$ cm^3/s in all panels. Points were calculated from the DM maps at each frequency and then interpolated. The first row shows the spectral dependence on the DM mass, the second row shows the dependence on the inner profile slope γ, and the third row shows the dependence on the MF and propagation model.

As for the MF and propagation model, higher MFs produce larger intensities. The spectral slope seems to be largely independent of the MF and propagation models, however the overall amplitude strongly depends on the propagation model, varying by up to one order of magnitude. As expected, configurations with higher vertical MF extent z_B produce larger emission. For the same $B(0,0)$ and z_B, models with reacceleration generate slightly larger intensities than those without reacceleration. Such inferences about DM spectra have interesting implications for a comparison with real sky data. In particular, the Planck team claimed in [18] that the average spectral index of the synchrotron emission from astrophysical Galactic CRs is ≈ -1.1. The anomalous microwave excess around the GC, on the other hand, has a very different index ≈ -0.6. This is one of the main motivations for the suggestion that the Haze comes from a distinct population of electrons, such as from DM annihilation. Comparing the DM indexes estimated above with the ones derived for the Haze and the synchrotron component of the WMAP and Planck data, we notice that while DM is able to generate an arbitrary amplitude for the intensity, the spectrum of the emission has a limited range of slopes (at least for DM masses of interest). Therefore, the DM component is only marginally able to mimic/contribute to regular synchrotron (for the largest WIMP masses considered), and at the same time its spectrum is too steep to fit the excess, which has $\beta \approx -0.6$. These simple considerations suggest that, even in the case that a DM signal is present, it is likely that another mechanism contributes the majority of the Haze signal. For this reason, we also considered a possible counterpart of the Fermi Bubbles in the component separation procedure presented in §4.6.

4.5 Conservative constraints on DM annihilation

In this subsection we present conservative DM constraints derived from the Planck sky maps when the emission is assumed to be composed only of the CMB emission and DM emission, with no other foregrounds considered. In performing this estimate, we considered only the CMB emission because it is very bright and well characterized, and thus very simple to model extremely accurately.

For this analysis, we chose to use Planck Low Frequency Instrument (LFI) channels only (28, 44 and 70 GHz) as the Planck noise level is far superior to that of WMAP while the frequency range covered is comparable.

The Planck 2013 maps that have been released have the monopole and dipole largely subtracted, but, after careful component separation, an estimate of the residual monopole and dipole in the maps was made and published by the Planck team. These residual values with their errors are shown in Table 2 of [88]. We performed subtraction of the quoted residual monopole and dipole values from all three Planck LFI channels. We then computed the average intensities in each frequency map. The impact of subtracting residual monopole and dipole on the average intensity is shown in Table 4. The first line of this table shows the average intensity inside our ROI from fig. 14 (left panel) without any map processing. The

Table 4. Average intensities in our ROI from the Planck LFI temperature maps and their associated uncertainties (all in units of erg/(cm^2 s sr Hz), converted from CMB temperature units using: $\Delta I(\nu) = \frac{\partial B_{bb}(\nu,T)}{\partial T}\Big|_{T=2.726K} \Delta T(\nu)$). These were used to derive the intensity upper limits from the data for the subsequent derivation of DM constraints. See §4.5 for more details.

Map	28 GHz	44 GHz	70 GHz
Nominal Planck LFI maps	$3.69 \cdot 10^{-20}$	$2.38 \cdot 10^{-20}$	$3.79 \cdot 10^{-20}$
Maps after residual monopole subtraction	$3.50 \cdot 10^{-20}$	$2.27 \cdot 10^{-20}$	$1.79 \cdot 10^{-20}$
Maps after residual mono/dipole subtraction	$3.64 \cdot 10^{-20}$	$2.27 \cdot 10^{-20}$	$1.79 \cdot 10^{-20}$
Standard deviation of residual monopole	$4.72 \cdot 10^{-22}$	$5.66 \cdot 10^{-22}$	$1.33 \cdot 10^{-21}$
Standard deviation of residual dipole	$6.17 \cdot 10^{-22}$	0	0
Standard deviation of CMB fluctuations	$6.00 \cdot 10^{-21}$	$1.44 \cdot 10^{-20}$	$3.37 \cdot 10^{-20}$
Total standard deviation	$6.05 \cdot 10^{-21}$	$1.44 \cdot 10^{-20}$	$3.38 \cdot 10^{-20}$

second and third lines of Table 4 show the ROI intensities after subtraction of the residual monopole and monopole+dipole respectively. These have a significant impact on the 70 GHz channel in particular, where the intensity decreases by about a factor of two.

Once the monopole and dipole were subtracted and the average intensities in the ROI were computed, we proceeded to estimate uncertainties due to Planck noise, errors in the residual monopole and dipole, and CMB fluctuations. The instrumental noise level was estimated using the maps provided as a part of the Planck data products, and it was found to be largely subdominant compared to the other uncertainties. The monopole and dipole uncertainties were taken from Table 2 of [88] and assumed to be the standard deviations of respective Gaussian distributions. Numerical values for the monopole and dipole "noise" (denoted $\sigma_\nu^{\rm mon}$, $\sigma_\nu^{\rm dip}$) are shown in the fourth and fifth line respectively of Table 4. The dipole-induced uncertainty slightly exceeds the monopole uncertainty for 28 GHz and does not exist for other channels by construction as it was not modeled in the Planck team fitting.

The most important contribution to the intensity uncertainty comes from the CMB temperature fluctuations, which we took to be an unknown realization of the underlying cosmological model, in our specific ROI. Here we aimed at deriving the standard deviation $\sigma_\nu^{\rm CMB}$ of the mean ROI intensity $I = 1/n \sum_{i=1}^{n} T_i$, where $n = 6427$ denotes the number of map pixels in our ROI at our resolution and T_i is the intensity (or, equivalently, thermodynamic temperature) value in each pixel i.

The variance of I was calculated as follows:

$$\langle (I - \langle I \rangle)^2 \rangle = \langle I^2 \rangle = \langle \frac{1}{n^2} \sum_{i=1}^{n} T_i \sum_{j=1}^{n} T_j \rangle = \frac{1}{n^2} \sum_{i,j=1}^{n} \langle T_i T_j \rangle = \frac{1}{n^2} \sum_{i,j=1}^{n} \sum_{l} \frac{2l+1}{4\pi} C_l B_l^2 W_l^2 P_l(\cos\theta_{ij}). \tag{4.4}$$

Here the brackets $\langle\rangle$ mean averaging effectively over all possible realizations of the underlying cosmological model in an area that matches our ROI. When considering CMB fluctuations, $\langle I \rangle = 0$. The well-known expression for $\langle T_i T_j \rangle$ in terms of the CMB power spectrum C_l can be found in, e.g., eq. (18.29) in [89].

The beam B_l and pixel window function W_l in eq. 4.4 account for the smoothing procedure we applied to the data (we smoothed the Planck maps down to 1° convolving them with a 2D Gaussian function) and map pixel size ($\sim 0.5°$ in our case). $P_l(x)$ denotes the Legendre polynomials of order l and θ_{ij} the angular distance between the i'th and j'th pixels.

The standard deviation given by eq. 4.4 was computed using the HEALPix tools [85] and summing from $l = 2$ to $l_{max} = 60$; it was found to be 25.4 $\mu K_{\rm CMB}$ (identical for all frequencies). As input C_l's we used the power spectrum theoretically derived from the conventional best-fit ΛCDM model [90]. Specifically, we took numerical values of C_l's from the "Ancillary Data" section of [91] and the Planck+WP+highL+lensing parameter set there. The σ_ν^{CMB} values are shown in the sixth line of Table 4.

The three sources of noise described above are uncorrelated, so the total noise σ_ν is the sum in quadrature: $\sigma_\nu = \sqrt{(\sigma_\nu^{\rm mon})^2 + (\sigma_\nu^{\rm dip})^2 + (\sigma_\nu^{\rm CMB})^2}$. Numerical values of σ_ν are shown in the last line of Table 4, where we see that the CMB fluctuations contribution completely dominates over the others. Regarding the signal to noise ratio, the CMB noise is at the level $\approx 20\%$ with respect to the mean intensity at 28 GHz, but it increases fast with frequency, and at 70 GHz it already exceeds the mean signal. We computed the 95% CL limits by setting $I_\nu + 1.64\sigma_\nu$ as the upper limit at each frequency. This chosen cut corresponds to the 95% CL upper limit for a one-dimensional Gaussian distribution. Our choice is justified by the fact that the main source of the noise is CMB fluctuations, which are correlated between the frequency channels.

After setting $I_\nu + 1.64\sigma_\nu$ as the intensity upper limit, we required that the DM emission intensity in our ROI should not exceed these limits in *any* of the frequency channels. Since the DM intensity is proportional to $\langle\sigma v\rangle$, this requirement translates to an upper limit for the cross section, which we display in fig. 16. In general, our exclusion curves are quite far from the canonical thermal relic cross section $\langle\sigma v\rangle = 3 \cdot 10^{-26}$ cm^3/s (red dashed line) for all considered configurations. The best constraint among all is $\langle\sigma v\rangle \lesssim 2 \cdot 10^{-25}$ cm^3/s. No clear dependence of the exclusions on the profile slope γ is apparent. However, the dependence on the annihilation channel is quite strong: constraints for $\tau^+\tau^-$ are $\gtrsim 3$ times stronger than for $b\bar{b}$ for the same MF/propagation models. Also the $\tau^+\tau^-$ channel forms a slightly narrower band of exclusion lines. Increases in both z_B and $B(0,0)$ values strengthen the constraints. All these parameter dependencies are indeed in agreement with those for DM intensities, which were described in §4.4. The most pessimistic constraints are typically realized by the Reacc z_{B1} $B(0,0) = 50$ μG configuration, while the most optimistic ones by MAX $B(0,0) = 100$ μG. The more moderate configuration is Reacc z_{B2} $B(0,0) = 50$ μG, which we set as our representative constraint (shown by the blue solid line in Figs. 15, 16 and 21). For this we chose the $B(0,0) = 50$ μG case rather than $B(0,0) = 100$ μG due to the MF considerations explained in §4.2.3. Note also that the fiducial configuration corresponds to the Reacc diffusion model, which is expected to be the newest and most accurate among all three considered.

Along with our exclusion lines, fig. 16 shows the parameter regions at 95% CL (unless stated otherwise), which are required to fit the GC gamma-ray excess by WIMP annihilation; see figure caption for details. In general, there is a good agreement between the parameter regions derived in independent studies for the same channel and profile slope pairs. While all these works only include DM prompt gamma rays in the fit, [92] showed that including secondary gamma rays from ICS and bremsstrahlung from DM leptons marginally changes the result (their signal region, derived for the configuration $\chi\chi \to b\bar{b}; \gamma = 1.2$, is almost completely inside the brown region shown). Therefore, overall our constraints on the cross section show no tension with the signal regions derived from gamma-ray data analyses of the excess.

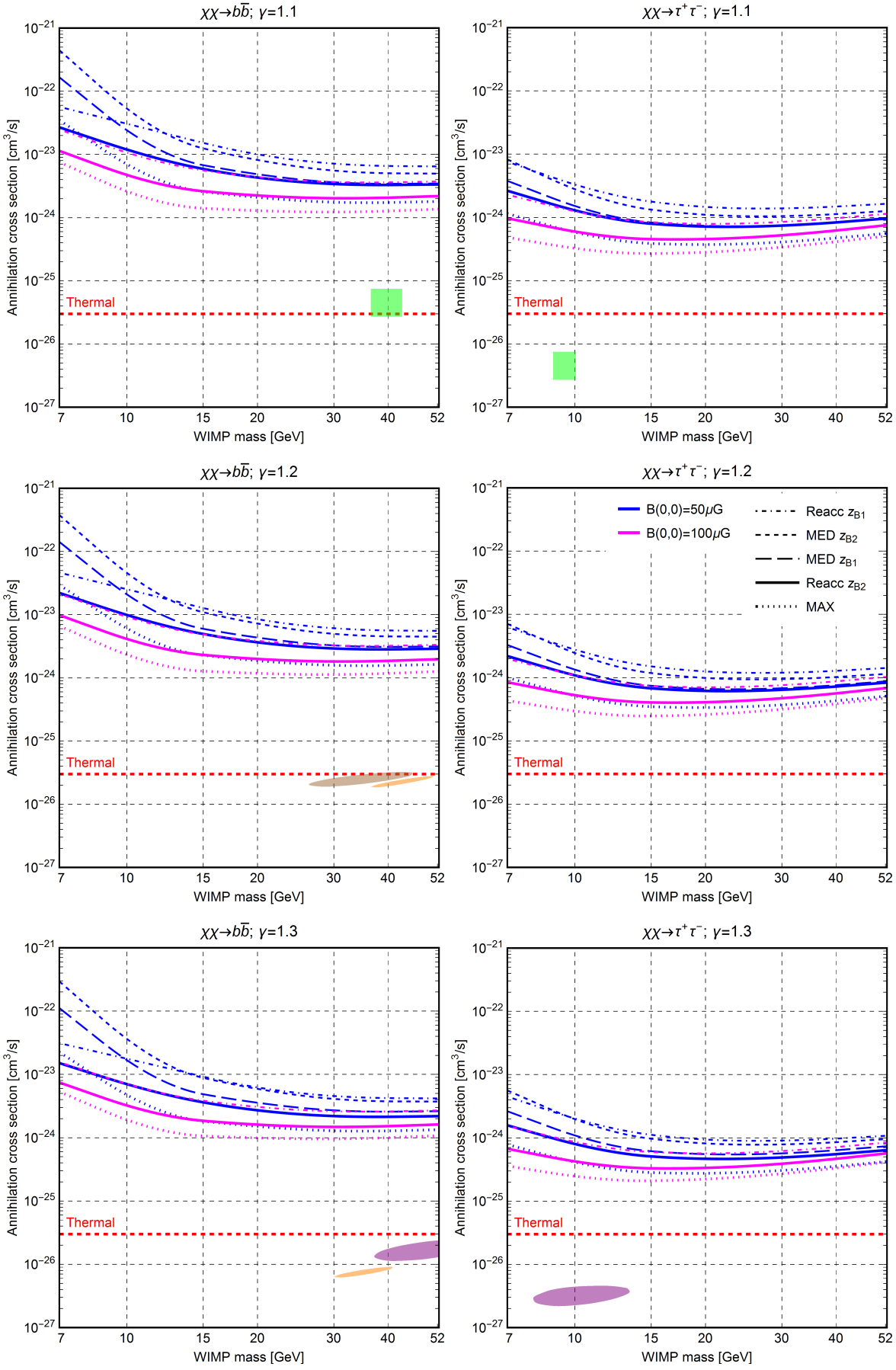

χχ→bb̄; γ=1.1
χχ→τ⁺τ⁻; γ=1.1
χχ→bb̄; γ=1.2
χχ→τ⁺τ⁻; γ=1.2
χχ→bb̄; γ=1.3
χχ→τ⁺τ⁻; γ=1.3
Annihilation cross section [cm³/s]
WIMP mass [GeV]
Thermal
B(0,0)=50μG
B(0,0)=100μG
Reacc z_B1
MED z_B2
MED z_B1
Reacc z_B2
MAX

Figure 16. *(preceding page)* DM constraints derived at 95% CL resulting from the Planck temperature maps with subtraction of the CMB emission only for various DM/MF/propagation models ($\langle\sigma v\rangle$ above the lines are excluded). The red dashed horizontal line indicates the thermal relic cross section $\langle\sigma v\rangle = 3\cdot 10^{-26}$ cm^3/s. Besides exclusion curves we also show here WIMP parameter regions (at 95% CL unless stated otherwise) needed to fit the GC gamma-ray excess. The brown region for the case $\chi\chi \to b\bar{b}; \gamma = 1.2$ was derived in the work [15], the orange ones for $\chi\chi \to b\bar{b}$ in [50], the green ones for $\gamma = 1.1$ in [16] (68% CL regions), and the purple ones for $\gamma = 1.3$ in [76]. For the optimistic high MF models with $B(0,0) = 100$ μG, only three exclusion curves out of five computed in total are shown. The two curves not shown lie inside the other curves. More details are in §4.5.

An alternative way to account for the CMB fluctuations in the emission map is to subtract at every frequency the reconstructed CMB fluctuation map as provided by the Planck team (see "all-sky-maps" folder at [91]). This map is the result of the emission component separation procedure performed by the team and reflects the most up-to-date knowledge of the actual realization of CMB fluctuation field. We attempted this strategy and found a relatively minor improvement in our derived constraints of $\approx 16\%$. Although more stringent, these constraints depend on the specific component separation procedure adopted to derive the map, and therefore we opted instead to show the results from the procedure described earlier in this section.

The DM limits described in this section are relatively weak, however we expect that foregrounds other than the CMB play a potentially important role in this region of the sky: dust, free-free from ionized hydrogen, synchrotron from regular CRs and the Bubbles. In the following subsection we perform a full component separation analysis to more accurately characterize a possible DM contribution.

4.6 DM constraints from a component separation approach

4.6.1 The WMAP-Planck Haze: history

A mysterious microwave excess above the canonical astrophysical foregrounds was first reported with the first WMAP data release [17], and was later interpreted as a possible signal of DM annihilation [62]. Further WMAP-based studies confirmed the existence of the Haze and characterized it in detail [93–95]. The most recent and comprehensive Haze study was performed after the Planck data releases in [18]. This work combined WMAP-9 and Planck data to separate out the Haze emission at 6 frequencies via frequency-by-frequency template fitting. The results showed the Haze properties to be highly consistent between the two data sets. This can be seen in fig. 8 in [18], where the derived Haze spectrum is presented. As we already mentioned, those authors claimed that the Haze spectrum $I \sim \nu^{-0.56}$ is indeed significantly harder than the usual synchrotron $I \sim \nu^{-1.1}$, which suggests the origin to be from a distinct population of electrons. The overall amplitude of the Haze emission was found to constitute $\approx 33\%$ of the total synchrotron and $\approx 23\%$ of the total Galactic emission at 23 GHz in the relevant region (fig. 14, left). Figs. 9-10 in [18] show the Haze morphology, which appears to be consistent with that of the Fermi Bubbles. This fact and other considerations (see, e.g., [68]), led the community to favor a scenario where the Haze is simply the microwave counterpart of the Fermi Bubbles.

The DM and the Bubbles interpretation of the Haze are in fact not mutually exclusive, and thus it is necessary to consider both in the analysis. In what follows, we will investigate whether the data are best fit with one of these components at a time, or both together. In

this part of the analysis, we will adopt the ROI shown in the right panel of fig. 14 for the component separation analysis.

4.6.2 Methodology

Our procedure relies on template fitting, which is described by the following equation:

$$d(\nu, b, l) = \sum_i a_i(\nu) t_i(\nu, b, l) + r(\nu, b, l), \tag{4.5}$$

where $d(\nu, b, l)$ is the data map at frequency ν in a pixel with coordinates (b, l); $t_i(\nu, b, l)$ is an assumed template intensity of the i-th component; $r(\nu, b, l)$ are residuals; $a_i(\nu)$ is a dimensionless amplitude of the i-th component, which is determined by the fitting. As for the sky maps $d(\nu, b, l)$, we used four WMAP channels: 23, 33, 41, 61 GHz (K, Ka, Q, and V bands from [96]) and three Planck LFI channels: 28, 44, 70 GHz from [91]. In contrast to [18], we also included in the fit the 70 GHz frequency channel, which provides further leverage for DM fitting and allows a better investigation of the frequency dependence of foregrounds.

In addition to DM, we included in the fit as foregrounds: dust, free-free, synchrotron and the Bubbles. A monopole and dipole component, as well as the CMB, are initially fit to the whole sky map, and removed from the data, so there is no monopole, dipole, or CMB fitting performed in the chosen ROI. As described in §4.2, the DM emission modeling predicts a specific emission at each frequency, therefore DM has only one free parameter, namely an overall amplitude a_{DM}, which sets the annihilation cross section value required by the fit. We ran the fitting procedure separately for each DM/MF/propagation model. We assumed spatially-constant power laws for all Galactic foregrounds. This means that the templates are rescaled by a single number, $a_i(\nu)$, in the ROI at every frequency independently. Therefore, unlike for the DM component, we did not impose a frequency dependence to foregrounds in the fit. We computed it, however, a posteriori.

The data at 23 GHz and the foreground templates are shown in fig. 17. Note that our units can be converted into thermodynamic units: 10^{-20} erg/(s cm^2 Hz sr) $\approx 62\ \mu K_{\rm CMB}$ at 23 GHz at temperatures of interest. For the CMB template we employed the Internal Linear Combination from Planck HFI channels (weights were derived from one single region, outside of the type-III Planck 2013 CO-based mask [97]). The reason for this choice rather than the Planck official map (SMICA) is that we wanted to avoid any of the LFI channels contributing to the CMB solution in order to avoid any circularity in the fit. The Galactic dust emission map is described in [98, 99]. Free-free emission naturally correlates with H_α, which provides an estimate of its morphology [100]. The synchrotron from conventional astrophysical CRs is assumed to have a similar morphology at radio and microwave frequencies (which is essentially equivalent to an assumption of constant spectral index across the sky). This allows us to use the canonical Haslam 408 MHz map as the synchrotron template [101]. Finally for the Bubbles we adopted the elliptical Gaussian template (with $\sigma_l = 15^\circ$ and $\sigma_b = 25^\circ$) proposed by [18] for the Haze emission, which was suggested to be suitable for the Fermi Bubbles counterpart. Indeed an exact Bubbles morphology is not known and may be quite complicated with both vertical and horizontal asymmetries (see, e.g., [67] for the morphology in radio). Our choice has the advantage of allowing comparison of our results with existing results in the literature (see [18] and references therein).

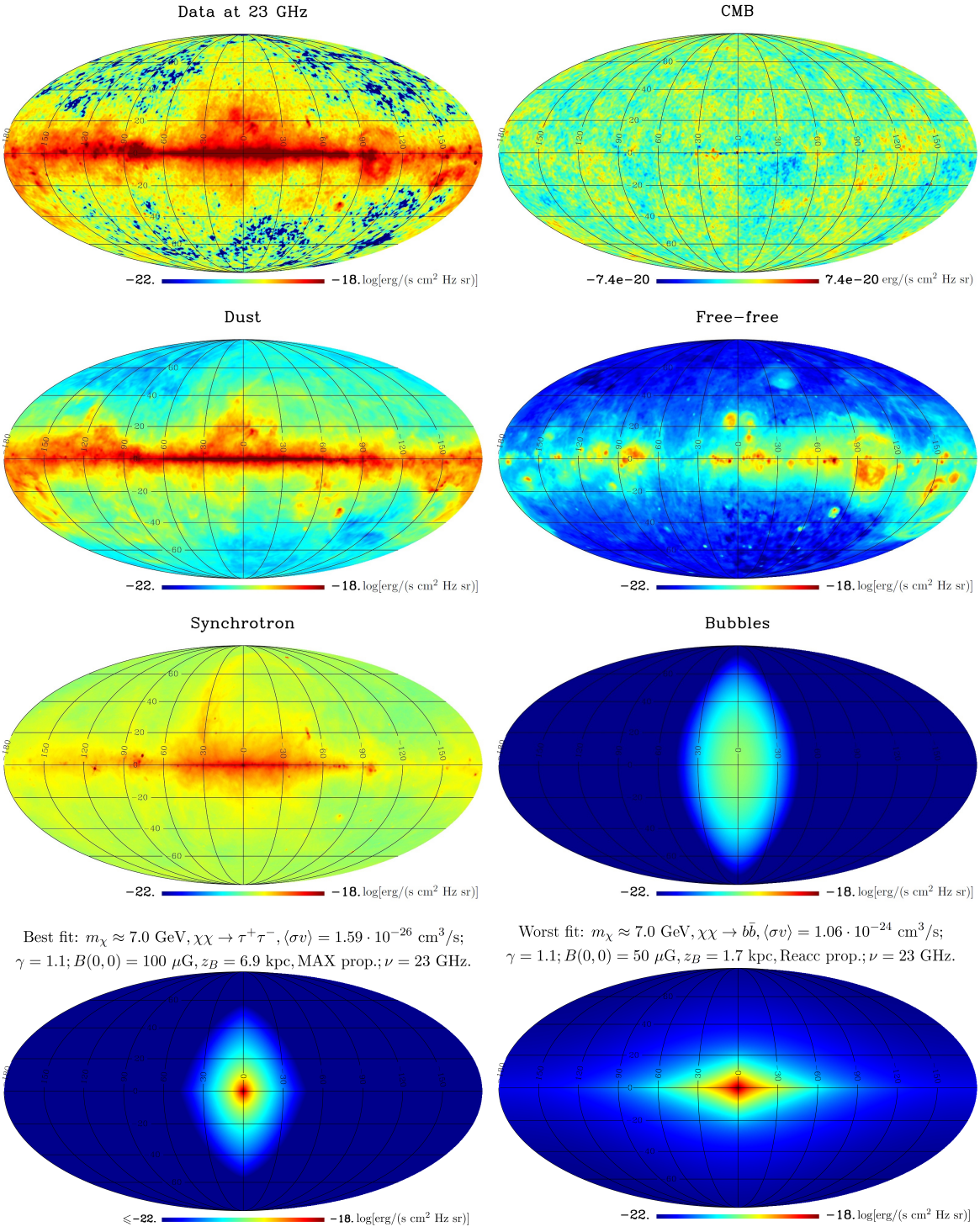


Figure 17. Data (total observed intensity at 23 GHz, top left panel) and templates (all other panels) used in the analysis. Morphology of all components except DM was assumed to be frequency-independent. Normalization of each template corresponds to that of the best-fit model at 23 GHz. The bottom panels show the best-fit and worst-fit DM sky maps among all the models considered. See more details in §4.6.2.

Additional foreground components could also be considered. For example, the authors of [18] also introduced a "disc" component (an elliptical Gaussian with $\sigma_l = 20°$ and $\sigma_b = 5°$) to account for a potential difference in the synchrotron morphology between 408 MHz and the typical CMB frequency range. This was intended to account for the energy dependence of the electron propagation length. Our attempt to add such component to the fitting provided unphysical results. Also, considering the relatively minor importance of the disc reported in [18], we decided not to include any further correction to the synchrotron emission in our final procedure.

The fitting procedure determines the amplitudes $a_i(\nu)$ by minimizing the residuals $r(\nu, b, l)$ in eq. 4.5. They are the solution of the following set of equations:

$$\frac{\partial \chi^2}{\partial a_i(\nu)} = 0. \tag{4.6}$$

If the sky model only included free amplitudes for each component at each frequency, the solution of the linear system eq. 4.6 would be:

$$\mathbf{a}(\nu) = \mathbf{T}^{-1}\, B_\nu \tag{4.7}$$

$$\Delta a(\nu)^2 = \mathrm{diag}\frac{1}{2}\, \mathbf{T}^{-1} \tag{4.8}$$

where $B_\nu = (d(\nu, b, l)/\sigma(\nu, b, l)) \cdot (t(b, l)/\sigma(\nu, b, l))$ and $T_{ij} = t_i(b, l)/\sigma(\nu, b, l) \cdot t_j(b, l)/\sigma(\nu, b, l)$. However, our DM modeling couples all frequencies so that we had to resort to a Markov-Chain procedure to find the values and errors for $a_i(\nu)$.

Modeling foregrounds by means of templates and assuming spatially-constant spectral indexes across the whole sky is a very crude approximation. Moreover, we expect the DM signal to be prominent near the GC but not everywhere. On the other hand, a residual monopole and dipole might be present in the WMAP and Planck maps, as well as in the templates, as a result of the map-making and calibration procedures, and on small areas of the sky these components are not properly fit.

For these reasons, we decided to perform the fit in two steps. First, we fit the data masking the Galactic plane and bright sources with a mask very similar to the one used by [18], and obtained the template amplitudes at all frequencies; we did not include the DM in this nearly full-sky fit. We then subtracted the CMB and monopole and dipole from the data and solved for the dust, free-free, synchrotron, Bubbles, and DM amplitudes in the larger ROI (right panel of fig. 14).

In order to determine the best-fitting DM/foreground amplitudes in our chosen ROI, we ran our own Markov Chain Monte Carlo (MCMC) sampler to study the multi-parameter likelihood, which is assumed to be:

$$L \sim \exp(-0.5\chi^2),\ \ \chi^2 = \sum_{j=1}^{7} \sum_{i=1}^{n_2} \frac{r_{ij}^2}{\sigma_{ij}^2}, \tag{4.9}$$

where r_{ij} is the residual in pixel i at frequency channel j according to eq. 4.5, σ_{ij} are map noise, and the summation runs over all seven frequencies and all $n_2 = 15481$ pixels in our ROI. The reduced χ^2 (χ^2_{r}), is computed dividing the full χ^2 in eq. 4.9 by the number of degrees of freedom $N_{\mathrm{dof}} = 7 \cdot n_2 - 7 \cdot 4 - 1 = 108338$.

Eq. 4.9 implicitly assumes that the noise in each pixel is uncorrelated. In fact, noise correlations are expected because of the spacecraft scanning strategy and the adopted smoothing

Table 5. All parameter values for the best-fitting (BF, $\chi^2_{\rm r} = 6.87$) and worst-fitting (WF, $\chi^2_{\rm r} = 7.03$) DM/MF/propagation models.

Model	Cross section $\langle\sigma v\rangle$ [cm^3/s]	Mass m_χ [GeV]	Channel	Profile slope γ	Central MF $B(0,0)$ [μG]	Vertical MF scale z_B [kpc]	Diffusion model
BF	$1.6 \cdot 10^{-26}$	7.0	$\tau^+\tau^-$	1.1	100	6.9	MAX
WF	$1.1 \cdot 10^{-24}$	7.0	$b\bar{b}$	1.1	50	1.7	Reacc

procedure. Despite being sub-optimal, this procedure is commonly used (e.g., [18]) because of the difficulty to treat the full complexity of the noise at intermediate and high resolution. The noise maps were computed as the standard deviation of full resolution Gaussian noise realizations, smoothed to one degree and downgraded to $N_{side} = 128$ (to match the DM template). The RMS maps derived were further rescaled to match the noise power spectrum level of the full-resolution smoothed maps. We did not put any prior on the amplitudes, aside from imposing that they should be positive.

4.6.3 Fitting results

We ran the MCMC fit for our grid of DM/MF/propagation models and obtained $\chi^2_{\rm r}$ for each of them. Overall the quality of the fit is quite poor, with a $\chi^2_{\rm r}$ ranging between 6.87 and 7.03. This is simply a confirmation of the challenge that the component separation poses, the limitations we face with the current, non-Planck-based foreground templates, and the simplicity of template fitting. As a result, the $\chi^2_{\rm r}$ difference cannot be considered a powerful discriminant between models. Nonetheless, we can rank the models based on their likelihood and draw conclusions. The parameter values of the best-fitting (BF) and worst-fitting (WF) configurations are presented in Table 5.

While overall the poor χ^2_r values indicate a poor fit, it is sensible to ask whether the Bubbles and/or DM substantially improve the fit, with respect to the case in which only standard foregrounds are included. The respective fit qualities for various setups are shown in Table 6, with fits to each individual frequency and all frequencies together reported. If only standard foregrounds are considered, the fit is very poor. The lowest frequencies show the largest residuals, hence they likely contain the largest contribution from the Haze. Above 40 GHz, residuals are less pronounced and quite acceptable, with a possible overfitting in the 60 GHz channel where the foregrounds are typically at their minimum. When adding the Bubbles template, we see a very significant improvement at low frequencies. Similarly, when adding only DM, there is an improvement is the fit. The value of $|\Delta\chi^2_{\rm r}|$ is slightly less than in the Bubbles-only case, but quite comparable. When allowing for both Bubbles and DM in the fit, $\chi^2_{\rm r}$ reduces by almost a factor of two; however remaining quite large (since naively we expect it to take the value of one in the case of a good fit).

In fig. 18 we show maps of the relative residuals $r(\nu, b, l)/[d(\nu, b, l) - md(\nu, b, l)]$ with $r(\nu, b, l)$ and $d(\nu, b, l)$ defined as in eq. 4.5 and $md(\nu, b, l)$ the fitted mono/dipole. The top row of fig. 18 shows the frequency dependence of the residuals with neither DM nor the Bubbles in the fit. At 23 GHz the Haze is very clearly visible, reaching up to about 50% of the total sky intensity at peak points. Note the vertically-elongated Haze morphology (which would be absorbed by the Bubbles template) slightly bent to the right relative to zero longitude

Table 6. Effects of addition of the Bubbles and DM on the quality of the fit. The BF DM model shown is described in Table 5. The second column shows results with "standard" foregrounds only. The third column shows the χ^2_r improvement after adding the Bubbles. The fourth column shows improvements after adding the BF DM model only (no Bubbles). The last column shows improvements in the most general case of the Bubbles and DM considered together.

ν	χ^2_r with CMB, mono/dipole, f-f, synchr., dust	$\Delta\chi^2_r$ after addition of the Bubbles	$\Delta\chi^2_r$ after addition of the BF DM model	$\Delta\chi^2_r$ after addition of the Bubbles and BF DM model
23	37.4	-15.9	-15.4	-17.8
28	21.4	-6.35	-5.42	-6.86
33	10.0	-3.13	-2.67	-3.47
41	2.23	-0.475	-0.363	-0.533
44	3.31	-0.343	-0.219	-0.379
61	0.563	-0.023	-0.013	-0.023
70	2.29	-0.078	-0.007	-0.077
Gl.	11.0	-3.75	-3.44	-4.16

(which visually matches the shape derived in [67]). The Haze becomes less prominent with frequency, and is almost absent at 70 GHz. This spectral trend agrees well with that in Table 6, which shows that χ^2_r reaches considerably lower values at higher frequencies, even if only standard foregrounds are considered. Moreover, looking at the top left panel, it is clear that the Haze tends to have rather irregular morphology with sharp edges, which seems more consistent with the Bubbles origin rather than smooth DM emission (e.g., fig. 13). The bottom row shows the residuals at the lowest and most relevant frequency for the cases of DM only, DM+Bubbles WF and DM+Bubbles BF. We can see that the addition of DM alone reduces residuals somewhat. Adding both the Bubbles and DM further improves the results, almost entirely absorbing the Haze. There is, however, essentially no difference in the DM BF and WF cases, which is consistent with our previous finding that the χ^2_r differs very little for these two models.

The computation of the fitting coefficients $a_i(\nu)$ also allowed us to evaluate the average intensity of each component within the ROI and its frequency dependence, as well as the components' relative amplitudes. This is reported in fig. 19 for the BF DM model. Other models did not show significant qualitative differences. Hence, for simplicity, in what follows we focus on the BF case. At essentially all frequencies, there is a hierarchy in intensity (from higher to lower): synchrotron, dust, Bubbles, free-free and DM. The CMB fluctuations average is negative in our ROI, and its absolute value grows from a subdominant 2.9% at 23 GHz up to a significant 61% at 70 GHz, which reflects the black-body spectrum and the overall foreground frequency dependence. DM has the smallest contribution at all frequencies, ranging from 2.2% to 0.27%. The synchrotron dominates at almost all frequencies, decreasing from 61% to 51%. Also we see that we reproduced well the canonically-expected (e.g., [18]) synchrotron spectral index $I \sim \nu^{-1.1}$. The dust spectrum is not monotonic; it contributes 29% at 23 GHz. The free-free contributes 2.7% and matches quite well the expected slope $I \sim \nu^{-0.15}$ (e.g., [102]). The Bubbles contribution is relatively flat in frequency and equal to 5-9%. Our Bubbles spectrum agrees very well with $I \sim \nu^{-0.56}$ derived in [18].

We also compared our foreground component intensities with those derived in [18], for

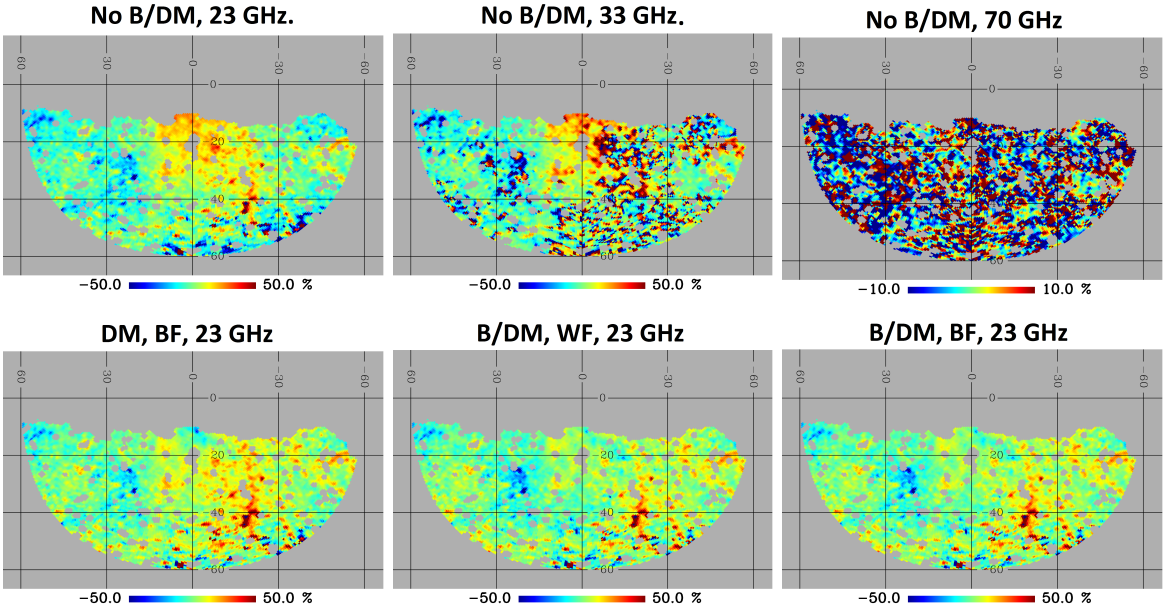


Figure 18. Residuals resulting from our component separation procedure in units of the total measured sky intensity. The top row shows the residuals at different frequencies without introducing either the Bubbles or DM template. We can see a clear excess in this case at low frequencies. The bottom row shows residuals at 23 GHz with DM only and Bubbles+DM. Adding DM improves residuals slightly, while adding both the Bubbles and DM improves the residuals much more. At the same time the difference between the BF and WF configurations is almost absent. More details are in §4.6.3.

Table 7. The breakdowns of the Galactic components (in % of the total non-CMB emission) at 23 GHz in the ROI (fig. 14, left) obtained in our work (BF case) and by the Planck team in [18]. More details are in §4.6.3.

Component	Planck team	Our work
Synchrotron	43	56
Dust	30	26
Free-free	4	3.1
Haze (DM+Bubbles)	23	12

the frequency where the Haze is most pronounced. For this exercise, we considered the ROI used in [18] and shown in fig. 14 (left panel). This comparison is shown in Table 7. While all standard astrophysical components have similar derived properties in both that work and ours, the Haze component in this work is about a factor of two smaller. This might be due to the mono/dipole removal strategy described above and/or to the modeling of the Haze which receives contributions from both Bubbles and DM in our work. Lastly, note that the sum of all components is well within the 3σ error bars on the data in all channels.

We also investigated the model dependence of the Bubbles and DM contributions. In Table 8 we reported the mean and variation ranges of the contributions of all DM/MF/propagation

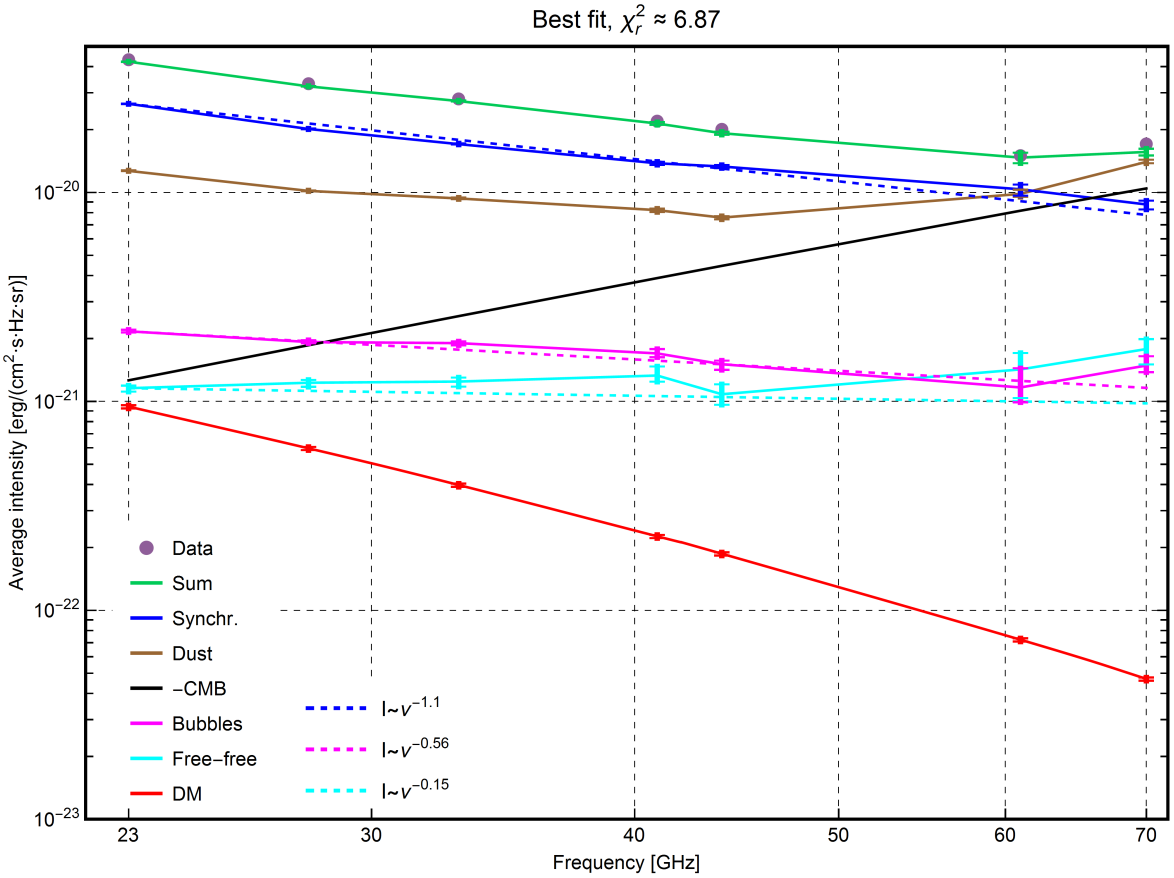


Figure 19. Spectra of all physical components (and their sum) for the BF DM configuration. Error bars correspond to statistical 68% CL. The data reported here have monopole and dipole subtracted, and the noise does not exceed the marker size used. Solid lines are results of this work, dashed lines are power-law spectra typically expected for the components considered. More details are in §4.6.3.

models at 23 and 70 GHz. The Haze contribution does not significantly fluctuate from model to model. At 23 GHz its amplitude is well above systematics, whereas at higher frequencies it is of the same order of magnitude as the residuals. The mean flux of the Haze represents 7.8% of the total sky emission compared to the best-fit amplitude of 7.2%. DM contributes a significant part of the Haze at 23 GHz: 21% on average (30% in the BF case). Because DM spectra usually fall off with frequency faster than the Bubbles spectrum, the DM contribution to the Haze decreases with frequency.

Note that in Table 8 we also quoted the range and mean of the residuals normalized to the data, which can give an indication of the systematic uncertainties (error bars in fig. 19 reflect statistical errors only). Systematic uncertainties may be due to inaccuracy in the templates, the foreground modeling error introduced by our component separation setup, as well as residual systematics in the WMAP and Planck data (e.g., calibration and map-making). Studying these in detail is beyond the scope of our work, however note that they are below 10% of the sky signal at all frequencies.

Statistical uncertainties in fig. 19 rarely exceed a few percent. The largest uncertainties are at high frequencies for the Bubbles and free-free component. Given the low map noise,

Table 8. Variation ranges and mean of the contributions for all our DM/MF/propagation models. The last row shows the residuals normalized to data. More details are in §4.6.3 and §4.6.4.

Parameter	23 GHz	70 GHz
Range/mean of Haze contribution to the data, %	[7.2-10]/7.8	[8.7-10]/9.2
Range/mean of DM contribution to the data, %	[0.43-6.3]/1.7	[0.0043-4.7]/0.59
Range/mean of DM contribution to the Haze, %	[5.5-62]/21	[0.047-45]/6.5
Range/mean of the residuals, %	[1.7-2.1]/2.0	[7.7-9.1]/8.6

our component separation strategy yields quite narrow N-dimensional likelihoods (N=29) for all parameters. Fig. 20 shows some examples of the marginalized likelihoods, for some components' amplitudes. The distributions are typically symmetric but not necessarily Gaussian, and the dispersion is below a few percent. Two of the bottom panels also show the 2D marginalized confidence regions for the most correlated pairs of components in the BF case. Thus, we see that the largest correlation is observed between the DM and Bubbles amplitudes at 23 GHz with the correlation coefficient $R = 0.70$ (defined in the standard way as the covariance divided by the square root of the product of the variances). This degeneracy between DM and the Bubbles is likely caused by similarity in the templates. The second largest correlation, with $R = 0.65$, is seen between the dust and synchrotron at 70 GHz.

4.6.4 DM implications

Table 8 shows that the derived DM contribution to the data, considering all DM/MF/propagation models, is small: at 23 GHz the mean contribution is 1.7% and the BF model 2.2%. This is at the level of the residuals at 23 GHz, implying no robust detection of DM. The signal-to-noise ratio does not improve at higher frequencies because the DM emission is less pronounced and the noise increases. Some models show a 6% contribution of DM to the data at 23GHz, which is well above the residuals. However, this is also not a highly significant detection, and the global fit is, in general, poor with $\chi^2_{\rm r} \simeq 7$ for all models.

We now examine correlations between the fit quality and DM parameters. For example, one may naively expect a preference for a specific DM spectral slope by the data. The DM spectral slope β (defined as $I \sim \nu^\beta$) varies over a wide range $-5.0 < \beta < -1.1$ for all models. The best fitting models have $\beta \approx -2.7$, which is much smaller than that of both the Bubbles and synchrotron (for which we found fitted values of -0.44 ± 0.05 and -1.17 ± 0.01 respectively). However, β is not linked unambiguously to any single DM/MF/propagation parameter. Looking at more physical parameters, one can see the following correlations. The fit quality mainly depends on the MF/propagation model, it depends significantly on WIMP mass, and is almost insensitive to the annihilation channel and profile slope γ. The smallest $\chi^2_{\rm r}$ typically corresponds to the strongest MF ($B(0,0) = 100$ μG) with medium to high vertical extent ($z_B = 2.7$, 6.9 kpc), strong diffusion models MAX and Reacc (see Table 3), and intermediate WIMP masses around 19 GeV. Instead, the worst fits are observed for low $z_B = 1.7$-2.0 kpc, MED and Reacc diffusion, and low WIMP masses around 7 GeV. These general trends should not be considered in a strict sense. Particularly, one may notice that the same WIMP mass 7 GeV serves for both BF and WF models (Table 5), which suggests only a weak correlation with mass. The correlation with MF/propagation configuration is stronger, and this has a quite straightforward interpretation. Comparing the BF and WF DM

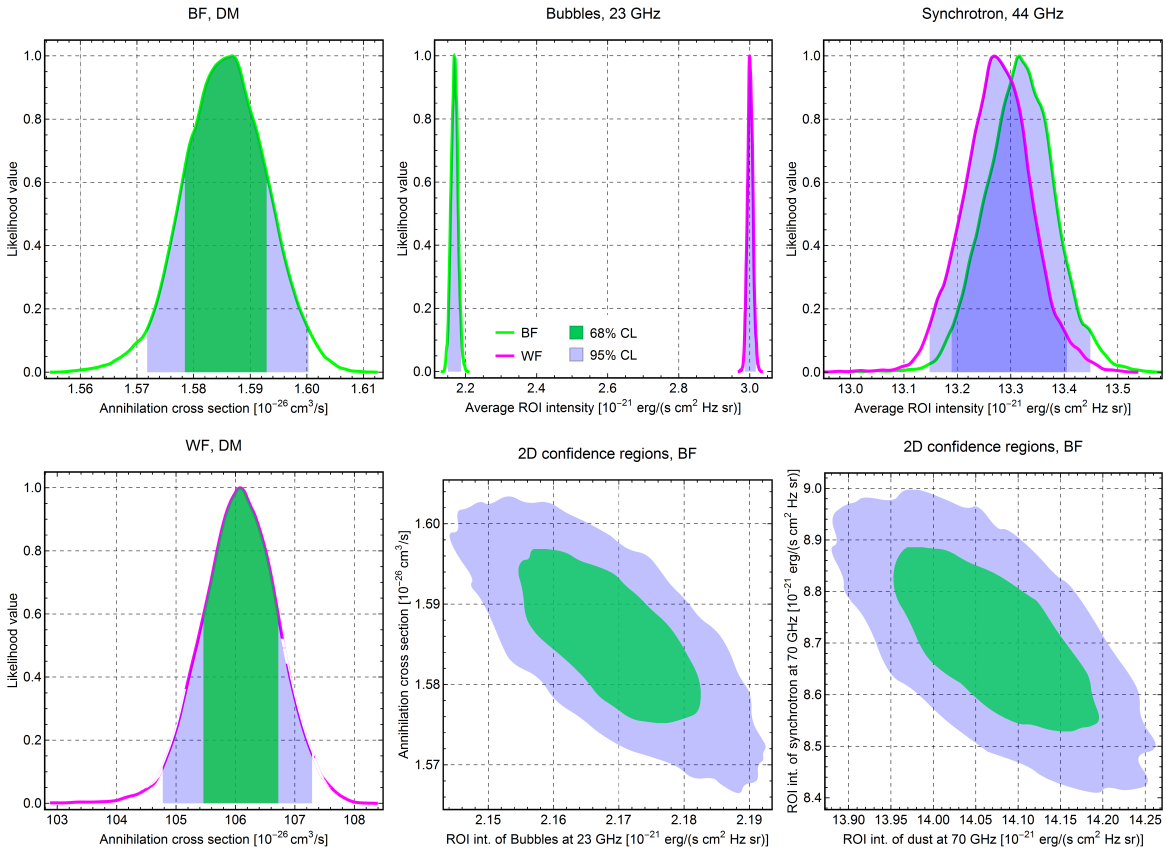


Figure 20. Examples of the marginalized 1D and 2D likelihoods for the components mentioned on each plot. The green regions show 68% confidence intervals while the blue regions 95%. 1D likelihoods are shown for both the BF and WF cases. 2D confidence regions are shown for the pairs of most correlated component intensities in the BF case. More details are in §4.6.3.

maps in fig. 17 two main differences are apparent: the BF map has a steeper brightness profile and a vertically elongated morphology instead of the horizontal morphology observed in the WF. The vertical elongation can be naturally explained by a strong and highly extended MF with the parameters mentioned above. The reason for such a preference by the fit could be related to the degeneracy between DM and the Bubbles: the BF DM template looks much more similar to the Bubbles template than the WF template.

Fig. 21 presents our main result: the best-fitting WIMP annihilation cross sections and masses for various DM/MF/propagation models. As for the more conservative constraints (fig. 16), $\langle\sigma v\rangle$ values vary over an order of magnitude for different MF/propagation models, with the $\tau^+\tau^-$ channel showing less of a spread than $b\bar{b}$ does. Indeed, the MF/propagation model uncertainties significantly exceed the statistical ones. The BF $\langle\sigma v\rangle$ values reside close to the canonical cross section $3\cdot10^{-26}$ cm^3/s, especially for $\tau^+\tau^-$ channel. It is interesting to compare the constraints in the $\langle\sigma v\rangle - m_\chi$ plane with those required to fit the GC gamma-ray excess, also reported in fig. 21. We see essentially no intersections between the allowed regions determined by gamma-ray data analysis and our BF values. A small intersection is visible only in the case $\chi\chi \to b\bar{b}, \gamma = 1.1$, but even there very optimistic MF/propagation models with $B(0,0) = 100$ μG would be required.

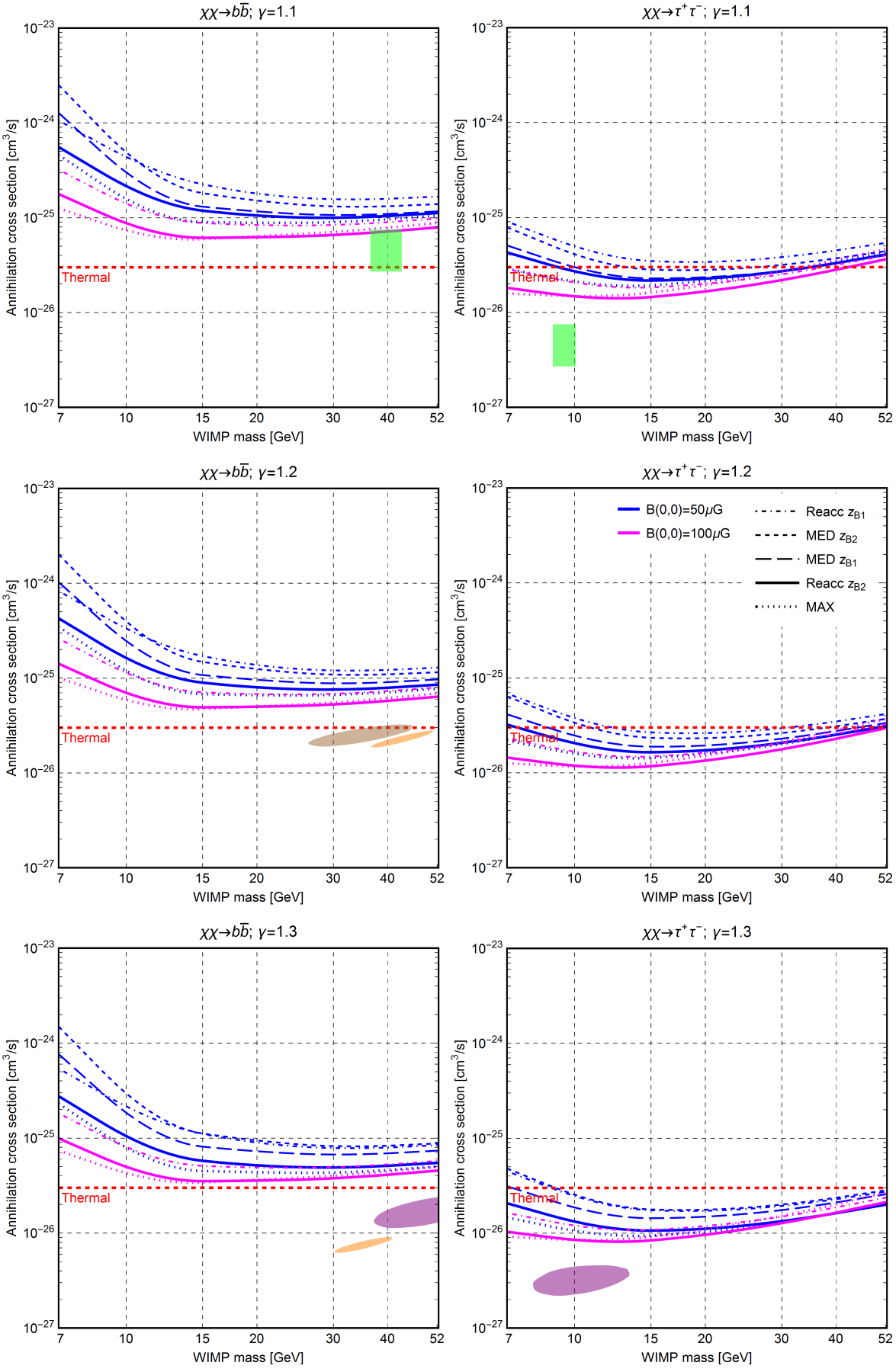

χχ→bb̄; γ=1.1
χχ→τ⁺τ⁻; γ=1.1
χχ→bb̄; γ=1.2
χχ→τ⁺τ⁻; γ=1.2
χχ→bb̄; γ=1.3
χχ→τ⁺τ⁻; γ=1.3
Annihilation cross section [cm³/s]
WIMP mass [GeV]
Thermal
B(0,0)=50μG
B(0,0)=100μG
Reacc z_B1
MED z_B2
MED z_B1
Reacc z_B2
MAX

Figure 21. *(preceding page)* DM constraints derived at 95% CL resulting from our component separation procedure for various DM/MF/propagation models. Limiting cross section values are indistinguishable from the BF ones at this line resolution. The red dashed horizontal line indicates the thermal relic cross section $\langle\sigma v\rangle = 3{\cdot}10^{-26}$ cm^3/s. In addition to the best-fit curves we also present here DM parameter regions (same as in fig. 16) needed to fit the GC gamma-ray excess. We see again that our constraints mainly do not contradict them. See more details in §4.6.4.

Thus, we can conclude that our fit of the microwave data with DM does not prefer similar DM parameters as the gamma-ray data fits [15, 16, 50, 76], but rather favors higher cross section values (by a factor $\sim (2-7)$) for similar masses and annihilation channels.

Finally, comparing DM best-fit values resulting from the component separation and the more conservative constraints derived in §4.5 (fig. 21 vs. fig. 16), it is apparent that foreground cleaning may improve the sensitivity of a DM search by a factor of 10-100. However, as was already mentioned in §4.5, any component separation procedure yields results whose validity depends on the foreground and signal modeling.

4.7 Summary and discussion

In this work, we addressed the DM implications of the WMAP-Planck Haze in the context of models that could explain the GC gamma-ray excess. We investigated whether the microwave observations are compatible with a DM contribution to the Haze emission, derived constraints on DM particle parameters, and compared them to those needed to fit the GC gamma-ray excess.

We modeled the synchrotron emission in the microwave portion of the electromagnetic spectrum due to DM annihilation, making various assumptions about the DM density distribution, the DM particle model, as well as the MF and CR propagation models. DM emission intensity sky maps for various DM/MF/propagation models were created and compared with the data at seven WMAP-Planck frequencies. To test the consistency of the DM models with the data, we adopted two approaches. First we adopted a conservative approach which only considered CMB and DM as contributing to the total sky intensity, while second we attempted to separate all the emission components including a potential DM signal using template fitting. The first approach yields relatively weak, but very robust DM constraints (see fig. 16). The second one probes much lower cross sections, with the best-fit cross-sections reaching the thermal relic expectation $\langle\sigma v\rangle = 3 \cdot 10^{-26}$ cm^3/s (see fig. 21), however this approach is more dependent on the details of the modeling and the results are less straightforward to interpret due to degeneracies between DM and other model components.

We summarize our results as follows:

- The (weak) upper limits obtained with the conservative approach are compatible with both the thermal cross section and the signal regions of DM models that fit the gamma-ray excess that have been determined in other works.

- In the component separation analysis, the overall quality of our fits is poor, indicating that we lack sufficient understanding of foregrounds, or that template fitting is a too simplistic procedure for explaining the observed signal in the sky area under consideration.

- Adding additional components that produce emission at tens of degrees around the GC to the standard astrophysical foregrounds and CMB considerably improves the fit.

Thus we confirmed the clear presence of the Haze: a microwave excess not explained by the CMB, (spinning) dust, free-free, and synchrotron emission, which contributes (7.2-10)% of the intensity at 23 GHz and (8.7-10)% at 70 GHz in our selected sky region near the GC. We also derived the Haze spectrum (here represented by the sum of the DM and Bubbles components), obtaining $I \sim \nu^{-0.84\pm0.04}$. This is somewhat different from the slope of -0.56 reported in [18]. However, this is not a completely equivalent comparison due to the presence of the DM template in our Haze fit. Our derived Haze spectrum significantly differs from that of the usual synchrotron ($I \sim \nu^{-1.17\pm0.01}$), which suggests that the Haze originates from a population of electrons distinct from typical Galactic CR electrons.

- We considered two possible origins of the Haze in constructing our templates: i) DM annihilation and ii) a counterpart of the Fermi Bubbles. We showed that the data do not have a strong preference for either of these two components when considered separately; they provide comparable fit qualities with a mild preference towards the Bubbles. However, inclusion of both templates together provides a better fit than adding either template individually. Thus, both emission mechanisms can be contributing to the Haze. In this scenario, DM constitutes (5.5-62)% (on average 21%) of the Haze emission and (0.43-6.3)% (on average 1.7%) of the total emission at 23 GHz. The DM spectrum, as derived from our modeling of the DM emission, is generally steeper than the Bubbles fit-inferred spectrum. The amplitude of the latter exceeds that of the DM, especially at high frequencies.

- Given the overall poor quality of the fits, it is not possible to confidently attribute any of the emission to a DM model, nor to single out a particular DM model as the one preferred by the data. In general the data show a mild preference for a strong MF that is extended above the plane. This kind of MF generates DM emission with a vertically elongated morphology that is aligned with the Bubbles observed in gamma rays.

- The best-fit cross-sections as determined by the component separation procedure are a factor ≈(2-7) higher than those favored to explain the GC gamma-ray excess, and are in tension with other constraints from indirect DM searches (e.g., [103]).

Looking forward, although multi-frequency studies clearly offer complementary information to that from indirect searches in gamma rays, to make these searches competitive it will be necessary to better understand the various non-DM contributions to the total microwave emission. This could be pursued by considering other component separation strategies and an optimization of the ROI.

5 Conclusions and future plans

Summarizing our big work, we can conclude that the study of the big Local Group galaxies in the radio-microwave band yielded interesting and valuable results for the field. Thus, the conducted study of M31 provided a quite strong evidence that the canonical WIMP is not lighter than 50-100 GeV (assuming the most probable thermal value for the annihilation cross section). Our extensive work on MW showed in fact quite good agreement with the work on M31: we did not find any strong evidences for the annihilating WIMPs with masses of few decades of GeV around the GC. These constraints also agree with the independent probe coming from gamma ray observations of MW satellites (see e.g. [5]). These

all together strongly suggest $m_\chi \gtrsim 100$ GeV as a hallmark for future searches. Thus, our work significantly contributed into the process of shrinking of a wide parameter space for the hypothetical WIMP, which was one of our main initial goals. WIMP at 100 GeV scale can be slightly more challenging to detect. However, such masses are absolutely possible and allowed by general particle physics considerations.

The conducted work indeed revealed various challenges. Even considering the same targets for the indirect detection, there are still many opportunities for further improvements of the sensitivity. Thus, for M31 one can develop the following aspects: gathering the newer radio observational data or even proposing the targeted observations, refinement of the propagation model with inclusion of the spatial diffusion, employment of newer data on the DM density distribution and others. Considering MW, the emission component separation can be done at more advanced level, using e.g. pixel-by-pixel fitting instead of a quite simplistic template fitting. And in both cases indeed one can vary the region of interest. This is especially relevant for MW, since sky areas far from the GC and Galactic plane have much weaker foregrounds and, hence, may potentially provide a better "signal-to-noise" ratio. Moreover, in recent years the new frequency window in the radio astronomy began to be actively explored - very low frequencies in the range $\sim (10 - 100)$ MHz. Recently launched instruments like LOFAR and LWA have a great sensitivity and resolution in this window. And they can provide very valuable data for the DM searches, since our targeted synchrotron signal grows up very fast with the frequency decrease as was showed in our work. Thus, studying M31 and MW by the mentioned instruments could be another productive direction too.

Acknowledgments

I would like to greatly thank: Elena Pierpaoli, my research advisor; Wendy Lane, the Principal Investigator of the VLSS radio survey, for valuable discussions regarding radio observational aspects; Loris Colombo for extensive help with the CMB emission modeling and Planck data interpretation; Andrew Strong for valuable consultations on GALPROP and Antony Lewis for assistance with GetDist. We also acknowledge the usage of the computers at the USC High Performance Computing Center and the LevelScheme package for Mathematica developed by Mark Caprio [104] (the latter greatly helped in preparation of high-quality plots). Some of the results in this work have been derived using the HEALPix package [85].

References

[1] F. Zwicky, *On the Masses of Nebulae and of Clusters of Nebulae*, *Astrophys. J.* **86** (Oct., 1937) 217.

[2] G. Bertone, *Particle dark matter - observations, models and searches*. Cambridge University Press, 2010.

[3] Particle Data Group: http://pdg.lbl.gov/.

[4] M. S. Madhavacheril, N. Sehgal, and T. R. Slatyer, *Current dark matter annihilation constraints from CMB and low-redshift data*, *Phys. Rev. D* **89** (May, 2014) 103508, [arXiv:1310.3815].

[5] Fermi-LAT Collaboration, *Searching for Dark Matter Annihilation from Milky Way Dwarf Spheroidal Galaxies with Six Years of Fermi-LAT Data*, *ArXiv e-prints* (Mar., 2015) [arXiv:1503.02641].

[6] E. Borriello, A. Cuoco, and G. Miele, *Radio constraints on dark matter annihilation in the galactic halo and its substructures*, *Phys. Rev. D* **79** (Jan., 2009) 023518.

[7] S. Colafrancesco, S. Profumo, and P. Ullio, *Multi-frequency analysis of neutralino dark matter annihilations in the Coma cluster*, *Astron. Astrophys.* **455** (Aug., 2006) 21–43.

[8] J. L. Feng, M. Kaplinghat, and H.-B. Yu, *Sommerfeld enhancements for thermal relic dark matter*, *Phys. Rev. D* **82** (Oct., 2010) 083525.

[9] J. Lavalle et al., *Indirect search for dark matter in M 31 with the CELESTE experiment*, *Astron. Astrophys.* **450** (Apr., 2006) 1–8.

[10] M. Fornasa, M. Taoso, and G. Bertone, *Gamma rays from dark matter minispikes in the Andromeda Galaxy M31*, *Phys. Rev. D* **76** (2007) 043517.

[11] A. E. Egorov and E. Pierpaoli, *Constraints on dark matter annihilation by radio observations of M31*, *Phys. Rev. D* **88** (July, 2013) 023504, [arXiv:1304.0517].

[12] M. Regis and P. Ullio, *Multiwavelength signals of dark matter annihilations at the Galactic center*, *Phys. Rev. D* **78** (Aug., 2008) 043505.

[13] L. Goodenough and D. Hooper, *Possible Evidence For Dark Matter Annihilation In The Inner Milky Way From The Fermi Gamma Ray Space Telescope*, arXiv:0910.2998.

[14] N. Fornengo, R. A. Lineros, M. Regis, and M. Taoso, *Galactic synchrotron emission from WIMPs at radio frequencies*, *JCAP* **1201** (2012) 005, [arXiv:1110.4337].

[15] C. Gordon and O. Macias, *Dark Matter and Pulsar Model Constraints from Galactic Center Fermi-LAT Gamma Ray Observations*, *Phys.Rev.* **D88** (2013) 083521, [arXiv:1306.5725].

[16] K. N. Abazajian, N. Canac, S. Horiuchi, and M. Kaplinghat, *Astrophysical and Dark Matter Interpretations of Extended Gamma-Ray Emission from the Galactic Center*, *Phys.Rev.* **D90** (2014) 023526, [arXiv:1402.4090].

[17] D. P. Finkbeiner, *Microwave ISM emission observed by WMAP*, *Astrophys.J.* **614** (2004) 186–193, [astro-ph/0311547].

[18] **Planck** Collaboration, P. Ade et al., *Planck Intermediate Results. IX. Detection of the Galactic haze with Planck*, *Astron.Astrophys.* **554** (2013) A139, [arXiv:1208.5483].

[19] D. Hooper and T. Linden, *Gamma Rays From The Galactic Center and the WMAP Haze*, *Phys.Rev.* **D83** (2011) 083517, [arXiv:1011.4520].

[20] A. E. Egorov, J. M. Gaskins, E. Pierpaoli, and D. Pietrobon, *Dark matter implications of the WMAP-Planck Haze*, arXiv:1509.05135.

[21] http://www.marcocirelli.net/PPPC4DMID.html.

[22] M. Cirelli, G. Corcella, A. Hektor, G. Hutsi, M. Kadastik, et al., *PPPC 4 DM ID: A Poor Particle Physicist Cookbook for Dark Matter Indirect Detection*, *JCAP* **1103** (2011) 051, [arXiv:1012.4515].

[23] P. Ciafaloni, D. Comelli, A. Riotto, F. Sala, A. Strumia, et al., *Weak Corrections are Relevant for Dark Matter Indirect Detection*, *JCAP* **1103** (2011) 019, [arXiv:1009.0224].

[24] A. Strong and I. Moskalenko, *Propagation of cosmic-ray nucleons in the galaxy*, *Astrophys.J.* **509** (1998) 212–228, [astro-ph/9807150].

[25] M. Longair, *High energy astrophysics*. Cambridge University Press, 2011.

[26] http://galprop.stanford.edu/.

[27] J. F. Navarro, C. S. Frenk, and S. D. M. White, *A Universal Density Profile from Hierarchical Clustering*, *Astrophys. J.* **490** (Dec., 1997) 493.

[28] A. W. Graham et al., *Empirical Models for Dark Matter Halos. II. Inner Profile Slopes, Dynamical Profiles, and ρ/σ^3*, *Astron. J.* **132** (Dec., 2006) 2701–2710.

[29] V. Springel et al., *The Aquarius Project: the subhaloes of galactic haloes*, *Mon. Not. R. Astron. Soc.* **391** (Dec., 2008) 1685–1711.

[30] E. Corbelli et al., *A wide-field H I mosaic of Messier 31. II. The disk warp, rotation, and the dark matter halo*, *Astron. Astrophys.* **511** (Feb., 2010) A89.

[31] J. J. Geehan, M. A. Fardal, A. Babul, and P. Guhathakurta, *Investigating the Andromeda stream - I. Simple analytic bulge-disc-halo model for M31*, *Mon. Not. R. Astron. Soc.* **366** (Mar., 2006) 996–1011.

[32] M. Kamionkowski, S. M. Koushiappas, and M. Kuhlen, *Galactic Substructure and Dark Matter Annihilation in the Milky Way Halo*, *Phys.Rev.* **D81** (2010) 043532, [arXiv:1001.3144].

[33] E. Borriello et al., *Searching for Dark Matter in Messier 33*, *Astrophys. J., Lett.* **709** (Jan., 2010) L32–L38.

[34] A. Fletcher, E. M. Berkhuijsen, R. Beck, and A. Shukurov, *The magnetic field of M 31 from multi-wavelength radio polarization observations*, *Astron. Astrophys.* **414** (Jan., 2004) 53–67.

[35] R. M. Crocker, D. Jones, F. Melia, J. Ott, and R. J. Protheroe, *A lower limit of 50 microgauss for the magnetic field near the Galactic Centre*, *Nature* **468** (2010) 65, [arXiv:1001.1275].

[36] R. Beck, *Magnetic Fields in Galaxies*, *Space Sci. Rev.* **166** (May, 2012) 215–230.

[37] P. Hoernes, R. Beck, and E. M. Berkhuijsen, *Properties of synchrotron emission and magnetic fields in the central region of M31*, in *The Central Regions of the Galaxy and Galaxies*, vol. 184 of *IAU Symposium*, p. 351, 1998.

[38] M. Haverkorn and V. Heesen, *Magnetic fields in galactic haloes*, *Space Sci.Rev.* **166** (2012) 133–144, [arXiv:1102.3701].

[39] R. P. van der Marel and M.-R. L. Cioni, *Magellanic Cloud Structure from Near-Infrared Surveys. I. The Viewing Angles of the Large Magellanic Cloud*, *Astron. J.* **122** (Oct., 2001) 1807–1826.

[40] A. S. Cohen et al., *The VLA Low-Frequency Sky Survey*, *Astron. J.* **134** (Sept., 2007) 1245–1262.

[41] R. B. Rengelink et al., *The Westerbork Northern Sky Survey (WENSS), I. A 570 square degree Mini-Survey around the North Ecliptic Pole*, *Astron. Astrophys. Suppl. Ser.* **124** (Aug., 1997) 259–280.

[42] J. J. Condon et al., *The NRAO VLA Sky Survey*, *Astron. J.* **115** (May, 1998) 1693–1716.

[43] J. J. Condon et al., *A 4.85 GHz sky survey. 3: Epoch 1986 and combined (1986+1987) maps covering 0 deg less than delta less than +75 deg*, *Astron. J.* **107** (May, 1994) 1829–1833.

[44] F. Bonnarel et al., *The ALADIN interactive sky atlas. A reference tool for identification of astronomical sources*, *Astron. Astrophys. Suppl. Ser.* **143** (Apr., 2000) 33–40.

[45] R. Trotta, *Bayes in the sky: Bayesian inference and model selection in cosmology*, *Contemporary Physics* **49** (Mar., 2008) 71–104.

[46] A. Tamm et al., *Stellar mass map and dark matter distribution in M 31*, *Astron. Astrophys.* **546** (Oct., 2012) A4.

[47] A. Geringer-Sameth and S. M. Koushiappas, *Exclusion of Canonical Weakly Interacting Massive Particles by Joint Analysis of Milky Way Dwarf Galaxies with Data from the Fermi Gamma-Ray Space Telescope*, *Phys. Rev. Lett.* **107** (Dec., 2011) 241303.

[48] D. Hooper and L. Goodenough, *Dark Matter Annihilation in The Galactic Center As Seen by the Fermi Gamma Ray Space Telescope*, *Phys.Lett.* **B697** (2011) 412–428, [arXiv:1010.2752].

[49] K. N. Abazajian and M. Kaplinghat, *Detection of a Gamma-Ray Source in the Galactic Center Consistent with Extended Emission from Dark Matter Annihilation and Concentrated Astrophysical Emission*, *Phys.Rev.* **D86** (2012) 083511, [arXiv:1207.6047].

[50] T. Daylan, D. P. Finkbeiner, D. Hooper, T. Linden, S. K. N. Portillo, et al., *The Characterization of the Gamma-Ray Signal from the Central Milky Way: A Compelling Case for Annihilating Dark Matter*, arXiv:1402.6703.

[51] F. Calore, I. Cholis, and C. Weniger, *Background model systematics for the Fermi GeV excess*, *JCAP* **1503** (2015) 038, [arXiv:1409.0042].

[52] D. Hooper, I. Cholis, T. Linden, J. Siegal-Gaskins, and T. Slatyer, *Pulsars Cannot Account for the Inner Galaxy's GeV Excess*, *Phys.Rev.* **D88** (2013) 083009, [arXiv:1305.0830].

[53] I. Cholis, D. Hooper, and T. Linden, *Challenges in Explaining the Galactic Center Gamma-Ray Excess with Millisecond Pulsars*, arXiv:1407.5625.

[54] Q. Yuan and B. Zhang, *Millisecond pulsar interpretation of the Galactic center gamma-ray excess*, *JHEAp* **3-4** (2014) 1–8, [arXiv:1404.2318].

[55] J. Petrovic, P. D. Serpico, and G. Zaharijas, *Millisecond pulsars and the Galactic Center gamma-ray excess: the importance of luminosity function and secondary emission*, arXiv:1411.2980.

[56] T. D. Brandt and B. Kocsis, *Disrupted Globular Clusters Can Explain the Galactic Center Gamma Ray Excess*, *Astrophys. J.* **812** (2015), no. 1 15, [arXiv:1507.05616].

[57] J. Petrovic, P. D. Serpico, and G. Zaharijas, *Galactic Center gamma-ray "excess" from an active past of the Galactic Centre?*, *JCAP* **1410** (2014), no. 10 052, [arXiv:1405.7928].

[58] E. Carlson and S. Profumo, *Cosmic Ray Protons in the Inner Galaxy and the Galactic Center Gamma-Ray Excess*, *Phys.Rev.* **D90** (2014), no. 2 023015, [arXiv:1405.7685].

[59] I. Cholis, C. Evoli, F. Calore, T. Linden, C. Weniger, and D. Hooper, *The Galactic Center GeV Excess from a Series of Leptonic Cosmic-Ray Outbursts*, arXiv:1506.05119.

[60] R. Bartels, S. Krishnamurthy, and C. Weniger, *Strong support for the millisecond pulsar origin of the Galactic center GeV excess*, arXiv:1506.05104.

[61] S. K. Lee, M. Lisanti, B. R. Safdi, T. R. Slatyer, and W. Xue, *Evidence for Unresolved Gamma-Ray Point Sources in the Inner Galaxy*, *ArXiv e-prints* (June, 2015) [arXiv:1506.05124].

[62] D. Hooper, D. P. Finkbeiner, and G. Dobler, *Possible evidence for dark matter annihilations from the excess microwave emission around the center of the Galaxy seen by the Wilkinson Microwave Anisotropy Probe*, *Phys.Rev.* **D76** (2007) 083012, [arXiv:0705.3655].

[63] M. Su, T. R. Slatyer, and D. P. Finkbeiner, *Giant Gamma-ray Bubbles from Fermi-LAT: AGN Activity or Bipolar Galactic Wind?*, *Astrophys.J.* **724** (2010) 1044–1082, [arXiv:1005.5480].

[64] **Fermi-LAT** Collaboration, M. Ackermann et al., *The Spectrum and Morphology of the Fermi Bubbles*, *Astrophys.J.* **793** (2014), no. 1 64, [arXiv:1407.7905].

[65] Y. Sofue, *Bipolar-hyper-shell galactic center statrburst model: further evidence from rosat data and new radio and x-ray simulations*, *Astrophys.J.* **540** (2000) 224, [astro-ph/9912528].

[66] J. Bland-Hawthorn and M. Cohen, *The Large scale bipolar wind in the Galactic Center*, *Astrophys.J.* **582** (2003) 246–256, [astro-ph/0208553].

[67] E. Carretti, R. Crocker, L. Staveley-Smith, M. Haverkorn, C. Purcell, et al., *Giant Magnetized Outflows from the Centre of the Milky Way*, *Nature* **493** (2013) 66, [arXiv:1301.0512].

[68] R. M. Crocker, G. V. Bicknell, A. M. Taylor, and E. Carretti, *A Unified Model of the Fermi Bubbles, Microwave Haze, and Polarized Radio Lobes: Reverse Shocks in the Galactic Center's Giant Outflows*, arXiv:1412.7510.

[69] GALPROP explanatory supplement at http://galprop.stanford.edu/code.php?option=manual.

[70] GNU Scientific Library: http://www.gnu.org/software/gsl/.

[71] F. Iocco, M. Pato, G. Bertone, and P. Jetzer, *Dark Matter distribution in the Milky Way: microlensing and dynamical constraints*, *JCAP* **1111** (2011) 029, [arXiv:1107.5810].

[72] F. Nesti and P. Salucci, *The Dark Matter halo of the Milky Way, AD 2013*, *JCAP* **1307** (2013) 016, [arXiv:1304.5127].

[73] F. Calore, N. Bozorgnia, M. Lovell, G. Bertone, M. Schaller, C. S. Frenk, R. A. Crain, J. Schaye, T. Theuns, and J. W. Trayford, *Simulated Milky Way analogues: implications for dark matter indirect searches*, arXiv:1509.02164.

[74] M. Pato, F. Iocco, and G. Bertone, *Dynamical constraints on the dark matter distribution in the Milky Way*, arXiv:1504.06324.

[75] F. Iocco, M. Pato, and G. Bertone, *Evidence for dark matter in the inner Milky Way*, *Nature Phys.* **11** (2015) 245248, [arXiv:1502.03821].

[76] F. Calore, I. Cholis, C. McCabe, and C. Weniger, *A Tale of Tails: Dark Matter Interpretations of the Fermi GeV Excess in Light of Background Model Systematics*, *Phys.Rev.* **D91** (2015), no. 6 063003, [arXiv:1411.4647].

[77] G. Dobler, I. Cholis, and N. Weiner, *The Fermi Gamma-Ray Haze from Dark Matter Annihilations and Anisotropic Diffusion*, *Astrophys.J.* **741** (2011) 25, [arXiv:1102.5095].

[78] D. Malyshev, I. Cholis, and J. D. Gelfand, *Fermi Gamma-ray Haze via Dark Matter and Millisecond Pulsars*, *Astrophys.J.* **722** (2010) 1939–1945, [arXiv:1002.0587].

[79] Y. Mambrini, M. H. Tytgat, G. Zaharijas, and B. Zaldivar, *Complementarity of Galactic radio and collider data in constraining WIMP dark matter models*, *JCAP* **1211** (2012) 038, [arXiv:1206.2352].

[80] R. M. Crocker, D. I. Jones, F. Aharonian, C. J. Law, F. Melia, et al., *Gamma-Rays and the Far-Infrared-Radio Continuum Correlation Reveal a Powerful Galactic Center Wind*, *Mon.Not.Roy.Astron.Soc.* **411** (2011) L11–L15, [arXiv:1009.4340].

[81] R. Stepanov, T. G. Arshakian, R. Beck, P. Frick, and M. Krause, *Magnetic field structures of galaxies derived from analysis of Faraday rotation measures, and perspectives for the SKA*, *Astronomy and Astrophysics* **480** (2008) 45–59, [arXiv:0711.1267].

[82] M. Haverkorn, *Magnetic Fields in the Milky Way*, arXiv:1406.0283.

[83] J. Lavalle, D. Maurin, and A. Putze, *Direct constraints on diffusion models from cosmic-ray positron data: Excluding the MIN model for dark matter searches*, arXiv:1407.2540.

[84] R. Trotta, G. Johannesson, I. Moskalenko, T. Porter, R. R. de Austri, et al., *Constraints on cosmic-ray propagation models from a global Bayesian analysis*, *Astrophys.J.* **729** (2011) 106, [arXiv:1011.0037].

[85] K. M. Górski, E. Hivon, A. J. Banday, B. D. Wandelt, F. K. Hansen, M. Reinecke, and M. Bartelmann, *HEALPix: A Framework for High-Resolution Discretization and Fast Analysis of Data Distributed on the Sphere*, *Astrophys. J.* **622** (Apr., 2005) 759–771, [astro-ph/0409513].

[86] http://lambda.gsfc.nasa.gov/product/map/dr5/masks_info.cfm.

[87] http://irsa.ipac.caltech.edu/data/Planck/release_2/ancillary-data/.

[88] **Planck** Collaboration, P. Ade et al., *Planck 2013 results. XII. Diffuse component separation*, *Astron.Astrophys.* **571** (2014) A12, [arXiv:1303.5072].

[89] J. Peacock, *Cosmological physics*. Cambridge University Press, 1999.

[90] **Planck** Collaboration, P. Ade et al., *Planck 2013 results. XVI. Cosmological parameters*, *Astron.Astrophys.* **571** (2014) A16, [arXiv:1303.5076].

[91] http://irsa.ipac.caltech.edu/data/Planck/release_1/.

[92] T. Lacroix, C. Boehm, and J. Silk, *Fitting the Fermi-LAT GeV excess: On the importance of including the propagation of electrons from dark matter*, *Phys.Rev.* **D90** (2014) 043508, [arXiv:1403.1987].

[93] G. Dobler and D. P. Finkbeiner, *Extended Anomalous Foreground Emission in the WMAP 3-Year Data*, *Astrophys. J.* **680** (2008) 1222–1234, [arXiv:0712.1038].

[94] D. Pietrobon, K. M. Gorski, J. Bartlett, A. J. Banday, G. Dobler, et al., *Analysis of WMAP 7-year Temperature Data: Astrophysics of the Galactic Haze*, *Astrophys.J.* **755** (2012) 69, [arXiv:1110.5418].

[95] G. Dobler, *Identifying the Radio Bubble Nature of the Microwave Haze*, *Astrophys. J.* **760** (2012) L8, [arXiv:1208.2690].

[96] http://lambda.gsfc.nasa.gov/product/.

[97] Planck Collaboration, P. A. R. Ade, N. Aghanim, M. I. R. Alves, C. Armitage-Caplan, M. Arnaud, M. Ashdown, F. Atrio-Barandela, J. Aumont, C. Baccigalupi, and et al., *Planck 2013 results. XIII. Galactic CO emission*, *Astronomy and Astrophysics* **571** (Nov., 2014) A13, [arXiv:1303.5073].

[98] D. J. Schlegel, D. P. Finkbeiner, and M. Davis, *Maps of Dust Infrared Emission for Use in Estimation of Reddening and Cosmic Microwave Background Radiation Foregrounds*, *Astrophys.J.* **500** (1998) 525–553, [astro-ph/9710327].

[99] D. P. Finkbeiner, M. Davis, and D. J. Schlegel, *Extrapolation of Galactic Dust Emission at 100 Microns to Cosmic Microwave Background Radiation Frequencies Using FIRAS*, *Astrophys.J.* **524** (1999) 867–886, [astro-ph/9905128].

[100] D. P. Finkbeiner, *A Full-Sky Hα Template for Microwave Foreground Prediction*, *Astrophys.J.Suppl.Ser.* **146** (2003) 407–415, [astro-ph/0301558].

[101] C. G. T. Haslam, C. J. Salter, H. Stoffel, and W. E. Wilson, *A 408 MHz all-sky continuum survey. II - The atlas of contour maps*, *Astron.Astrophys.Suppl.Ser.* **47** (1982) 1.

[102] **Planck** Collaboration, R. Adam et al., *Planck 2015 results. X. Diffuse component separation: Foreground maps*, arXiv:1502.01588.

[103] **Fermi-LAT** Collaboration, M. Ackermann et al., *Searching for Dark Matter Annihilation from Milky Way Dwarf Spheroidal Galaxies with Six Years of Fermi-LAT Data*, arXiv:1503.02641.

[104] http://scidraw.nd.edu/levelscheme/.

[105] E. Casuso and J. E. Beckman, *Explaining the Galactic Interstellar Dust Grain Size Distribution Function*, *Astron. J.* **139** (Apr., 2010) 1406–1412.

[106] K. Ferrière, W. Gillard, and P. Jean, *Spatial distribution of interstellar gas in the innermost 3 kpc of our galaxy*, *Astron. Astrophys.* **467** (May, 2007) 611–627.

[107] G. Rybicki and A. Lightman, *Radiative processes in astrophysics*. WILEY-VCH Verlag GmbH, Weinheim, 2004.

A Absorption analysis for M31

Here we discuss all potentially relevant mechanisms of absorption of radio emission during its propagation from the M31 center to the observer. We focused only on a potential absorption inside M31 and did not consider possible absorption in MW, because the Andromeda galaxy lies far enough from the Galactic plane, and we do not expect any significant absorption in this direction on the sky. In general, inside the Andromeda there are two main agents of interstellar medium relevant for our purposes: a dust and an ionized gas. Among them a dust can be excluded as an absorber rather easily: typically a dust grain size does not exceed 10^{-4} cm (see e.g. [105]). And the wavelengths of radio emission involved are $10 - 1000$ cm, which is many orders of magnitude larger than grain sizes. In such case, when a wavelength is much greater than an obstacle size, it is well known that radiation does not interact with obstacles. Thus, we can conclude that a dust does not affect radiation in the considered frequency range.

A situation with the absorption by the interstellar plasma is more tricky. Here we can distinguish several possible ways of absorption. First of all, let's check the Langmuir frequency of plasma involved. As well known, a radiation can not propagate through plasma, if its frequency is less than the Langmuir frequency of the propagation medium. The Langmuir frequency is defined as

$$\nu_{pl} = \frac{\omega_{pl}}{2\pi} = \sqrt{\frac{e^2 n_{pl}}{\pi m_e}}, \tag{A.1}$$

where n_{pl} is the concentration of plasma electrons, which needs to be estimated. For this purpose we used the results of [106], where the gas density distribution was obtained for the central region of MW. Taking into account that MW and M31 are very similar galaxies, we can extrapolate results for MW on M31 staying at necessary level of accuracy. From [106] we can easily see, that the plasma concentration in a galactic center can not exceed $n_{pl} \lesssim 10$ cm^{-3} in the worst case, which yields $\nu_{pl} \lesssim 30$ kHz. Thus, the Langmuir frequency is much smaller than the observational frequencies of MHz-GHz, which means that the interstellar plasma is transparent with respect to this absorption mechanism.

Another potentially relevant mechanism is a synchrotron self-absorption. Synchrotron emission, generated by relativistic leptons from DM annihilation, can be absorbed by neighbour emitting leptons. In order to estimate the level of this absorption quantitatively we computed the corresponding optical depth along our line of sight, which goes through the M31 center:

$$\tau_{ss} = \int\limits_{l.o.s.} \alpha_{ss} dl, \tag{A.2}$$

where α_{ss} is the synchrotron self-absorption coefficient. We used the derived expression for α_{ss} from [107] (formula 6.50 there):

$$\alpha_{ss} = -\frac{c^2}{8\pi\nu^2} \int\limits_{m_e c^2}^{m_\chi c^2} dE P_e(E, \nu, \vec{r}) \cdot E^2 \frac{\partial}{\partial E} \left(E^{-2} \cdot 2n(E, \vec{r}) \right), \tag{A.3}$$

where $P_e(E, \nu, \vec{r})$ is the synchrotron power of one lepton defined by eq. 2.3–2.4, $n(E, \vec{r})$ is the stationary energy spectrum of emitting leptons of one kind defined by eq. 3.1. Then we substituted all relevant values of the parameters involved. Particularly, for WIMP mass and

frequency of observations we used as an example $m_\chi = 100$ GeV and $\nu = 74$ MHz. Such combination of all parameters yields $\tau_{ss} \sim 10^{-3}$, which means that we can neglect by the synchrotron self-absorption completely and reliably. And this conclusion is valid for all other frequencies used in our work, because α_{ss} decreases with frequency, and 74 MHz is the lowest frequency of observations. In general, this conclusion agrees with the results of [12], where the authors solved similar DM annihilation problem with application to MW. And they also showed an irrelevance of synchrotron self-absorption on all frequencies.

And the last potential absorption mechanism, which has to be checked, is a free-free absorption by plasma. Here we also estimated the corresponding optical depth:

$$\tau_{ff} = \int\limits_{l.o.s.} \alpha_{ff} dl, \tag{A.4}$$

where the absorption coefficient α_{ff} was also taken from [107] (formula 5.18b there):

$$\alpha_{ff} = 3.7 \cdot 10^8 T^{-1/2} Z^2 n_{pl}^2 \nu^{-3} \left(1 - \exp\left(-\frac{h\nu}{kT}\right)\right) g_{ff}, \tag{A.5}$$

where n_{pl} and T are plasma concentration and temperature respectively. As for the spatial distribution $n_{pl}(\vec{r})$, it does not appear to be obtained in the literature for M31. That's why we decided to use such distribution for MW again as an approximation. Taking all relevant information from [106] and assuming $g_{ff} \approx 1$ and $Z = 1$ (hydrogen plasma) we estimated $\tau_{ff} \lesssim 0.01$ in the worst case scenario. Thus, we can see that the free-free absorption is not relevant for our work as well in the first approximation.

Summarizing, in this section we have conducted the detailed analysis of all potentially relevant absorption mechanisms for the radio emission generated by DM annihilation. None of these mechanisms achieves significant level. This conclusion is in agreement with similar studies [12], [6] for the MW. Thus we can ignore any absorption in our analysis without significant loss of accuracy.

B Spatial diffusion of annihilation products in M31

Here we study the role of the spatial diffusion of annihilation products in our problem. In order to understand the importance of the spatial diffusion for final results, we should compare the characteristic distance, which annihilation products travel while they are emitting the relevant radiation, with the characteristic size of the emitting region. According to e.g. [6], the diffusion path traveled by leptons can be calculated as $l_D \approx \sqrt{D(E)\tau_{loss}(E)}$, where $D(E)$ is the diffusion coefficient for leptons participating in eq. 2.5; $\tau_{loss}(E)$ is the cooling time of leptons, during which they are emitting the expected radiation and losing their energy until escaping the relevant energy domain. We took the diffusion coefficient $D(E)$ from [6], where it is provided for the MW, and expected to work roughly for the Andromeda galaxy as well:

$$D(E) = D_0 \left(\frac{E}{E_0}\right)^\delta, \tag{B.1}$$

with $D_0 = 10^{28}$ cm^2/s, $E_0 = 3$ GeV and a Kolmogorov spectrum $\delta = 1/3$. The cooling time for leptons can be estimated as

$$\tau_{loss}(E) \sim \frac{E}{\dot{E}} = \frac{E}{b(E, \vec{r})}, \tag{B.2}$$

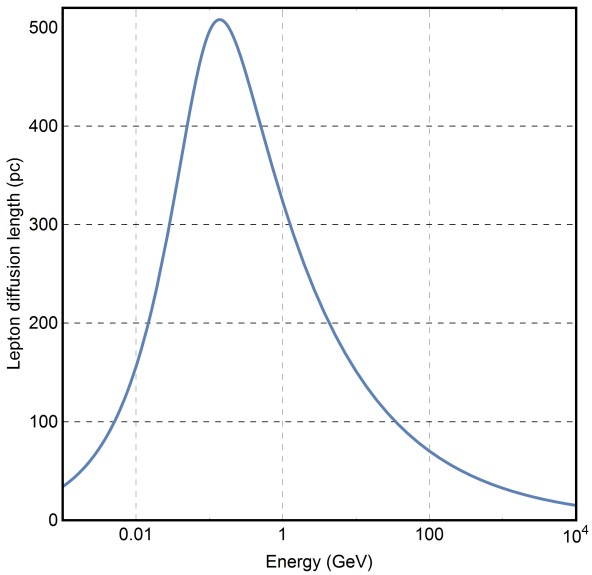


Figure 22. The dependence of the lepton diffusion length l_D on the energy E. The MF used is $B = 50$ μG, concentration is $n_{pl} = 0.1$ cm^{-3}.

where $b(E, \vec{r}) = b_{ICS} + b_{sync} + b_{brem} + b_{Col}$ (see eqs. 2.9–2.12). After all necessary substitutions we obtained l_D dependence on the lepton energy E, which is shown on fig. 22. For the MF B and the concentration n_{pl} we used the expected values for the M31 center ~ 50 μG and ~ 0.1 cm^{-3} respectively. These parameter values were justified in the section 3.2. As we can see in fig. 22, the lepton diffusion path over the relevant range of energies does not exceed $\sim$ 500 pc. Our emitting region, which we capture by our ROI with angular radius $\alpha \approx 5'$, would have the form of the cylinder with the radius $\rho_{max} \approx \alpha d \approx 1100$ pc. Thus, the smallest size of the emitting region is about 2 times larger than the diffusion length of leptons in the M31 center. It means, in turn, that the leptons do not have enough time to migrate significantly and escape from the emitting volume, before they cool down and discontinue radiation. Also taking into account the fact that a majority of the total radiation flux due to DM annihilation is formed in the very central region, we can conclude that inclusion of the spatial diffusion in our calculations should not affect our results significantly. And neglecting by the diffusion is an acceptable approximation in our computation procedure. Such conclusion is in general agreement with the work [6], where the similar procedure of constraints derivation was conducted for the MW. However, since the spatial scale of the emitting volume and the lepton diffusion path do not differ drastically, we allow an opportunity to include the diffusion in our calculations in a future work in order to improve accuracy of our results.